Steam reforming of methane over alumina supported nickel catalysts: Influence of calcination temperature, gold doping and sulfur addition

Elizabeth L. Norris

Doctor of Philosophy

June 2013

Keele University

Abstract

Alumina supported nickel and gold-doped nickel catalysts have been investigated for their use as hydrocarbon steam reforming catalysts. The influence of calcination temperature during preparation has been investigated using a variety of techniques including X-ray powder diffraction (XRD), X-ray photoelectron spectroscopy (XPS), BET surface area analysis, scanning electron microscopy (SEM) and temperature-programmed reduction (TPR). It has been shown that the nickel phases present and their subsequent reducibility are strongly dependent upon the calcination temperature during preparation. As the calcination temperature is increased nickel aluminate ($NiAl_2O_4$) is formed and nickel oxide–support interactions increase. The addition of gold to the catalyst increases nickel oxide–support interactions, lowering the sample reducibility and increasing formation of $NiAl_2O_4$ at lower calcination temperatures.

The calcination temperature significantly influences the steam methane reforming characteristics under both stoichiometric and methane-rich reaction conditions and the presence of unreduced $NiAl_2O_4$ significantly alters catalytic activity. Under the reaction conditions employed, the presence of gold provides no long-term benefit towards catalyst performance, resulting in a reduced reforming activity, especially at lower reaction temperatures, and in certain cases an increase in carbon laydown. Sulfur addition to the reaction mixture results in catalyst poisoning and in some cases complete deactivation, particularly at low reaction temperatures. However, sulfur addition does significantly increase resistance to carbon deposition. The addition of sulfur to the reaction mixtures and gold-doping of catalysts provides an increase in carbon resistance, whilst significantly reducing the rate of sulfur poisoning and increasing catalyst lifetime.

This research discusses the influence of calcination temperature on steam methane reforming activity, catalyst resistance towards carbon formation and sulfur tolerance under variable reforming conditions over alumina supported nickel and gold-doped alumina supported nickel catalysts.

‘Research is what I'm doing when I don't know what I'm doing’

Wemher von Braun

‘In my world everyone is a pony, and they all eat rainbows, and poop butterflies’

Dr Seuss

Acknowledgements

This research and thesis would not have been possible without the guidance and help of several individuals, who have in one way or another contributed and provided valuable support in the completion and preparation of this study.

First and foremost, my utmost thanks to my PhD supervisor Prof. Mark Ormerod for the years of guidance and invaluable knowledge. You have provided me with unwavering support and assistance through the years and ensured that I have remained focused on achieving all my research aims. Thank you for giving me the opportunity of a lifetime!

For your door always being open, Dr Richard Darton, you have ensured that the direction of this project remained focused. You always reminded me that research is about trying ideas out and seeing what happens! You guidance has been vital, without your knowledge and expertise areas of this research would not have progressed and developed into major areas of work.

The most enthusiastic post-doc I have had the pleasure of knowing, Dr John Staniforth, thank you for the many hours of assistance throughout my time at Keele.

I would like to thank the Surface Chemistry and Heterogeneous Catalysis Group at the University of Glasgow, specifically Andy McFarlane and Dr David Lennon and Dr Stewart Parker at the Rutherford Appleton Laboratories for their continuing support and collaboration. The research carried out by the group is truly inspiring and I am honoured to have been a part of it.

Thank you to everyone at Keele University who has helped me in some way with my research, amongst many, Dr Frank Rutten for your assistance with the XPS, Karen Walker for your time and

help with the SEM and Dave Evans for your overall support with the analytical machines and lab equipment.

Thank you to the research group led by Prof. Ormerod at Keele University and the members of the Birchall Centre office, specifically Christian Laycock and Lina Meghani, for always making it a great place to work. Also, a little cheers to the KPA for providing the perfect getaway after extremely long days!

A special thank you to Dave Nixon, you have never doubted my ability to complete this research. You have been by my side every step of the way. It has been the most amazing, challenging and life changing experience and I am so glad we have experienced it all together.

Last but not the least, my family - Mum, Dad, Jim and Casper - for always being there for me and believing in me, thank you so much.

Table of Contents

List of Abbreviations

QMS	Quadrupole mass spectrometer
TPR	Temperature-programmed reduction
TPO	Temperature-programmed oxidation
XRD	X-ray powder diffraction
XPS	X-ray photoelectron spectroscopy
BET	Brunauer-Emmett-Teller surface area analysis
SEM	Scanning electron microscopy
TEM	Transmission electron microscopy
UV	Ultraviolet
INS	Inelastic neutron scattering
SPARG	Sulfur passivated reforming
AFC	Alkaline fuel cell
PAFC	Phosphoric acid fuel cell
PEM	Polymer electrolyte membrane fuel cell
MCFC	Molten carbonate fuel cell

SOFC	Solid oxide fuel cell
YSZ	Yittria stabalised zirconia
GHSV	Gas hourly space velocity

Post-calcination catalyst sample abbreviations:

NiO/Al_2O_3 (600)	20 wt % Ni/Al_2O_3 catalyst calcined at 600 °C
NiO/Al_2O_3 (700)	20 wt % Ni/Al_2O_3 catalyst calcined at 700 °C
NiO/Al_2O_3 (800)	20 wt % Ni/Al_2O_3 catalyst calcined at 800 °C
NiO/Al_2O_3 (900)	20 wt % Ni/Al_2O_3 catalyst calcined at 900 °C
NiO/Al_2O_3 (1000)	20 wt % Ni/Al_2O_3 catalyst calcined at 1000 °C
Au-NiO/Al_2O_3 (600)	5 mol % Au doped 20 wt % Ni/Al_2O_3 catalyst calcined at 600 °C
Au-NiO/Al_2O_3 (700)	5 mol % Au doped 20 wt % Ni/Al_2O_3 catalyst calcined at 700 °C
Au-NiO/Al_2O_3 (800)	5 mol % Au doped 20 wt % Ni/Al_2O_3 catalyst calcined at 800 °C
Au-NiO/Al_2O_3 (900)	5 mol % Au doped 20 wt % Ni/Al_2O_3 catalyst calcined at 900 °C
Au-NiO/Al_2O_3 (1000)	5 mol % Au doped 20 wt % Ni/Al_2O_3 catalyst calcined at 1000 °C

Post-reduction catalyst sample abbreviations:

Ni/Al_2O_3 (600)	20 wt % Ni/Al_2O_3 catalyst calcined at 600 °C and reduced in hydrogen

Ni/Al_2O_3 (700)	20 wt % Ni/Al_2O_3 catalyst calcined at 700 °C and reduced in hydrogen
Ni/Al_2O_3 (800)	20 wt % Ni/Al_2O_3 catalyst calcined at 800 °C and reduced in hydrogen
Ni/Al_2O_3 (900)	20 wt % Ni/Al_2O_3 catalyst calcined at 900 °C and reduced in hydrogen
Ni/Al_2O_3 (1000)	20 wt % Ni/Al_2O_3 catalyst calcined at 1000 °C and reduced in hydrogen
Au-Ni/Al_2O_3 (600)	5 mol % Au doped 20 wt % Ni/Al_2O_3 catalyst calcined at 600 °C and reduced in hydrogen
Au-Ni/Al_2O_3 (700)	5 mol % Au doped 20 wt % Ni/Al_2O_3 catalyst calcined at 700 °C and reduced in hydrogen
Au-Ni/Al_2O_3 (800)	5 mol % Au doped 20 wt % Ni/Al_2O_3 catalyst calcined at 800 °C and reduced in hydrogen
Au-Ni/Al_2O_3 (900)	5 mol % Au doped 20 wt % Ni/Al_2O_3 catalyst calcined at 900 °C and reduced in hydrogen
Au-Ni/Al_2O_3 (1000)	5 mol % Au doped 20 wt % Ni/Al_2O_3 catalyst calcined at 1000 °C and reduced in hydrogen

List of Figures

List of Tables

1 Introduction

The use of oil as a primary fuel source has dominated the global market for many years and its use as a fuel cannot be underestimated. In 2011, the world's primary energy consumption rose by 2.5 %, however, world proven oil reserves are significantly dwindling and only estimated to last for another 50 years at current extraction rates and costs [1]. The use of hydrogen as an alternative fuel is a rapidly developing market, since the need and desire for more economical and environmentally friendly energy sources increases. It is currently a valuable feedstock for many industries including petrochemical and chemical industries and its use within additional technologies such as fuel cells is a highly developing area.

Hydrogen is, in principle, abundantly available and possesses the highest energy content per unit of weight (120 kJ/g) compared to any other fuel [2]. Although hydrogen is highly abundant, it does not exist freely in its molecular form and is conventionally generated via a number of methods including thermal decomposition and reforming of hydrocarbons and electrolysis of water [3]. Steam reforming of methane (natural gas) currently accounts for up to 95 % of current hydrogen production in the U.S. [4]. However, the use of steam reforming in hydrogen production has been subject to extensive research and investigation due to the need for improved process efficiency, in particular lower steam concentrations, and constantly developing fuel requirements [5, 6]. Due to the loss of heat and production of unwanted by-products during the steam reforming process, lower efficiencies are obtained compared to other methods of hydrogen production, such as electrolysis [3].

Specific industrial and academic research is focused on the development and optimisation of the catalysts used during the reforming process, in order to increase the hydrogen yield, whilst

minimising CO production. Among the various hydrocarbon compounds used in the production of hydrogen, natural gas, which is predominantly methane, is the most common [7]. It is expected that the UK will need to import over 80 % of all gas requirements by 2020. Therefore, the use of additional resources within the UK would provide both economic and environmental benefits [8]. One such alternative fuel source is biogas. The use of waste biogas as an alternative source of methane has attracted significant interest in recent years [9-12].

Biogas is the volatile organic fraction of biomass, predominantly formed from sewage, animal waste and industrial effluents [13]. Biogas is a complex and variable mixture of methane, carbon dioxide and other gases, in which the concentration can vary with location and time [10], with the main constituents accounting for 55-70 vol % CH_4 and 27-44 vol % CO_2 [14]. The development of biogas as a viable fuel source and major methane source in the production of hydrogen could significantly improve both the environmental impact of steam reforming whilst utilising a valuable fuel source.

Research undertaken by the Ormerod group at Keele University has predominantly focused on the development of highly selective nickel based catalysts, for use within the hydrocarbon reforming industry [15, 16] and in solid oxide fuel cell technology [10, 17]. This has involved the development and use of catalysts with various supports and active metal phases. Specific research areas have focused on the development of highly selective catalysts for use within solid oxide fuel cells and the development of biogas both as a primary source of hydrogen and as a fuel for use within solid oxide fuel cells [10, 17-21].

This thesis is focused on the development of more carbon resistant and sulfur tolerant nickel based alumina supported catalysts for use during steam methane reforming. Specific attention has been devoted to the catalyst preparation and in particular the calcination temperature and influence of catalyst composition, calcination temperature and steam to methane ratio have on the catalyst

properties and steam reforming characteristics. This research aims to provide fundamental information relevant to the future development of catalysts for the steam reforming of biogas. The work includes detailed studies relating to the influence of calcination temperature on steam methane reforming activity, catalyst resistance towards carbon formation and sulfur tolerance under variable reforming conditions.

The catalysts developed within this study have also been used in a major collaboration project with the University of Glasgow and Rutherford Appleton Lab, aimed at gaining an increased understanding of the surface chemical reaction pathways, and steam and carbon dioxide reforming mechanisms over supported nickel catalysts, through the use of a wide range of characterisation techniques including inelastic neutron scattering spectroscopy (INS) [22-24].

The research presented within this thesis has been divided into sub-sections of research. These principal research areas include:

- The influence of calcination temperature on the structural properties of alumina supported nickel catalysts, including gold doped alumina supported nickel catalysts.
- The influence of calcination temperature on steam methane reforming characteristics of alumina supported nickel based and gold doped alumina supported nickel catalysts.
- The impact of steam concentration on the steam reforming reaction and carbon forming reaction over alumina supported nickel catalysts and gold doped alumina supported nickel catalysts.
- The effect of adding sulfur to methane steam mixtures on the steam reforming reaction and carbon forming reactions over alumina supported nickel catalysts and gold doped alumina supported nickel catalysts.

1.1 References

1. *BP Statistical Review of World Energy* June 2012.
2. *NIST Chemistry WebBook*. NIST Standard Reference Database Number 69 2012; Available from: http://webbook.nist.gov/chemistry/.
3. Holladay, J.D., J. Hu, D.L. King, and Y. Wang, *An overview of hydrogen production technologies.* Catalysis Today, 2009. **139**(4): p. 244-260.
4. *U.S. Department of Energy, Fuel Cell Technologies Program.* Energy Efficiency and Renewable Energy, November 2012.
5. Ming, Q., T. Healey, L. Allen, and P. Irving, *Steam reforming of hydrocarbon fuels.* Catalysis Today, 2002. **77**(51-64).
6. Rakass, S., H. Oudghiri-Hassani, P. Rowntree, and N. Abatzoglou, *Steam reforming of methane over unsupported nickel catalysts.* Journal of Power Sources, 2006. **158**(1): p. 485-496.
7. Wilhelm, D.J., D.R. Simbeck, A.D. Karp, and R.L. Dickenson, *Syngas production for gas-to-liquids applications: technologies, issues and outlook.* Fuel Processing Technology, 2001. **71**(1-3): p. 139-148.
8. *A study for British Energy undertaken by AEA Technology, The Feasibility, Costs and Markets for Hydrogen Production.* September 2009.
9. Ashrafi, M., T. ProÌˆll, C. Pfeifer, and H. Hofbauer, *Experimental Study of Model Biogas Catalytic Steam Reforming: 1. Thermodynamic Optimization.* Energy & Fuels, 2008. **22**(6): p. 4182-4189.
10. Staniforth, J. and R.M. Ormerod, *Implications for using biogas as a fuel source for solid oxide fuel cells: Internal dry reforming in a small tubular solid oxide fuel cell.* Catalysis Letters, 2002. **81**: p. 19-23.
11. Sato, T., T. Suzuki, M. Aketa, Y. Ishiyama, K. Mimura, and N. Itoh, *Steam reforming of biogas mixtures with a palladium membrane reactor system.* Chemical Engineering Science, 2010. **65**(1): p. 451-457.

12. Komiyama, M., T. Misonou, S. Takeuchi, K. Umetsu, and J. Takahashi, *Biogas as a reproducible energy source: Its steam reforming for electricity generation and for farm machine fuel.* International Congress Series, 2006. **1293**: p. 234-237.

13. Demirbas, A., *Biofuels sources, biofuel policy, biofuel economy and global biofuel projections.* Energy Conversion and Management, 2008. **49**(8): p. 2106-2116.

14. Kolbitsch, P., C. Pfeifer, and H. Hofbauer, *Catalytic steam reforming of model biogas.* Fuel, 2008. **87**(6): p. 701-706.

15. Diskin, A.M., *The oxidative chemistry of methane over supported nickel catalysts* in *PhD Thesis.* 2000, Keele University.

16. Diskin, A.M., R.H. Cunningham, and R.M. Ormerod, *The oxidative chemistry of methane over supported nickel catalysts.* Catalysis Today, 1998. **46**(2-3): p. 147-154.

17. Staniforth, J. and K. Kendall, *Biogas powering a small tubular solid oxide fuel cell.* Journal of Power Sources, 1998. **71**(1-2): p. 275-277.

18. Finnerty, C.M., N.J. Coe, R.H. Cunningham, and R.M. Ormerod, *Carbon formation on and deactivation of nickel-based/zirconia anodes in solid oxide fuel cells running on methane.* Catalysis Today, 1998. **46**(2-3): p. 137-145.

19. Finnerty, C.M. and R.M. Ormerod, *Internal reforming over nickel/zirconia anodes in SOFCS operating on methane: Influence of anode formulation, pre-treatment and operating conditions.* Journal of Power Sources 2000. **86**: p. 390-394.

20. Laycock, C.J., J.Z. Staniforth, and R.M. Ormerod, *Improving the Sulphur Tolerance of Nickel Catalysts for Running Solid Oxide Fuel Cells on Waste Biogas.* ECS Transactions, 2009. **16**(50): p. 177-188.

21. Laycock, C., J. Staniforth, and R.M. Ormerod, *Biogas as a fuel for solid oxide fuel cells and synthesis gas production: effects of ceria-doping and hydrogen sulfide on the performance of nickel-based anode materials.* Dalton Transactions, 2011. **40**: p. 5494.

22. McFarlane, A., I.P. Silverwood, E.L. Norris, R.M. Ormerod, C.D. Frost, S.F. Parker, and D. Lennon, *The application of inelastic neutron scattering and isotopic substitution*

experiments to examine the CO_2 reforming of methane over alumina-supported catalysts. Chemical Science, paper in preparation.

23. Silverwood, I.P., E.L. Norris, R.M. Ormerod, C.D. Frost, S.F. Parker, and D. Lennon, *The application of inelastic neutron scattering to investigate the steam reforming of methane over alumina-supported nickel catalysts.* Journal of Catalysis, paper in preparation.

24. Silverwood, I.P., N.G. Hamilton, A.R. McFarlane, J. Kapitan, L. Hecht, E.L. Norris, R. Mark Ormerod, C.D. Frost, S.F. Parker, and D. Lennon, *Application of inelastic neutron scattering to studies of CO_2 reforming of methane over alumina-supported nickel and gold-doped nickel catalysts.* Physical Chemistry Chemical Physics, 2012.

2 Applications and limitations of hydrocarbon reforming over supported nickel catalysts

Hydrocarbon reforming has been extensively studied by numerous researchers over many years. There are diverse range of applications associated with hydrocarbon reforming and many catalysts have been studied. This literature review highlights some of the main areas of interest from the point of view of this research. The processes and applications of hydrocarbon reforming have been detailed, focusing on steam reforming due to its significance in this research. Some of the limitations and challenges associated with the use of supported nickel catalysts for hydrocarbon reforming, have also been reviewed.

2.1 Synthesis gas

Synthesis gas (syngas), a key intermediate in the chemical industry, is predominantly a mixture of carbon monoxide and hydrogen. It is an intermediate in a number of syntheses of chemicals and fuels [1, 2] and an essential source of pure hydrogen and carbon monoxide.

Syngas is produced via a number of key technologies, of which hydrocarbon steam reforming is the most widespread commercial reforming technology. Reforming processes are described in detail in Section 2.3. In theory each method of syngas production results in a specific H_2/CO ratio, which is crucial to the subsequent use of syngas and the syntheses employed. The syngas ratio can be manipulated for particular applications by selecting a specific reforming process, altering the various reforming conditions (such as oxidant to carbon ratio, temperature, pressure and the catalyst itself) or through the addition of process steps, such as the water-gas shift reaction.

The major commercial uses of syngas as a chemical intermediate include the production of methanol and liquid hydrocarbons. Hydrogen produced from syngas and the application of the water-gas shift reaction, can also be used in the production of ammonia and other hydrogenation applications.

2.1.1 Methanol synthesis

Methanol is a primary feedstock for the chemical industry. In 2004, 32.1 million tonnes of methanol were manufactured as an intermediate for the production of a variety of chemicals [3]. Methanol synthesis from syngas requires a H_2/CO ratio of 2, and the presence of carbon dioxide. Carbon dioxide is added to maximise methanol production, utilising additional hydrogen present. The key reactions are summarised below in Reactions 2.1 – 2.3.

$$\mathbf{CO + 2H_2 \leftrightarrow CH_3OH} \qquad \textbf{(2.1)}$$

$$\mathbf{CO_2 + 3H_2 \leftrightarrow CH_3OH + H_2O} \qquad \textbf{(2.2)}$$

$$\mathbf{CO + H_2O \leftrightarrow CO_2 + H_2} \qquad \textbf{(2.3)}$$

Both Reaction 2.1 and Reaction 2.2 are exothermic and favoured by increased pressure and reduced temperature. Reaction 2.2 results from the sum of Reaction 2.1 and the water-gas shift reaction (Reaction 2.3). Each reaction is reversible and thus limited by thermodynamic equilibrium, depending on reaction conditions. Methanol is thermodynamically less stable than other products, such as methane and therefore the catalyst employed must be highly selective. Large-scale methanol plants require rapid heat removal or cooling through the introduction of fresh gas, due to the strong temperature dependence and increasing side reactions at higher temperatures. However, modern methanol synthesis plants have selectivities above 99 % and energy efficiencies over 70 % [3]. Catalysis is carried out in a recycle process, allowing carbon dioxide and unused syngas to be fed back into the reactor.

2.1.2 Ammonia synthesis

Synthesis of ammonia from hydrogen and nitrogen (the Haber process) is one of the most important processes in the chemical industry. Up to 100 million tonnes of ammonia are produced worldwide per year [4]. Ammonia synthesis requires a syngas H_2/CO ratio of 3, from which hydrogen is utilised in Reaction 2.4.

$$\mathbf{N_2 + 3H_2 \rightarrow 2NH_3} \qquad \textbf{(2.4)}$$

Equilibrium is favoured by low temperature and high pressure, although the rate of the reaction is slow below *ca.* 400 °C – 500 °C.

Ammonia synthesis occurs via three main stages, where * denotes adsorbed species:

1) Dissociative chemisorption of starting materials

$$\mathbf{N_2\,(g) \rightarrow {*N_2} \rightarrow 2{*N}} \qquad \textbf{(2.5)}$$

$$\mathbf{H_2\,(g) \rightarrow 2{*H}} \qquad \textbf{(2.6)}$$

2) Reaction of adsorbed atoms

$$\mathbf{{*N} + {*H} \rightarrow {*NH} \rightarrow {*NH} + {*H} \rightarrow {*NH_2} + {*H} \rightarrow {*NH_3}} \qquad \textbf{(2.7)}$$

3) Desorption of product

$$\mathbf{{*NH_3} \rightarrow NH_3\,(g)} \qquad \textbf{(2.8)}$$

The dissociative chemisorption of nitrogen (Reaction step 2.5) is the rate determining step in this process. Industrial catalysts consist of iron oxides (60 – 70 % iron), doped with mixed oxides of alumina, calcium, magnesium and potassium to increase selectivity and activity. As with methanol synthesis, either heat removal or cooling through the addition of gasses is required in order to maintain reaction conditions. Ammonia has a wide variety of applications including its use as a fertiliser, cleaning agent and in fermentation processes.

2.1.3 Fischer-Tropsch synthesis

The Fischer-Tropsch process involves the conversion of synthesis gas to liquid hydrocarbons, shown generally in Reactions 2.9 and 2.10.

$$\mathbf{2nCO + nH_2 \rightarrow [CH_2]_n + nCO_2} \qquad \textbf{(2.9)}$$

$$\mathbf{nCO + 2nH_2 \rightarrow [CH_2]_n + nH_2O} \qquad \textbf{(2.10)}$$

The hydrocarbon products can be a complex mixture of straight chain alkenes and alkanes, although oxygen containing compounds (oxygenates, such as alcohols and aldehydes) are also formed. Fischer-Tropsch reactions are highly exothermic and therefore, the removal of the heat of reaction is important to reduce the risk of overheating and catalyst deactivation.

Excess hydrogen can suppress chain growth and decrease selectivity to higher hydrocarbons. Therefore, an optimum H_2/CO ratio is required for the formation of ranges of hydrocarbon chain lengths. Chain growth during the Fischer-Tropsch process occurs in a similar manner to polymerisation. Currently there are two Fischer-Tropsch process operating modes, high and low temperature processeses [5]. The high temperature process (300 – 350 °C) involves the use of an iron based catalyst to produce gasoline and linear low molecular mass alkenes. The low temperature process (200 – 240 °C) involves the use of either iron or cobalt catalysts to produce high molecular mass linear waxes.

Fuels produced via Fischer-Tropsch synthesis are frequently classed as ‘green’ alternative fuels as they are much cleaner than those derived from crude oil.

2.1.4 Fuel cells

In addition to being used as a major chemical intermediate, syngas or the individual constituents of syngas can be used as a fuel for electricity generation in fuel cells. A fuel cell is a device that directly converts chemical energy of reactants into low voltage DC electricity [6]. Fuel cells were

invented over 160 years ago [7]. However, due to the costs associated with the development of technologies only recently have the high efficiencies and environmental advantages become of genuine technical interest [8].

The basic principle of a fuel cell consists of an anode, cathode and ion conducting, but electronically insulating, electrolyte [8]. At the anode a fuel is oxidised, whilst at the cathode oxygen reacts with migrating hydrogen ions or incoming electrons depending on the type of fuel cell. The electrodes are connected electrically by a conducting metallic external circuit.

Fuel cells [9] can be solid state and mechanically ideal (no moving parts), resulting in highly reliable, silent and very durable systems. Although they offer significant advantages due to high energy conversion, very low harmful pollutant emissions and significant reduction in greenhouse gas emissions, a major problem for hydrogen dependant fuel cells is fuel storage. Depending on the fuel cell employed [10, 11] a number of fuel compositions could be used other than pure hydrogen. This fuel flexibility and use of alternative hydrocarbon fuel supplies offers significant additional benefits.

There are a number of different types of fuel cell, which are characterised by the nature of their electrolyte [12, 13]. These are represented in Table 2.1.

Table 2.1: Overview of major fuel cell types and major characteristics

Fuel cell	Electrolyte	Fuel	Oxidant	Operating T / ºC	Main characteristics
Alkaline Fuel Cell (AFC)	Aqueous solution of sodium or potassium hydroxide	Hydrogen	Air or pure oxygen	70	poisoned by low levels of CO and CO_2
Phosphoric Acid Fuel Cell (PAFC)	Phosphoric acid	Hydrogen	Air or pure oxygen	Up to 200	Tolerant to CO_2
Polymer Electrolyte Membrane Fuel Cell (PEM)	Proton conducting polymer membrane	Hydrogen	Air or pure oxygen	80	Poisoned by low levels of CO
Molten Carbonate Fuel Cell (MCFC)	Molten potassium and lithium carbonate	Hydrogen and carbon monoxide (syngas)	Air, pure oxygen or carbon dioxide	650	Operate on syngas [a]
Solid Oxide Fuel Cell (SOFC)	Solid ceramic inorganic oxide	Hydrogen (syngas) or various hydrocarbon fuels	Air or pure oxygen	650 – 1000	Operate on syngas [a]

[a] produced by internal or external reforming of hydrocarbon fuels

Both MCFCs and SOFCs allow direct use of syngas with little or no need for fuel 'clean up' and removal of either carbon monoxide or carbon dioxide. Despite the major advantages of fuel cells, a number of challenges are still to be overcome, such as the high cost of fuel cells compared to conventional power systems, and for hydrogen fuel cells, the use of hydrogen as a fuel requiring on-site production via reforming. Although a number of major problems are still to be overcome, the use of fuel cells potentially provides major benefits for future energy generation.

2.2 Heterogeneous catalysis

Heterogeneous catalysis refers to conditions where the catalyst and the substrate are in different phases. Generally this refers to a system where the catalyst is a solid and the reactants are gases or liquids. In every solid/gas phase catalytic reaction, at least one of the reactants, at some point, must be adsorbed on the catalyst surface. There are two main mechanisms of heterogeneously catalysed gas-phase reactions, the Langmuir-Hinshelwood mechanism and the Eley-Rideal mechanism [14, 15]. The mechanistic reactions are discussed for the following reaction type:

$$\mathbf{A_{(g)} + B_{(g)} \rightarrow C_{(g)}} \qquad \mathbf{(2.11)}$$

The Langmuir-Hinshelwood mechanism assumes that both the reactants must be adsorbed on the catalyst surface before reacting. The reaction will occur at the active site, between neighbouring chemisorbed molecules. The final step involves product desorption from the catalyst into the gas phase. The following reaction sequence is assumed, where * denotes adsorbed species:

$$\mathbf{A_{(g)} \leftrightarrow A^* \text{ and } B_{(g)} \leftrightarrow B^*} \qquad \mathbf{(2.12)}$$

$$\mathbf{A^* + B^* \leftrightarrow C^*} \qquad \mathbf{(2.13)}$$

$$\mathbf{C^* \leftrightarrow C_{(g)}} \qquad \mathbf{(2.14)}$$

Each of the above steps can be rate determining depending on the specific reaction occurring and conditions employed.

On the other hand, the Eley-Rideal mechanism assumes that only one reactant is adsorbed on the catalyst surface. The reaction occurs at the active site with a reactant in the gas phase, producing the chemisorbed product. The final step involves the product desorbing from the catalyst into the gas phase. The following reaction sequence is assumed, where * denotes adsorbed species:

$$\mathbf{A_{(g)} \leftrightarrow A^*} \qquad \mathbf{(2.15)}$$

$$\mathbf{A^* + B_{(g)} \leftrightarrow C^*} \qquad \mathbf{(2.16)}$$

$$\mathbf{C^* \leftrightarrow C_{(g)}} \qquad \mathbf{(2.17)}$$

The degree of coverage of adsorbed reactants onto the catalyst surface (Reaction step 2.15) is the rate determining step during such reactions.

The above mechanisms rely on the reactant undergoing activated adsorption on the catalyst surface. Thus, the catalyst surface plays a crucial role in the reaction process and is a major factor in heterogeneous catalysis. Surfaces are rarely uniform, containing steps and kinks which can facilitate and enhance catalysis. This is shown schematically in Figure 2.1.

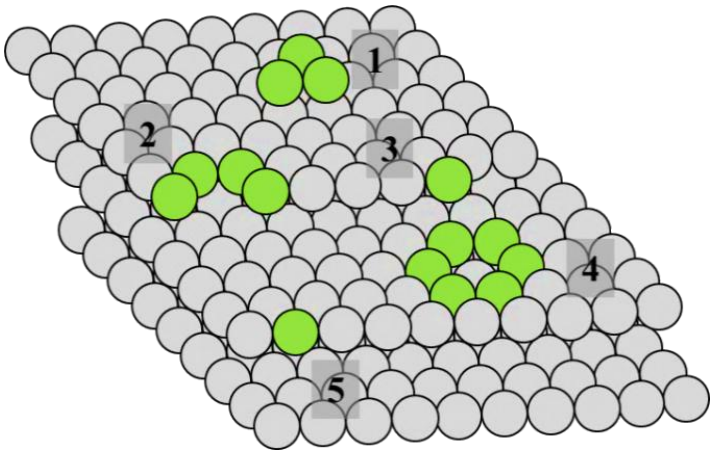

Figure 2.1: Schematic representation of catalytic surface 1, surface cluster; 2, step vacancy; 3, kink edge; 4, terrace vacancy and 5 step site, adapted from [15]

Atoms adsorbed at surface steps and kinks are not fully coordinated, and thus have higher interactions with neighbouring adsorbed species. Such ‘active sites’ can dramatically influence the

reaction rate and catalysis that occurs on the catalyst surface. Active sites may not always be the most energetically favourable sites for adsorption as the strength of adsorption of the molecules is crucial for optimum activity. Any reactants adsorbed on the catalyst surface should be able to be adsorbed but, following the reaction, product species should be able to effectively and easily desorb. The catalyst surface and active sites on the surface will affect the extent of adsorption and hence the reaction kinetics.

2.3 Hydrocarbon reforming

Natural gas and light hydrocarbons are major feedstocks for the production of syngas. Although steam reforming is the most established process, there are a number of reforming processes utilised for syngas production. Hydrocarbon reforming is a complex process involving not only the transfer and diffusion of reactants between the catalyst bulk and surface phase, but numerous reactions both in parallel and series.

Supported nickel catalysts are commonly used during methane reforming due to their high reforming activity and low cost [11]. Other group VIII metals, specifically platinum, palladium and ruthenium are also highly active towards methane reforming [16-18]. However, as well as being highly active, nickel poses the benefit of being significantly cheaper than the above mentioned precious metals, with reforming activity not significantly affected.

Supports which have been shown to be highly active and stable during methane reforming include Al_2O_3, SiO_2, TiO_2, ZrO_2 MgO and CeO_2 [16, 19-21]. The most common support used for steam reforming of methane is alumina, which provides high surface area and good porosity, allowing long contact time between reactants and the catalyst. Gamma alumina (γ-Al_2O_3) provides a high surface area, however, at temperatures above 1200 °C it can undergo a phase transformation forming α-Al_2O_3 [22]. Alpha alumina (α-Al_2O_3) has a lower surface area but higher thermal stability during reforming reactions. Therefore, α-Al_2O_3 is commonly selected for high temperature reforming investigations due to its enhanced stability at elevated temperatures. The catalyst support

must be chosen carefully and attention must be paid to the reforming conditions and specific use of each catalyst. Each support provides specific benefits towards each reforming process, providing increased activity, reactivity or selectivity.

In addition to the chemical composition of reforming catalysts, the physical properties and morphology can also dramatically influence the activity and stability of catalysts. The specific parameters employed during catalyst preparation can significantly influence the physical and morphological properties. The most common methods used for preparation of Ni/Al_2O_3 catalysts are wet impregnation and co-precipitation. Wet impregnation involves the dispersion of a metal salt in an aqueous solution onto the oxide support material, whereas, co-precipitation involves mixing solutions of metal salts together at a constant pH, allowing the desired product to precipitate out. Although both methods are effective at producing highly active catalysts, studies have shown they can have different influences on catalyst activity during reforming reactions [23, 24]. As well as conventional techniques, a number of other preparative methods are increasingly used to generate an active hydrocarbon reforming catalyst, such as the citric acid method [25], post-hydrolysis [26] and the more widely used sol-gel method [27, 28].

Both the catalyst formulation and preparation parameters significantly affect catalyst reactivity during methane reforming and are extremely important to the objective of achieving high activity and selectivity during reforming reactions.

2.3.1 Steam reforming

Steam reforming is the most important route to hydrogen and the one which is most commonly used in industry [29]. Currently 80 – 85 % of all global hydrogen production is derived via steam methane reforming of natural gas [30]. This process has been known and widely researched since the 1800's. Steam reacts with a fuel in the presence of a catalyst to produce hydrogen, carbon monoxide and carbon dioxide. Carbon monoxide can be removed via a further reaction known as the water-gas shift reaction (Reaction 2.20). Steam is normally added well in excess of the

stoichiometric requirement of Reaction 2.18, so the equilibrium of Reaction 2.20 is shifted to favour carbon dioxide production and increase hydrogen yield. Carbon dioxide is not only produced through the water-gas shift reaction but directly via steam methane reforming in the presence of excess steam (Reaction 2.19).

$$\mathbf{CH_4 + H_2O \leftrightarrow CO + 3H_2} \qquad \mathbf{\Delta H^{\Theta}_{298} = + 206\ kJ\ mol^{-1}} \qquad \mathbf{(2.18)}$$

$$\mathbf{CH_4 + 2H_2O \leftrightarrow CO_2 + 4H_2} \qquad \mathbf{\Delta H^{\Theta}_{298} = + 165\ kJ\ mol^{-1}} \qquad \mathbf{(2.19)}$$

$$\mathbf{CO + H_2O \leftrightarrow CO_2 + H_2} \qquad \mathbf{\Delta H^{\Theta}_{298} = - 41\ kJ\ mol^{-1}} \qquad \mathbf{(2.20)}$$

Due to its endothermic nature, steam methane reforming is favoured at higher reaction temperatures. Methane conversion is strongly dependent on both the temperature and the reactant gas composition. Although a high steam ratio is advantageous for carbon gasification and methane conversion, the thermal cost of excess steam makes this reaction mode less favourable. Thermodynamic calculations indicate that methane conversion increases with increasing reaction temperature for all ratios of methane to steam, although complete conversion is unlikely at high methane to steam ratios. Thermodynamic simulations and experimental studies suggest that a high steam to methane ratio (above 2) and a reaction temperature of *ca.* 700 - 750 °C provide ideal operating conditions [11, 31, 32]. Higher steam concentrations favour Reaction 2.19, increasing selectivity towards carbon dioxide formation from methane directly and inhibiting the reverse water gas shift reaction. At higher reaction temperatures, steam methane reforming is sensitive to pressure, significantly promoting the reverse reactions (Reaction 2.18 and 2.19). Thus, high pressure conditions are not favourable to methane conversion [33]. Low space velocities also increase methane conversion [31, 32] due to increased contact time between the catalyst and the reactant gases.

Although it is generally accepted that the rate of steam methane reforming is first order with respect to methane [33-35], there is less agreement regarding additional kinetic parameters. This is due to the influence of various catalyst modifications or properties, adaptable reaction parameters

and additional reactions and processes that can occur on the catalyst during reforming, such as carbon deposition and sintering. Reforming kinetics over supported metallic catalysts are significantly affected by pore diffusion influences, heat and mass transfer factors and adsorption characteristics.

Although specific kinetic factors are still a highly debated and greatly researched area [33, 35, 36], most models are still based on the mechanism proposed by Froment and Xu [37]. Froment and Xu based their surface mechanistic reactions on an early study undertaken by Temkin [38] who proposed the following mechanistic route:

$$CH_4 + * \leftrightarrow *CH_2 + H_2 \quad (2.21)$$

$$*CH_2 + H_2O \leftrightarrow *CHOH + H_2 \quad (2.22)$$

$$*CHOH \leftrightarrow *CO + H_2 \quad (2.23)$$

$$*CO \leftrightarrow CO + * \quad (2.24)$$

$$* + H_2O \leftrightarrow *O + H_2 \quad (2.25)$$

$$*O + CO \leftrightarrow CO_2 + * \quad (2.26)$$

Steps 2.25 and 2.26 are linked to the water-gas shift reaction (Reaction 2.20) and * denotes a free nickel surface adsorption site and * preceding a chemical moiety refers to corresponding chemisorbed species. Although this was a very simple mechanism, Tempkin was able to demonstrate the dependence of reaction rates on the partial pressures of reaction components.

Based on the above mechanistic routes, a detailed and more extensive mechanism was proposed by Froment and Xu [37], developed taking into account the following assumptions:

- Steam reacts with surface nickel atoms, producing gaseous hydrogen and adsorbed oxygen
- Methane is adsorbed on surface nickel atoms
- Adsorbed methane either reacts with adsorbed oxygen or dissociates forming adsorbed radical species

- The concentration of adsorbed radical species is considerably lower than the concentration of active nickel sites
- Adsorbed oxygen and carbon radicals react to form adsorbed intermediates
- Hydrogen formed directly desorbs into the gas phase

With the above assumptions taken into account and based on experimental and theoretical analysis, the following reaction mechanism was proposed relating to Reactions 2.18, 2.19 and 2.20:

$$H_2O + * \leftrightarrow *O + H_2 \quad (2.26)$$

$$CH_4 + * \leftrightarrow *CH_4 \quad (2.27)$$

$$*CH_4 + * \leftrightarrow *CH_3 + *H \quad (2.28)$$

$$*CH_3 + * \leftrightarrow *CH_2 + *H \quad (2.29)$$

$$*CH_2 + *O \leftrightarrow *CH_2O + * \quad (2.30)$$

$$*CH_2O + * \leftrightarrow *CHO + *H \quad (2.31)$$

$$*CHO + * \leftrightarrow *CO + *H \quad (2.32)$$

$$*CO + *O \leftrightarrow *CO_2 + * \quad (2.33)$$

$$*CHO + *O \leftrightarrow *CO_2 + *H \quad (2.34)$$

$$*CO \leftrightarrow CO + * \quad (2.35)$$

$$*CO_2 \leftrightarrow CO_2 + * \quad (2.35)$$

$$2*H \leftrightarrow *H_2 + * \quad (2.36)$$

$$*H_2 = H_2 + * \quad (2.37)$$

Where * denotes a free nickel surface adsorption site and * preceding a chemical moiety refers to corresponding chemisorbed species. Froment and Xu proposed that steps 2.32 – 2.34 are rate determining. However, recent advances in mechanistic studies of steam methane reforming have proposed that methane adsorption and the dissociation of C-H bonds is in fact the rate determining step of the kinetic process [35]. It has been shown that step and kink surface sites have lower activation barriers than terrace sites, and are more reactive towards methane activation [35, 39].

There are a number of important factors that influence steam methane reforming reactions that must be taken into account and considered when undertaking experimental investigations. Catalyst selection and reaction parameters are crucial in obtaining maximum reforming activity and selectivity.

2.3.2 Water-gas shift reaction

The water-gas shift reaction (Reaction 2.20) is mildly exothermic which means that it is favoured at lower temperatures. Table 2.2 shows that as the temperature increases ΔG^{Θ} becomes more positive, limiting the forward reaction. ΔG^{Θ} for the reaction becomes more negative below *ca.* 709 °C. However, the reaction is reversible and the reverse water-gas shift reaction can occur in the presence of carbon dioxide at elevated temperatures.

Table 2.2: Thermodynamic data for the water-gas shift reaction, produced using data from [40]

	$\Delta G^{\Theta}_{298\ K}$ / kJ mol^{-1}	$\Delta G^{\Theta}_{1200\ K}$ / kJ mol^{-1}	$T_{\Delta G=0}$ / K	$T_{\Delta G=0}$ / °C
$CO + H_2O \leftrightarrow CO_2 + H_2$ **Reaction 2.20**	-41.15	9.3	979.2	706.1

It has also been shown that the water-gas shift reaction is more favourable when methane conversion is relatively low, and reaches equilibrium at temperatures between 600 °C and 700 °C [35]. The mechanistic process for the water-gas shift reaction is shown in Section 2.3.1 (Reaction steps 2.25 and 2.26). The simple mechanism proposed is based on the Eley-Rideal mechanism, where adsorbed oxygen species react with carbon monoxide in the gas phase to produce carbon dioxide.

Commercial shift reactors/converters are commonly employed during industrial reforming processes, reducing the amount of carbon monoxide in synthesis gas, allowing the ratio of H_2/CO to be tailored to specific requirements. Either excess steam can be utilised from the product gases or additional steam is added to the shift reactor. This shift process can occur over two phases, at different temperatures, operating between either 200 – 400 °C or 130 – 175 °C [30]. The water gas shift reaction can occur as a side reaction during reforming reactions that use steam as an oxidant or produce steam during the process, such as oxygen or carbon dioxide reforming.

2.3.3 Carbon dioxide reforming

Carbon dioxide reforming, also referred to as 'dry' reforming, utilises carbon dioxide to produce syngas, as shown in Reaction 2.38. This reaction is more endothermic than steam reforming. However, it generates a more desirable H_2/CO ratio for processes such as Fischer-Tropsch.

$$\mathbf{CH_4 + CO_2 \rightarrow 2CO + 2H_2} \qquad \mathbf{\Delta H^{\Theta}_{298} = +247\ kJ\ mol^{-1}} \qquad \mathbf{(2.38)}$$

Like steam reforming, carbon dioxide reforming is favoured at high temperatures, due to the strongly endothermic nature of the reaction.

It has been shown that the reforming reaction mechanism is not dramatically altered on replacing steam with carbon dioxide and follows a similar reaction mechanism, as shown in Section 2.3.1 [29]. The reaction is first order with respect to methane dissociation [35]. The water-gas shift reaction (Reaction 2.20) is limited during carbon dioxide reforming as the carbon dioxide present in the gas feed inhibits the forward reaction. The highly endothermic nature and, in particular, the significantly carbon rich nature of carbon dioxide reforming means its commercial use is limited.

2.3.4 Catalytic partial oxidation

When the oxygen to fuel ratio is less than that required for complete combustion partial oxidation can take place, producing syngas. This is a mildly exothermic reaction (Reaction 2.39), and is thus favoured at lower temperatures than either the steam or carbon dioxide reforming reactions. Complete oxidation can also occur during reactions involving oxygen, Reaction 2.40. The complete oxidation of methane is undesirable due to its highly exothermic nature, which reduces the reforming process efficiency, as excess energy is generated as heat.

$$\mathbf{CH_4 + \frac{1}{2}O_2 \rightarrow CO + 2H_2} \qquad \mathbf{\Delta H^{\Theta}_{298} = -36\ kJ\ mol^{-1}} \qquad \mathbf{(2.39)}$$

$$\mathbf{CH_4 + 2O_2 \rightarrow CO_2 + 2H_2O} \qquad \mathbf{\Delta H^{\Theta}_{298} = -890\ kJ\ mol^{-1}} \qquad \mathbf{(2.40)}$$

The product gas stoichiometry means that this method of syngas production is ideal for methanol synthesis, avoiding the need for hydrogen removal. Although partial oxidation offers product gas composition and operating temperature advantages, the oxidation of product gases during reactions can occur, reducing efficiency. The slight exothermic nature of partial oxidation reactions means that reactor operating temperatures are easier to manage than in conventional steam and dry reforming reactors. Partial oxidation can occur in a non-catalytic environment at very high reaction temperatures, although the use of a catalyst significantly reduces this operating temperature.

2.3.5 Combined oxidative reforming

Combined oxidative reforming refers to reforming involving the addition of oxygen to both the steam and carbon dioxide reforming process, altering selectivity towards specific syngas product ratios. Oxygen can be added to both the steam methane reforming reaction (Reaction 2.41) and to the dry reforming reaction (Reaction 2.42).

$$4CH_4 + 2H_2O + O_2 \rightarrow 4CO + 10H_2 \quad (2.41)$$

$$CH_4 + CO_2 + O_2 \rightarrow 3CO + 3H_2 + H_2O \quad (2.42)$$

As noted above, partial oxidation is an exothermic reaction. Thus, additional heat produced by this reaction can be utilised during both steam and dry reforming reactions, keeping reaction temperatures high, increasing methane conversion. As well as benefiting reactor operating temperatures and product compositions, the addition of oxygen and use of two oxidants provides additional benefits through fuel flexibility. While natural gas is the predominant source of methane used in the production of syngas, other sources of methane are being researched. For example, the use of biogas, a mixture of both methane and carbon dioxide, has been investigated for its use during reforming in the presence of oxygen, to produce synthesis gas [41]. This reduces the need for removal of carbon dioxide from methane mixtures and provides additional reforming benefits.

2.4 Catalyst deactivation

The hydrocarbon reforming processes described above require highly active catalysts in order to maximise reforming activity and product formation. As discussed, supported nickel catalysts are commonly used for reforming processes, exhibiting a high activity towards hydrocarbon reforming. However, nickel is highly susceptible to deactivation during reforming reactions.

The life, stability, activity and selectivity of a catalyst can be influenced by the possibility of sintering, poisoning or coking. Sintering is a form of structural deactivation through the deformation or alteration of the catalyst during its lifetime. While, poisoning and coking are both forms of chemical deactivation, formed by the deposition of feed stream impurities and formation of surface residues by side reactions.

2.4.1 Sintering

Sintering refers to the loss of active surface, usually via a thermally activated structural transformation of the catalyst, often leading to the deactivation of the catalyst through blocking of pores and reduction of the catalytic surface area [42, 43]. Loss of surface area can result from the loss of support area due to support collapse, metal crystallite growth or a combination of the two processes.

Three principle mechanisms of sintering by metal crystallite growth have been proposed [44] and are shown in Figure 2.2. Crystallite grown can occur by crystalline migration, atomic migration and vapour transport (at high temperatures).

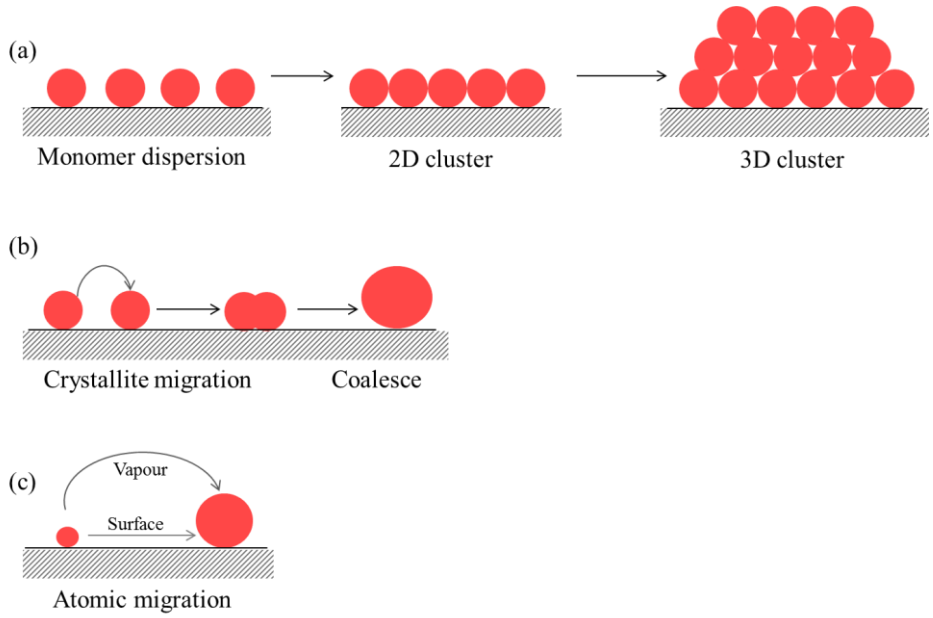

Figure 2.2: Schematic representation of various stages in the formation and growth of particles via (a) surface diffusion (b) crystallite migration and (c) atomic migration (adapted from [45])

Surface diffusion (Figure 2.2 (a)) occurs when atoms are present as small clusters of metal particles (monomer dispersion). Diffusion of atoms leads to the growth of two-dimensional clusters and on further diffusion larger three-dimensional particles will be formed. Once these particles are formed crystallite and atomic migration may occur, thus forming larger particles [45]. Crystallite migration

(Figure 2.2 (b)) involves the migration of entire crystallites over the support, followed by collision and coalescence. Atomic migration (Figure 2.2 (c)) involves separation of metal atoms from larger crystallites, migration of these atoms over the support (or in gas phase) and finally capture of larger crystallites on collision with another metal crystallite. Atomic migration is also referred to as the Ostwald ripening process, characterised by mass transport between the metal particles. During crystalline growth, small crystallites diminish in size whilst larger ones increase, since larger crystallites are more stable due to metal-metal bond energies being greater than metal-support interactions. Chemical transformations of catalyst phases can also result in loss of catalytic surface area, for example, the formation of a bulk metal aluminate phase during reactions or preparation of alumina supported metal catalysts [46].

Important factors that influence the sintering process are particle size, structure and composition of the support, reaction temperature and reaction environment. At elevated temperatures the control of the thermally induced sintering is critical for maintaining catalytic activity. The loss of metal surface area increases dramatically with increasing temperature, and following sintering average particle sizes are significantly increased [47, 48]. A shift in the metal sintering mechanism can occur as the reaction temperature is altered, changing from crystallite migration at low temperatures and short sintering times, to atomic migration at higher temperatures and longer sintering times [47, 49, 50].

Support properties and metal-support interactions can influence sintering behaviour and the extent of metal sintering. The influence a catalyst support has on the ability of metal particles to migrate across the surface is shown in Figure 2.3.

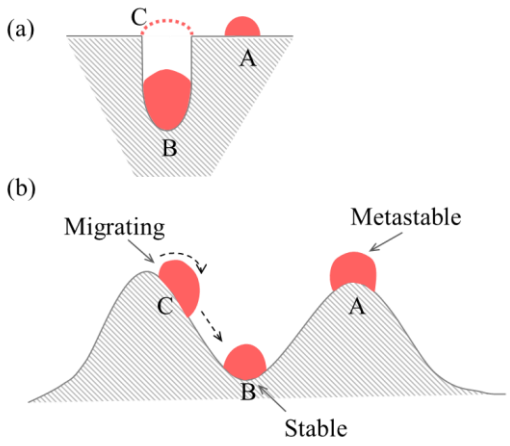

Figure 2.3: Schematic representation of metal particle morphologies on irregular support surfaces (adapted from [45])

The stabilising influence of a support pore is demonstrated in Figure 2.3 (a). Assuming the contact angle of particle A and B to the support are the same, particle A can migrate randomly as described earlier. However, if the particle is contained in a cylindrical shaped pore, B, it is stable and cannot effectively migrate. Particle A is unstable with respect to particle B, therefore, particles will migrate to fill the pore with stable metallic species, until it begins to protrude from the pore, C [45]. If the support surface has similar curvatures in size to the particle sizes, as shown in Figure 2.3 (b), particles can experience different stabilising effects. A particle on the convex portion of the support profile (A) will be metastable. If changes occur causing the particle to move from position A, a greater curvature will develop on the side of the particle (C) and cause it to move and migrate to a more stable position (B) in the concave portion of the support profile. The change in particle curvature develops from the need for the particle to maintain an optimum contact angle between it and the support surface. Particle sintering may be retarded for particles dispersed in the smallest pores or in stable support positions. As the support morphology changes during reactions, metal particles may experience a change in stability and so increased particle migration [45].

Under high pressures and elevated temperatures it has been shown that nickel aluminate is formed, reducing alumina surface area [46, 51]. The support particles are rearranged to accommodate the rearrangement and possible growth of nickel particles, resulting in a change in the catalyst

microstructure from a supported catalyst to a suspended catalyst where the nickel particle sizes are comparable or larger than support pore sizes. The influence of support collapse and loss of surface area towards the extent of sintering has been shown to occur to a greater extent over alumina supported catalysts compared to metals supported on silica [47]. This is due to the higher surface area, and therefore, a greater surface is available for the release of metal atoms [52]. It has also been shown that supported nickel catalysts with higher nickel loadings exhibit reduced nickel dispersion and increased sintering [53]. Sintering can occur for supported and unsupported catalysts, although it has been shown that sintering has little effect on the activity of unsupported nickel catalysts [31].

Increasing reaction temperature significantly increases metal particle sintering [54] as well as reducing support surface areas [55]. The Tamman and Hüttig [43] temperatures are directly related to the melting temperature, providing an indication of the temperature at which the sintering process may occur for specific atoms.

$$\mathbf{T_{Hüttig} = 0.3\ T_{melting}} \qquad \mathbf{(2.43)}$$

$$\mathbf{T_{Tamman} = 0.5\ T_{melting}} \qquad \mathbf{(2.44)}$$

Atom mobility increases with increasing temperature. When the Hüttig temperature (Reaction 2.43) is reached, atoms at surface defects may become mobile and at the Tamman temperature (Reaction 2.44) atoms from the bulk may exhibit mobility. From the melting point data for nickel, a Tamman temperature of *ca.* 720 °C can be predicted and crystalline migration may become an important sintering mechanism at temperatures above this. Supports such as alumina and silica possess high Tamman temperatures, increasing their thermostability and effectiveness as catalytic supports.

As well as temperature, the reactant gas composition and catalyst morphology can also influence sintering behaviour. The presence of steam has been shown to influence and enhance nickel sintering processes [50, 52, 56] through the formation of mobile Ni_2-OH complexes, enhancing the rate of migration and coalescence. Teixiera *et al.* [50] have demonstrated that addition of lanthanum stabilising promoters to Ni/Al_2O_3 can act to decrease mobility of nickel atoms and

particles due to strong interactions, so reducing migration and, ultimately, sintering. However, Sehested *et al.* [46] show that the addition of potassium promoters to nickel based catalysts, at low pressures, has little effect on sintering rates compared to un-promoted catalysts.

Although sintering is a largely irreversible process some researchers have shown that metal re-dispersion is possible in certain oxidative environment [57]. For example, the addition of carbon dioxide to the gas feed at elevated temperatures has been shown to significantly re-disperse agglomerated nickel particles, reducing the effects of sintering over $Ni/CaAl_2O_4$ [48].

Although other deactivation mechanisms such as carbon deposition and sulfur poisoning are more widely discussed and researched, sintering is a major cause of catalyst deactivation in reforming processes and one which must be taken into account during investigations involving supported catalysts at elevated temperatures and pressures.

2.4.2 Carbon deposition

The main problem encountered through the use of nickel in reforming catalysts is its high activity towards carbon forming reactions such as the Boudouard reaction (Reaction 2.45), methane decomposition (Reaction 2.46) and CO reduction (Reaction 2.47).

$$\mathbf{2CO \leftrightarrow C + CO_2} \qquad \mathbf{(2.45)}$$

$$\mathbf{CH_4 \rightarrow C + 2H_2} \qquad \mathbf{(2.46)}$$

$$\mathbf{CO + H_2 \leftrightarrow C + H_2O} \qquad \mathbf{(2.47)}$$

Thermodynamic data shown in Table 2.3, for gas phase reactions, predicts that, for Reactions 2.45 and 2.47, as the temperature is increased, ΔG^{Θ} becomes more positive, limiting the forward reaction. Both the Boudouard reaction and CO reduction are favoured at lower temperatures, below *ca.* 670 °C. However, Reaction 2.46 is favoured at higher temperatures, as the temperature is increased ΔG^{Θ} becomes more negative. Methane decomposition is favoured at temperatures above

ca. 714 °C. All thermodynamic predictions assume that all reactants and products are in the gas phase, and that ΔH and ΔS are independent of temperature. Under reaction conditions, in the presence of a catalyst, such thermodynamic predictions can vary dramatically. For example, Shah *et al.* [58] have shown that the use of binary catalysts reduces the temperature at which methane decomposition occurs, by up to 400 °C – 500 °C.

Table 2.3: Thermodynamic data for the principal carbon deposition reactions (Boudouard reaction, methane decomposition and CO reduction) produced using data from [40]

	$\Delta G^{\Theta}_{298\ K}$ / kJ mol^{-1}	$\Delta G^{\Theta}_{1200\ K}$ / kJ mol^{-1}	$T_{\Delta G=0}$ / K	$T_{\Delta G=0}$ / °C
$2CO \leftrightarrow C + CO_2$ **Reaction 2.45**	-118.5	44.7	953.0	679.8
$CH_4 \rightarrow 2H_2 + C$ **Reaction 2.46**	52.0	-16.0	987.2	714.1
$CO + H_2 \leftrightarrow C + H_2O$ **Reaction 2.47**	-89.8	35.4	945.0	672.0

Such carbon formation reactions can lead to carbon deposition on the catalyst surface, also known as fouling or coking [43], where a surface is covered with a deposit whose origin is not always related to the primary process occurring on the catalyst. 'Carbon' is typically referred to as a product of carbon monoxide disproportionation, whereas 'coke' is produced by decomposition of hydrocarbons on the catalyst surface. However, the origin of carbon and coke is not always known and is generally referred to as carbon irrespective of its origin. The reverse of the above reactions may also provide a basis for carbon removal via gasification.

Depending on the carbon deposition reaction occurring and the temperature at which the carbon is formed, a number of different species of carbon have been identified on the catalyst surface. The main forms are encapsulating, pyrolytic, filament and whisker. These different types of carbon can affect the activity of the catalyst in different ways; some lead to catalyst deactivation [59, 60], whilst others have little effect on reforming activity [61], and in some cases carbon formation can enhance the activity of reforming catalysts [59]. The specific forms of carbon are discussed in more detail in Sections 2.4.2.1 - 2.4.2.3.

The nature of carbon and hence its location on the catalyst can change significantly with pressure, temperature, oxidant/hydrocarbon ratio and catalyst pre-treatments [61-63]. Gasification of hydrocarbon intermediates, and so reduction in the transformation of intermediates into carbon deposits, occurs at certain concentrations of oxidant, such as steam. In the presence of high steam partial pressures and a steam-rich system (methane to steam ratio >2), chemisorbed OH species increase on the catalyst surface, resulting in carbon removal by gasification and suppression of carbon deposition [31, 52]. Carbon gasification by steam is limited by thermodynamics and becomes increasingly favoured at higher temperatures [63].

When using temperature-programmed oxidation (TPO) as a method of carbon quantification and identification, as discussed in Chapter 3, it is important to note the temperature at which carbon monoxide and carbon dioxide are evolved. This can provide an indication as to the carbon species present on the catalyst surface [61, 64, 65 and references therein]. Finnerty *et al*. [64] identified three types of carbon species during TPO analysis. The three species are removed by oxygen during TPO reactions, at *ca.* 597 °C, > 627 °C and > 727 °C.

Menon indicates the importance of control over coking rates [65]. Rapid coke lay-down can lead to pore-mouth blockage and thus rapid catalyst deactivation. A slow rate of coverage over the entire catalyst ensures that activity remains constant and pore blocking is kept to a minimum. This is illustrated in Figure 2.4. Theoretically, by deliberately coking catalysts, the rate of coking through subsequent reactions can be controlled.

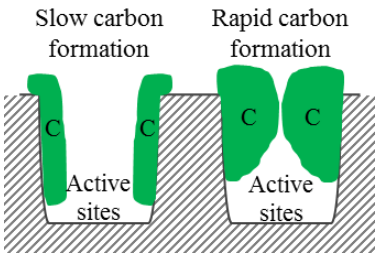

Figure 2.4: Schematic representation of carbon formation in active sites during fast and slow rates of formation (adapted from [65])

Both filament and whisker carbon have very similar morphologies and effects on catalyst activity and reforming. In the following sections both filament and whisker carbon are discussed in the same section, due to their similar methods of formation, highlighting the main differences where appropriate. However, it is important to note that some authors do not distinguish between the two carbon forms when discussing formation and deposition, often referring to both as filament species.

2.4.2.1 Filament and whisker carbon

Carbon nanotubes or filaments are cylindrical or tubular carbon formations. The main difference between these two species of carbon is the orientation of graphite basal planes with respect to the tube axis [66]. A schematic representation is shown in Figure 2.5. Filaments consist of stacked basal plane sheets and grow with a metal particle at the tip, $0° < \theta > 90°$, where θ is the tube axis (Figure 2.5 (a)). Nanotubes are cylindrical carbon deposits whose graphite basal planes are parallel to the tube axis, $\theta = 0°$ (Figure 2.5 (b)).

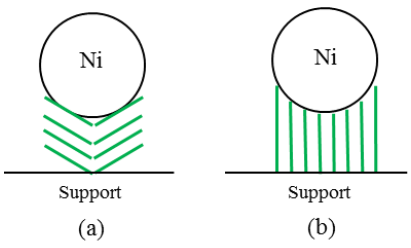

Figure 2.5: Schematic illustration of (a) filament and (b) nanotube carbon present on nickel supported catalysts (adapted from [66])

Filament and whisker carbon is produced through the dissolution of carbon in nickel and the subsequent formation of filaments, with a polymeric structure. This is proposed to occur in the temperature range from *ca*. 250 °C to 500 °C [67]. It has been suggested [68-70] that carbon filaments are formed by the precipitation of dissolved carbon or nucleation of graphitic carbon at the bottom side of metal crystallites, resulting in metal particles growing away from the support, as shown in Figure 2.6. At the top of the nickel particle, away from the support, a selvedge is created with a high carbon concentration [71]. This is created due to the segregation behaviour of carbon in nickel, where the surface is enriched with carbon, also referred to as carbide [72], with the dissolved carbon concentration decreasing towards the support.

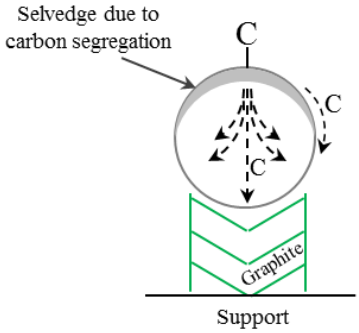

Figure 2.6: Schematic representation of the mechanism of whisker/filament carbon formation on a supported nickel particle (adapted from [71])

There have been many different theories proposed as to whether bulk diffusion of carbon through nickel is driven by a concentration gradient or by a temperature gradient. However, the most accepted mechanism for the elementary steps in the formation of filament carbon from methane decomposition, can be summarised as follows [68, 71, 73]:

Surface reactions:

$$CH_4 + 2* \rightarrow *CH_3 + *H \qquad (2.48)$$

$$*CH_3 + * \rightarrow *CH_2 + *H \qquad (2.49)$$

$$*CH_2 + * \rightarrow *CH + *H \quad (2.50)$$

$$*CH + * \rightarrow *C + *H \quad (2.51)$$

$$2*H + * \rightarrow H_2 + 2* \quad (2.52)$$

Dissolution:

$$*C \rightarrow C_{Nit} + * \quad (2.53)$$

Diffusion:

$$C_{Nit} \rightarrow C_{Nib} \quad (2.54)$$

Dissolution of carbon:

$$C_{Nib} \rightarrow C_f \quad (2.55)$$

Where * is the surface adsorption site, C_{Nit} is the carbon dissolved in the nickel at the top of the nickel particle below the selvage, C_{Nib} is the carbon dissolved in the nickel at the bottom of the particle close to the support and C_f is carbon filament.

At low temperatures, the initial rate of nucleation is low compared to the rate of carbon diffusion. Nucleation is uniform over the whole metal interface and the nickel crystallite is lifted from the support as shown in Figure 2.6. Full filaments are usually formed in this way, with no hollow channel. Initially, following filament formation, the coking and deactivation rate is high, resulting in a steady-state growth of filaments [73].

A carbide intermediate is formed preceding the nucleation of graphite. Carbon filament growth is facilitated by the continuous decomposition of carbide intermediates until a regime of steady state growth is reached, where the rate of coking is equal to the rate of carbon diffusion through the crystallite [59, 72]. Filament growth increases with increasing temperature, until a maximum rate of growth is reached at an optimum temperature [73]. Strong interactions between the nickel and support has been shown to inhibit filamentous carbon formation during reforming reactions [59].

Filament growth is proposed to cease when sufficient filaments are formed and begin encapsulating the nickel particle.

At high temperatures, carbon nucleation occurs as soon as the metal-support interface reaches saturation, much faster than the rate of diffusion. Rapid nucleation lifts nickel crystallites in only the areas where rapid carbon laydown has occurred. Following carbon formation, the concentration of dissolved carbon drops and nucleation decreases. This results in reduced carbon formation and formation of hollow filaments. Strong metal-support interactions where there is no carbon formation, results in the distortion of the metal crystallite as carbon filaments grow, shown in Figure 2.7 [71, 74].

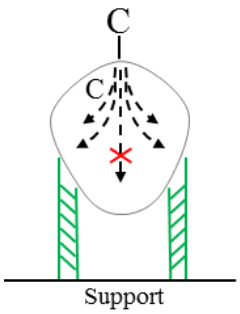

Figure 2.7: Schematic representation of the deformation of metal particle due to formation of hollow filaments

Nickel crystallite size is a major parameter in the formation and control of carbon filament growth [52, 73]. Smaller crystallite sizes can have differing effects on the rate of carbon growth [73]. A small nickel crystallite size provides a high surface area for surface reactions and diffusion of carbon, leading to higher coking rates. However, a nickel crystallite which is too small results in a large saturation concentration, leading to a slow diffusion rate and a reduced rate of coking, as the filament saturation concentration becomes the dominating factor. Initiation of filament nucleation has been shown to be more difficult on smaller nickel crystals [52, 73]. Kim *et al.*[75] have shown that a minimum diameter of *ca.* 7 nm is required for nickel particles to facilitate filament carbon growth. Following initiation, the rate of filament growth has been shown to increase over catalysts

containing smaller nickel crystallites [52, 67], although, it has been suggested that nickel crystallites must have a diameter >10 nm to be involved exclusively in filament growth [72].

It has been reported [59, 76] that this type of carbon (particularly filament carbon) does not directly cause catalyst deactivation, unless it is formed in sufficient quantities to block pores or inhibit gas flow to the catalyst. However, it has been shown to deactivate steam reforming catalysts mechanically [65]. The activity of steam ethanol reforming has been shown to increase over α-Al_2O_3 supported nickel catalysts following filamentous carbon formation [59], this is attributed to the formation of small nickel particles on the filament tip, increasing nickel activity. This demonstrates that although the majority of carbon deposition results in catalyst deactivation, in limited cases filamentous carbon can in fact increase catalytic activity.

2.4.2.2 Encapsulating carbon

Encapsulating carbon consists of carbon layers or films covering the nickel particle, resulting in loss of nickel activity. Encapsulating carbon is usually formed at temperatures below 500 °C. This form of deposition can result in direct deactivation by covering active phases.

The schematic representation in Figure 2.8, shows deactivation is a progressive process. Encapsulating carbon can be catalytically produced by the decomposition of carbon containing gases on the catalyst surface and subsequent polymerisation of CH_x fragments [77]. Encapsulating carbon is ascribed to an advanced state of graphite formation.

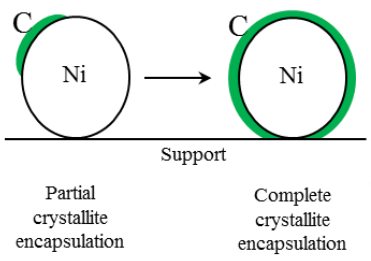

Figure 2.8: Schematic representation of encapsulating carbon formation over a supported nickel particle

It has been shown [59] that the initial rate of encapsulating carbon is high, although the rate of formation decreases with time, as the majority of metallic sites become inactive and unavailable. The high carbon saturation level in small crystallites may lead to the formation of encapsulating coke, due to the high surface coverage of carbon [52, 73]. Although low reaction temperatures favour encapsulating carbon formation, Piao *et al.* [62] have proposed that high reaction temperatures increase the methane decomposition rate, leading to rapid amorphous carbon formation resulting in encapsulation of nickel particles. It is also proposed that encapsulation could terminate filament growth [78]. Encapsulating carbon is usually limited to *ca.* 30 or 40 layers of graphene sheets, irrespective of the size of the nickel crystallite or formation conditions [66]. However, the thickness of the coating is dependent on the carbon source, the higher the carbon mass the greater the thickness [79].

Metal crystallites can be encapsulated with carbon deliberately, in order to isolate metal particles from environmental influences, protect against oxidation and increase stability in air and corrosive liquids. Such carbon-encapsulated metal nanoparticles can be used for various applications including drug delivery [80] and isolation of highly reactive materials [81].

2.4.2.3 Pyrolytic carbon

Pyrolytic carbon is formed during exposure to higher hydrocarbons and subsequent thermal cracking and deposition of carbon precursors on the nickel surface. This carbon is formed as a result of C-C bond cleavage at high temperatures. Formation occurs above 600 °C in the presence of low oxidant levels. Formation of pyrolytic carbon leads to the ultimate encapsulation of metallic particles. Pyrolytic carbon has a polycrystalline structure, resulting in dense polyaromatic deposits [82]. However, due to the graphite-like nature of pyrolytic carbon, microstructures can have different forms depending on reaction conditions [44]. Pyrolytic carbon is made up of layers of different ‘textured’ carbon. Textures can be classified into three main types: smooth laminar, rough

laminar and isotropic. Unlike graphite, pyrolytic carbon has a distorted lattice structure with random un-associated carbon atoms.

2.4.2.4 Catalyst modification to improve tolerance towards carbon deposition

Supported metal catalysts can be modified in a number of ways in order to increase activity and tolerance towards deactivation through carbon deposition.

Both the preparation method and activation parameters selected during preparation can dramatically influence the catalyst morphology and hence the propensity towards carbon formation. The preparation procedure used, such as wet co-impregnation, sequential impregnation, co-precipitation or sol-gel method, can influence a catalyst's ability to form carbon [17, 19, 83, 84]. The calcination temperature selected during preparation can also have a dramatic effect on the subsequent carbon deposition during reforming reactions and methane decomposition, especially for metals supported on oxide materials such as alumina. Calcination temperatures can influence structural morphology and metal support interactions. It has been suggested that greater metal support interactions, resulting from higher calcination temperatures, result in greater catalyst resilience towards carbon deposition via methane decomposition [26, 54]. As well as the amount of carbon formed, the type of carbon produced during methane decomposition can be influenced by calcination temperature. Joo *et al*. [61] have demonstrated that Ni/Al_2O_3 catalysts calcined at lower temperatures deactivate due to the formation of amorphous carbon during methane decomposition, whereas following calcination at 850 °C, catalysts facilitate the formation of filamentous carbon which does not lead to catalyst deactivation.

The support chosen for nickel based catalysts can significantly influence the extent of carbon deposition during reforming reactions. An increase in support surface area has been shown to provide better resistance towards coke formation [85]. Zirconia (ZrO_2) has proven to increase stability and suppress carbon deposition, compared to alumina (Al_2O_3) [21]. These beneficial effects are also observed when ZrO_2 is incorporated into a Ni/Al_2O_3 catalyst, significantly reducing

carbon deposition [19, 84, 86]. It has been proposed that ZrO_2 enhances carbon dioxide dissociation, which increases surface oxygen intermediates. These intermediates enhance oxidation of hydrocarbon intermediates, thus facilitating carbon removal via gasification.

The addition of a gold promoter to Ni/YSZ and Ni/$MgAl_2O_4$ has been shown to significantly reduce carbon deposition [87-89]. This is attributed to the preferential binding of gold to nickel step sites, which are highly active towards carbon nucleation [39]. Additionally, gold lowers the rate of methane dehydrogenation and increases the lifetime, stability and concentration of adsorbed CH_x species. Gold has been shown to induce electronic and catalytic property changes in surface nickel, resulting in an increase in both the activation barrier of methane dissociation and the energy of the resulting adsorbed species, reducing carbon formation [89].

Alkaline earth metals have been reported to have contradictory effects on the extent and type of carbon deposition. The introduction of calcium to a Ni/Al_2O_3 catalyst has been reported to reduce carbon deposition, whilst the addition of magnesium have been reported to increase the catalyst capacity for methane decomposition [90]. However, Lisboa *et al.* [83] have shown that the addition of calcium and magnesium to 10 % Ni/Al_2O_3 catalysts dramatically increases carbon deposition. However, the coke deposited did not block the nickel surface for reforming reactions, due to a change in the type of coke formed on addition of the promoters. It has been proposed that the addition of magnesium reduces the nickel ensemble particle size, thus inhibiting the formation of less reactive coke through the blocking of carbon nucleation sites. The influence of calcium addition has been linked to enhanced gasification of adsorbed carbon by steam. In the presence of calcium and magnesium promoters, two types of carbon were deposited on the catalyst surface, whereas only one type was deposited for un-promoted samples. It has also been shown that the addition of 10 wt % sodium, potassium, magnesium and calcium to Ni/Al_2O_3 catalysts dramatically reduces carbon deposition through suppression of methane decomposition [91].

The addition of precious metals to reforming catalysts has proved to be a successful method of increasing activity, as well as suppressing carbon formation. Ruthenium, palladium, platinum and

iridium have all been reported to increase reforming activity when incorporated into a variety of supported nickel catalysts [17, 18, 92-94]. Precious metal promoted catalysts can suppress carbon deposition via two main mechanisms. The addition of a precious metal to the nickel catalyst increases the number of surface active metal sites due to clustering of precious metals and nickel, resulting in higher nickel dispersion and reduction in nickel particle size, ultimately acting to restrain carbon nucleation [92, 94]. Precious metals also promote hydrogen spill-over to nickel and carbon species. Hydrogen formed during methane decomposition can be spilled over to the carbon intermediates on the surface, suppressing C-C bond formation [18]. This effect also reduces the need for catalyst pre-reduction, as this spill-over effect has been shown to effectively reduce NiO species in reforming conditions [93, 94].

Ceria has been widely used to modify reforming catalysts, improving tolerance towards carbon formation due to its self de-coking ability [95]. Removal of coke via gasification has been shown to increase on incorporation of CeO_2 into catalyst samples, due to its ability to store, release and transfer oxygen species. Intimate contact between the metal and ceria phase must be achieved, leading to accelerated gasification of adsorbed carbon species on the metal-oxide interface [96]. Although ceria is beneficial towards reduction in carbon formation, it has reported to be detrimental towards reforming activity, as it has been shown to oxidise nickel species within the catalyst, thus limiting the active metal phase [95, 97].

The modification of a catalyst to suppress carbon formation is undertaken with the knowledge that the promoter may suppress carbon formation or increase gasification, but can also reduce catalytic reforming activity. An optimum balance between carbon suppression and catalytic performance must be achieved for any promoted reforming catalyst to be effective.

2.4.3 Sulfur poisoning

Poisoning of catalysts essentially refers to the preferential adsorption of species which are usually foreign to the reactive system. The effect is highly dependent on the formation of strong adsorption

bonds between the catalyst and the adsorbed species. Species are regarded as poisons if they act to inhibit catalysis, even if only present in small concentrations. A poison can act by blocking active sites (geometric effects) or by altering the adsorption of other species by electronic effects. Poisons can also modify the chemical nature of active sites, resulting in the formation of new species that alter the catalyst behaviour and performance. Such effects will influence the reactions occurring on the catalyst surface and result in the deactivation of reforming reactions. Poisons are generally classified as either 'selective' or 'non-selective', which is shown schematically in Figure 2.9. Selective poisoning generally involves the poisoning of the most active sites first. Non-selective poisoning involves chemisorption of the poison in a more uniform manner generally showing a linear decrease in activity with poison concentration.

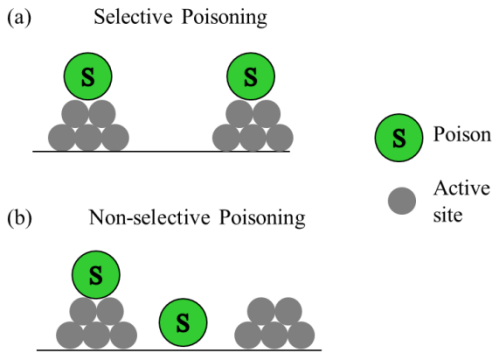

Figure 2.9: Schematic representation of (a) selective and (b) non-selective poisoning

Maxted [98] reported that metal groups VIII B and IB (iron, ruthenium, osmium, cobalt, rhodium, iridium, nickel, palladium, platinum and copper, silver, gold) are most susceptible to poisoning. As stated above, poisons are usually strongly adsorbed species which limit catalyst activity. Three main classes of catalyst poisons are: molecules containing elements of periodic group VA (nitrogen, phosphorus, arsenic, antimony) and V1A (oxygen, sulfur, selenium and tellurium, including the free elements, with the exception of nitrogen), compounds with a large number of catalytically toxic metals, and molecules containing multiple bonds (such as carbon monoxide, cyanogen compounds and in some cases benzene).

Sulfur containing compounds found in the gas feed are typically converted to hydrogen sulfide, H_2S, under reforming conditions. Other sulfur containing compounds, such as COS, SO_2, CS, SO_3, methanethiol, ethanethiol, and thiophene, act in a similar way to H_2S due to the sulfur compounds having an unshared electron pair, leading to strong chemisorption to the metal surface. In order to show the major properties and characteristics of sulfur poisoning, H_2S is generally referred to, as this is the most studied in the literature and is the most applicable within current research undertaken.

Sulfur poisoning of nickel based catalysts is strongly dependent on a number of parameters, such as sulfur concentration, reaction temperature and the nature of the catalyst. An exponential decrease in catalyst activity is reported to be observed on increased sulfur poisoning [99]. Stabilisation of catalyst activity following poisoning is faster with higher sulfur concentrations, while the poisoning effect takes longer to stabilise at lower levels of sulfur. The chemisorption of hydrogen sulfide is an exothermic process, with sulfur adsorption on nickel surfaces occurring more strongly at low to mid operating temperatures (below 800 °C) [100]. The rate of surface nickel sulfide formation increases as the temperature is increased up to 850 °C, due to sulfur chemisorption and nickel sulfide formation until an equilibrium and saturation of the surface is reached [101]. Steam reforming, due to its endothermic nature, lowers the catalyst bed temperature at the top of the catalyst bed where reactions are more prevalent, therefore, sulfur content and poisoning at this point is increased compared to the middle and bottom of the bed [100, 102]. At high temperatures (*ca.* 900 °C) activity is reported to be maintained at a higher level, even at higher sulfur concentrations [99].

Kinetic studies have shown that the rate of H_2S adsorption on metals is generally rapid and no barrier to adsorption is present until saturation levels are approached [103 and references therein]. H_2S chemisorbs dissociatively on nickel surfaces [104-106], although the number of surface nickel atoms involved in H_2S chemisorption is a strongly debated area. Rostrup-Nielsen [105] suggest a one-site mechanism for H_2S adsorption (Reaction 2.56) at temperatures of *ca.* 550 °C.

$$\mathbf{H_2S_{(g)} + Ni \leftrightarrow Ni - S + H_2} \qquad \textbf{(2.56)}$$

In contrast, Saleh *et al.* [107] suggest a three site mechanism for chemisorption of H_2S with the nickel surface, occurring at significantly low temperatures (-80 °C), Reaction 2.57. It has been proposed that complete dissociation takes place and each atom in hydrogen sulfide occupies one nickel site.

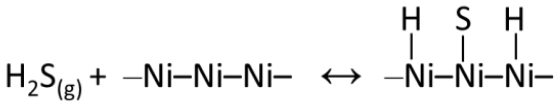

(2.57)

Den Besten and Selwood [106] and Ng and Martin [108] have suggested a mechanism at low temperatures for dissociative H_2S adsorption involving the formation of four chemisorptive bonds with the nickel surface (Reaction 2.58). If surface coverage is high, the dissociated hydrogen is forced into the gas phase rather than adsorbing to free nickel sites (Reaction 2.59) resulting in chemical rearrangement and possible formation of bulk sulfides.

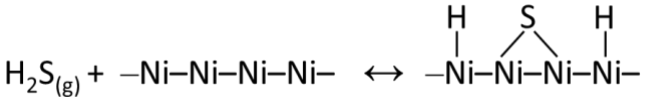

(2.58)

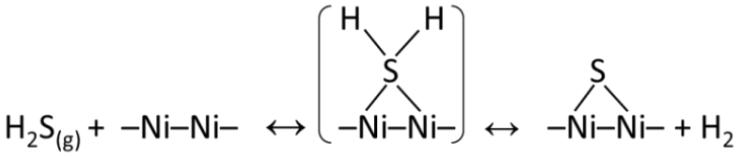

(2.59)

It is clear that the adsorption of sulfur on metal surfaces is a complex dissociative chemisorption process, with potentially several metal sites involved in sulfur adsorption. It is considered that sulfur interacts with only the metallic phase and the amount of sulfur adsorbed on the support at low temperatures is negligible [104].

Sulfur has been shown to remain on the nickel surface in three different states, corresponding to H_2S which desorbs at *ca.* 200 °C and *ca.* 500 °C, and irreversible sulfur which does not desorb at temperatures above *ca.* 600 °C [104].

Following the formation of surface metallic sulfides, sulfur can form bulk sulfides, formed slowly by the attack of deeper metallic layers. The amount of such species depends on the nature of the catalyst [104], such as the catalyst metal loading and ratio of H_2S/H_2 in the gas feed [109]. A high ratio of H_2S/ H_2 and low reaction temperature can result in bulk nickel sulfide formation [109]. Bulk sulfide formation involves ion diffusion through the metallic layer to the surface, followed by formation of a metal sulfide layer on the surface beyond the original metallic layer.

2.4.3.1 Regeneration of sulfur poisoned catalysts

Theoretically the chemisorption process is reversible and in some cases sulfur can be removed from the surface by either hydrogen or by oxidation in controlled conditions. Due to the exothermic nature of sulfur chemisorption (Reaction 2.56), removal of surface sulfur is favoured at higher temperatures.

Regeneration in the presence of hydrogen provides the additional benefit of keeping metallic species in an active reduced state (Reaction 2.60). During reforming reactions, the removal of sulfur from the reactive gas stream has been shown to regenerate catalytic activity [99, 100]. Sulfur oxidation by carbon dioxide, oxygen and steam has also been used to regenerate poisoned catalysts. It has been reported [48] that the addition of carbon dioxide at elevated temperatures restored activity to 76 % (Reaction 2.61). Steam has been shown to effectively regenerate nickel catalysts poisoned by sulfur chemisorption at temperatures above 500 °C [100, 110], although this requires complete oxidation of the nickel (Reaction 2.62) ensuring that hydrogen sulfide is not retained at the surface. Sulfur dioxide can be formed in the presence of excess steam and is more thermodynamically stable than H_2S and sulfur, Reaction 2.63. Regeneration in the presence of air at temperatures below 600 °C has been shown to be unsuccessful over both nickel and platinum

based catalysts, as surface sulfates do not decompose at such low temperatures [99, 111]. However, in the presence of hydrogen, surface sulfur species are removed easily at lower temperatures (Reaction 2.60).

$$\mathbf{Ni - S + H_2 \rightarrow Ni + H_2S} \qquad \mathbf{(2.60)}$$

$$\mathbf{CO_2 + H_2S \rightarrow COS + H_2O} \qquad \mathbf{(2.61)}$$

$$\mathbf{Ni - S + H_2O \rightarrow NiO + H_2S} \qquad \mathbf{(2.62)}$$

$$\mathbf{H_2S + 2H_2O \rightarrow SO_2 + 3H_2} \qquad \mathbf{(2.63)}$$

2.4.3.2 Influence of sulfur adsorption towards carbon resistance

Although sulfur is classed as a poison and has been shown to deactivate nickel catalysts, it has also shown to be beneficial at low levels towards some reforming processes. The process by which carbon-free steam reforming of methane operates on partially sulfur-passivated catalysts is known as the SPARG process (Sulfur PAssivated ReforminG) [112-114]. As sulfur is introduced into a steam methane reforming reaction, the rate of carbon formation is inhibited more than the rate of reforming. 'Ensemble control' ensures that steam reforming selectivity is increased on increased sulfur coverage, as ensembles of nickel atoms available for the conversion of adsorbed methane are sufficient for the conversion of steam, but not the nucleation of carbon, due to the larger ensemble size required for dissolution-precipitation of carbon. Carbon nucleation and coverage over a nickel surface can be reduced due to preferential binding to nickel step sites [115]. Sulfur adsorption at step sites increases the activation energy for methane decomposition, occurring over less favourable terrace sites. Steps could be blocked by either gold or sulfur, eliminating unwanted side reactions, such as carbon formation, with only a moderate impact on methane dissociation rate. The impact of sulfur on reducing carbon deposition, over the support material alone is minimal and no significant reduction in carbon is observed when no active metal is used [116]. The impact of sulfur adsorption on carbon nucleation is also reflected in the morphology of carbon formed. Above a

certain coverage, amorphous carbon is reported to be formed as opposed to whisker carbon [112]. Although it has been shown to reduce carbon deposition, it has also been reported to promote carbon deposition [116, 117], preventing hydrocarbon reforming and reducing carbon gasification. However, although promoting the formation of graphitic islands, sulfur has been shown to hinder the growth of filamentous carbon due to the preferential binding of sulfur on reactive nickel sites [116].

Under precise operating conditions and reactive gas compositions, it is possible to operate a carbon-free operating regime in the presence of sulfur, with little impact on the reforming characteristics.

2.5 References

1. J.M. Thomas and W.J. Thomas, *Setting the Scene*, in *Principles and Practice of Heterogeneous Catalysis* 1996, VCH. p. 1.
2. I. Wender, *Reactions of synthesis gas.* Fuel Processing Technology, 1996. **48**(3): p. 189-297.
3. G.A. Olah, A. Goeppert, and G.K.S. Prakash, *Methanol as a Fuel and Energy Carrier*, in *Beyond Oil and Gas: The Methanol Economy*. 2006, Wiley-VCH. p. 173.
4. J. Hagen, *Heterogeneously Catalyzed Processes in Industry*, in *Industrial Catalysis* 2006, Wiley-VCH. p. 261.
5. M.E. Dry, *The Fischer-Tropsch process: 1950-2000.* Catalysis Today, 2002. **71**(3-4): p. 227-241.
6. A.J. Appleby and F.R. Foulkes, *Fuel Cell Handbook*. 1993, Krieger Publishing Company: Florida.
7. W.R. Grove, Phil. Mag., 1839. **14**: p. 137.
8. R.M. Ormerod, *Solid Oxide Fuel Cells.* Chemical Society Reviews, 2003. **32**: p. 17-28.

9. C. Song, *Fuel processing for low-temperature and high-temperature fuel cells: Challenges, and opportunities for sustainable development in the 21st century.* Catalysis Today, 2002. **77**(1-2): p. 17-49.

10. R.M. Ormerod, *Fuels and Fuel Procesing*, in *High Temperature Solid Oxide Fuel Cells - Fundamentals, Design and Applications*, S.C. Singhai and K. Kendall, Editors. 2003, Elsevier. p. 333-361.

11. Q. Ming, T. Healey, L. Allen, and P. Irving, *Steam reforming of hydrocarbon fuels.* Catalysis Today, 2002. **77**(51-64).

12. D. Deublein and A. Steinhauser, *Biogas from Waste and Renewable Sources*. 2008: WILEY-VCH. 376.

13. J. Chorkendorff and J.W. Niemantsverdriet, *Concepts in Modern Catalysis* 2007: WILEY-VCH. 346-350.

14. J. Hagen, *Heterogeneous Catalysis: Fundamentals*, in *Industrial Catalysis* 2006, Wiley-VCH. p. 109 - 113.

15. G. Rothenberg, *Heterogeneous Catalysis*, in *Catalysis: Concepts and Green Applications*. 2008, WILEY-VCH.

16. M.E.S. Hegarty, A.M. O'Connor, and J.R.H. Ross, *Syngas production from natural gas using ZrO_2-supported metals.* Catalysis Today, 1998. **42**(3): p. 225-232.

17. J.H. Jeong, J.W. Lee, D.J. Seo, Y. Seo, W.L. Yoon, D.K. Lee, and D.H. Kim, *Ru-doped Ni catalysts effective for the steam reforming of methane without the pre-reduction treatment with H_2.* Applied Catalysis A: General, 2006. **302**(2): p. 151-156.

18. T. Takeguchi, R. Kikuchi, T. Yano, K. Eguchi, and K. Murata, *Effect of precious metal addition to Ni-YSZ cermet on reforming of CH_4 and electrochemical activity as SOFC anode.* Catalysis Today, 2003. **84**(3-4): p. 217-222.

19. S. Therdthianwong, C. Siangchin, and A. Therdthianwong, *Improvement of coke resistance of Ni/Al_2O_3 catalyst in CH_4/CO_2 reforming by ZrO_2 addition.* Fuel Processing Technology, 2008. **89**(2): p. 160-168.

20. S.B. Tang, F.L. Qiu, and S.J. Lu, *Effect of supports on the carbon deposition of nickel catalysts for methane reforming with CO_2*. Catalysis Today, 1995. **24**(3): p. 253-255.

21. K. Nagaoka, K. Seshan, K.-i. Aika, and J.A. Lercher, *Carbon Deposition during Carbon Dioxide Reforming of Methane--Comparison between Pt/Al_2O_3 and Pt/ZrO_2.* Journal of Catalysis, 2001. **197**(1): p. 34-42.

22. C.S. Nordahl and G.L. Messing, *Thermal analysis of phase transformation kinetics in α-Al_2O_3 seeded boehmite and γ-Al_2O_3.* Thermochimica Acta, 1998. **318**(1-2): p. 187-199.

23. A.M. Diskin, *The oxidative chemistry of methane over supported nickel catalysts* in *PhD Thesis*. 2000, Keele University.

24. A.M. Diskin, R.H. Cunningham, and R.M. Ormerod, *The oxidative chemistry of methane over supported nickel catalysts.* Catalysis Today, 1998. **46**(2-3): p. 147-154.

25. M. Barroso, M. Gomez, L. Arrúa, and M. Abello, *Reactivity of Aluminum Spinels in the Ethanol Steam Reforming Reaction.* Catalysis Letters, 2006. **109**(1): p. 13-19.

26. P. Kim, Y. Kim, H. Kim, I.K. Song, and J. Yi, *Synthesis and characterization of mesoporous alumina with nickel incorporated for use in the partial oxidation of methane into synthesis gas.* Applied Catalysis A: General, 2004. **272**(1-2): p. 157-166.

27. H. Cui, M. Zayat, and D. Levy, *A sol-gel route using propylene oxide as a gelation agent to synthesize spherical $NiAl_2O_4$ nanoparticles.* Journal of Non-Crystalline Solids, 2005. **351**(24-26): p. 2102-2106.

28. M. Salavati-Niasari, F. Davar, and M. Farhadi, *Synthesis and characterization of spinel-type $CuAl_2O_4$ nanocrystalline by modified sol–gel method.* Journal of Sol-Gel Science and Technology, 2009. **51**(1): p. 48-52.

29. J.R. Rostrup-Nielsen, *Production of Synthesis gas.* Catalysis Today, 1993. **18**: p. 305-324.

30. A.P. Simpson and A.E. Lutz, *Exergy analyis of hydrogen production via steam methane reforming* International Journal of Hydrogen Energy, 2007. **32**: p. 4811-4820.

31. S. Rakass, H. Oudghiri-Hassani, P. Rowntree, and N. Abatzoglou, *Steam reforming of methane over unsupported nickel catalysts.* Journal of Power Sources, 2006. **158**(1): p. 485-496.

32. M. Ashrafi, T. ProÌˆll, C. Pfeifer, and H. Hofbauer, *Experimental Study of Model Biogas Catalytic Steam Reforming: 1. Thermodynamic Optimization.* Energy & Fuels, 2008. **22**(6): p. 4182-4189.

33. K. Hou and R. Hughes, *The kinetics of methane steam reforming over a Ni/α-Al_2O catalyst.* Chemical Engineering Journal, 2001. **82**(1-3): p. 311-328.

34. J.R.H. Ross and M.C.F. Steel, *Mechanism of the steam reforming of methane over a coprecipitated nickel-alumina catalyst.* Journal of the Chemical Society, Faraday Transactions 1: Physical Chemistry in Condensed Phases, 1973. **69**: p. 10-21.

35. J. Wei and E. Iglesia, *Structural requirements and reaction pathways in methane activation and chemical conversion catalyzed by rhodium.* Journal of Catalysis, 2004. **225**(1): p. 116-127.

36. A.K. Avetisov, J.R. Rostrup-Nielsen, V.L. Kuchaev, J.H. Bak Hansen, A.G. Zyskin, and E.N. Shapatina, *Steady-state kinetics and mechanism of methane reforming with steam and carbon dioxide over Ni catalyst.* Journal of Molecular Catalysis A: Chemical, 2010. **315**(2): p. 155-162.

37. J. Xu and G.F. Froment, *Methane steam reforming, methanation and water-gas shift: I. Intrinsic kinetics.* AIChE Journal, 1989. **35**(1): p. 88-96.

38. M.I. Temkin, *The Kinetics of Some Industrial Heterogeneous Catalytic Reactions*, in *Advances in Catalysis*, H.P. D.D. Eley and B.W. Paul, Editors. 1979, Academic Press. p. 173-291.

39. H.S. Bengaard, J.K. Nørskov, J. Sehested, B.S. Clausen, L.P. Nielsen, A.M. Molenbroek, and J.R. Rostrup-Nielsen, *Steam Reforming and Graphite Formation on Ni Catalysts.* Journal of Catalysis, 2002. **209**(2): p. 365-384.

40. *CRC Handbook of Chemistry and Physics*, ed. D.R. Lide. 1995-1996 76h Edition: CRC Press.

41. C.S. Lau, A. Tsolakis, and M.L. Wyszynski, *Biogas upgrade to syn-gas (H_2-CO) via dry and oxidative reforming.* International Journal of Hydrogen Energy, 2011. **36**(1): p. 397-404.

42. P. Forzatti and L. Lietti, *Catalyst deactivation.* Catalysis Today, 1999. **52**(2-3): p. 165-181.

43. J.A. Moulijn, A.E. van Diepen, and F. Kapteijn, *Catalyst deactivation: is it predictable?: What to do?* Applied Catalysis A: General, 2001. **212**(1-2): p. 3-16.

44. C.H. Bartholomew, *Mechanisms of catalyst deactivation.* Applied Catalysis A: General, 2001. **212**(1-2): p. 17-60.

45. P. Wynblatt and N.A. Gjostein, *Supported metal crystallites.* Progress in Solid State Chemistry, 1975. **9**: p. 21-58.

46. J. Sehested, J.A.P. Gelten, and S. Helveg, *Sintering of nickel catalysts: Effects of time, atmosphere, temperature, nickel-carrier interactions, and dopants.* Applied Catalysis A: General, 2006. **309**(2): p. 237-246.

47. C.H. Bartholomew and W.L. Sorensen, *Sintering kinetics of silica- and alumina-supported nickel in hydrogen atmosphere.* Journal of Catalysis, 1983. **81**(1): p. 131-141.

48. S.M. Hashemnejad and M. Parvari, *Deactivation and Regeneration of Nickel-Based Catalysts for Steam-Methane Reforming.* Chinese Journal of Catalysis. **32**(1): p. 273-279.

49. J.R. Rostrup-Nielsen, K. Pedersen, and J. Sehested, *High temperature methanation: Sintering and structure sensitivity.* Applied Catalysis A: General, 2007. **330**: p. 134-138.

50. A.C.S.C. Teixeira and R. Giudici, *Deactivation of steam reforming catalysts by sintering: experiments and simulation.* Chemical Engineering Science, 1999. **54**(15-16): p. 3609-3618.

51. P. Salagre, J.L.G. Fierro, F. Medina, and J.E. Sueiras, *Characterization of nickel species on several γ-alumina supported nickel samples.* Journal of Molecular Catalysis A: Chemical, 1996. **106**(1-2): p. 125-134.

52. K.O. Christensen, D. Chen, R. Lødeng, and A. Holmen, *Effect of supports and Ni crystal size on carbon formation and sintering during steam methane reforming.* Applied Catalysis A: General, 2006. **314**(1): p. 9-22.

53. M.A. Goula, A.A. Lemonidou, W. Grünert, and M. Baerns, *Methane partial oxidation to synthesis gas using nickel on calcium aluminate catalysts.* Catalysis Today, 1996. **32**(1-4): p. 149-156.

54. J. Chen, Q. Ma, T.E. Rufford, Y. Li, and Z. Zhu, *Influence of calcination temperatures of Feitknecht compound precursor on the structure of Ni-Al_2O_3 catalyst and the corresponding catalytic activity in methane decomposition to hydrogen and carbon nanofibers.* Applied Catalysis A: General, 2009. **362**(1-2): p. 1-7.

55. W.S. Brey and K.A. Krieger, *The Surface Area and Catalytic Activity of Aluminum Oxide.* Journal of the American Chemical Society, 2002. **71**(11): p. 3637-3641.

56. J. Sehested, J.A.P. Gelten, I.N. Remediakis, H. Bengaard, and J.K. Nørskov, *Sintering of nickel steam-reforming catalysts: effects of temperature and steam and hydrogen pressures.* Journal of Catalysis, 2004. **223**(2): p. 432-443.

57. E. Ruckenstein and X.D. Hu, *Mechanism of redispersion of supported metal catalysts in oxidative atmospheres.* Langmuir, 1985. **1**(6): p. 756-760.

58. N. Shah, D. Panjala, and G.P. Huffman, *Hydrogen Production by Catalytic Decomposition of Methane.* Energy & Fuels, 2001. **15**(6): p. 1528-1534.

59. A.L. Alberton, M.M.V.M. Souza, and M. Schmal, *Carbon formation and its influence on ethanol steam reforming over Ni/Al_2O_3 catalysts.* Catalysis Today, 2007. **123**(1-4): p. 257-264.

60. H.-S. Roh, K.-W. Jun, and S.-E. Park, *Methane-reforming reactions over Ni/Ce-ZrO_2/θ-Al2O3 catalysts.* Applied Catalysis A: General, 2003. **251**(2): p. 275-283.

61. O.-S. Joo and K.-D. Jung, *CH 4 Dry Reforming on Alumina-Supported Nickel Catalyst.* Bulletin of the Korean Chemical Society 2002. **23**(8): p. 1149-1153.

62. L. Piao, Y. Li, J. Chen, L. Chang, and J.Y.S. Lin, *Methane decomposition to carbon nanotubes and hydrogen on an alumina supported nickel aerogel catalyst.* Catalysis Today, 2002. **74**(1-2): p. 145-155.

63. V.R. Choudhary, S. Banerjee, and A.M. Rajput, *Hydrogen from step-wise steam reforming of methane over Ni/ZrO_2: factors affecting catalytic methane decomposition and*

gasification by steam of carbon formed on the catalyst. Applied Catalysis A: General, 2002. **234**: p. 259-270.

64. C.M. Finnerty, N.J. Coe, R.H. Cunningham, and R.M. Ormerod, *Carbon formation on and deactivation of nickel-based/zirconia anodes in solid oxide fuel cells running on methane.* Catalysis Today, 1998. **46**(2-3): p. 137-145.

65. P.G. Menon, *Coke on catalysts-harmful, harmless, invisible and beneficial types.* Journal of Molecular Catalysis, 1990. **59**(2): p. 207-220.

66. P.E. Nolan, David C. Lynch, and A.H. Cutler, *Carbon Deposition and Hydrocarbon Formation on Group VIII Metal Catalysts.* The Journal of Physical Chemistry B, 1998. **102**: p. 4165-4175.

67. C.H. Bartholomew, *Carbon Deposition in Steam Reforming and Methanation.* Catalysis Reviews, Science and Engineering, 1982. **24**: p. 67-112.

68. J. Rostrup-Nielsen and D.L. Trimm, *Mechanisms of carbon formation on nickel-containing catalysts.* Journal of Catalysis, 1977. **48**(1-3): p. 155-165.

69. M. Audier and M. Coulon, *Kinetic and microscopic aspects of catalytic carbon growth.* Carbon, 1985. **23**(3): p. 317-323.

70. I. Alstrup, *A new model explaining carbon filament growth on nickel, iron, and Ni-Cu alloy catalysts.* Journal of Catalysis, 1988. **109**(2): p. 241-251.

71. J.W. Snoeck, G.F. Froment, and M. Fowles, *Filamentous Carbon Formation and Gasification: Thermodynamics, Driving Force, Nucleation, and Steady-State Growth.* Journal of Catalysis, 1997. **169**(1): p. 240-249.

72. A.J.H.M. Kock, P.K. de Bokx, E. Boellaard, W. Klop, and J.W. Geus, *The formation of filamentous carbon on iron and nickel catalysts : II. Mechanism.* Journal of Catalysis, 1985. **96**(2): p. 468-480.

73. D. Chen, K.O. Christensen, E. Ochoa-Fernández, Z. Yu, B. Tøtdal, N. Latorre, A. Monzón, and A. Holmen, *Synthesis of carbon nanofibers: effects of Ni crystal size during methane decomposition.* Journal of Catalysis, 2005. **229**(1): p. 82-96.

74. W.L. Holstein, *The Roles of Ordinary and Soret Diffusion in the Metal-Catalyzed Formation of Filamentous Carbon.* Journal of Catalysis, 1995. **152**(1): p. 42-51.

75. J.-H. Kim, D.J. Suh, T.-J. Park, and K.-L. Kim, *Effect of metal particle size on coking during CO_2 reforming of CH_4 over Ni-alumina aerogel catalysts.* Applied Catalysis A: General, 2000. **197**(2): p. 191-200.

76. H. He and J.M. Hill, *Carbon deposition on Ni/YSZ composites exposed to humidified methane.* Applied Catalysis A: General, 2007. **317**(2): p. 284-292.

77. P.E. Nolan, D.C. Lynch, and A.H. Cutler, *Graphite encapsulation of catalytic metal nanoparticles.* Carbon, 1996. **34**(6): p. 817-819.

78. R.T. Yang and J.P. Chen, *Mechanism of carbon filament growth on metal catalysts.* Journal of Catalysis, 1989. **115**(1): p. 52-64.

79. U. Narkiewicz and M. Podsiadly, *Synthesis of carbon-encapsulated nickel nanoparticles.* Applied Surface Science, 2010. **256**(17): p. 5249-5253.

80. M.J. Wozniak, P. Wozniak, M. Bystrzejewski, S. Cudzilo, A. Huczko, P. Jelen, W. Kaszuwara, J.A. Kozubowski, H. Lange, M. Leonowicz, and M. Lewandowska-Szumiel, *Magnetic nanoparticles of Fe and Nd-Fe-B alloy encapsulated in carbon shells for drug delivery systems: Study of the structure and interaction with the living cells.* Journal of Alloys and Compounds, 2006. **423**(1-2): p. 87-91.

81. P.J.F. Harris and S.C. Tsang, *Encapsulating uranium in carbon nanoparticles using a new technique.* Carbon, 1998. **36**(12): p. 1859-1861.

82. J.R. Rostrup-Nielsen, *Industrial relevance of coking.* Catalysis Today, 1997. **37**(3): p. 225-232.

83. J.d.S. Lisboa, D.C.R.M. Santos, F.B. Passos, and F.B. Noronha, *Influence of the addition of promoters to steam reforming catalysts.* Catalysis Today, 2005. **101**(1): p. 15-21.

84. S. Therdthianwong, A. Therdthianwong, C. Siangchin, and S. Yongprapat, *Synthesis gas production from dry reforming of methane over Ni/Al_2O_3 stabilized by ZrO_2.* International Journal of Hydrogen Energy, 2008. **33**(3): p. 991-999.

85. A.S.A. Al-Fatish, A.A. Ibrahim, A.H. Fakeeha, M.A. Soliman, M.R.H. Siddiqui, and A.E. Abasaeed, *Coke formation during CO_2 reforming of CH_4 over alumina-supported nickel catalysts.* Applied Catalysis A: General, 2009. **364**(1-2): p. 150-155.

86. N. Srisiriwat, S. Therdthianwong, and A. Therdthianwong, *Oxidative steam reforming of ethanol over Ni/Al_2O_3 catalysts promoted by CeO_2, ZrO_2 and CeO_2-ZrO_2.* International Journal of Hydrogen Energy, 2009. **34**(5): p. 2224-2234.

87. Y.-H. Chin, D.L. King, H.-S. Roh, Y. Wang, and S.M. Heald, *Structure and reactivity investigations on supported bimetallic AuNi catalysts used for hydrocarbon steam reforming.* Journal of Catalysis, 2006. **244**(2): p. 153-162.

88. L. Guczi, G. Stefler, O. Geszti, I. Sajó, Z. Pászti, A. Tompos, and Z. Schay, *Methane dry reforming with CO_2: A study on surface carbon species.* Applied Catalysis A: General, 2010. **375**(2): p. 236-246.

89. N.C. Triantafyllopoulos and S.G. Neophytides, *Dissociative adsorption of CH_4 on NiAu/YSZ: The nature of adsorbed carbonaceous species and the inhibition of graphitic C formation.* Journal of Catalysis, 2006. **239**(1): p. 187-199.

90. J. Requies, M.A. Cabrero, V.L. Barrio, J.F. Cambra, M.B. Güemez, P.L. Arias, V. La Parola, M.A. Peña, and J.L.G. Fierro, *Nickel/alumina catalysts modified by basic oxides for the production of synthesis gas by methane partial oxidation.* Catalysis Today, 2006. **116**(3): p. 304-312.

91. T. Horiuchi, K. Sakuma, T. Fukui, Y. Kubo, T. Osaki, and T. Mori, *Suppression of carbon deposition in the CO_2-reforming of CH_4 by adding basic metal oxides to a Ni/Al_2O_3 catalyst.* Applied Catalysis A: General, 1996. **144**(1-2): p. 111-120.

92. C. Crisafulli, S. Scirè, S. Minicò, and L. Solarino, *Ni-Ru bimetallic catalysts for the CO_2 reforming of methane.* Applied Catalysis A: General, 2002. **225**(1-2): p. 1-9.

93. J.A.C. Dias and J.M. Assaf, *Autoreduction of promoted Ni/γ-Al_2O_3 during autothermal reforming of methane.* Journal of Power Sources, 2005. **139**(1-2): p. 176-181.

94. J.A.C. Dias and J.M. Assaf, *Autothermal reforming of methane over Ni/γ-Al_2O_3 catalysts: the enhancement effect of small quantities of noble metals.* Journal of Power Sources, 2004. **130**(1-2): p. 106-110.

95. N. Laosiripojana, W. Sangtongkitcharoen, and S. Assabumrungrat, *Catalytic steam reforming of ethane and propane over CeO_2-doped Ni/Al_2O_3 at SOFC temperature: Improvement of resistance toward carbon formation by the redox property of doping CeO_2.* Fuel, 2006. **85**(3): p. 323-332.

96. J. Xu, C.M.Y. Yeung, J. Ni, F. Meunier, N. Acerbi, M. Fowles, and S.C. Tsang, *Methane steam reforming for hydrogen production using low water-ratios without carbon formation over ceria coated Ni catalysts.* Applied Catalysis A: General, 2008. **345**(2): p. 119-127.

97. N. Laosiripojana, W. Sutthisripok, and S. Assabumrungrat, *Synthesis gas production from dry reforming of methane over CeO_2 doped Ni/Al_2O_3: Influence of the doping ceria on the resistance toward carbon formation.* Chemical Engineering Journal, 2005. **112**(1-3): p. 13-22.

98. E.B. Maxted, *The Poisoning of Metallic Catalysts*, in *Advances in Catalysis*, W.G. Frankenburg, et al., Editors. 1951, Academic Press. p. 129-178.

99. M. Ashrafi, C. Pfeifer, T. Pröll, and H. Hofbauer, *Experimental Study of Model Biogas Catalytic Steam Reforming: 2. Impact of Sulfur on the Deactivation and Regeneration of Ni-Based Catalysts.* Energy & Fuels, 2008. **22**(6): p. 4190-4195.

100. J. Srinakruang, K. Sato, T. Vitidsant, and K. Fujimoto, *Highly efficient sulfur and coking resistance catalysts for tar gasification with steam.* Fuel, 2006. **85**(17-18): p. 2419-2426.

101. C. Laycock, J. Staniforth, and R.M. Ormerod, *Biogas as a fuel for solid oxide fuel cells and synthesis gas production: effects of ceria-doping and hydrogen sulfide on the performance of nickel-based anode materials.* Dalton Transactions, 2011. **40**: p. 5494.

102. J. Hepola and P. Simell, *Sulphur poisoning of nickel-based hot gas cleaning catalysts in synthetic gasification gas: I. Effect of different process parameters.* Applied Catalysis B: Environmental, 1997. **14**(3-4): p. 287-303.

103. C.H. Bartholomew, P.K. Agrawal, J.R. Katzer, and H.P.a.P.B.W. D.D. Eley, *Sulfur Poisoning of Metals*, in *Advances in Catalysis*. 1982, Academic Press. p. 135-242.

104. P. Mare´cot, E. Paraiso, J.M. Dumas, and J. Barbier, *Deactivation of nickel catalysts by sulphur compounds: II. Chemisorption of hydrogen sulphide.* Applied Catalysis A: General, 1992. **80**(1): p. 89-97.

105. J.R. Rostrup-Nielsen, *Chemisorption of hydrogen sulfide on a supported nickel catalyst.* Journal of Catalysis, 1968. **11**(3): p. 220-227.

106. I.E. Den Besten and P.W. Selwood, *The chemisorption of hydrogen sulfide, methyl sulfide, and cyclohexene on supported nickel catalysts.* Journal of Catalysis, 1962. **1**(2): p. 93-102.

107. J.M. Saleh, C. Kemball, and M.W. Roberts, *Interaction of hydrogen sulphide with nickel, tungsten and silver films.* Transactions of the Faraday Society, 1961. **57**: p. 1771-1780.

108. C.F. Ng and G.A. Martin, *Poisoning of Ni/SiO_2 catalysts with H_2S: Chemisorption of H_2, CO, C_6H_6, and C_2H_2 studied by magnetic methods.* Journal of Catalysis, 1978. **54**(3): p. 384-396.

109. J. Hepola and P. Simell, *Sulphur poisoning of nickel-based hot gas cleaning catalysts in synthetic gasification gas: II. Chemisorption of hydrogen sulphide.* Applied Catalysis B: Environmental, 1997. **14**(3-4): p. 305-321.

110. J.R. Rostrup-Nielsen, *Some principles relating to the regeneration of sulfur-poisoned nickel catalyst.* Journal of Catalysis, 1971. **21**(2): p. 171-178.

111. D.J. Fullerton, A.V.K. Westwood, R. Brydson, M.V. Twigg, and J.M. Jones, *Deactivation and regeneration of Pt/γ-alumina and Pt/ceria-alumina catalysts for methane combustion in the presence of H_2S.* Catalysis Today, 2003. **81**(4): p. 659-671.

112. J.R. Rostrup-Nielsen, *Sulfur-passivated nickel catalysts for carbon-free steam reforming of methane.* Journal of Catalysis, 1984. **85**(1): p. 31-43.

113. H.C. Dibbern, P. Olesen, J.R. Rostrup-Nielsen, P.B. Tottrup, and N.R. Udengaard, *Make low H_2/CO syngas using sulfur passivated reforming.* Hydrocarbon Processing, 1986. **65**: p. 71 - 74.

114. J.R. Rostrup-Nielsen, I.B. Alstrup, and J.W. Ward, *Ensemble Control By Sulfur Poisoning of Nickel Catalysts for Steam Reforming*, in *Studies in Surface Science and Catalysis*. 1988, Elsevier. p. 725-732.

115. F. Abild-Pedersen, O. Lytken, J. Engbæk, G. Nielsen, I. Chorkendorff, and J.K. Nørskov, *Methane activation on Ni(1 1 1): Effects of poisons and step defects.* Surface Science, 2005. **590**(2-3): p. 127-137.

116. C. Xie, Y. Chen, Y. Li, X. Wang, and C. Song, *Influence of sulfur on the carbon deposition in steam reforming of liquid hydrocarbons over CeO_2-Al_2O_3 supported Ni and Rh catalysts.* Applied Catalysis A: General, 2011. **394**(1-2): p. 32-40.

117. S.L. Lakhapatri and M.A. Abraham, *Deactivation due to sulfur poisoning and carbon deposition on Rh-Ni/Al_2O_3 catalyst during steam reforming of sulfur-doped n-hexadecane.* Applied Catalysis A: General, 2009. **364**(1-2): p. 113-121.

3 Methodology

3.1 Catalyst preparation

A total of ten alumina supported nickel catalyst samples were prepared, Ni/Al_2O_3, with a nickel loading of 20 wt % and a set which were doped with 5 mol % gold, again with a nickel loading of 20 wt %. Both sets of catalysts were prepared by wet impregnation, and subsequently subjected to calcination and reduction, discussed in Section 3.2.

Nickel oxide (NiO) samples used as standards for characterisation (Chapter 4) were prepared by calcination of nickel nitrate hexahydrate ($Ni(NO_3)_2.6H_2O$), using the calcination procedure discussed in Figure 3.2, Section 3.2. Nickel samples used as standards for characterisation were prepared by reduction of standard NiO, as described in Section 3.6.2.

3.1.1 20 wt % Ni/Al_2O_3

60.00 g 20 wt % Ni/Al_2O_3 was prepared. 59.32 g of nickel nitrate hexahydrate, Ni $(NO_3)_2.6H_2O$, (Fischer Scientific) was dissolved into solution. Alpha aluminium oxide, α-Al_2O_3, (Alfa Aesar, 99.98 %, < 1 µm APS powder, Surface area 10 $m^2\ g^{-1}$) was dried at 100 °C overnight to remove any physically bound water. 48.00 g of this dried aluminium oxide was suspended in the minimal amount of water and added to the Ni $(NO_3)_2$ solution. The mixture was stirred whilst gently heated at *ca*. 80 °C. All samples were dried in ceramic boats at 100 °C overnight. The samples were then activated by calcination and reduction, as discussed in Sections 3.2 and 3.6.2 respectively. Following calcination, the catalyst was ground using a pestle and mortar and sieved to a particle size <106 µm using a stainless steel Laboratory Test Sieve (BS410/1986).

3.1.2 5 mol % Au doped 20 wt % Ni/Al_2O_3

60.00 g of 5 mol % Au 20 wt % Ni/Al_2O_3 was prepared. 59.32 g of nickel nitrate hexahydrate, $Ni(NO_3)_2.6H_2O$, (Fischer Scientific) was dissolved into solution and 48.00 g of dried alpha aluminium oxide, α-Al_2O_3, (Alfa Aesar) was added, as above. Gold was added in the form of gold chloride trihydrate, $HAuCl_4.3H_2O$, (Acros Organics) to a level of 5 mol % with respect to the nickel content, which equated to 4.06 g. This was suspended in a minimal amount of water and added to the $Ni(NO_3)_2$ solution. The mixture was stirred whilst gently heated at *ca*. 80 °C. All samples were dried in ceramic boats at 100 °C overnight and then activated by calcination and reduction, as discussed in Sections 3.2 and 3.6.2 respectively. Following calcination, the catalysts were ground using a pestle and mortar and were sieved to a particle size <106 μm using stainless steel Laboratory Test Sieve (BS410/1986).

3.2 Catalyst calcination

All the catalyst precursor samples were calcined in air at elevated temperatures in order to burn off any impurities and residual organic matter, and convert nickel nitrate to nickel oxide. Following preparation, as described above, the samples were loaded into alumina ceramic boats (unglazed alumina ceramic combustion boat, maximum heat 1250 °C, 8.5 cm x 1 cm x 1 cm, Fisher Scientific), Figure 3.1. The samples were then dried overnight in an oven followed by calcination in a furnace (Carbolite Furnace RHF 1600).

Figure 3.1: Catalyst precursor sample loaded into ceramic boat, following overnight drying in oven, prior to activation by calcination

A standard calcination procedure was used for all samples. The samples were heated to 500 °C at a heating rate of 1 °C min^{-1} and then to the desired calcination temperature (600 °C, 700 °C, 800 °C, 900 °C or 1000 °C) at 5 °C min^{-1}. This temperature was then held for 2 hours. Following the high temperature calcination, the temperature was reduced to room temperature at 5 °C min^{-1}. A temperature-programmed representation of the calcination treatments are shown in Figure 3.2.

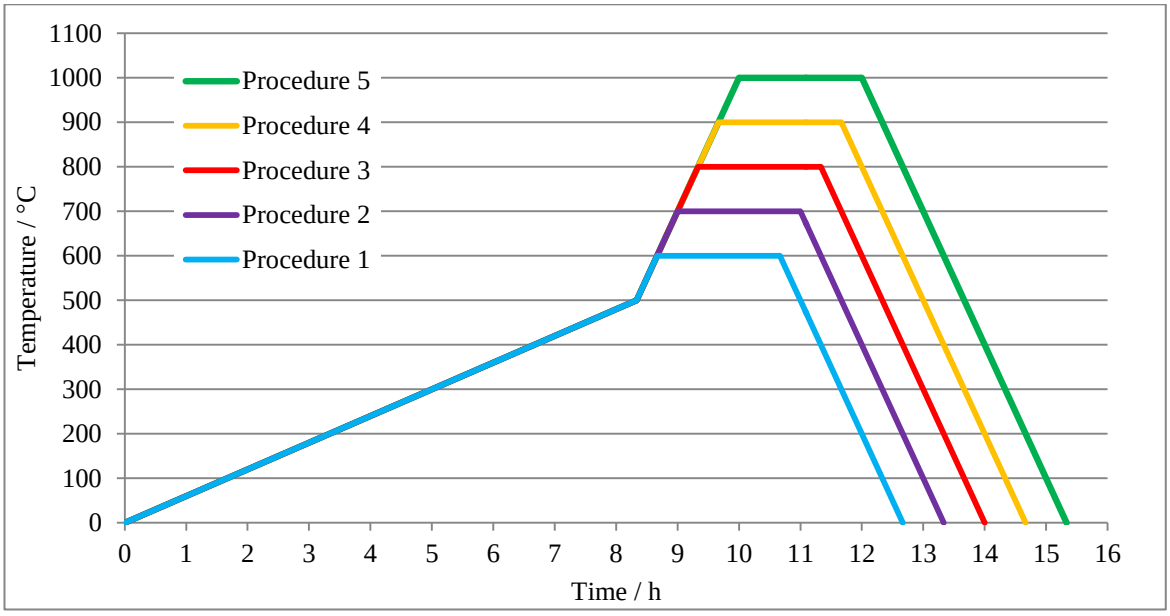

Figure 3.2: Temperature-programmed representation of the calcination treatments for the catalyst samples

The 20 wt % Ni/Al_2O_3 sample was calcined at five different calcination temperatures, 600 °C, 700 °C, 800 °C, 900 °C and 1000 °C, denoted hereon as Ni/Al_2O_3 (600), Ni/Al_2O_3 (700), Ni/Al_2O_3 (800), Ni/Al_2O_3 (900) and Ni/Al_2O_3 (1000), respectively.

The 5 mol % Au doped 20 wt % Ni/Al_2O_3 was calcined, to the same temperatures as the 20 wt % Ni/Al_2O_3 catalyst, 600 °C, 700 °C, 800 °C, 900 °C and 1000 °C, denoted hereon as Au-Ni/Al_2O_3 (600), Au-Ni/Al_2O_3 (700), Au-Ni/Al_2O_3 (800), Au-Ni/Al_2O_3 (900) and Au-Ni/Al_2O_3 (1000), respectively.

Prior to any catalytic measurements, all samples were reduced using the procedure discussed in Section 3.6.2.

3.3 Catalytic test apparatus

All catalytic measurements were undertaken on a custom built catalytic test system shown schematically in Figure 3.3. The apparatus consisted of three main sections: gas manifold, catalytic micro-reactor and gas analysis system. The gas manifold comprised of a gas tight stainless steel manifold, which was fed by hydrogen, methane, carbon dioxide, carbon monoxide, oxygen, helium, and hydrogen sulfide. All gases were of BOC high purity scientific grade and the H_2S was delivered to the sample in a helium carrier (10 ppm). Gases were fed to the reactor via the gas manifold. $^1/_8$ inch stainless steel tubing was used throughout the manifold. 13X (10 Å) molecular sieve traps were used to dry all the gases. Sulfur was introduced to the gas feed through the oxygen line, bypassing the molecular sieve traps to ensure complete gas flow and no adsorption of sulfur. Each gas line was fitted with mass flow controllers (Mass-Stream D-5111) to enable complete control over reactant gas flow and any mixture of gases to be attained, up to a total flow of 20 ml min^{-1}. Precision low-flow stainless steel metering valves (Swagelok) were used to control the inert helium flow (valve 1). Helium was used as a carrier gas, with a typical flow rate of 18 ml min^{-1} employed.

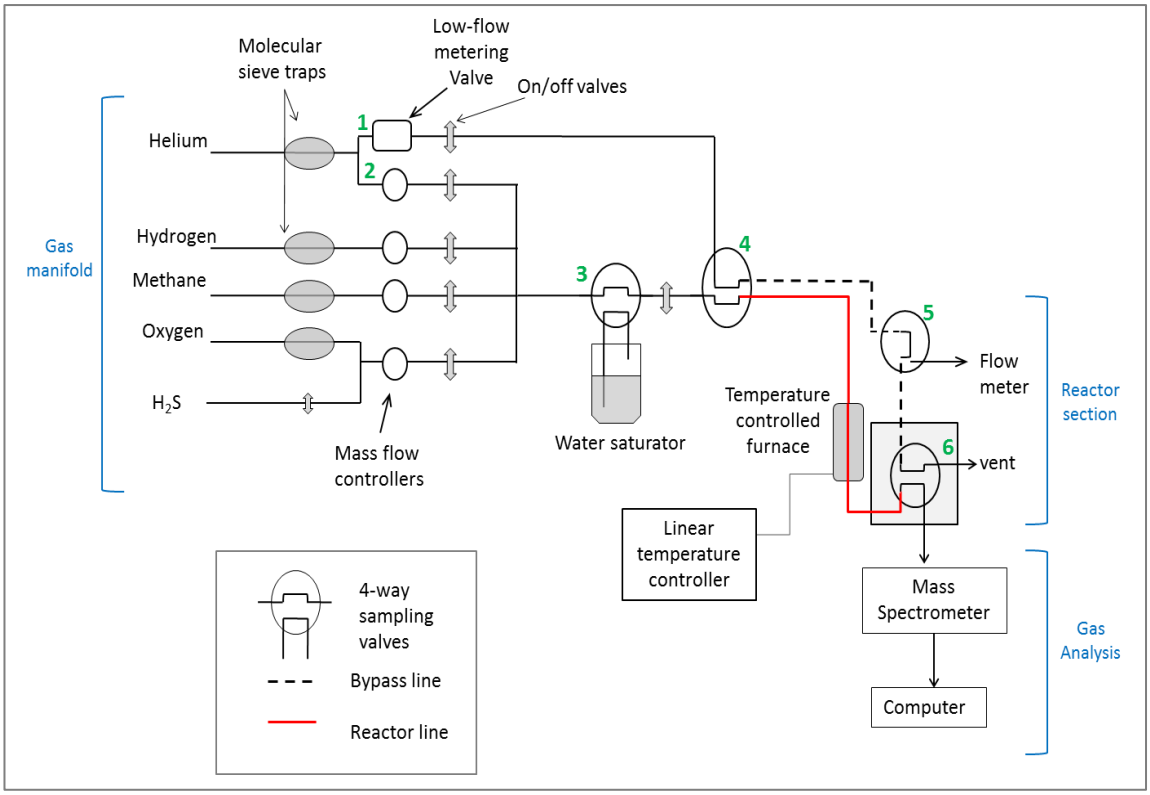

Figure 3.3: Schematic representation of custom built catalytic test apparatus

The reactant gas mixtures were fed to a quartz reactor tube, in which the catalyst sample was housed (see Section 3.4). The reactor tube was connected to a heated quartz capillary (150 °C) which, in turn, was connected to a continually sampling gas analysis system containing a quadrupole mass spectrometer (MKS Spectra MiniLab LM80), allowing real time analysis of up to 12 gas masses simultaneously. The MiniLab is a bench top, on-line gas analysis system housing a Microvision Plus quadrupole mass spectrometer, fitted with a turbomolecular pump, backed by a dry diaphragm pump. The system was run at an elevated temperature of 80 °C to prevent condensation of vapours in the vacuum chamber. Gas entered the vacuum system via a capillary inlet, with the diaphragm pump also serving as a by-pass pump for the capillary inlet.

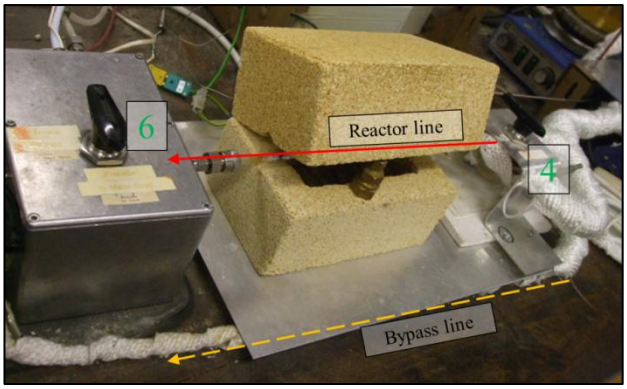

Figure 3.4: Photograph showing the layout of the reactor and bypass line in relation to the temperature controlled furnace and the 4-way sampling valves (labelled 4 and 6, corresponding to Figure 3.3)

The test system was designed to always have two parallel gas flows, one through the bypass (dashed line in Figure 3.4) and one through the reactor line (red line in Figure 3.4). Valve 1 controlled the non-carrier gas helium, allowing a constant flow of inert gas through either the reactor or bypass line (selected using the 4-way sampling valve 4). This allowed an inert gas flow to pass over the catalyst at all times during stabilisation, and the reactant gas composition to be changed and precisely monitored through the bypass line. The reactant carrier gas, helium, was controlled by a mass flow controller and valve 2. All other gases were independently controlled by mass flow controllers and on/off valves.

Steam could be introduced into the reactive gas flow via a 4-way sampling valve (valve 3), connected to the temperature controlled water saturator. This allowed the reactant gas stream to flow through the water saturator, allowing a continuous flow of water vapour to be delivered. The water saturator consisted of a 15 cm length of stainless steel tubing of diameter $^{1}/_{8}$ inches sealed at one end, filled with deionised water. The top of the saturator comprised of a Swagelok T-junction seal, through which the stainless steel reactant pipe passed to the bottom of the saturator. This ensured that all reactant gases bubbled through the water before exiting via the remaining junction, back to the 4-way valve. The water saturator was placed in an oil bath mounted on a temperature

controlled hot plate, enabling the temperature and hence steam concentrations to be accurately controlled and maintained.

Gas products leaving either the reactor tube or the bypass could be directed to the vent or the mass spectrometer, using the 4-way sampling valve (valve 6). Valve 6 was housed in a post-reactor heating unit (hot box), in order to prevent any water condensing before reaching the analysis chamber. The hot box was constructed using a metal box, housing a ceramic brick with a nichrome wound filament, similar to that used for the reactor furnace. This was independently run at *ca.* 100 °C. Reactant gases could be directed through the bypass to achieve specific reactant gas mixture compositions before being directed through the reactor tube and passed over the catalyst. Exact total flow rates, were determined by directing gases to the bubble flow meter, value 5. All stainless steel tubes of the manifold and reactor system were independently heated using a transformer, heater wire and insulated using woven glass webbing (RS 5364028), ensuring that the steam remained in the gas phase throughout the whole manifold with no cold spots.

The home-built ceramic furnace housing the reactor tube had dimensions of 18 cm x 11.5 cm x 15 cm and was temperature controlled via a K-type thermocouple connected to a Eurotherm 2416 programmable temperature controller. The thermocouple was inserted into the ceramic furnace, located outside the quartz reactor tube wall at the position corresponding to the middle of the catalyst bed. The furnace consists of two hollowed out (depth of *ca*. 2 cm) ceramic bricks of (single brick dimension 18 cm x 11.5 cm x 7.5 cm). Both bricks contained nickel/chromium (nichrome) wire (Ni80/Cr20, temper annealed, diameter 0.5 mm, Advent) heating filaments of 5.32 Ω m^{-1} resistance. The nichrome filament in each brick was wound around 6 hollow alumina tubes of 4.5 cm in length and 0.5 cm diameter, which were placed along the hollowed area of the brick, as shown in Figure 3.5. Each alumina tube was held in place by two U-shaped metal clips pressed into the furnace brick. The top and bottom furnace were wired together with the filament in series. Using this set-up it was possible to ramp the furnace to a temperature of 1000 °C, at heating rates between 1 and 20 °C min^{-1}, or to maintain a stable temperature up to 1000 °C.

Figure 3.5: Custom built ceramic furnace displaying heating filaments and quartz reactor tube

Where the quartz reactor tube was connected to the system by stainless steel ultra-torr vacuum fittings (Swagelok) outside of the heated furnace, an independent heating line was installed to ensure no cold spots occurred during investigations involving steam (Heating tape HT9 with a maximum temperature of 450 °C, resistance wires covered in a glass fibre fabric 25 mm width 0.6 m length, Fischer Scientific HEF445070W).

The mass spectrometer used for gas detection was interfaced to a computer running Residual Gas Analysis (RGA) for Windows. During analysis, the quadrupole mass spectrometer was able to monitor 12 masses simultaneously in fast scan mode. The interval between stored scans could be altered allowing suitable data storage depending on the length and type of reaction being undertaken. Any data obtained was then exported to Microsoft Excel (Windows) for analysis and processing.

3.4 Reactor tube preparation

For catalytic investigations, each catalyst was loaded into a quartz reactor tube 25 cm in length, 0.7 cm external diameter and 0.5 cm internal diameter (Multi-Lab). A small amount of quartz wool (Fischer-scientific) was firmly pushed into the centre of the reactor tube, corresponding to the point in which the thermocouple enters the furnace. The reactor tube was then weighed. The catalyst was then loaded into the reactor, resting on the quartz wool. The reactor tube was re-weighed in order to

determine the actual weight of catalyst sample. Approximately 50 mg (± 0.2 mg) of catalyst was used during catalytic reactions, unless otherwise stated. Following this, another quantity of quartz wool was inserted, ensuring that the catalyst was held in the centre of the reactor tube, as shown in Figure 3.6.

Figure 3.6: Sample loaded into quartz reactor tube, placed between quartz wool

Quartz wool was used to ensure that no catalyst movement occurred during reactions and accurate positioning of the catalyst was gained, with adequate porosity to ensure free flow of the reactant gases. A large amount of quartz wool was required for reactions involving steam, as shown in Figure 3.6, due to the pressure created during such reactions. In such cases where smaller amounts of quartz wool were used, the additional pressure when reactive gases were passed over the furnace resulted in catalyst movement, to a position outside the furnace. Once prepared, the reactor tube was connected to the gas manifold system.

3.5 Quadrupole mass spectrometer

Mass spectrometry is a technique widely used for determining relative atomic or molecular masses. Quadrupole mass spectrometery was first realised by Wolfgang Paul in the 1950's, for which he received a Nobel prize in 1989 [1]. Quadrupole mass spectrometers (QMS) contain a quadrupole mass filter, which consists of four metal rods held in alignment with one another allowing the ions to be suffused in both an electric and radio frequency field as they pass along the rods. The use of a QMS allows the advantage of selected ion monitoring, allowing ions of specific m/z values to traverse the analyser and rejecting all others. This increases sensitivity when detecting low concentrations of compounds. Selected ion monitoring allows only the most intense and most

characteristic ions to pass through the analyser more often, so increasing the amount of time that the analyser focuses on given values of m/z. This substantially increases the amount of specific ions that reach the detector and so a lower limit of detection can be reached.

3.5.1 Calibration

Gases entering the mass spectrometer were not ionised equally. Therefore, in order to make a quantitative interpretation of the data the sensitivity of the mass spectrometer towards each mass signal was determined. These were then normalised with respect to oxygen, mass 32, in terms of relative ionisation sensitivities, oxygen was assigned a sensitivity of 1. Thus, in order to determine the sensitivity towards methane, for example, oxygen and methane were directed towards the mass spectrometer at equal flow rates of 1 ml min^{-1}. The relative gas pressure signals produced by the gases in the mass spectrometer were noted and the sensitivity of methane compared to oxygen was calculated, as shown in Equation 3.1.

$$\textbf{Sensitivity of methane} = \frac{\textbf{Methane signal}}{\textbf{Oxygen signal}} \qquad \textbf{(3.1)}$$

Different multiples of flow rates of each gas were directed to the mass spectrometer, in order to obtain a range of sensitivities, from which an average could be taken. For example, if the methane flow rate were doubled to 2 ml min^{-1} and oxygen flow rate kept at 1 ml min^{-1}, the relative sensitivity would be calculated as shown in Equation 3.2. This was undertaken for helium, methane, hydrogen, carbon monoxide and carbon dioxide.

$$\textbf{Sensitivity of methane} = \frac{\textbf{Methane signal/2}}{\textbf{Oxygen signal}} \qquad \textbf{(3.2)}$$

Relative sensitivities, for the above mentioned gases and water, were also gained from sensitivity experiments calculated in a similar way as described above. These reactions involved monitoring the reaction progress over a range of temperatures. The gases entering and the final concentration of gases exiting the reactor were then normalised. For example, in order to gain relative

sensitivities of hydrogen and water, hydrogen and oxygen were passed over the furnace while the temperature was linearly ramped up to 1000 °C and held at this temperature until all gases had stabilised. The product gases were compared to those entering the reactor and relative sensitivities calculated. This was done for reactions involving oxygen and methane, hydrogen, oxygen and carbon monoxide, hydrogen and oxygen.

All relative sensitivities gained were used for data analysis and processing, see Section 3.5.2.

The amount of carbon produced during a catalytic reaction was also calibrated. Temperature-programmed oxidation (TPO) reactions on known amounts of carbon were undertaken, as discussed in Section 3.6.5. The sum of carbon dioxide and carbon monoxide produced during each reaction was tabulated and a carbon calibration graph was obtained, an example of which is shown in Figure 3.7. The carbon dioxide and carbon monoxide peak gained during a post-reaction TPO of the catalyst sample was then quantitatively compared to the carbon calibration graph. This allowed an accurate mass of deposited carbon to be determined, for specific reactions undertaken.

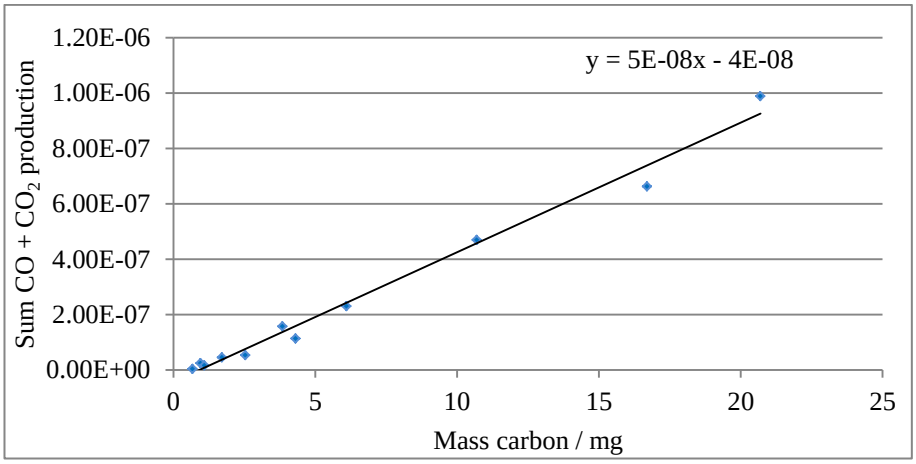

Figure 3.7: Example carbon calibration graph, showing the sum of carbon monoxide and carbon dioxide produced against mass of carbon

3.5.2 Data analysis

Upon completion of a reaction, any data stored on the computer interfaced to the mass spectrometer, was exported to a separate computer for analysis in Windows Microsoft Excel. Data was time disk stored in the form of relative signal intensities for each gas monitored. The relative sensitivities for each gas determined during calibration, as discussed above, were then applied to the relative gas signal intensities in order to gain the actual respective amounts of each gas detected by the mass spectrometer. A helium correction was also applied to all relative signal intensities. Helium was used as a carrier gas and its flow rate and signal intensity varied throughout the reaction, therefore, this change needed to be taken into consideration when analysing data. With this in mind, the helium correction was determined using the initial helium signal compared to subsequent values. This difference was then applied to all signal values for all reactive gases. Equation 3.3 shows an example of how raw partial pressures of gases were corrected for using relative sensitivity and helium correction values, using methane as an example.

$$\textbf{Corrected } PCH_4 = \frac{PCH_4}{\text{Sensitivity } CH_4} \times \textbf{helium correction} \qquad (3.3)$$

This data, once relative sensitivities and helium correction were applied, was then plotted against time or temperature, depending on whether the reaction undertaken was isothermal or temperature-programmed, in order to determine reactive gas ratios and any changes throughout the course of the reaction.

3.6 Catalytic analysis using quadrupole mass spectrometry

3.6.1 Temperature-programmed reactions

Temperature-programmed reactions, in heterogeneous materials chemistry, allow changes in the bulk and/or surface of the catalyst to be obtained and reaction progress to be monitored over a temperature range.

One such example of a widely used temperature-programmed technique is temperature-programmed reduction. Temperature-programmed reduction (TPR) reactions ensure that a catalyst has a fully reduced metal species, allowing maximum catalytic activity to be achieved. A reducing gas, such as methane or hydrogen is passed over the catalyst bed, while the temperature is raised linearly with time. A TPR profile is gained by measuring hydrogen consumption and water evolution as a function of temperature. TPR profiles can be used to help determine the chemical nature and environment of the catalyst surface, whilst the area under the TPR peak can represent the concentration of active components on the catalyst surface. The reduction of Ni^{2+} by hydrogen (Reaction 3.9) can occur over a wide range of temperatures from 0 to 1000 °C depending on the interaction between nickel and the support.

$$\mathbf{NiO + H_2 \rightarrow Ni + H_2O} \qquad \mathbf{(3.9)}$$

In 1924, Benton and Emmett [2] reported the first measurement of bulk NiO reduction, they proposed a mechanism for the reduction process that implied the rate of reduction was proportional to the interface area, where the interface area present depends not only on the extent to which the reaction has preceded but also the manner in which it begins. Benton and Emmett investigated reduction reactions through the collection of water at specific time intervals during the reaction. However in 1930, Taylor and Starkeweather [3] were one of the first to investigate reduction of metal oxides by following the rate of reduction by measuring the volume of hydrogen consumption, a technique widely used today. Early researchers [4, 5] have shown the importance of appropriate experimental conditions during TPR reactions, such as the amount of reducible species, carrier gas flow rate, hydrogen concentration and heating rate. A detailed description of the TPR theory is presented by Gentry et al. [4].

Another example of an important temperature-programmed technique is temperature-programmed oxidation. Temperature-programmed oxidation (TPO) reactions (Reaction 3.10) undertaken following reforming reactions, are widely used to quantify the amount of carbon deposited on a catalyst surface during a reforming reaction [6-8].

$$XO_2 + YC_{surface} \rightarrow WCO_2 + ZCO \qquad (3.10)$$

The temperature at which the carbon is removed during a TPO reaction can provide an insight into the nature of the carbon deposited on the catalyst surface [9], as discussed in Chapter 2.

3.6.2 Temperature-programmed reduction

Temperature-programmed reduction (TPR) reactions allowed catalyst pre-treatment prior to catalytic reactions, whist also allowing the nature of the catalyst and catalytic properties to be investigated.

TPR reactions were undertaken prior to catalytic reforming reactions, typically on 50 mg ± 0.2 mg catalyst. Catalyst reducibility investigations were undertaken using the same reaction procedures used for pre-catalytic reactions, as discussed in Chapter 4 and 5.

A mixture of 10 % H_2 in helium, total flow 20 ml min^{-1}, was passed over the catalyst while the temperature was linearly ramped at 10 °C min^{-1}, to 1000 °C. Unless otherwise stated, following this, the temperature was allowed to settle back to room temperature ensuring hydrogen was passed over the catalyst. In some cases, where stated, the temperature was held at 1000 °C for a period of time, allowing complete catalyst reduction, until hydrogen consumption and water evolution had ceased. Following TPR reactions, hydrogen was passed over the catalyst until the temperature settled below 200 °C, to ensure the catalyst was not re-oxidised. After cooling, the sample was not exposed to air and kept in a flow of helium at room temperature until further reactions were performed. A profile of hydrogen consumption and water evolution leaving the reactor, against temperature was plotted.

3.6.3 Temperature-programmed reactions of methane and steam

Temperature-programmed reactions of methane and steam were carried out over 50 mg (± 0.2 mg) of pre-reduced catalyst sample. A mixture of methane, steam and helium was used with the steam

flow adjusted using the heated saturator. An approximate methane flow rate of 2 ml min^{-1} was employed, with the total flow rate 20 ml min^{-1} excluding steam flow. Gas ratios and approximate saturator temperatures are shown below in Table 3.1.

Table 3.1: Gas reactant ratios and corresponding saturator temperatures

Methane to steam gas ratio		**Approximate saturator temperature / °C**
2:1	Methane-rich	34
1:1	Stoichiometric	38

Reactions were carried out with a reverse temperature ramp, from 1000 °C to room temperature at a rate of 5 °C min^{-1}. This ensured that the catalyst was not re-oxidised by the steam present in a forward temperature-programmed reaction, so affecting catalytic activity (as discussed in Appendix B). Reactant gas ratios of methane and steam were gained through the bypass line. Once the furnace temperature reached 1000 °C, reactants were passed to the reactant line over the catalyst, allowed to settle and the reaction temperature ramp initiated. Following reactions, inert helium was passed over the catalyst while the temperature was held at room temperature. Plots of gas partial pressures against temperature were gained.

Parameters concerning the description of reaction gas ratios (methane/steam) in the reformer are defined as follows, for corrected gas pressure values:

$$\textbf{methane to steam ratio} = \frac{\textbf{Pin } CH_4}{\textbf{Pin } H_2O} \qquad \textbf{(3.11)}$$

Data gained allowed reaction activity calculations to be made, including conversion, yield and product ratio information for reaction profiles and product gases. CH_4 conversion, H_2 yield, CO selectivity and gas hourly space velocity (GHSV) are defined as follows:

$$\mathbf{CH_4\ Conversion\ (\%) = \left(\frac{(Pin\ CH_4 - P\ CH_4)}{Pin\ CH_4}\right) x\ 100} \qquad \mathbf{(3.12)}$$

$$\mathbf{H_2\ yield\ (\%) = \left(\frac{PH_2}{Pin\ CH_4 \times 3}\right)\ x\ 100} \qquad \mathbf{(3.13)}$$

$$\mathbf{CO\ selectivity\ (\%) = \left(\frac{PCO}{(PCO + PCO_2)}\right)\ x\ 100} \qquad \mathbf{(3.14)}$$

$$\mathbf{GHSV = \frac{F}{V}\left(h^{-1}\right)} \qquad \mathbf{(3.15)}$$

Where P is the gas partial pressure, F is the volume of the reaction mixture introduced per unit of time and V is the volume of catalyst.

3.6.4 Isothermal reactions of methane and steam

Isothermal analysis allowed catalytic activity to be monitored over time, at a specific reaction temperature. Reaction gas ratios were gained through the bypass line and were the same as those shown in Table 3.1. Once gases had settled through the bypass line, gas partial pressures were stored for 10 minutes, allowing accurate reactant gas ratios to be recorded. The gases were then passed over the catalyst sample, at a specific temperature, for a desired length of time. Following this, reactant gases were once again passed over the bypass line and stored for a further 20 minutes, in order to ensure correct ratios were maintained throughout the reaction process. Following reactions, the temperature was reduced back to room temperature and helium was passed over the catalyst. Catalyst samples were not exposed to air following reactions, but kept in a flow of helium until further reactions were performed. Profiles of gas partial pressures against time were gained. As with temperature-programmed reactions, reaction activity calculations were performed on data gained.

3.6.5 Temperature-programmed oxidation

Temperature-programmed oxidation (TPO) reactions were carried out on catalysts following catalytic reactions, allowing any carbon deposition during reforming reactions to be analysed.

TPO reactions were carried in a similar way to TPR reactions, Section 3.6.2. However, TPO reactions were carried out in 10 % O_2 in helium, total flow 20 ml min^{-1}, whilst the temperature was ramped up to 900 °C at a heating rate of 10 °C min^{-1}. At certain temperatures, oxygen reacted with any surface carbon producing carbon dioxide and carbon monoxide (Reaction 3.10), detected by the mass spectrometer. Profiles of carbon monoxide and carbon dioxide production against temperature were gained. The sum of any carbon monoxide and carbon dioxide produced was calculated via integration of the peak area. This was then compared to a carbon calibration, example shown in Section 3.5.1, to determine the amount of carbon deposited on the surface.

TPO reactions were also used for *in situ* calcination experiments, allowing oxygen to be passed over a pre-calcined catalyst and gas evolution monitored. All TPO experimental parameters were maintained, such as oxygen flow rate and heating rate. However, the masses monitored by the mass spectrometer were modified accordingly. For example, mass 30 was selected to monitor NO evolution. This allowed the calcination of the catalysts to be monitored in real-time and complete calcination profiles to be obtained. Profiles of gas production against temperature were gained.

3.6.6 Sulfur addition to isothermal reactions of methane and steam

Reactions involving sulfur were conducted in a similar way to isothermal reactions involving methane and steam, Section 3.6.4. Hydrogen sulfide (10 ppm H_2S in helium) was introduced at concentrations relative to the methane within the reaction gas flow. Table 3.2 shows flow rates of reactive gases in order to gain desired hydrogen sulfide concentration and methane to steam ratio.

Table 3.2: Concentration of hydrogen sulfide relative to methane and required flow rates for reactive gases during reactions involving methane and steam

Methane flow rate / ml min^{-1}	Hydrogen sulfide * flow rate / ml min^{-1}	Concentration of hydrogen sulfide relative to methane / ppm	Helium flow rate / ml min^{-1}	Total flow / ml min^{-1}
2	16	80	2	20

* 10 ppm H_2S in He

Initially the desired methane to steam flow rates were gained through the bypass line, as described previously in Section 3.6.3, with a helium flow of 18 ml min^{-1}. Following this, the steam flow was stopped and the desired hydrogen sulfide flow rate was obtained relating to the exact flow rate of methane. Finally, the steam was once again added to the reactive gas flow, and the helium flow rate reduced to 2 ml min^{-1}. This allowed an overall flow rate (excluding steam) of 20 ml min^{-1} to be achieved and the correct methane to steam ratio maintained. Once all ratios and gas flow rates were obtained, the reactive gases were allowed to settle through the bypass. The reactions were then run as previously discussed for isothermal reactions of methane and steam, gas partial pressures were stored over a desired reaction time, including 10 minutes prior and 20 minutes post reaction to gain reactive gas ratios. Profiles of gas partial pressures against time were gained.

3.7 Catalyst characterisation

X-ray diffraction (XRD), X-ray photoelectron spectroscopy (XPS), Brunauer-Emmett-Teller surface area analysis (BET) and scanning electron microscopy (SEM) were all employed to characterise catalyst samples. TPR studies were also used for reducibility investigations, as discussed in Section 3.6.2.

3.7.1 Crystallite size determination: Powder X-ray diffraction (XRD)

3.7.1.1 XRD theory

X-ray diffraction (XRD) is widely used to determine crystal structure. This technique can provide information regarding the lattice type and location of all atoms in the molecule.

Max von Laue was awarded [10] the Nobel Prize in Physics, in 1914[1], '*for his discovery of the diffraction of X-rays by crystals*'. W. Friedrich and P. Knipping undertook much of Laue's experimental work into proving the theory behind the diffraction of X-rays by crystals and the determination of space-lattices within crystals. They proved that diffracted X-rays pass through the crystal due to the comparable X-ray and atom separation. This major milestone in crystallography allowed positions of atoms in crystals to be determined and major advances to be made in the area of X-ray spectroscopy.

Short wavelength electromagnetic radiation (X-rays) is produced by bombarding a metal with high energy electrons. Bremsstrahlung radiation is also generated with a continuous range of wavelengths, produced from electrons decelerating as they bombard the metal. High intensity radiation can arise from the interaction of incoming electrons with electrons in the outer shells of atoms in the crystal. A collision expels an electron, and so an electron of higher energy drops into the vacant site, emitting excess photon energy. This is known as Kα radiation.

X-rays are generated by heating a filament, producing electrons. By applying a voltage, electrons are accelerated towards a target material. If these electrons have sufficient energy, X-rays are produced, with a wavelength characteristic for that material (commonly Cu). Cu Kα radiation has a wavelength of 1.5418 Å. X-rays are then collimated and directed towards the sample. Both the sample and detector are rotated and the intensity of reflected rays are detected. X-ray signals are converted to count rate.

[1] Announced November 1915

Bragg law allows determination of the angle the crystal must be, in order for constructive interference to occur. Bragg Law (Equation 3.16) can be used to identify the spacing of layers of atoms and a reflection should be observed when the glancing angle, θ, satisfies Bragg Law.

$$\boldsymbol{\lambda = 2dsin\theta} \qquad \textbf{(3.16)}$$

Where λ is the incident wavelength and d is the spacing between planes in the lattice.

Powder diffraction relies on the fact that some of the randomly orientated crystals in the powder will satisfy Bragg Law. Each set of hkl values will produce reflections at different angles. Data is gained as a set of intensities (count rate), arising from miller planes (hkl), each with differing intensities. Therefore, each material will have a specific and unique diffraction pattern.

The average crystallite size of the different phases present can be obtained through XRD line broadening analysis, using the Debye-Scherrer equation (peak width at half peak height), Equation 3.17.

$$\boldsymbol{L = \frac{k\lambda}{\left(\frac{\pi}{180}\right)(B^2 - b^2)^{\frac{1}{2}} cos\theta}} \qquad \textbf{(3.17)}$$

Where, L is the crystallite size, B is the width of the diffraction peaks at half height (radians), λ is the wavelength of incident radiation (Cu $K\alpha_1$ = 1.5406 Å), θ is the glancing angle and k is the particle shape factor (spherical particles, value of 0.89 or cubic particles, value of 0.94). Instrumental line broadening is taken into account, through the incorporation of b into the Scherrer equation (0.08), this is determined experimentally and discussed in more detail in Section 3.7.1.2.

Powder XRD instrumentation consists of 3 main elements: X-ray tube, sample holder and X-ray detector, shown below in Figure 3.8. The corresponding laboratory instrument, as described in section 3.7.1.2, is shown in Figure 3.9.

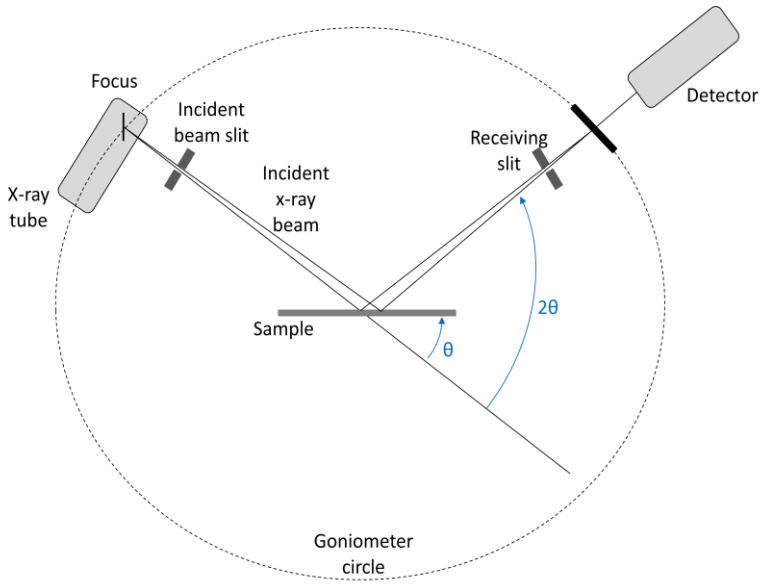

Figure 3.8: Schematic representation of typical powder XRD instrumentation

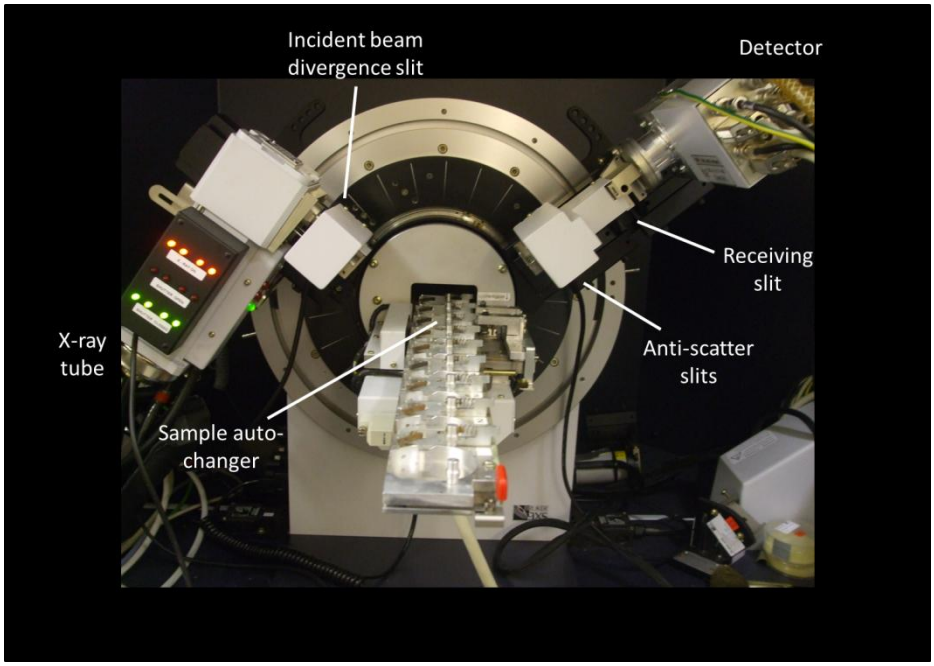

Figure 3.9: Laboratory Bruker D8 Advance corresponding to above schematic XRD representation, Figure 3.8

3.7.1.2 XRD measurement

Powder X-ray diffraction spectra were recorded on a Bruker D8 Advance X-ray diffractometer using Cu $K\alpha_1$ radiation with a wavelength of 1.5406 Å at 40 kV tube voltage and 40 mA tube current. Scanning was undertaken between 2θ values of 5° and 80°, time per step 2.0 s, at a step size of either 0.02° for full scans or 0.01° for close scans, focusing upon peaks of interest. Samples were loaded onto PMMA sample holders with a sample reception diameter of 25 mm and 1 mm depth (set specimen holder rings for reflection, C79298A3244D82/84, Bruker AXS) and mounted onto a sample auto-changer unit.

A heating stage was used for investigations involving *in situ* high temperature XRD studies. A reaction chamber (XRK 900, solid state and solid state-gas reactions up to 900 °C and 10 bar, Anton Paar) was fitted in place of the sample auto-changer unit. This heating stage allowed temperatures from room temperature to 900 °C to be reached, whilst XRD investigations were run *in situ*, at specific temperatures.

The XRD patterns were recorded as EVA raw files. XRD spectra were referenced to powder diffraction files, ICDD-PDF-2 Powder Diffraction Data base, released 2008, for identification of specific elemental compounds. Following elemental phase analysis, EVA raw files were converted to Windows Excel files for additional analysis. The Chemical Database Service was also used for crystal structure determination.

Where possible, the most distinct peaks relating to the crystallite were selected and crystallite size was determined via the Scherrer equation, as described in Section 3.7.1.1. At higher resolution the Kα peak was readily seen to be a doublet, $K\alpha_1$ and $K\alpha_2$, due to the splitting of the 2p orbital in copper, so splitting of energy levels (Cu $K\alpha_1$ radiation wavelength = 1.5406 Å, Cu $K\alpha_2$ radiation wavelength = 1.5444 Å). Prior to EVA analysis, $K\alpha_2$ peaks were stripped from XRD profiles using EVA software.

The width of diffraction peaks at half height and corresponding 2θ values for use in the Scherrer equation were determined using EVA software.

Instrumental line broadening, for use in Scherrer analysis, was determined through the analysis of crystalline materials with a known crystallite size for example, CeO_2 with a crystallite size of 500 Å. Using the Scherrer equation, without line broadening taken into account, the crystallite size was determined and the difference in these values with respect to the actual crystallite size was determined. A value for the instrumental line broadening was determined as 0.08. This procedure was repeated for a number of known samples, ensuring that this value was accurate.

3.7.2 Surface analysis: X-ray photoelectron spectroscopy (XPS)

3.7.2.1 XPS theory

X-ray photoelectron spectroscopy (XPS), also known as electron spectroscopy for chemical analysis (ESCA), is a technique undertaken for surface elemental and chemical state analysis.

A sample is illuminated by Mg Kα X-rays, emitting photoelectrons from the top millimetre of the surface. The kinetic energy of emitted electrons is characteristic of the element from which it originated. The chemical state of an atom alters the binding energy of the emitted photoelectron, therefore, a change in kinetic energy is observed. The relationship can be simply defined as: binding energy = hv – kinetic energy (where hv is the X-ray photon energy). The spectra are defined using the Koopmans' theorem approximation stating that the ionisation energy is equal to the orbital energy of the ejected electron. Therefore, the ionisation energy, specific to the energy of the orbital from which it is ejected can be identified. X-ray photoelectron spectroscopy is used when core electrons are being studied, so higher energy photons are required to expel them.

A background is observed during XPS analysis that increases with binding energy. At low binding energy, the background is principally due to continuous emission of Bremsstrahlung radiation. At higher binding energies, the background is dominated by electrons from inelastic scattering.

The position and intensity of peaks in the spectrum provides the desired quantitative information into surface characteristics. The intensity of the peak is directly proportional to the density of the

atom, within the sampled volume from which it derives. Although core level binding energies for specific elements are unique, thus allowing identification, they are not fixed values. Small detectable shifts can be observed during XPS analysis, due to core ionisation energies slightly affected by bond formation and atom environments. For example, chemically inequivalent atoms of the same element can be differentiated. A difference in charge and so core ionisation energy could result in a split peak and shift in binding energy observed during XPS analysis. Satellite peaks may be observed during XPS studies where non-monochromated X-ray sources are used, due to the difference in energy of the X-rays of the anode material and X-ray gun.

3.7.2.2 XPS measurement

X-ray photoelectron studies (XPS) were undertaken on a Kratos Amicus (ESCA 3400) surface analysis system equipped with non-monochromated Mg Kα X-ray source. The measurement conditions were chosen to be X-ray power of 12 kV, 15 mA, an electron flood gun voltage of 2 eV and analyser pass energy of 150 eV. The system was kept at an operating pressure (X-ray gun on) below 10^{-5} Pa and the standard resolution was 1.15 eV. Air was used to drive pneumatic valves and nitrogen used as a vent gas. Samples were inserted via a sample insertion chamber, ensuring a high vacuum was maintained within the analysis chamber. Specific regions of analysis, including binding energy and dwell times are given in Table 3.3. Initially a wide scan over all regions was undertaken, followed by specific elemental regions.

Table 3.3: XPS specific regions of analysis for wide scan and specific elemental analysis

Region Name	Centre / eV	Width / eV	Step / eV	Dwell / ms	Sweeps
Wide scan	500.00	1100	0.5	200	2
Ni 2p	859.00	40.2	0.1	600	10
O 1s	532.95	20.1	0.1	350	2
Al 2p	72.95	20.1	01	350	2
Au 4f	86.95	20.1	0.1	350	4

Powdered samples were mounted on stainless steel sample holders with a diameter of 6 mm upon sticky tape mounts, with dimensions of approximately 5 mm x 5 mm. Sample holders and mounting tools were cleaned prior to use, to ensure no contaminants were present. Powder samples were pressed onto the mounting tape ensuring a full and even distribution and any excess powder was removed using an air blower. This step was repeated twice to ensure complete sample coverage. Samples were mounted such that the sample surface was at optimum analysis height and the sample stub was raised and lowered on a screw mechanism. Examples of mounted XPS samples are shown in Figure 3.10.

Figure 3.10: XPS sample holders and mounted powder samples

Integrated VISION control software, on a computer interfaced to the XPS instrument, was used for XPS data acquisition and processing. Peak fitting of experimental peaks involved Shirley

background subtraction and subsequent deconvolution, with the use of mixed Gaussian-Lorentzian functions. This was undertaken using VISION control software. Experimental and peak fitted data were exported to Microsoft Excel for presentation of data.

3.7.3 Surface area analysis: Brunauer-Emmett-Teller analysis (BET)

3.7.3.1 BET theory

Gas sorption is a process originating from the tendency of all solid surfaces to attract surrounding gas molecules, from which surface area and pore size information can be obtained.

BET aims to use the physical adsorption of gas molecules on a solid surface, in order to measure the specific surface area of the material. 'BET' is derived from the surnames of the authors who first proposed this theory [11], in 1938, Stephen Brunauer, Paul Emmett and Edward Teller. A material that is surrounded by and is in equilibrium with a gas, at a certain temperature and relative vapour pressure, will adsorb a specific amount of gas. The amount of gas adsorbed depends upon the relative vapour pressure and is proportional to the surface area of the material, both external and internal. An adsorption isotherm links the vapour pressure to the amount of adsorbed gas, at a constant temperature. The type of material under investigation (porous, non-porous and those with narrow pores such as gels) can be characterised depending upon by the type of isotherm gained, shown in Figure 3.11. Type I isotherms are given by microporous solids with small external surface areas, type II from non-porous or macroporous adsorbents with unrestricted monolayer-multilayer adsorption, type III isotherms are not common and are usually from non-porous materials, type IV isotherms are given by a mesoporous adsorbents and type V, are again uncommon, and from a porous adsorbent. Type III and V are related in that the adsorbent-adsorbate interaction is weak.

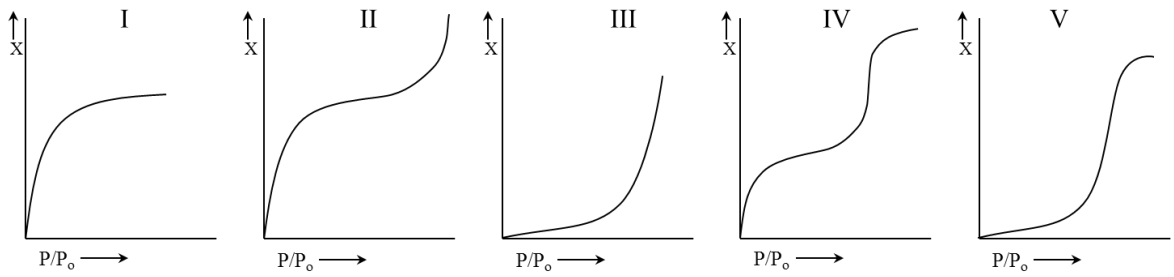

Figure 3.11: Schematic representation of physisorption isotherm types, according to Brunauer classification (adapted from [12]) where X is the mass adsorbed at relative vapour pressure P/P_o

The fractional surface coverage is equal to the ratio of the volume of gas adsorbed, to the volume required to form a monolayer. This is based upon 5 assumptions: the gas is ideal, adsorbed gas is confined to a monolayer, there are no lateral interactions between adsorbed species, the surface is homogenous and adsorbed gas stays in the position where it first collides.

Degassing of samples prior to analysis ensures that all contaminants such as water and oils are removed. This is carried out under vacuum at elevated temperatures. Following degassing, the sample is bought to a constant temperature, through the use of an external bath containing liquid nitrogen. Small amounts of adsorbate (nitrogen) are introduced into the sample chamber and adsorbed to the sample (adsorbent). The surface area is then calculated from the monolayer amount of adsorbed gas using BET method.

The BET equation in its linear form (Equation 3.19) is commonly used as a standard procedure for the determination of surface area.

$$\frac{P}{V(P_o - P)} = \frac{1}{V_m C} + \frac{C-1}{V_m C}\frac{P}{P_o} \qquad \textbf{(3.19)}$$

Where V is the amount adsorbed at the relative pressure P/P_o and V_m is the monolayer capacity. C is related exponentially to the enthalpy of adsorption in the first adsorbed layer, Equation 3.20.

$$C = exp\frac{(H_1 - H_2)}{RT} \qquad \textbf{(3.20)}$$

The BET equation requires a linear relationship between $P/V(P_o-P)$ and P/P_o, thereby producing a BET plot. The BET plot can be used to determine the true value of V_m. In order to calculate the surface area from the monolayer capacity, the average area (a_m) occupied by the adsorbate molecule in the complete monolayer is required. The total surface area (A_s) is then calculated by Equation 3.21 and specific surface area (a_s) by Equation 3.22, where m is the mass of adsorbent and L Avogadro constant. When nitrogen gas is used as the adsorbate, $a_m = 0.162$ nm^2 at 77 K.

$$\boldsymbol{A_s = V_m\, L\, a_m} \qquad \textbf{(3.21)}$$

$$\boldsymbol{a_s = \frac{A_s}{m}} \qquad \textbf{(3.22)}$$

3.7.3.2 BET measurement

BET surface area analysis was undertaken on a Quantachrome Autosorb-1 Series, Surface Area and Pore Size Analyser. Typically, 0.20 g of sample was used for analysis. Samples were placed in sample cells, with appropriate bulb size at base to hold powder sample. Sample surface contaminants were removed by outgassing under vacuum at 350 °C for 12 hours. Following this, the samples were bought to a constant temperature, through the use of liquid nitrogen, at 77 K. Sample bulbs were immersed by at least 5 cm into the liquid nitrogen. Nitrogen gas was used as the adsorbate (BOC high purity scientific gases). A working range of P/P_o (relative vapour pressure) of 0 to 1 was used. N_2 adsorption and desorption isotherms were used to determine the surface area BET models. BET isotherm and surface area data were gained for each sample. Integrated AUTOSORB software, on a computer interfaced to the Autosorb-1 analyser, was used for data acquisition and processing.

3.7.4 Surface/crystallographic analysis: Scanning electron microscopy (SEM)

3.7.4.1 SEM theory

SEM allows information relating to surface morphology, chemical composition and crystalline structure to be investigated. SEM offers depth of field allowing a greater area of the sample to be focused at one time, as well as high resolution allowing high magnification [13]. This is a non-destructive form of surface analysis.

An electron beam is produced from a filament at the top of the microscope. In a vacuum, this beam follows a vertical path through the microscope. Magnetic fields and lenses focus the beam towards the sample. An objective lens focuses the beam to a fine point on the sample. The magnification can be controlled by varying the voltage of the scanning coils. As the beam collides with the sample, X-rays and electrons are ejected. Secondary electrons and backscattered electrons are detected and most commonly used for imaging samples.

If the sample under investigation is conductive then limited sample preparation is required. However, all other samples require coating with a conductive material, prior to sample analysis. This involves dispersing a thin layer of conductive material, commonly gold, on the sample. The sample is placed in a chamber, under vacuum. The presence of argon gas and an electric field results in an electron to be removed from the argon, thus resulting in positively charged atoms. The positively charged ions are attracted to the negatively charged gold foil, resulting in the loss of gold atoms from the surface. This results in a thin dispersion of gold on the sample surface.

3.7.4.2 SEM measurement

SEM analysis was undertaken on a high resolution Hitachi field emission scanning electron microscope (FE-SEM) S-4500. An emission current of 10 mA was used with magnification up to x 60k employed. Samples were mounted on conductive carbon adhesive pads, fixed to 15 mm Hitachi stubs (Agar Scientific). Samples were then sputter coated with gold using Emscope FD500,

at a current of 25 mA in an argon atmosphere. Following preparation, samples were viewed and imaged using Quartz PCL Image Management System software.

3.8 References

1. W. Paul, *Electromagnetic traps for charged and neutral particles.* Nobel Lecture, 1989.
2. A.F. Benton and P.H. Emmet, *The reduction of nickelous and ferric oxides by hydrogen.* Journal of the American Chemical Society 1924. **46**: p. 2728-2737.
3. G.B. Taylor and H.W. Starkweather, *Reduction of metal oxides by hydrogen* Journal of the American Chemical Society, 1930. **52**: p. 2314-2325.
4. S.J. Gentry, N.W. Hurst, and A. Jones, *Temperature programmed reduction of copper ions in zeolites.* Journal of the Chemical Society, Faraday Transactions 1: Physical Chemistry in Condensed Phases, 1979. **75**: p. 1688-1699.
5. P. Malet and A. Caballero, *The selection of experimental conditions in temperature-programmed reduction experiments.* Journal of the Chemical Society, Faraday Transactions 1: Physical Chemistry in Condensed Phases, 1988. **84**(7): p. 2369-2375.
6. C.M. Finnerty, N.J. Coe, R.H. Cunningham, and R.M. Ormerod, *Carbon formation on and deactivation of nickel-based/zirconia anodes in solid oxide fuel cells running on methane.* Catalysis Today, 1998. **46**(2-3): p. 137-145.
7. C.M. Finnerty and R.M. Ormerod, *Internal reforming over nickel/zirconia anodes in SOFCS operating on methane: Influence of anode formulation, pre-treatment and operating conditions.* Journal of Power sources 2000. **86**: p. 390-394.
8. H. He and J.M. Hill, *Carbon deposition on Ni/YSZ composites exposed to humidified methane.* Applied Catalysis A: General, 2007. **317**(2): p. 284-292.
9. P.G. Menon, *Coke on catalysts-harmful, harmless, invisible and beneficial types.* Journal of Molecular Catalysis, 1990. **59**(2): p. 207-220.
10. M.v. Laue, *Concerning the detection of X-ray interferences.* Nobel Lecture, 1915.

11. S. Brunauer, P.H. Emmett, and E. Teller, *Adsorption of Gases in Multimolecular Layers.* Journal of the American Chemical Society, 1938. **60**(2): p. 309-319.

12. G. Fagerlund, *Determination of specific surface by the BET method*. Materials and Structures, 1973. **6**(3): p. 239-245.

13. G.H. Michler, *Scanning Electron Microscopy (SEM)*, in *Electron Microscopy of Polymers*. 2008, Springer. p. 87-120.

4 Catalyst characterisation: Influence of calcination temperature on 20 wt % Ni/Al_2O_3 samples

Nickel aluminate has a structure relating to the magnesium aluminate spinel, $MgAl_2O_4$, and is given the general formula AB_2O_4 [1]. This structure consists of face centred cubic O^{2-} ions where the A ions reside in one-eighth of the tetrahedral sites and the B ions inhabit half of the octahedral sites, denoted as $A[B_2]O_4$.

The formation of such spinel phases is common during catalyst preparation, although the parameters determining and influencing its formation is a highly debated area. Preparation parameters have been reported to have different effects on the Ni^{2+} phases formed. For example, Li *et al.* [2] have reported using TPR and XRD, that different co-precipitation and impregnation methods have different effects on $NiAl_2O_4$ spinel formation. Nickel loading has also been shown to influence the extent of spinel formation in supported catalysts, Sahli *et al.* [3] and Roh *et al.* [4] have reported that lower nickel loading increases nickel aluminate formation. However, it has also been shown [5, 6] that nickel loading and calcination temperature during preparation have no influence on the extent of nickel aluminate formation, and that the resulting nickel aluminate species are due to the surface properties of the support, whilst Cui *et al.* [7] have proposed that both the nickel loading and calcination temperature have an influence upon formation of spinel compounds.

Despite the conflicting nature of previous research relating to nickel aluminate formation, studies have shown that calcination temperature clearly has a significant impact on the extent of nickel aluminate formation [7-14]. It is proposed that two reactions can occur concurrently when an alumina supported nickel sample is heated: one produces a surface spinel, like $NiAl_2O_4$, and the other results in segregation of free NiO. Higher calcination

temperatures have been shown to increase nickel aluminate formation and increase nickel support interactions. Studies suggest that during calcination the diffusion of nickel ions into the alumina support is limited to the first outer layers, so the formation of surface nickel aluminate, as opposed to bulk species, is more likely [6].

Due to the conflicting nature of previous research relating to alumina supported nickel catalysts and their use during catalytic steam reforming investigations, the influence of calcination temperature on catalyst samples was studied. Prior to catalytic testing, all the catalyst samples were characterised using powder X-ray diffraction (XRD), X-ray photoelectron spectroscopy (XPS), scanning electron microscopy (SEM) and nitrogen sorption (BET). As well as conventional analytical techniques, the reduction characteristics were studied using temperature-programmed reduction (TPR). These techniques provide complementary information regarding the sample structure and morphology at different stages of catalyst preparation (calcination) and activation (reduction).

4.1 Standard samples

Nickel nitrate hexahydrate ($Ni(NO_3)_2.6H_2O$), nickel oxide (NiO), nickel (Ni) and alpha-alumina (α-Al_2O_3, surface area 9.89 $m^2\ g^{-1}$) were investigated as standard samples. The NiO standard was obtained from the thermal decomposition of $Ni(NO_3)_2.6H_2O$ in air, at 1000 °C. The nickel standard was obtained from the subsequent temperature-programmed reduction (in hydrogen up to 1000 ºC) of the NiO derived from $Ni(NO_3)_2.6H_2O$. The calcination and reduction procedures are described in Chapter 3.

4.1.1 Temperature-programmed X-ray diffraction (XRD)

α-Al_2O_3 was used as a standard precursor and support for all samples. *In situ* temperature-programmed XRD of α-Al_2O_3 was undertaken in order to investigate the thermal stability of

α-Al_2O_3 at high temperatures. The temperature-programmed XRD patterns are shown in Figure 4.1.

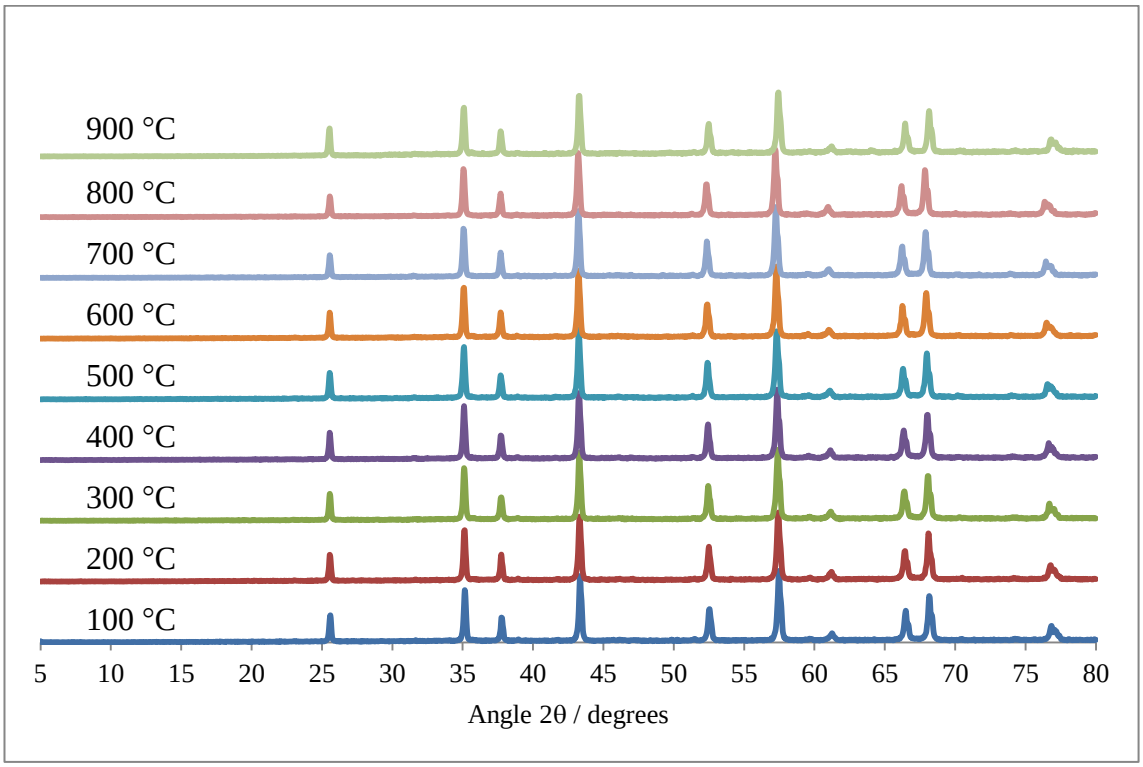

Figure 4.1: Temperature-programmed XRD analysis of α-Al_2O_3 from 100 °C to 900 °C

It has been shown that at high temperatures of *ca.*1200 °C a phase transformation can occur, transforming γ- Al_2O_3 into α-Al_2O_3 [15]. Figure 4.1 shows that α-Al_2O_3 is stable and remains in the alpha form at all temperatures, up to 900 °C. On this basis, no phase transformation from the alpha phase should occur under the reforming temperature conditions employed in this study.

In situ temperature-programmed XRD calcination of nickel nitrate hexahydrate was undertaken in order to investigate the thermal decomposition of nickel nitrate hexahydrate to NiO. XRD profiles at different temperature intervals in the range 50 ºC to 600 °C, are shown in Figure 4.2. It is not possible to identify the major phases present in the XRD profiles in Figure 4.2 using the Chemical Database Service or the Inorganic Crystal Structure Database.

However, it is possible to distinguish the major stages which occur during the thermal decomposition of nickel nitrate hexahydrate.

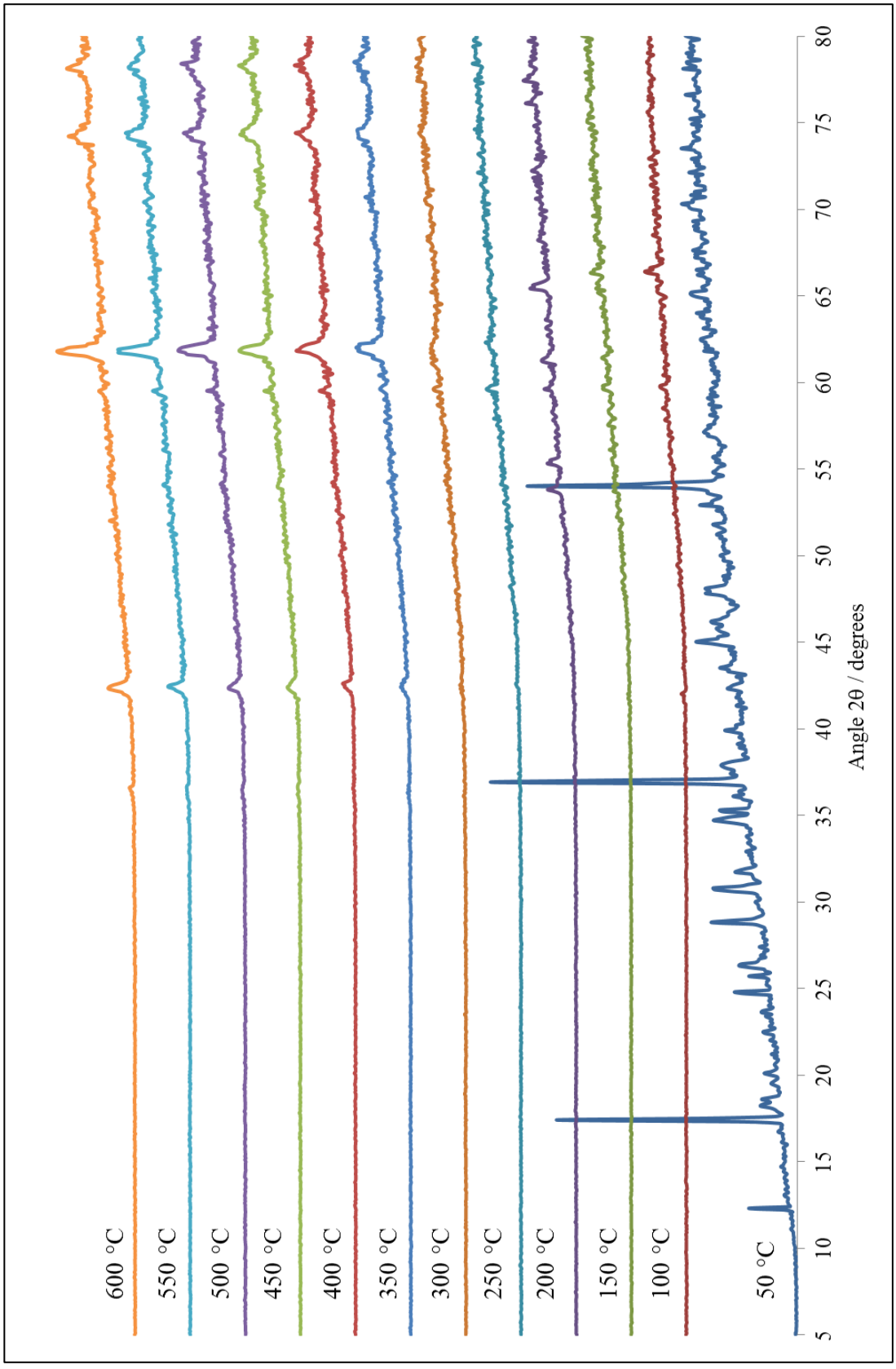

Figure 4.2: **XRD profiles of the thermal decomposition of $Ni(NO_3)_2.6H_2O$ over a temperature range 50 °C to 600 °C**

At 100 °C, the only peaks remaining relating to the nickel nitrate precursor observed at 50 °C, are at 2θ values of 42.0°, 59.7° and 66.4°. These peaks are still present at 150 °C apart from the peak at 42.0°. However, by 200 °C additional peaks are present at 53.9°, 55.3°, 61.3°, 65.4°, 76.1° and 77.4°. At 250 °C, these peaks have disappeared, apart from the peak at 59.60°, and a new peak is present at 62.0°. Upon further heating from 300 °C to 600 °C peaks at 37.0°, 42.4°, 61.8°, 74.2° and 78.1° appear, becoming sharper and more defined as the temperature increases. These peaks can be attributed to NiO (see Section 4.1.2.2). The peak at 59.6° suggests that some precursor nitrate phase may remain in the sample at 600 °C and higher temperatures may be required for complete decomposition of nickel nitrate.

The main steps proposed [16, 17] for the decomposition of nickel nitrate are shown in Table 4.1. The results gained may differ from suggested mechanistic routes, due to the presence of oxygen during calcination and to the influence of support interactions.

Table 4.1: Thermal decomposition of $Ni(NO_3)_2.6H_2O$ and approximate decomposition temperatures (adapted from [17])

Reaction/step	Temperature [a] / °C
Water separation	
1. $Ni(NO_3)_2.6H_2O \rightarrow Ni(NO_3)_2.4H_2O + 2H_2O$	50 – 125
2. $Ni(NO_3)_2.4H_2O \rightarrow Ni(NO_3)_2.2H_2O + 2H_2O$	
Partial decomposition	
3. $Ni(NO_3)_2.4H_2O \rightarrow Ni(NO_3)(OH)_2.H_2O + NO_2$	145
4. $Ni(NO_3)(OH)_2.H_2O \rightarrow Ni(NO_3)(OH)_{1.5}.O_{0.25}.H_2O + 0.25H_2O$	190

Decomposition		
5.	**$Ni(NO_3)(OH)_{1.5}.O_{0.25}.H_2O \rightarrow 0.5Ni_2O_3 + HNO_3 + 1.25H_2O$**	250 [b]
Oxide decomposition to NiO		
6.	**$3Ni_2O_3 \rightarrow 2Ni_2O_4 + 0.5O_2$**	250 [b]
7.	**$2Ni_2O_4 \rightarrow 3NiO + 0.5O_2$**	300 [b]

[a] Decomposition temperature

[b] Beginning of reaction

The temperature-programmed XRD analysis is consistent with the thermal decomposition reactions proposed above. Although not all stages proposed above would be observed during XRD analysis, the main stages during thermal decomposition may be identified. Three main stages are observed for the thermal decomposition of nickel nitrate hexahydrate. XRD analysis indicates that decomposition commences between 50 °C and 100 °C, as at 100 °C few peaks can be identified corresponding to the initial XRD pattern of nickel nitrate. The next stage of decomposition occurs around 200 °C, followed by the final stage starting at around 250 °C. Peaks corresponding to NiO begin to appear at 250 °C and 300 °C, increasing in intensity as the temperature is increased. Temperatures above 600 °C may be required for complete decomposition and conversion to NiO.

4.1.2 Characterisation of standard samples

4.1.2.1 Scanning electron microscopy (SEM)

SEM investigations, using a range of magnifications from 15,000 to 60,000, were undertaken on the NiO and α-Al_2O_3 standards (Figure 4.3 and Figure 4.4, respectively).

Figure 4.3: SEM image of NiO standard (magnification of 15,000)

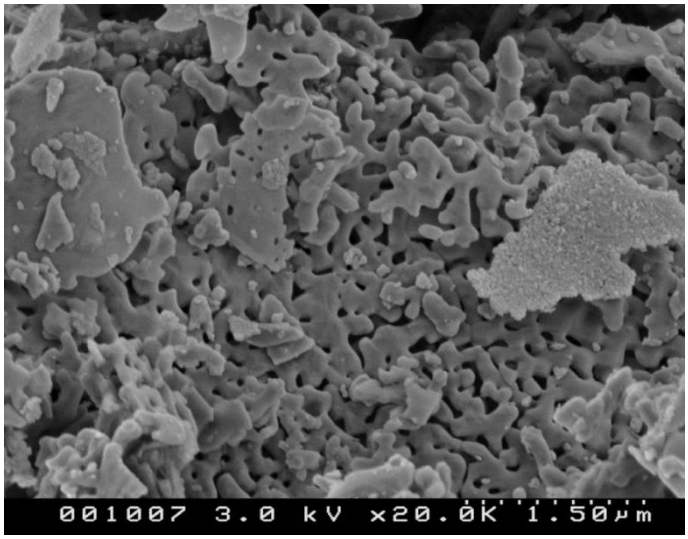

Figure 4.4: SEM image of α-Al_2O_3 standard (magnification of 20,000)

Figure 4.3 shows two NiO grains, comprising of cubic NiO crystallites. Thus, calculations involving XRD line broadening analysis, with the Scherrer equation, have assumed a cubic structure for NiO and therefore, a particle shape factor of 0.94, as discussed in Chapter 3.

SEM images indicate a range of particle sizes for the NiO, with the particle sizes ranging from below 200 nm to above 600 nm. The α-Al_2O_3 has a particle size of *ca.* 150 nm, as well as some much larger amorphous sheet species. Crystallite size determination from XRD using the Scherrer equation should be taken as an average representation of the crystallites

present, whilst SEM images provide an indication of the average particle sizes and morphologies present in the sample.

4.1.2.2 X-ray diffraction (XRD)

XRD was carried out on NiO, nickel and α-Al_2O_3 standards in order to aid identification of the major phases present in catalyst samples. The XRD patterns for NiO, nickel and α-Al_2O_3 are shown in Figure 4.5, Figure 4.6 and Figure 4.7 respectively.

The Chemical Database Service and the Inorganic Crystal Structure Database were used for XRD line profile analysis and crystal structure determination. The ICDD-PDF database, within EVA software, was used for the identification of major species present in the XRD patterns, File card numbers: NiO, 65-6920; Ni, 01-1266; α-Al_2O_3, 43-1484.

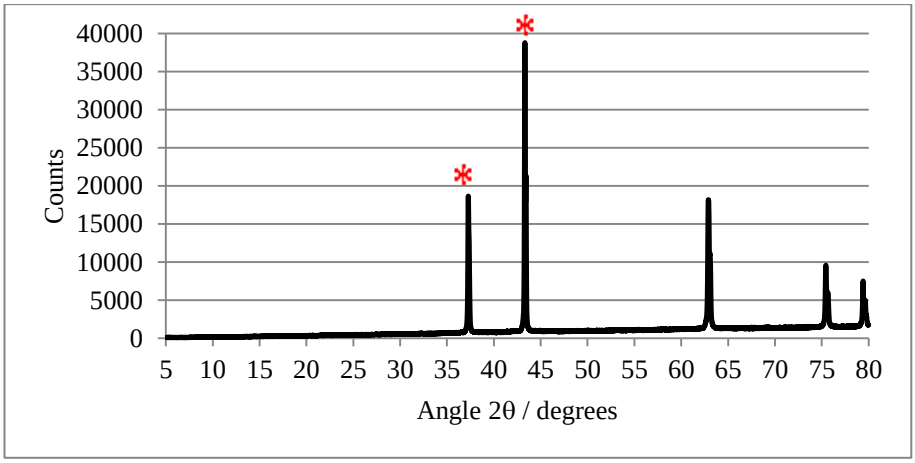

Figure 4.5: XRD pattern of NiO standard

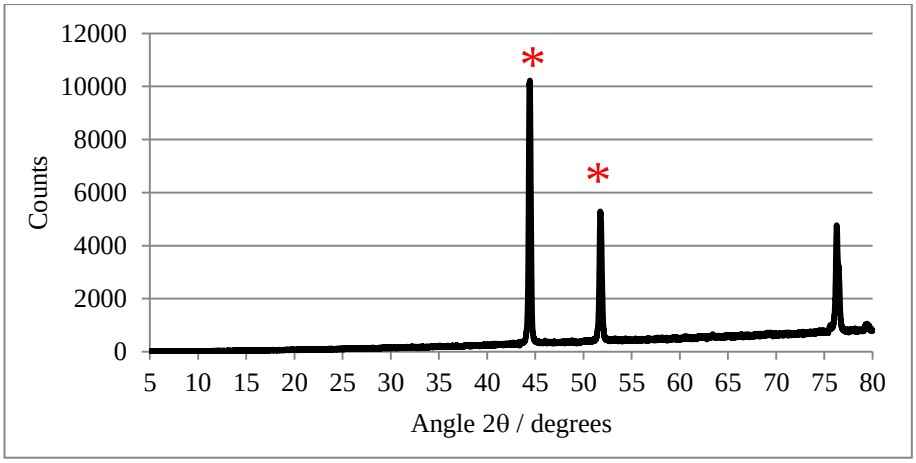

Figure 4.6: XRD pattern of nickel standard

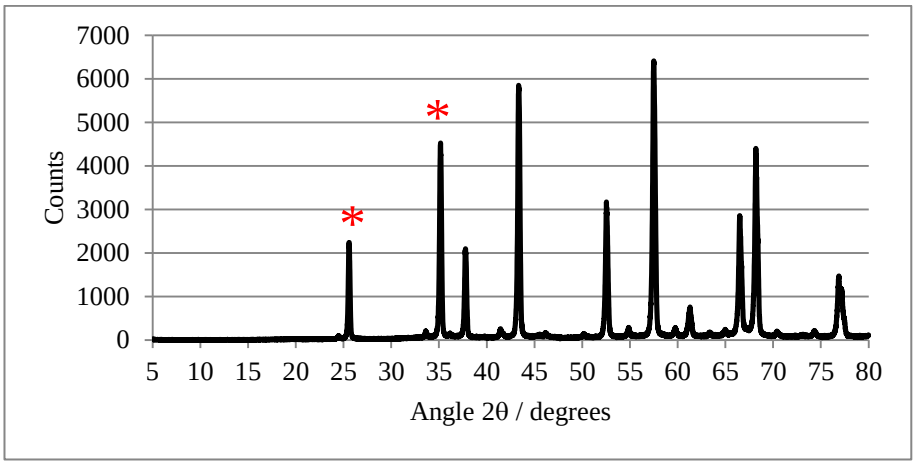

Figure 4.7: XRD pattern of α-Al_2O_3 standard

Table 4.2 shows the peak positions and the average crystallite size (obtained by the Scherrer equation) for the most distinct peaks, shown by * in the XRD patterns of NiO, nickel and α-Al_2O_3.

Table 4.2: Average crystallite size of NiO, nickel and α-Al_2O_3 determined via Scherrer analysis for the two most distinct peaks in XRD profile and corresponding peak positions

Sample	Peak position (*) Angle 2θ / degrees		Average crystallite size / nm
NiO	37.3	43.3	170
Nickel	44.4	51.7	48
α-Al_2O_3	25.6	35.1	55

In Sections 4.2.2.3 and 4.2.4.1, the peaks corresponding to the major crystallite phases present within the XRD patterns corresponding to the catalyst samples are identified. Those attributed to the alumina support are not identified.

4.1.2.3 X-ray photoelectron spectroscopy (XPS)

XP spectra of NiO and α-Al_2O_3 were obtained. The O 1s and Ni $2p^{3-2}$ spectra of NiO are shown in Figure 4.8, and the O 1s and Al 2p spectra of α-Al_2O_3 are shown in Figure 4.9. Where possible, peak fitting involving background subtraction and subsequent deconvolution of experimental data was undertaken and is shown in the spectra. This allows surface properties and elemental environments to be investigated for all standard samples. XPS can be used for characterisation of major surface species in the catalyst samples. All spectra show experimental data (black), peak fitted components (blue, green, yellow and purple) and the peak fitted spectrum curve (red).

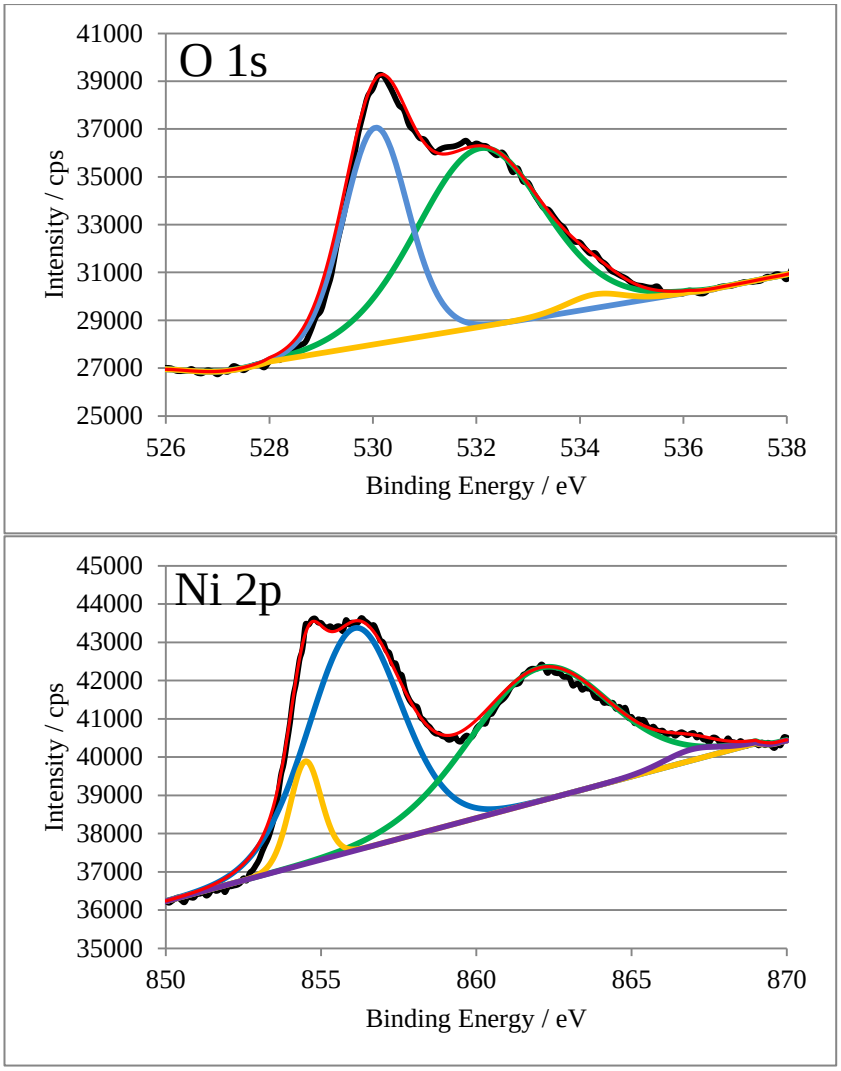

Figure 4.8: Peak fitted O 1s and Ni 2p spectra of NiO standard

The O 1s peak fitted spectrum of unsupported NiO in Figure 4.8 shows two primary peaks, at binding energies of 530.0 and 532.3 eV. The primary peak at 530.0 eV is attributed to oxide species and the peak at 532.3 eV is attributed to surface hydroxyl species [18].

The Ni 2p peak fitted spectrum in Figure 4.8, shows two characteristic primary peaks at binding energies of 854.0 and 856.5 eV, which are attributed to Ni^{2+} and Ni^{3+}, respectively. The observed peaks at binding energies of 862.0 and 867.5 eV are satellite peaks which are obtained for Ni^{2+} and Ni^{3+}, respectively. The Ni^{3+} satellite peak is important in this study, for the identification of additional species and determination of overlapping peaks [11]. The Ni

2p spectrum for the unsupported NiO agrees well with literature values of *ca.* 855 and 857 eV for Ni^{2+} and Ni^{3+} respectively [13, 19].

The O 1s peak fitted spectrum of α-Al_2O_3 (Figure 4.9) shows two primary peaks at binding energies of 534.0 and 536.3 eV. The peak at 534.0 eV is attributed to O^{2-} species, whilst, the small shoulder attached to this peak at 536.3 eV, is often attributed to either adsorbed water or hydroxyl groups [20]. The peak fitted Al 2p spectrum of α-Al_2O_3, shows the presence of one predominant primary peak at 77.0 eV, attributed to the Al^{3+} species.

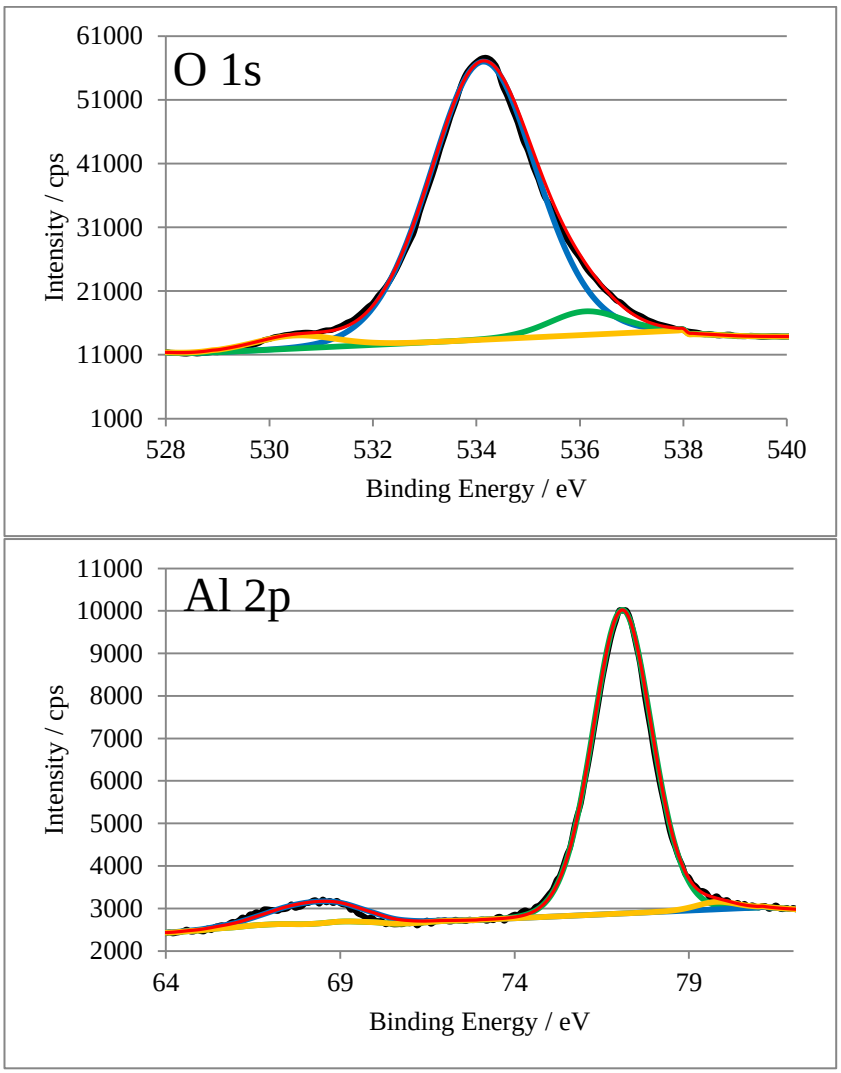

Figure 4.9: Peak fitted O 1s and Al 2p spectra of α-Al_2O_3 standard

4.1.3 Temperature-programmed reduction (TPR)

Temperature-programmed reduction measurements were conducted on both NiO and α-Al_2O_3, to investigate the sample reducibility. As expected due to its high thermal stability, no reduction of α-Al_2O_3 was observed. The TPR profile for the NiO standard is shown in Figure 4.10. Only one reduction peak is present at *ca.* 400 °C, which corresponds to the reduction of NiO to metallic nickel. Reduction is complete by *ca.* 550 °C. This is consistent with previous TPR studies, which show a single reduction peak at a temperature between 350 °C and 400 °C [2, 6, 21].

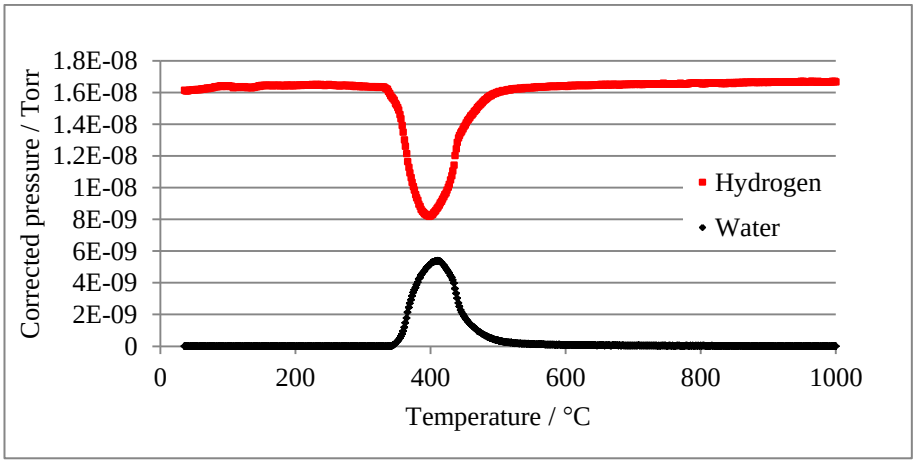

Figure 4.10: TPR profile of NiO showing hydrogen consumption and water evolution

Hydrogen consumption and water evolution were both recorded during TPR measurements, as shown in Figure 4.10. However, subsequent TPR profiles will show only the water evolution, since the hydrogen consumption mirrors the water evolution.

4.2 20 wt % Ni/Al_2O_3 samples

The 20 wt % Ni/Al_2O_3 samples are denoted hereon as NiO/Al_2O_3 (calcination temperature) for post-calcined samples and Ni/Al_2O_3 (calcination temperature) for post-reduced samples. For example, Ni/Al_2O_3 (600) refers to the 20 wt % Ni/Al_2O_3 sample following calcination at 600 °C and subsequent temperature-programmed reduction in hydrogen.

4.2.1 Calcination

In situ calcination of the $Ni(NO_3)_2/Al_2O_3$ precursor was carried out under a flow of oxygen. This was undertaken to investigate the calcination properties of the catalyst precursor and identify the temperatures at which decomposition occurs and calcination is complete. The calcination process was also studied using *in situ* temperature-programmed XRD to study major phases present during the calcination process.

Temperature-programmed decomposition of $Ni(NO_3)_2/Al_2O_3$ was carried out, under a flow of 10 % O_2 in helium, following the reaction procedure described for TPO investigations in Chapter 3. The temperature-programmed decomposition profile is shown in Figure 4.11.

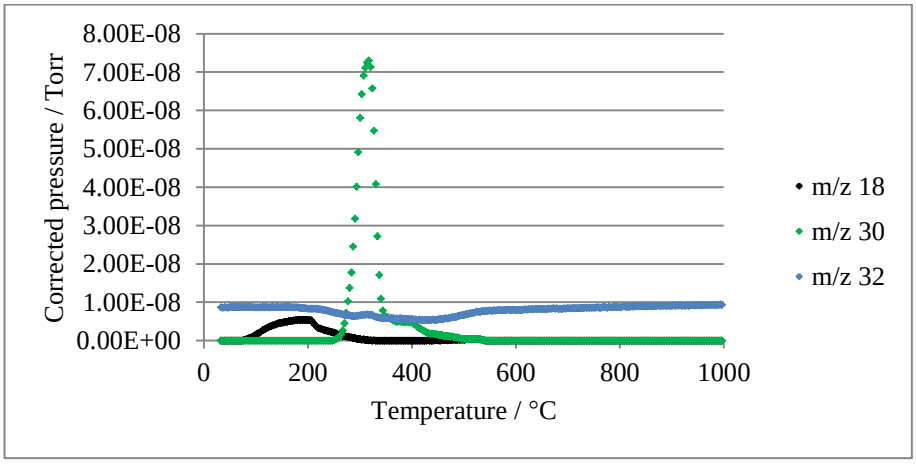

Figure 4.11: Temperature-programmed decomposition of $Ni(NO_3)_2/Al_2O_3$ under a flow of oxygen

Product gases monitored included NO and NO_2. However, the only masses observed were 18 and 30, respectively due to H_2O and NO evolution. Evolution of all gases was complete by *ca*. 500 °C. No higher nitrate compounds, such as NO_2 and N_2O, were detected.

XRD profiles at different temperature intervals, in the range of 50 ºC to 900 °C for the temperature-programmed thermal oxidative decomposition of $Ni(NO_3)_2/Al_2O_3$ are shown in Figure 4.12 and Figure 4.13.

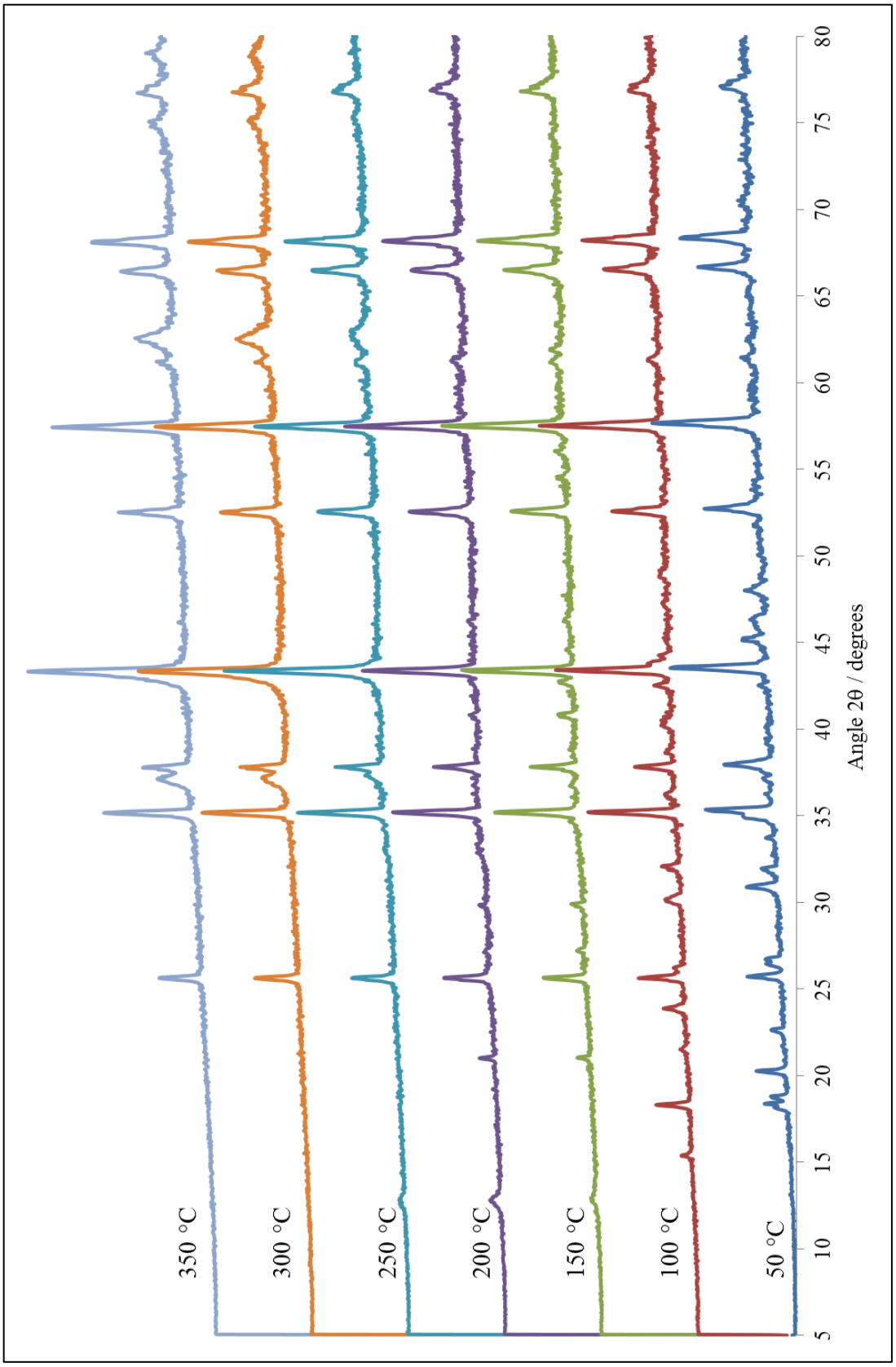

Figure 4.12: XRD profiles of the thermal decomposition of $Ni(NO_3)_2/Al_2O_3$ over the temperature range of 50 °C to 350 °C

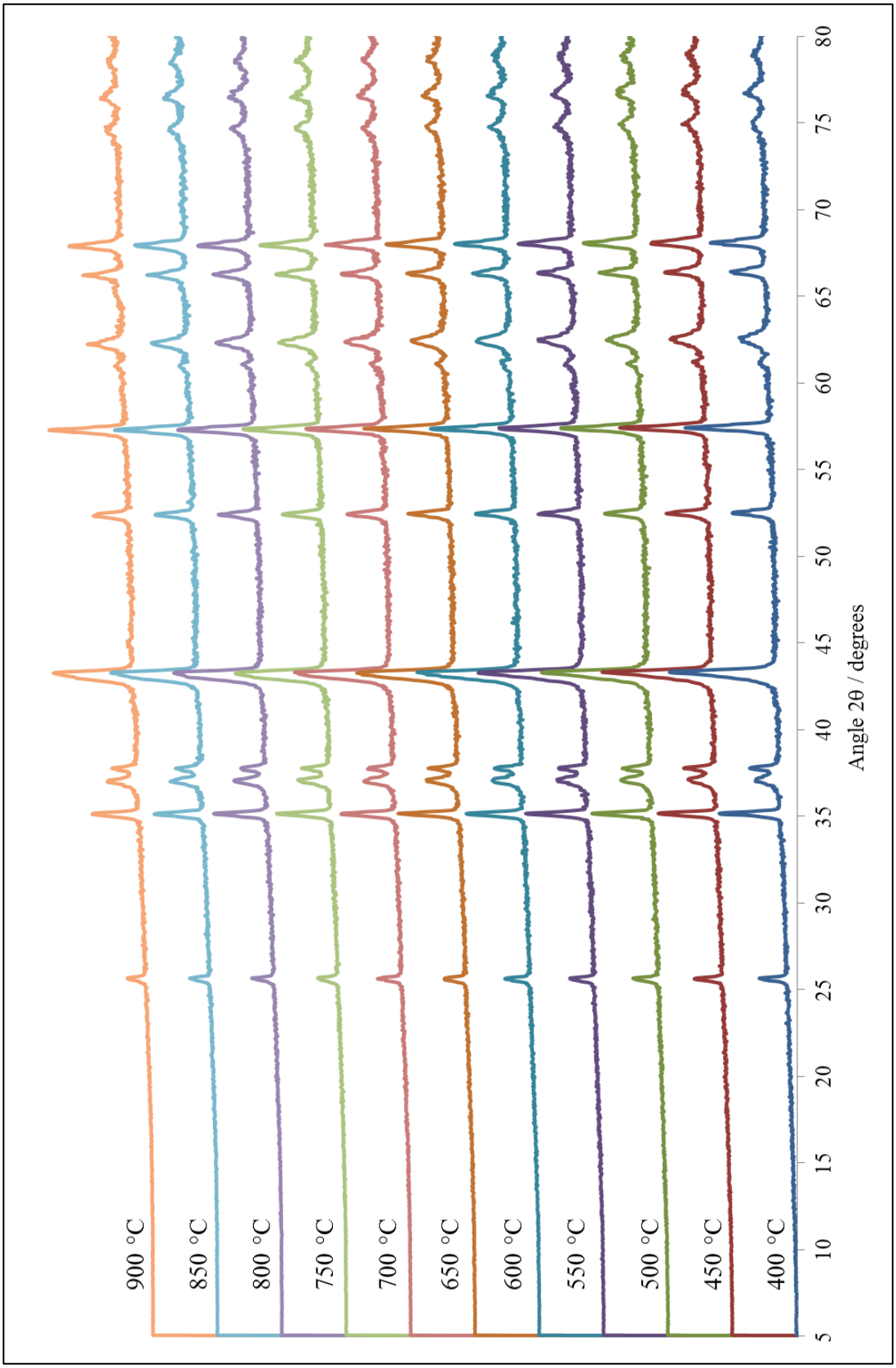

Figure 4.13: XRD profiles of the thermal decomposition of $Ni(NO_3)_2/Al_2O_3$ over the temperature range of 400 °C to 900 °C

The XRD peaks at 2θ values of 25.5°, 35.1°, 37.8°, 43.5°, 52.5°, 57.5°, 66.5° and 68.2°, present in XRD profiles at all calcination temperatures are attributed to α-Al_2O_3.

Three major stages are observed in the calcination of $Ni(NO_3)_2/Al_2O_3$. Decomposition initiates at 50 ºC to 100 °C. At 100 °C, the XRD profile is different from that of the precursor at 50 °C. The precursor peaks have disappeared and additional peaks are observed at 15.3°, 21.5°, 23.8°, 30.1°, 32.0° and 40.2°. At 150 °C, peaks at 12.9°, 21.0° and 27.1° appear whilst peaks at 21.5° and 30.1° shift to lower values. At 250 °C, peaks at 37.3° and 62.9° appear, which can be attributed to the formation of NiO (Figure 4.5). However, a peak at 12.4°, corresponding to the precursor remains. By 300 °C, no nitrate precursor peaks are observed and the NiO peaks progressively increase in intensity as the temperature is increased to 900 °C. This decomposition process links to the thermal decomposition of nickel nitrate observed in Section 4.1.1.

4.2.2 Characterisation of calcined NiO/Al_2O_3 samples

Following calcination, the samples were characterised by XRD, SEM and XPS allowing an insight into both bulk and surface properties of the calcined samples.

4.2.2.1 Visual appearance

The sample appearance following calcination at different temperatures is shown in Figure 4.14. Stoichiometric NiO is dark green, therefore, suggesting the presence of NiO in the samples calcined up to 900 °C. However, NiO/Al_2O_3 (1000) is a distinct blue colour, not typical of NiO. All samples showed no change in colour over time.

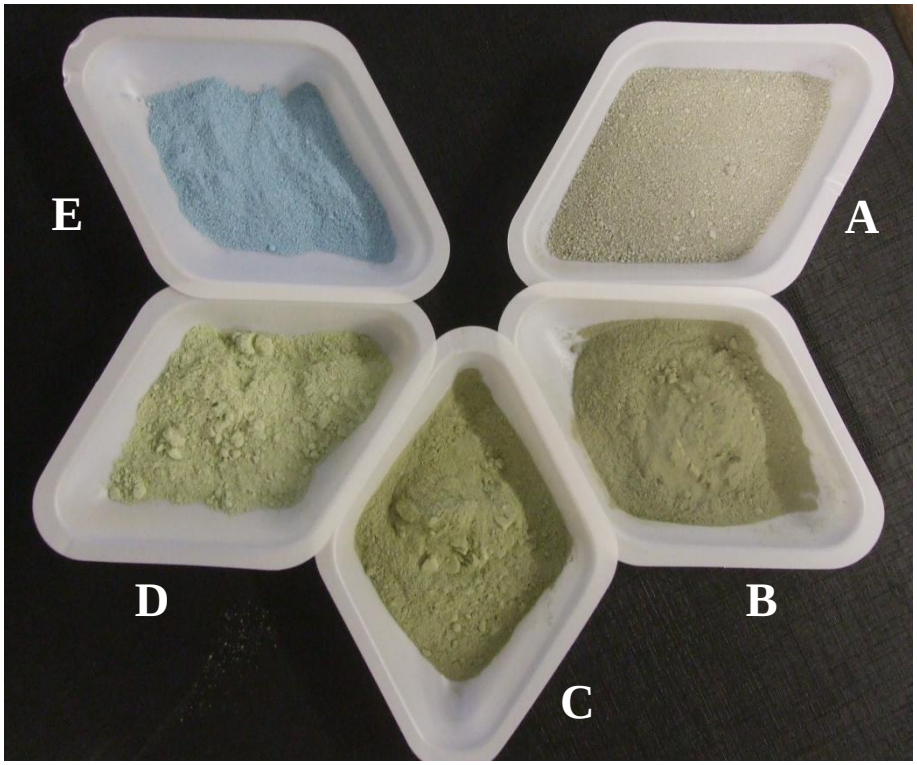

Figure 4.14: **NiO/Al_2O_3 catalyst appearance following calcination A, NiO/Al_2O_3 (600); B, NiO/Al_2O_3 (700); C, NiO/Al_2O_3 (800); D, NiO/Al_2O_3 (900) and E, NiO/Al_2O_3 (1000)**

$NiAl_2O_4$ is known to have a distinct blue colour [10, 11, 21]. This suggests that NiO/Al_2O_3 (1000) could contain additional species produced during high temperature calcination, such as $NiAl_2O_4$. Gavalas *et al.* [22] have shown that the colour of NiO/Al_2O_3 samples changes from a grey/green to green/blue colour, with increasing calcination temperature from 750 °C to 1050 °C.

4.2.2.2 Surface area

The surface areas were determined by the BET method for all samples following calcination, results are shown in Table 4.3.

Table 4.3: The BET surface area for samples following calcination

Sample	Surface area / $m^2 g^{-1}$
NiO/Al_2O_3 (600)	10.0
NiO/Al_2O_3 (700)	10.2
NiO/Al_2O_3 (800)	7.9
NiO/Al_2O_3 (900)	4.8
NiO/Al_2O_3 (1000)	6.8

The surface areas significantly decrease following calcination at 800 °C and 900 °C, which could be attributed to increased crystallinity. The surface area of NiO/Al_2O_3 (900) is dramatically reduced. However, following calcination at 1000 °C the surface area is slightly increased. The change observed following calcination at 900 °C and 1000°C could indicate a variation in both the surface morphology and the crystallinity, following high temperature calcination. This is confirmed by both XRD and SEM results shown in Sections 4.2.2.3 and 4.2.2.4, which indicate a dramatic change in the surface morphology at 900 and 1000 °C and an additional phase formed at 1000 °C. TPR results also indicate a change in Ni^{2+} reducibility, most significantly observed following calcination at 900 °C and 1000 °C, which may also account for the variation in surface areas.

4.2.2.3 X-ray diffraction (XRD)

XRD profiles of the samples following calcination are shown in Figure 4.15, whilst the crystallite sizes of the major species estimated via the Scherrer equation are shown in Table 4.4.

Peaks corresponding to NiO, α-Al_2O_3 and additional phases overlap at low angles. To estimate NiO crystallite size, a peak at higher angle (*ca.* 62.8°, marked * in Figure 4.15) which does not overlap with any other peaks was used. This peak has been used for all NiO crystallite size determinations in this study. The XRD pattern obtained for NiO/Al_2O_3 (1000), shows additional peaks which correspond to an additional phase, these have been identified and labelled within the profile.

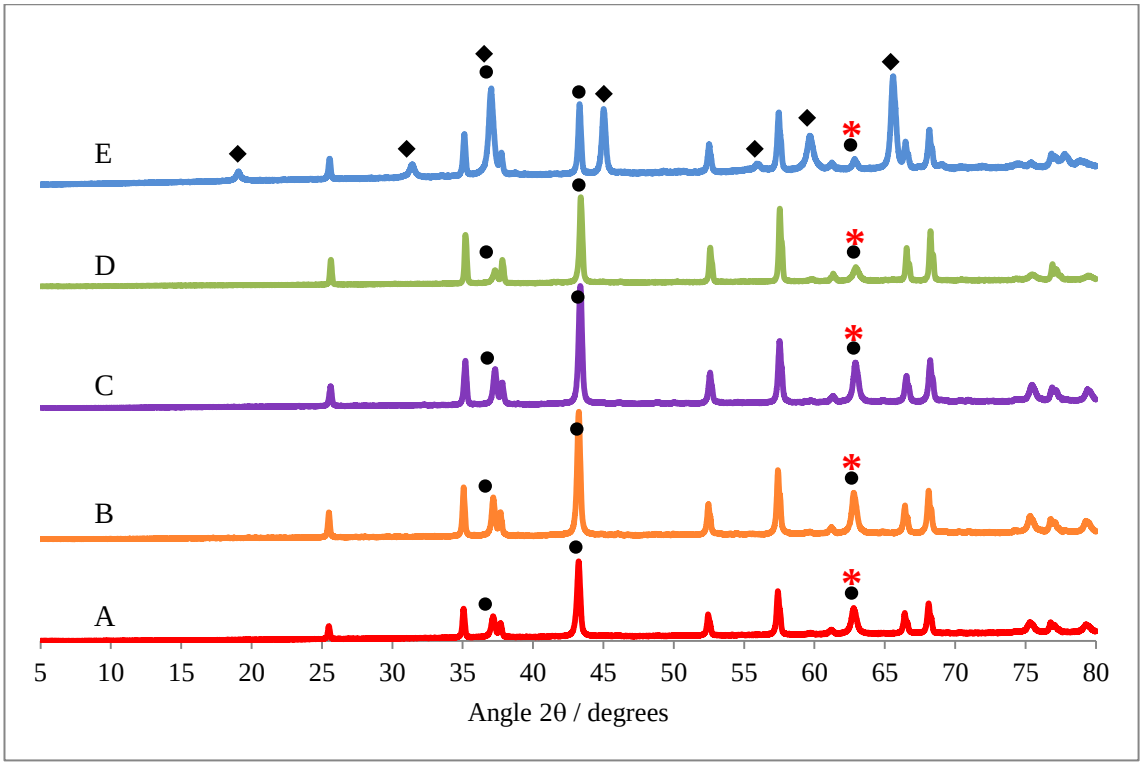

Figure 4.15: XRD profiles of A, NiO/Al_2O_3 (600); B, NiO/Al_2O_3 (700); C, NiO/Al_2O_3 (800); D, NiO/Al_2O_3 (900) and E, NiO/Al_2O_3 (1000) (● NiO, ♦$NiAl_2O_4$)

Table 4.4: Approximate NiO crystallite size determined via the Scherrer equation for the most distinct peak in XRD profile

Sample	Approximate NiO crystallite size / nm
NiO/Al_2O_3 (600)	29
NiO/Al_2O_3 (700)	35
NiO/Al_2O_3 (800)	32
NiO/Al_2O_3 (900)	30
NiO/Al_2O_3 (1000)	54

All the calcined samples exhibit diffraction peaks characteristic of α-Al_2O_3 (25.5°, 35.0°, 37.8°, 43.3°, 52.5°, 57.5°, 66.5° and 68.2°) and NiO (37.2°, 43.3° and 62.8°). The presence of an additional phase with peaks at 19.1°, 31.4°, 36.9°, 45.0°, 57.2°, 59.6° and 65.6° is observed for NiO/Al_2O_3 (1000). This phase is attributed to the formation of nickel aluminate, $NiAl_2O_4$ (ICDD-PDF database File card number: $NiAl_2O_4$, 01-1299). $NiAl_2O_4$ formation is not observed by XRD for catalysts calcined below 900 °C.

As the calcination temperature is increased from 600 °C to 800 °C, the NiO diffraction peaks at *ca.* 62.8° become sharper and more intense, indicating increased crystallinity. However, as the calcination temperature increases from 900 °C to 1000 °C, this peak becomes smaller and less defined. The crystallite size data determined from Scherrer analysis (Table 4.2) shows that as the calcination temperature is increased to 900 °C crystallite sizes remain *ca.* 30 nm. However, at the highest calcination temperature of 1000 °C, application of the Scherrer equation suggests that the NiO crystallite size almost doubles in size to 54 nm. This could indicate either significant sintering of the NiO crystallites or reduced crystallinity, at

high calcination temperatures. Chen *et al.* [8] also observe that calcination temperature is the main factor causing sintering of NiO species, as the calcination temperature increases the particle size of NiO increases.

4.2.2.4 Scanning electron microscopy (SEM)

SEM studies were undertaken in order to investigate sample morphology and approximate particle sizes of NiO crystallites. SEM studies over a magnification range of 15,000 to 60,000 were undertaken on all calcined samples. SEM images for all samples following calcination are shown in Figure 4.16 - Figure 4.20. The arrows displayed on SEM images indicate the possible presence of cubic NiO crystallites.

Figure 4.16: SEM image of NiO/Al_2O_3 (600) (magnification 30,000)

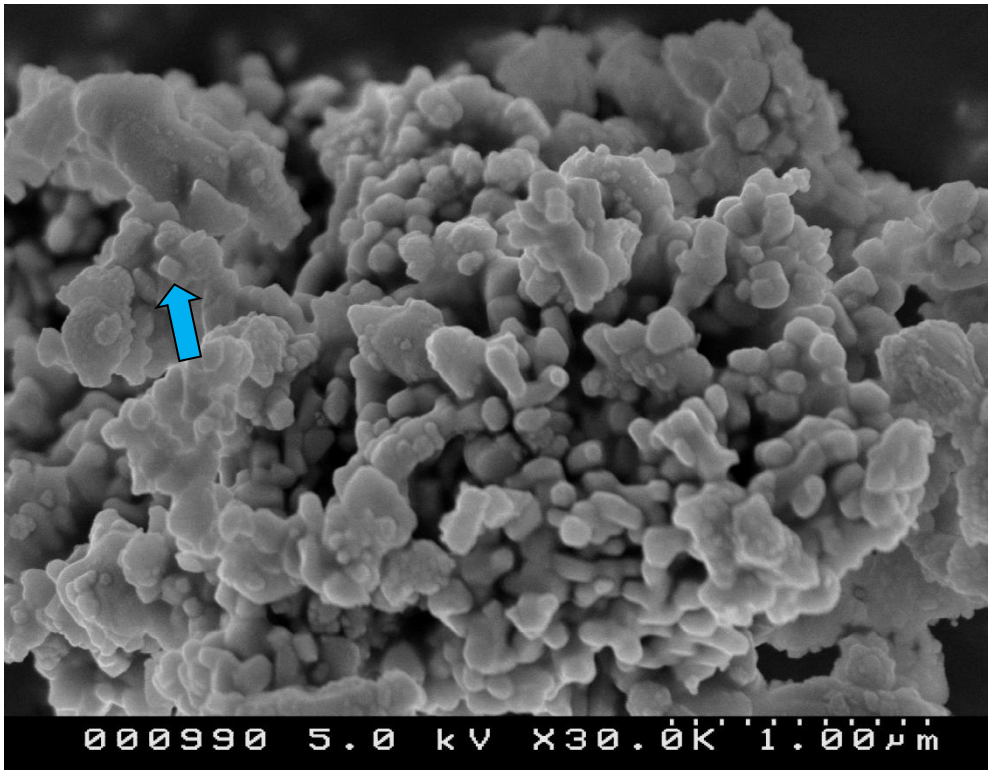

Figure 4.17: SEM image of NiO/Al_2O_3 (700) (magnification 30,000)

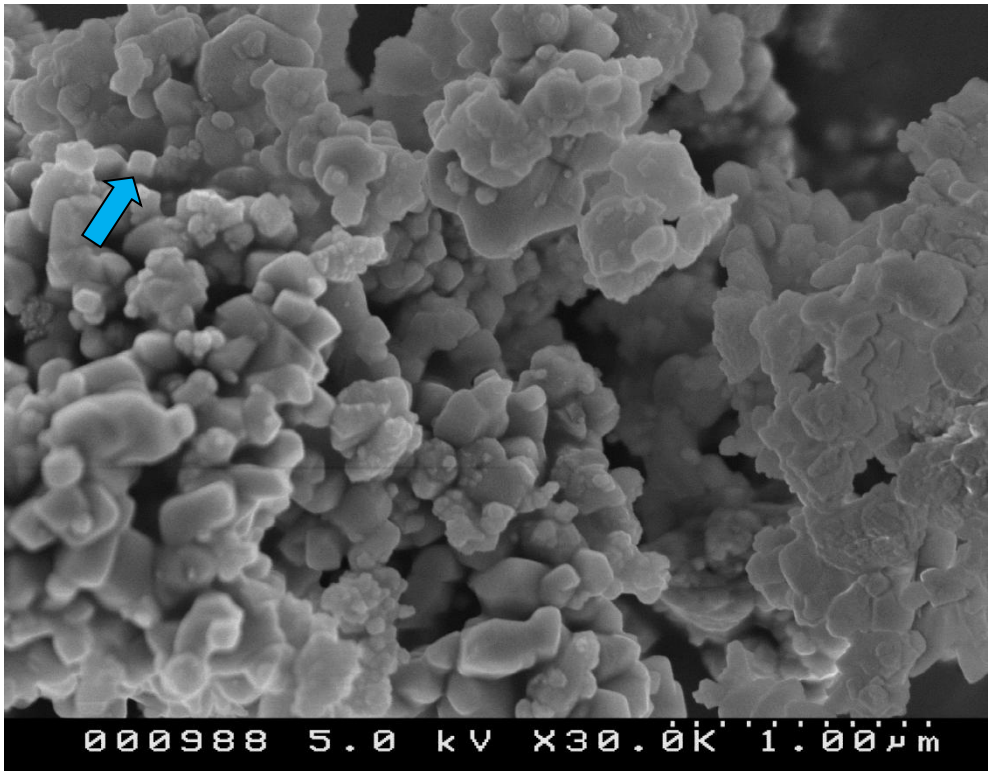

Figure 4.18: SEM image of NiO/Al_2O_3 (800) (magnification 30,000)

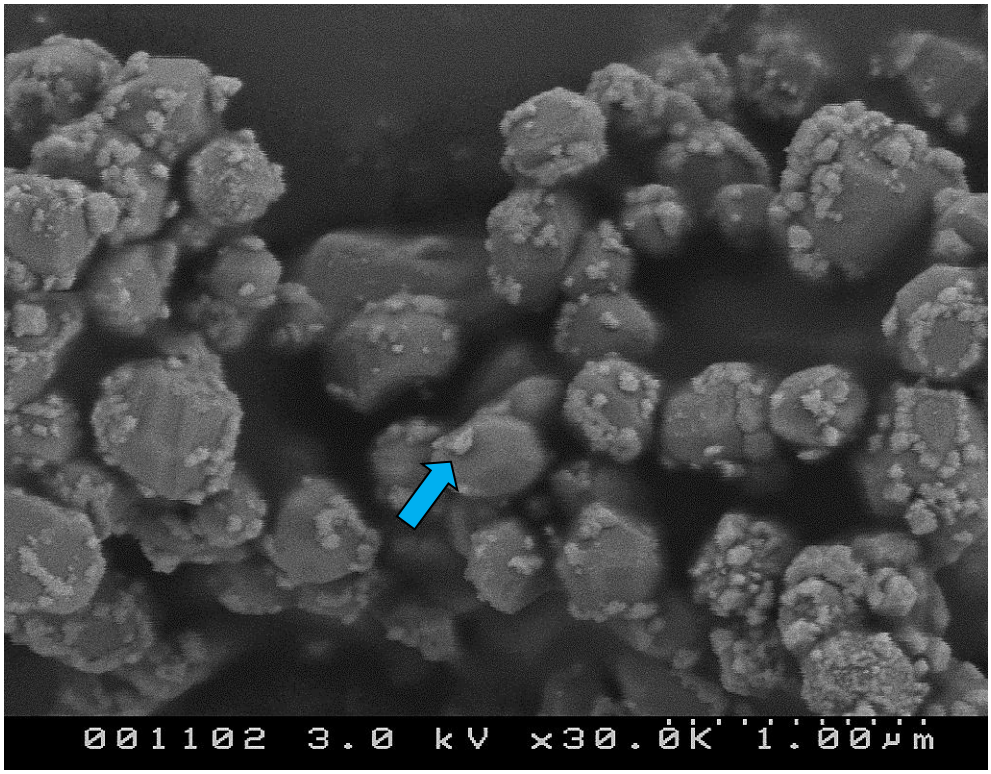

Figure 4.19: SEM image of NiO/Al_2O_3 (900) (magnification 30,000)

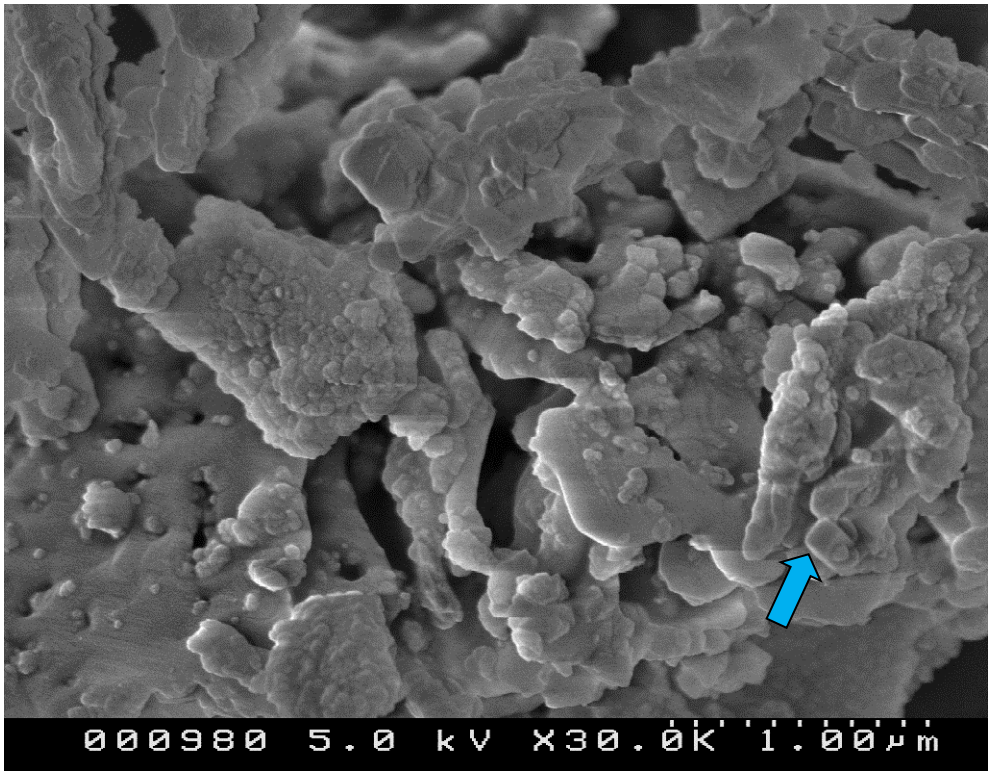

Figure 4.20: SEM image of NiO/Al_2O_3 (1000) (magnification 30,000)

The SEM images show that the support morphology is dramatically influenced by calcination temperature. At temperatures between 600 °C and 900 °C, the formation of uniform well defined support species is observed, becoming more pronounced as the temperature is increased. Small well distributed support particles observed in all samples, but most prominently in NiO/Al_2O_3 (600), conglomerate as the calcination temperature is increased forming larger species [22]. Uniform, spherical support species are observed as the temperature is increased to 900 °C (Figure 4.19). However, the SEM image for NiO/Al_2O_3 (1000) (Figure 4.20) shows the formation of large non-uniform sheets with a less defined morphology, significantly different to that of NiO/Al_2O_3 (900). This indicates that temperature is affecting support morphology most dramatically, at the highest calcination temperatures.

Few cubic well distributed NiO crystallites are observed on the support in NiO/Al_2O_3 (1000), compared to NiO/Al_2O_3 (900). This suggests that following high temperature calcination at 1000 °C, NiO is no longer highly dispersed on the support surface, but may be incorporated into the bulk structure.

The SEM images suggest that at calcination temperatures between 600 °C and 900 °C, NiO particle sizes remain relatively constant ranging from *ca.* 50 nm to 200 nm in all samples calcined up to 900 ºC. However, at 1000 °C due to the amorphous nature of NiO/Al_2O_3 (1000), the NiO crystallite sizes appear to be significantly larger. This is consistent with crystallite data determined using XRD, indicating sintering of NiO at this temperature. As NiO is incorporated into the bulk structure at high calcination temperatures, the morphology of the sample is considerably altered, becoming less uniform and defined.

4.2.2.5 X-ray photoelectron spectroscopy (XPS)

SEM studies show that the structural morphology and surface properties of the samples are altered with increasing calcination temperature. XPS measurements of the calcined samples were carried out to further study the surface properties.

The Ni 2p and O 1s spectra of NiO/Al_2O_3 (600) are shown in Figure 4.21 and Figure 4.23, respectively. The Ni 2p and O 1s spectra of NiO/Al_2O_3 (900) and NiO/Al_2O_3 (1000) are shown in Figure 4.22 and Figure 4.24 respectively. Curve fitting of the spectra was carried out in an attempt to more easily assign the different surface species present in the Ni 2p and O 1s spectra. All spectra show the experimental data (black), peak fitted components (blue, green, yellow and purple) and peak fitted spectra curve (red).

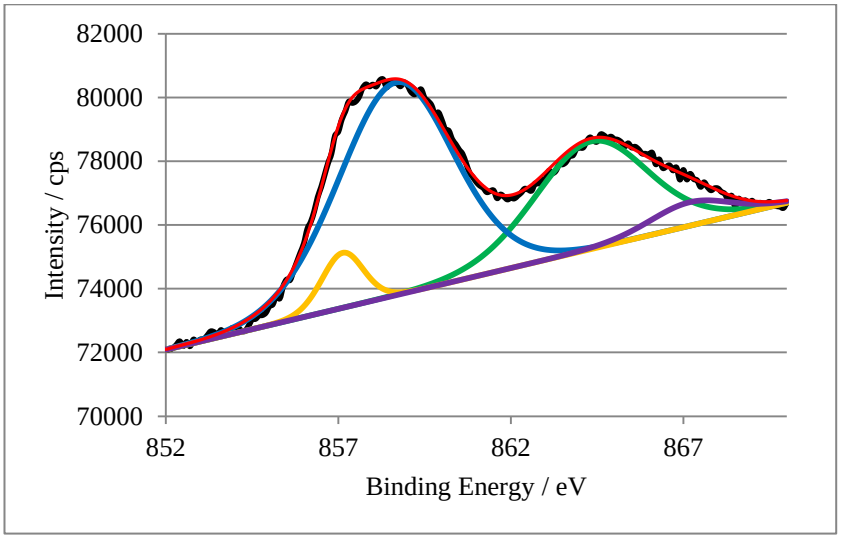

Figure 4.21: Peak fitted Ni 2p XP spectrum of NiO/Al_2O_3 (600)

The Ni 2p peak fitted spectrum shows the presence of two primary peaks at binding energies of 857.1 and 858.7 eV and two satellite deconvoluted peaks at 864.3 and 867.2 eV (Figure 4.21). The two primary peaks and corresponding satellite peaks, are similar to those observed for unsupported NiO (Figure 4.8) and are generally assigned by the presence or absence of satellite peaks. The primary peaks at 857.1 and 858.7 eV can be attributed to Ni^{2+} and Ni^{3+} respectively, due to the presence of the two satellite peaks as observed for

unsupported standard NiO. The Ni 2p peaks are shifted to higher binding energies, than for unsupported NiO, which is attributed to the interaction of NiO with the support, an increase of 3.1 and 2.2 eV is observed for Ni^{2+} and Ni^{3+} respectively.

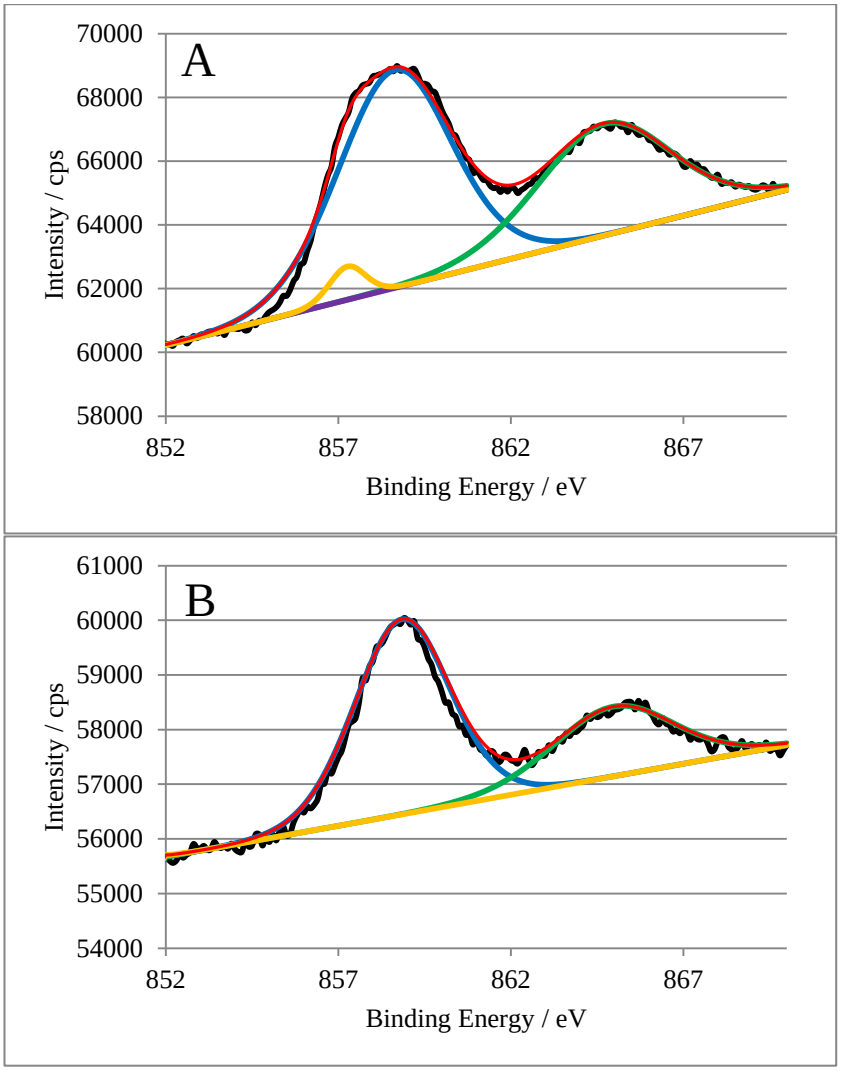

Figure 4.22: Peak fitted Ni 2p XP spectra of A, NiO/Al_2O_3 (900) and B, NiO/Al_2O_3 (1000)

The Ni 2p peak fitted spectra for both samples (Figure 4.22), shows the presence of a primary peak, at a binding energy of 858.6 eV for NiO/Al_2O_3 (900) and 858.9 eV for NiO/Al_2O_3 (1000). This peak can be attributed to nickel aluminate, $NiAl_2O_4$. This primary peak is not assigned to Ni^{3+}, due to the absence of a Ni^{3+} satellite peak [11]. Ni^{2+} ions present in both the NiO and the $NiAl_2O_4$ phase have satellite peaks at a very similar binding energy,

therefore, only one satellite peak is observed when both phases are present [13]. Additionally, the XP spectrum of NiO/Al_2O_3 (900) shows the presence of a peak at 857.3 eV, this is attributed to the presence of stoichiometric NiO.

As with NiO/Al_2O_3 (600), the peaks are shifted to higher binding energies due to nickel-support interactions. In NiO/Al_2O_3 (900), the presence of NiO, in addition to $NiAl_2O_4$, shifts the Ni^{2+} satellite peak by 0.2 eV to a slightly lower binding energy, compared to NiO/Al_2O_3 (1000).

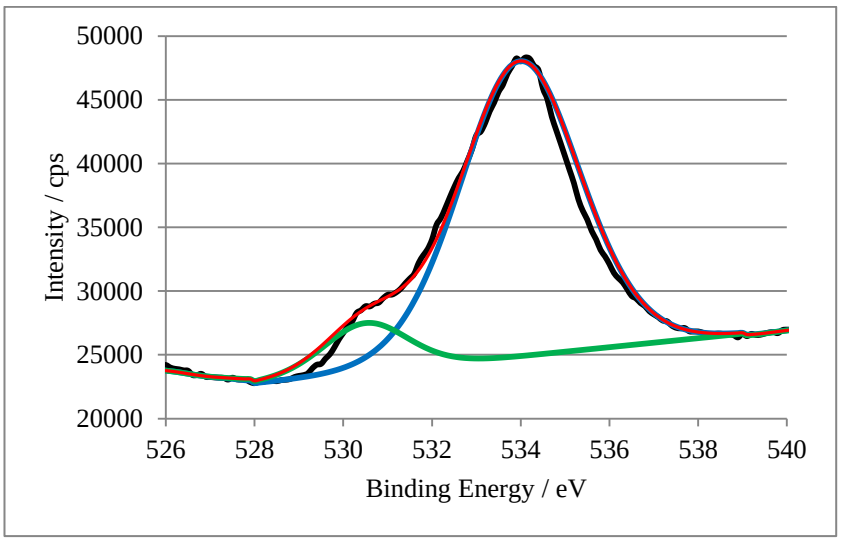

Figure 4.23: Peak fitted O 1s XP spectrum of NiO/Al_2O_3 (600)

The O 1s peak fitted spectrum shows the presence of two peaks at 530.5 and 534.0 eV (Figure 4.23), which are attributed to oxygen associated with Ni and Al_2O_3 [23], respectively.

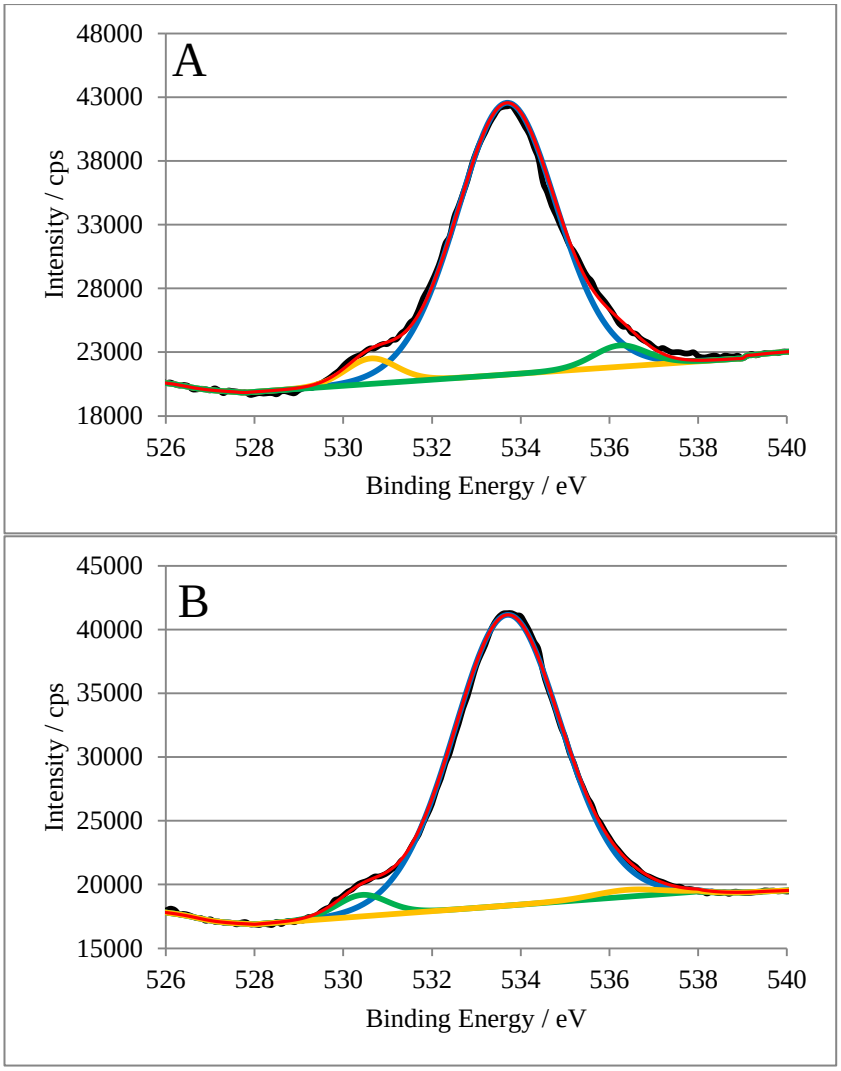

Figure 4.24: Peak fitted O 1s XP spectra of A, NiO/Al_2O_3 (900) and B, NiO/Al_2O_3 (1000)

The O 1s peak fitted spectra of the samples calcined at 900 and 1000 °C suggests the presence of three peaks (Figure 4.24). Peaks at 530.6 eV for Ni/Al_2O_3 (900) and 530.4 eV for Ni/Al_2O_3 (1000), are attributed to oxygen bonding to Ni [23]. The peak at 533.7 eV, in both spectra, is attributed to oxygen bonding with Al [23]. Both samples show the presence of an additional peak at *ca*. 536 eV, which is attributed to surface hydroxyl groups [18]. This peak is also observed in the O 1s spectrum of unsupported NiO (Figure 4.8). Hydroxyl groups are reported to have been introduced to the catalyst during the preparative stage and retained by alumina during preparation [24].

Analysis of the Ni 2p spectra suggests two different surface states of Ni^{2+} are present, corresponding to NiO and $NiAl_2O_4$. Both surface species are present following calcination at 900 °C. However, only surface NiO is present following calcination at 600 °C and only surface $NiAl_2O_4$ is present following calcination at 1000 °C. Analysis of the O 1s spectra distinguishes the oxygen bonded to the nickel and Al_2O_3, as well as adsorbed hydroxyl groups in some samples. Hydroxyl groups are present as samples are stored in air at room temperature. The Al 2p spectra of all samples show peaks at *ca.* 76 eV, corresponding to Al bonding with O. The O 1s and Al 2p spectra were less useful in the identification of surface nickel phases present.

The XP spectra clearly shows that as the calcination temperature is increased from 900 °C to 1000 °C, surface NiO is no longer present or able to be detected, and the presence of surface $NiAl_2O_4$ increases. XPS data is consistent with XRD results indicating the presence of an additional phase in samples that undergo calcination at 1000 ºC. However, it is important to note that XPS clearly identifies the presence of surface $NiAl_2O_4$ following calcination at 900 °C, whereas XRD analysis does not detect this phase.

4.2.3 Temperature-programmed reduction (TPR)

TPR profiles of NiO/Al_2O_3 (600), NiO/Al_2O_3 (700), NiO/Al_2O_3 (800), NiO/Al_2O_3 (900) and NiO/Al_2O_3 (1000) are shown in Figure 4.25 - Figure 4.29. The temperatures corresponding to maximum water evolution during reduction are listed in Table 4.5.

The TPR peaks correspond to different reducible Ni^{2+} states, each with a certain interaction with the alumina support. The ratio of the reduction peak area provides an indication of the ratio of different Ni^{2+} states in each sample, as shown in Table 4.5. A higher reduction peak temperature indicates a stronger interaction between NiO and Al_2O_3. Three reduction peaks

have been observed during reduction of alumina supported nickel catalysts [25, 26]. Unsupported NiO reduces at relatively low temperatures, *ca*. 400 °C, as shown in Figure 4.10. Peaks at such temperatures can be attributed to surface Ni^{2+}. Slightly higher temperature reduction peaks at around 600 °C relate to surface Ni^{2+} interacting with the support. Higher temperature reduction peaks present, above 600 °C, can be attributed to Ni^{2+} interacting more strongly with the alumina support and incorporation into the bulk support structure.

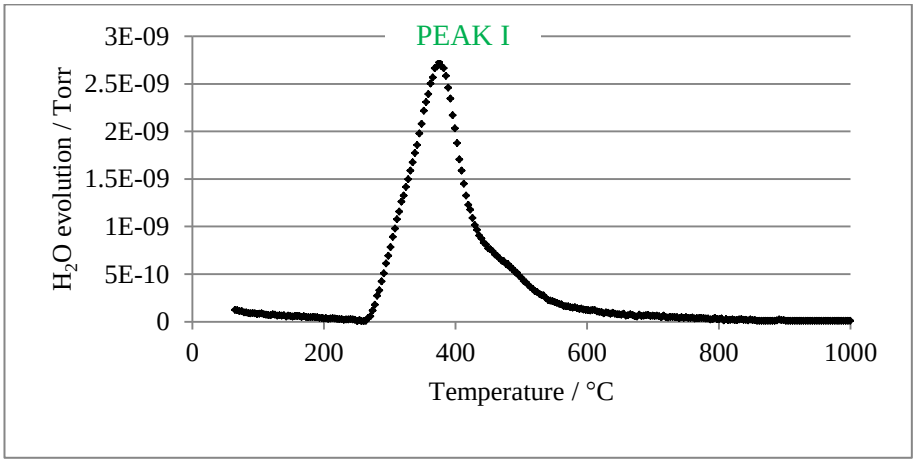

Figure 4.25: TPR profile of NiO/Al_2O_3 (600)

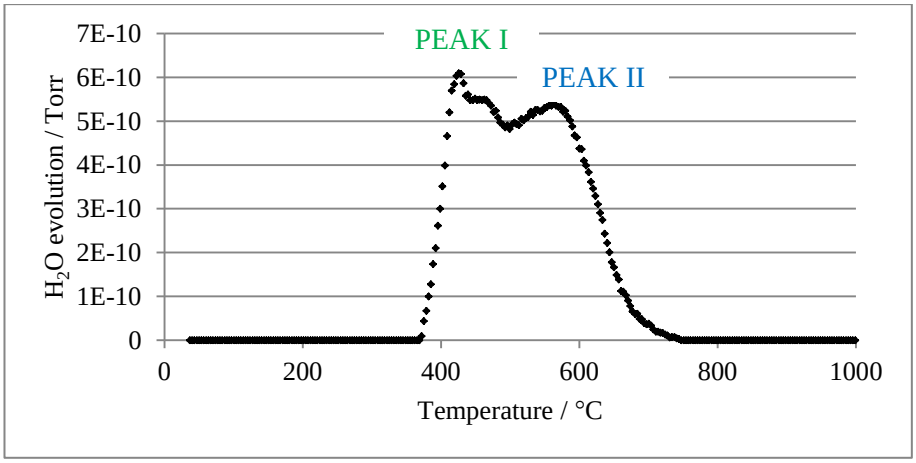

Figure 4.26: TPR profile of NiO/Al_2O_3 (700)

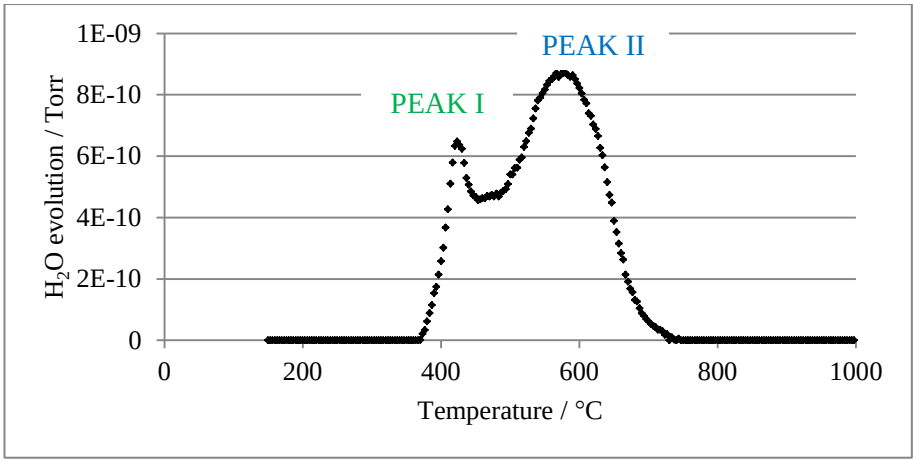

Figure 4.27: TPR profile of NiO/Al_2O_3 (800)

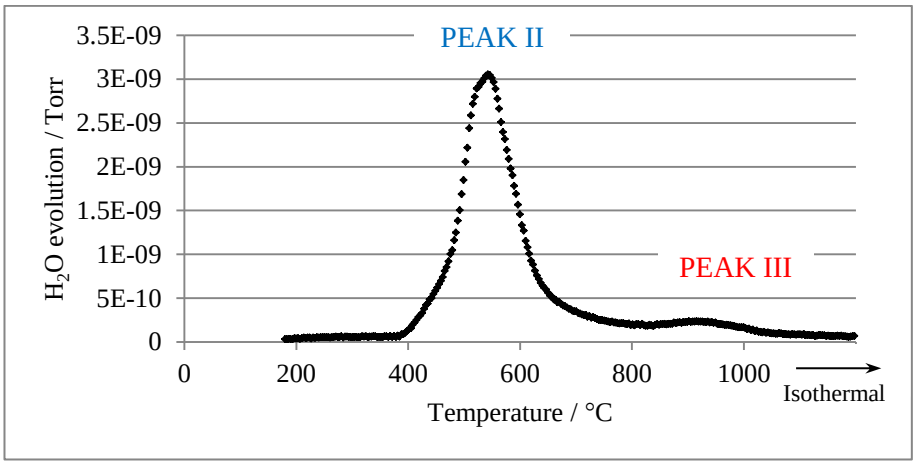

Figure 4.28: TPR profile of NiO/Al_2O_3 (900)

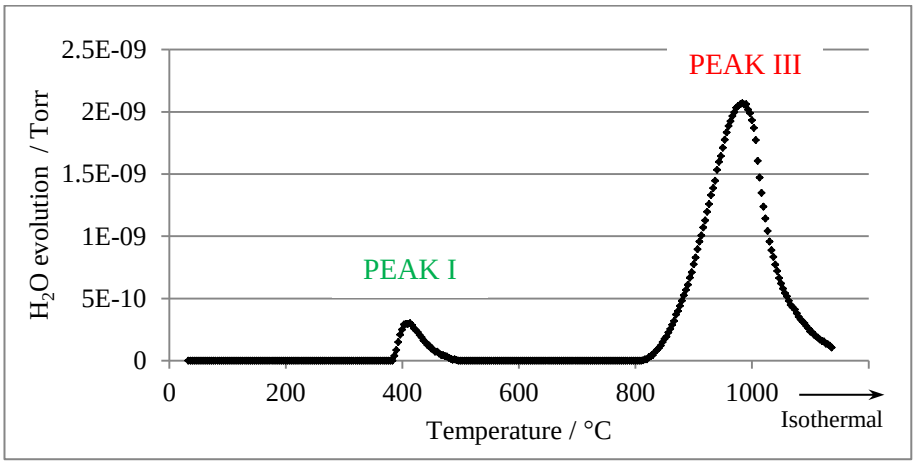

Figure 4.29: TPR profile of NiO/Al_2O_3 (1000)

Table 4.5: Reduction peak temperatures and approximate ratios of reduction peak areas obtained from the TPR profiles of NiO/Al_2O_3 (600), NiO/Al_2O_3 (700), NiO/Al_2O_3 (800), NiO/Al_2O_3 (900) and NiO/Al_2O_3 (1000)

Sample	Reduction peak temperature [a] / °C			Approximate area ratios of peaks (I:II:III)
	Peak I	Peak II	Peak III	
NiO/Al_2O_3 (600)	375	-	-	100 : 0 : 0
NiO/Al_2O_3 (700)	426	563	-	44 : 56 : 0
NiO/Al_2O_3 (800)	423	580	-	28 : 72 : 0
NiO/Al_2O_3 (900)	-	542	915	0 : 87 : 13
NiO/Al_2O_3 (1000)	406	-	951	18 : 0 : 82

[a] Temperature at maximum water evolution

TPR peaks at *ca.* 400 °C correspond to the reduction of 'free' surface NiO (Peak I). A peak at this temperature is observed for all the calcined samples, except NiO/Al_2O_3 (900). A higher temperature shoulder is observed on Peak I in the TPR profile of NiO/Al_2O_3 (600). This increases in size and is observed as a distinct peak (Peak II) in the samples calcined at 700 °C, 800 °C and 900 °C (Figure 4.26 - Figure 4.28). This indicates the presence of Ni^{2+} with a stronger interaction with the support. Such intimate contact between the nickel oxide and support results in moderately strong interactions, even if only through charge transfer, resulting in a reducibility intermediate between that of bulk NiO (Peak I) and $NiAl_2O_4$ (Peak III). Peak II varies in temperature depending upon the extent of the oxide-support interactions, the stronger the interaction the higher reduction temperature.

Higher temperature reduction peaks above 600 °C (Peak III), are observed for the samples calcined at 900 ºC and 1000 °C, (Figure 4.28 and Figure 4.29). The Ni^{2+} is harder to reduce

due to strong interactions with the alumina support or incorporation of Ni^{2+} into the bulk support structure, forming $NiAl_2O_4$, characterised by the high temperatures required for complete reduction [2, 4, 6, 21, 27-29].

Peak II is not observed for NiO/Al_2O_3 (1000) (Figure 4.29). This suggests that Ni^{2+} is either incorporated into the bulk structure or present as 'free' surface NiO. Salhi *et al.* [26] have proposed that $NiAl_2O_4$ is not a 'tolerant' structure and excess nickel will be rejected and dispersed as NiO. This would account for the presence of only the low and high temperature reduction peaks at this calcination temperature. 1000 °C may not be a high enough temperature to facilitate the complete formation of $NiAl_2O_4$, thus limited formation is observed.

The reduction profile obtained for NiO/Al_2O_3 (900) (Figure 4.28) is consistent with results reported by Teixeira *et al.* [25], where two reduction peak maxima were observed at higher temperatures. These correspond to an oxide strongly interacting with the support (Peak II) and stoichiometric $NiAl_2O_4$ (Peak III). No low temperature peak corresponding to 'free' NiO with weak interaction with the support is observed.

No high temperature reduction peak is observed for samples calcined below 800 °C, indicating that this calcination temperature is not high enough to facilitate such strong interactions and incorporation of Ni^{2+} into the bulk support structure. Higher calcination temperatures promote the incorporation of Ni^{2+} into the bulk structure forming $NiAl_2O_4$, which is more difficult to reduce [2, 4, 21]. Up to 82 % of the nickel is present in this state for NiO/Al_2O_3 (1000), compared to *ca.* 9 % for NiO/Al_2O_3 (900). Numaguchi *et al.* [14] have reported that as the calcination temperature of a Ni/Al_2O_3 sample is increased the ratio of $NiAl_2O_4$ formed increases, reducing NiO content, so resulting in a greater amount of species that are difficult to reduce. This has been confirmed by Molina and Poncelet [13], who reported that at high temperatures redistribution of nickel species between octahedral and tetrahedral sites is accompanied by the formation of $NiAl_2O_4$ and a decrease in surface nickel

species. Nickel located in tetrahedral sites are reported to be more difficult to reduce than Ni located in octahedral sites, due to a higher binding energy [2]. This is consistent with the XPS data (Section 4.1.2.3) for the 900 °C and 1000 °C calcined samples, which shows that Ni^{2+} present as $NiAl_2O_4$ has a higher binding energy than NiO. This accounts for the high reduction temperature observed (Peak III) upon incorporation of Ni^{2+} into the bulk structure.

Although a small high temperature reduction peak is observed in the TPR of NiO/Al_2O_3 (900), no additional phases are observed in the XRD pattern (Section 4.2.2.3, Figure 4.15). This phase could be attributed to a non-crystalline form of $NiAl_2O_4$. The presence of such a species has been suggested by Salgare *et al.* [11] and Chen *et al.* [9]. Alternatively, as TPR results show that only a small amount of $NiAl_2O_4$ is present compared to NiO, its detection could be below the XRD detection limits. Calcination at 900 °C may be a fundamental temperature in formation of $NiAl_2O_4$ and increased interactions between the oxide and support phase.

4.2.4 Characterisation of reduced Ni/Al_2O_3 samples

Prior to any catalytic reaction, all the catalyst samples were activated by reduction in hydrogen at elevated temperatures. Characterisation of the reduced samples using XRD, SEM and XPS was undertaken.

4.2.4.1 X-ray diffraction (XRD)

XRD patterns for the reduced samples are shown in Figure 4.30, whilst Table 4.6 shows the corresponding crystallite sizes of the nickel species. The peak corresponding to nickel at *ca.* 51.7º (*) was used for nickel crystallite size determination.

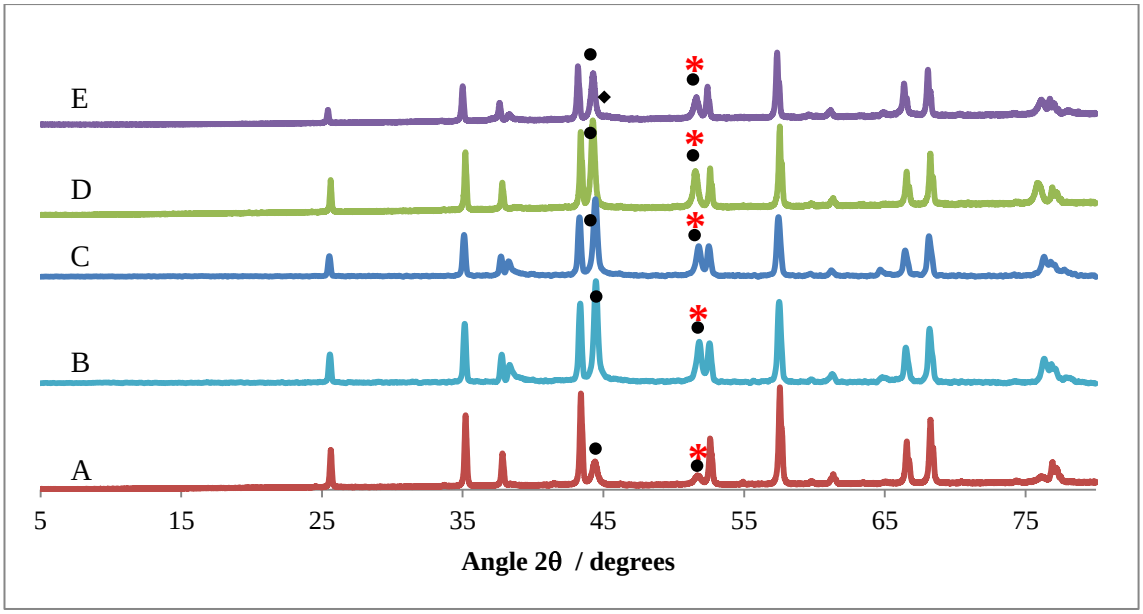

Figure 4.30: **XRD profiles of A, Ni/Al_2O_3 (600); B, Ni/Al_2O_3 (700); C, Ni/Al_2O_3 (800); D, Ni/Al_2O_3 (900); E, Ni/Al_2O_3 (1000) (● Ni, ♦ $NiAl_2O_4$)**

Table 4.6: **Approximate nickel crystallite size determined via the Scherrer equation for the most distinct peak in XRD profile**

Sample	Approximate nickel crystallite size / nm
Ni/Al_2O_3 (600)	34
Ni/Al_2O_3 (700)	34
Ni/Al_2O_3 (800)	33
Ni/Al_2O_3 (900)	39
Ni/Al_2O_3 (1000)	33

Post-reduction XRD patterns clearly show metallic nickel at *ca.* 44.5° and 51.7°, produced from the reduction of NiO and $NiAl_2O_4$. This metallic phase is observed in all post-reduction profiles. No NiO phase is present in post-reduction XRD profiles for the samples calcined at 600 °C to 900 °C, indicating complete reduction. The $NiAl_2O_4$ phase (with peaks at *ca.* 45°) is identified in the post-reduction XRD profile of Ni/Al_2O_3 (1000), indicating that some Ni^{2+} species are not reducible under the reduction conditions employed and remain in as $NiAl_2O_4$. Isobe *et al.* [30] have reported that $NiAl_2O_4$ does not completely decompose (to NiO and Al_2O_3) until *ca.* 1300 °C. However, it is important to note that this is an extremely small diffraction peak compared to those observed for $NiAl_2O_4$ species in the calcined samples (Section 4.2.2.3).

The nickel crystallite sizes are all *ca.* 32 to 38 nm, indicating that the reduction treatment has little effect on nickel particle sintering. In some cases, the nickel crystallite sizes are smaller following reduction than those of the calcined NiO. In Ni/Al_2O_3 (1000), the approximate nickel crystallite size is smaller than the NiO crystallite size. This is consistent with the results gained for standard samples, where the NiO crystallite size was significantly larger than the nickel particles. Although sintering of NiO may occur during calcination at 1000 °C, during reduction nickel is re-dispersed on the support and substantial sintering of nickel does not occur at the reduction temperatures used in this study. Chen *et al.* [8] have reported that the nickel particle size in samples following reduction is larger than that of NiO in pre-reduced samples, particularly at lower calcination temperatures. This is consistent with this study where nickel crystallite sizes, following low temperature calcination, are slightly increased following reduction. However, this behaviour is not observed following higher calcination temperatures.

4.2.4.2 Scanning electron microscopy (SEM)

SEM investigations were undertaken on samples Ni/Al_2O_3 (900) and Ni/Al_2O_3 (1000), following reduction. The SEM images are shown in Figure 4.31 and Figure 4.32, respectively.

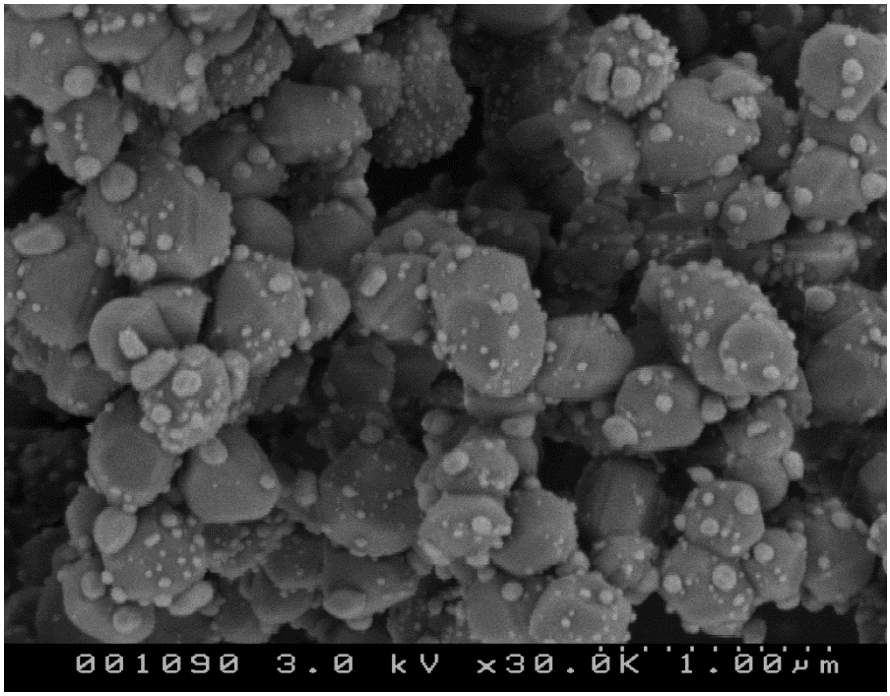

Figure 4.31: SEM image of Ni/Al_2O_3 (900) (magnification 30,000)

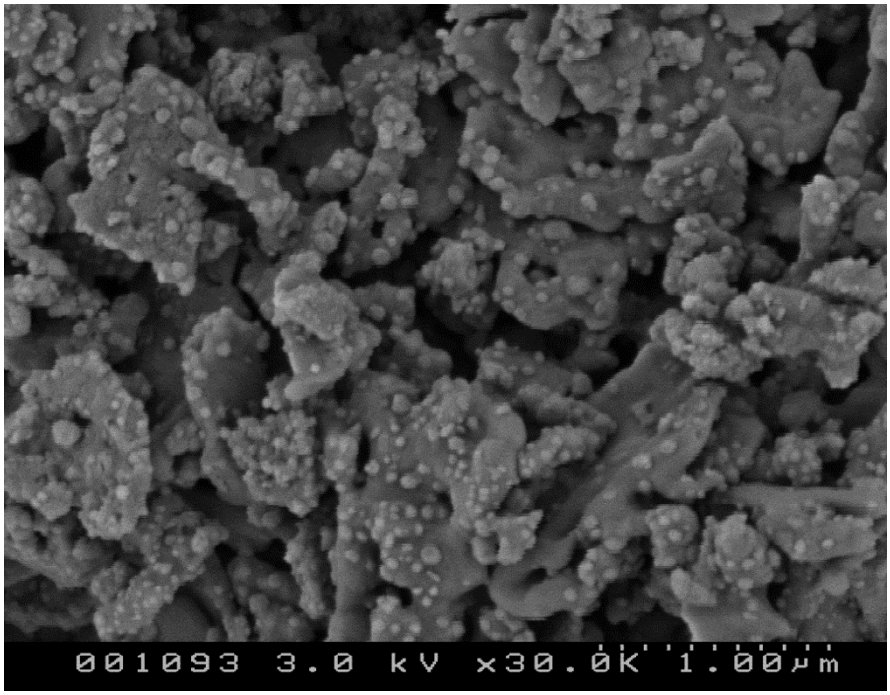

Figure 4.32: SEM image of Ni/Al_2O_3 (1000) (magnification 30,000)

The sample morphology of post-reduction images for Ni/Al_2O_3 (900) and (1000) (Figure 4.31 and Figure 4.32), relate to the corresponding post-calcination images (Figure 4.19 and Figure 4.20). The post-reduction images, following high temperature reduction show that the structure of the support remains the same as samples following calcination. Ni/Al_2O_3 (900) shows uniform support morphology and Ni/Al_2O_3 (1000) shows less defined support species. In both the post-reduction images, highly dispersed nickel can be observed on the Al_2O_3 support. The nickel species observed in both samples range from *ca.* 20 nm to 100 nm in size, which is consistent with crystallite size determined by Scherrer analysis (Section 4.2.4.1). Following reduction of Ni/Al_2O_3 (1000), an increase in the nickel dispersion on the support surface is observed, relating to the dispersion of NiO on the support (Figure 4.20). This suggests that following reduction Ni^{2+} that may have been incorporated into the bulk structure or sintered, during calcination, is reduced and re-dispersed on the support surface.

4.2.4.3 X-ray photoelectron spectroscopy (XPS)

XPS analysis was undertaken on both the Ni/Al_2O_3 (900) and Ni/Al_2O_3 (1000) following reduction, to try to determine if the surface $NiAl_2O_4$ species identified following calcination were fully reduced. However, the Ni 2p spectra obtained were not representative of metallic nickel. Following reduction, the samples were transferred in air to the XPS instrument for sample loading. It is likely that this resulted in surface oxidation of the nickel species, such that no peaks relating to Ni^0 (characteristic E_b values of *ca.* 853 eV) were identified in the XP spectra, only those relating to Ni^{2+} and Ni^{3+}. This problem has also been reported by Guczi *et al*. [31] who observed oxidation of surface Ni^0 to Ni^{2+} during XPS sample preparation and exposure to air.

Therefore, it is not possible to use XPS to validate the XRD results which indicate that all the Ni^{2+} ions present in the NiO phase are effectively reduced to metallic nickel and those present in $NiAl_2O_4$ phase are not fully reduced upon high temperature reduction.

4.2.5 Reducibility following reduction and re-calcination

Re-calcination of the samples was undertaken in order to investigate whether $NiAl_2O_4$ species are re-formed during calcination or if, once reduced, they will re-oxidise to NiO. This study also allows an insight into the sample reducibility following reduction and re-calcination.

Initially, NiO/Al_2O_3 (1000) was reduced under the TPR conditions and was then held at 1000 °C to ensure complete reduction of all $NiAl_2O_4$ species, as shown in Section 4.2.3. Following reduction the sample was re-oxidised, using the *in situ* TPO procedure discussed in Section 4.2.1. Following re-calcination, the sample was once again reduced under TPR conditions. Samples were not removed from the reactor unit between any of the reduction or oxidation procedures.

Following re-oxidation, the sample appeared the same blue colour as shown in Section 4.2.2.1. The initial TPR profile is shown in Figure 4.33. The reduction profile for the sample following re-calcination is shown in Figure 4.34.

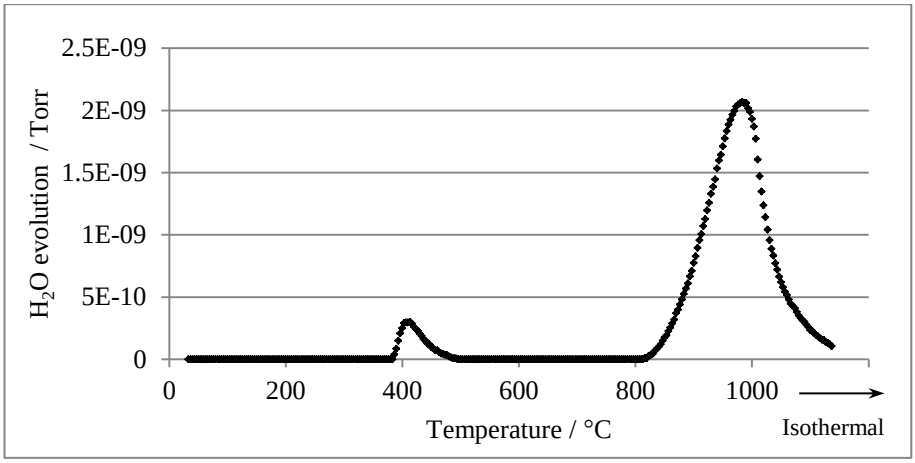

Figure 4.33: TPR profile of NiO/Al_2O_3 (1000)

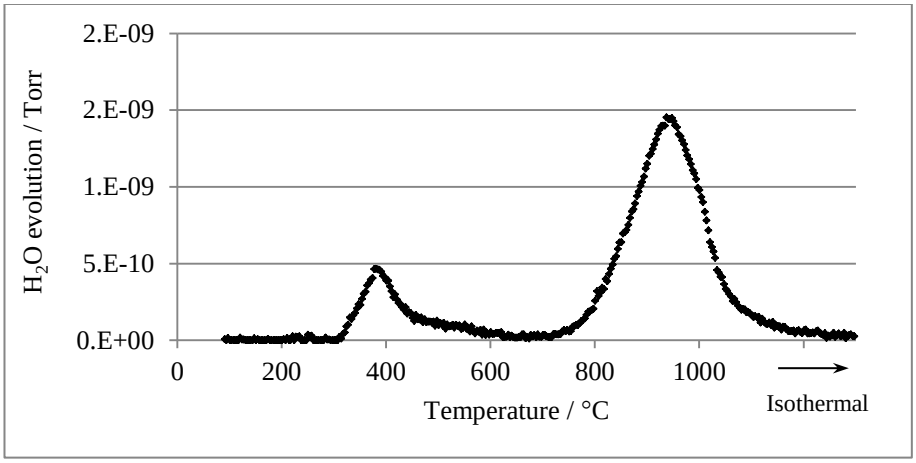

Figure 4.34: TPR profile of NiO/Al_2O_3 (1000) following reduction and re-calcination

$NiAl_2O_4$ species were identified in NiO/Al_2O_3 (1000) during characterisation of calcined samples (Section 4.1.2) and although a small proportion of $NiAl_2O_4$ remains unreduced following TPR reactions, the majority of the Ni^{2+} species were shown by XRD to reduce to Ni^0 during the reduction procedure. Following re-calcination of Ni/Al_2O_3 (1000), Ni^{2+} species are reduced at low and high temperatures, exactly as observed in the initial TPR. Thus, although Ni^{2+} species are reduced and re-dispersed on the support surface following

initial reduction, upon re-calcination the reduced nickel species re-oxidise to their original forms, as NiO and $NiAl_2O_4$. This indicates that although reduction effectively reduces all Ni^{2+} species, oxidation at high temperatures results in the formation of $NiAl_2O_4$ and the re-incorporation of Ni^{2+} into the bulk support structure. This suggests that this behaviour may be completely reversible on successive cycles of oxidation and reduction.

4.3 Summary

This study shows that, a low calcination temperature of 600 °C ensures that $NiAl_2O_4$ is not formed and all Ni^{2+} species can be reduced at relatively low reduction temperatures, due to limited interactions between the oxide and support. TPR and SEM results indicate that calcination at temperatures of 700 °C and 800 °C, results in increased interactions between the oxide and support, although no incorporation of Ni^{2+} into the bulk support structure is observed.

900 °C is a fundamental temperature during calcination, as XRD, XPS and TPR studies indicate the initial stages of $NiAl_2O_4$ formation occurring. Results suggest the formation of non-crystalline $NiAl_2O_4$ species and increased interactions between Ni^{2+} and the support. Two Ni^{2+} phases are present in the catalyst, both NiO and $NiAl_2O_4$. However, this calcination temperature is not high enough to facilitate the formation of a crystalline $NiAl_2O_4$.

Upon calcination at 1000 °C, crystalline $NiAl_2O_4$ is formed. Although bulk NiO is detected by TPR and XRD, no surface NiO was detected by XPS. This may due to low levels present on the sample surface or suggests that no surface NiO is present. TPR and XRD show that during calcination at 1000 °C two reactions occur, one forming crystalline surface $NiAl_2O_4$ species, the other segregation of free NiO. Calcination at 1000 ºC, also results in significant sintering of NiO crystallites.

High reduction temperatures are required for complete reduction of all Ni^{2+} species, especially those incorporated into the bulk support structure. $NiAl_2O_4$ is difficult to reduce at temperatures below 700 °C [2, 4, 27-29]. A number of authors [21, 32, 33] have shown that without such high reduction temperatures, insufficient reduction of $NiAl_2O_4$ phase will occur, resulting in reduced reforming activity of the catalyst. This shows the importance of holding the sample at 1000 °C, ensuring complete reduction of all Ni^{2+} species. XRD indicates that Ni^{2+} is effectively reduced to metallic nickel. However, in Ni/Al_2O_3 (1000), a small majority of $NiAl_2O_4$ is not effectively reduced, remaining as Ni^{2+} in the spinel phase. Despite this, following reduction, nickel is highly dispersed on the support surface and the support morphology is not altered during high temperature reduction. There is no indication that high temperature reduction conditions result in any further sintering of the nickel particles and all nickel crystallite sizes are comparable in all catalysts.

Re-calcination of Ni/Al_2O_3 (1000) following reduction, results in the re-formation of $NiAl_2O_4$ species. This shows that upon initial formation of spinel phases during calcination, re-oxidation to this phase from dispersed nickel is entirely reversible and temperature dependant.

Despite the contradicting literature relating to this area, the use of analytical techniques in this study, confirm that the calcination temperature selected during preparation can have a dramatic influence upon the morphology, structure, phases formed and reducibility of 20 wt % Ni/Al_2O_3 samples. The calcination temperature of Ni/Al_2O_3 catalysts must be chosen with care and attention paid to subsequent phases formed during preparation. Additionally, the activation procedure employed must be carefully considered in order to obtain a fully active catalyst with high distribution of active metallic species.

4.4 References

1. A.R. West, *Basic Solid State Chemistry*. 1988: John Whiley & Sons.
2. G. Li, L. Hu, and J.M. Hill, *Comparison of reducibility and stability of alumina-supported Ni catalysts prepared by impregnation and co-precipitation.* Applied Catalysis A: General, 2006. **301**(1): p. 16-24.
3. N. Sahli, C. Petit, A.C. Roger, A. Kiennemann, S. Libs, and M.M. Bettahar, *Ni catalysts from $NiAl_2O_4$ spinel for CO_2 reforming of methane.* Catalysis Today, 2006. **113**(3-4): p. 187-193.
4. H.-S. Roh, K.-W. Jun, and S.-E. Park, *Methane-reforming reactions over Ni/Ce-ZrO_2/θ-Al_2O_3 catalysts.* Applied Catalysis A: General, 2003. **251**(2): p. 275-283.
5. P. Kim, Y. Kim, H. Kim, I.K. Song, and J. Yi, *Synthesis and characterization of mesoporous alumina with nickel incorporated for use in the partial oxidation of methane into synthesis gas.* Applied Catalysis A: General, 2004. **272**(1-2): p. 157-166.
6. C. Li and Y.-W. Chen, *Temperature-programmed-reduction studies of nickel oxide/alumina catalysts: effects of the preparation method.* Thermochimica Acta, 1995. **256**(2): p. 457-465.
7. H. Cui, M. Zayat, and D. Levy, *A sol-gel route using propylene oxide as a gelation agent to synthesize spherical $NiAl_2O_4$ nanoparticles.* Journal of Non-Crystalline Solids, 2005. **351**(24-26): p. 2102-2106.
8. I. Chen, S.-Y. Lin, and D.-W. Shiue, *Calcination of nickel/alumina catalysts.* Industrial and Engineering Chemistry Research, 1988. **27**: p. 926-929.
9. J. Chen, Q. Ma, T.E. Rufford, Y. Li, and Z. Zhu, *Influence of calcination temperatures of Feitknecht compound precursor on the structure of Ni-Al_2O_3 catalyst and the corresponding catalytic activity in methane decomposition to hydrogen and carbon nanofibers.* Applied Catalysis A: General, 2009. **362**(1-2): p. 1-7.

10. P. Jeevanandam, Y. Koltypin, and A. Gedanken, *Preparation of nanosized nickel aluminate spinel by a sonochemical method.* Materials Science and Engineering B, 2002. **90**(1-2): p. 125-132.

11. P. Salagre, J.L.G. Fierro, F. Medina, and J.E. Sueiras, *Characterization of nickel species on several γ-alumina supported nickel samples.* Journal of Molecular Catalysis A: Chemical, 1996. **106**(1-2): p. 125-134.

12. Y. Cesteros, P. Salagre, F. Medina, and J.E. Sueiras, *Preparation and Characterization of Several High-Area $NiAl_2O_4$ Spinels. Study of Their Reducibility.* Chemistry of Materials, 2000. **12**(2): p. 331-335.

13. R. Molina and G. Poncelet, *α-Alumina-Supported Nickel Catalysts Prepared with Nickel Acetylacetonate. 2. A Study of the Thermolysis of the Metal Precursor.* Journal of Physical Chemistry: B, 1999. **103**: p. 11290-11296.

14. T. Numaguchi, H. Eida, and K. Shoji, *Reduction of $NiAl_2O_4$ containing catalysts for steam methane reforming reaction.* International Journal of Hydrogen Energy, 1997. **22**(12): p. 1111-1115.

15. C.S. Nordahl and G.L. Messing, *Thermal analysis of phase transformation kinetics in α-Al_2O_3 seeded boehmite and γ-Al_2O_3.* Thermochimica Acta, 1998. **318**(1-2): p. 187-199.

16. B. Mile, D. Stirling, M.A. Zammitt, A. Lovell, and M. Webb, *The location of nickel oxide and nickel in silica-supported catalysts: Two forms of "NiO" and the assignment of temperature-programmed reduction profiles.* Journal of Catalysis, 1988. **114**(2): p. 217-229.

17. W. Brockner, C. Ehrhardt, and M. Gjikaj, *Thermal decomposition of nickel nitrate hexahydrate, $Ni(NO_3)_2{\cdot}6H_2O$, in comparison to $Co(NO_3)_2{\cdot}6H_2O$ and $Ca(NO_3)_2{\cdot}4H_2O$.* Thermochimica Acta, 2007. **456**(1): p. 64-68.

18. M.A. Langell and M.H. Nassir, *Stabilization of NiO(111) Thin Films by Surface Hydroxyls.* The Journal of Physical Chemistry, 1995. **99**(12): p. 4162-4169.

19. E. Heracleous, A.F. Lee, K. Wilson, and A.A. Lemonidou, *Investigation of Ni-based alumina-supported catalysts for the oxidative dehydrogenation of ethane to ethylene: structural characterization and reactivity studies.* Journal of Catalysis, 2005. **231**(1): p. 159-171.

20. B.V. Crist, *Handbook of Monochromatic XPS Spectra*. Vol. 2 - Commercially Pure Binary Oxides: Wiley-Blackwell.

21. O.-S. Joo and K.-D. Jung, *CH 4 Dry Reforming on Alumina-Supported Nickel Catalyst.* Bulletin of the Korean Chemical Society 2002. **23**(8): p. 1149-1153.

22. G.R. Gavalas, C. Phichitkul, and G.E. Voecks, *Structure and activity of NiO/α-Al_2O_3 and NiO/ZrO_2 calcined at high temperatures : I. Structure.* Journal of Catalysis, 1984. **88**(1): p. 54-64.

23. J. Jun, M. Dhayal, J.-H. Shin, Y.H. Han, and N. Getoff, *Surface chemistry and catalytic activity of Ni/Al_2O_3 irradiated with high-energy electron beam.* Applied Surface Science, 2008. **254**(15): p. 4557-4564.

24. I.P. Silverwood, N.G. Hamilton, A.R. McFarlane, J. Kapitan, L. Hecht, E.L. Norris, R. Mark Ormerod, C.D. Frost, S.F. Parker, and D. Lennon, *Application of inelastic neutron scattering to studies of CO_2 reforming of methane over alumina-supported nickel and gold-doped nickel catalysts.* Physical Chemistry Chemical Physics, 2012.

25. A.C.S.C. Teixeira and R. Giudici, *Deactivation of steam reforming catalysts by sintering: experiments and simulation.* Chemical Engineering Science, 1999. **54**(15-16): p. 3609-3618.

26. N. Salhi, A. Boulahouache, C. Petit, A. Kiennemann, and C. Rabia, *Steam reforming of methane to syngas over $NiAl_2O_4$ spinel catalysts.* International Journal of Hydrogen Energy, 2011. **36**(17): p. 11433-11439.

27. Y.-H. Chin, D.L. King, H.-S. Roh, Y. Wang, and S.M. Heald, *Structure and reactivity investigations on supported bimetallic AuNi catalysts used for hydrocarbon steam reforming.* Journal of Catalysis, 2006. **244**(2): p. 153-162.

28. Y. Zhang, G. Xiong, S. Sheng, and W. Yang, *Deactivation studies over NiO/γ-Al_2O_3 catalysts for partial oxidation of methane to syngas.* Catalysis Today, 2000. **63**(2-4): p. 517-522.

29. J.A. Peña, J. Herguido, C. Guimon, A. Monzón, and J. Santamaría, *Hydrogenation of Acetylene over Ni/$NiAl_2O_4$ Catalyst: Characterization, Coking, and Reaction Studies.* Journal of Catalysis, 1996. **159**(2): p. 313-322.

30. T. Isobe, K. Daimon, K. Ito, T. Matsubara, Y. Hikichi, and T. Ota, *Preparation and properties of Al_2O_3/Ni composite from $NiAl_2O_4$ spinel by in situ reaction sintering method.* Ceramics International, 2007. **33**(7): p. 1211-1215.

31. L. Guczi, G. Stefler, O. Geszti, I. Sajó, Z. Pászti, A. Tompos, and Z. Schay, *Methane dry reforming with CO_2: A study on surface carbon species.* Applied Catalysis A: General, 2010. **375**(2): p. 236-246.

32. M. Barroso, M. Gomez, L. Arrúa, and M. Abello, *Reactivity of Aluminum Spinels in the Ethanol Steam Reforming Reaction.* Catalysis Letters, 2006. **109**(1): p. 13-19.

33. Y. Matsumura and T. Nakamori, *Steam reforming of methane over nickel catalysts at low reaction temperature.* Applied Catalysis A: General, 2004. **258**(1): p. 107-114.

5 Catalyst characterisation: Influence of calcination temperature on 5 mol % Au doped 20 wt % Ni/Al_2O_3 samples

The results described in Chapter 4 have shown that the calcination temperature used in the preparation of 20 wt % Ni/Al_2O_3 significantly influences the structure and morphology of catalyst samples. As both 20 wt % Ni/Al_2O_3 and 5 mol % Au doped 20 wt % Ni/Al_2O_3 catalysts have been used during catalytic investigations involving methane and steam, the influence of calcination temperature on 5 mol % Au doped 20 wt % Ni/Al_2O_3 sample was also investigated.

The samples are denoted hereon as Au-NiO/Al_2O_3 (calcination temperature) for calcined samples and Au-Ni/Al_2O_3 (calcination temperature) for samples following reduction. For example, Au-Ni/Al_2O_3 (600) refers to the 5 mol % Au doped 20 wt % Ni/Al_2O_3 sample following calcination at 600 °C and subsequent temperature-programmed reduction in hydrogen.

5.1 Calcination

In situ calcination of the $HAuCl_4$ $Ni(NO_3)_2/Al_2O_3$ precursor was carried out, under a flow of oxygen as described in Chapter 4, Section 4.2.1. The calcination process was also studied using *in situ* temperature-programmed XRD, to identify the major phases present during the calcination process.

The temperature-programmed profiles for the thermal oxidative decomposition of $HAuCl_4$ $Ni(NO_3)_2/Al_2O_3$ are shown in Figure 5.1 and Figure 5.2.

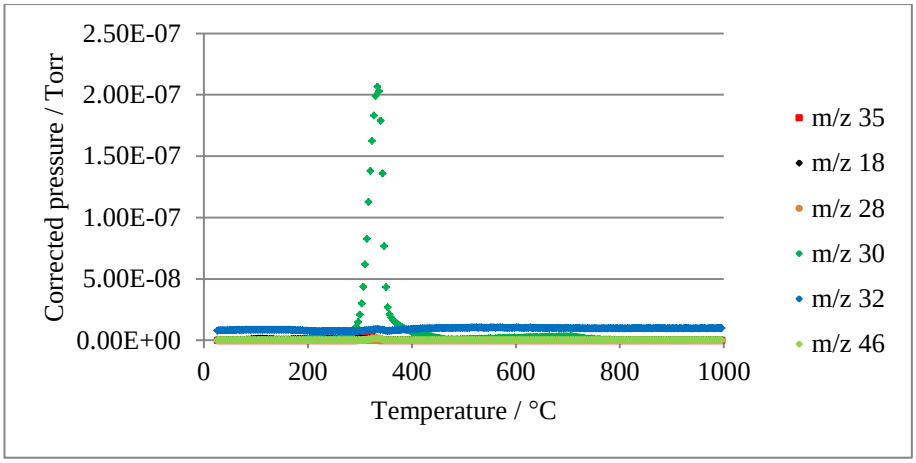

Figure 5.1: Temperature-programmed decomposition of $HAuCl_4$ $Ni(NO_3)_2/Al_2O_3$ under a flow of oxygen

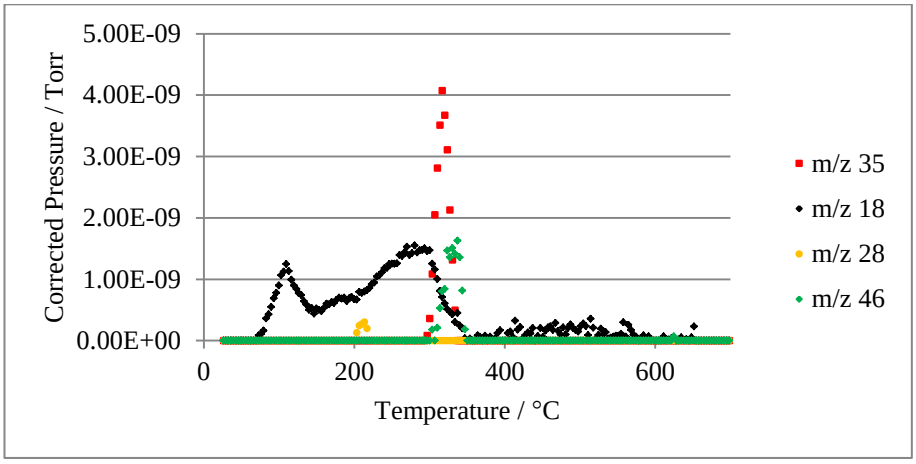

Figure 5.2: Enhanced image of Figure 5.1, showing desorption profiles of minor products

Mass 18, 28, 30, 35 and 46 were all identified during temperature-programmed studies, corresponding to the evolution of H_2O, N_2, NO, HCl and NO_2, respectively. Evolution of all gases was complete by *ca*. 800 °C (Figure 5.1).

In situ XRD profiles were recorded at 50 °C temperature intervals in the range of 50 °C to 900 °C, for the temperature-programmed decomposition of $HAuCl_4$ $Ni(NO_3)_2/Al_2O_3$. These are shown in Figure 5.3 and Figure 5.4.

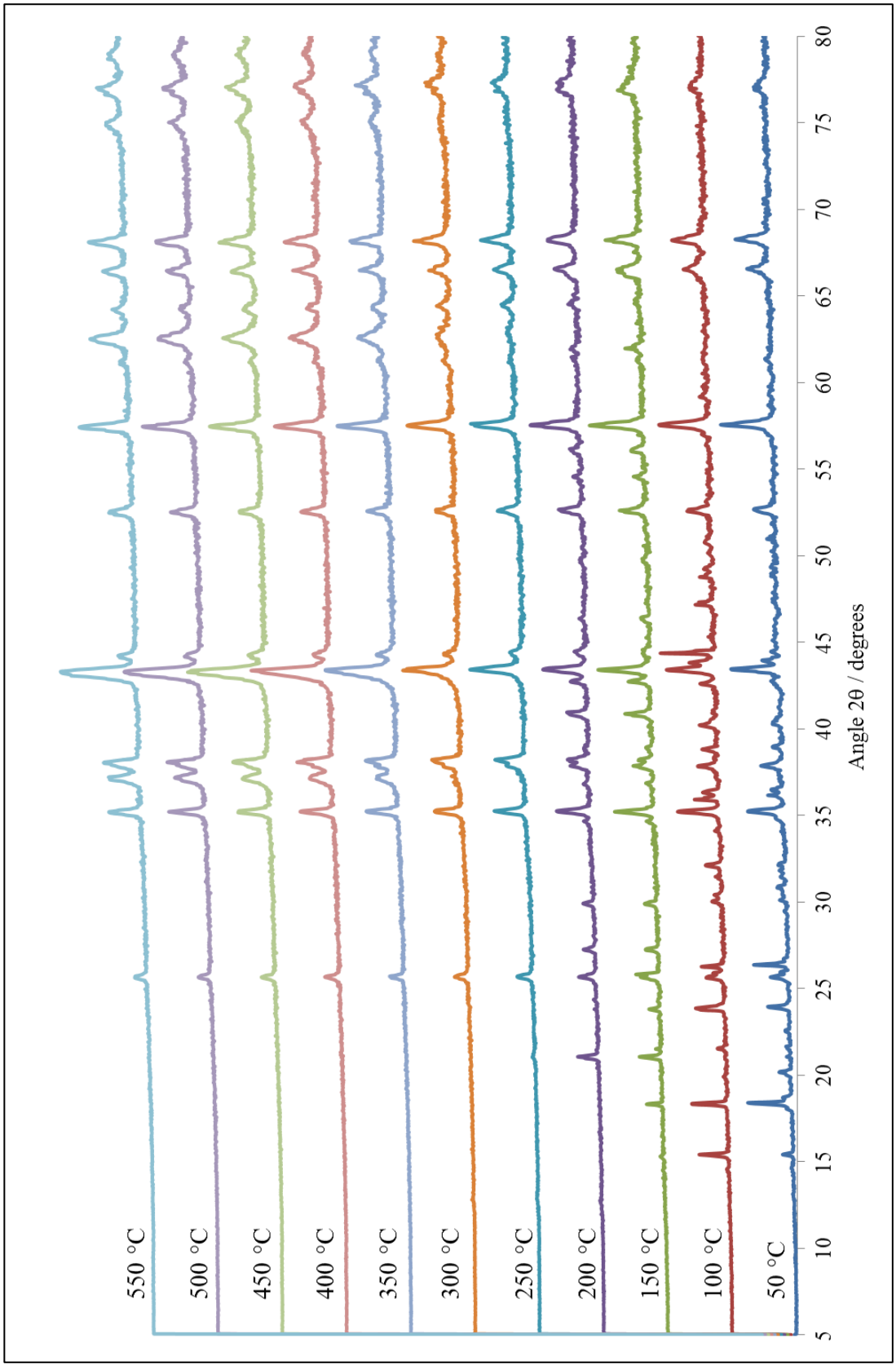

Figure 5.3: XRD profiles of the thermal decomposition of $HAuCl_4$ $Ni(NO_3)_2/Al_2O_3$, over the temperature range of 50 °C to 550 °C

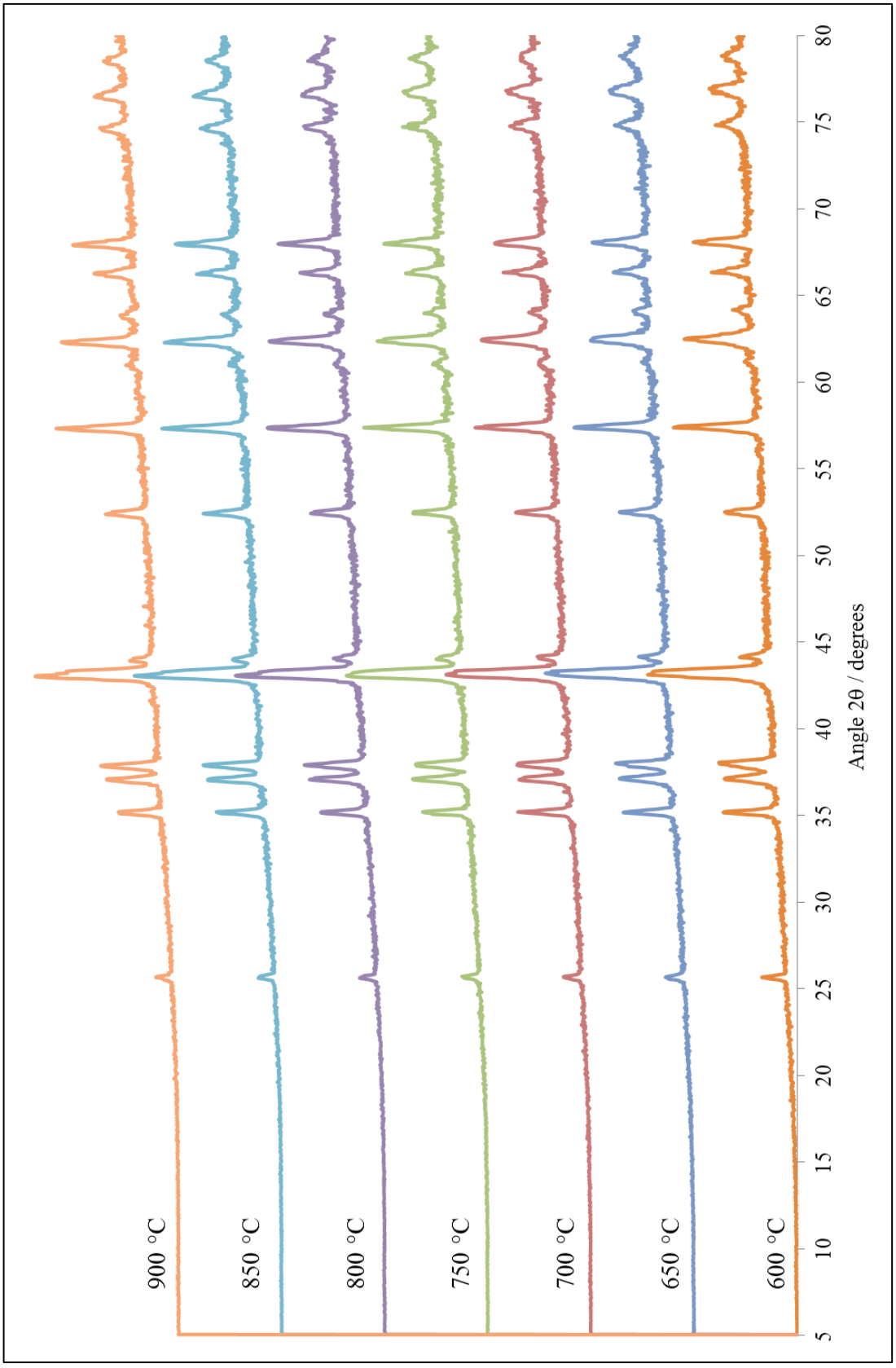

Figure 5.4: XRD profiles of the thermal decomposition of $HAuCl_4$ $Ni(NO_3)_2/Al_2O_3$, over the temperature range of 600 °C to 900 °C

The XRD peaks at 2θ values of 25.5°, 35.1°, 37.8°, 42.3°, 52.5°, 57.5°, 66.5° and 68.2° present in the XRD profiles at all calcination temperatures are attributed to α-Al_2O_3.

As identified during temperature-programmed XRD studies of the thermal decomposition of $Ni(NO_3)_2/Al_2O_3$ (Chapter 4), three major stages are present in the decomposition of $HAuCl_4$ $Ni(NO_3)_2/Al_2O_3$. At 100 °C, diffraction peaks relating to the precursor sample remain, although additional peaks are observed at 21.5°, 32.1° and 47.1°. At 150 °C, additional peaks are observed at 21.0°, 27.2°, 46.3°, 54.5°, 56.0° and 61.9°. By 250 °C, most peaks corresponding to the precursor material have disappeared, and a small peak at 62.8° appears, which is attributed to the formation of nickel oxide (Chapter 4, Section 4.1.2.2). Additional peaks attributed to NiO at 37.1° and 75.0° appear at 300 °C, increasing in intensity as the temperature is increased. Peaks at *ca.* 44.2° and 64.2° which correspond to gold are observed at all calcination temperatures.

Thus, *in situ* temperature-programmed XRD measurements show that decomposition of $HAuCl_4$ $Ni(NO_3)_2/Al_2O_3$ initiates at 100 °C. The next stage occurs around 150 °C, followed by the final decomposition stage at 250 °C. Peaks relating to NiO appear at 250 °C and increase in intensity as the temperature is increased to 900 °C. This decomposition process is consistent with the thermal decomposition of nickel nitrate observed in Chapter 4 (Section 4.1.1).

5.2 Characterisation of calcined Au-NiO/Al_2O_3 samples

5.2.1 Visual appearance

The sample appearance following calcination at different temperatures is shown in Figure 5.5. All samples are grey in colour, although a distinct blue colour is observed for Au-NiO/Al_2O_3 (1000) and a purple colour for Au-NiO/Al_2O_3 (600). All samples showed no change in colour over time.

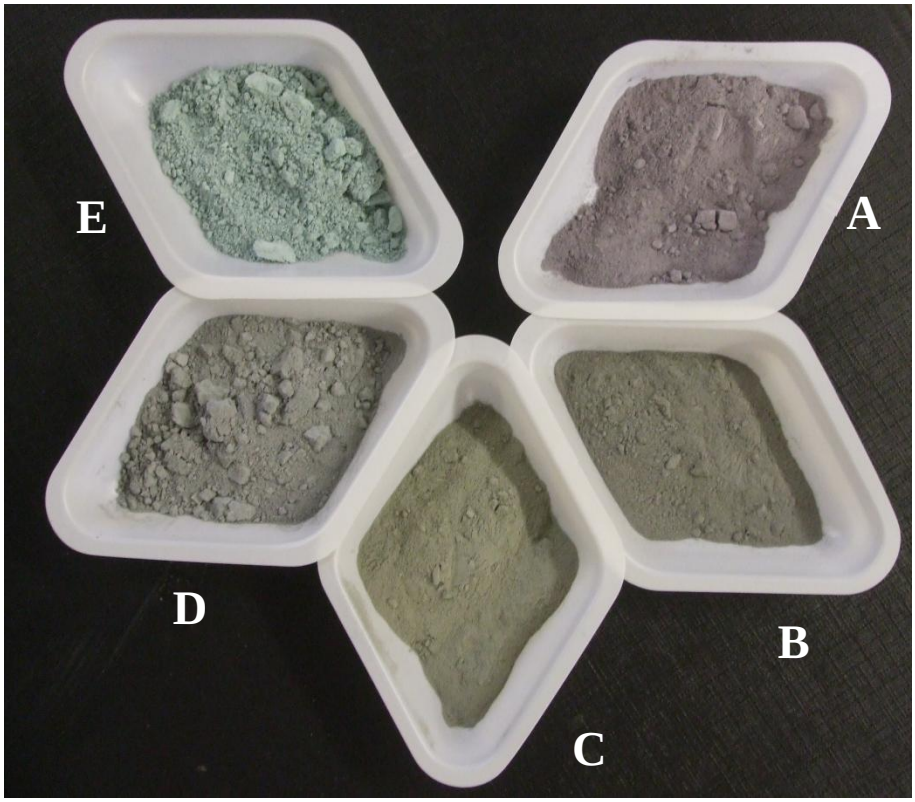

Figure 5.5: **Au-NiO/Al_2O_3 sample appearance following calcination A, Au-NiO/Al_2O_3 (600); B, Au-NiO/Al_2O_3 (700); C, Au-NiO/Al_2O_3 (800); D, Au-NiO/Al_2O_3 (900) and E, Au-NiO/Al_2O_3 (1000)**

The samples show a gradual change in colour as the calcination temperature is increased. *In situ* decomposition results in Section 5.1 suggest that calcination is not complete until *ca*. 800 °C. Therefore, the purple colour of Au-NiO/Al_2O_3 (600) could be attributed to incomplete calcination. This seems at variance with the work by Daté *et al*. [1] who observe a purple colour for Au/TiO_2 samples calcined at 300 °C, which they attribute to complete calcination of samples. The green colour of samples calcined from 700 ºC to 900 ºC, can be attributed to the formation of NiO. The distinct blue colour of Au-NiO/Al_2O_3 (1000) could be attributed to the formation of an additional phase, such as nickel aluminate, $NiAl_2O_4$ [2, 3]. This is consistent with XRD studies shown in Section 5.2.3 and results for NiO/Al_2O_3 (1000), as shown in Section 4.2.2.1.

5.2.2 Surface area

The surface areas were all determined by the BET method for all samples following calcination, results are shown in Table 5.1.

Table 5.1: The BET surface area for samples following calcination

Sample	Surface area / $m^2 g^{-1}$
Au-NiO/Al_2O_3 (600)	10.3
Au-NiO/Al_2O_3 (700)	9.9
Au-NiO/Al_2O_3 (800)	7.1
Au-NiO/Al_2O_3 (900)	8.5
Au-NiO/Al_2O_3 (1000)	3.0

The surface area is highest following calcination at 600 °C and significantly decreases following high temperature calcination at 1000 °C. The reduction in surface area observed following calcination at 1000 °C, could indicate a variation in both the surface morphology and the crystallinity, following high temperature calcination. This is confirmed by both XRD and SEM results (Section 5.2.3 and 5.2.4), which indicate a dramatic change in the surface morphology following calcination at 1000 °C and the formation of $NiAl_2O_4$. This phase is identified by XRD in the sample calcined at 900 °C, although no dramatic change in surface area is detected. The surface area results correspond to the SEM images obtained for both Au-NiO/Al_2O_3 and NiO/Al_2O_3 samples. The lowest surface areas are obtained for both NiO/Al_2O_3 (900) and Au-NiO/Al_2O_3 (1000), where SEM images show a uniform almost spherical support species.

5.2.3 X-ray diffraction (XRD)

XRD profiles of the samples following calcination are shown in Figure 5.6, whilst average crystallite sizes of the major phases present, extracted by the Scherrer equation are shown in Table 5.2.

Peaks corresponding to NiO, gold, α-Al_2O_3 and additional phases present overlap at low angles. To estimate NiO and gold crystallite sizes, peaks at higher angles which do not overlap with any other phases were used. The peak at *ca.* 62.8º (marked * in Figure 5.6) was used for NiO and the peak at *ca.* 44.3º (marked *) was used for gold crystallite size determination. However, an alternative gold peak at *ca.* 38.0º also marked with * was used for Au-NiO/Al_2O_3 (900) and Au-NiO/Al_2O_3 (1000), due to the slight overlapping of peaks in those XRD patterns.

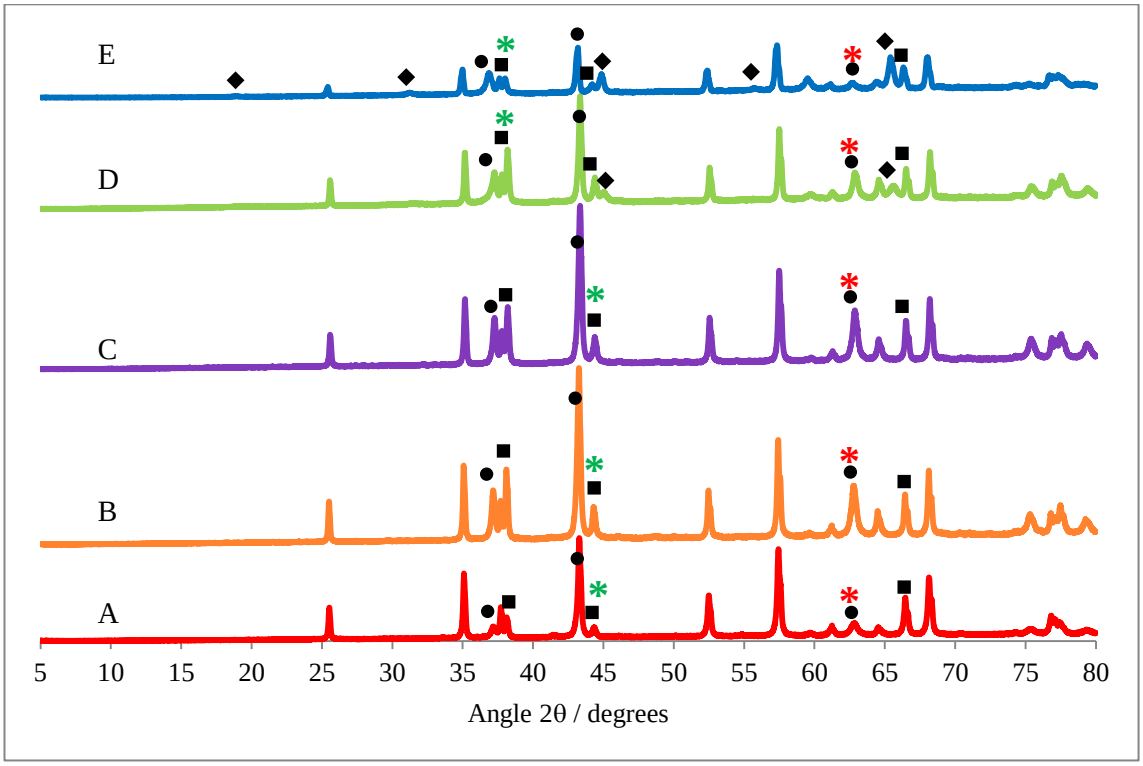

Figure 5.6: **XRD profiles of A, Au-NiO/Al_2O_3 (600); B, Au-NiO/Al_2O_3 (700); C, Au-NiO/Al_2O_3 (800); D, Au-NiO/Al_2O_3 (900) and E, Au-NiO/Al_2O_3 (1000) (● NiO, ▪ Au, ♦$NiAl_2O_4$)**

Table 5.2: Approximate NiO and gold crystallite size determined via the Scherrer equation for the most distinct peak in the XRD profile

Sample	Approximate NiO crystallite size / nm	Approximate gold crystallite size / nm
Au-NiO/Al_2O_3 (600)	26	58
Au-NiO/Al_2O_3 (700)	32	56
Au-NiO/Al_2O_3 (800)	32	48
Au-NiO/Al_2O_3 (900)	35	46
Au-NiO/Al_2O_3 (1000)	49	42

All calcined samples show diffraction peaks characteristic of the α-Al_2O_3 support (25.5°, 35.0°, 37.8°, 43.3°, 52.5°, 57.5°, 66.5° and 68.2°) and NiO (37.2º, 43.3º, 62.7º 75.4º and 79.5º).

The presence of an additional phase, with peaks at 19.2°, 31.5°, 45.0°, 57.2° and 65.6°, is observed in the profiles of Au-NiO/Al_2O_3 (900) and Au-NiO/Al_2O_3 (1000). This phase is attributed to the formation of nickel aluminate, $NiAl_2O_4$ (ICDD-PDF database File card number: $NiAl_2O_4$, 01-1299). This phase is not observed for the samples calcined below 800 °C. As the calcination temperature is increased from 900 ºC to 1000 ºC, the diffraction peaks due to $NiAl_2O_4$ increase in intensity and additional peaks for this phase appear, indicating increased crystallinity.

Chang *et al.* [4] have identified an $AuAl_2O_4$ spinel species during TPR analysis, formed through the diffusion of gold ions into alumina sub layers, although no such phase was identified during XRD analysis. If $AuAl_2O_4$ species were formed during calcination in this study, its presence may be too low to detect by XRD analysis, due to the relatively low gold loading in the samples.

The crystallite size data determined by Scherrer analysis in Table 5.2 shows that as the calcination temperature is increased sintering of NiO crystallites occurs, resulting in increased NiO crystallite

size. Although, the crystallite size does not increase to the same extent, this result is consistent with crystallite size data determined from Scherrer analysis for the NiO/Al_2O_3 samples (Chapter 4, Section 4.2.2.2).

Diffraction peaks corresponding to metallic gold, at *ca.* 38.0º and 44.3º are identified in all profiles (ICDD-PDF database File card number: Au, 01-1174). As the calcination temperature is increased, the gold crystallite size appears to reduce slightly, which suggests that gold does not undergo high temperature sintering during calcination. The Tamman and Hüittig temperatures are indicative of the temperature at which sintering can occur. The low melting temperature of gold, and so the low Tamman temperature (395 °C), indicates that sintering of gold may occur at lower calcination temperatures compared to those studied. Thus, sintering may have already occurred at lower temperatures, during the calcination procedure. Gold crystallite sizes for supported gold catalysts in the literature [1, 5, 6] range from *ca.* 2 to 12 nm. These are considerably smaller than the crystallite sizes determined reported in this study following calcination, consistent again with sintering having occurred below 600 °C. The XRD spectra show no evidence of gold-nickel alloy formation [7].

5.2.4 Scanning electron microscopy (SEM)

SEM studies were undertaken on all samples at magnifications from 15,000 to 60,000. SEM images for all calcined samples are shown in Figure 5.7 - Figure 5.11. Arrows displayed on the SEM images indicate examples of the possible presence of NiO particles.

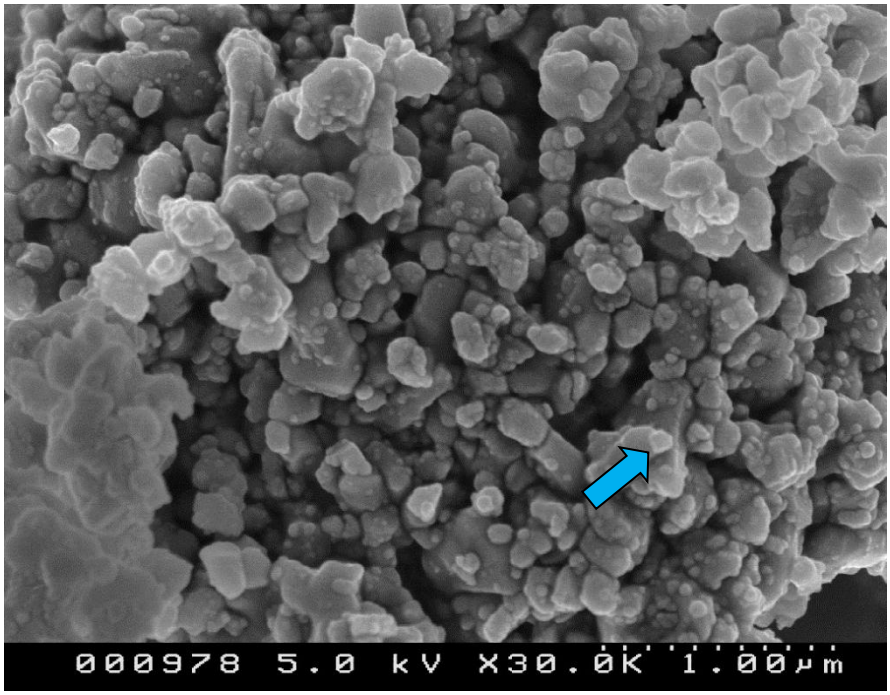

Figure 5.7: SEM image of Au-NiO/Al_2O_3 (600) (magnification 30,000)

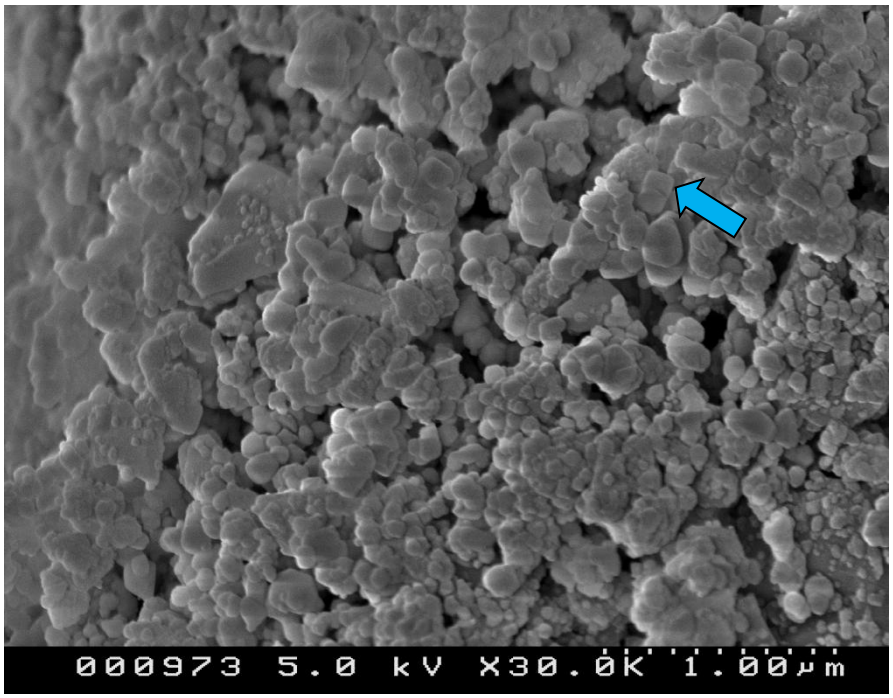

Figure 5.8: SEM image of Au-NiO/Al_2O_3 (700) (magnification 30,000)

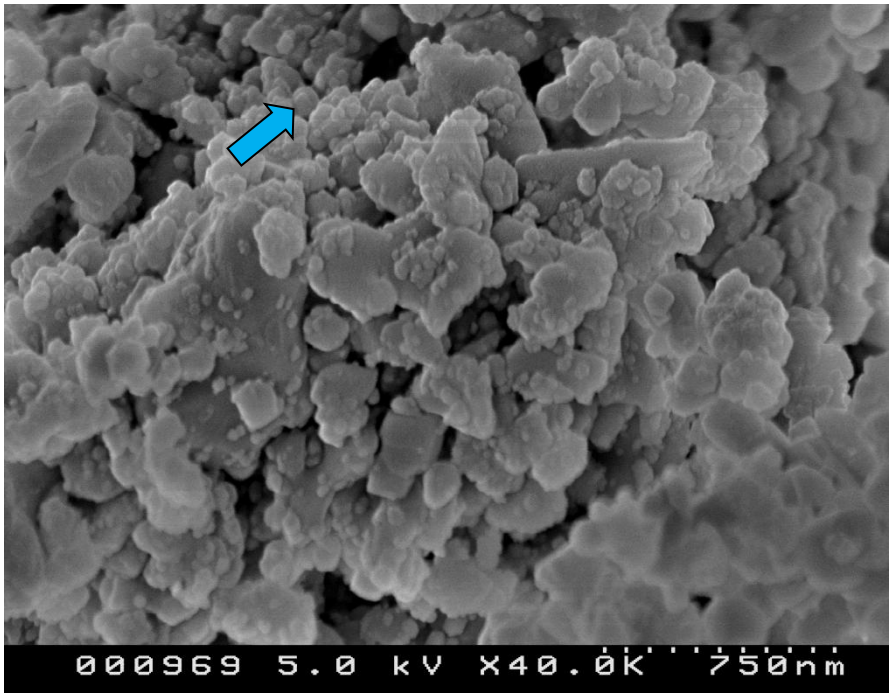

Figure 5.9: SEM image of Au-NiO/Al_2O_3 (800) (magnification 40,000)

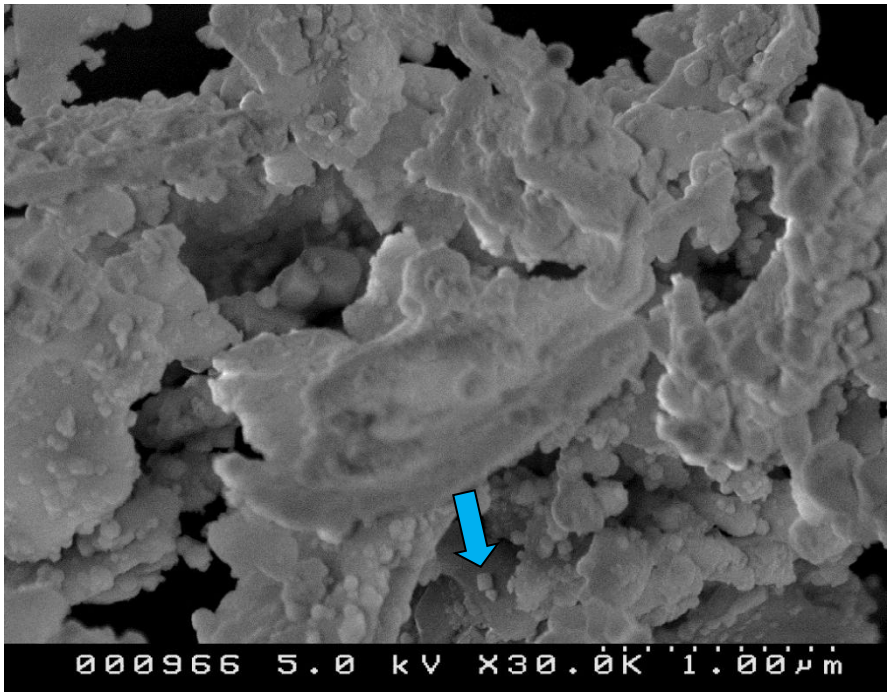

Figure 5.10: SEM image of Au-NiO/Al_2O_3 (900) (magnification 30,000)

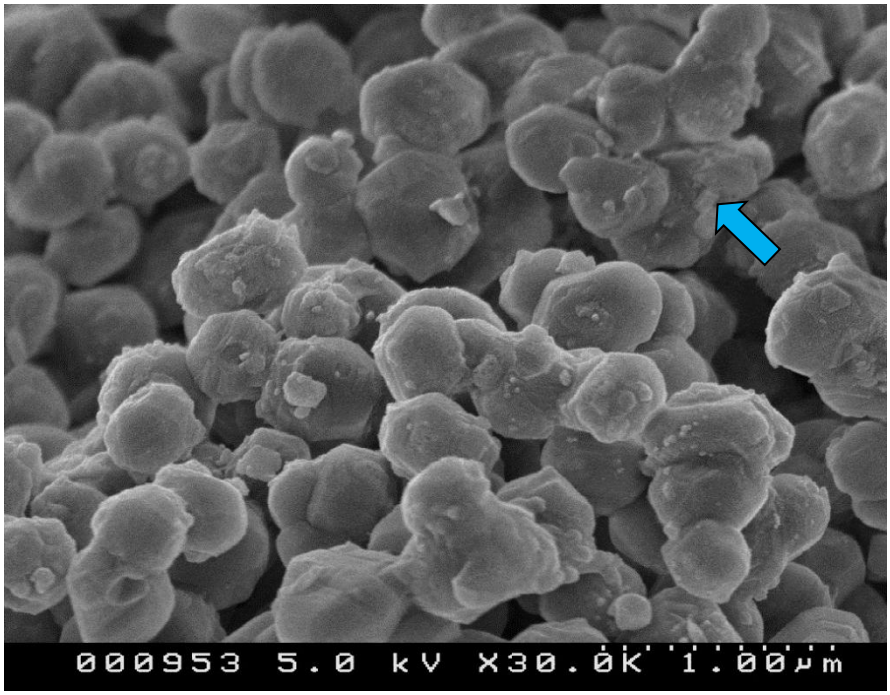

Figure 5.11: SEM image of Au-NiO/Al_2O_3 (1000) (magnification 30,000)

The presence of amorphous 'sheet' support structures are observed for all samples calcined below 900 °C, and are observed to a greater extent following calcination at 900 °C. The smaller support species, most predominantly present in Au-NiO/Al_2O_3 (600), conglomerate as the calcination temperature is increased, forming larger less defined species. The NiO particle sizes range from *ca.* 50 to 100 nm. Crystallite size determination using XRD indicates that NiO crystalline sizes remain fairly stable for all samples, increasing slightly as the calcination temperature is increased. Some particles identified in the SEM image of Au-NiO/Al_2O_3 (1000) are *ca.* 100 nm larger than other Au-NiO/Al_2O_3 samples. This could be attributed to sintering of NiO at 1000 ºC. NiO is less well distributed on the support surface in all Au-NiO/Al_2O_3 samples, compared to NiO/Al_2O_3 (Section 4.2.2.3). This could indicate increased incorporation of NiO into the bulk support structure.

Uniform support species are formed in Au-NiO/Al_2O_3 (1000) (Figure 5.11), similar to results observed by Salavati-Niasari *et al.* [8] and Isobe *et al.* [9] for other nickel alumina systems. Salavati-Niasari *et al.* studied $CuAl_2O_4$ and have proposed that the formation of uniform species is facilitated by the presence of copper. This uniform morphology is not observed for the NiO/Al_2O_3 sample calcined at 1000 °C, (Figure 4.20). This suggests that the presence of gold in the sample

may increase the formation of uniform support species. The small amount of gold incorporated into the sample makes it difficult to distinguish such species in the SEM images.

5.2.5 X-ray photoelectron spectroscopy (XPS)

Given the significant changes in catalyst morphology identified during SEM studies, surface XPS analysis was carried out to further study to surface properties of calcined samples. The Ni $2p^{3/2}$ spectrum for Au-Ni/Al_2O_3 (600) is shown in Figure 5.12 and spectra for Au-Ni/Al_2O_3 (900) and Au-Ni/Al_2O_3 (1000) are shown in Figure 5.13. The O 1s spectrum for Au-Ni/Al_2O_3 (600) is shown in Figure 5.14 and spectra for Au-Ni/Al_2O_3 (900) and Au-Ni/Al_2O_3 (1000) are shown in Figure 5.15. The Au 4f spectra are shown in Figure 5.16. Curve fitting of the spectra was carried out in an attempt to assign the surface species present in both the Ni 2p and O 1s spectra. The Ni 2p and O 1s spectra show the experimental data (black), peak fitted components (blue, green, yellow and purple) and peak fitted spectra curve (red).

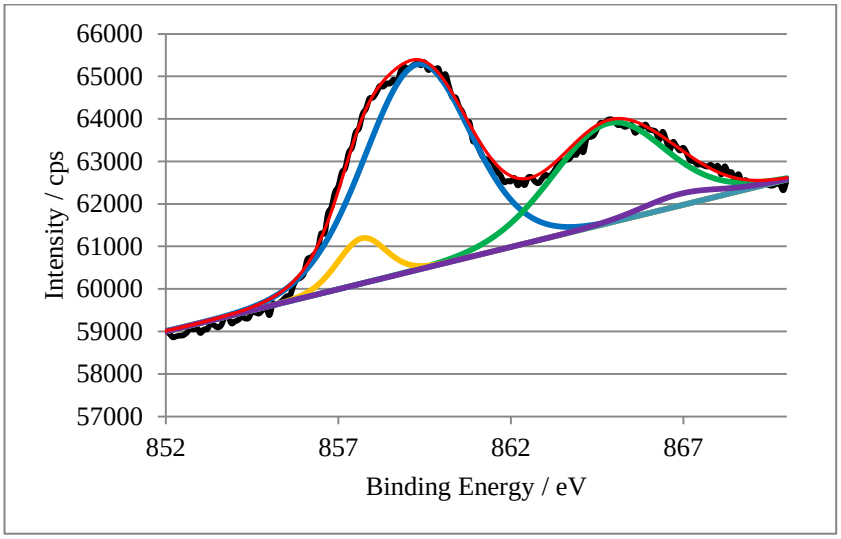

Figure 5.12: Peak fitted Ni 2p XP spectrum of Au-NiO/Al_2O_3 (600)

The Ni 2p peak fitted spectrum of Au-NiO/Al_2O_3 (600) shown in Figure 5.12 suggests two primary and two satellite peaks. The two primary peaks at binding energies of 857.1 and 858.7 eV, and corresponding satellite peaks at 864.3 and 867.2 eV, are similar to those observed for unsupported

NiO (Section 4.1.2.3) and NiO/Al_2O_3 (600) (Section 4.2.2.4). The primary peaks at 857.1 and 858.7 eV can be attributed to Ni^{2+} and Ni^{3+}respectively, due to the presence of both satellite peaks [10, 11].

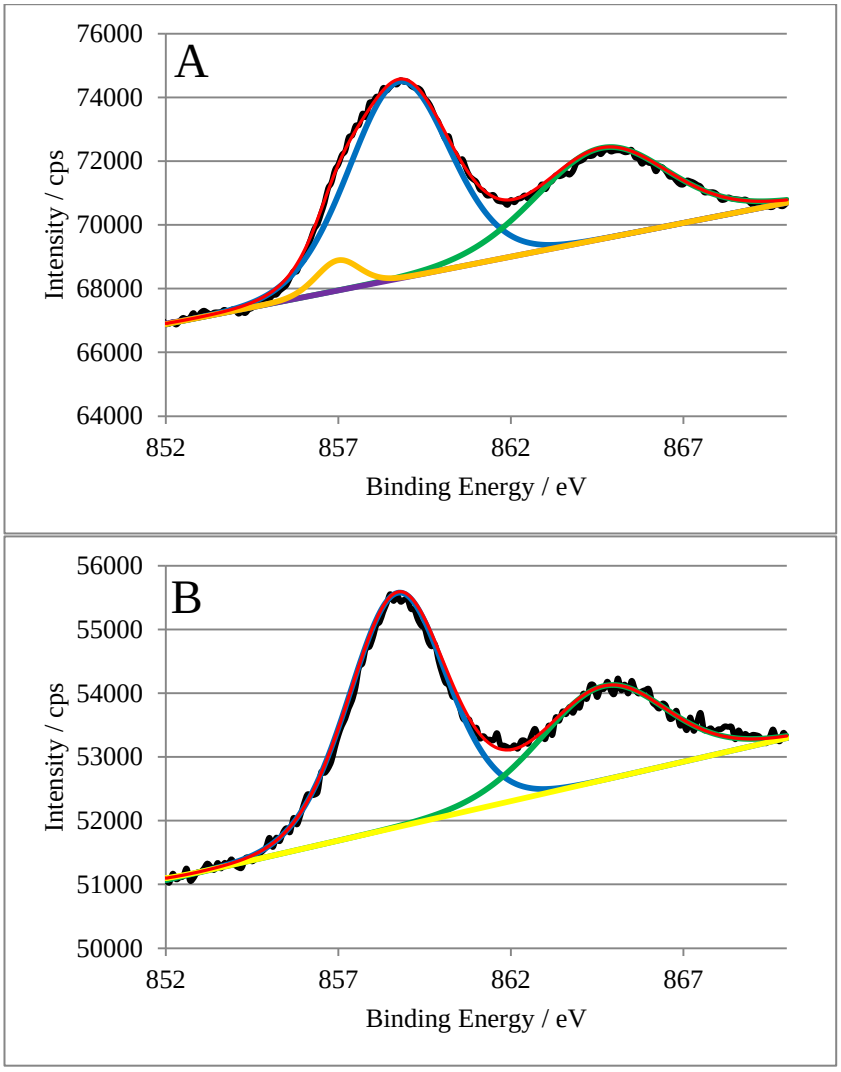

Figure 5.13: Peak fitted Ni 2p XP spectra of A, Au-NiO/Al_2O_3 (900) and B, Au-NiO/Al_2O_3 (1000)

The Ni 2p peak fitted spectra for both samples (Figure 5.13) show the presence of a primary peak at 858.8 eV for Au-NiO/Al_2O_3 (900) and 858.7 eV for Au-NiO/Al_2O_3 (1000). This peak can be attributed to nickel aluminate, $NiAl_2O_4$ [2, 10]. This peak was also identified in the NiO/Al_2O_3 samples calcined at 900 ºC and 1000 ºC (Section 4.2.2.4). This primary peak is not assigned to Ni^{3+}

due to the absence of a Ni^{3+} satellite peak. Additionally, Au-NiO/Al_2O_3 (900) shows the presence of a Ni^{2+} peak at 857.0 eV, which is attributed to the presence of 'stoichiometric' NiO.

The Ni 2p peaks obtained for Au-NiO/Al_2O_3 samples are comparable to those gained for NiO/Al_2O_3 samples, identifying surface $NiAl_2O_4$ phases present following calcination at 900 ºC and 1000 ºC. This is consistent with XRD data gained, indicating the presence of crystalline $NiAl_2O_4$ in both Au-NiO/Al_2O_3 samples calcined at 900 °C and 1000 °C.

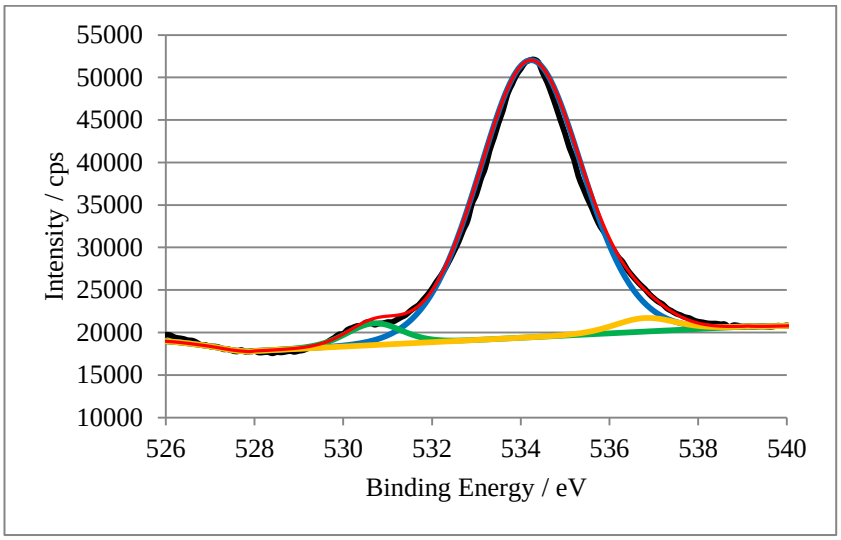

Figure 5.14: Peak fitted O 1s XP spectrum of Au-NiO/Al_2O_3 (600)

The O 1s peak fitted spectrum of Au-NiO/Al_2O_3 (600) shows the presence of primary peaks at 530.5 eV and 534.0 eV, which are attributed to oxygen associated with Ni and Al_2O_3 [12], respectively. The small peak identified by peak fitting at 536.8 eV, is generally attributed to surface hydroxyl species [13]. Hydroxyl groups are reported to have been introduced to the catalyst during the preparative stage and retained by alumina [7].

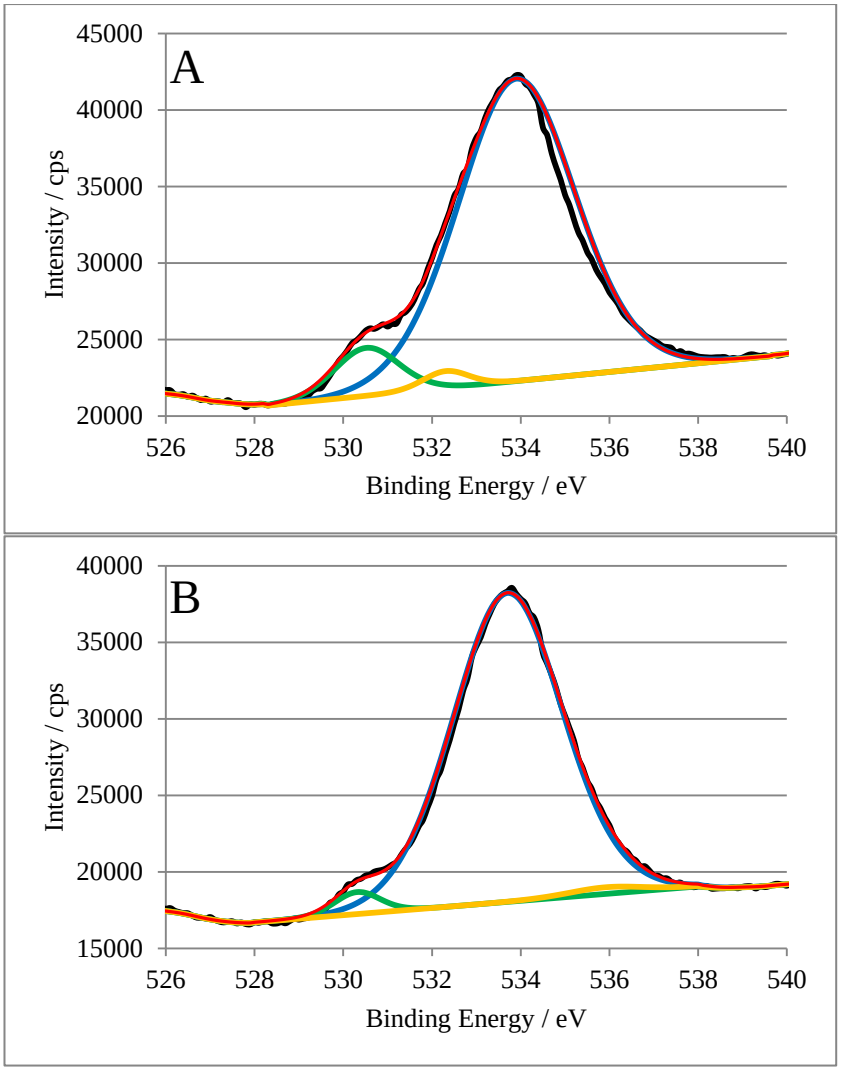

Figure 5.15: Peak fitted O 1s XP spectra of A, Au-NiO/Al_2O_3 (900) and B, Au-NiO/Al_2O_3 (1000)

The O 1s peak fitted spectra for the samples calcined at 900 °C and 1000 °C shows two primary peaks at E_b 530.5 eV and 533.9 eV for Au-NiO/Al_2O_3 (900) and 530.3 eV and 533.7 eV for Au-NiO/Al_2O_3 (1000), attributed to oxygen bonding with Ni and Al atoms respectively. The XP spectrum of Au-NiO/Al_2O_3 (1000) suggests the presence of an additional peak at 535.9 eV, which is attributed to surface hydroxyl species [7, 13]. The spectrum of Au-NiO/Al_2O_3 (900) suggests the presence of an additional peak at 532.3 eV. This peak is unable to be identified and may be a consequence of curve fitting limitations.

The Au 4f peak fitted spectra are shown in Figure 5.16. All spectra show the presence of a small peak at *ca.* 86 eV. The intensity of the Au 4f peak is very small, due to the small amount of gold present in the sample. The peak intensity and signal to noise ratio are too small for peak fitting and specific components are unable to be determined.

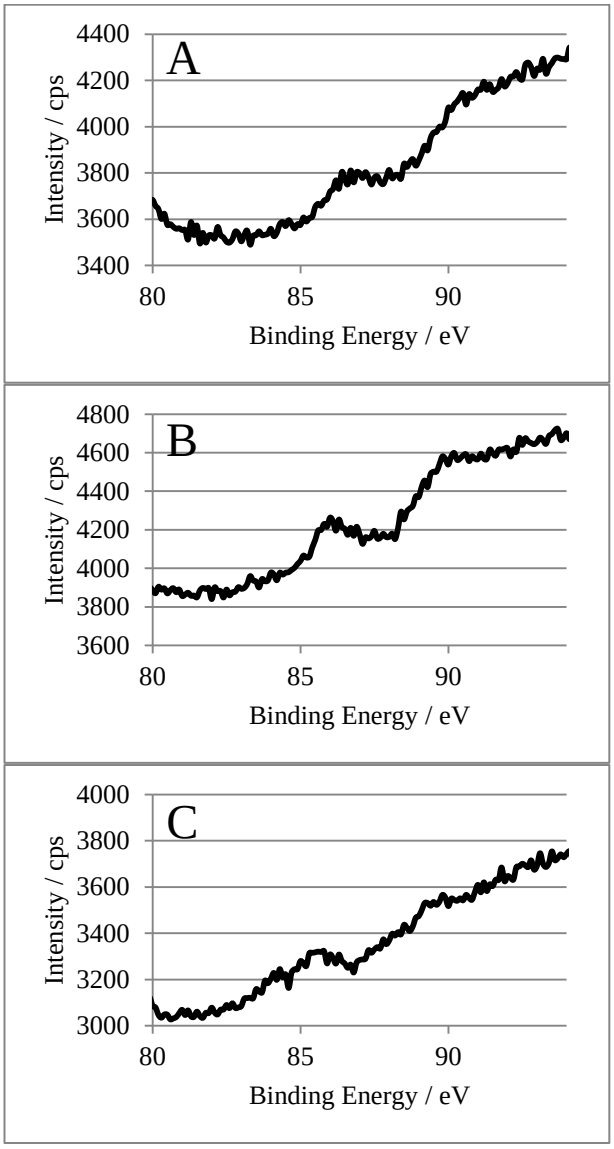

Figure 5.16: Au 4f XP spectra of A, Au-NiO/Al_2O_3 (600); B, Au-NiO/Al_2O_3 (900) and C, Au-NiO/Al_2O_3 (1000)

Analysis of the Ni 2p spectra suggests two different surface states of Ni^{2+} are present, corresponding to NiO and $NiAl_2O_4$. Both species are present following calcination at 900 ºC. However, only surface $NiAl_2O_4$ is present following calcination at 1000 ºC. Following calcination

at 600 ºC only NiO is present. This is consistent with the results for NiO/Al_2O_3 shown in Section 4.2.2.4. Gold surface species are observed for all the samples, although Au 4f peaks are small.

XPS results confirm that as the calcination temperature is increased a reduction in the amount of surface NiO occurs, indicating that calcination temperature strongly influences the surface species present. This is consistent with the results gained for NiO/Al_2O_3 samples. The XPS results confirm the data gained by XRD, indicating the formation of $NiAl_2O_4$ as the calcination temperature is increased to 900 ºC.

5.3 Temperature-programmed reduction (TPR)

TPR profiles of Au-NiO/Al_2O_3 (600), Au-NiO/Al_2O_3 (700), Au-NiO/Al_2O_3 (800), Au-NiO/Al_2O_3 (900) and Au-NiO/Al_2O_3 (1000) are shown in Figure 5.17 - Figure 5.21. The temperatures corresponding to maximum water evolution during reduction are listed in Table 5.3.

As discussed previously in Section 4.2.3, the TPR peaks correspond to different reducible Ni^{2+} states, each with a certain interaction with the alumina support. A higher reduction peak temperature indicates a stronger interaction between the Ni^{2+} oxide species and the support.

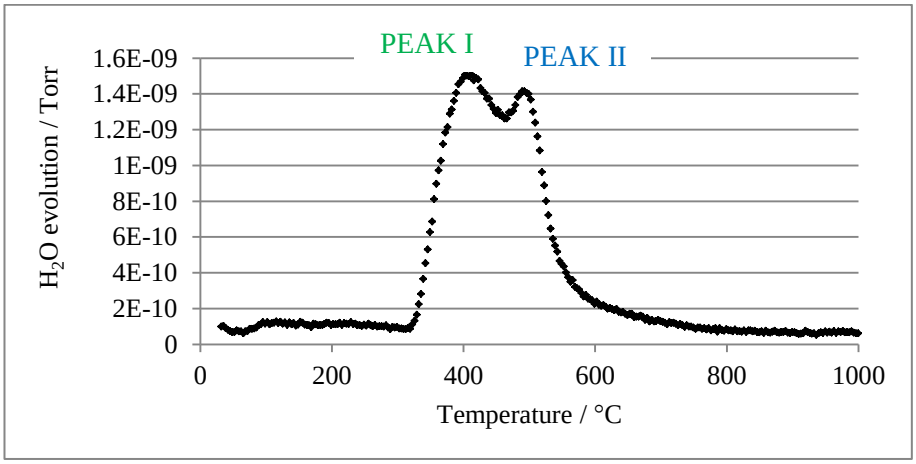

Figure 5.17: TPR profile of Au-NiO/Al_2O_3 (600)

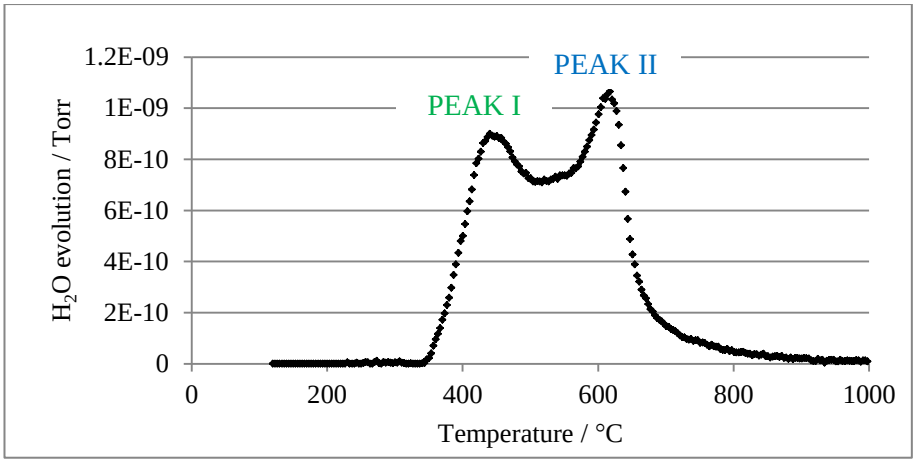

Figure 5.18: TPR profile of Au-NiO/Al_2O_3 (700)

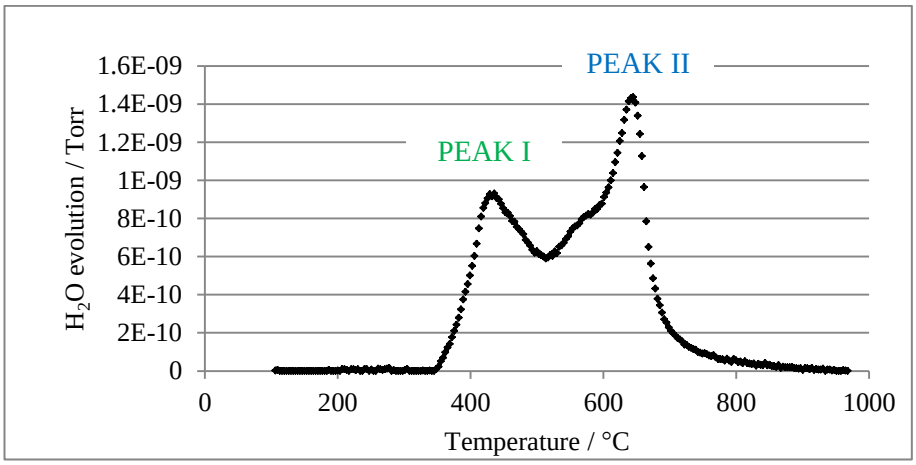

Figure 5.19: TPR profile of Au-NiO/Al_2O_3 (800)

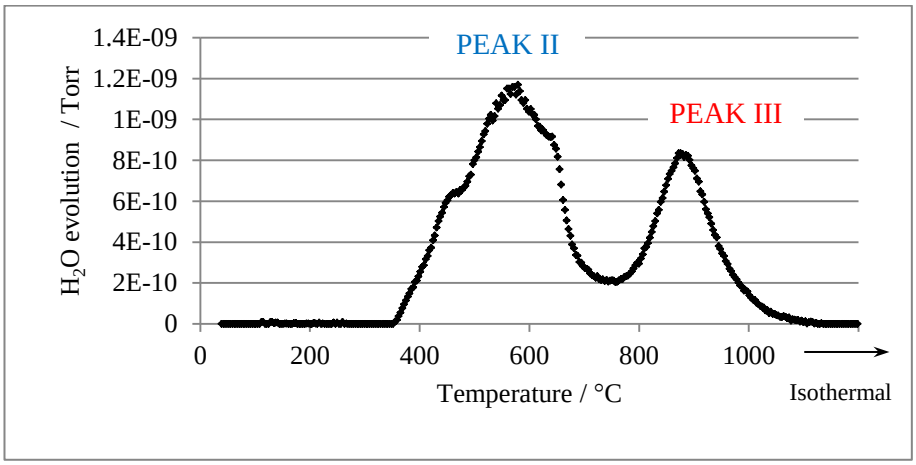

Figure 5.20: TPR profile of Au-NiO/Al_2O_3 (900)

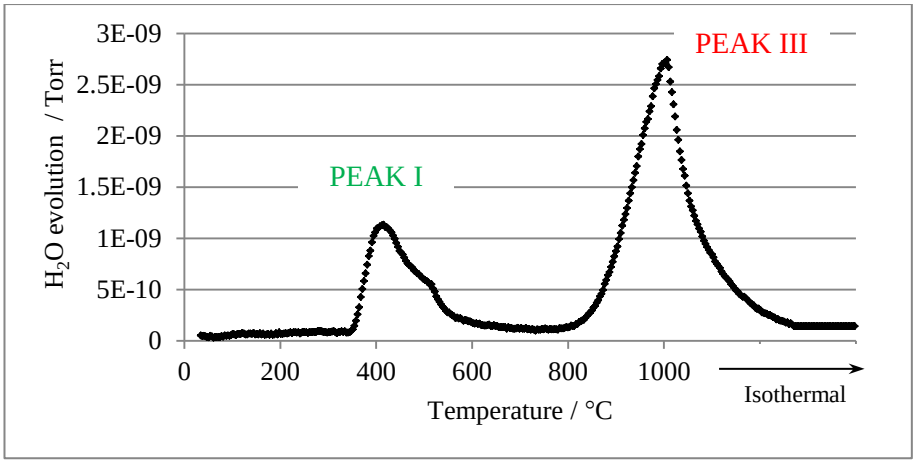

Figure 5.21: TPR profile of Au-NiO/Al_2O_3 (1000)

Table 5.3: Reduction peak temperatures and approximate ratios of reduction peak areas obtained from the TPR profiles of Au-NiO/Al_2O_3 (600), Au-NiO/Al_2O_3 (700), Au-NiO/Al_2O_3 (800), Au-NiO/Al_2O_3 (900) and Au-NiO/Al_2O_3 (1000)

Sample	Reduction peak temperature [a] / °C			Approximate area ratios of peaks (I:II:III)
	Peak I	Peak II	Peak III	
Au-NiO/Al_2O_3 (600)	402	482	-	54 : 46 : 0
Au-NiO/Al_2O_3 (700)	440	617	-	44 : 56 : 0
Au-NiO/Al_2O_3 (800)	436	645	-	34 : 66 : 0
Au-NiO/Al_2O_3 (900)	-	579	875	0 : 67 : 33
Au-NiO/Al_2O_3 (1000)	415	-	1000	29 : 0 : 71

[a] Temperature at maximum water evolution

Low temperature (Peak I) and medium temperature (Peak II) reduction peaks are present for samples calcined up to and including 800 °C (Figure 5.17 - Figure 5.19). These reduction peaks are

due to the reduction of surface NiO and NiO with a weak interaction with the alumina support. The temperature of Peak II increases significantly from 482 °C to 645 °C, as the calcination temperature is increased from 600 °C to 800 °C. This suggests that the interaction between Ni^{2+} and the support increases considerably as the calcination temperature is increased.

The TPR profiles for the reduction of Au-NiO/Al_2O_3 (900) and Au-NiO/Al_2O_3 (1000) (Figure 5.20 and Figure 5.21) show the presence of a distinct high temperature reduction peak (peak III). This can be attributed to Ni^{2+} with a strong interaction with the alumina support or more likely incorporation into the bulk support structure forming a $NiAl_2O_4$ species [14]. Although high temperature peaks (Peak III) are observed for both these samples, the temperature of these peaks are significantly different, for Au-NiO/Al_2O_3 (1000) Peak III is shifted to a considerably higher temperature indicating that the interactions between the oxide and support are significantly stronger.

The formation of an $AuAl_2O_4$ phase has been reported in literature [4] and has been identified by a high temperature reduction peak. It has been suggested [4] that gold may interact with the alumina support at high calcination temperatures and that the reduction of the $AuAl_2O_4$ phase by hydrogen occurs at temperatures above 1000 ºC. The formation of a $AuAl_2O_4$ phase during calcination may account for the high reduction temperature of peak III in Au-NiO/Al_2O_3 (1000). However, the low gold loading in this sample makes the formation of significant amounts of this phase unlikely.

As shown previously for NiO/Al_2O_3 calcined at 900 °C (Section 4.2.3), two reduction peak maxima are observed for Au-NiO/Al_2O_3 (900). These correspond to Ni^{2+} strongly interacting with the support (Peak II) and stoichiometric $NiAl_2O_4$ (Peak III), indicating that this temperature is fundamental to the incorporation of Ni^{2+} into the bulk support structure.

The interaction between the support and the oxide phase is increased as the calcination temperature of NiO/Al_2O_3 and Au-NiO/Al_2O_3 increases. However, the TPR spectra also show that this interaction further increases upon the incorporation of gold into the sample. All the reduction peaks in the TPR spectra are shifted to higher reduction temperatures compared to the equivalent

NiO/Al_2O_3 sample, indicating that Ni^{2+} species are harder to reduce in Au-NiO/Al_2O_3 samples. This is most noticable when comparing the TPR profiles for NiO/Al_2O_3 and Au-NiO/Al_2O_3 samples calcined at 600 °C. NiO/Al_2O_3 (600) shows only the reduction of simple NiO, whereas, reduction of NiO with an interaction with the support as well as simple NiO are observed in the reduction of Au-NiO/Al_2O_3 (600). Gold both lowers the temperature at which the oxide and support interact and increases the reduction temperature of nickel. These results differ from those reported by Yoshida *et al.* [15] who have shown that the addition of gold reduces the Ni^{2+} reduction temperature. Following the incorporation of gold in the sample calcined at 900 °C, an increase in Peak III area of *ca.* 20 % is obtained. Gold also increases the temperature at which the subsequently formed $NiAl_2O_4$ is reduced (Peak III).

Although the incorporation of gold into the sample increases reduction temperature and the interactions between the oxide and support, the area ratio of peaks indicate that similar amounts of $NiAl_2O_4$ are formed in both NiO/Al_2O_3 and Au-NiO/Al_2O_3 samples calcined at 1000 °C. This could indicate that although gold facilitates the formation of $NiAl_2O_4$, maximum formation is reached following calcination at 1000 °C and is no longer influenced by the addition of gold. The formation of $NiAl_2O_4$ has been shown [9] not to decompose until 1300 ºC, indicating high formation temperatures.

5.4 Characterisation of reduced Au-Ni/Al_2O_3 samples

In the same way as the Ni/Al_2O_3 samples, all the Au-NiO/Al_2O_3 samples were activated by being reduced in hydrogen at elevated temperatures prior to catalytic reaction. Characterisation of reduced catalytic samples using XRD, SEM and XPS has been undertaken.

5.4.1 X-ray diffraction (XRD)

XRD patterns for the reduced samples are shown in Figure 5.22, whilst the corresponding nickel crystallite sizes estimated using the Scherrer equation are shown in Table 5.4. The peak corresponding to nickel at *ca.* 51.7° (*) was used to estimate nickel crystallite size. Gold crystallite sizes were unable to be accurately calculated due to overlapping of gold, nickel and α-Al_2O_3 diffraction peaks.

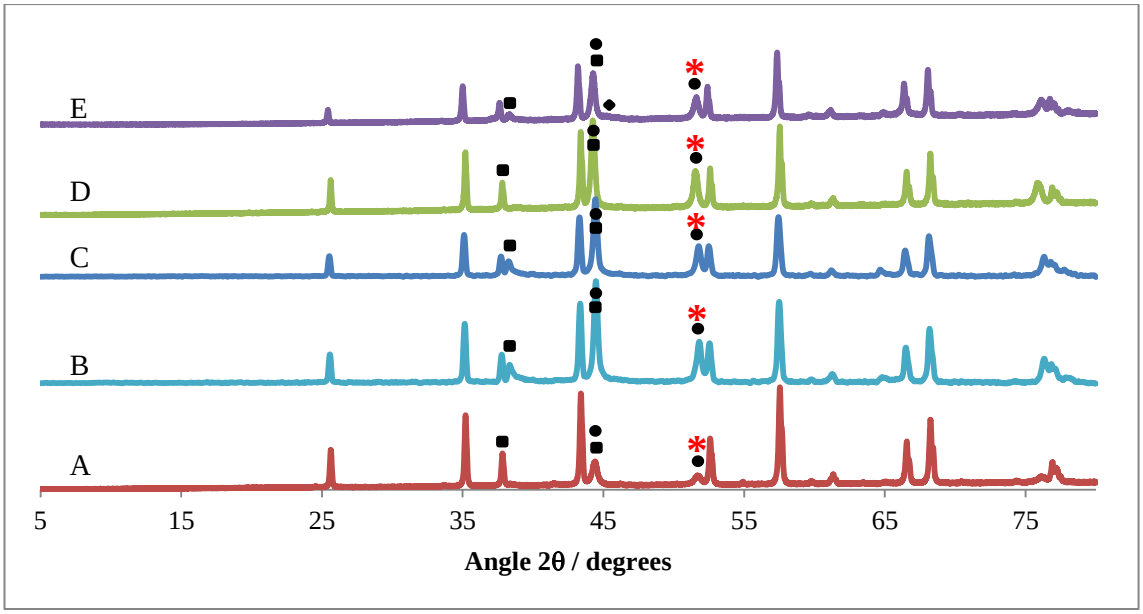

Figure 5.22: XRD profile of A, Au-Ni/Al_2O_3 (600); B, Au-Ni/Al_2O_3 (700); C, Au-Ni/Al_2O_3 (800); D, Au-Ni/Al_2O_3 (900); E, Au-Ni/Al_2O_3 (1000) (● Ni, ▪ Au, ♦ $NiAl_2O_4$)

Table 5.4: Approximate nickel crystallite size determined via the Scherrer equation for the most distinct peak in the XRD profile

Sample	Approximate nickel crystallite size / nm
Au-NiO/Al_2O_3 (600)	27
Au-NiO/Al_2O_3 (700)	29
Au-NiO/Al_2O_3 (800)	28
Au-NiO/Al_2O_3 (900)	36
Au-NiO/Al_2O_3 (1000)	33

Post-reduction XRD clearly show the presence of metallic nickel, with peaks at *ca.* 44.5° and 51.5°, produced from the reduction of NiO and $NiAl_2O_4$. This metallic phase is observed in all post-reduction profiles and no NiO phase is present in any of the post-reduction XRD profiles. However, the $NiAl_2O_4$ phase can be identified in the XRD pattern of Au-Ni/Al_2O_3 (1000), indicating that some Ni^{2+} species are not fully reducible under the reduction conditions employed and remain as $NiAl_2O_4$. These results are consistent with XRD analysis of the reduced Ni/Al_2O_3 (1000) sample (Section 4.2.4.1), where the $NiAl_2O_4$ phase is also observed. It is again important to note that this diffraction peak is extremely small compared to those observed for the $NiAl_2O_4$ phase in the calcined samples (Section 5.2.3).

The nickel crystallite sizes do not increase as the calcination temperature is increased, but remain around *ca.* 30 nm. In Au-Ni/Al_2O_3 (1000), the average nickel crystallite sizes are smaller than the average particle size of NiO, indicating that the nickel is re-dispersed on the surface. This indicates that the reduction conditions employed do not affect the crystallite size and further sintering does not occur when Au-NiO/Al_2O_3 (900) and Au-NiO/Al_2O_3 (1000) samples are held for a prolonged period of time at 1000 °C during reduction.

5.4.2 Scanning electron microscopy (SEM)

SEM investigations were undertaken on Au-Ni/Al_2O_3 (900) and Au-Ni/Al_2O_3 (1000) samples, following reduction. The SEM images are shown in Figure 5.23 and Figure 5.24.

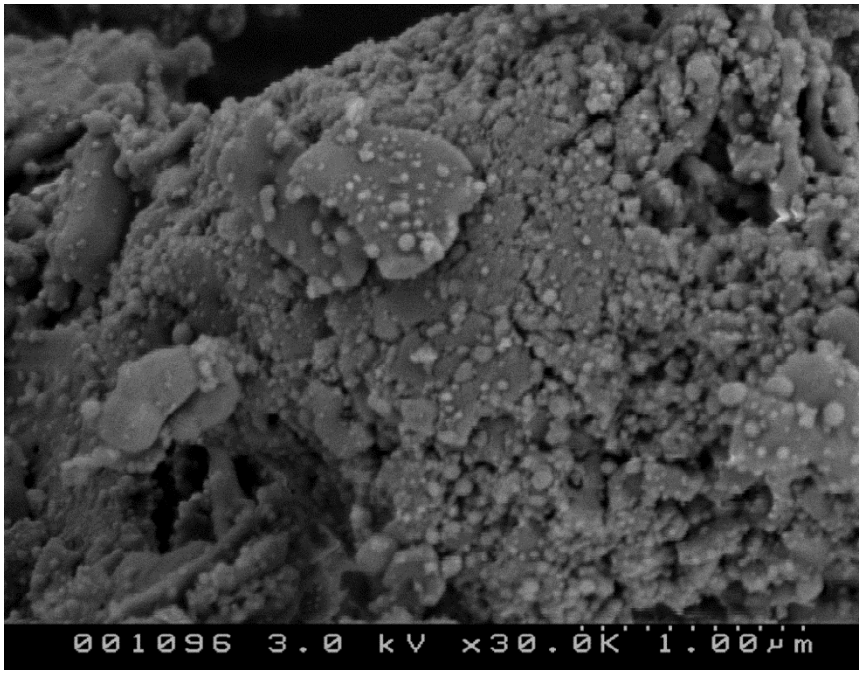

Figure 5.23: SEM image of Au-Ni/Al_2O_3 (900) (magnification 30,000)

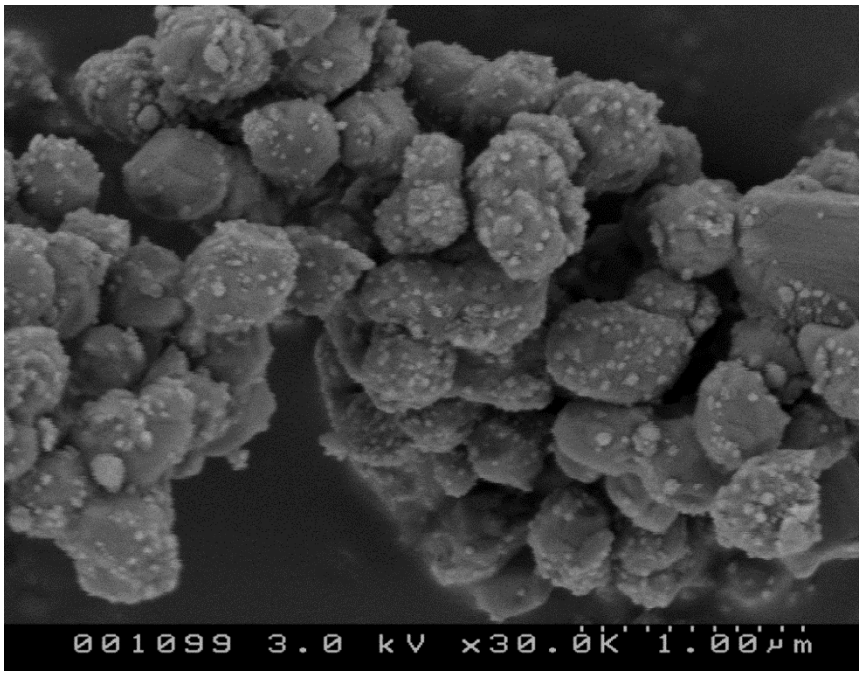

Figure 5.24: SEM image of Au-Ni/Al_2O_3 (1000) (magnification 30,000)

The sample morphology of post-reduction SEM images for Au-Ni/Al_2O_3 (900) and (1000) (Figure 5.23 and Figure 5.24) relate to the corresponding images following calcination (Figure 5.10 and Figure 5.11). The post-reduction images show that following high temperature reduction, the structure of the support remains the same. The post-reduction image of Au-Ni/Al_2O_3 (900) shows a poorly defined support morphology, whereas Au-Ni/Al_2O_3 (1000) shows more uniform support species. Following reduction nickel is highly dispersed on the support surface. The nickel species observed range in size from *ca.* 20 to 150 nm in both samples, consistent with XRD analysis. Again, due to the small amount of gold incorporated into the sample makes it difficult to distinguish such species in the SEM images.

5.4.3 X-ray photoelectron spectroscopy (XPS)

XPS analysis was undertaken on both the Au-Ni/Al_2O_3 (900) and Au-Ni/Al_2O_3 (1000) samples following reduction, to try to determine if surface $NiAl_2O_4$ species identified following calcination were fully reduced. As with Ni/Al_2O_3 samples (Section 4.2.4.3), the Ni 2p spectra obtained were not representative of metallic nickel. Following reduction, the samples were transferred in air to the XPS instrument for sample loading. It is likely that this resulted in oxidation of surface nickel, such that no peaks relating to Ni^0 (E_b values of *ca.* 853 eV) were identified in the XP spectra [16].

However, the Au 4f spectra for both Au-Ni/Al_2O_3 (900) and Au-Ni/Al_2O_3 (1000) (Figure 5.25) showed significantly more intense gold peaks than those observed following calcination. This could indicate that reduction results in gold particles segregating on the support surface. This could be facilitated by the high mobility of gold particles at elevated temperatures.

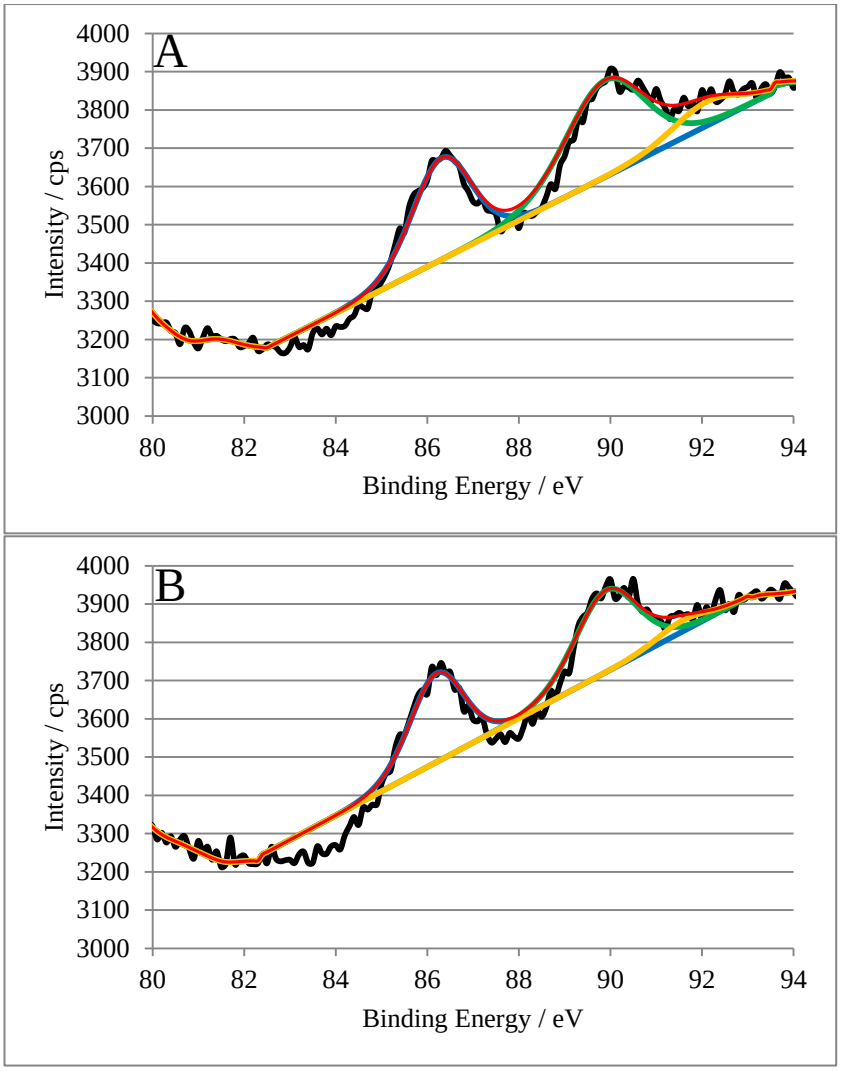

Figure 5.25: Peak fitted Au 4f XP spectra of A, Au-Ni/Al_2O_3 (900) and B, Au-Ni/Al_2O_3 (1000)

The peaks at *ca.* 86 and 90 eV for both samples are attributed to a surface gold phase. However, literature values for metallic gold have significantly lower binding energies at *ca.* 84 and 88 eV [17, 18]. The Au^+ phase has Au 4f peaks at *ca.* 86 eV and 90 eV [19], corresponding to those observed in Figure 5.25. Thus, the high binding energy values of the Au 4f peaks could be attributed to Au^+, formed by the partial oxidation of surface gold species during sample preparation.

5.5 Reducibility following reduction and re-calcination

As in Section 4.2.6, Au-NiO/Al_2O_3 (1000) was reduced and re-calcined in order to investigate the reducibility of Ni^{2+} species following re-oxidation.

Following re-oxidation, the sample appeared the same colour as shown in Figure 5.5. The initial TPR profile is shown in Figure 5.26. The reduction profile for the sample following re-calcination is shown in Figure 5.27.

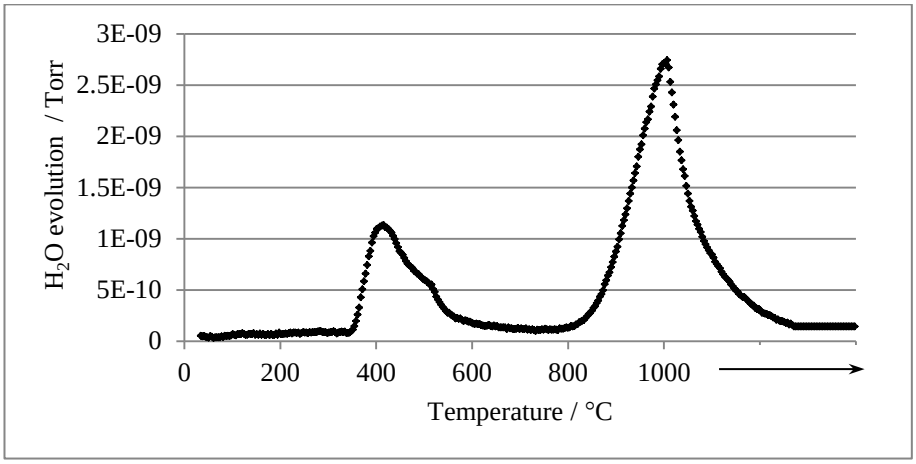

Figure 5.26: TPR profile of Au-NiO/Al_2O_3 (1000)

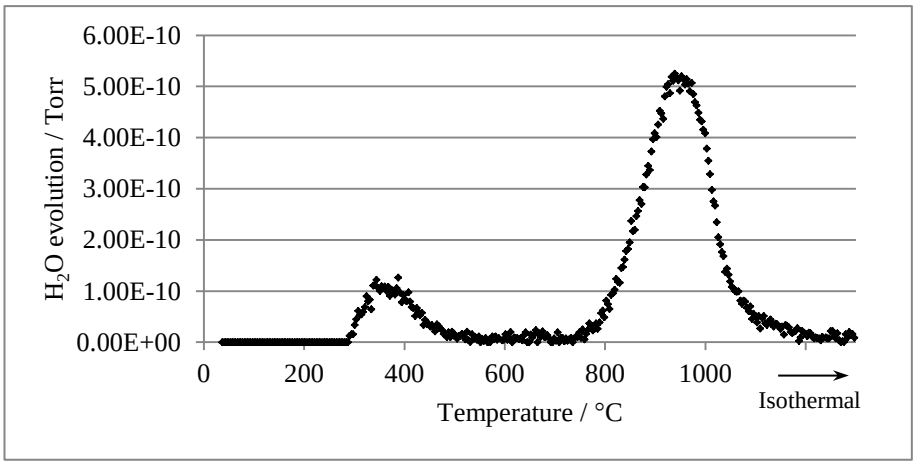

Figure 5.27: TPR profile of Au-NiO/Al_2O_3 (1000) following reduction and re-calcination

Following re-calcination of Au-Ni/Al_2O_3 (1000), reduction of Ni^{2+} species is observed at *ca.* 380 °C and 980 °C, as observed in the original TPR investigations. Thus, although Ni^{2+} species are

reduced and re-dispersed on the support surface following initial reduction, upon re-calcination nickel species re-oxidise to their original forms, as NiO and $NiAl_2O_4$. As with Ni/Al_2O_3, this indicates that although reduction effectively reduces most of the Ni^{2+} species, oxidation at high temperatures results in the formation of $NiAl_2O_4$ species and the re-incorporation of Ni^{2+} into the bulk support structure.

5.6 Summary

TPR and SEM studies show that as the calcination increases from 600 °C to 800 °C, the interaction of NiO with the alumina support increases. As the calcination temperature is increased to 800 °C NiO interacts more strongly with the support, and the sample reducibility is affected.

At 900 °C the initial stages of $NiAl_2O_4$ formation are observed by XRD, TPR and XPS analysis. Results indicate the formation of crystalline $NiAl_2O_4$ species and increased interactions between NiO and the support. XRD, XPS and TPR identify two Ni^{2+} phases present on the catalyst surface, NiO and $NiAl_2O_4$.

Following calcination at 1000 °C, crystalline $NiAl_2O_4$ species are formed. Although observed during both TPR and XRD studies, no surface NiO was identified by XPS in Au-NiO/Al_2O_3 (1000). This may be due to low levels present on the sample surface. The results have shown that during calcination at 1000 ºC two reactions occur, one forming crystalline surface $NiAl_2O_4$ species, the other segregation of surface NiO.

Gold crystallite sizes post-calcination are significantly larger than expected for all samples [1, 5, 6], and no significant increase in gold crystallite size is observed when calcined at 600 °C to 1000 °C. It is suggested that gold particle sintering occurs during calcination at temperatures below 600 °C. Following reduction, gold surface segregation occurs and is detected to a greater degree by XPS.

All Ni^{2+} species present in a NiO phase are effectively reduced to metallic nickel following the reduction treatment. Ni^{2+} species present in the $NiAl_2O_4$ phase are effectively reduced in Au-

Ni/Al_2O_3 calcined at 900 °C. However, following calcination to 1000 °C a small quantity of $NiAl_2O_4$ remains unreduced (identified by XRD studies), indicating that this phase is unable to be fully reduced in the reduction conditions employed. Following reduction of Ni^{2+} species, metallic nickel is dispersed on the support surface, with no sintering of nickel occurring following reduction at high temperatures.

Upon incorporation of gold into Ni/Al_2O_3, more Ni^{2+} is present in a form that is harder to reduce. This occurs to a greater degree for samples calcined at 1000 °C. Gold significantly influences the formation of $NiAl_2O_4$, confirmed by the formation of a crystalline $NiAl_2O_4$ phase following calcination at 900 °C. The temperature at which nickel oxide interacts with the support is significantly lowered upon incorporation of gold into the sample. When both Ni/Al_2O_3 and Au-Ni/Al_2O_3 samples are calcined at 1000 ºC, maximum $NiAl_2O_4$ formation is reached, shown by the relative area ratio of TPR peaks corresponding to $NiAl_2O_4$ (Ni/Al_2O_3 (1000) *ca.* 82 % and Au-Ni/Al_2O_3 (1000) *ca.* 71 %). At this highest calcination temperature the presence of gold no longer influences the amount of aluminate phase formed, only the extent of the interaction between nickel oxide and the support and so the sample reducibility.

The apparent influence that gold has on the catalyst morphology could be attributed to the preparation procedure employed as well as the different nature of gold. Depending upon the pH during catalyst preparation, aluminium ions are displaced into solution by the hydrogen ions [20]. The aluminium ions are then subsequently readsorbed together with the other adsorbing ions, resulting in a mixed adsorption process [21]. Dissolution of alumina and the adsorption of dissolved species can initiate immediately the diffusion of alumina in the aqueous acidic solution occurs [20, 22]. The addition of gold chloride trihydrate during preparation may lower the pH of the solution, resulting in an acidic environment. This acidic environment may increase aluminium dissolution during preparation, resulting in a mixed adsorption process which may enhance the metal adsorption rate, and so contribute to the formation of $NiAl_2O_4$ species on the oxide surface. This could account for the high Ni^{2+} interaction with the support observed in the Au-Ni/Al_2O_3 samples.

Gold addition to 20 wt % Ni/Al_2O_3 catalyst samples has been shown to significantly influence the morphology, structure and species formed, increasing interactions between Ni^{2+} and the support and the formation of additional spinel phases at high calcination temperatures. This can be attributed to the preparation procedure and the possible influence of pH upon the incorporation of nickel into the support structure as well as the influence of having gold incorporated in the catalyst structure. This shows the significant influence such preparation and activation parameters have upon the catalyst structure and morphology and the formation of $NiAl_2O_4$. The use of Au doped Ni/Al_2O_3 catalysts during steam reforming must be done so with care, attention must be paid to the specific physical properties of the catalyst and potential influence towards their ultimate activity.

5.7 References

1. M. Daté, Y. Ichihashi, T. Yamashita, A. Chiorino, F. Boccuzzi, and M. Haruta, *Performance of Au/TiO_2 catalyst under ambient conditions.* Catalysis Today, 2002. **72**(1-2): p. 89-94.
2. P. Salagre, J.L.G. Fierro, F. Medina, and J.E. Sueiras, *Characterization of nickel species on several γ-alumina supported nickel samples.* Journal of Molecular Catalysis A: Chemical, 1996. **106**(1-2): p. 125-134.
3. O.-S. Joo and K.-D. Jung, *CH 4 Dry Reforming on Alumina-Supported Nickel Catalyst.* Bulletin of the Korean Chemical Society 2002. **23**(8): p. 1149-1153.
4. C.-K. Chang, Y.-J. Chen, and C.-t. Yeh, *Characterizations of alumina-supported gold with temperature-programmed reduction.* Applied Catalysis A: General, 1998. **174**(1-2): p. 13-23.
5. M. Maciejewski, P. Fabrizioli, J.-D. Grunwaldt, O.S. Becker, and A. Baiker, *Supported gold catalysts for CO oxidation: Effect of calcination on structure, adsorption and catalytic behaviour.* Physical Chemistry Chemical Physics, 2001. **3**(17): p. 3846-3855.

6. J. Hua, K. Wei, Q. Zheng, and X. Lin, *Influence of calcination temperature on the structure and catalytic performance of Au/iron oxide catalysts for water-gas shift reaction.* Applied Catalysis A: General, 2004. **259**(1): p. 121-130.

7. I.P. Silverwood, N.G. Hamilton, A.R. McFarlane, J. Kapitan, L. Hecht, E.L. Norris, R. Mark Ormerod, C.D. Frost, S.F. Parker, and D. Lennon, *Application of inelastic neutron scattering to studies of CO_2 reforming of methane over alumina-supported nickel and gold-doped nickel catalysts.* Physical Chemistry Chemical Physics, 2012.

8. M. Salavati-Niasari, F. Davar, and M. Farhadi, *Synthesis and characterization of spinel-type $CuAl_2O_4$ nanocrystalline by modified sol–gel method.* Journal of Sol-Gel Science and Technology, 2009. **51**(1): p. 48-52.

9. T. Isobe, K. Daimon, K. Ito, T. Matsubara, Y. Hikichi, and T. Ota, *Preparation and properties of Al_2O_3/Ni composite from $NiAl_2O_4$ spinel by in situ reaction sintering method.* Ceramics International, 2007. **33**(7): p. 1211-1215.

10. R. Molina and G. Poncelet, *α-Alumina-Supported Nickel Catalysts Prepared with Nickel Acetylacetonate. 2. A Study of the Thermolysis of the Metal Precursor*. Journal of Physical Chemistry: B, 1999. **103**: p. 11290-11296.

11. E. Heracleous, A.F. Lee, K. Wilson, and A.A. Lemonidou, *Investigation of Ni-based alumina-supported catalysts for the oxidative dehydrogenation of ethane to ethylene: structural characterization and reactivity studies.* Journal of Catalysis, 2005. **231**(1): p. 159-171.

12. J. Jun, M. Dhayal, J.-H. Shin, Y.H. Han, and N. Getoff, *Surface chemistry and catalytic activity of Ni/Al_2O_3 irradiated with high-energy electron beam.* Applied Surface Science, 2008. **254**(15): p. 4557-4564.

13. M.A. Langell and M.H. Nassir, *Stabilization of NiO(111) Thin Films by Surface Hydroxyls.* The Journal of Physical Chemistry, 1995. **99**(12): p. 4162-4169.

14. C. Li and Y.-W. Chen, *Temperature-programmed-reduction studies of nickel oxide/alumina catalysts: effects of the preparation method.* Thermochimica Acta, 1995. **256**(2): p. 457-465.

15. K. Yoshida, N. Begum, S.-i. Ito, and K. Tomishige, *Oxidative steam reforming of methane over Ni/α-Al_2O_3 modified with trace noble metals.* Applied Catalysis A: General, 2009. **358**(2): p. 186-192.

16. L. Guczi, G. Stefler, O. Geszti, I. Sajó, Z. Pászti, A. Tompos, and Z. Schay, *Methane dry reforming with CO_2: A study on surface carbon species.* Applied Catalysis A: General, 2010. **375**(2): p. 236-346.

17. O. Tkachenko, L. Kustov, S. Nikolaev, V. Smirnov, K. Klementiev, A. Naumkin, I. Volkov, A. Vasil'kov, and D. Murzin, *DRIFT, XPS and XAS Investigation of Au–Ni/Al_2O_3 Synergetic Catalyst for Allylbenzene Isomerization.* Topics in Catalysis, 2009. **52**(4): p. 344-350.

18. J.L. Rousset, F.J. Cadete Santos Aires, B.R. Sekhar, P. Mélinon, B. Prevel, and M. Pellarin, *Comparative X-ray Photoemission Spectroscopy Study of Au, Ni, and AuNi Clusters Produced by Laser Vaporization of Bulk Metals.* The Journal of Physical Chemistry B, 2000. **104**(23): p. 5430-5435.

19. L. Minati, S. Torrengo, and G. Speranza, *Characterization of gold nanoclusters synthesized on carbon nanotubes film: Evaluation of the size distributions by means of X-ray photoelectron spectroscopy.* Surface Science, 2010. **604**(5-6): p. 508-512.

20. J.T. Richardson and M.V. Twigg, *Reduction of impregnated NiO/α-Al_2O_3 association of Al^{3+} ions with NiO.* Applied Catalysis A: General, 1998. **167**(1): p. 57-64.

21. S.L. Chen, H.L. Zhang, J. Hu, C. Contescu, and J.A. Schwarz, *Effect of alumina supports on the properties of supported nickel catalysts.* Applied Catalysis, 1991. **73**(2): p. 289-312.

22. U. Olsbye, R. Wendelbo, and D. Akporiaye, *Study of Pt/alumina catalysts preparation.* Applied Catalysis A: General, 1997. **152**(1): p. 127-141.

6 Reactions of methane and steam over 20 wt % Ni/Al_2O_3: Influence of calcination temperature

Characterisation studies (Chapter 4) have shown that the calcination temperature employed during the preparation of Ni/Al_2O_3 catalysts can significantly affect the catalyst structure, morphology and reducibility. Following high temperature calcination, Ni^{2+} reducibility and support morphology are considerably altered and the formation of a nickel aluminate ($NiAl_2O_4$) phase is detected. The formation of nickel aluminate and changes in the morphology of the support and active phase may result in modifications to the catalyst behaviour, specifically with respect to methane reforming. To investigate this, reactions involving methane and steam were undertaken to allow an insight into the reactivity and activity of Ni/Al_2O_3 catalysts, over a range of temperatures. The catalysts selected in this study represent those with significant variations in their physical characteristics, such as the formation of nickel aluminate. This has allowed the influence of physical properties on the steam methane reforming characteristics to be investigated. With this in mind, reactions involving methane and steam were carried out over 20 wt % Ni/Al_2O_3, calcined at 600 °C, 900 °C and 1000 °C, denoted hereon as Ni/Al_2O_3 (600), Ni/Al_2O_3 (900) and Ni/Al_2O_3 (1000).

All reforming reactions presented were carried out under near stoichiometric conditions, methane to steam ratio of 1:1. As discussed in Chapter 2, two fundamental reactions can occur during reactions involving methane and steam under stoichiometric reaction conditions, steam methane reforming (Reaction 6.1) and the water-gas shift reaction (Reaction 6.2).

$$\mathbf{CH_4 + H_2O \leftrightarrow CO + 3H_2} \qquad \mathbf{(6.1)}$$

$$CO + H_2O \leftrightarrow CO_2 + H_2 \qquad (6.2)$$

All catalysts were reduced in hydrogen at elevated temperatures prior to catalytic reactions. Temperature-programmed reduction (TPR) profiles for each catalyst are presented in Chapter 4.

6.1 Reverse temperature-programmed reactions of methane and steam under stoichiometric conditions over 20 wt % Ni/Al_2O_3

Reverse temperature-programmed reactions were undertaken in the presence of methane and steam, over the temperatures range 1000 °C to 200 °C. Reactions were undertaken in reverse as initial experiments demonstrated that catalytic data, such as reactivity and activity, could not to be accurately monitored during forward temperature-programmed reactions. This is discussed in more detail in Appendix B.

6.1.1 The influence of calcination temperature on the reactivity of Ni/Al_2O_3 during reactions of methane and steam

The reverse temperature-programmed reaction profile of methane and steam, under stoichiometric conditions over Ni/Al_2O_3 (600) is shown in Figure 6.1.

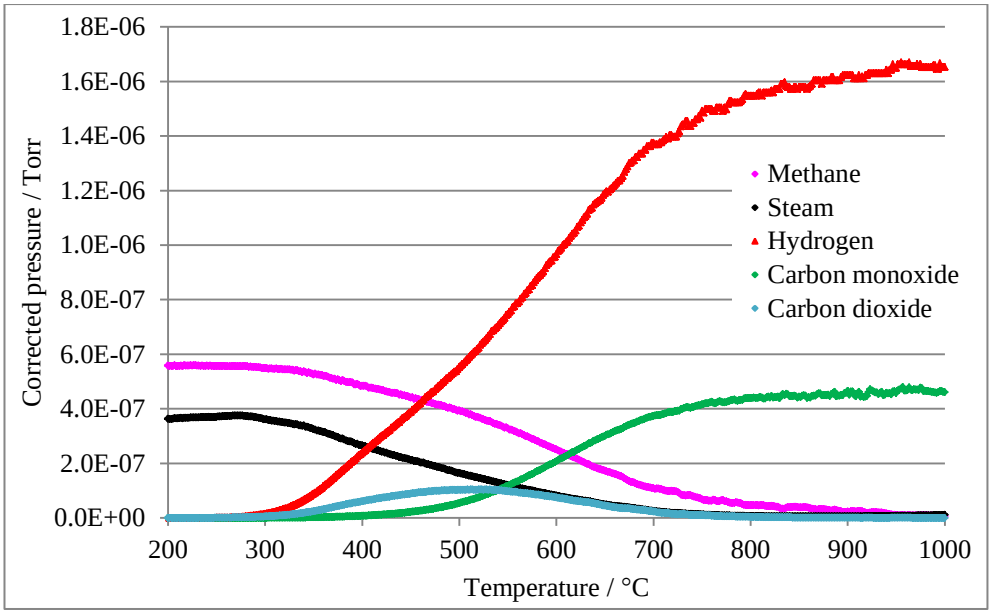

Figure 6.1: Reverse temperature-programmed reaction of methane and steam over Ni/Al_2O_3 (600) under near stoichiometric conditions (methane: steam = 1:1)

The reaction profiles over all the catalysts exhibit a similar reaction progression over the temperature range investigated, to that observed for Ni/Al_2O_3 (600) in Figure 6.1. As the temperature increases, consumption of methane and steam increases and the onset of hydrogen, carbon monoxide and carbon dioxide production are observed. Carbon monoxide and hydrogen production rises with increasing reaction temperature, reaching steady production at temperatures above *ca.* 850 °C. Carbon dioxide reaches maximum production at an intermediate temperature of *ca.* 500 °C.

Reverse temperature-programmed reaction profiles can be used to determine catalyst reactivity. Product gas onset temperatures during reactions of methane and steam, over Ni/Al_2O_3 (600), Ni/Al_2O_3 (900) and Ni/Al_2O_3 (1000) are shown in Table 6.1.

Table 6.1: Product gas onset temperatures during reverse temperature-programmed reactions of methane and steam under stoichiometric conditions

Catalyst	H_2 onset temperature / °C	CO onset temperature / °C	CO_2 onset temperature / °C
Ni/Al_2O_3 (600)	225	240	225
Ni/Al_2O_3 (900)	280	323	326
Ni/Al_2O_3 (1000)	237	286	261

The product gas onset reaction temperatures over Ni/Al_2O_3 (600) are lower than both Ni/Al_2O_3 (900) and Ni/Al_2O_3 (1000). Both hydrogen and carbon dioxide production occur simultaneously at 225 °C, whilst carbon monoxide is not detected until 240 °C. A similar trend is observed over Ni/Al_2O_3 (1000), where hydrogen onset is shortly followed by carbon dioxide, and finally carbon monoxide production. However, over Ni/Al_2O_3 (900) a significant reduction in catalytic reactivity is observed. The product gas onset temperatures are *ca.* 50 °C higher than for other catalysts and carbon monoxide and carbon dioxide production occur almost simultaneously, following hydrogen production.

Over Ni/Al_2O_3 (600) and Ni/Al_2O_3 (1000), carbon monoxide is detected at a higher reaction temperature, than both hydrogen and carbon dioxide. This could be attributed to the water-gas shift reaction occurring (Reaction 6.2). As soon as steam reforming occurs (Reaction 6.1) carbon monoxide produced could be utilised in the water-gas shift reaction, producing carbon dioxide. As the reaction temperature is increased, production of carbon monoxide occurs in excess of the water-gas shift requirements, due to the higher steam methane reforming activity, lowering the available steam concentration at higher reaction temperatures. Over Ni/Al_2O_3 (900), carbon monoxide is not utilised to the same extent as the other catalysts, and carbon dioxide production is observed

following carbon monoxide onset. Ni/Al_2O_3 (900) is less reactive towards both steam reforming and the water-gas shift reaction, thus product gas onset is significantly inhibited.

6.1.2 The influence of calcination temperature on the activity and selectivity of Ni/Al_2O_3 during reactions of methane and steam

Under stoichiometric conditions at optimum operating temperatures, if the steam methane reforming reaction (Reaction 6.1) were at equilibrium, CH_4 conversion and H_2 yield would be expected to reach 100 % and an H_2/CO ratio of 3 would be gained. This is assuming that additional side reactions, such as the water-gas shift reaction or carbon formation are not occurring and catalyst deactivation through sintering or carbon deposition do not occur or influence the steam reforming reaction. H_2 yield is calculated with respect to the steam methane reforming reaction only.

The catalyst selectivity and maximum activity over all catalysts is shown in Table 6.2, relating to reverse temperature-programmed reaction profiles. The H_2 yield and CH_4 conversion profiles for each catalyst are shown in Figure 6.2 and Figure 6.3, respectively and the CO selectivity profiles are shown in Figure 6.4. Minimum CO selectivity values are shown in Table 6.2, in order to give an indication of the extent of carbon dioxide produced relative to carbon monoxide production.

Table 6.2: Catalyst selectivity and maximum activity during reactions of methane and steam

Catalyst	Maximum CH_4 conversion / %	Maximum H_2 yield / %	Average final H_2/CO ratio	Minimum CO selectivity / %
Ni/Al_2O_3 (600)	99	100	3.5	15
Ni/Al_2O_3 (900)	100	103	2.5	38
Ni/Al_2O_3 (1000)	100	78	2.1	26

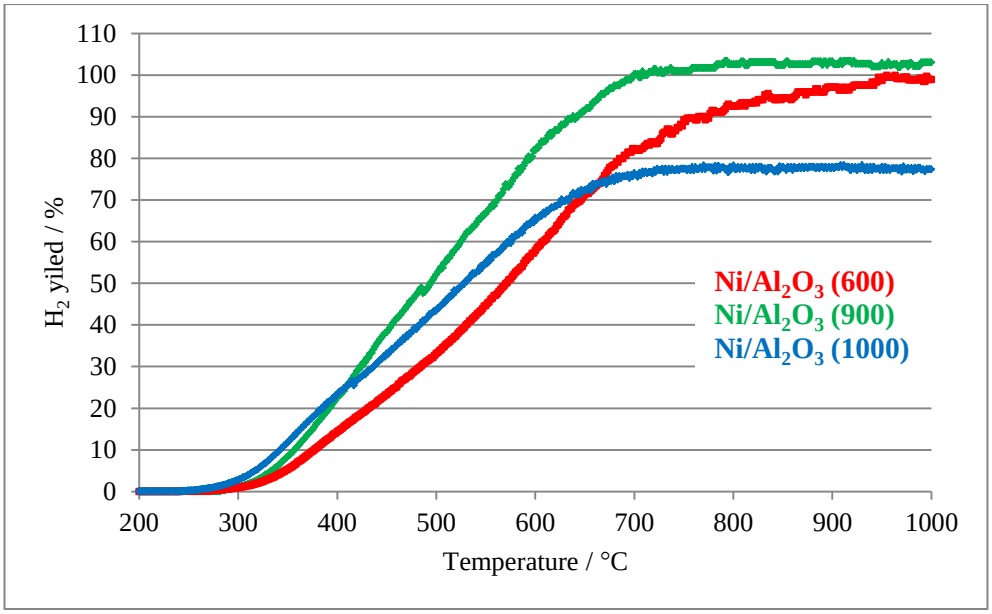

Figure 6.2: **H_2 yield during reactions of methane and steam over Ni/Al_2O_3 (600), Ni/Al_2O_3 (900) and Ni/Al_2O_3 (1000)**

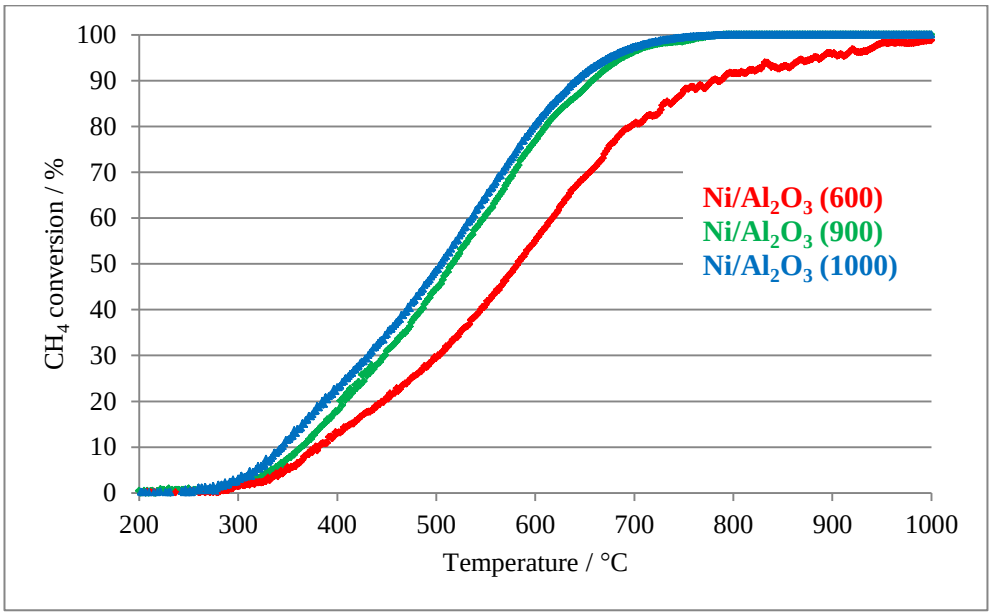

Figure 6.3: **CH_4 conversion during reactions of methane and steam over Ni/Al_2O_3 (600), Ni/Al_2O_3 (900) and Ni/Al_2O_3 (1000)**

Although CH_4 conversion and H_2 yield reach almost 100 % over Ni/Al_2O_3 (600), the final H_2/CO ratio indicates that additional reactions must be occurring at high temperatures producing additional hydrogen. This could be attributed to incomplete steam reforming occurring at temperatures above

ca. 900 °C. Thus, excess methane present undergoes decomposition, producing additional hydrogen (Reaction 6.3), which accounts for the increased H_2/CO ratio. As the reaction temperature is increased above 900 °C, a steady increase in methane consumption is observed, with additional hydrogen produced concurrently. No variation in carbon monoxide production or steam utilisation is observed, consistent with methane decomposition.

$$\mathbf{CH_4 \rightarrow C + 2H_2} \qquad \mathbf{(6.3)}$$

Over Ni/Al_2O_3 (900), at high temperatures, the H_2 yield increases to 103 %. Additional hydrogen may be produced by carbon gasification in the presence of steam. This could occur via the reverse CO reduction, producing hydrogen and carbon monoxide (reverse of Reaction 6.4). However, this does not account for the low H_2/CO ratio.

$$\mathbf{CO + H_2 \leftrightarrow C + H_2O} \qquad \mathbf{(6.4)}$$

It is likely in this case given the stability of the H_2 yield above 750 °C (Figure 6.2) and the very slight increase above 100 % observed, that this is due to the slight limitations in the sensitivity of the mass spectrometer. This trend is discussed in more detail in Section 6.2.2.

Over Ni/Al_2O_3 (1000), the H_2 yield is significantly less by *ca.* 22 %, than the CH_4 conversion. This suggests that hydrogen produced during steam reforming is utilised in additional reactions or processes. In Chapter 4, it was shown that Ni/Al_2O_3 (1000) was not fully reduced during TPR reactions and the $NiAl_2O_4$ phase formed during calcination remained partially unreduced. At high reaction temperatures, hydrogen produced via steam methane reforming could be reducing Ni^{2+} species present in the $NiAl_2O_4$ phase to metallic nickel, resulting in a lower H_2 yield and H_2/CO ratio. Any water produced by this reduction process would be utilised by the steam reforming reaction, thus no change in the steam gas signal would be observed, furthermore increasing methane conversion. The results in Chapter 4 suggest that $NiAl_2O_4$ is only present in an unreduced form in Ni/Al_2O_3 (1000) and the low H_2 yield observed over Ni/Al_2O_3 (1000) is not observed over other catalysts, consistent with the suggestion of $NiAl_2O_4$ reduction under reforming conditions.

Joo *et al.* [1] have made similar observations during reforming studies undertaken over a partially reduced Ni/Al_2O_3 catalyst, containing a $NiAl_2O_4$ phase formed during calcination. During these studies, the catalyst was ineffectively reduced prior to reforming studies and during reforming the catalyst was slowly reduced under the atmosphere of hydrogen produced during steam reforming, progressively becoming more active.

Other than the variation in the H_2 yield, both Ni/Al_2O_3 (900) and Ni/Al_2O_3 (1000) exhibit similar activity profiles, resulting in complete methane conversion at temperatures above *ca.* 750 °C.

The minimum CO selectivity and corresponding CO selectivity profiles are shown in Table 6.2 and Figure 6.4, respectively. CO selectivity gives an indication of carbon dioxide formation with respect to carbon monoxide production. Due to the thermodynamic nature of the water-gas shift reaction and the availability of steam, carbon dioxide production at temperatures below 700 °C is most likely due to the occurrence of this reaction. Additionally, it is worth noting that carbon dioxide can also be produced by the Boudouard reaction (Reaction 6.5) at temperatures below 680 °C (as discussed in Chapter 2).

$2CO \leftrightarrow C + CO_2$ (6.5)

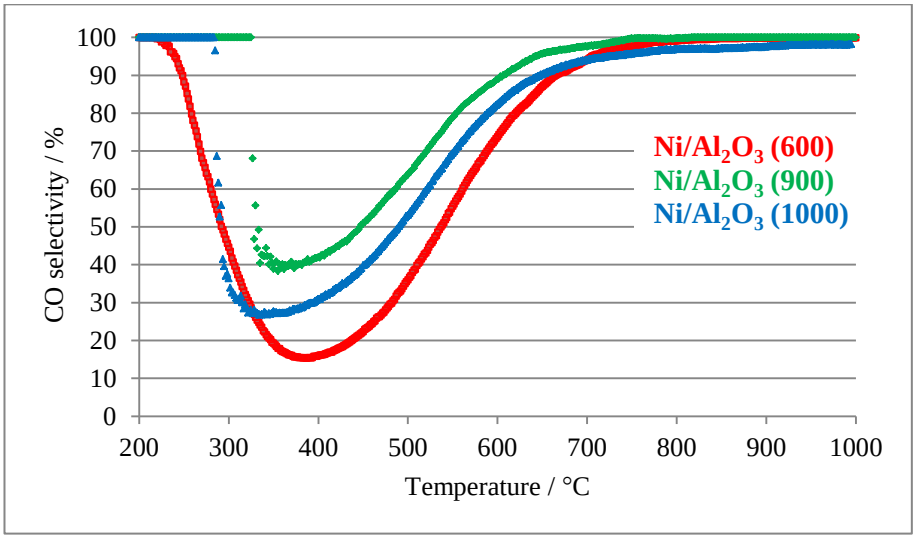

Figure 6.4: CO selectivity during reactions of methane and steam over Ni/Al_2O_3 (600), Ni/Al_2O_3 (900) and Ni/Al_2O_3 (1000)

As discussed in Section 6.1.1, Ni/Al_2O_3 (600) is highly active towards the water-gas shift reaction, which is confirmed by the CO selectivity profiles in Figure 6.4 showing *ca.*15 % CO selectivity at *ca.* 400 °C. The CO selectivity data suggests Ni/Al_2O_3 (900) is least active towards the water-gas shift reaction.

The high water-gas shift activity over Ni/Al_2O_3 (600) may account for the reduction in CH_4 conversion compared to other catalysts as observed in Figure 6.3. The high activity may inhibit steam reforming, as steam is utilised in the water-gas shift reaction, reducing the extent to which steam reforming occurs at temperatures between *ca.* 300 °C to 700 °C, where the water-gas shift reaction is highly active. Ni/Al_2O_3 (900) and Ni/Al_2O_3 (1000) are more active towards steam methane reforming than the water-gas shift reaction.

6.1.3 Carbon deposition during reverse temperature-programmed reactions of methane and steam

The dynamic nature of temperature-programmed reactions means it would be inaccurate and misleading to present carbon deposition data, due to the different carbon forming reactions that can occur over the temperatures studied. Any carbon deposition data would not provide an accurate indication regarding catalyst activity towards specific carbon deposition reactions. As discussed in Chapter 2, carbon deposition can occur via a number of reactions favoured at various temperatures and reaction conditions. Each catalyst may promote specific carbon forming reactions at various temperatures and to various extents. Thus, any carbon deposition data following temperature-programmed reactions does not provide specific information regarding the temperature at which carbon was formed or specific amounts of carbon formed at certain temperatures.

Carbon deposition data (presented in Section 6.3) has been obtained following isothermal reactions using post-reaction temperature-programmed oxidation, in order to obtain a better understanding into the specific carbon forming reactions occurring at different reforming temperatures.

6.2 Effect of temperature on the reactions of methane and steam under stoichiometric conditions over 20 wt % Ni/Al_2O_3

Reactions of methane and steam were carried out over a range of temperatures, over a 20 hour reaction period. This duration was selected in order to gain an insight into the catalytic activity over an extended period, allowing any substantial changes in the catalytic behaviour to be monitored. This allowed a steady reaction regime to be reached, as well as any catalyst deactivation trends to be detected. The temperatures studied (500 °C, 600 °C, 700 °C, 800 °C and 900 °C) were selected with regard to the catalytic activity during temperature-programmed reactions. Below 500 ºC, the catalytic activity was very low and would not provide accurate or useful data. Temperature-programmed reaction data suggests that high reforming activity is reached by 900 °C, so temperatures above 900 °C were not investigated.

An example of a reaction carried out over Ni/Al_2O_3 (600) for 20 hours in the presence of methane and steam at 700 °C is shown in Figure 6.5.

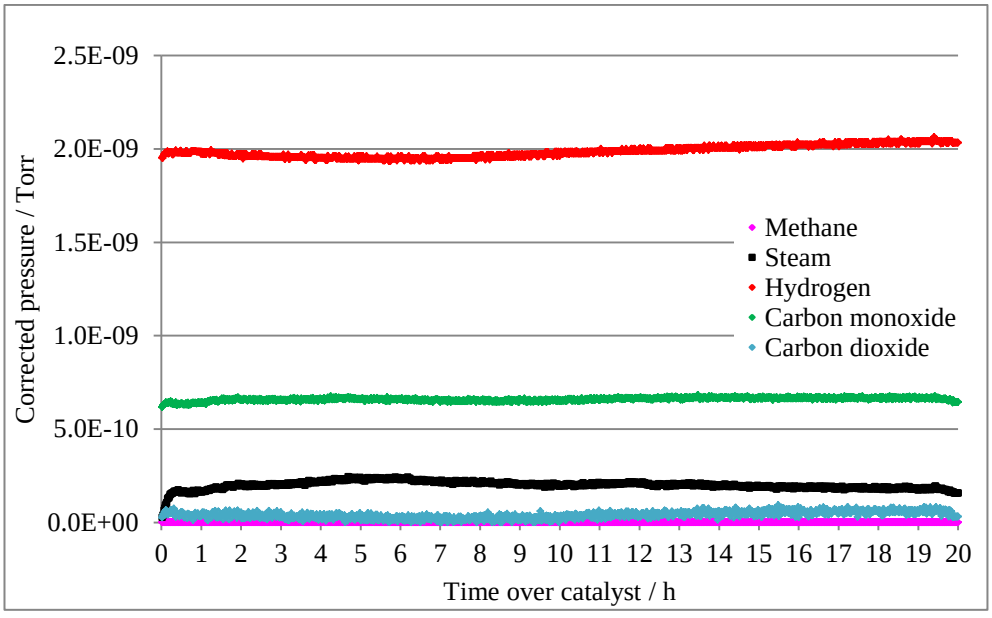

Figure 6.5: Reaction profile for reaction of methane and steam over Ni/Al_2O_3 (600) for 20 hours under stoichiometric conditions at 700 °C

A full set of similar reaction profiles were obtained for Ni/Al_2O_3 (900) and Ni/Al_2O_3 (1000) over the temperature range studied. Catalytic data, including the activity and selectivity, were obtained from reaction profiles.

It can be seen in Figure 6.5, that the reaction reaches a stable activity after *ca.* 1 hour. However, in some situations changes in the laboratory temperature resulted in a small fluctuation in the methane to steam reactant gas ratios during the reaction. An example of a subsequent reaction profile is shown in Figure 6.6.

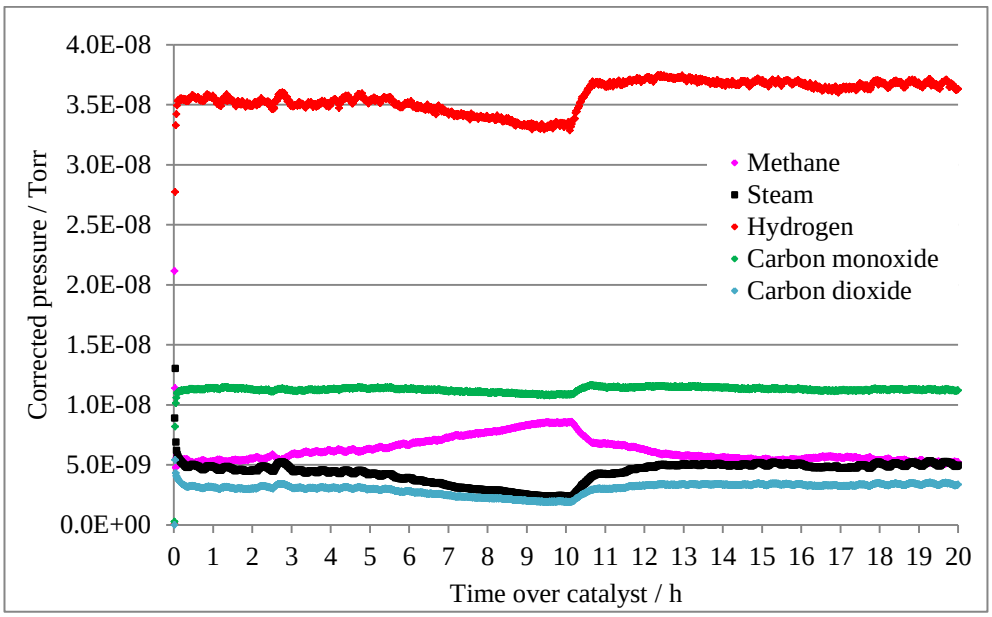

Figure 6.6: Reaction profile for reaction of methane and steam over Ni/Al_2O_3 (900) for 20 hours under stoichiometric conditions at 600 °C

The variation in the exit gas composition in Figure 6.6, from *ca.* 4 to 11 hours, can be attributed to a change in the steam pressure. This results in fluctuations of all the reactant and product gas signals, mirroring or following that exhibited by steam. Changes such as these must be viewed with care and not mistaken for changes in catalytic activity or selectivity at a fixed methane to steam ratio. Due to the reaction stoichiometry, a small change in the steam pressure can significantly affect the catalytic activity. With this in mind, activity and selectivity data presented in this study shows minimum, maximum and average activity data, taken from the 20 hour reaction profiles at

the corresponding temperature. Every effort was made to minimise any changes in the steam partial pressure during the course of this study. Unless otherwise stated, the variation in catalytic activity and selectivity presented in this study is attributed to a change in the methane to steam ratio.

6.2.1 Reactions of methane and steam under stoichiometric conditions over Ni/Al_2O_3 (600)

The average CH_4 conversion and H_2 yield are shown in Figure 6.7 and the average CO selectivity and H_2/CO ratio in Table 6.3, for reactions of methane and steam over Ni/Al_2O_3 (600) across the temperature range 500 °C to 900 °C.

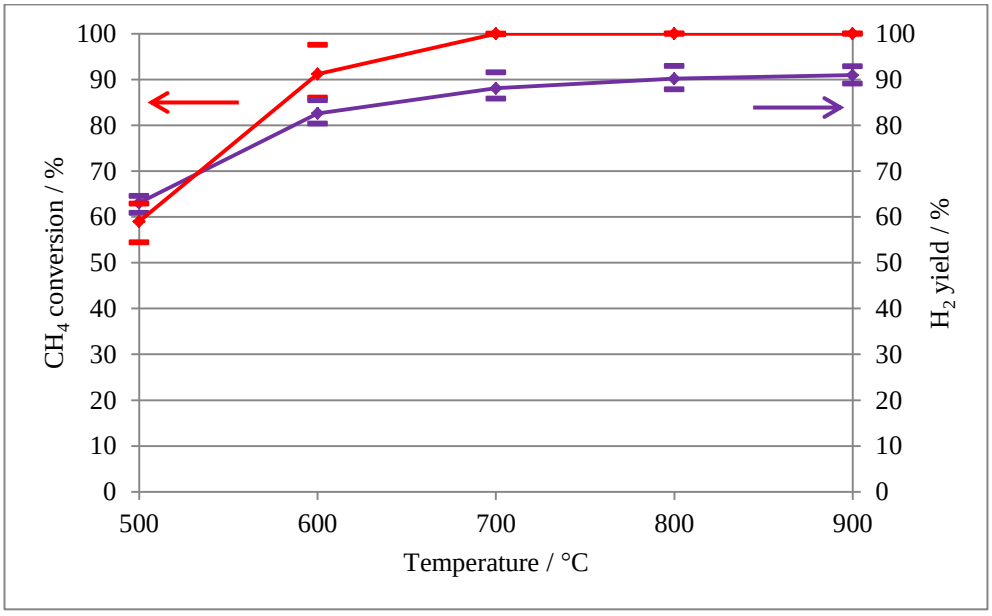

Figure 6.7: Average CH_4 conversion and H_2 yield during reactions of methane and steam over Ni/Al_2O_3 (600) for 20 hours under stoichiometric conditions (methane: steam = 1:1) at reaction temperatures 500 °C to 900 °C

Table 6.3: Average CO selectivity and H_2/CO ratio during reactions of methane and steam over Ni/Al_2O_3 (600) for 20 hours under stoichiometric conditions (methane: steam = 1:1) at reaction temperatures 500 °C to 900 °C

Reaction temperature / °C	Average CO selectivity / %	Average H_2/CO ratio
500	63	3.0
600	100	3.0
700	94	3.0
800	98	3.2
900	100	3.5

The data shows an increase of *ca.* 30 % in both CH_4 conversion and H_2 yield at 500 °C and 600 °C, compared to temperature-programmed results. This could be due to increased stability of reforming reactions over a prolonged period of time, compared to temperature-programmed studies. Both CH_4 conversion and H_2 yield data exhibit similar trends over the temperatures investigated during isothermal studies.

The low CO selectivity at 500 °C indicates that the water-gas shift reaction is occurring, although not to the extent observed during temperature-programmed studies. At 500 °C, it is assumed that the only reactions occurring are steam reforming and the water-gas shift reaction. As the reaction temperature is increased to 600 °C, the CO selectivity data indicates that the water-gas shift reaction is no longer occurring and the primary reaction occurring is steam methane reforming

At temperatures above 600 °C, reforming activity increases and maximum CH_4 conversion is achieved. Figure 6.7 shows that the H_2 yield is *ca.* 10 % lower than the CH_4 conversion, for reactions carried out at reaction temperatures between 700 °C and 900 °C. The reduction in H_2 yield could be attributed to additional side reactions occurring. CO selectivity is slightly below 100

% (Table 6.3) indicating additional carbon dioxide may be produced. At these reaction temperatures, the reverse water-gas shift reaction is thermodynamically favoured, as discussed in Chapter 2, and may be occurring. Carbon dioxide could be produced via the Boudouard reaction (Reaction 6.5), utilising carbon monoxide to produce surface carbon. However, due to the presence of steam, carbon gasification may also occur. This is confirmed by post-reaction TPO studies undertaken (Section 6.3) which indicate that no carbon is produced on the catalyst during reactions over Ni/Al_2O_3 (600). The additional side reactions occurring would account for the low hydrogen yield and slightly higher than expected H_2/CO ratio.

6.2.2 Reactions of methane and steam under stoichiometric conditions over Ni/Al_2O_3 (900)

The average CH_4 conversion and H_2 yield are shown in Figure 6.8 and the average CO selectivity and H_2/CO ratio in Table 6.4, for reactions of methane and steam over Ni/Al_2O_3 (900) across the temperature range 500 °C to 900 °C.

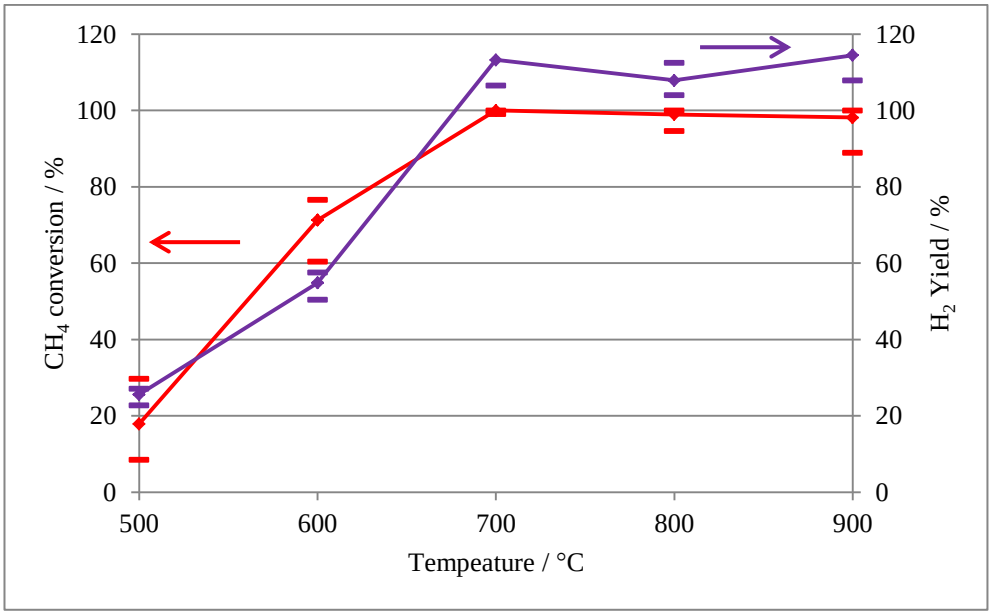

Figure 6.8: Average CH_4 conversion and H_2 yield during reactions of methane and steam over Ni/Al_2O_3 (900) for 20 hours under stoichiometric conditions (methane: steam = 1:1) at reaction temperatures 500 °C to 900 °C

Table 6.4: Average CO selectivity and H_2/CO ratio during reactions of methane and steam over Ni/Al_2O_3 (900) for 20 hours under stoichiometric conditions (methane: steam = 1:1) at reaction temperatures 500 °C to 900 °C

Reaction temperature / °C	Average CO selectivity / %	Average H_2/CO ratio
500	49	4.2
600	79	3.2
700	95	3.0
800	100	2.8
900	100	2.9

Lower CH_4 conversion and H_2 yield are obtained during reactions undertaken at 500 °C and 600 °C, than exhibited during reverse temperature-programmed studies, which suggests that Ni/Al_2O_3 (900) exhibits low reactivity towards steam methane reforming. The reaction at 500 °C exhibits low CO selectivity and a high H_2/CO ratio (Table 6.4), suggesting a high activity towards the water-gas shift reaction. Although a minimal amount, carbon deposition is observed following the reaction at 500 °C (Section 6.3) and may be formed either by the Boudouard reaction or CO reduction. However, it is most likely that this is occurring by the Boudouard reaction, contributing to the low CO selectivity, and increase in H_2/CO ratio to a value above 4.

An increase in the reaction temperature to 600 °C, results in the H_2 yield being *ca.* 15 % lower than CH_4 conversion, although maximum and minimum data points are comparable. CO selectivity data indicates that the water-gas shift reaction is occurring, although not to the extent observed at 500 °C. The slightly lower than expected H_2/CO ratio gained is attributed to the formation of carbon (Section 6.3) via CO reduction.

At temperatures above 700 °C higher H_2 yield compared to CH_4 conversion is observed. This could possibly be due to experimental error relating to the sensitivity of the mass spectrometer. However, this trend is also observed during reverse temperature-programmed reactions over Ni/Al_2O_3 (900) at high reaction temperatures, suggesting that additional reactions or processes may be occurring over this catalyst, resulting in a high H_2 yield. H_2 yield is calculated with respect to methane (as shown in Chapter 3), thus additional hydrogen production could be related to additional reactions involving steam directly. With this in mind, the additional hydrogen production could be attributed to H_2O dissociation and subsequent desorption of adsorbed H_2 species. During reverse temperature-programmed reactions H_2O adsorption and subsequent desorption may also be occurring, however, the low H_2/CO ratio suggests this is only occurring to a small extent. No carbon deposition is observed following reactions at elevated temperatures (Section 6.3). As well as H_2O dissociation, steam reforming is the primary reaction occurring during reactions above 700 °C and at this temperature CO selectivity data indicates that the water-gas shift may be occurring, to a relatively minor extent.

6.2.3 Reactions of methane and steam under stoichiometric conditions over Ni/Al_2O_3 (1000)

The average CH_4 conversion and H_2 yield are shown in Figure 6.9 and the average CO selectivity and H_2/CO ratio in Table 6.5, for reactions of methane and steam over Ni/Al_2O_3 (1000) across the temperature range 500 °C to 900 °C.

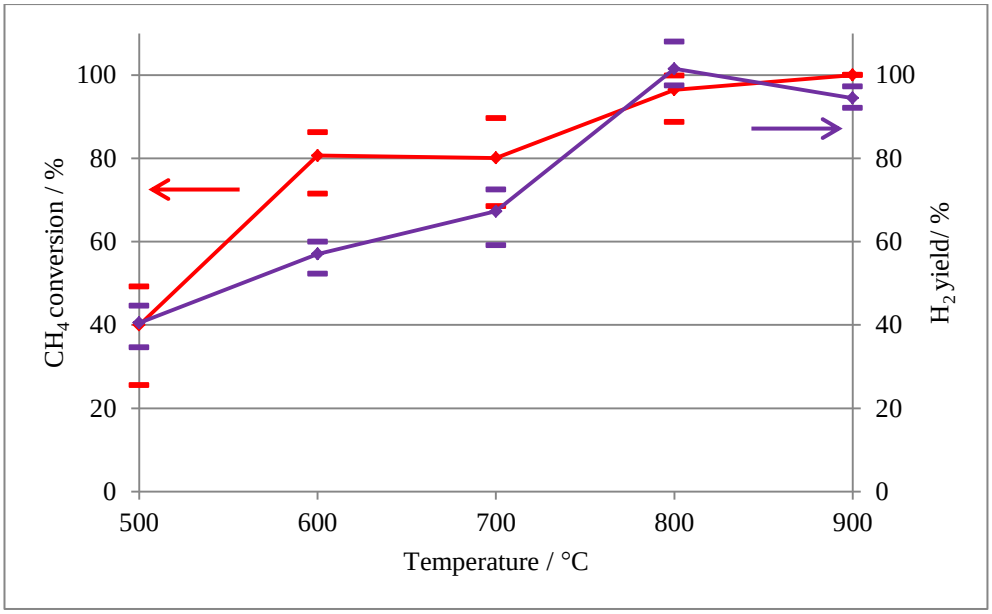

Figure 6.9: **Average CH_4 conversion and H_2 yield during reactions of methane and steam over Ni/Al_2O_3 (1000) for 20 hours under stoichiometric conditions (methane: steam = 1:1) at reaction temperatures 500 °C to 900 °C**

Table 6.5: **Average CO selectivity and H_2/CO ratio during reactions of methane and steam over Ni/Al_2O_3 (1000) for 20 hours under stoichiometric conditions (methane: steam = 1:1) at reaction temperatures 500 °C to 900 °C**

Reaction temperature / °C	**Average CO selectivity / %**	**Average H_2/CO ratio**
500	55	3.4
600	83	2.3
700	93	2.4
800	98	1.9
900	100	4.1

The reaction at 500 °C exhibits characteristics indicating that the primary reactions occurring are steam reforming and the water-gas shift reaction. The H_2 yield is lower than expected, which could be due to carbon formation by the Boudouard reaction also occurring, possibly followed by carbon gasification in the presence of steam. At 600 °C, the H_2 yield is *ca.* 20 % lower than the CH_4 conversion. The reduction in H_2 yield is also apparent in the low H_2/CO ratio. This indicates that hydrogen is being utilised in additional reactions or processes. A similar trend was observed during the reverse temperature-programmed studies, although at higher temperatures. In this case, this trend was attributed to the reduction of $NiAl_2O_4$ species by hydrogen, thus lowering the hydrogen yield. A similar process may be occurring during the reaction at 600 °C in the presence of hydrogen produced during steam reforming. However, this is unlikely to rapidly reduce $NiAl_2O_4$ due to the low reaction temperature and high temperatures required for complete reduction, as observed in Chapter 4. Therefore at 600 °C, reduction may be occurring gradually over 20 hours. At higher reaction temperatures, this may be a rapid process occurring over the first few hours due to the increased reaction temperature and higher product gas ratio. Therefore, a significant variation in the H_2 yield would not be observed over the course of the reaction. Similar behaviour was observed by Joo *et al.* [1], during reforming studies undertaken over a partially reduced Ni/Al_2O_3 catalyst. As well as this reduction process occurring, CO selectivity data indicates that the water-gas shift reaction is also occurring at 600 °C.

The difference between CH_4 conversion and H_2 yield observed during the reaction at 700 °C is small and possibly within experimental error, as maximum and minimum values are comparable. Alternatively this could be attributed to the reduction of $NiAl_2O_4$ or the formation of carbon via either or both the Boudouard reaction and CO reduction, accounting for the low H_2/CO ratio obtained. Both CH_4 conversion and H_2 yield reach *ca.* 100 % during reactions at 800 °C and 900 °C. However, the H_2/CO ratio is significantly different at these temperatures. At 800 °C, the low H_2/CO ratio (1.9) could be attributed to the Boudouard reaction and reverse water-gas shift reaction occurring. This would reduce the product gas ratio whilst maintaining a high H_2 yield. At 900 °C, the H_2/CO ratio is dramatically increased to 4.1. This is most likely due to some methane

decomposition occurring (Reaction 6.3), however, due to the extent of the steam reforming activity at this temperature, methane is not present in excess amounts, thus the amount of methane available for methane decomposition would be low.

6.2.4 The influence of calcination temperature on the activity and selectivity of Ni/Al_2O_3 during reactions of methane and steam at different reaction temperatures

The average CH_4 conversion and H_2 yield comparison profiles for Ni/Al_2O_3 (600), Ni/Al_2O_3 (900) and Ni/Al_2O_3 (1000) are shown in Figure 6.10 and Figure 6.11. Average CO selectivites and H_2/CO ratio profiles for the above mentioned catalysts are shown in Figure 6.12 and Figure 6.13.

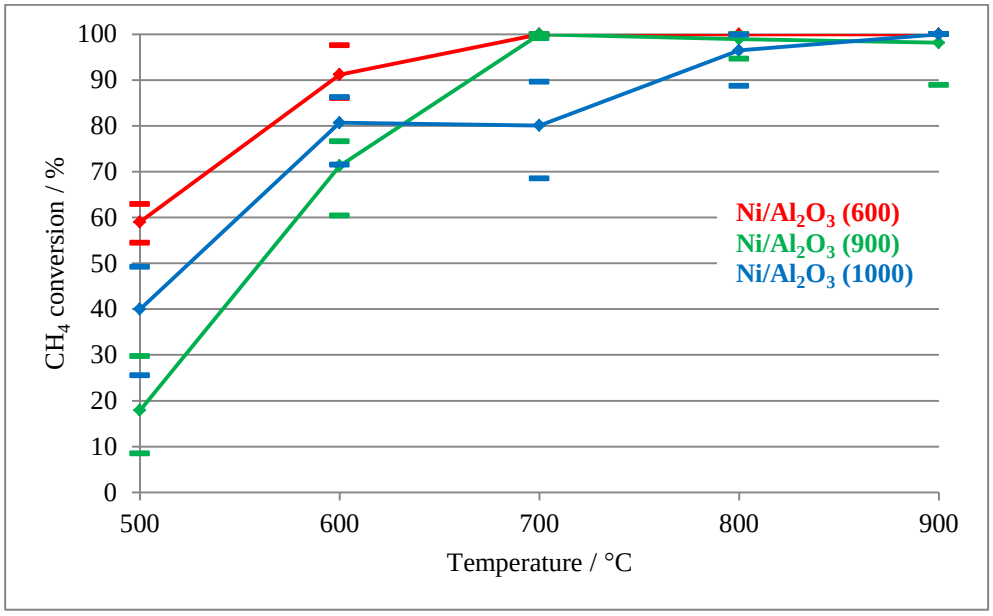

.

Figure 6.10: Average CH_4 conversion during reactions of methane and steam over Ni/Al_2O_3 (600), Ni/Al_2O_3 (900) and Ni/Al_2O_3 (1000) for 20 hours under stoichiometric conditions (methane: steam = 1:1) at reaction temperatures 500 °C to 900 °C

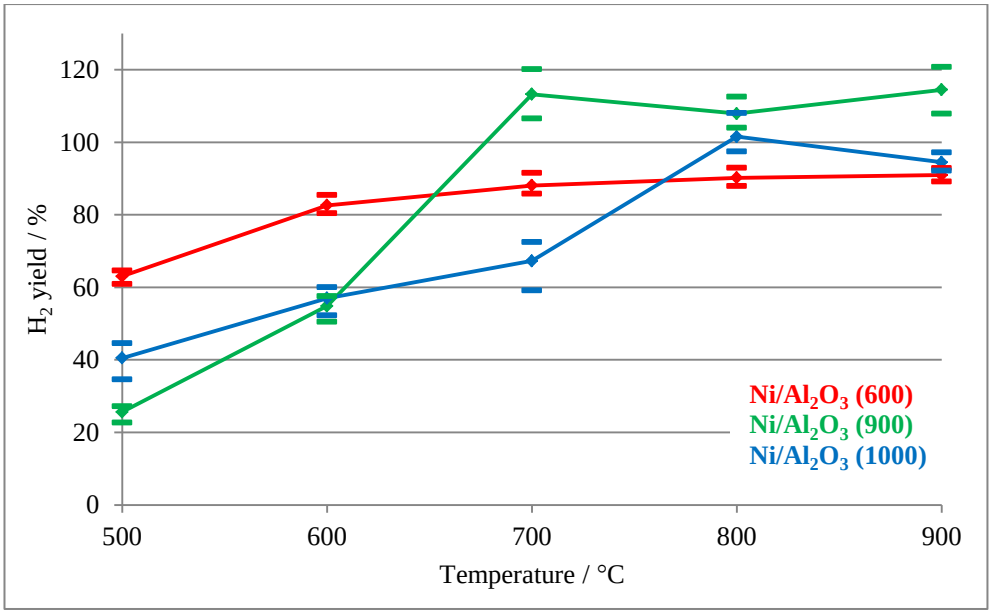

Figure 6.11: **Average H_2 yield during reactions of methane and steam over Ni/Al_2O_3 (600), Ni/Al_2O_3 (900) and Ni/Al_2O_3 (1000) for 20 hours under stoichiometric conditions (methane: steam = 1:1) at reaction temperatures 500 °C to 900 °C**

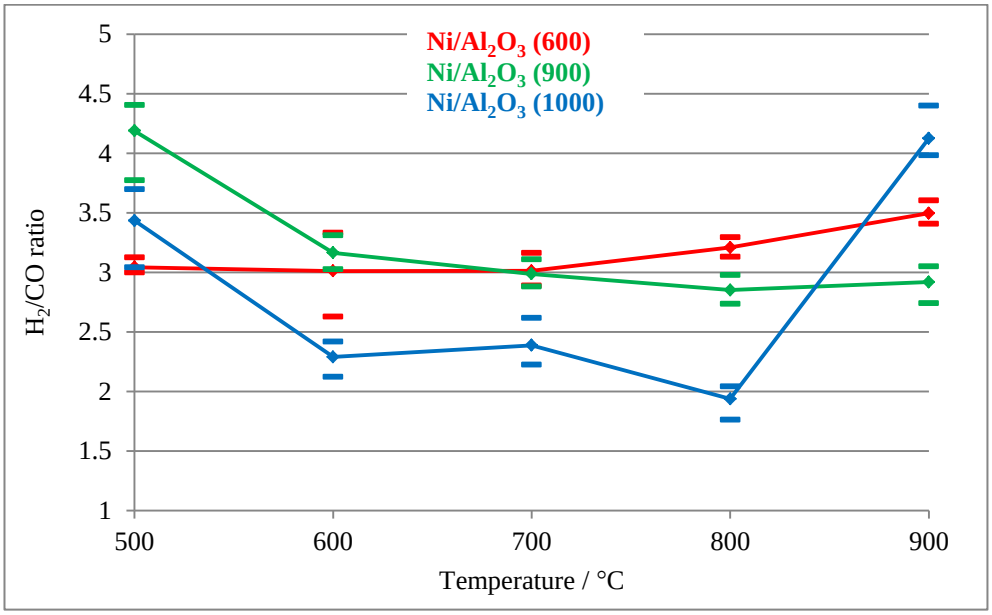

Figure 6.12: **Average H_2/CO ratio during reactions of methane and steam over Ni/Al_2O_3 (600), Ni/Al_2O_3 (900) and Ni/Al_2O_3 (1000) for 20 hours under stoichiometric conditions (methane: steam = 1:1) at reaction temperatures 500 °C to 900 °C**

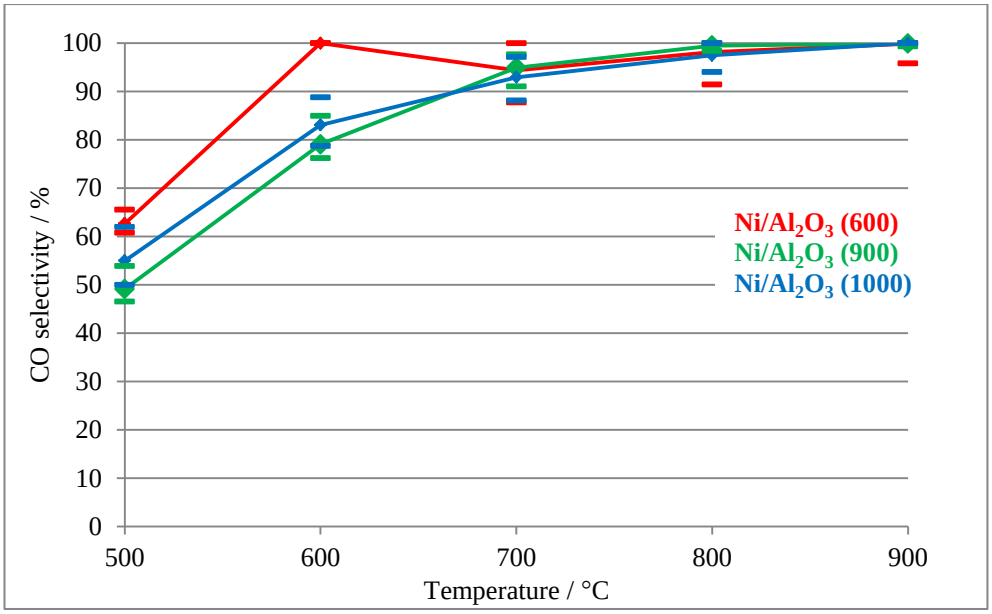

Figure 6.13: Average CO selectivity during reactions of methane and steam over Ni/Al_2O_3 (600), Ni/Al_2O_3 (900) and Ni/Al_2O_3 (1000) for 20 hours under stoichiometric conditions (methane: steam = 1:1) at reaction temperatures 500 °C to 900 °C

Temperature-programmed studies shown in Section 6.1.1 indicate that Ni/Al_2O_3 (600) was most reactive towards steam reforming. This is also observed in the CH_4 conversion and H_2 yield data for reactions at 500 °C and 600 °C, shown in Figure 6.10. Ni/Al_2O_3 (900) exhibits the lowest activity at 500 °C and 600 °C (Figure 6.10), and could be attributed to carbon formation, resulting in a reduction in reforming activity (Section 6.3). Although Ni/Al_2O_3 (900) promotes carbon deposition at temperatures below 600 °C (Figure 6.14), slightly reducing the catalytic activity, the CH_4 conversion and H_2 yield data are comparable to Ni/Al_2O_3 (1000).

The activity over Ni/Al_2O_3 (1000) is as low as Ni/Al_2O_3 (900) at 500 °C, although it is not limited by carbon deposition. Reforming activity may be low over Ni/Al_2O_3 (1000) due to the presence of partially unreduced $NiAl_2O_4$. As discussed in Chapter 4, $NiAl_2O_4$ is formed following calcination at 1000 °C and is ineffectively reduced in hydrogen during TPR reactions (Chapter 4 Section 4.2.4.1). At low reaction temperatures, the $NiAl_2O_4$ phase may not be reduced during the reforming reaction, as observed in Section 6.2.3. $NiAl_2O_4$ has been reported to have very little or no reforming activity

if ineffectively reduced prior to reforming reactions [1-5], accounting for the low activity at 500 °C. Low reactivity and activity (at low temperatures) may not have been observed during the temperature-programmed reaction over Ni/Al_2O_3 (1000), as the reaction is undertaken in reverse. Therefore, $NiAl_2O_4$ may be reduced to metallic nickel at high reaction temperatures (Section 6.1.2), potentially increasing low temperature activity, compared to the isothermal reaction studies.

The reaction undertaken over Ni/Al_2O_3 (1000) at 600 °C, exhibits a significantly lower H_2 yield, compared to CH_4 conversion (Figure 6.11). During reforming reactions, hydrogen produced by steam reforming may be reducing the remaining $NiAl_2O_4$ phase to metallic nickel, thus a reduction in hydrogen yield is observed [1]. At higher reaction temperatures, the $NiAl_2O_4$ phase will be reduced rapidly during the initial stages of the reaction, so no sustained effect on the product gases is observed. A significant reduction in H_2 yield is not observed over the other catalysts, and $NiAl_2O_4$ was not identified during post-reduction XRD studies in these catalysts.

At temperatures above 700 °C, Ni/Al_2O_3 (900) could be promoting H_2O adsorption and dissociation, with subsequent desorption of hydrogen accounting for the high hydrogen yield obtained (Figure 6.11). This also contributes to the increase in carbon gasification and low levels of carbon deposition observed over Ni/Al_2O_3 (900), as discussed in Section 6.3. No other catalysts appear to promote hydrogen formation through this mechanism. Apart from H_2O dissociation, the primary reaction occurring at high temperatures over Ni/Al_2O_3 (900) is steam reforming. However, over Ni/Al_2O_3 (600) and Ni/Al_2O_3 (1000) this does not occur and additional side reactions occurring above 700 °C result in a shift in the H_2/CO ratio (Figure 6.12) and H_2 yield (Figure 6.11).

Over Ni/Al_2O_3 (600), greater activity towards the reverse water-gas shift reaction, Boudouard reaction and carbon gasification would account for the higher than expected H_2/CO ratio (Figure 6.12) and low H_2 yield (Figure 6.11) obtained at reaction temperatures above 700 °C. The H_2/CO ratio is significantly affected by additional side reactions over Ni/Al_2O_3 (1000). This is due to carbon formation reactions occurring at 800 °C and 900 °C and a likely shift from the Boudouard reaction to methane decomposition occurring.

Both Ni/Al_2O_3 (600) and Ni/Al_2O_3 (1000) are active towards the reverse water-gas shift reaction at temperatures above 700 °C. However, Ni/Al_2O_3 (600) is less active than Ni/Al_2O_3 (1000) towards the water-gas shift reaction (Figure 6.12). Ni/Al_2O_3 (900) exhibits moderately low CO selectivity at 500 °C and 600 °C (Figure 6.12), which is not only attributed to the water-gas shift reaction but also the Boudouard reaction, thus lowering CO selectivity to a greater extent.

6.3 Carbon deposition following reactions of methane and steam under stoichiometric conditions over 20 wt % Ni/Al_2O_3 at different reaction temperatures

Carbon deposition determined by post-reaction temperature-programmed oxidation (TPO) studies, is shown in Figure 6.14. Specific TPO profiles are not shown due to the low levels of carbon deposition during stoichiometric studies and resulting lack of obtainable information from the profiles. TPO profiles are shown following reforming studies carried out under methane-rich conditions (Chapter 7).

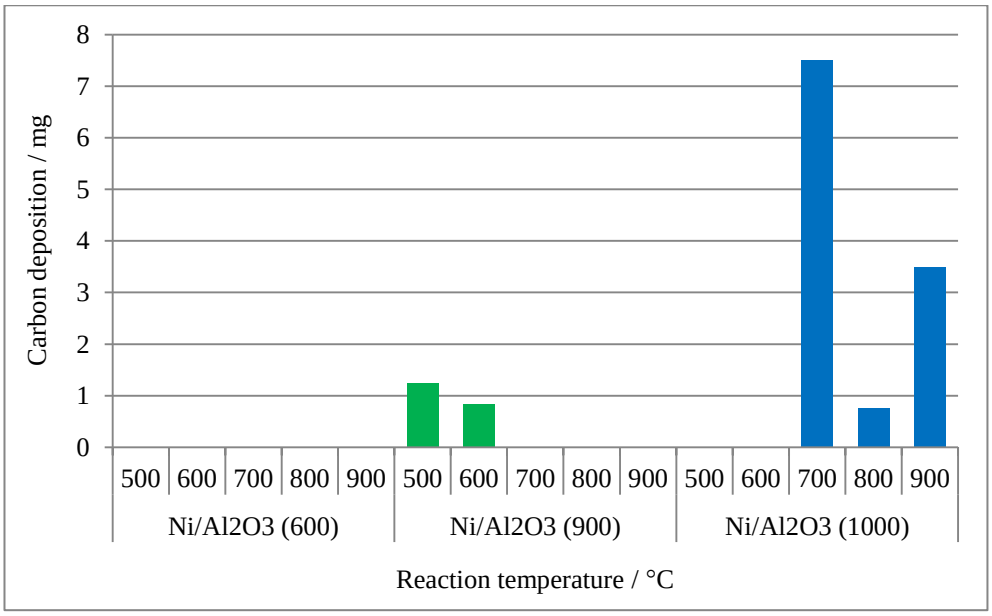

Figure 6.14: Amount of carbon deposition following reactions of methane and steam under stoichiometric conditions over Ni/Al_2O_3 (600), Ni/Al_2O_3 (900) and Ni/Al_2O_3 (1000) at different temperatures

A number of carbon-forming reactions can occur during reforming, at various temperatures. As well as carbon-forming reactions, carbon gasification in the presence of steam can also occur, minimising carbon deposition. Both CO reduction and the Boudouard reaction are favoured at temperatures below *ca.* 670 °C and thus the reverse reactions may be the mechanism for carbon removal at temperatures above this. Methane decomposition is favoured at temperatures above 714 °C. Due to the stoichiometry of the above reforming reactions, significant carbon gasification may occur in the presence of steam, as discussed in Appendix C. Appendix C shows that the presence of steam can significantly aid carbon removal by gasification during reforming reactions at temperatures as low as 200 °C. Additionally it is shown that carbon gasification by steam increases as the reaction temperature is increased. Removal of carbon has been shown by Choudhary *et al.* [6] to be strongly dependent on both methane concentration and the amount of carbon deposited on the catalyst surface.

As discussed in Section 6.2, a number of carbon-forming reactions are occurring during reforming studies. As expected, it is shown that the Boudouard reaction and CO reduction are the primary carbon formation reactions occurring at and below 800 °C. Although the Boudouard reaction may be occurring over Ni/Al_2O_3 (600) at temperatures from 700 °C to 900 °C, carbon removal by steam occurs. This results in complete removal of carbon from the surface and thus no carbon is observed during post-reaction TPO studies (Figure 6.14).

TPO studies identify carbon deposition following reactions over Ni/Al_2O_3 (900) at 500 °C and 600 °C, as shown in Figure 6.14. This can be attributed to the Boudouard reaction and CO reduction occurring, although carbon gasification may also be occurring at these temperatures, limiting deposition to minor amounts (*ca.* 1 mg). As discussed in Section 6.2.2, Ni/Al_2O_3 (900) appears to substantially promote the adsorption and dissociation of H_2O at temperatures above 700 °C. The adsorbed oxygen species resulting from H_2O adsorption may increase carbon gasification, therefore, limiting carbon deposition during reforming reactions. This would account for the lack of carbon formation above 700 °C. This is supported by Rostrup-Nielsen [7], who have proposed that

the rate of H_2O dissociation on catalysts is the main factor resulting in improved resistance towards carbon formation. This group have proposed that the amount of adsorbed OH species enhances the removal of adsorbed CH_x species, retarding the full dehydrogenation of CH_x species to surface carbon.

Carbon formation reactions are observed to the greatest extent over Ni/Al_2O_3 (1000), at temperatures of 700 °C and above. At 500 °C the Boudouard reaction may be occurring, however, any carbon formed is removed by gasification in the presence of steam. Additionally, the presence of $NiAl_2O_4$ reduces catalytic activity towards carbon-forming reactions. At higher temperatures (700 °C and 800 °C) carbon is deposited during reforming reactions by the Boudouard reaction and CO reduction, and carbon removal by gasification is not sufficient to remove all the carbon formed. At 700 °C, over 7 mg of carbon is deposited during reforming reactions, due to the occurrence of both the Boudouard reaction and CO reduction, whilst at 900 °C carbon deposition is proposed to occur by methane decomposition.

In summary, carbon formation is more strongly favoured over Ni/Al_2O_3 (1000) at reaction temperatures of 700 °C and above, following reduction of $NiAl_2O_4$. Although carbon gasification in the presence of steam may be occurring, it has least influence on carbon deposition over Ni/Al_2O_3 (1000) at higher reaction temperatures. Carbon formation is observed following reactions over Ni/Al_2O_3 (900) at low reaction temperatures. However, the promotion of H_2O adsorption during reforming reactions increases carbon gasification at temperatures above 700 °C. Carbon deposition is not observed following reactions over Ni/Al_2O_3 (600) and is effectively removed by reverse CO reduction in the presence of steam. Piao *et al.* [8] have reported that the influence of calcination temperature on carbon formation is extremely variable and can depend on many factors. They have shown that an optimum calcination temperature exists in which carbon deposition occurs. Low levels of carbon deposition are observed during this study carried out under stoichiometric reforming conditions. However, the results show that the influence of calcination

temperature on carbon formation is complex due to the different carbon-forming reactions and other surface reaction which all have different temperature dependencies.

6.4 Summary

Ni/Al_2O_3 calcined at 900 °C has been shown to be highly active towards the adsorption and subsequent dissociation of H_2O, resulting in an increase in hydrogen production at reaction temperatures above 700 °C. This also increases carbon gasification during reactions carried out at 700 °C and above, due to an increase in surface oxygen species.

The catalytic activity of Ni/Al_2O_3 calcined at 1000 °C is dramatically affected by the formation of $NiAl_2O_4$ during preparation and the incomplete reduction of this phase during reduction in hydrogen. Low temperature reaction activity is limited due to the minimal activity of the $NiAl_2O_4$ phase. However, at reaction temperatures above 600 °C the $NiAl_2O_4$ phase is reduced under reforming conditions, by the hydrogen produced by steam methane reforming. During the reaction at 600 °C, $NiAl_2O_4$ reduction to metallic nickel is observed resulting in a reduced hydrogen yield. This increases the activity at higher temperatures, compared to that observed in temperature-programmed studies.

Carbon deposition is significantly increased over Ni/Al_2O_3 calcined at 1000 °C and to a greater extent at elevated reaction temperatures due to an increase in catalytic activity following $NiAl_2O_4$ reduction. Despite results indicating that carbon-forming reactions are occurring over Ni/Al_2O_3 calcined at 600 °C above 600 °C, carbon removal in the presence of steam effectively removes all carbon deposited on the catalyst and no carbon is observed during TPO reactions.

Calcination at different temperatures has shown to significantly alter the characteristics of the catalyst (Chapter 4), causing significant differences in activity during reforming at different reaction temperatures. As well as significantly affecting the activity towards steam methane reforming, the activity towards carbon-forming reactions and subsequent carbon deposition is

altered. Due to the stoichiometry of the above reactions and the promotion of carbon gasification in the presence of steam, it is difficult to state with certainty which carbon-forming reactions are occurring. This also affects catalytic reforming activity data and product ratios, making it difficult to differentiate between specific reactions occurring over the different catalyst and linking these to specific catalyst properties.

6.5 References

1. O.-S. Joo and K.-D. Jung, *CH 4 Dry Reforming on Alumina-Supported Nickel Catalyst.* Bulletin of the Korean Chemical Society 2002. **23**(8): p. 1149-1153.
2. P. Kim, Y. Kim, H. Kim, I.K. Song, and J. Yi, *Synthesis and characterization of mesoporous alumina with nickel incorporated for use in the partial oxidation of methane into synthesis gas.* Applied Catalysis A: General, 2004. **272**(1-2): p. 157-166.
3. Y. Matsumura and T. Nakamori, *Steam reforming of methane over nickel catalysts at low reaction temperature.* Applied Catalysis A: General, 2004. **258**(1): p. 107-114.
4. N. Sahli, C. Petit, A.C. Roger, A. Kiennemann, S. Libs, and M.M. Bettahar, *Ni catalysts from $NiAl_2O_4$ spinel for CO_2 reforming of methane.* Catalysis Today, 2006. **113**(3-4): p. 187-193.
5. H.-S. Roh, K.-W. Jun, and S.-E. Park, *Methane-reforming reactions over Ni/Ce-ZrO_2/θ-Al_2O_3 catalysts.* Applied Catalysis A: General, 2003. **251**(2): p. 275-283.
6. V.R. Choudhary, S. Banerjee, and A.M. Rajput, *Hydrogen from step-wise steam reforming of methane over Ni/ZrO_2: factors affecting catalytic methane decomposition and gasification by steam of carbon formed on the catalyst.* Applied Catalysis A: General, 2002. **234**: p. 259-270.
7. J.R. Rostrup-Nielsen, *New aspects of syngas production and use.* Catalysis Today, 2000. **63**(2-4): p. 159-164.

8. L. Piao, Y. Li, J. Chen, L. Chang, and J.Y.S. Lin, *Methane decomposition to carbon nanotubes and hydrogen on an alumina supported nickel aerogel catalyst.* Catalysis Today, 2002. **74**(1-2): p. 145-155.

7 Reactions of methane and steam over 20 wt % Ni/Al_2O_3: Influence of methane to steam ratio

Reforming studies performed under stoichiometric conditions (Chapter 6) have shown that the calcination temperature can significantly influence catalytic activity and selectivity of Ni/Al_2O_3 catalysts. However, with this reaction stoichiometry it is difficult to distinguish between the primary reactions and specific carbon-forming reactions occurring.

Chapter 6 has shown that high steam ratios benefit carbon gasification and result in high catalyst reforming activity. However, the requirement for high steam conditions has been shown to be problematic, in the specific laboratory conditions, with variations in the laboratory temperature result in changes in steam pressure, significantly influencing the reforming activity and product gas ratios obtained. Increasing the methane to steam ratio minimises this problem, and more importantly allows catalyst deactivation to be studied.

Reactions were carried out in this study under methane-rich conditions with a methane to steam ratio of 2:1 (theoretically Reaction 7.1 and 7.2). Due to the reaction stoichiometry, higher methane concentrations should reduce the formation of carbon dioxide by inhibiting the water-gas shift reaction (Reaction 7.3).

$$\mathbf{2CH_4 + H_2O \rightarrow CO + 3H_2 + CH_4} \qquad \mathbf{(7.1)}$$

$$\mathbf{CH_4 \rightarrow C + 2H_2} \qquad \mathbf{(7.2)}$$

$$\mathbf{CO + H_2O \leftrightarrow CO_2 + H_2} \qquad \mathbf{(7.3)}$$

Under ideal reforming conditions and assuming methane decomposition is not occurring, only 50 % of methane can be reformed in the presence of steam to produce carbon monoxide and hydrogen.

Thus, lower reforming activities are observed during reactions undertaken in steam-deficient reaction conditions.

Carrying out reactions under methane-rich conditions is likely to increase carbon deposition through methane decomposition (Reaction 7.2), during reactions due to the presence of methane in excess of the steam methane reforming requirements (Reaction 7.1). These studies will allow an insight into catalyst behaviour and the propensity and selectivity towards specific carbon-forming reactions at different reaction temperatures. This was not possible during studies undertaken in stoichiometric conditions due to extensive carbon gasification.

In order to study the effect of methane to steam, were carried out over 20 wt % Ni/Al_2O_3, calcined at 600 °C, 900 °C and 1000 °C, denoted hereon as Ni/Al_2O_3 (600), Ni/Al_2O_3 (900) and Ni/Al_2O_3 (1000).

7.1 Reverse temperature-programmed reactions of methane and steam under methane-rich conditions over 20 wt % Ni/Al_2O_3

7.1.1 The influence of calcination temperature on the reactivity of Ni/Al_2O_3 during reactions of methane and steam

The reverse temperature-programmed reaction of methane and steam under methane-rich conditions over Ni/Al_2O_3 (600) is shown in Figure 7.1.

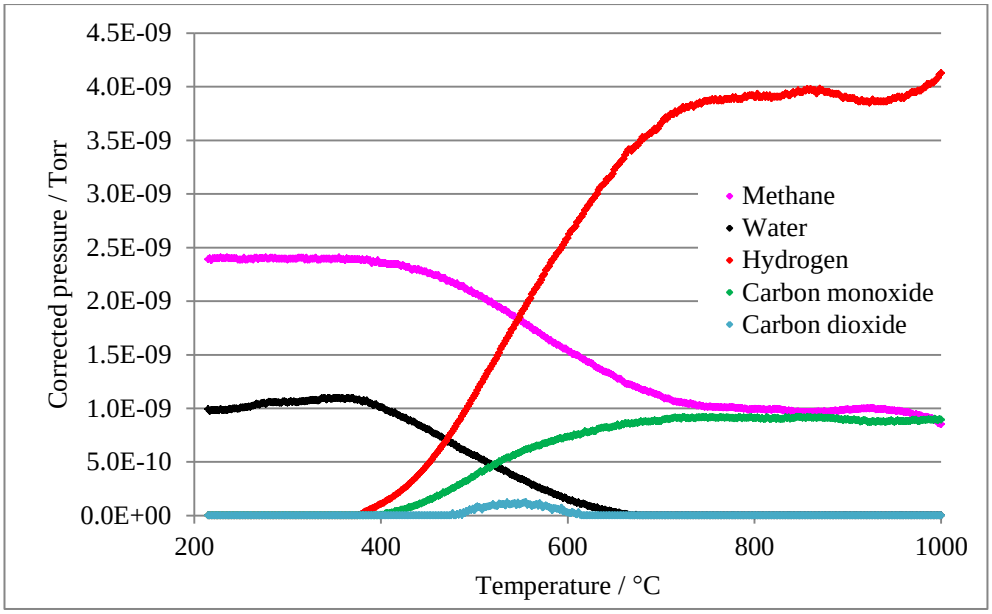

Figure 7.1: Reverse temperature-programmed reaction of methane and steam over Ni/Al_2O_3 (600) under methane-rich conditions (methane: steam = 2:1)

The reaction profiles over all the catalysts exhibit a similar reaction profile to that observed over Ni/Al_2O_3 (600) in Figure 7.1. As the reaction temperature increases, consumption of methane and steam increases and the onset of production of hydrogen and carbon monoxide are observed from *ca.* 380 °C. Hydrogen and carbon monoxide production rises with increasing reaction temperature and reaches steady production at temperatures above *ca.* 750 °C, mirrored by the methane and steam consumption. Above *ca.* 950 °C, hydrogen production and methane consumption increase. A small amount of carbon dioxide formation is also observed in the temperature range 480 °C to 620 °C with a peak in production at *ca.* 550 °C.

Reverse temperature-programmed reaction profiles can be used to determine catalytic reactivity. Product gas onset temperatures during reactions of methane and steam, over Ni/Al_2O_3 (600), Ni/Al_2O_3 (900) and Ni/Al_2O_3 (1000) are summarised in Table 7.1.

Table 7.1: Product gas onset temperature during reactions of methane and steam under methane-rich conditions (methane: steam = 2:1)

Catalyst	H_2 onset temperature / °C	CO onset temperature / °C	CO_2 onset temperature / °C
Ni/Al_2O_3 (600)	377	400	477
Ni/Al_2O_3 (900)	410	410	455
Ni/Al_2O_3 (1000)	360	373	385

The product gas onset reaction temperatures are comparable over all catalysts, although the onset temperatures for hydrogen and carbon monoxide production are higher over Ni/Al_2O_3 (900).

Over all catalysts, carbon dioxide formation occurs after both hydrogen and carbon monoxide production. This could be attributed to a small level of water-gas shift reaction occurring at a higher reaction temperature under these conditions. Alternatively, due to the reaction stoichiometry and low steam availability the Boudouard reaction (Reaction 7.4) could be occurring, producing carbon dioxide.

$$2CO \rightarrow CO_2 + C \qquad (7.4)$$

Ni/Al_2O_3 (900) is the least reactive towards steam reforming at low temperatures. However, carbon monoxide and hydrogen production occurs simultaneously over Ni/Al_2O_3 (900), which is not observed over the other catalysts.

7.1.2 The influence of calcination temperature on the activity and selectivity of Ni/Al_2O_3 during reactions of methane and steam

Under methane-rich conditions at optimum operating conditions, if the steam methane reforming reaction were at equilibrium, CH_4 conversion and H_2 yield would be expected to reach 50 % and a

H_2/CO product gas ratio of 3 would be gained. This assumes that no additional side reactions are occurring, such as the water-gas shift reaction. However, this also assumes that in the presence of a significant excess of methane, that methane decomposition (Reaction 7.2) does not occur, and the catalyst is not influenced by catalyst deactivation through sintering or carbon deposition.

The catalyst selectivity and maximum activity over all catalysts, extracted from the reverse temperature-programmed reaction profiles are shown in Table 7.2. The H_2 yield and CH_4 conversion profiles for each catalyst are shown in Figure 7.2 and Figure 7.3, respectively and the CO selectivity profiles are shown in Figure 7.4.

Table 7.2: Catalyst selectivity and maximum activity during reactions of methane and steam in a methane-rich environment (methane: steam = 2:1)

Catalyst	**Maximum CH_4 conversion / %**	**Maximum H_2 yield / %**	**Average final H_2/CO ratio**	**Minimum CO selectivity / %**
Ni/Al_2O_3 (600)	64	57	4.5	82
Ni/Al_2O_3 (900)	75	71	2.6	61
Ni/Al_2O_3 (1000)	66	47	1.9	27

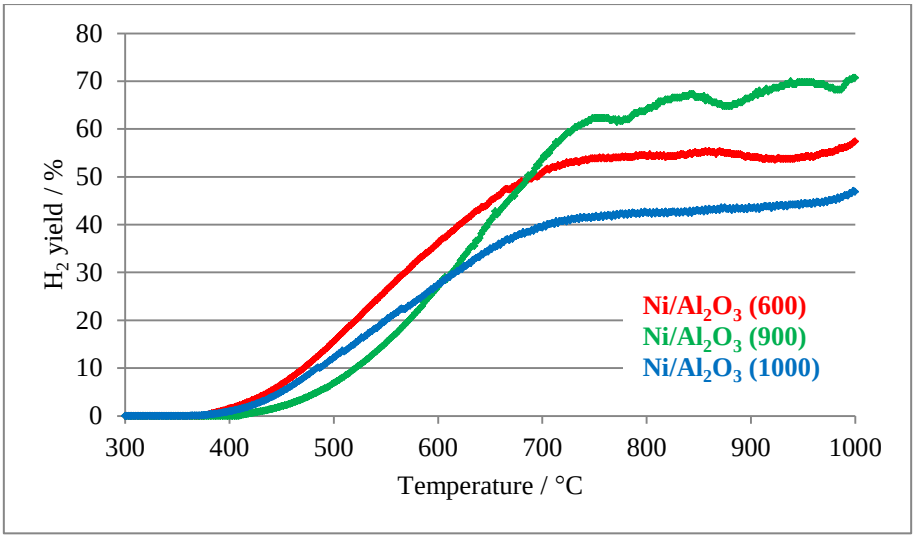

Figure 7.2: **H_2 yield during temperature-programmed reaction of methane and steam over Ni/Al_2O_3 (600), Ni/Al_2O_3 (900) and Ni/Al_2O_3 (1000) under methane-rich conditions (methane: steam = 2:1)**

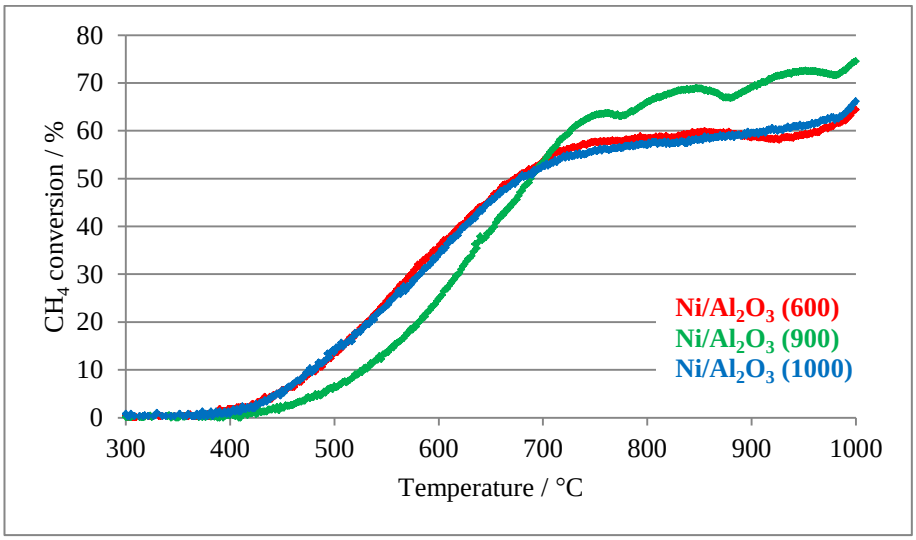

Figure 7.3: **CH_4 conversion during temperature-programmed reaction of methane and steam over Ni/Al_2O_3 (600), Ni/Al_2O_3 (900) and Ni/Al_2O_3 (1000) under methane-rich conditions (methane: steam = 2:1)**

Over Ni/Al_2O_3 (600) similar CH_4 conversion and H_2 yield data is observed, although the H_2 yield is slightly less than the CH_4 conversion. The high maximum CH_4 conversion and H_2 yield exhibited

over this catalyst at temperatures above *ca.* 900 °C can be attributed to methane decomposition occurring at these temperatures. This also accounts for the high final H_2/CO ratio observed.

Over Ni/Al_2O_3 (900), the high maximum CH_4 conversion and H_2 yield obtained can again be attributed to methane decomposition occurring at temperatures above *ca.* 900 °C. However, the low H_2/CO ratio obtained indicates additional reactions are occurring, in addition to steam reforming and methane decomposition, and could be a result of the reverse water-gas shift reaction occurring (Reaction 7.5).

$$\mathbf{H_2 + CO_2 \rightarrow CO + H_2O} \qquad \mathbf{(7.5)}$$

The fluctuation in both the CH_4 conversion and H_2 yield (Figure 7.2 and Figure 7.3) observed at temperatures above *ca.* 750 °C is due to the use of heated insulating tape over the reactor tube fittings. This was used to ensure that the steam remained vaporised throughout the reactor system. However, during this temperature-programmed reaction the heating caused changes in the steam pressure due to subsequent condensation and evaporation which resulted in fluctuations in the product and reactant gas ratios.

Over Ni/Al_2O_3 (1000) the H_2 yield is *ca.* 20 % less than the CH_4 conversion. The CH_4 conversion is *ca.* 66 %, indicating methane decomposition is occurring at elevated reaction temperatures. The significant reduction in H_2 yield could indicate that hydrogen produced is utilised in additional reactions or processes at temperatures above *ca.* 700 °C. It has been shown in Chapter 4, that following TPR reactions $NiAl_2O_4$ formed during catalyst preparation is not fully reduced during TPR reactions. During temperature-programmed reactions, in the presence of hydrogen produced during reforming reactions, $NiAl_2O_4$ may be reduced to metallic nickel [1]. Therefore, a lower H_2 yield and H_2/CO ratio will be observed. Due to the stoichiometry of the reactions, any water produced during reduction would be utilised in the steam reforming reaction, increasing methane conversion, and no change in the water signal would be observed.

The minimum CO selectivity and corresponding CO selectivity profiles are shown in Table 7.2 and Figure 7.4, respectively. Due to the reaction stoichiometry, the water-gas shift reaction may be limited during temperature-programmed reactions, due to the low levels of steam present.

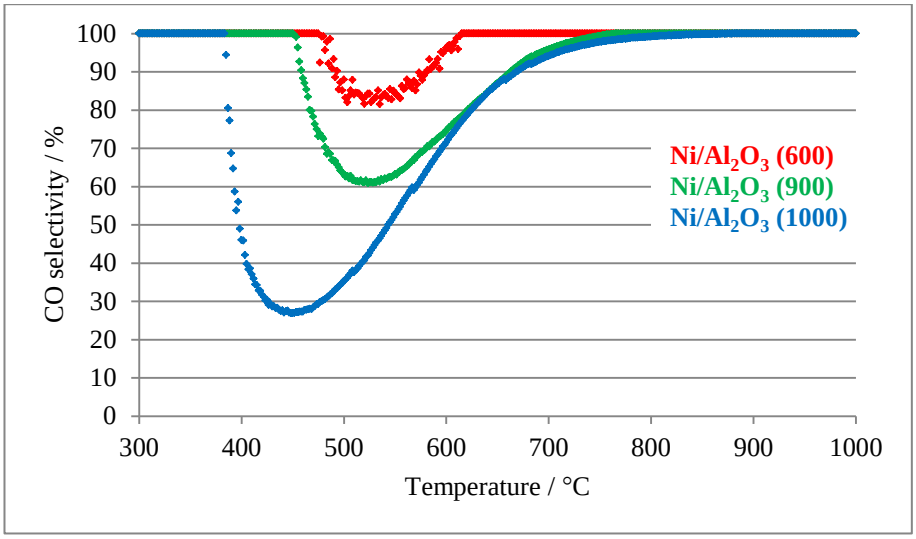

Figure 7.4: CO selectivity during reactions of methane and steam over Ni/Al_2O_3 (600), Ni/Al_2O_3 (900) and Ni/Al_2O_3 (1000) under methane-rich conditions (methane: steam = 2:1)

The CO selectivity profiles indicate that carbon dioxide is produced at significantly different reaction temperatures over all the different catalysts. Ni/Al_2O_3 (600) is least active towards carbon dioxide production, whereas Ni/Al_2O_3 (1000) is highly active. Ni/Al_2O_3 (600) is least active towards the water-gas shift reaction, due to the high activity towards steam methane reforming, reducing the amount of steam available for the water-gas shift reaction. Over Ni/Al_2O_3 (1000), additional water produced by the reduction of $NiAl_2O_4$ to metallic nickel in the temperature range 380 °C to 600 °C, may be promoting the water-gas shift reaction increasing the formation of carbon dioxide, lowering CO selectivity.

7.1.3 The influence of methane to steam ratio on the reactivity and activity during reactions of methane and steam

The H_2 yield and CH_4 conversion profiles for temperature-programmed reactions under stoichiometric and methane-rich conditions are shown in Figure 7.5 and Figure 7.6. The CO selectivity and H_2/CO ratio data are summarised in Table 7.3.

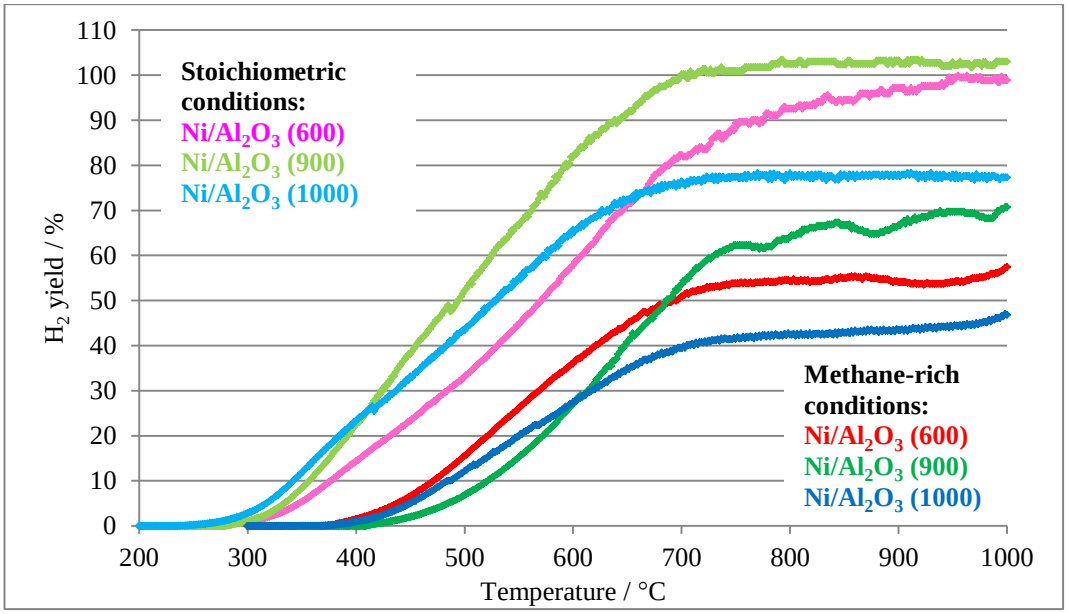

Figure 7.5: **H_2 yield during reactions of methane and steam over Ni/Al_2O_3 (600), Ni/Al_2O_3 (900) and Ni/Al_2O_3 (1000), under methane-rich (methane: steam = 2:1) and stoichiometric (methane: steam = 1:1) conditions**

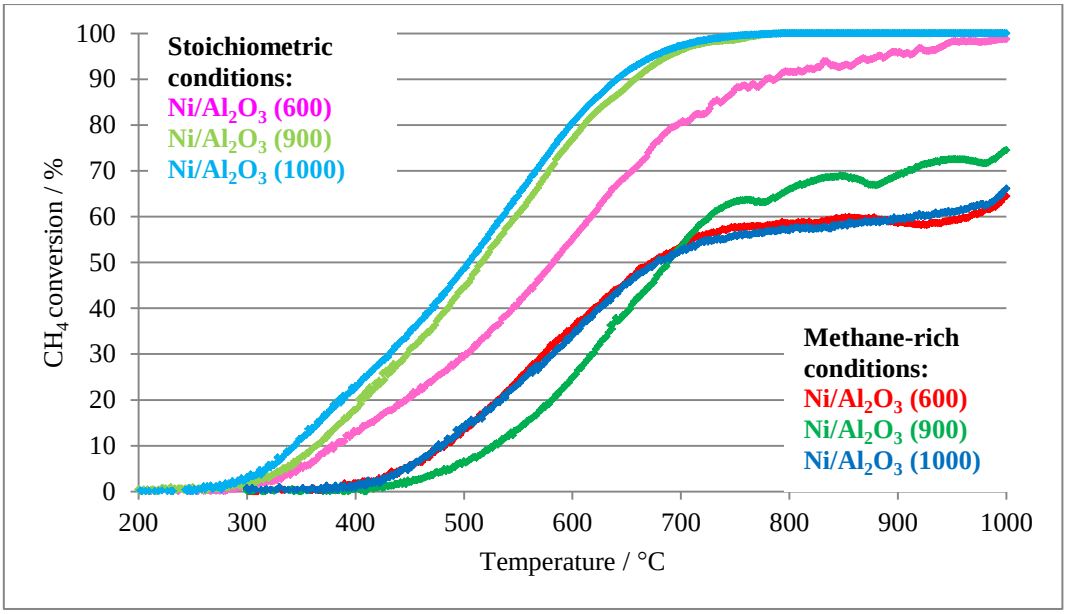

Figure 7.6: **CH_4 conversion during reactions of methane and steam over Ni/Al_2O_3 (600), Ni/Al_2O_3 (900) and Ni/Al_2O_3 (1000), under methane-rich (methane: steam = 2:1) and stoichiometric (methane: steam = 1:1) conditions**

Table 7.3: **CO selectivity and H_2/CO ratio during reactions of methane and steam over Ni/Al_2O_3 (600), Ni/Al_2O_3 (900) and Ni/Al_2O_3 (1000) under methane-rich (methane: steam = 2:1) and stoichiometric (methane: steam = 1:1) conditions**

	Catalyst	Minimum CO selectivity / %	Minimum CO selectivity temperature / °C	Average final H_2/CO ratio
Stoichiometric	**Ni/Al_2O_3 (600)**	15	387	3.5
	Ni/Al_2O_3 (900)	38	355	2.5
	Ni/Al_2O_3 (1000)	27	335	2.1
Methane-rich	**Ni/Al_2O_3 (600)**	82	535	4.5
	Ni/Al_2O_3 (900)	61	523	2.6
	Ni/Al_2O_3 (1000)	27	448	1.9

Under methane-rich conditions, catalyst reactivity is significantly reduced resulting in the product onset temperatures increasing by *ca.* 100 °C for all catalysts studied. In addition, the product yield and conversions at elevated reaction temperatures are also significantly reduced under steam-deficient conditions [2]. The H_2 yield is significantly reduced under methane-rich conditions (Figure 7.5) [3, 4], due to the increased methane concentration and insufficient levels of oxidant to satisfy the steam methane reforming requirements. Although the H_2 yield is reduced over all the catalysts studied the trend behaviour within the set of catalysts remain similar, despite the change in steam concentration.

Under both reaction conditions, Ni/Al_2O_3 (1000) exhibits a low H_2 yield compared to CH_4 conversion at temperatures above *ca.* 700 °C. This is due to the presence of unreduced $NiAl_2O_4$ formed during catalyst preparation. This phase is reduced during the reforming reaction under both stoichiometric and methane-rich conditions, leading to a reduction in the H_2 yield and H_2/CO ratio.

Ni/Al_2O_3 (900) is highly active during reforming reactions under both stoichiometric and methane-rich conditions, exhibiting high reactant conversion and product yields. With the exception of Ni/Al_2O_3 (600), the final H_2/CO ratios (Table 7.3) are not significantly altered following an increase in the methane to steam ratio. Over Ni/Al_2O_3 (600), the final H_2/CO ratio is increased in the methane-rich environment, due to higher methane decomposition activity. Although the H_2 yield is reduced, the final H_2/CO ratios are not significantly altered following a reduction in oxidant level.

As expected CO selectivity data (Table 7.3) shows that under methane-rich conditions the water-gas shift reaction is less favoured and the temperature at which minimum CO selectivity is observed is significantly increased by *ca.* 100 °C under such conditions. This may be due to a reduction in reactivity and activity, consistent with the decrease in steam reforming reactivity observed under methane-rich conditions. Alternatively, the carbon dioxide produced during reactions may be a product of the Boudouard reaction thus a change in the temperature of carbon

dioxide formation may be observed. Both Ni/Al_2O_3 (600) and Ni/Al_2O_3 (900) exhibit a reduction in carbon dioxide production under methane-rich conditions, compared to stoichiometric conditions. However, over Ni/Al_2O_3 (1000) although the temperature where minimum CO selectivity occurs increases, minimum CO selectivity values are comparable under both reaction conditions. This may be attributed to the promotion of the water-gas shift reaction due to an increase in water produced during the reduction of $NiAl_2O_4$ under both reaction conditions. This is discussed in more detail in Section 7.2.3.

As discussed in Chapter 6, carbon deposition results determined following temperature-programmed reactions are not shown, due to the nature of the carbon formation over the temperature range investigated. Carbon deposition results are presented in Section 7.3, following studies at different reaction temperatures.

7.2 Effect of temperature on the reactions of methane and steam under methane-rich conditions over 20 wt % Ni/Al_2O_3

Reactions were carried out under methane-rich conditions for 20 hours at 500 °C, 600 °C, 700 °C, 800 °C and 900 °C. The reaction data are presented in a similar manner to Chapter 6, displaying minimum, maximum and average activity data, allowing any changes in the activity to be shown. However, due to notable catalyst deactivation over time and thus variations in catalyst activity and selectivity, specific activity profiles are also presented.

7.2.1 Reactions of methane and steam under methane-rich conditions over Ni/Al_2O_3 (600)

The average CH_4 conversion and H_2 yield are shown in Figure 7.7 and the average CO selectivity and H_2/CO ratio are shown in Table 7.4 for reactions of methane and steam over Ni/Al_2O_3 (600) under methane-rich conditions across the temperature range 500 °C to 900 °C. The H_2 yield profiles at each reaction temperature are shown in Figure 7.8.

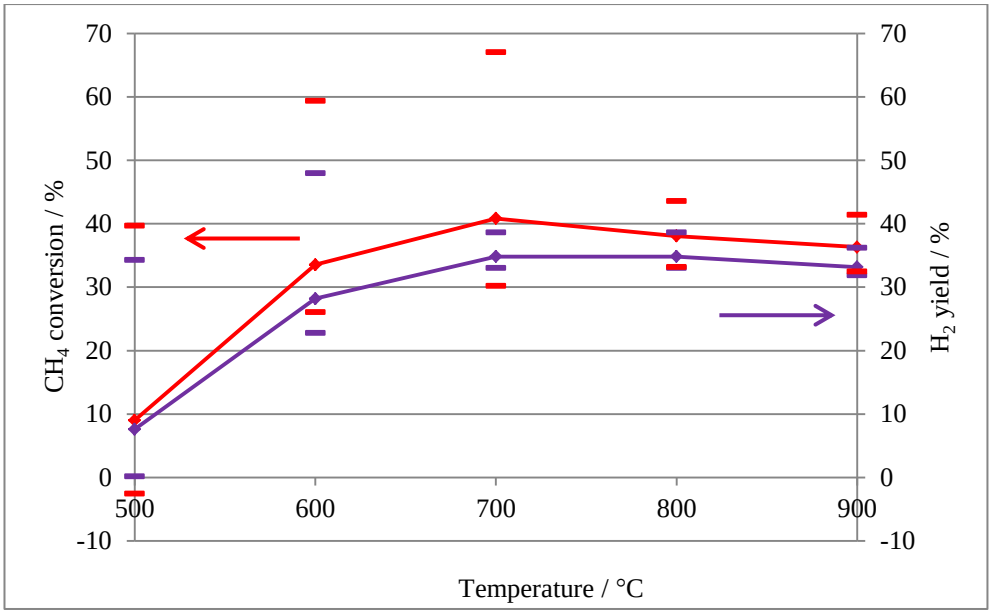

Figure 7.7: **Average CH_4 conversion and H_2 yield during reactions of methane and steam over Ni/Al_2O_3 (600) for 20 hours under methane-rich conditions (methane: steam = 2:1) at reaction temperatures 500 °C to 900 °C**

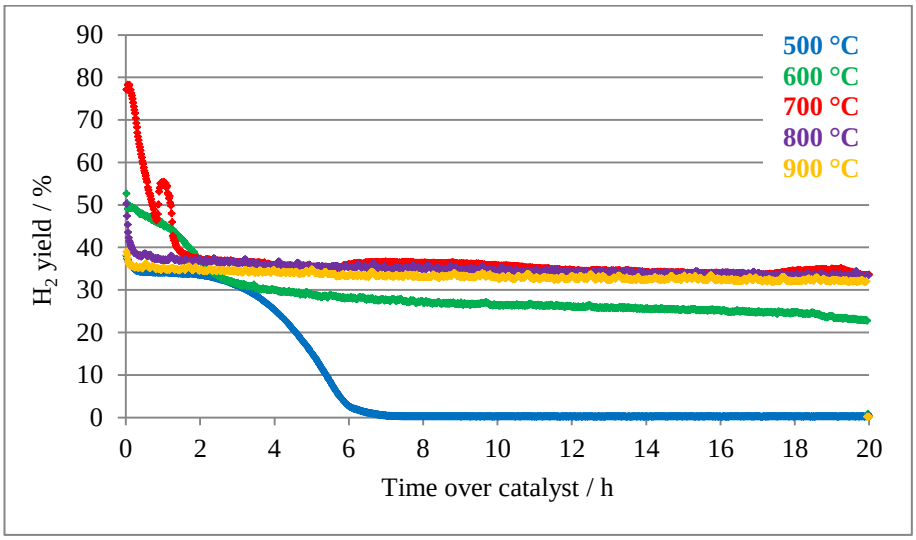

Figure 7.8: **H_2 yield profiles for reactions of methane and steam over Ni/Al_2O_3 (600) for 20 hours under methane-rich conditions (methane: steam = 2:1) at reaction temperatures 500 °C to 900 °C**

Table 7.4: Average CO selectivity and H_2/CO ratio during reactions of methane and steam over Ni/Al_2O_3 (600) for 20 hours under methane-rich conditions (methane: steam = 2:1) at reaction temperatures 500 °C to 900 °C

Reaction temperature / °C	Average CO selectivity / %	Average H_2/CO ratio
500	90 [a]	3.8 [a]
600	96	3.6
700	98	3.3
800	100	2.9
900	100	2.9

[a] Average taken between 1 and 2 hours, before complete catalyst deactivation

Significant deactivation of the Ni/Al_2O_3 (600) catalyst is observed during reactions at temperatures below 700 °C. Catalyst deactivation results in complete loss of reforming activity after *ca.* 7 hours during the reaction at 500 °C and H_2 yield is reduced by over 25 % throughout the course of the reaction at 600 °C. The higher than expected H_2/CO ratio and carbon dioxide production indicates that the Boudouard reaction may be occurring, resulting in significant carbon deposition (Section 7.3) and catalyst deactivation. Additionally, CO reduction may also be occurring (Reaction 7.6), resulting in carbon deposition via Reaction 7.6.

$$\mathbf{CO + H_2 \leftrightarrow H_2O + C} \qquad \mathbf{(7.6)}$$

During the reaction at 700 °C, significant reduction in initial reforming activity is observed and CH_4 conversion indicates that methane decomposition may be occurring during the first *ca.* 2 hours. Following deactivation, the H_2/CO ratio is slightly higher than expected and low levels of

carbon dioxide are produced, indicating that the Boudouard reaction may be occurring. The reduction in reforming activity observed is attributed to carbon deposition (Section 7.3).

At 800 °C and 900 °C, steam methane reforming is the predominant reaction occurring, although carbon deposition is observed following both reactions (Section 7.3). The reaction profiles shown in Figure 7.8 indicate that methane decomposition may be occurring during the initial few hours of the reaction, resulting in carbon deposition and slight catalyst deactivation. Alternatively, carbon may be formed via CO reduction at elevated temperatures, accounting for the H_2/CO ratio obtained. The possible shift in the primary source of carbon deposition over the temperatures studied could affect the type of carbon formed during the reactions, exhibiting different influences on reforming activity.

In summary, a significant loss in reforming activity is observed following reactions over Ni/Al_2O_3 (600) from 500 °C to 700 °C under methane-rich conditions, due to carbon deposition. Carbon formation primarily occurs via the Boudouard reaction at lower reaction temperatures and methane decomposition or CO reduction at higher reaction temperatures. Methane decomposition appears not to be highly favoured below 900 °C, occurring only during the initial stages of the reforming reaction. During characterisation studies of calcined samples shown in Chapter 4, Ni^{2+} is shown to have weak interactions with the alumina support following calcination at 600 °C. Sahli *et al*. [5] have demonstrated that catalysts shown to have 'free' nickel with minimal interactions with the support give rapid deactivation through carbon formation, similar to the results observed for Ni/Al_2O_3 (600).

7.2.2 Reactions of methane and steam under methane-rich conditions over Ni/Al_2O_3 (900)

The average CH_4 conversion and H_2 yield are shown in Figure 7.9 and the average CO selectivity and H_2/CO ratio are shown in Table 7.5 for reactions of methane and steam over Ni/Al_2O_3 (900) under methane-rich conditions across the temperature range 500 °C to 900 °C. The H_2 yield profiles at each reaction temperature are shown in Figure 7.10.

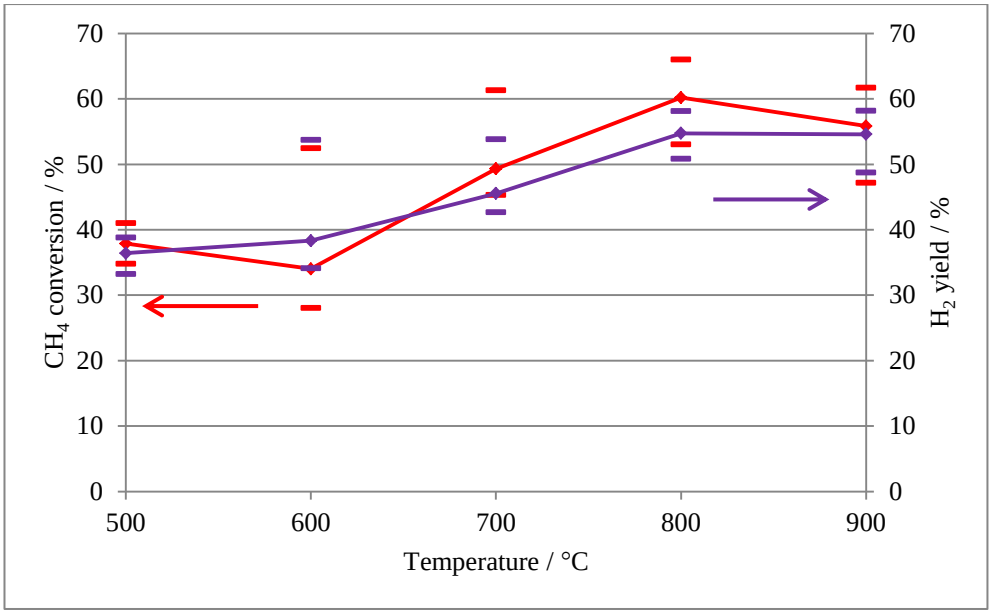

Figure 7.9: **Average CH_4 conversion and H_2 yield during reactions of methane and steam over Ni/Al_2O_3 (900) for 20 hours under methane-rich conditions (methane: steam = 2:1) at reaction temperatures 500 °C to 900 °C**

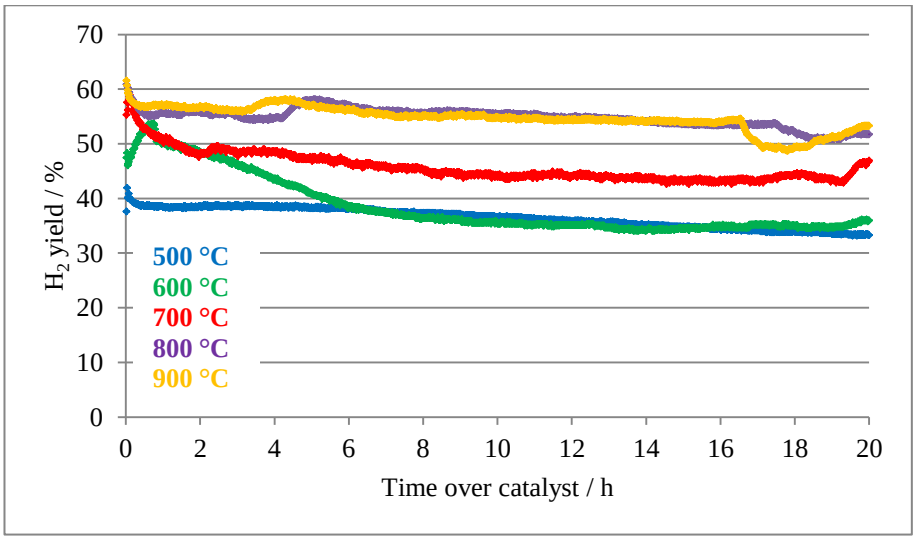

Figure 7.10: **H_2 yield profiles for reactions at over Ni/Al_2O_3 (900) for 20 hours under methane-rich conditions (methane: steam = 2:1) at reaction temperatures 500 °C to 900 °C**

Table 7.5: Average CO selectivity and H_2/CO ratio during reactions of methane and steam over Ni/Al_2O_3 (900) for 20 hours under methane-rich conditions (methane: steam = 2:1) at reaction temperatures 500 °C to 900 °C

Reaction temperature / °C	Average CO selectivity / %	Average H_2/CO ratio
500	83	3.4
600	88	3.0
700	99	2.3
800	100	4.5
900	99	4.0

The reaction at 500 °C exhibits a slightly higher than expected H_2/CO ratio and low CO selectivity, whilst CH_4 conversion and H_2 yield are relatively high and stable over the 20 hour period. This trend may be attributed to the Boudouard reaction occurring, which also results in high levels of carbon deposition (Section 7.3). Although carbon deposition is high, reforming activity is only reduced by *ca.* 10 %, in marked contrast to the complete deactivation observed for Ni/Al_2O_3 (600) under these conditions. As the reaction temperature is increased to 600 °C catalyst deactivation is observed and H_2 yield is reduced by *ca.* 15 % over the course of the reaction. This can be attributed to carbon formation (Section 7.3) via CO reduction, also accounting for the lower CO selectivity.

Although high reforming activity is observed, a low H_2/CO ratio is obtained during the reaction at 700 °C, which may be attributed to the reverse water-gas shift reaction. Additionally, significant carbon deposition is attained following the reaction at 700 °C. It is likely that carbon is formed via methane decomposition during the initial stages of the reaction, accounting for the high CH_4 conversion observed during the initial 2 hours. At reaction temperatures above 800 °C, CH_4

conversion exceeds 50 % and the H_2/CO ratio increases to 4 and above. This clearly indicates that Ni/Al_2O_3 (900) is active towards methane decomposition at elevated reaction temperatures. Despite the high activity towards methane decomposition at such temperatures, both carbon deposition (Section 7.3) and catalyst deactivation is reduced, compared to reactions undertaken at lower temperatures. The fluctuations in the product gases in the H_2 yield profiles at 800 °C and 900 °C at *ca.* 4 and 17 hours, may be attributed to a change in steam pressure (as observed and discussed in Chapter 6).

7.2.3 Reactions of methane and steam under methane-rich conditions over Ni/Al_2O_3 (1000)

The average CH_4 conversion and H_2 yield are shown in Figure 7.11 and the average CO selectivity and H_2/CO ratio are shown in Table 7.6 for reactions of methane and steam over Ni/Al_2O_3 (1000) under methane-rich conditions across the temperature range 500 °C to 900 °C. The H_2 yield profiles at each temperature are shown in Figure 7.12.

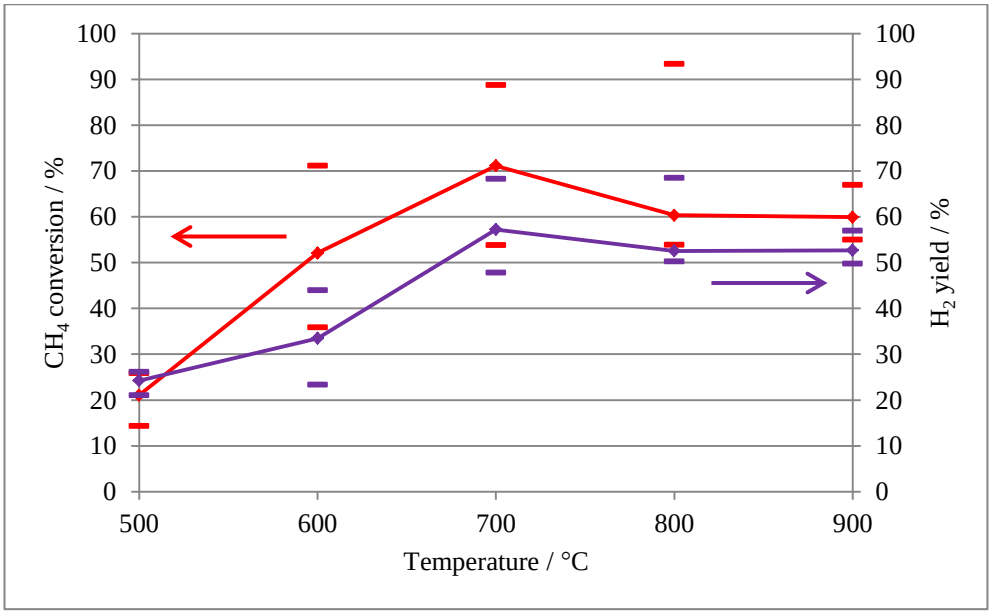

Figure 7.11: Average CH_4 conversion and H_2 yield during reactions of methane and steam over Ni/Al_2O_3 (1000) for 20 hours under methane-rich conditions (methane: steam = 2:1) at reaction temperatures 500 °C to 900 °C

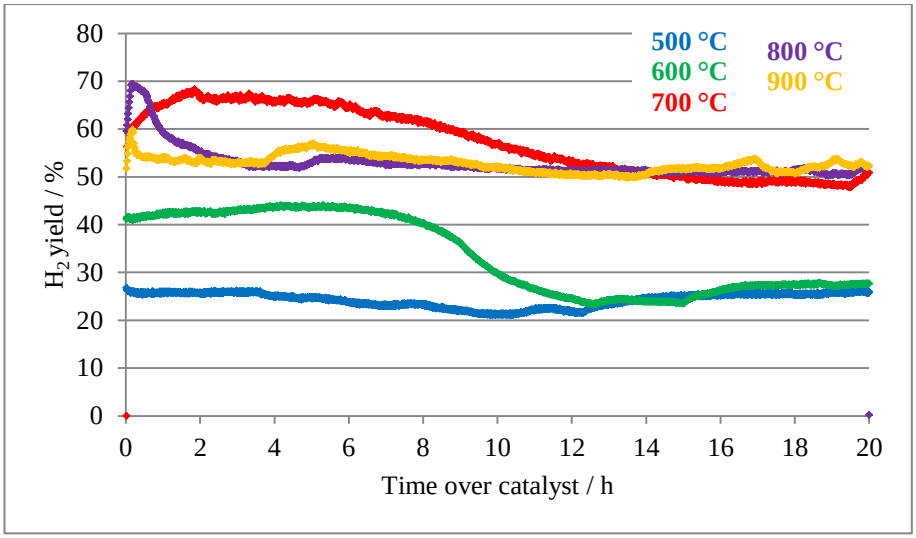

Figure 7.12: **H_2 yield profiles for reactions over Ni/Al_2O_3 (1000) for 20 hours under methane-rich conditions (methane: steam = 2:1) at reaction temperatures 500 °C to 900 °C**

Table 7.6: **Average CO selectivity and H_2/CO ratio during reactions of methane and steam over Ni/Al_2O_3 (1000) for 20 hours under methane-rich conditions (methane: steam = 2:1) at reaction temperatures 500 °C to 900 °C**

Reaction temperature / °C	Average CO selectivity / %	Average H_2/CO ratio
500	57	3.3
600	95	2.5
700	100	4.1
800	100	5.1
900	100	4.9

The reaction at 500 °C exhibits low reforming activity, observed in both the CH_4 conversion and the H_2 yield data, whilst a high H_2/CO ratio is observed. The carbon dioxide formation and CO selectivity data indicates that the water-gas shift reaction is occurring, accounting for the high H_2/CO ratio. It has been shown in Chapter 4 that $NiAl_2O_4$ formed during calcination is not fully reduced during TPR studies. $NiAl_2O_4$ has been shown to have little or no activity towards methane reforming [1, 6, 7]. Thus, the low reforming activity observed during the reaction at 500 °C is attributed to the presence of $NiAl_2O_4$. Due to the low methane reforming activity on this catalyst at this reaction temperature, steam is present in sufficient quantity to catalyse the water-gas shift reaction. Carbon deposition is also low and most likely occurs by the Boudouard reaction. Ni/Al_2O_3 (1000) may be relatively tolerant towards carbon-forming reactions during reactions at 500 °C due to the presence of $NiAl_2O_4$ [8].

At 600 °C, the catalyst activity is increased. However, a difference in the CH_4 conversion and H_2 yield is observed. The H_2 yield is *ca*. 25 % lower than the CH_4 conversion at certain stages of the reaction, as shown in Figure 7.13. This is also reflected in the low H_2/CO ratio also obtained and was also observed during reactions under stoichiometric conditions over this catalyst.

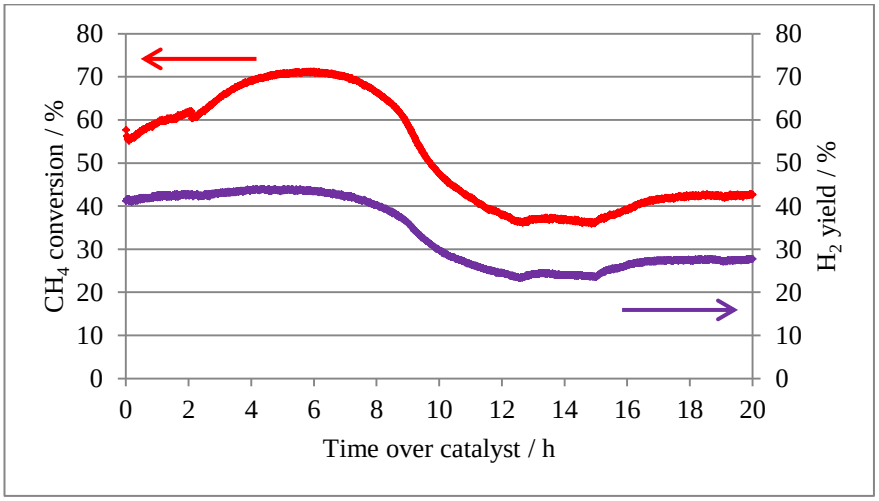

Figure 7.13: CH_4 conversion and H_2 yield for the reaction of methane and steam over Ni/Al_2O_3 (1000) under methane-rich conditions at 600 °C

The low H_2 yield exhibited during the reaction can be attributed to the presence of unreduced $NiAl_2O_4$ formed during calcination (Chapter 4). Thus, in the presence of hydrogen produced by steam reforming and methane decomposition, the $NiAl_2O_4$ phase is reduced, consuming hydrogen [1, 9]. The CH_4 conversion increases to over 70 % during the course of the reaction from *ca.* 4 to 8 hours (Figure 7.13), which indicates methane decomposition is occurring. This trend is not mirrored by a significant increase in H_2 yield, due to the consumption of additional hydrogen in the reduction of $NiAl_2O_4$ [9]. After *ca.* 8 hours the catalytic activity is significantly reduced, due to deactivation as a result of carbon deposition (Section 7.3).

Above 700 ºC, the predominant reactions occurring are steam reforming and methane decomposition. This is confirmed by the high H_2/CO ratio gained and the CH_4 conversion exceeding 50 %. Catalyst deactivation is observed during the reaction at 700 ºC and CH_4 conversion is reduced by over 20 %. Similarly, at 800 ºC, catalyst deactivation occurs during the initial *ca.* 4 hours, where CH_4 conversion is reduced by *ca.* 20 %. However, interestingly significant reduction in catalyst activity is not observed during the reaction at 900 ºC. The presence of $NiAl_2O_4$ does not alter the catalytic behaviour during higher temperature reactions due to rapid reduction of this phase during the initial phase of the reaction. Chen *et al.* [10] have demonstrated that the activity and stability of nickel particles towards methane decomposition is dependent on the interaction between nickel and the support and that the higher the Ni 2p binding energy observed during XPS studies, the higher the nickel activity towards methane decomposition. XPS analysis of NiO/Al_2O_3 (1000) has shown (Chapter 4) higher Ni 2p binding energies compared to other catalysts, due to an increased interaction between nickel and the support. This corresponds to an increase in methane decomposition and carbon formation over Ni/Al_2O_3 (1000).

7.2.4 The influence of calcination temperature on the activity and selectivity of Ni/Al_2O_3 during reactions of methane and steam under methane-rich conditions at different reaction temperatures

The average CH_4 conversion and H_2 yield comparison profiles for Ni/Al_2O_3 (600), Ni/Al_2O_3 (900) and Ni/Al_2O_3 (1000) are shown in Figure 7.14 and Figure 7.15.

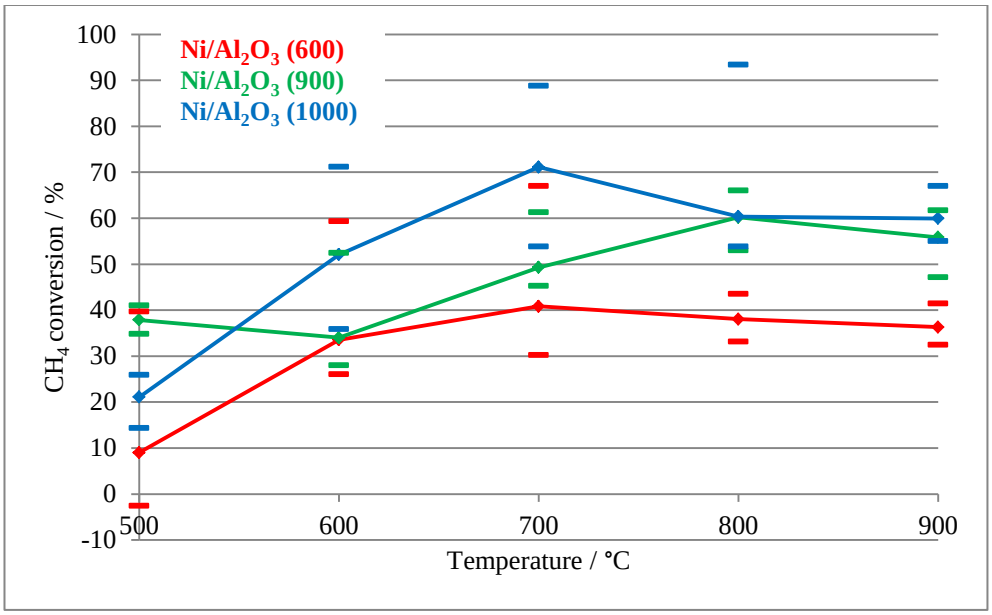

Figure 7.14: Average CH_4 conversion during reactions of methane and steam over Ni/Al_2O_3 (600), Ni/Al_2O_3 (900) and Ni/Al_2O_3 (1000) for 20 hours under methane-rich conditions (methane: steam = 2:1) at reaction temperatures 500 °C to 900 °C

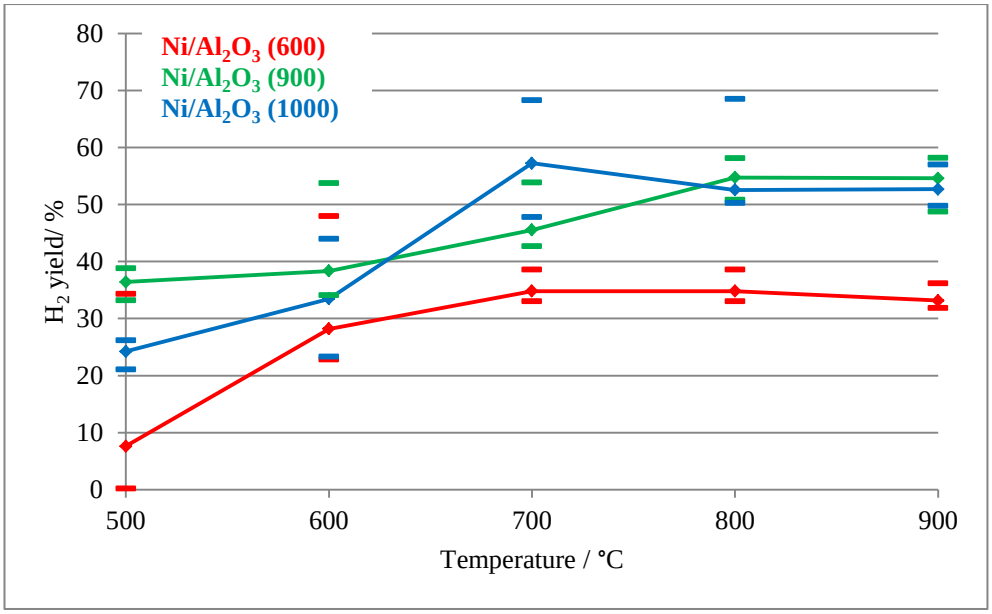

Figure 7.15: Average H_2 yield during reactions of methane and steam over Ni/Al_2O_3 (600), Ni/Al_2O_3 (900) and Ni/Al_2O_3 (1000) for 20 hours under methane-rich conditions (methane: steam = 2:1) at reaction temperatures 500 °C to 900 °C

Over Ni/Al_2O_3 (600), CH_4 conversion and H_2 yield are low over all reaction temperatures investigated (Figure 7.14 and Figure 7.15), compared to Ni/Al_2O_3 (900) and Ni/Al_2O_3 (1000). This is attributed to the suppression of CH_4 decomposition. However, considerable catalyst deactivation is observed over Ni/Al_2O_3 (600) at 500 °C, resulting in complete loss of catalytic activity. As the reaction temperature is increased, catalyst deactivation becomes less severe. Ni/Al_2O_3 (600) exhibits the most substantial catalyst deactivation and loss of catalytic activity from carbon deposition, formed by both the Boudouard reaction and CO reduction. Despite the high levels of carbon deposition, minimal methane decomposition is observed over Ni/Al_2O_3 (600) at any reaction temperature, except at 600 °C and 700 °C (for the initial few hours).

Ni/Al_2O_3 (900) exhibits the highest activity at 500 °C, although a similar activity is exhibited by Ni/Al_2O_3 (600) prior to catalyst deactivation (Figure 7.16). Due to the presence of unreduced $NiAl_2O_4$, which is relatively inactive towards reforming [6, 7], Ni/Al_2O_3 (1000) exhibits low reforming activity at 500 °C, which subsequently results in the water-gas shift reaction being favoured. As the reaction temperature is increased to 600 °C (Figure 7.16), both Ni/Al_2O_3 (600)

and Ni/Al_2O_3 (900) exhibit similar reaction profiles (Figure 7.16), deactivating to similar extents. While Ni/Al_2O_3 (1000) shows a high activity towards methane decomposition over the first half of the reaction, followed by significant catalyst deactivation due to carbon deposition.

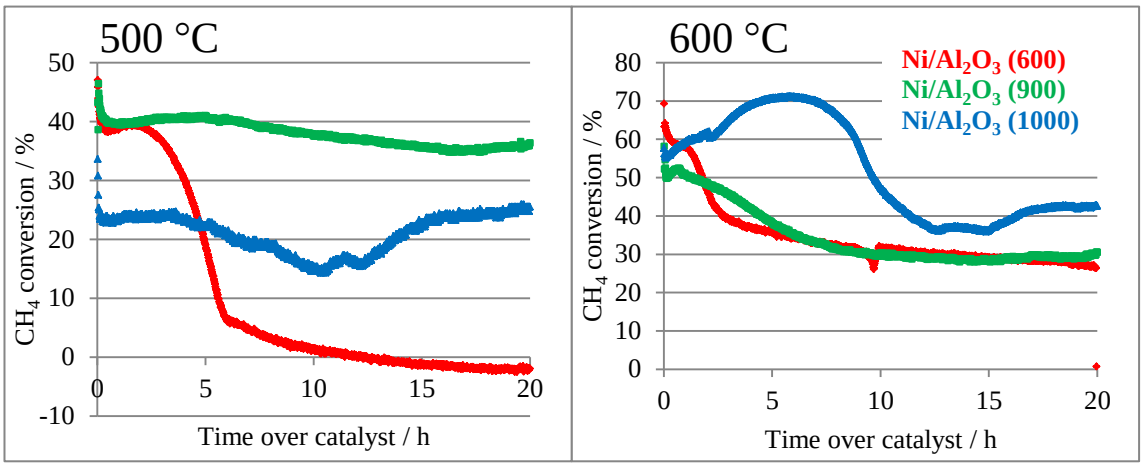

Figure 7.16: CH_4 conversion profiles for reaction of methane and steam over Ni/Al_2O_3 (600), Ni/Al_2O_3 (900) and Ni/Al_2O_3 (1000) under methane-rich conditions at 500 °C and 600 °C

The presence of a partially unreduced $NiAl_2O_4$ phase in Ni/Al_2O_3 (1000) results in a significant reduction in the H_2 yield compared to the CH_4 conversation at 600 °C. The $NiAl_2O_4$ phase is reduced in the steam reforming environment, consuming hydrogen, resulting in a reduction in the H_2 yield. Additional hydrogen produced by methane decomposition occurring between 4 to 8 hours (Figure 7.16), is utilised in the reduction process and a similar increase is not observed in the H_2 yield profile. This trend was also observed during reverse temperature-programmed studies undertaken over this catalyst (Section 7.1.2). This *in situ* reduction process is not observed over the other Ni/Al_2O_3 catalysts. As the reaction temperature is increased, $NiAl_2O_4$ is reduced during the initial stages of the reaction in the presence of hydrogen, becoming more active towards reforming [8] and less variation in reforming characteristics are observed as a result of this process. As a result, at elevated reaction temperatures the reforming activity of Ni/Al_2O_3 (1000) is comparable to other catalysts.

Above 700 °C, both Ni/Al_2O_3 (900) and Ni/Al_2O_3 (1000) exhibit similar H_2 yield and CH_4 conversion profiles. The main difference is observed at 800 °C, as shown in Figure 7.17, where a much higher H_2 yield and CH_4 conversion is observed over Ni/Al_2O_3 (1000) during the initial phase of the reaction. This is attributed to higher activity towards methane decomposition, such that almost all the methane is utilised during the first 2 hours by a combination of steam reforming and methane decomposition. However, following this transient behaviour, both Ni/Al_2O_3 (900) and Ni/Al_2O_3 (1000) subsequently follow similar activity trends and show comparable conversions and deactivation profiles.

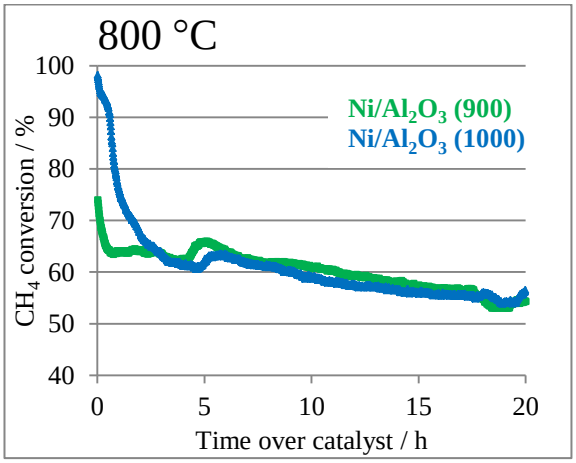

Figure 7.17: CH_4 conversion for reaction of methane and steam over Ni/Al_2O_3 (900) and Ni/Al_2O_3 (1000) under methane-rich conditions at 800 °C

Both Ni/Al_2O_3 (900) and Ni/Al_2O_3 (1000) are highly active towards methane decomposition at temperatures above 700 °C, resulting in high levels of carbon deposition (Section 7.3) and decreased catalytic activity over time. Calcination at 1000 °C results in a higher activity towards methane decomposition at lower reaction temperatures. Whereas calcination at 600 °C and 900 °C exhibit high activity towards CO reduction and the Boudouard reaction at reaction temperatures below 800 °C. As the reaction temperature is increased catalyst activity becomes more stable and less deactivation is observed during the reaction, especially at 900 °C. This is mirrored by the reduction in carbon deposition over all catalysts following reaction at 900 °C (Section 7.3). Clearly,

the calcination temperature selected considerably affects the carbon formation reactions and the reforming activity of each catalyst.

7.2.5 The influence of methane to steam ratio on the activity and selectivity of Ni/Al_2O_3 during reactions of methane and steam at different reaction temperatures

The average CH_4 conversion and H_2 yield data under methane-rich and stoichiometric conditions over Ni/Al_2O_3 (600) are shown in Figure 7.18, and the average CO selectivity and H_2/CO ratios are shown in Table 7.7.

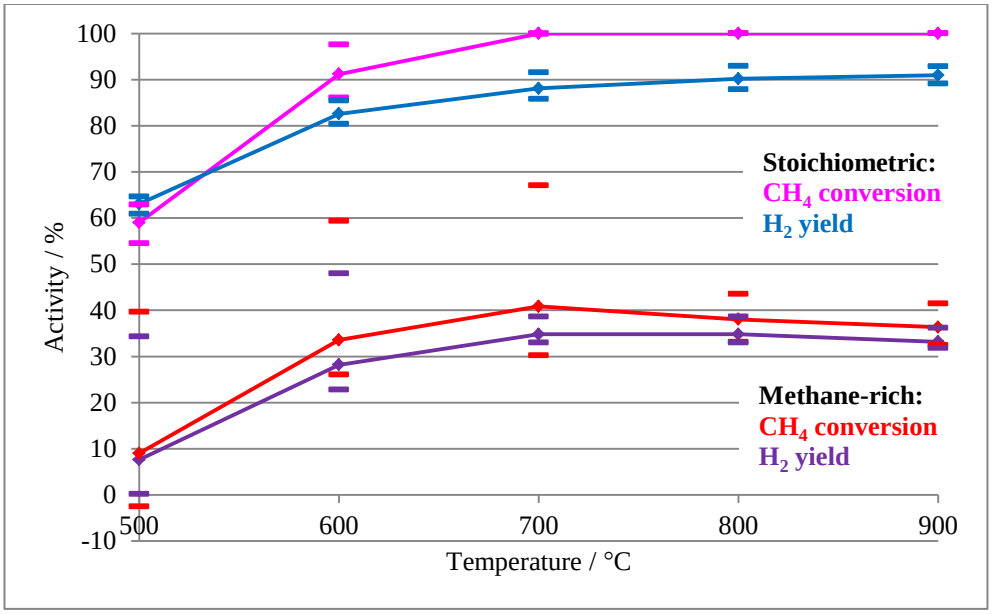

Figure 7.18: Average CH_4 conversion and H_2 yield during reactions over Ni/Al_2O_3 (600) for 20 hours under methane-rich (methane: steam = 2:1) and stoichiometric (methane: steam = 1:1) conditions at reaction temperatures 500 °C to 900 °C

Table 7.7: Average CO selectivity and H_2/CO ratio during reactions over Ni/Al_2O_3 (600) for 20 hours under methane-rich (methane: steam = 2:1) and stoichiometric (methane: steam = 1:1) conditions at reaction temperatures 500 °C to 900 °C

Reaction temperature / °C	Average CO selectivity / %		Average H_2/CO ratio	
	Stoichiometric	Methane-rich	Stoichiometric	Methane-rich
500	63	90 [a]	3.0	3.8 [a]
600	100	96	3.0	3.6
700	94	98	3.0	3.3
800	98	100	3.2	2.9
900	100	100	3.5	2.9

[a] Average taken between 1 and 2 hours, before complete catalyst deactivation

The average activity is reduced by *ca.* 50 % under methane-rich conditions, which might be expected due to the methane-rich nature of reforming reactions and limited oxidant concentrations present [3, 4]. Although reforming activity is lower under methane-rich conditions, the results indicate that minimal methane decomposition is occurring over Ni/Al_2O_3 (600), especially at thermodynamically favoured temperatures above 700 °C, and only occurs for a short period of time during reactions at 600 °C and 700 °C. The CO selectivity results indicate that the Boudouard reaction is favoured at reaction temperatures below 700 °C, under both reaction conditions. However, the Boudouard reaction occurs to a greater extent under methane-rich conditions, resulting in greater carbon deposition and considerable loss in catalyst activity. This is attributed to a reduction in carbon gasification in the presence of 'excess' steam, observed during the reaction under stoichiometric conditions at these temperatures. As well as an increase in carbon gasification

under stoichiometric conditions, the presence of excess adsorbed steam on the surface results in a greater water-gas shift reaction activity. Under methane-rich conditions, minimal water-gas shift activity is observed and the main route to carbon dioxide production is via the Boudouard reaction.

A shift from the Boudouard reaction to CO reduction is observed from reaction temperatures of 500 °C – 700 °C to 800 °C – 900 °C, resulting in significant carbon deposition and loss in reforming activity, especially during low temperature reforming reactions. This is in marked contrast to the lack of carbon deposition observed under stoichiometric conditions and clearly demonstrates the efficiency of steam in carbon gasification.

Highly efficient reforming and carbon gasification accounts for the high H_2/CO ratio obtained under stoichiometric conditions at reaction temperatures above 800 °C. In contrast, the lower product ratio obtained during methane-rich studies can be attributed to steam reforming and CO reduction occurring. The higher H_2/CO ratios obtained during the reactions at 600 °C and 700 °C are due to minimal levels of methane decomposition occurring over the initial reaction stage, which is reinforced by the maximum CH_4 conversion data observed at 600 °C and 700 °C.

The average CH_4 conversion and H_2 yield data under methane-rich and stoichiometric reaction conditions over Ni/Al_2O_3 (900) are shown in Figure 7.19 and the average CO selectivity and H_2/CO ratios are shown in Table 7.8.

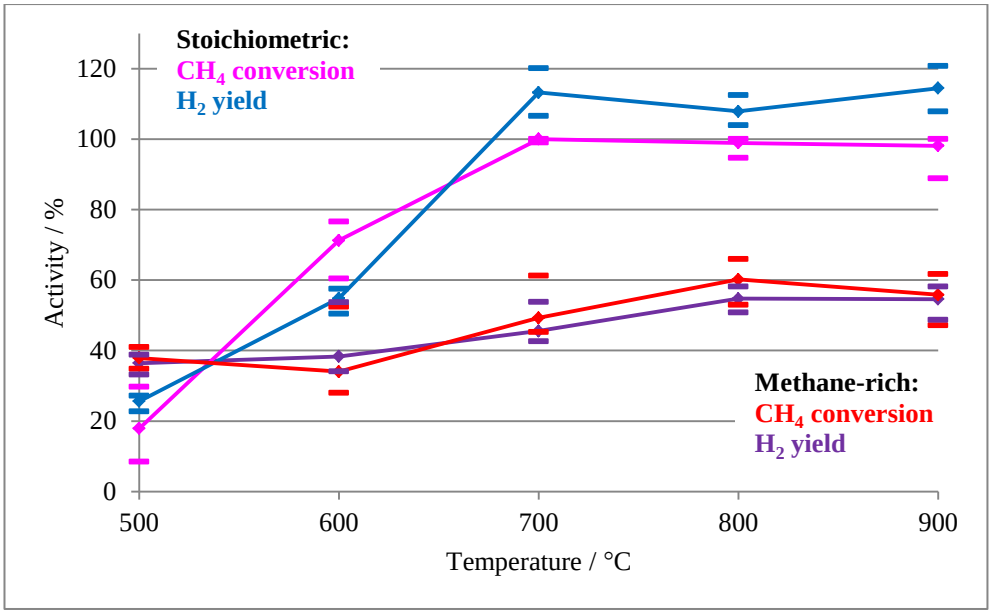

Figure 7.19: **Average CH_4 conversion and H_2 yield during reactions over Ni/Al_2O_3 (900) for 20 hours under methane-rich (methane: steam = 2:1) and stoichiometric (methane: steam = 1:1) conditions at reaction temperatures 500 °C to 900 °C**

Table 7.8: **Average CO selectivity and H_2/CO ratio during reactions over Ni/Al_2O_3 (900) for 20 hours under methane-rich (methane: steam = 2:1) and stoichiometric (methane: steam = 1:1) conditions at reaction temperatures 500 °C to 900 °C**

Reaction temperature / °C	Average CO selectivity / %		Average H_2/CO ratio	
	Stoichiometric	Methane-rich	Stoichiometric	Methane-rich
500	49	83	4.2	3.4
600	79	88	3.2	3.0
700	95	99	3.0	2.3
800	100	100	2.8	4.5
900	100	99	2.9	4.0

A similar reforming activity trend is observed following reactions at 500 °C, under both methane-rich and stoichiometric conditions. As might be expected, a greater amount of carbon is deposited during reactions undertaken in steam-deficient reaction conditions (Section 7.3). Although less carbon was deposited under stoichiometric conditions, it appears to have a greater impact on reforming activity, resulting in a significant reduction in CH_4 conversion and H_2 yield. Alternatively, this could also indicate that carbon may not be the only reason for catalyst deactivation. Nickel sintering has been shown [11] to significantly influence catalyst activity, resulting in loss of catalyst activity during reforming reactions. Furthermore, it has been shown [12-14] that the presence of steam enhances the nickel sintering processes through the formation of mobile Ni_2-OH complexes.

The Boudouard reaction is proposed to be the main form of carbon deposition at 500 °C and CO reduction at 600 °C, under both reforming conditions. However, above 700 °C reaction pathways occurring vary substantially depending on the reforming conditions. Under stoichiometric conditions, at temperatures above 700 °C additional hydrogen is potentially produced by H_2O adsorption and dissociation. This process enhances carbon gasification at high reaction temperatures. However, under methane-rich conditions this does not occur due to the utilisation of all the steam in the reforming of methane. Instead, methane decomposition occurs in the presence of excess methane, increasing CH_4 conversion to *ca.* 60 %, which is mirrored by an increase in the H_2 yield and high H_2/CO ratio.

A significant variation in the H_2/CO ratio is observed following reactions under different reforming conditions. The high H_2/CO ratio exhibited at 500 °C under stoichiometric conditions is attributed to the high activity towards the water-gas shift reaction, confirmed by the level of carbon dioxide formation and thus CO selectivity data. However, under methane-rich conditions the water-gas shift reaction is not favoured and the slightly higher than expected H_2/CO ratio is attributed to the Boudouard reaction occurring. Product ratios are similar at 600 °C due to CO reduction occurring, although slightly higher under stoichiometric conditions due to the water-gas shift reaction still

occurring at these temperatures. At reaction temperatures above 700 °C, the H_2/CO ratio remains stable under stoichiometric conditions, whereas under methane-rich conditions the ratio is significantly increased at 800 °C and 900 °C, because of methane decomposition.

Steam plays an important role in the variation of reforming trends depending on the extent different reaction pathways are favoured. This results in the promotion of different reaction pathways over Ni/Al_2O_3 (900) under methane-rich and stoichiometric conditions.

The average CH_4 conversion and H_2 yield data under methane-rich and stoichiometric reaction conditions over Ni/Al_2O_3 (1000) are shown in Figure 7.20 and the average CO selectivity and H_2/CO ratios are shown in Table 7.9.

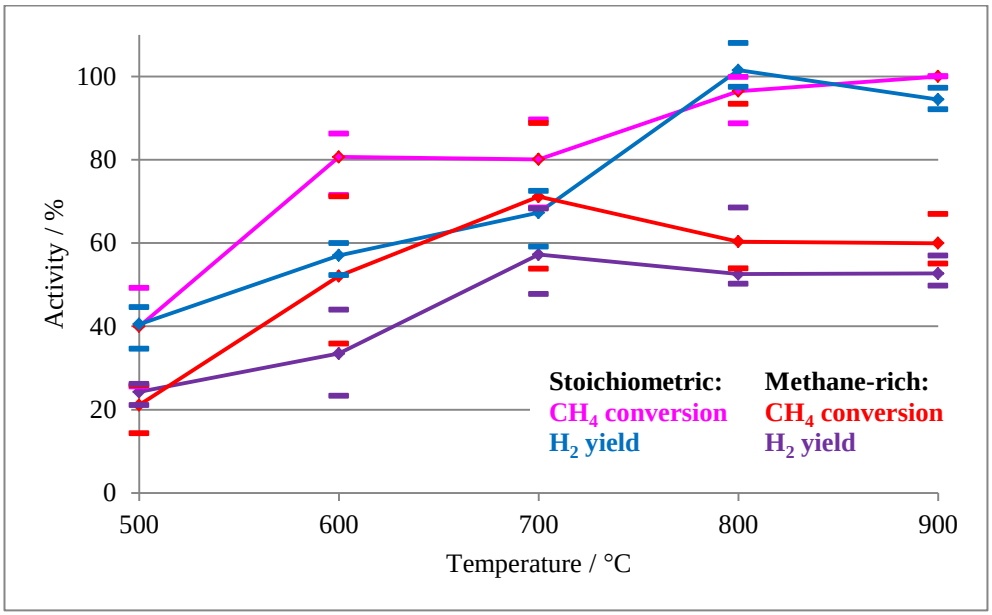

Figure 7.20: Average CH_4 conversion and H_2 yield during reactions over Ni/Al_2O_3 (1000) for 20 hours under methane-rich (methane: steam = 2:1) and stoichiometric (methane: steam = 1:1) conditions at reaction temperatures 500 °C to 900 °C

Table 7.9: Average CO selectivity and H_2/CO ratio during reactions over Ni/Al_2O_3 (1000) for 20 hours under methane-rich (methane: steam = 2:1) and stoichiometric (methane: steam = 1:1) conditions at reaction temperatures 500 °C to 900 °C

Reaction temperature / °C	Average CO selectivity / %		Average H_2/CO ratio	
	Stoichiometric	Methane-rich	Stoichiometric	Methane-rich
500	55	57	3.4	3.3
600	83	95	2.3	2.5
700	93	100	2.4	4.1
800	98	100	1.9	5.1
900	100	100	4.1	4.9

The activity and selectivity at 500 ºC shows a difference of *ca.* 15 % in both the CH_4 conversion and H_2 yield observed under both methane-rich and stoichiometric conditions. Characterisation studies (Chapter 4) have showed that $NiAl_2O_4$ formed during calcination is not fully reduced during TPR reaction of Ni/Al_2O_3 (1000). This results in a low product yield and no carbon formation at 500 °C due to the low reforming activity of $NiAl_2O_4$ [5]. Under methane-rich conditions, low reforming activity results in a higher steam availability, increasing the formation of carbon monoxide via the water-gas shift reaction, thus comparable CO selectivity values are observed under both reaction conditions. During the reaction at 600 ºC, under both reaction conditions, the H_2 yield is significantly less than CH_4 conversion, attributed to the reduction of $NiAl_2O_4$ under the atmosphere of hydrogen produced during steam methane reforming. This process results in a low H_2 yield and lower than expected H_2/CO ratio. During methane-rich studies methane

decomposition is favoured over Ni/Al_2O_3 (1000) at temperatures above 600 ºC, resulting in catalyst deactivation. However, methane decomposition is not observed under stoichiometric conditions until 900 ºC and at temperatures below this carbon deposition occurs predominantly by the Boudouard reaction.

The presence of unreduced $NiAl_2O_4$ at low reaction temperatures means that similar reaction behaviours are observed, which are not solely dependent on the methane to steam ratio. The $NiAl_2O_4$ phase limits the reactions that are able to proceed, both controlling carbon formation whilst also limiting methane reforming.

In addition to the calcination temperature, the reaction conditions have been shown to significantly affect the catalytic behaviour during methane reforming reactions. The major differences observed relate to the occurrence of additional reaction pathways, such as methane decomposition and the water-gas shift reaction, which affect both the product gas ratios and the extent of catalyst deactivation.

7.3 Carbon deposition during reactions of methane and steam over 20 wt % Ni/Al_2O_3 under methane-rich conditions at different reaction temperatures

Carbon deposition during reaction was determined using post-reaction temperature-programmed oxidation (TPO). In certain TPO experiments, carbon deposition exceeded the limit that was able to be accurately monitored using the flow rate of oxygen employed, an example of which is shown in Figure 7.21. This resulted in a TPO profile that was unable to be used to accurately quantify the specific amount of carbon deposited during the reaction. A TPO profile that demonstrates this behaviour is termed ‘oxygen deficient’. Oxygen deficient TPO profiles contain in excess of 25 mg of carbon and are represented by arrows on bar charts, as shown in Figure 7.23.

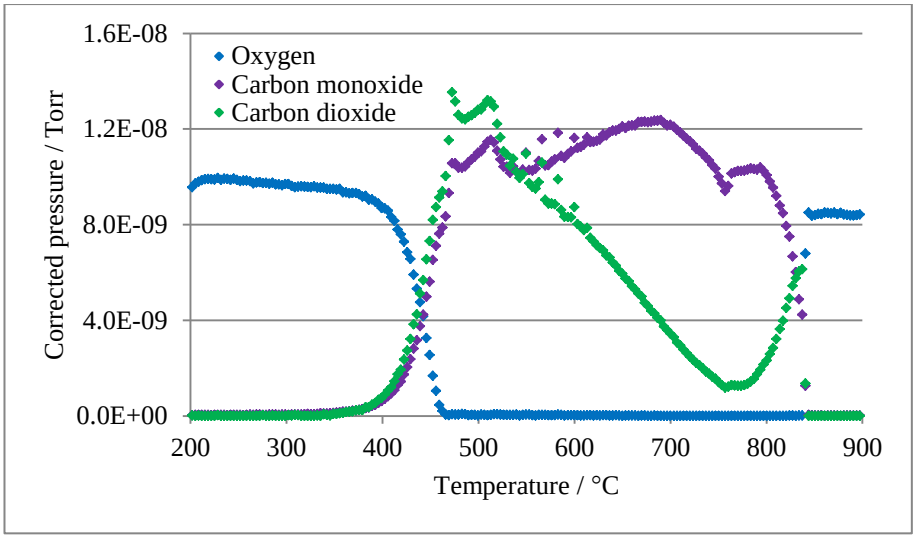

Figure 7.21: Oxygen deficient TPO profile following reaction of methane and steam at 600 °C for 20 hours under methane-rich conditions over Ni/Al_2O_3 (600)

In order to quantify the amount of carbon deposited during reactions, the sum of any carbon monoxide and carbon dioxide produced was determined and compared to a carbon calibration, as discussed in Chapter 3. The carbon removal profiles, achieved by summing the carbon monoxide and carbon dioxide profiles obtained during TPO reactions, following reactions of methane and steam at various temperatures over Ni/Al_2O_3 (600) are shown in Figure 7.22.

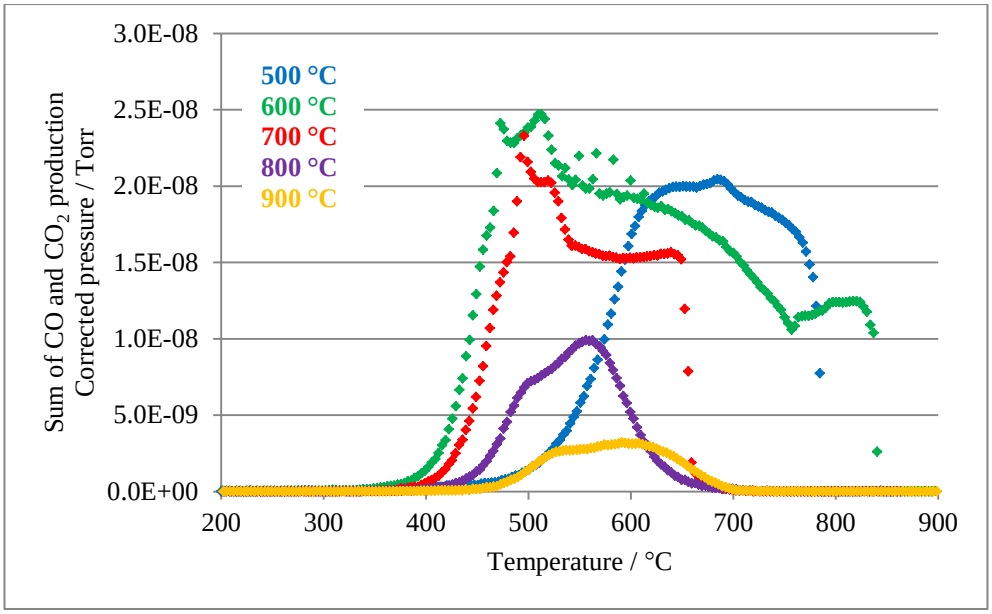

Figure 7.22: Carbon removal during TPO studies following reaction of methane and steam over Ni/Al_2O_3 (600) under methane-rich conditions at reaction temperatures between 500 °C and 900 °C

As well as allowing quantification of the amount of carbon deposited during reaction, TPO profiles can give some insight into the nature of carbon formed during reforming reactions. The temperature at which carbon is removed during TPO depends on the type of carbon and its stability on the catalyst surface [15]. However, oxygen deficient TPO profiles should be viewed with care. In Figure 7.22, the TPO profiles following the reaction undertaken at 600 °C and 700 °C are oxygen deficient and contain in excess of 25 mg of carbon. Therefore, the temperature at which the carbon is removed by oxygen may not be representative of the process occurring due to poorly defined carbon oxide peaks. A higher peak maximum is observed following the reaction at 500 °C, compared to profiles observed following reactions undertaken at 800 °C and 900 °C. This suggests that a different form of carbon may be produced during reaction at 500 °C. However, it is difficult to compare TPO peak maxima and state with certainty the carbon type formed, due to varying amounts of carbon formed slightly shifting peak positions. Additionally, there is evidence of carbon 'ageing' between 800 °C and 900 °C [2]. Despite less carbon deposited following the

reaction at 900 °C, it is more strongly bound to the surface, thus the temperature at which the carbon is removed is increased.

The carbon deposited following reactions under methane-rich conditions are shown in Figure 7.23 by solid bars and under stoichiometric conditions are shown by dashed bars. A general trend is exhibited by all catalysts over the reaction temperatures studied. Carbon deposition appears to be greater following reactions below 700 °C. Generally, less carbon is deposited at 800 °C and 900 °C. It has been shown (Section 7.2) that at temperatures below 800 °C a number of carbon formation reactions can occur, namely CO reduction, the Boudouard reaction and methane decomposition. However, at higher temperatures the predominant reaction occurring is methane decomposition.

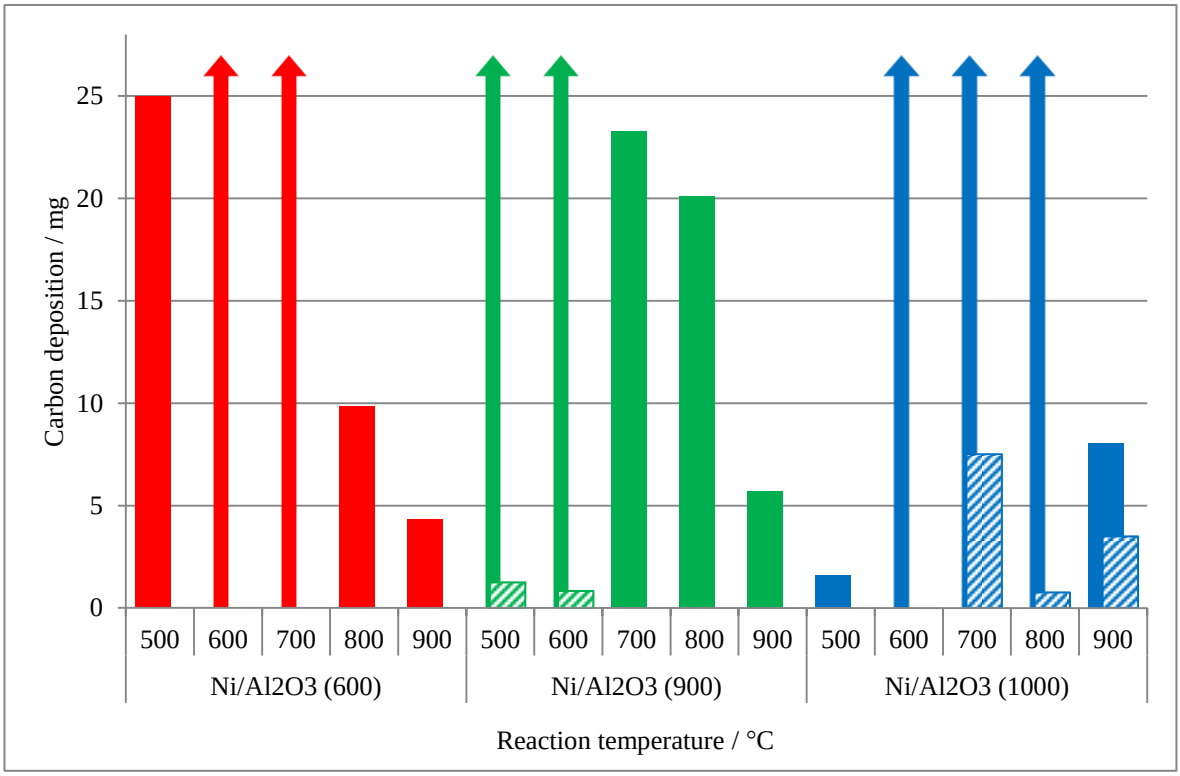

Figure 7.23: Carbon deposition following reaction of methane and steam under methane-rich conditions (bold) and stoichiometric conditions (dashed), over Ni/Al_2O_3 (600), Ni/Al_2O_3 (900) and Ni/Al_2O_3 (1000) at different reaction temperatures

Ni/Al_2O_3 (600) has been shown (Section 7.2) to be substantially influenced by carbon deposition, resulting in complete loss of catalytic activity during reactions at 500 °C. However, TPO results indicate that less carbon is deposited at 500 °C than during reactions undertaken at 600 °C and 700 °C. This suggests that a different form of carbon may be produced during reaction at these temperatures. This would seem to be confirmed by the TPO profiles shown in Figure 7.22, which shows that the carbon removal peak maximum is shifted to a much higher temperature following reaction at 500 °C, compared to higher reaction temperatures. SEM studies would potentially give an additional insight into the type of carbon formed during the reactions [1, 8, 9]. Although undertaken during carbon dioxide reforming conditions, it has been shown that different forms of carbon are produced depending on the calcination temperature employed during catalyst preparation [1, 8], resulting in significantly different effects on the catalyst reforming activity.

Over Ni/Al_2O_3 (600) a shift from the Boudouard reaction to CO reduction was observed as the reaction temperature is increased. However, some methane decomposition is observed during the initial phases of the reactions at 600 °C and 700 °C. Methane decomposition is not highly favoured over Ni/Al_2O_3 (600). This results in a reduction in carbon deposition during reactions undertaken at higher temperatures, where methane decomposition is thermodynamically favoured. Methane decomposition is favoured over Ni/Al_2O_3 (1000) and Ni/Al_2O_3 (900) compared to Ni/Al_2O_3 (600), shown by an increase in carbon deposition at reaction temperatures above 800 °C.

Over Ni/Al_2O_3 (1000), minimal carbon deposition is observed following the reaction at 500 °C. This is attributed to the presence of unreduced $NiAl_2O_4$, limiting activity towards carbon-forming reactions as well as methane reforming activity [8]. Following reduction of $NiAl_2O_4$ during reactions at 600 °C and above, significant carbon deposition is observed. Methane decomposition is the primary carbon-forming reaction favoured over Ni/Al_2O_3 (1000). Methane decomposition occurs over Ni/Al_2O_3 (900), although as the calcination temperature is increased to 1000 °C, methane decomposition occurs to a greater extent.

Methane-rich reforming conditions dramatically promote carbon deposition at all temperatures investigated [4]. This is attributed to the suppression of carbon gasification by steam and the promotion of methane decomposition in high methane concentrations. During studies under stoichiometric reaction conditions, excessive carbon removal by steam occurred resulting in minimal carbon deposition over the catalysts studied. Significant carbon removal by steam is observed over both Ni/Al_2O_3 (600) and Ni/Al_2O_3 (900) during reactions at temperatures above 700 °C, resulting in no carbon deposition observed by TPO. This is most significantly observed during reactions undertaken over Ni/Al_2O_3 (900) at temperatures above 700 °C, where H_2O dissociation is promoted and the resulting adsorbed oxygen species act to limit carbon deposition during reforming reactions through carbon gasification. Carbon gasification by steam is limited during reactions undertaken in methane-rich conditions, due to the reaction stoichiometry.

7.4 Summary

Following calcination at lower temperatures carbon formation on the Ni/Al_2O_3 catalyst occurs predominantly by the Boudouard reaction and CO reduction. However, at the higher calcination temperatures methane decomposition is favoured, occurring to a greater extent following calcination at 1000 °C. Although less carbon is formed over Ni/Al_2O_3 calcined at 600 °C, significant catalyst deactivation is observed during the reaction at 500 °C, resulting in complete loss of reforming activity. This could indicate that Ni/Al_2O_3 calcined at 600 °C results in a more deactivating form of carbon depending on the reaction temperature or that sintering of the nickel particles is also occurring. Apart from variations in activity due to carbon deposition induced deactivation, Ni/Al_2O_3 calcined at 600 °C and 900 °C have comparable activities at low reaction temperatures. It is only as the reaction temperature is increased that differences occur resulting from increased promotion of methane decomposition over Ni/Al_2O_3 calcined at 900 °C, altering both conversion and yield data obtained.

Ni/Al_2O_3 calcined at 1000 °C exhibits significantly different reforming characteristics than the catalysts calcined at 600 °C and 900 °C. This is attributed to the presence of unreduced $NiAl_2O_4$ limiting reforming activity at lower reaction temperatures. Ni/Al_2O_3 (1000) has extremely low reforming activity at 500 °C, increasing the steam concentration at the surface resulting in higher than expected activity towards the water-gas shift reaction. The presence of $NiAl_2O_4$ also results in suppression of carbon formation during the reaction at 500 °C. A reduction in H_2 yield is observed during the reaction at 600 °C as a result of hydrogen utilisation in the reduction of $NiAl_2O_4$ to metallic nickel. This process is not observed during reactions at temperatures above 700 °C due to the rapid reduction at these temperatures. Carbon deposition over Ni/Al_2O_3 (1000) occurs by methane decomposition, which is favoured over this catalyst at all reaction temperatures studied, except at the lowest temperature of 500 °C.

Methane-rich conditions significantly promote carbon formation over all catalysts at all reforming temperatures studied [4]. This is due to the steam deficient nature of reforming, limiting carbon gasification [16] and excess methane promoting methane decomposition. As well as promoting carbon deposition, reforming activity under methane-rich conditions [2] is reduced as a result of catalyst deactivation due to carbon deposition and insufficient steam present to reform all the methane.

Temperature-programmed reactions of methane and steam show that reactivity is significantly lowered during reactions under methane-rich conditions and gas onset temperatures are increased up to 100 °C. During isothermal reactions reforming activity at 500 °C is comparable whether under methane-rich or stoichiometric conditions, for each catalyst. However, as the reaction temperature is increased the variation of reforming trends becomes greater as steam plays a significant role in the extent different reaction pathways are favoured. For example, under stoichiometric conditions Ni/Al_2O_3 calcined at 900 °C promotes the adsorption and subsequent desorption of H_2O to form additional hydrogen, whilst also aiding carbon gasification during the

reaction. This however is not observed under methane-rich conditions and results in a vast difference in carbon deposition and hydrogen yield obtained. Although steam alters the reaction processes and reactions occurring during reforming, those that occur over Ni/Al_2O_3 calcined at 1000 °C at low reaction temperatures remain similar under both reaction conditions, due to the presence of $NiAl_2O_4$.

7.5 References

1. O.-S. Joo and K.-D. Jung, *CH 4 Dry Reforming on Alumina-Supported Nickel Catalyst.* Bulletin of the Korean Chemical Society 2002. **23**(8): p. 1149-1153.
2. C.M. Finnerty and R.M. Ormerod, *Internal reforming over nickel/zirconia anodes in SOFCS operating on methane: Influence of anode formulation, pre-treatment and operating conditions.* Journal of Power Sources 2000. **86**: p. 390-394.
3. Z.W. Liu, K.W. Jun, H.S. Roh, and S.E. Park, *Hydrogen production for fuel cells through methane reforming at low temperatures.* Journal of Power Sources, 2002. **111**: p. 283-287.
4. S. Rakass, H. Oudghiri-Hassani, P. Rowntree, and N. Abatzoglou, *Steam reforming of methane over unsupported nickel catalysts.* Journal of Power Sources, 2006. **158**(1): p. 485-496.
5. N. Sahli, C. Petit, A.C. Roger, A. Kiennemann, S. Libs, and M.M. Bettahar, *Ni catalysts from $NiAl_2O_4$ spinel for CO_2 reforming of methane*. Catalysis Today, 2006. **113**(3-4): p. 187-193.
6. P. Kim, Y. Kim, H. Kim, I.K. Song, and J. Yi, *Synthesis and characterization of mesoporous alumina with nickel incorporated for use in the partial oxidation of methane into synthesis gas.* Applied Catalysis A: General, 2004. **272**(1-2): p. 157-166.
7. H.-S. Roh, K.-W. Jun, and S.-E. Park, *Methane-reforming reactions over Ni/Ce-ZrO_2/θ-Al_2O_3 catalysts.* Applied Catalysis A: General, 2003. **251**(2): p. 275-283.

8. Y.-g. Chen and J. Ren, *Conversion of methane and carbon dioxide into synthesis gas over alumina-supported nickel catalysts. Effect of Ni-Al_2O_3 interactions.* Catalysis Letters, 1994. **29**(1): p. 39-48.

9. M.J. Lázaro, Y. Echegoyen, I. Suelves, J.M. Palacios, and R. Moliner, *Decomposition of methane over Ni-SiO_2 and Ni-Cu-SiO_2 catalysts: Effect of catalyst preparation method.* Applied Catalysis A: General, 2007. **329**(0): p. 22-29.

10. J. Chen, Q. Ma, T.E. Rufford, Y. Li, and Z. Zhu, *Influence of calcination temperatures of Feitknecht compound precursor on the structure of Ni-Al_2O_3 catalyst and the corresponding catalytic activity in methane decomposition to hydrogen and carbon nanofibers.* Applied Catalysis A: General, 2009. **362**(1-2): p. 1-7.

11. S.M. Hashemnejad and M. Parvari, *Deactivation and Regeneration of Nickel-Based Catalysts for Steam-Methane Reforming.* Chinese Journal of Catalysis. **32**(1): p. 273-279.

12. K.O. Christensen, D. Chen, R. Lødeng, and A. Holmen, *Effect of supports and Ni crystal size on carbon formation and sintering during steam methane reforming.* Applied Catalysis A: General, 2006. **314**(1): p. 9-22.

13. A.C.S.C. Teixeira and R. Giudici, *Deactivation of steam reforming catalysts by sintering: experiments and simulation.* Chemical Engineering Science, 1999. **54**(15-16): p. 3609-3618.

14. J. Sehested, J.A.P. Gelten, I.N. Remediakis, H. Bengaard, and J.K. Nørskov, *Sintering of nickel steam-reforming catalysts: effects of temperature and steam and hydrogen pressures.* Journal of Catalysis, 2004. **223**(2): p. 432-443.

15. C.M. Finnerty, N.J. Coe, R.H. Cunningham, and R.M. Ormerod, *Carbon formation on and deactivation of nickel-based/zirconia anodes in solid oxide fuel cells running on methane.* Catalysis Today, 1998. **46**(2-3): p. 137-145.

16. A.L. Alberton, M.M.V.M. Souza, and M. Schmal, *Carbon formation and its influence on ethanol steam reforming over Ni/Al_2O_3 catalysts.* Catalysis Today, 2007. **123**(1-4): p. 257-264.

8 Reactions of methane and steam over 5 mol % Au doped 20 wt % Ni/Al_2O_3: Influence of gold addition, calcination temperature and methane to steam ratio

---

Although gold has been used both as a promoter and primary active component in reforming catalysts [1-4], its use and influence on bimetallic nickel based catalysts remains an intensively researched area. The addition of gold to a nickel based catalyst has shown to be both detrimental and beneficial towards hydrocarbon reforming. It has been shown that the addition of gold to reforming catalysts can significantly reduce carbon formation during reforming studies [3, 5-7]. In bimetallic nickel based catalysts, gold is preferentially located at low coordination sites and is more stable at nickel surface step and kink sites than surface terrace sites [3, 7]. It has also been demonstrated by Bengaard *et al.* [7] that even at elevated temperatures, gold atoms are not located in the bulk of a nickel nanoparticle but are evenly spread over the nickel surface.

When gold atoms are alloyed to the nickel surface, neighbouring nickel atoms experience a change in geometry and electronic structure, due to a higher coordination number and change in surface energy. Gold can impede methane dissociation on the nickel surface, as nickel atoms in the vicinity of gold atoms have higher dissociation energy barriers and thus a lower dissociation rate [6, 8]. The changes induced in the nickel surface can also result in a decreased rate of methane dehydrogenation and an increase in both the stability and lifetime of adsorbed CH_x species, limiting formation of atomic carbon on the nickel surface [6]. As well as altering the electronic properties of nickel, the binding of gold to specific sites on the nickel surface can also be an important factor. Methane activation and graphite nucleation have been shown to be highly active at nickel step sites. Therefore, the preferential binding of gold to step sites may inhibit carbon nucleation, limiting

carbon formation during reforming reactions. As well as carbon deposition, gold has also shown to lessen catalyst deactivation by preventing nickel sintering at elevated temperatures [3, 4]. Although beneficial effects have been proposed, specifically relating to the suppression of carbon formation during reforming studies, the addition of gold to reforming catalysts has also shown to inhibit the reforming process [1, 2, 4]. In order for a promoted catalyst to be effective, gold must be incorporated in sufficient concentrations to effectively supress carbon formation without considerably inhibiting hydrocarbon reforming.

Characterisation studies described in Chapter 5 have shown that the calcination temperature used in the preparation of gold-doped Ni/Al_2O_3 significantly affects the catalyst structure, morphology and nickel interactions with the alumina support. This study aims to investigate the influence that the addition of gold to Ni/Al_2O_3 and the calcination temperature selected during preparation have on the catalyst activity and reactivity during steam methane reforming. The catalysts studied are those with significant variations in physical characteristics, allowing the influence of physical properties on steam methane reforming to be investigated. With this in mind, reactions involving methane and steam were conducted over 5 mol % Au doped 20 wt % Ni/Al_2O_3 catalysts calcined at 600 °C, 900 °C and 1000 °C, denoted hereon as Au-Ni/Al_2O_3 (600), Au-Ni/Al_2O_3 (900) and Au-Ni/Al_2O_3 (1000).

Reactions in this study were undertaken under both stoichiometric (methane: steam = 1:1) and methane-rich conditions (methane: steam = 2:1). Reactions 8.1 - 8.3 show the effect of complete methane conversion using these stoichiometries.

$$\mathbf{CH_4 + H_2O \rightarrow CO + 3H_2} \qquad \mathbf{(8.1)}$$

$$\mathbf{2CH_4 + H_2O \rightarrow CO + 3H_2 + CH_4} \qquad \mathbf{(8.2)}$$

$$\mathbf{CH_4 \rightarrow C + 2H_2} \qquad \mathbf{(8.3)}$$

Carbon dioxide may be produced during the water-gas shift reaction via Reaction 8.4, and carbon formation may also occur via the Boudouard reaction and CO reduction, as shown in Reactions 8.5 and 8.6, respectively, as well as by methane decomposition via Reaction 8.3.

$$\mathbf{CO + H_2O \leftrightarrow CO_2 + H_2} \qquad \mathbf{(8.4)}$$

$$\mathbf{CO_2 \rightarrow C + CO} \qquad \mathbf{(8.5)}$$

$$\mathbf{CO + H_2 \rightarrow C + H_2O} \qquad \mathbf{(8.6)}$$

Prior to all reforming reactions, all catalysts were reduced in hydrogen, using the TPR procedure discussed in Chapter 3 and the reduction profiles for the Au-Ni/Al_2O_3 catalysts are presented in Chapter 5.

8.1 Reverse temperature-programmed reactions of methane and steam under stoichiometric conditions over 5 mol % Au doped 20 wt % Ni/Al_2O_3

The selectivity and maximum activity over all catalysts are shown in Table 8.1, relating to the reverse temperature-programmed reaction profiles. The H_2 yield, CH_4 conversion and CO selectivity profiles for each catalyst are shown in Figure 8.1 to Figure 8.3, respectively.

Table 8.1: **Catalyst selectivity and maximum activity during temperature-programmed reactions of methane and steam over Au-Ni/Al_2O_3 catalysts under stoichiometric conditions (methane: steam = 1:1)**

Catalyst	Maximum CH_4 conversion / %	Maximum H_2 yield / %	Average final H_2/CO ratio	Minimum CO selectivity / %
Au-Ni/Al_2O_3 (600)	95	95	3.0	38
Au-Ni/Al_2O_3 (900)	97	94	3.1	74
Au-Ni/Al_2O_3 (1000)	100	66	2.1	61

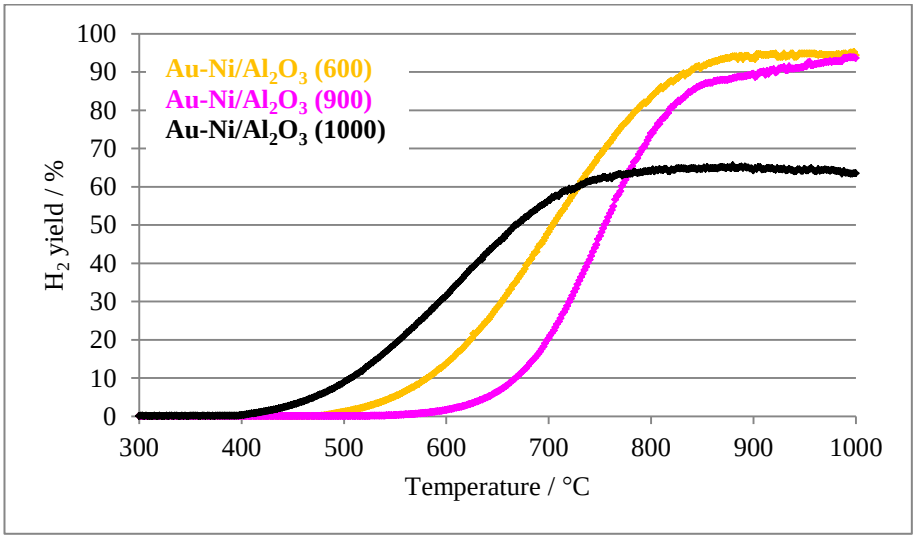

Figure 8.1: **H_2 yield during temperature-programmed reactions of methane and steam over Au-Ni/Al_2O_3 (600), Au-Ni/Al_2O_3 (900) and Au-Ni/Al_2O_3 (1000) under stoichiometric conditions (methane: steam = 1:1)**

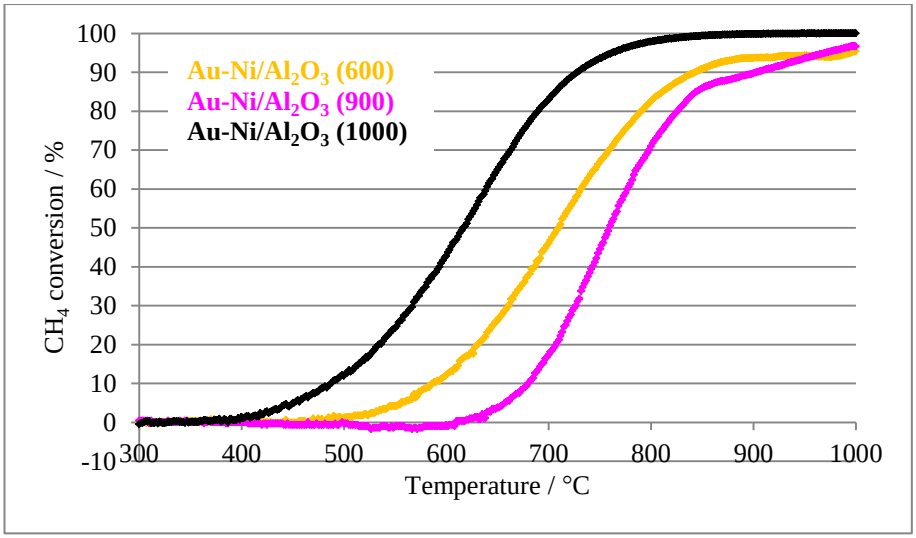

Figure 8.2: **CH_4 conversion during temperature-programmed reactions of methane and steam over Au-Ni/Al_2O_3 (600), Au-Ni/Al_2O_3 (900) and Au-Ni/Al_2O_3 (1000) under stoichiometric conditions (methane: steam = 1:1)**

The reaction profiles show clearly that the reactivity of Au-Ni/Al_2O_3 catalysts for stoichiometric methane to steam mixtures varies considerably depending on the calcination temperature used, and the onset temperatures for the reactions range from *ca.* 400 °C to *ca.* 600 °C.

The H_2 yield and CH_4 conversion results indicate that Au-Ni/Al_2O_3 (600) is highly active towards steam methane reforming, although maximum activity is not achieved. Incomplete steam methane reforming over Au-Ni/Al_2O_3 (900) results in methane decomposition at temperatures above *ca.* 850 °C, observed by a simultaneous increase in H_2 yield and CH_4 conversion. It should be noted that if a catalyst exhibits reduced steam methane reforming activity it can be difficult to infer if methane decomposition is occurring at elevated temperatures.

Over Au-Ni/Al_2O_3 (1000), the H_2 yield is *ca.* 35 % less than the CH_4 conversion. This indicates that hydrogen produced during steam methane reforming is being utilised in additional reactions or processes, as observed over Ni/Al_2O_3 (1000). In Chapter 5 it was shown that Au-Ni/Al_2O_3 (1000) was not fully reduced during temperature-programmed reduction and the $NiAl_2O_4$ phase formed during calcination remained partially unreduced. At high temperatures, hydrogen produced during

steam reforming is clearly reducing Ni^{2+} species present in the $NiAl_2O_4$ phase to metallic nickel [9]. This also accounts for the low H_2 yield and H_2/CO ratio obtained. No change in the water signal is observed, as steam produced is immediately utilised in steam reforming at elevated temperatures. Characterisation studies also suggest that $NiAl_2O_4$ is formed during calcination of Au-Ni/Al_2O_3 (900). However, this phase is not observed during post-reduction XRD studies, suggesting that this phase is effectively reduced, thus no change in catalytic activity is observed.

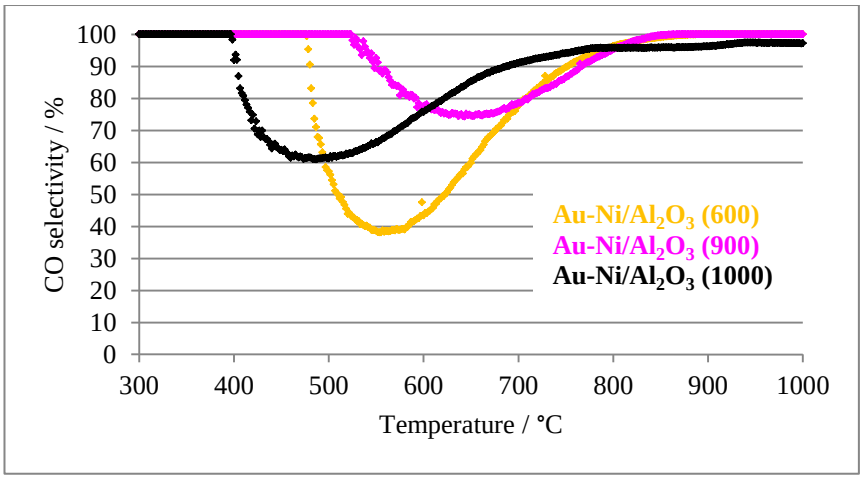

Figure 8.3: CO selectivity during temperature-programmed reactions of methane and steam over Au-Ni/Al_2O_3 (600), Au-Ni/Al_2O_3 (900) and Au-Ni/Al_2O_3 (1000) under stoichiometric conditions (methane: steam = 1:1)

The CO selectivity data indicates that Au-Ni/Al_2O_3 (600) is highly active towards carbon dioxide production in the temperature range 500 °C to 750 °C, either via the water-gas shift reaction or the Boudouard reaction. Au-Ni/Al_2O_3 (1000) also shows high activity towards carbon dioxide production from 400 °C. However, unlike the other catalysts, Au-Ni/Al_2O_3 (1000) continues to produce some carbon dioxide at temperatures above *ca.* 800 ºC. This could be attributed to the formation of additional steam via the reduction of $NiAl_2O_4$, increasing activity towards the water-gas shift reaction. This trend is not observed over other Au-Ni/Al_2O_3 catalysts. Au-Ni/Al_2O_3 (900) is least active and selective towards carbon dioxide production.

8.2 Reverse temperature-programmed reactions of methane and steam under methane-rich conditions over 5 mol % Au doped 20 wt % Ni/Al_2O_3

The catalyst selectivity and maximum activity over all catalysts is shown in Table 8.2, relating to reverse temperature-programmed reaction profiles. The H_2 yield, CH_4 conversion and CO selectivity profiles for each catalyst are shown in Figure 8.4 to Figure 8.6, respectively.

Table 8.2: Catalyst selectivity and maximum activity during temperature-programmed reactions of methane and steam $Au-Ni/Al_2O_3$ catalysts under methane-rich conditions (methane: steam = 2:1)

Catalyst	Maximum CH_4 conversion / %	Maximum H_2 yield / %	Average final H_2/CO ratio	Minimum CO selectivity / %
$Au-Ni/Al_2O_3$ (600)	47	47	3.5	24
$Au-Ni/Al_2O_3$ (900)	80	68	3.4	83
$Au-Ni/Al_2O_3$ (1000)	53	43	3.9	41

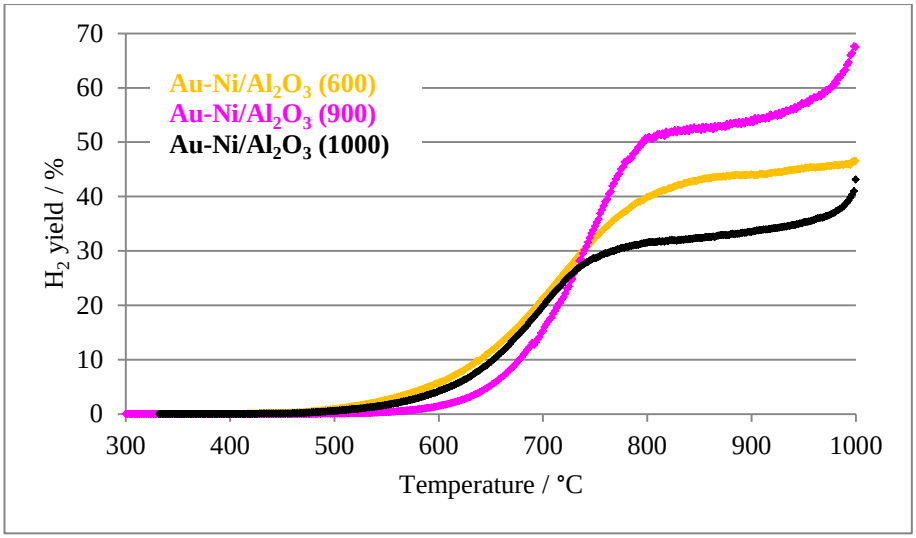

Figure 8.4: **H_2 yield during temperature-programmed reactions of methane and steam over Au-Ni/Al_2O_3 (600), Au-Ni/Al_2O_3 (900) and Au-Ni/Al_2O_3 (1000) under methane-rich conditions (methane: steam = 2:1)**

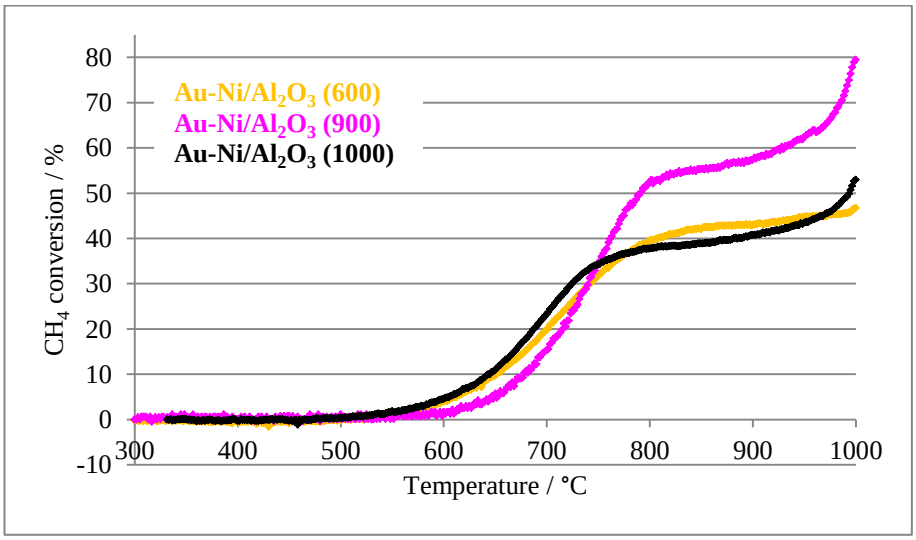

Figure 8.5: **CH_4 conversion during temperature-programmed reactions of methane and steam over Au-Ni/Al_2O_3 (600), Au-Ni/Al_2O_3 (900) and Au-Ni/Al_2O_3 (1000) under methane-rich conditions (methane: steam = 2:1)**

As opposed to reactions under stoichiometric conditions, marginal differences in the onset temperatures are observed between the catalysts studied.

Over Au-Ni/Al_2O_3 (600), high H_2 yield and CH_4 conversion are observed at temperatures above *ca.* 850 °C. It is possible that at low temperatures incomplete steam methane reforming increases steam concentration, catalysing the water-gas shift reaction. At elevated temperatures the Boudouard reaction may be occurring accounting for the very low CO selectivity and high H_2/CO ratio obtained.

Both the CH_4 conversion and H_2 yield exceed 50 % at elevated temperatures over Au-Ni/Al_2O_3 (900), indicating methane decomposition must be occurring. Before methane decomposition becomes favourable, Au-Ni/Al_2O_3 (1000) exhibits the lowest steam reforming activity between *ca.* 800 °C and 900 °C. However, above 900 °C methane decomposition is promoted and a simultaneous increase in both CH_4 conversion and H_2 yield is observed. Additionally, as was observed under stoichiometric conditions at elevated temperatures, the slight reduction in H_2 yield, compared to CH_4 conversion may be attributed to the reduction of $NiAl_2O_4$.

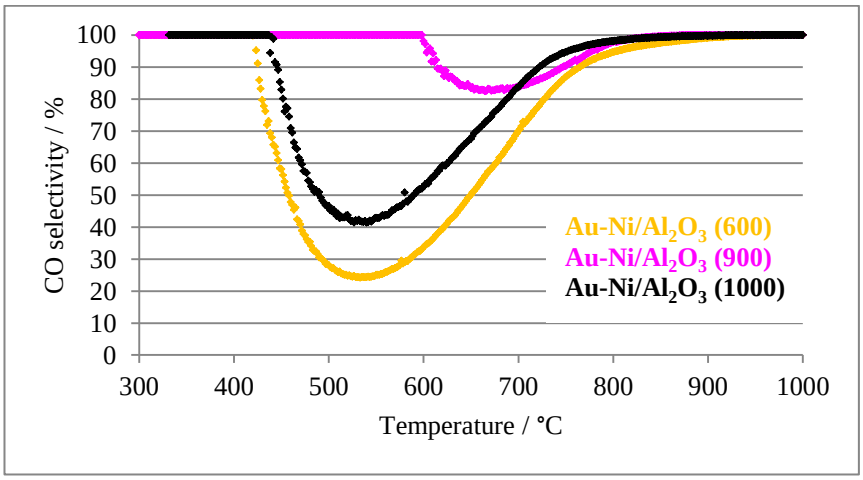

Figure 8.6: **CO selectivity during temperature-programmed reactions of methane and steam over Au-Ni/Al_2O_3 (600), Au-Ni/Al_2O_3 (900) and Au-Ni/Al_2O_3 (1000) under methane-rich conditions (methane: steam = 2:1)**

The CO selectivity profile indicates that Au-Ni/Al_2O_3 (900) does not produce carbon dioxide until a significantly higher temperature than other catalysts, *ca.* 600 °C compared to *ca.* 420 °C. This could be attributed to higher methane reforming activity at elevated temperatures and reduced

activity towards the water-gas shift reaction and/or the Boudouard reaction. As discussed above, Au-Ni/Al_2O_3 (600) is active towards carbon dioxide formation even at elevated temperatures. This may indicate that Au-Ni/Al_2O_3 (600) is less active towards steam reforming and more active towards carbon dioxide production. Au-Ni/Al_2O_3 (1000) is also highly active towards the water-gas shift reaction. In this case, this may be due to the reduction of $NiAl_2O_4$, increasing water production and availability for the water-gas shift reaction.

8.3 The influence of gold addition to 20 wt % Ni/Al_2O_3 on the reactivity and activity during temperature-programmed reactions of methane and steam under stoichiometric and methane-rich conditions

The H_2 yield and CH_4 conversion profiles of temperature-programmed reactions under stoichiometric conditions over Ni/Al_2O_3 and Au-Ni/Al_2O_3 are shown in Figure 8.7 and Figure 8.8, respectively.

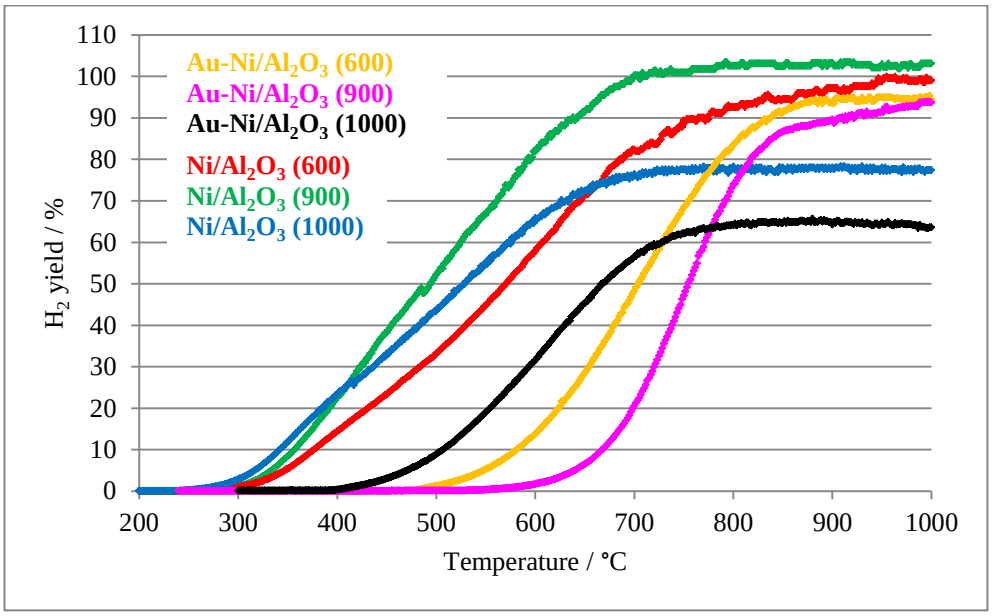

Figure 8.7: **H_2 yield profiles during temperature-programmed reactions of methane and steam over Ni/Al_2O_3 and Au-Ni/Al_2O_3 catalysts under stoichiometric reaction conditions (methane: steam = 1:1)**

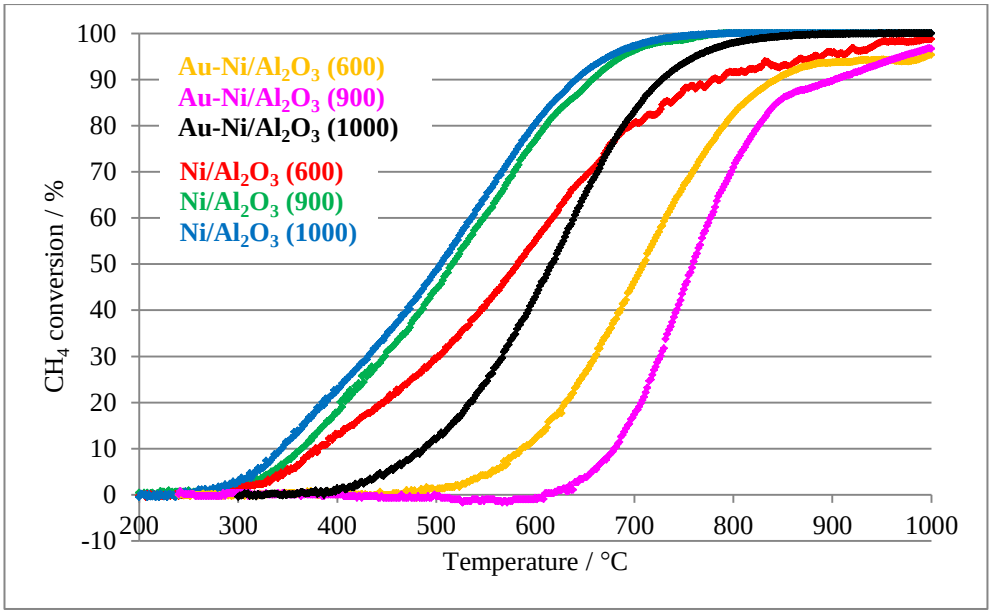

Figure 8.8: **CH_4 conversion during temperature-programmed reactions of methane and steam over Ni/Al_2O_3 and $Au\text{-}Ni/Al_2O_3$ catalysts under stoichiometric reaction conditions (methane: steam = 1:1)**

CH_4 conversion and H_2 yield profiles show that catalyst reactivity is considerably reduced with the addition of gold to Ni/Al_2O_3 catalysts. For example, over $Au\text{-}Ni/Al_2O_3$ (900) reaction onset temperatures are increased by up to *ca.* 300 °C. The addition of gold to Ni/Al_2O_3 catalysts also results in a greater sensitivity of the reactivity to the calcination temperature. For example, the reaction onset temperatures of the $Au\text{-}Ni/Al_2O_3$ catalysts vary by up to *ca.* 200 °C depending on the calcination temperature, but over Ni/Al_2O_3 catalysts a difference of only *ca.* 50 °C is observed across these catalysts. This may be attributed to the greater variability in the structure and phases formed during calcination and the location and distribution of gold on the surface, which in turn influences methane and steam adsorption and the stability of adsorbed hydrocarbon species.

Ni/Al_2O_3 and $Au\text{-}Ni/Al_2O_3$ catalysts calcined at 600 °C and 900 °C exhibit slightly different reaction profiles and activity characteristics, promoting steam methane reforming and methane decomposition to varying extents. However, over both Ni/Al_2O_3 (1000) and $Au\text{-}Ni/Al_2O_3$ (1000) similar reaction profiles are observed. Complete CH_4 conversion is reached over both catalysts calcined at 1000 °C, although H_2 yield is significantly reduced. In Chapters 4 and 5, it was shown

that both catalysts produce $NiAl_2O_4$ during calcination at 1000 °C which is not fully reduced during temperature-programmed reduction. The $NiAl_2O_4$ is reduced at elevated temperatures during reverse temperature-programmed reactions. Although characterisation studies have shown that similar amounts of $NiAl_2O_4$ are formed during calcination of both catalysts, a greater reduction in H_2 yield is observed over Au-Ni/Al_2O_3 (1000). The reduced low temperature activity over Au-Ni/Al_2O_3 (1000) may limit reduction at such temperatures, thus a greater amount of hydrogen is consumed at elevated temperatures in order to effectively reduce the $NiAl_2O_4$ phase. It has also been shown in Chapter 5 that Au-Ni/Al_2O_3 (1000) is more difficult to reduce.

The minimum CO selectivity obtained follow a similar trend following gold-doping. The catalysts calcined at 600 °C exhibit the lowest CO selectivity, promoting carbon dioxide production and those calcined at 900 °C the highest selectivity. Although the minimum CO selectivity is similar, the temperature at which maximum carbon dioxide formation occurs is significantly increased following the addition of gold to Ni/Al_2O_3 catalysts, reflecting the reduced activity of the Au-Ni/Al_2O_3 catalysts. Over both Ni/Al_2O_3 (1000) and Au-Ni/Al_2O_3 (1000) carbon dioxide production is observed at elevated temperatures, as shown in Figure 8.9.

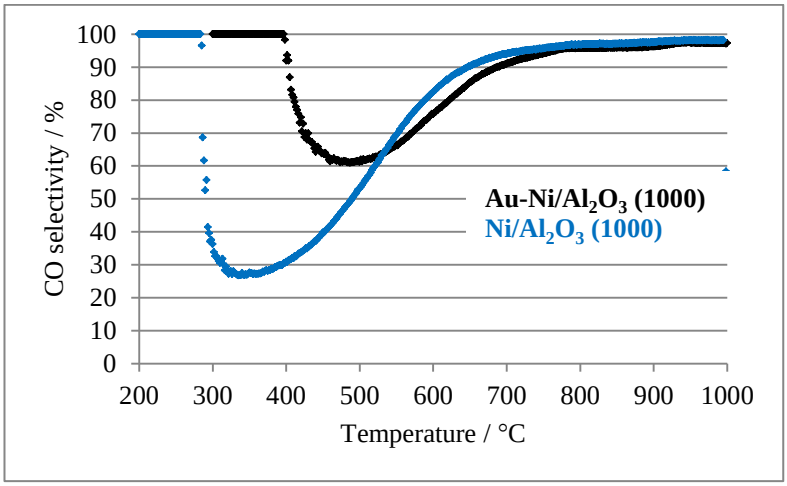

Figure 8.9: CO selectivity profiles for Ni/Al_2O_3 (1000) and Au-Ni/Al_2O_3 (1000) under stoichiometric reaction conditions (methane: steam = 1:1)

Continuous production of carbon dioxide at elevated reaction temperatures is not observed over any other catalyst. This can be attributed to the production of water via the reduction of $NiAl_2O_4$ at elevated reaction temperatures. The presence of additional steam promotes the formation of carbon dioxide via the water-gas shift reaction. Although a greater amount of carbon dioxide is produced over Ni/Al_2O_3 (1000), carbon dioxide is produced at higher temperatures over Au-Ni/Al_2O_3 (1000), accounting for the variation in catalytic reactivity and reducibility of $NiAl_2O_4$ over the temperature range studied.

The H_2 yield and CH_4 conversion profiles during temperature-programmed reactions over Ni/Al_2O_3 and Au-Ni/Al_2O_3 under methane-rich conditions are shown in Figure 8.10 and Figure 8.11, respectively.

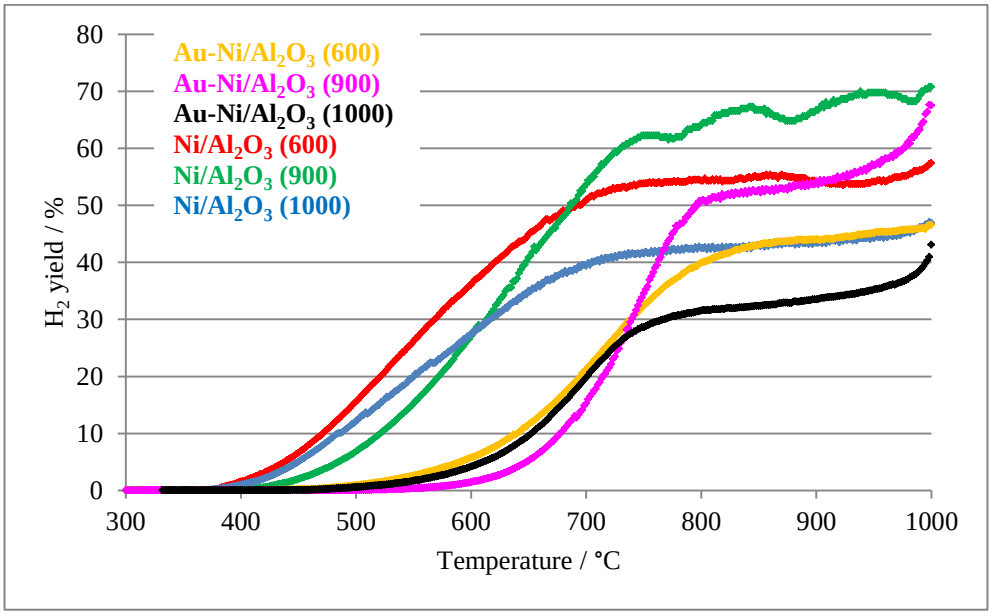

Figure 8.10: **H_2 yield during temperature-programmed reactions of methane and steam over Ni/Al_2O_3 and Au-Ni/Al_2O_3 catalysts under methane-rich reaction conditions (methane: steam = 2:1)**

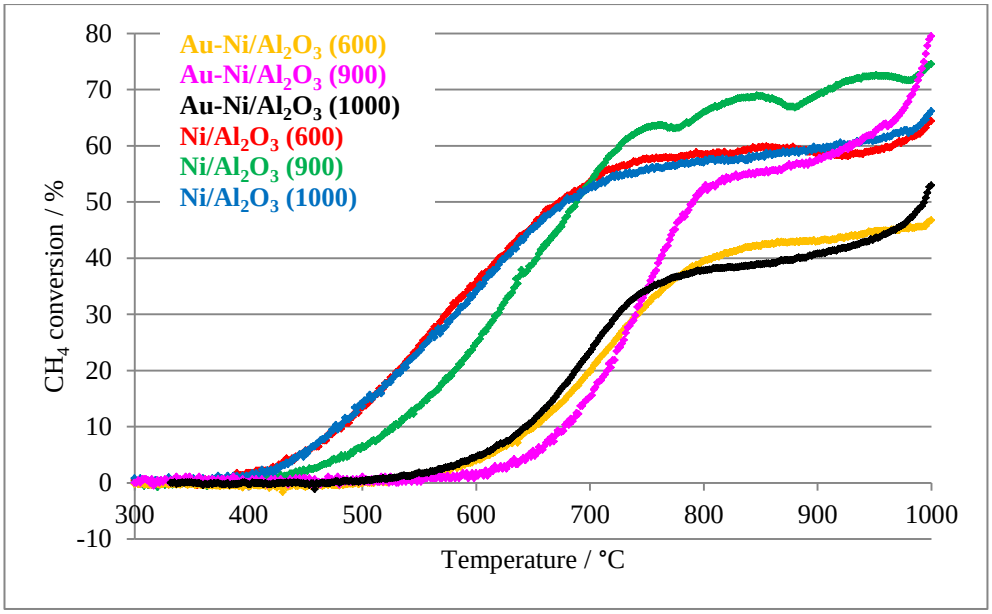

Figure 8.11: CH_4 conversion during temperature-programmed reactions of methane and steam over Ni/Al_2O_3 and $Au\text{-}Ni/Al_2O_3$ catalysts under methane-rich reaction conditions (methane: steam = 2:1)

The addition of gold to Ni/Al_2O_3 considerably lowers reactivity and onset reaction temperatures are increased by *ca.* 200 °C compared to Ni/Al_2O_3 catalysts. Although $Au\text{-}Ni/Al_2O_3$ catalysts show reduced activity at lower temperatures, all catalysts exhibit similar activity trends for a given calcination temperature. A reduction in the sensitivity of the reactivity of $Au\text{-}Ni/Al_2O_3$ catalysts to the calcination temperature is observed under methane-rich conditions, compared to stoichiometric conditions. For example under methane-rich conditions, the reaction onset temperatures of the $Au\text{-}Ni/Al_2O_3$ catalysts vary by up to *ca.* 20 °C depending on the calcination temperature, similar to Ni/Al_2O_3 catalysts.

Ni/Al_2O_3 (600) is highly active towards both methane reforming and methane decomposition at elevated temperatures. $Au\text{-}Ni/Al_2O_3$ (600) exhibits a similar activity trend, promoting methane decomposition at elevated temperatures, although the Boudouard reaction is also promoted at such temperatures. Both catalysts calcined at 900 °C are highly active towards steam reforming and methane decomposition at temperatures above 800 °C. H_2 yield is reduced by *ca.* 20 % compared to CH_4 conversion over Ni/Al_2O_3 (1000), which is attributed to the reduction of $NiAl_2O_4$ during the

reforming reaction. This is observed over Au-Ni/Al_2O_3 (1000) although not to the same extent, due to the increased stability of $NiAl_2O_4$ as shown in Chapters 4 and 5.

8.4 The influence of calcination temperature on the activity of 5 mol % Au doped 20 wt % Ni/Al_2O_3 during reactions of methane and steam under stoichiometric conditions at different reaction temperatures

The average CH_4 conversion and H_2 yield are shown in Figure 8.12 to Figure 8.14 and the average CO selectivity and H_2/CO ratio in Table 8.3 and Table 8.4, respectively for reactions of methane and steam over Au-Ni/Al_2O_3 (600), Au-Ni/Al_2O_3 (900) and Au-Ni/Al_2O_3 (1000) under stoichiometric conditions across the temperature range 500 °C to 900 °C.

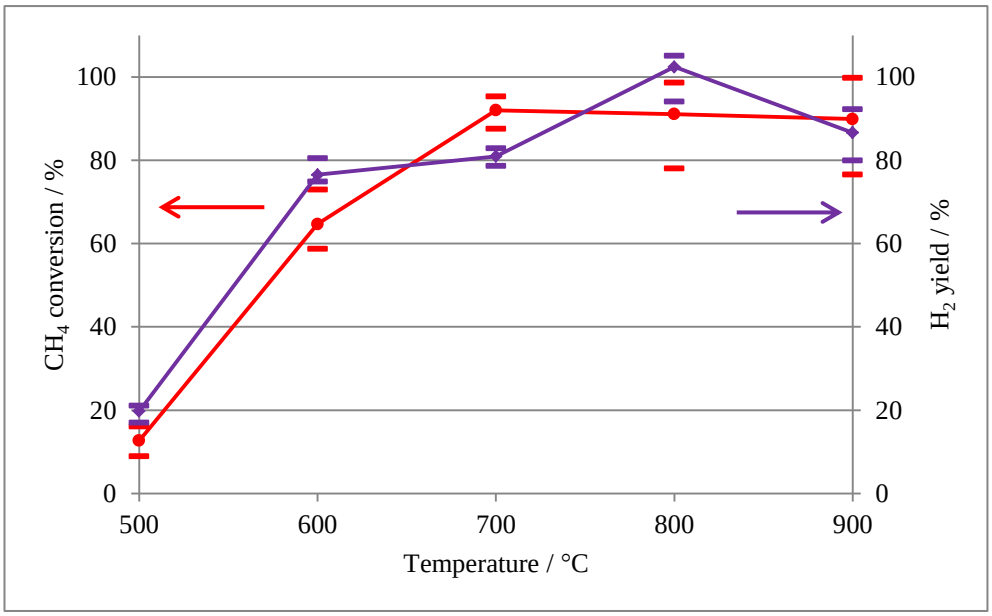

Figure 8.12: Average CH_4 conversion and H_2 yield during reactions of methane and steam over Au-Ni/Al_2O_3 (600) for 20 hours under stoichiometric conditions (methane: steam = 1:1) at reaction temperatures 500 °C to 900 °C

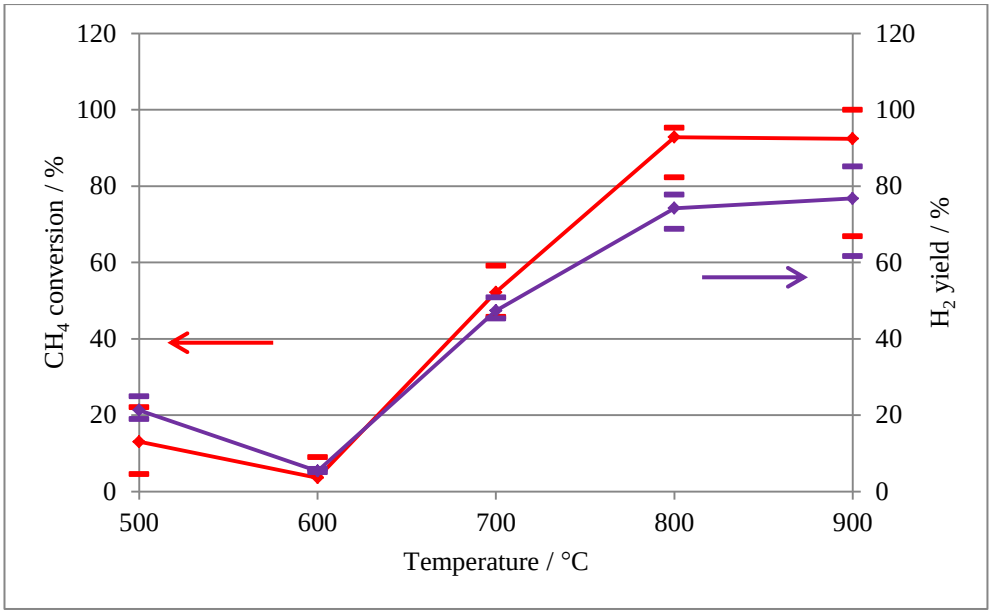

Figure 8.13: **Average CH_4 conversion and H_2 yield during reactions of methane and steam over Au-Ni/Al_2O_3 (900) for 20 hours under stoichiometric conditions (methane: steam = 1:1) at reaction temperatures 500 °C to 900 °C**

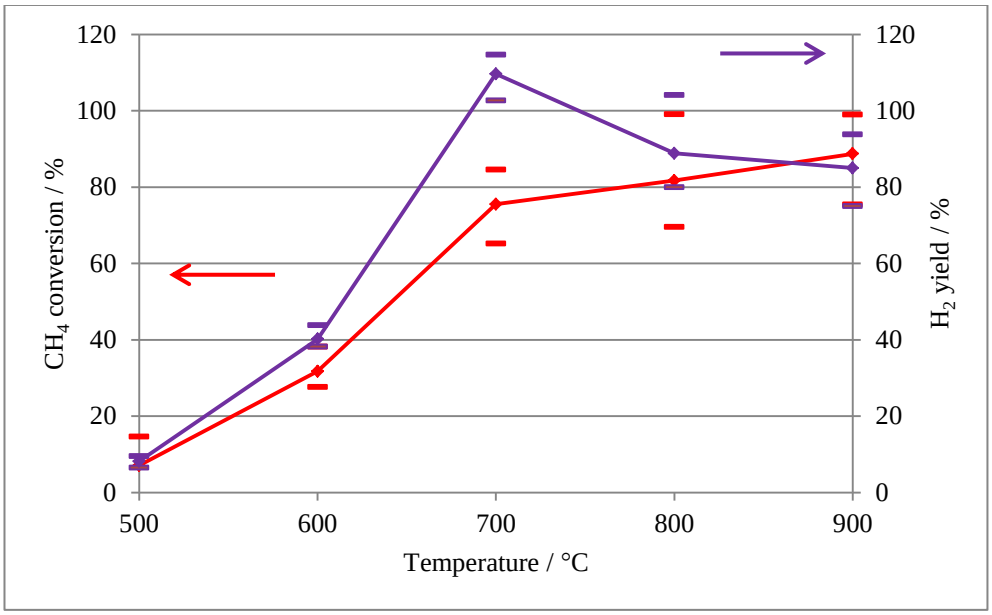

Figure 8.14: **Average CH_4 conversion and H_2 yield during reactions of methane and steam over Au-Ni/Al_2O_3 (1000) for 20 hours under stoichiometric conditions (methane: steam = 1:1) at reaction temperatures 500 °C to 900 °C**

Table 8.3: **Average CO selectivity during reactions of methane and steam over Au-Ni/Al_2O_3 (600), Au-Ni/Al_2O_3 (900) and Au-Ni/Al_2O_3 (1000) for 20 hours under stoichiometric conditions (methane: steam = 1:1) at reaction temperatures 500 °C to 900 °C**

Reaction temperature / °C	**Au-Ni/Al_2O_3 (600)**	**Au-Ni/Al_2O_3 (900)**	**Au-Ni/Al_2O_3 (1000)**
500	57	41	70
600	80	71	72
700	93	81	97
800	95	97	100
900	96	100	100

Table 8.4: **Average H_2/CO ratio during reactions of methane and steam over Au-Ni/Al_2O_3 (600), Au-Ni/Al_2O_3 (900) and Au-Ni/Al_2O_3 (1000) for 20 hours under stoichiometric conditions (methane: steam = 1:1) at reaction temperatures 500 °C to 900 °C**

Reaction temperature / °C	**Au-Ni/Al_2O_3 (600)**	**Au-Ni/Al_2O_3 (900)**	**Au-Ni/Al_2O_3 (1000)**
500	2.2	5.1	10.0
600	3.1	2.9	3.2
700	3.5	2.5	2.8
800	3.4	2.1	2.8
900	3.7	2.3	2.2

As expected from the temperature-programmed reactions, minimal reforming activity is observed over Au-Ni/Al_2O_3 (600) at 500 °C, increasing activity towards the water-gas shift reaction. Carbon deposition is observed following reaction the at 600 °C as shown in Section 8.8 and may occur via CO reduction, such that no significant change in the product gas ratio is observed. Although high reforming activities are observed at reaction temperatures above 700 °C, the H_2/CO ratios indicate that either additional hydrogen is produced or carbon monoxide is utilised in additional reactions. It is most likely that carbon monoxide is utilised during the Boudouard reaction, which accounts for the CO selectivity falling below 100 % and carbon formation observed following reactions at elevated temperatures (Section 8.8).

Extremely low steam methane reforming activity is observed over Au-Ni/Al_2O_3 (900) at 500 °C and 600 °C. Despite the low reforming activity, CO selectivity results indicate the water-gas shift reaction is highly favoured at this temperature, possibly due to the availability of excess steam not utilised in methane reforming. The occurrence of the reverse water-gas shift reaction (Reaction 8.7) may account for the low H_2/CO ratio obtained at reaction temperatures above 700 °C. Following the reaction at 900 °C, significant carbon deposition (Section 8.8) results in a 30 % reduction in CH_4 conversion over the duration of the reaction.

$$\mathbf{CO_2 + H_2 \leftrightarrow CO + H_2O} \qquad \mathbf{(8.7)}$$

Au-Ni/Al_2O_3 (1000) also exhibits very low methane reforming activity at 500 °C. As the reaction temperature is increased to 600 °C, reforming activity increases and both the H_2/CO ratio and activity data indicate that the primary reactions occurring are steam methane reforming and the water-gas shift reaction. An unexpected increase in the H_2 yield is obtained during the reaction at 700 °C, although CH_4 conversion does not follow the same trend. This activity trend is not reflected by an increase in the H_2/CO ratio obtained, therefore could be attributed to experimental error relating to the sensitivity of the mass spectrometer. Carbon deposition is observed following reactions at 800 °C and 900 °C (Section 8.8) and may be occurring via CO reduction, thus a

dramatic change in the H_2/CO ratio is not observed. However, during reaction at 900 °C the H_2/CO ratio is slightly lower than expected, which may be attributed to the reverse water-gas shift reaction occurring, following catalyst deactivation as a result of carbon deposition.

During the temperature-programmed reaction over Au-Ni/Al_2O_3 (1000), hydrogen produced during steam reforming is utilised in the reduction of $NiAl_2O_4$. However, this is not observed during reactions undertaken at elevated reaction temperatures over Au-Ni/Al_2O_3 (1000). In the temperature-programmed reduction of Au-Ni/Al_2O_3 (1000) shown in Chapter 5, the reaction was held at 1000 °C for a period of time to ensure $NiAl_2O_4$ reduction. Additionally, temperature-programmed reactions of methane and steam are conducted at temperatures above 900 °C, higher than isothermal reaction temperatures studied. This may indicate that $NiAl_2O_4$ formed during calcination of Au-Ni/Al_2O_3 (1000) is only able to be reduced during steam methane reforming reactions at temperatures above 900 °C. Thus, no trend relating to the reduction of the $NiAl_2O_4$ phase is observed during steam reforming reactions at temperatures below 900 °C.

In summary, a significant variation in catalytic activity and selectivity is observed over Au-Ni/Al_2O_3 catalysts under stoichiometric reaction conditions. Low temperature reactivity is significantly influenced by calcination temperature and minimal reforming activity is observed during reactions at 500 °C. Au-Ni/Al_2O_3 (900) is least active at low reaction temperatures, whereas Au-Ni/Al_2O_3 (600) is highly active at reaction temperatures above 600 °C.

8.5 The influence of gold addition to 20 wt % Ni/Al_2O_3 on the activity during reactions of methane and steam under stoichiometric conditions at different reaction temperatures

The average CH_4 conversion and H_2 yield data are presented in Figure 8.15, Figure 8.16 and Figure 8.17 for reactions over Ni/Al_2O_3 and Au-Ni/Al_2O_3 calcined at 600 °C, 900 °C and 1000 °C under stoichiometric conditions across the temperature range 500 °C to 900 °C.

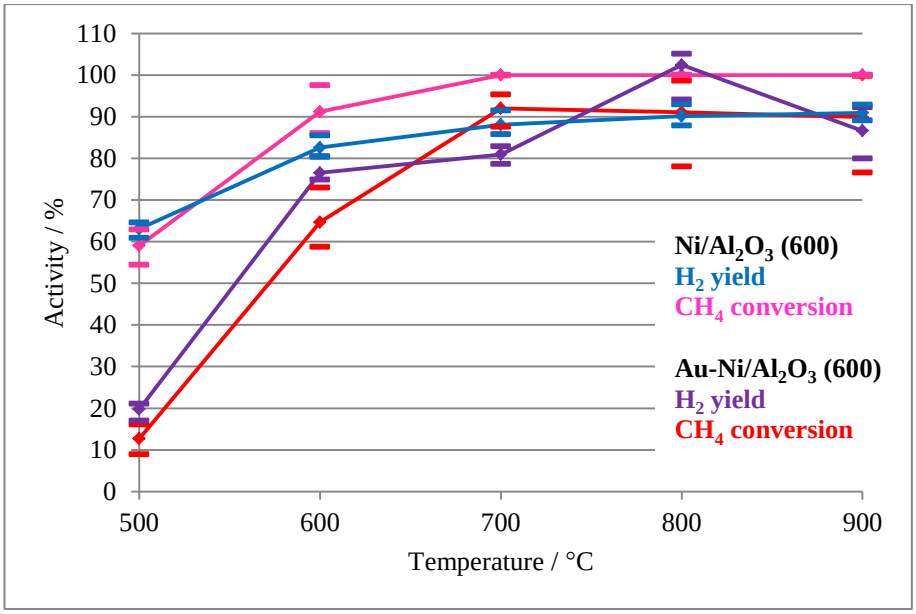

Figure 8.15: **Average CH_4 conversion and H_2 yield during reactions over Ni/Al_2O_3 (600) and Au-Ni/Al_2O_3 (600) for 20 hours under stoichiometric conditions (methane: steam = 1:1) at reaction temperatures 500 °C to 900 °C**

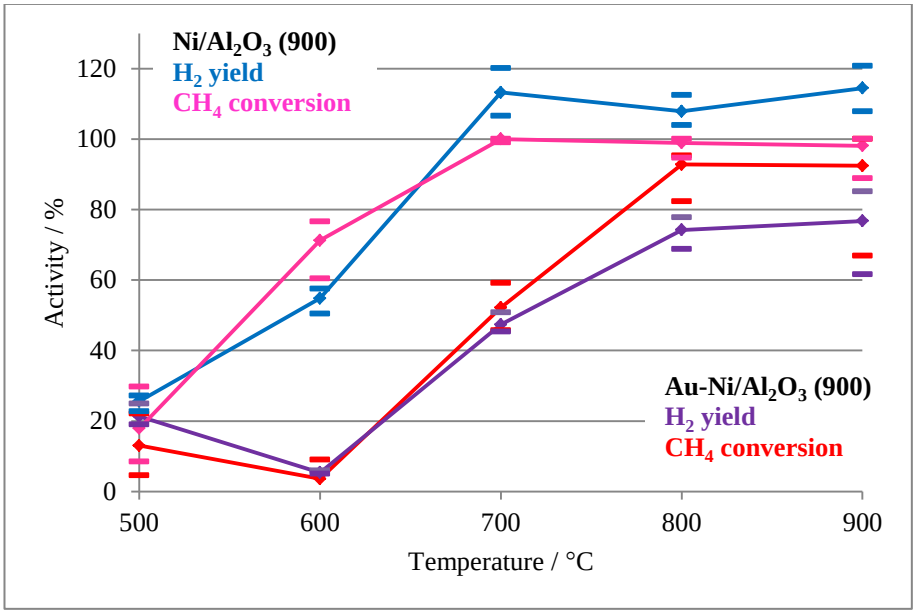

Figure 8.16: **Average CH_4 conversion and H_2 yield during reactions over Ni/Al_2O_3 (900) and Au-Ni/Al_2O_3 (900) for 20 hours under stoichiometric conditions (methane: steam = 1:1) at reaction temperatures 500 °C to 900 °C**

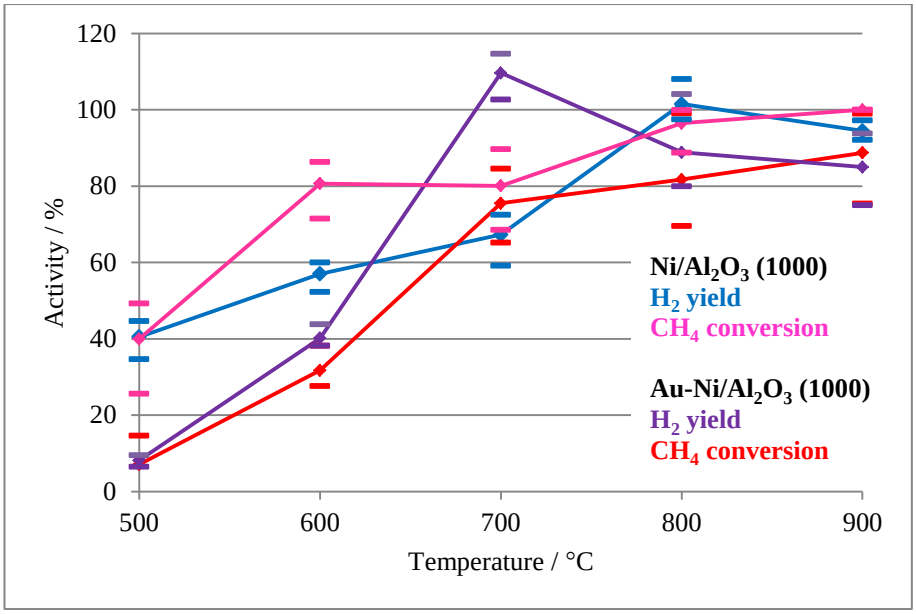

Figure 8.17: Average CH_4 conversion and H_2 yield during reactions over Ni/Al_2O_3 (1000) and Au-Ni/Al_2O_3 (1000) for 20 hours under stoichiometric conditions (methane: steam = 1:1) at reaction temperatures 500 °C to 900 °C

The addition of gold to Ni/Al_2O_3 subsequently calcined at 600 °C results in *ca*. 60 % reduction in activity at 500 °C, as shown in Figure 8.15. However, for reactions at temperatures above 600 °C, activity is only reduced by *ca*.10 %. With the exception of the significantly reduced activity at low temperatures, the most significant change following gold-doping Ni/Al_2O_3 (600) is the suppression of carbon gasification (Reaction 8.8) at temperatures above 700 °C, resulting in increased carbon deposition over Au-Ni/Al_2O_3 at temperatures above 600 °C (Section 8.8).

$$\mathbf{C + H_2O \rightarrow CO + H_2} \qquad \mathbf{(8.8)}$$

Both Ni/Al_2O_3 and Au-Ni/Al_2O_3 calcined at 600 °C promote the Boudouard reaction at elevated temperatures, although carbon gasification over Ni/Al_2O_3 (600) effectively reduces carbon laydown. With the exception of carbon removal reactions and low temperature activity, the addition of gold does not significantly influence the water-gas shift and steam methane reforming activity during reactions above 600 °C.

Low temperature activity is reduced by up to 40 % following the addition of gold to Ni/Al_2O_3 (900) as shown in Figure 8.16. Over Ni/Al_2O_3 (900), carbon deposition occurs via the Boudouard reaction and CO reduction, at reaction temperatures below 600 °C. However, following the addition of gold and the subsequent reduction in low temperature catalytic activity, carbon deposition is inhibited. At reaction temperatures above 700 °C, the formation of hydrogen by H_2O dissociation is catalysed over Ni/Al_2O_3 (900), acting to limit carbon deposition via carbon gasification. However, this is not observed over $Au\text{-}Ni/Al_2O_3$ (900) and carbon is formed at 900 °C via the Boudouard reaction (Section 8.8).

There is no indication of $NiAl_2O_4$ reduction during reforming reactions under stoichiometric conditions over $Au\text{-}Ni/Al_2O_3$ (1000). This is due in part to the reduced reforming activity, thus a lesser reducing environment, and in part due to the increased stability of $NiAl_2O_4$ in $Au\text{-}Ni/Al_2O_3$ (1000), than Ni/Al_2O_3 (1000). With the exception of reduced low temperature activity and the reduction of $NiAl_2O_4$, the primary reactions which occur over the catalysts calcined at 1000 °C are not significantly altered following the addition of gold.

TPO results in Section 8.8 indicate increased carbon formation following the addition of gold to Ni/Al_2O_3 catalysts. However, due to the limited reforming activity and promotion of various side reactions the exact carbon-forming reaction cannot be unequivocally deduced. The addition of gold to Ni/Al_2O_3 appears to result in the suppression of carbon gasification over all the catalysts. This is principally observed over the catalysts calcined at 900 °C, where dissociative adsorption of H_2O appears to be significantly limited. As well as CO reduction and the Boudouard reaction occurring during reforming, methane decomposition may also occur at elevated temperatures, due to the reduction in steam methane reforming activity over $Au\text{-}Ni/Al_2O_3$ catalysts.

Following gold-doping of Ni/Al_2O_3 catalysts, a significant reduction in low temperature reforming activity is exhibited. However, as the reaction temperature is increased, the influence of gold addition on activity is reduced. This could be attributed to the presence of gold on the catalyst surface, limiting the nickel surface sites available for low temperature reforming. At low reaction

temperatures gold may be well distributed across the nickel surface, limiting the amount of active nickel sites available for reforming. However, as the reaction temperature is increased gold sintering may occur to a greater extent (as discussed in Chapter 5), resulting in a reduction in active nickel sites 'blocked' by gold atoms. A schematic example of this process is shown in Figure 8.18. Thus, reforming activity at elevated reaction temperatures may be less inhibited by the addition of gold and more similar reforming activity to Ni/Al_2O_3 catalysts is observed.

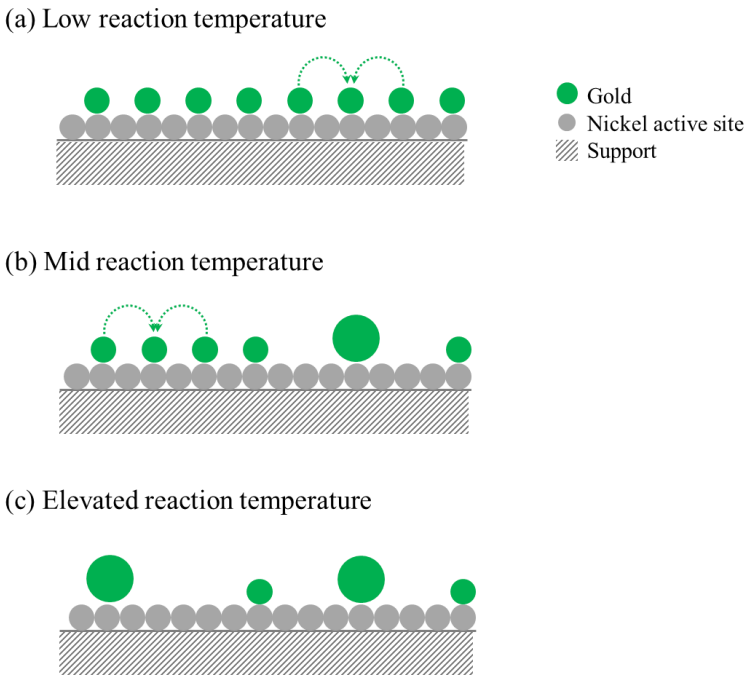

Figure 8.18: Schematic representation of increased gold sintering as reaction temperature is increased, influencing availability of active nickel sites (not to scale)

Gold-doping of Ni/Al_2O_3 catalysts, results in a significant reduction in reforming activity at low reaction temperatures, with minimal change in reforming activity at high temperature reforming. Under stoichiometric reaction conditions, gold-doping of Ni/Al_2O_3 catalysts appears to inhibit carbon gasification reactions leading to increased carbon build up compared to Ni/Al_2O_3 catalysts.

8.6 The influence of calcination temperature on the activity of 5 mol % Au doped 20 wt % Ni/Al_2O_3 during reactions of methane and steam under methane-rich conditions at different reaction temperatures

Reactions of methane and steam over Au-Ni/Al_2O_3 (600) under methane-rich conditions were initially conducted for 20 hours. However, this resulted in significant carbon deposition leading to a physical blockage of the quartz reactor tube, ultimately resulting in the quartz reactor tube breaking. The reaction profile obtained for the reaction of methane and steam under methane-rich conditions at 600 °C for 20 hours is shown in Figure 8.19.

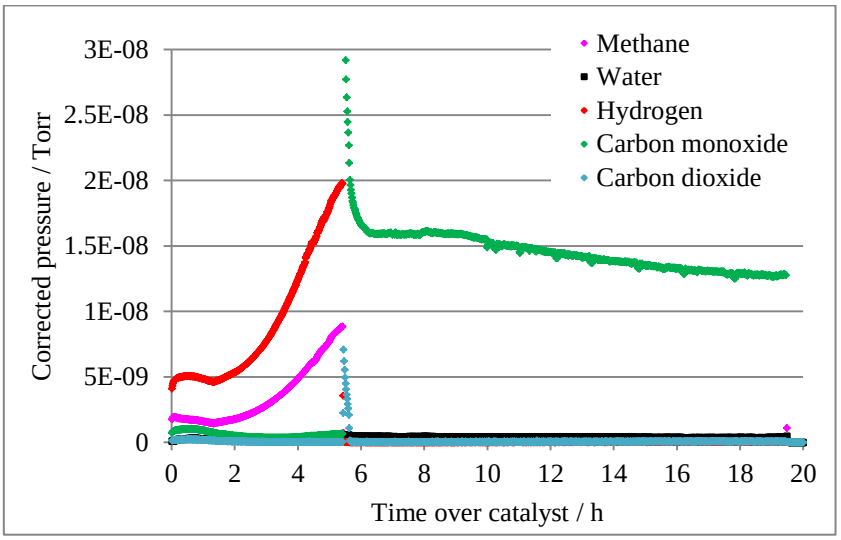

Figure 8.19: Reaction profile for reaction of methane and steam over Au-Ni/Al_2O_3 (600) at 600 °C for 20 hours under methane-rich conditions (methane: steam 2:1)

It is observed that the reactor tube becomes progressively blocked due to carbon laydown, with the reactor tube breaking after *ca.* 5.5 hours. Prior to the reactor tube breaking, a build-up of pressure is observed, causing irregularities in the gas flow observed during the reaction making subsequent data analysis problematic. As a result 20 hour reactions were not performed over Au-Ni/Al_2O_3 (600) under methane-rich conditions and instead reactions were carried out for 2 hours. This ensured that catalyst activity prior to significant carbon deposition was able to be monitored, thus activity data for reactions over Au-Ni/Al_2O_3 (600) is taken from 2 hour reaction profiles.

The average CH_4 conversion, H_2 yield and H_2 yield profiles are shown in Figure 8.20 to Figure 8.25 and the CO selectivity and H_2/CO ratios are shown in Table 8.5 and Table 8.6 respectively, for reactions of methane and steam over Au-Ni/Al_2O_3 (600), Au-Ni/Al_2O_3 (900) and Au-Ni/Al_2O_3 (1000) under methane-rich conditions across the temperature range 500 °C to 900 °C.

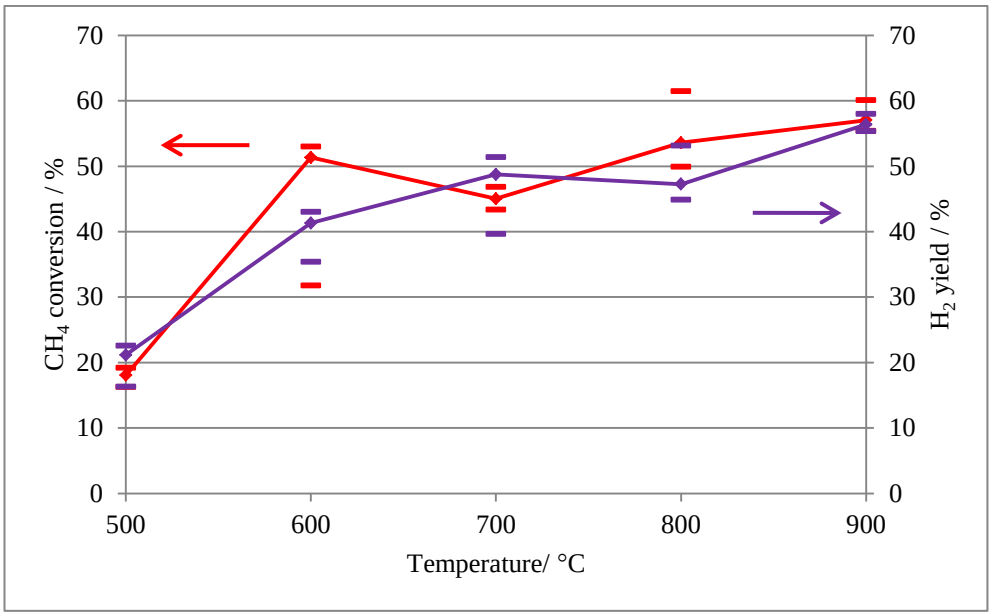

Figure 8.20: Average CH_4 conversion and H_2 yield during reactions of methane and steam over Au-Ni/Al_2O_3 (600) for 2 hours under methane-rich conditions (methane: steam = 2:1) at reaction temperatures 500 °C to 900 °C

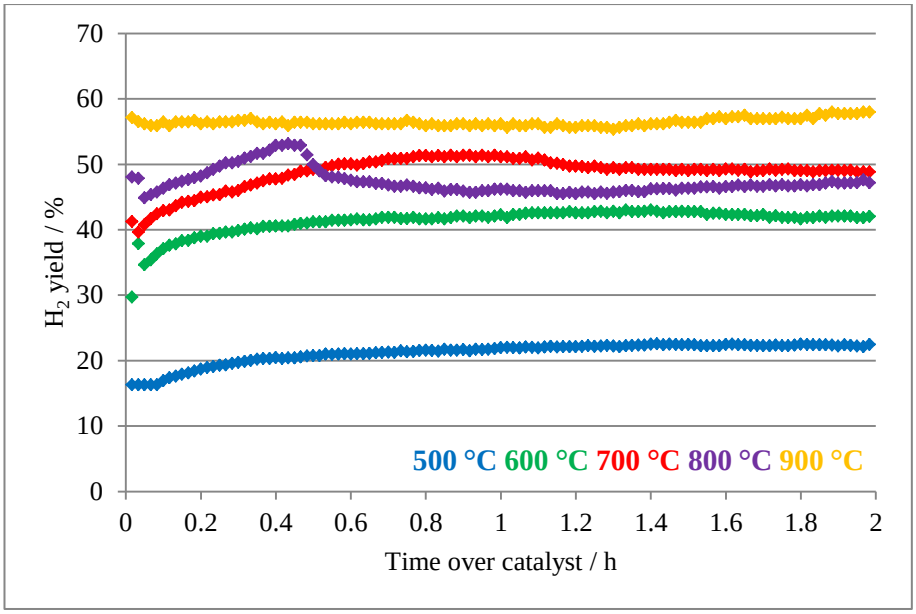

Figure 8.21: **H_2 yield profiles for reactions of methane and steam over Au-Ni/Al_2O_3 (600) for 2 hours under methane-rich conditions (methane: steam = 2:1) at reaction temperatures 500 °C to 900 °C**

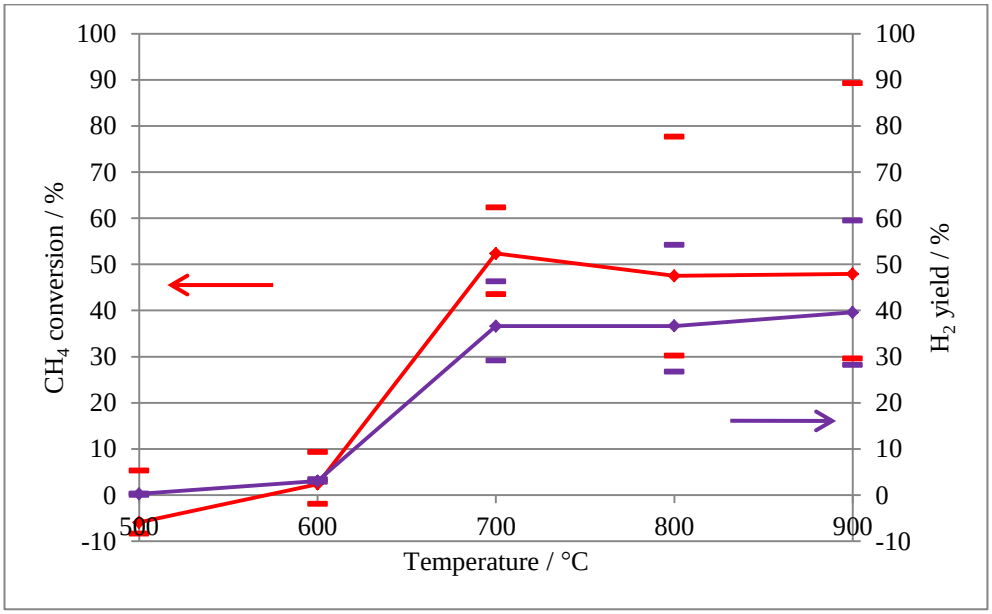

Figure 8.22: **Average CH_4 conversion and H_2 yield during reactions of methane and steam over Au-Ni/Al_2O_3 (900) for 20 hours under methane-rich conditions (methane: steam = 2:1) at reaction temperatures 500 °C to 900 °C**

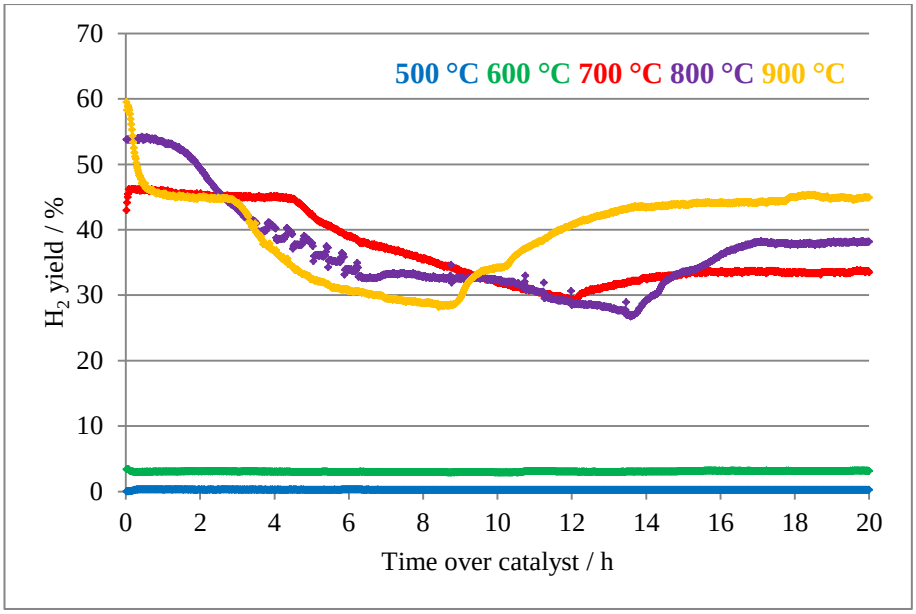

Figure 8.23: **H_2 yield profiles for reactions of methane and steam over Au-Ni/Al_2O_3 (900) for 20 hours under methane-rich conditions (methane: steam = 2:1) at reaction temperatures 500 °C to 900 °C**

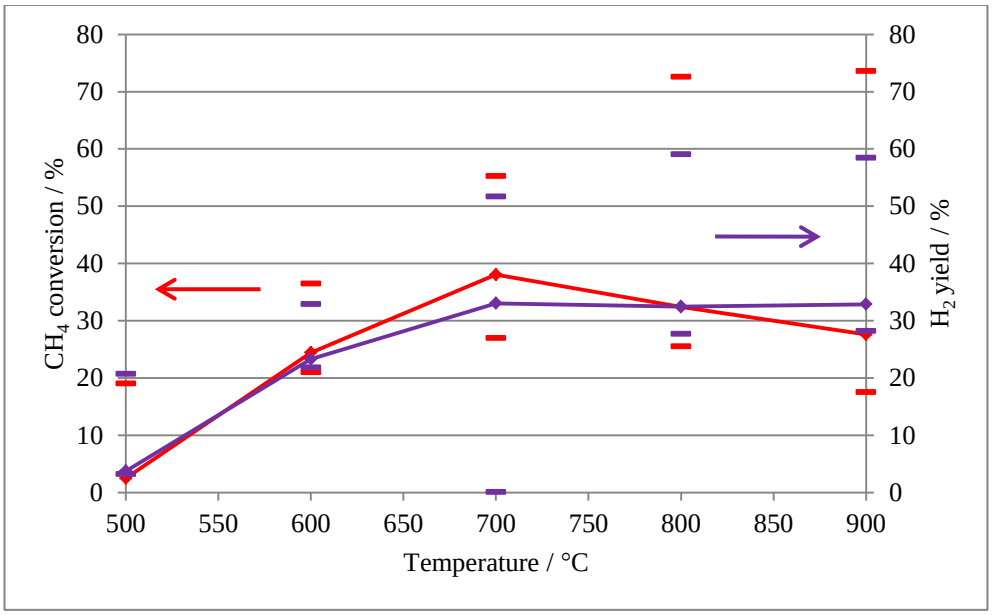

Figure 8.24: **Average CH_4 conversion and H_2 yield during reactions of methane and steam over Au-Ni/Al_2O_3 (1000) for 20 hours under methane-rich conditions (methane: steam = 2:1) at reaction temperatures 500 °C to 900 °C**

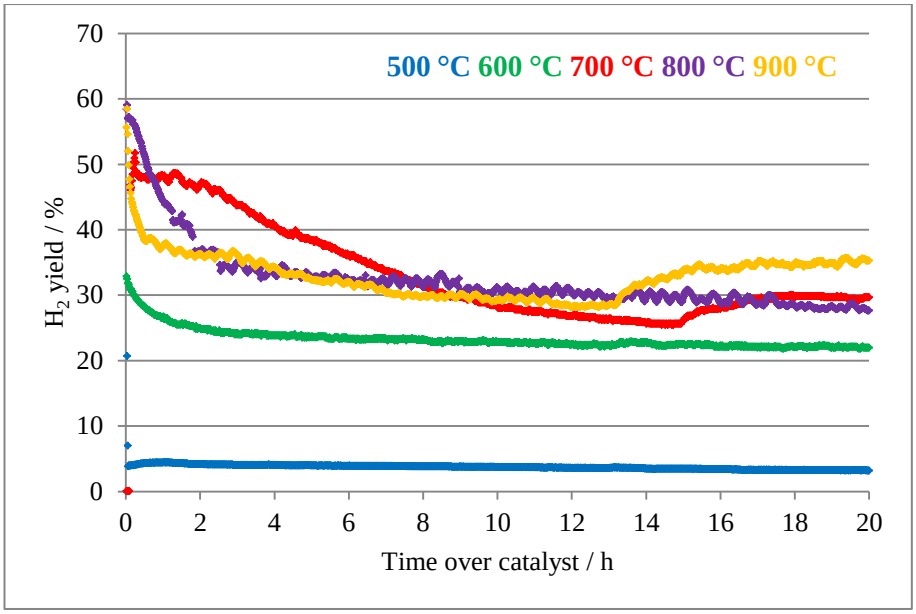

Figure 8.25: **H_2 yield profiles for reactions of methane and steam over Au-Ni/Al_2O_3 (1000) for 20 hours under methane-rich conditions (methane: steam = 2:1) at reaction temperatures 500 °C to 900 °C**

Table 8.5: **Average CO selectivity during reactions of methane and steam over Au-Ni/Al_2O_3 (600), Au-Ni/Al_2O_3 (900) and Au-Ni/Al_2O_3 (1000) under methane-rich conditions at reaction temperatures 500 °C to 900 °C**

Reaction temperature / °C	**Au-Ni/Al_2O_3 (600)***	**Au-Ni/Al_2O_3 (900)**	**Au-Ni/Al_2O_3 (1000)**
500	70	100	46
600	82	76	77
700	92	99	99
800	95	100	100
900	100	100	100

* 2 hour reaction

Table 8.6: Average H_2/CO ratio during reactions of methane and steam over Au-Ni/Al_2O_3 (600), Au-Ni/Al_2O_3 (900) and Au-Ni/Al_2O_3 (1000) under methane-rich conditions at reaction temperatures 500 °C to 900 °C

Reaction temperature / °C	Au-Ni/Al_2O_3 (600)*	Au-Ni/Al_2O_3 (900)	Au-Ni/Al_2O_3 (1000)
500	2.3	1.4	4.8
600	4.3	2.4	2.5
700	3.9	2.5	1.9
800	4.2	2.1	1.8
900	4.2	1.8	1.3

* 2 hour reaction

No apparent catalyst deactivation is observed at any reaction temperature, over Au-Ni/Al_2O_3 (600) over the 2 hour reaction period (Figure 8.21). At 500 °C minimal reforming activity is observed as expected from the temperature-programmed reaction studies shown in Section 8.2. As the reaction temperature is increased to 600 °C, catalytic activity is significantly improved by *ca.* 30 %. Significant carbon deposition is observed (Section 8.8), formed via the Boudouard reaction. Similar reaction pathways are occurring at 700 °C, although the Boudouard reaction may be occurring to a marginally reduced extent. Above 800 °C, the primary reactions occurring are steam methane reforming and methane decomposition, resulting in a high H_2/CO ratio and CH_4 conversion exceeding 50 %. A shift from the Boudouard reaction to methane decomposition occurs for reaction temperatures above 800 °C with both reactions resulting in considerable carbon deposition on the catalyst surface following only 2 hours of the reaction. Despite considerable carbon deposition no apparent catalyst deactivation is observed. This may indicate that the carbon formed during methane-rich reactions over Au-Ni/Al_2O_3 (600), is not significantly detrimental towards the activity of the catalyst, but results primarily in the mechanical damage of the reactor system due to

the extent of carbon formation, as observed during the 20 hour reaction shown in Figure 8.19 [10]. As noted previously in Chapter 7, Sahli *et al*. [11] have demonstrated that catalysts shown to have 'free' nickel with minimal interactions with the support give rapid deactivation through carbon formation. Characterisation studies of calcined samples in Chapter 5 showed Ni^{2+} has weak interactions with the alumina support following calcination at 600 °C, which may be contributing to the significant carbon deposition observed.

Au-Ni/Al_2O_3 (900) has extremely low reforming activity at 500 °C and 600 °C. As the reaction temperature is increased the activity increases considerably. However, rapid deactivation is observed over the first few hours of the reaction, followed by continuous deactivation over the course of the reaction. The high CH_4 conversion during the initial period of the reaction indicates that deactivation is due to carbon deposition formed via methane decomposition. Similar reaction characteristics are observed over Au-Ni/Al_2O_3 (1000). Minimal activity is observed at low reaction temperatures, with activity increasing with reaction temperature and the Boudouard reaction and/or CO reduction also promoted. Above 700 °C, significant catalyst deactivation is observed and a reduction of *ca.* 30 % in activity is observed over the course of the reaction, attributed to carbon formation via methane decomposition. Following initial deactivation, the reverse water-gas shift reaction may be occurring, accounting for the low H_2/CO ratio observed.

The similarities in the reforming characteristics of Au-Ni/Al_2O_3 catalysts calcined at 900 °C and 1000 °C can be accounted for by the results presented in Chapter 5. It was shown by XRD and XPS that the formation of $NiAl_2O_4$ occurs during calcination of Au-Ni/Al_2O_3 at 900 °C and 1000 °C and both catalysts exhibit similar TPR profiles. The variation in low temperature activity between the two catalysts may be due to differences in the distribution of gold on the surface and/or differences in morphologies identified during SEM analysis, limiting reforming activity to different extents.

As discussed in Section 8.5, as the reaction temperature is increased sintering of the gold particles on the catalyst surface may occur, resulting in similar reforming activities at high reaction temperatures over the catalysts studied.

8.7 The influence of gold addition to 20 wt % Ni/Al_2O_3 on the activity during reactions of methane and steam under methane-rich conditions at different reaction temperatures

The average CH_4 conversion and H_2 yield data are presented in Figure 8.26 - Figure 8.28 for reactions under methane-rich conditions over Ni/Al_2O_3 and $Au\text{-}Ni/Al_2O_3$ calcined at 600 °C, 900 °C and 1000 °C across the temperature range 500 °C to 900 °C.

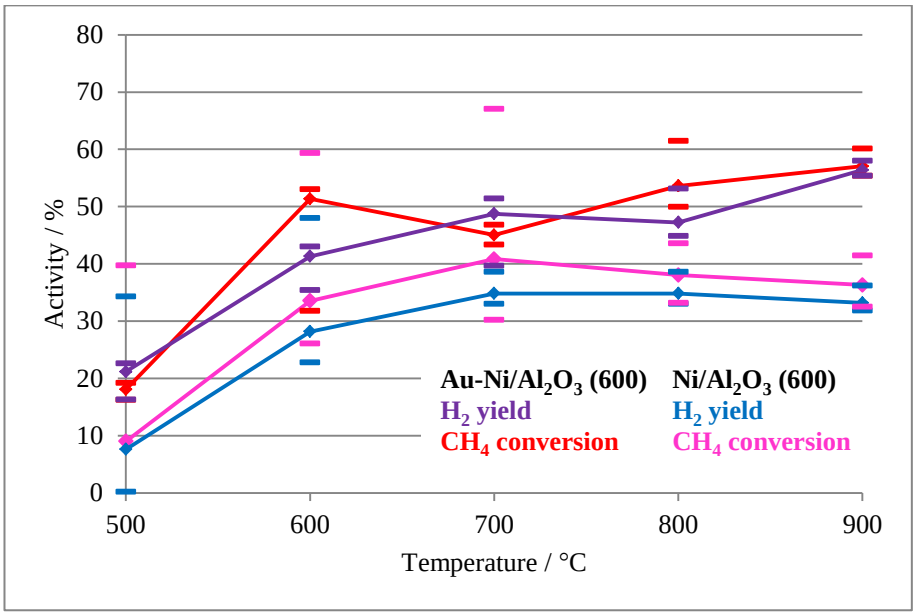

Figure 8.26: Average CH_4 conversion and H_2 yield during reactions over Ni/Al_2O_3 (600) for 20 hours and $Au\text{-}Ni/Al_2O_3$ (600) for 2 hours under methane-rich conditions (methane: steam = 2:1) at reaction temperatures 500 °C to 900 °C

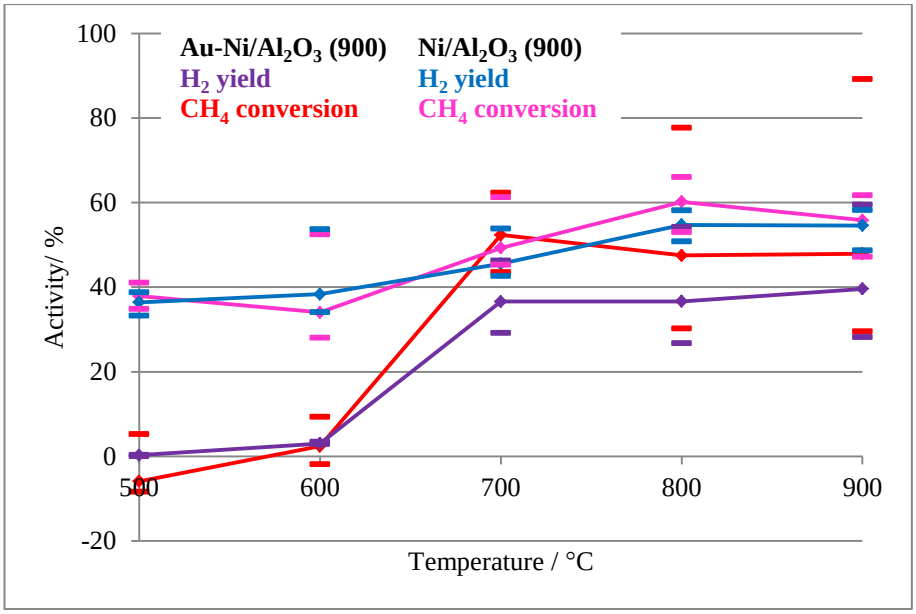

Figure 8.27: **Average CH_4 conversion and H_2 yield during reactions over Ni/Al_2O_3 (900) and $Au\text{-}Ni/Al_2O_3$ (900) for 20 hours under methane-rich conditions (methane: steam = 2:1) at reaction temperatures 500 °C to 900 °C**

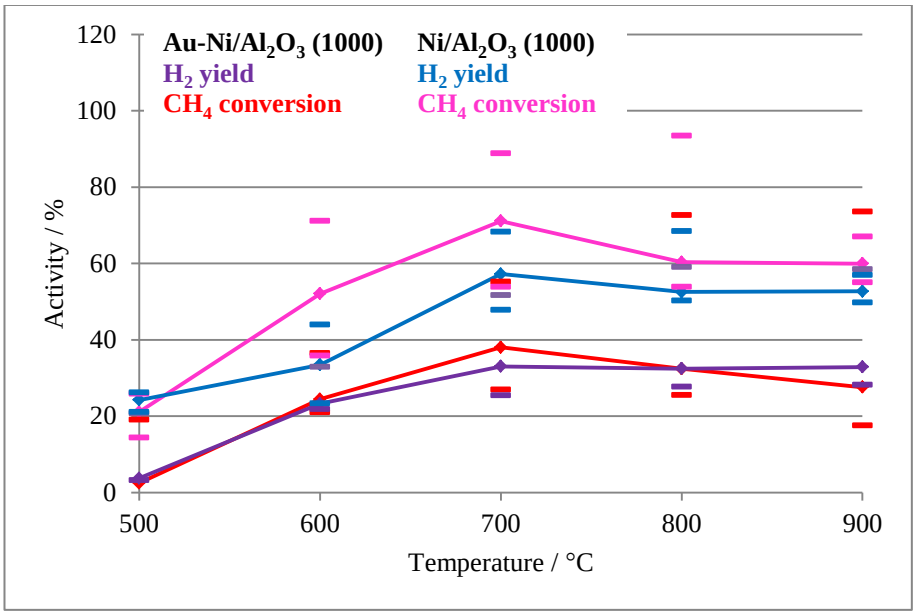

Figure 8.28: **Average CH_4 conversion and H_2 yield during reactions over Ni/Al_2O_3 (1000) and $Au\text{-}Ni/Al_2O_3$ (1000) for 20 hours under methane-rich conditions (methane: steam = 2:1) at reaction temperatures 500 °C to 900 °C**

As under stoichiometric conditions, the addition of gold to Ni/Al_2O_3 results in the promotion of steam reforming and carbon-forming reactions to varying extents over the reforming temperatures studied.

It may appear from Figure 8.26 that Ni/Al_2O_3 (600) has a lower activity than Au-Ni/Al_2O_3 (600), over the temperature range studied. However, these results must be viewed with caution due to the different lengths of time the reactions were studied for; Ni/Al_2O_3 (600) was studied for 20 hours and Au-Ni/Al_2O_3 (600) for 2 hours. Prior to deactivation, the maximum activity of Ni/Al_2O_3 (600) for reactions below 700 °C is higher than Au-Ni/Al_2O_3 (600). The low average activity of Ni/Al_2O_3 (600) is attributed to catalyst deactivation over time, which is not observed over Au-Ni/Al_2O_3 (600). For reactions above 700 °C, Au-Ni/Al_2O_3 (600) promotes methane decomposition, whereas this is promoted at lower temperatures on Ni/Al_2O_3 (600). During reactions at lower temperatures both catalysts calcined at 600 °C promote the Boudouard reaction and CO reduction resulting in significant carbon deposition, which results in significant catalyst deactivation and a reduction in performance.

Activity at low temperatures is reduced by up to *ca.* 30 % following the addition of gold to Ni/Al_2O_3 catalysts calcined at 900 °C. Although average activities are comparable at temperatures above 700 °C deactivation is increased over Au-Ni/Al_2O_3 (900). Both catalysts promote methane decomposition at elevated reaction temperatures under methane-rich conditions, although the subsequent carbon formation has variable effects on catalyst activity. Methane decomposition results in significant carbon formation over Au-Ni/Al_2O_3 (900), leading to *ca*. 60 % reduction in activity at temperatures above 800 °C.

Similar activity trends are observed for the catalysts calcined at 1000 °C, to those observed for the catalysts calcined at 900 °C. Over Au-Ni/Al_2O_3 (1000), minimal activity is observed at low reaction temperatures. However, over Ni/Al_2O_3 (1000) methane decomposition is promoted at considerably low reaction temperatures resulting in a high CH_4 conversion and catalyst deactivation. As the reaction temperature is increased above 700 °C methane decomposition occurs over Au-Ni/Al_2O_3

(1000) and significant catalyst deactivation is evident. As for the catalysts calcined at 900 °C, methane decomposition and the resulting carbon formation has a greater impact on the activity of Au-Ni/Al_2O_3 catalysts. In addition to catalyst deactivation as a result of carbon deposition, the lower reforming activity observed over Au-Ni/Al_2O_3 (1000) at high reaction temperatures may also be a consequence of an unreduced $NiAl_2O_4$ phase.

Generally, the addition of gold to Ni/Al_2O_3 catalysts results in the suppression of low temperature methane reforming, which in turn supresses carbon deposition. However, at elevated temperatures the addition of gold to Ni/Al_2O_3 catalysts under these conditions enhances catalyst deactivation due to carbon formation.

8.8 Carbon deposition during reactions of methane and steam over 5 mol % Au doped 20 wt % Ni/Al_2O_3

8.8.1 Carbon deposition during reactions of methane and steam under stoichiometric and methane-rich reaction conditions over 5 mol % Au doped 20 wt % Ni/Al_2O_3 at different reaction temperatures

The amount of carbon deposition following reactions under methane-rich and stoichiometric conditions is shown in Figure 8.29 by solid bars and dashed bars, respectively. Note that carbon deposition following reactions over Au-Ni/Al_2O_3 (600) under methane-rich conditions cannot be accurately compared with other catalysts or reaction conditions due to reduced reaction time employed.

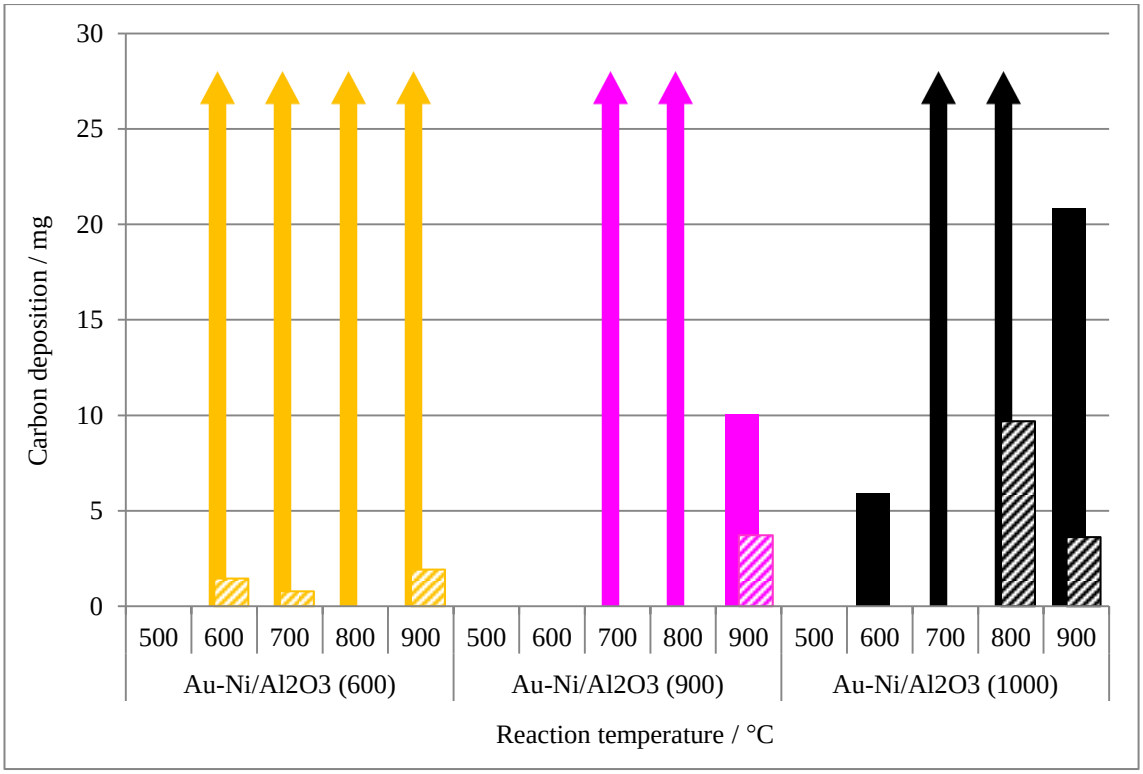

Figure 8.29: Carbon deposition following reactions of methane and steam under methane-rich conditions (solid) and stoichiometric conditions (dashed), over Au-Ni/Al_2O_3 (600), Au-Ni/Al_2O_3 (900) and Au-Ni/Al_2O_3 (1000) at different temperatures

Post-reaction TPO measurements indicate that carbon formation is not favoured at 500 °C, under either methane-rich or stoichiometric reaction conditions over any Au-Ni/Al_2O_3 catalyst. This is attributed to the reduced catalytic activity at low reaction temperatures.

During reactions under stoichiometric conditions, although levels are minimal lower temperature carbon formation is observed over Au-Ni/Al_2O_3 (600), whilst over Au-Ni/Al_2O_3 (900) and Au-Ni/Al_2O_3 (1000) deposition is favoured at temperatures above 800 °C.

During reactions under methane-rich conditions a substantial increase in carbon deposition is observed over all catalysts and reaction temperatures studied. Although carbon deposition cannot be absolutely compared for Au-Ni/Al_2O_3 (600), a significant increase in carbon deposition is observed under methane-rich conditions. Over both Au-Ni/Al_2O_3 (600) and Au-Ni/Al_2O_3 (900)

methane decomposition occurs above 800 °C resulting in considerable carbon deposition and reduced catalytic activity. However, over Au-Ni/Al_2O_3 (1000) methane decomposition occurs from 700 °C. At lower reaction temperatures, over all catalysts, carbon deposition primarily occurs via the Boudouard reaction and/or CO reduction. Due to the large quantity of carbon deposition resulting in oxygen deficient TPO reactions (as observed in Chapter 7) it is not possible to further analyse profiles, in order to define specific types of carbon formed during reforming reactions.

8.8.2 The influence of gold addition to 20 wt % Ni/Al_2O_3 on carbon deposition during reactions of methane and steam under stoichiometric and methane-rich reaction conditions at different reaction temperatures

The amount of carbon deposition following reactions under stoichiometric and methane-rich conditions over Ni/Al_2O_3 and Au- Ni/Al_2O_3 catalysts are shown in Figure 8.30 and Figure 8.31, respectively.

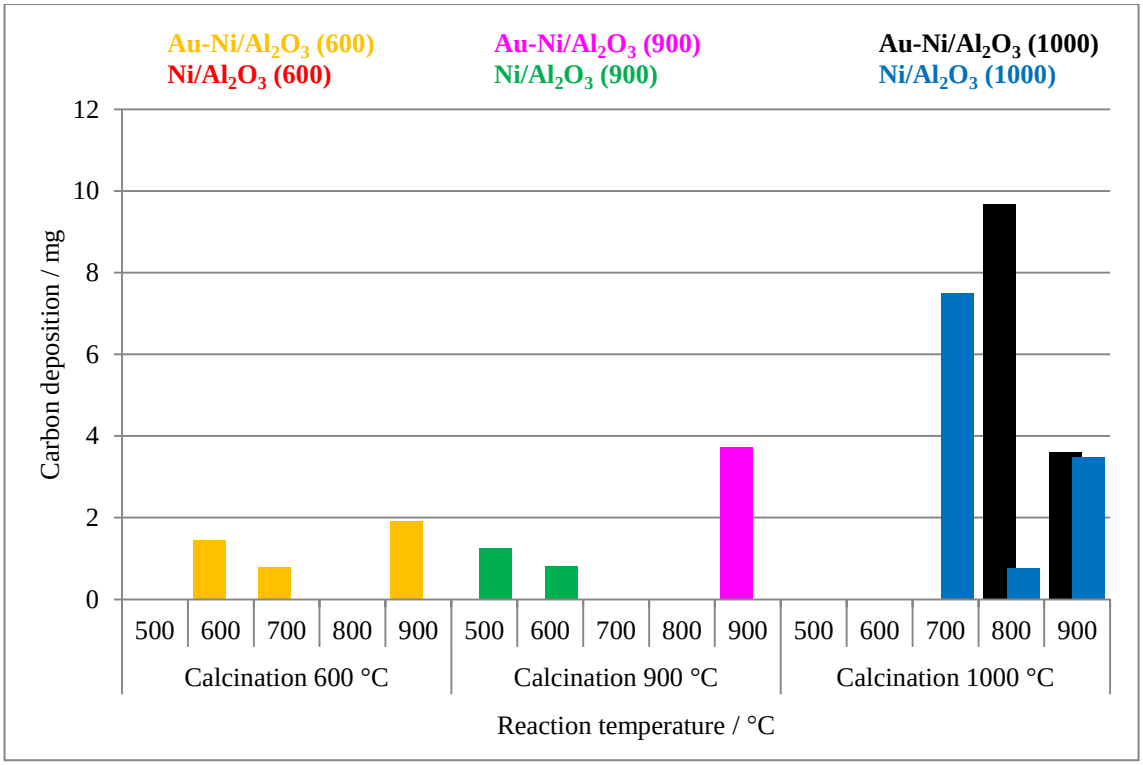

Figure 8.30: Carbon deposition following reactions of methane and steam under stoichiometric conditions at different temperatures over Au-Ni/Al_2O_3 and Ni/Al_2O_3 calcined at 600 °C, 900 °C and 1000 °C

Minimal carbon deposition is observed following reactions under stoichiometric conditions over both Au-Ni/Al_2O_3 and Ni/Al_2O_3 catalysts. For the catalyst calcined at 600 °C an increase in carbon deposition is observed following gold-doping, over most temperatures studied. However, carbon deposition levels are extremely low and do not result in catalyst deactivation. This may be attributed to some reduction in carbon gasification over Au-Ni/Al_2O_3 (600).

It has been shown in Chapter 6 that Ni/Al_2O_3 (900) promotes the dissociative adsorption of H_2O at high reaction temperatures, increasing carbon gasification and inhibiting carbon formation. However, following the addition of gold to Ni/Al_2O_3 (900), carbon deposition is observed at 900 °C. Gold appears to supress H_2O adsorption and thus reduce carbon gasification. Over catalysts calcined at 1000 °C, no low temperature carbon formation is observed due to the presence of

inactive unreduced $NiAl_2O_4$. However, at temperatures above 800 °C, methane decomposition is favoured and carbon deposition is increased over Au-Ni/Al_2O_3 (1000).

In general, following the addition of gold to Ni/Al_2O_3 catalysts, carbon deposition is increased during reactions under stoichiometric conditions. However, during reactions at temperatures below 600 °C, catalytic activity is significantly reduced following the addition of gold and as a result no or minimal carbon deposition is observed.

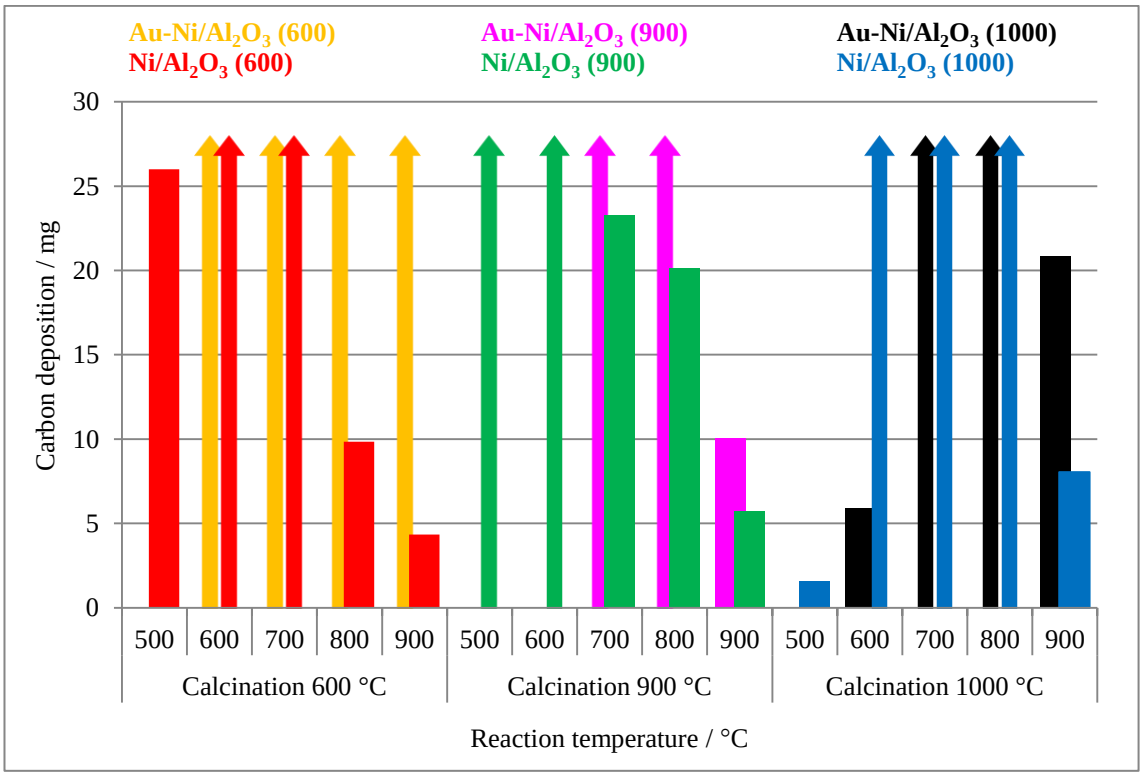

Figure 8.31: Carbon deposition following reactions of methane and steam under methane-rich conditions at different temperatures over Au-Ni/Al_2O_3 and Ni/Al_2O_3 calcined at 600 °C, 900 °C and 1000 °C

Over all Au-Ni/Al_2O_3 catalysts, carbon deposition is minimal for reaction temperatures at and below 600 °C due to the low catalytic activity. Over both Ni/Al_2O_3 and Au-Ni/Al_2O_3 calcined at 600 °C substantial carbon laydown is observed following reactions. It has been shown that carbon deposition during the reaction over Ni/Al_2O_3 (600) at 500 °C, results in a complete loss of

reforming activity. However, due to the limited reforming activity of Au-Ni/Al_2O_3 catalysts at 500 °C, no carbon is observed following this reaction. During reactions at temperatures between 500 °C and 700 °C, both the Boudouard reaction and CO reduction occur and at temperatures above 700 °C methane decomposition is promoted. Following the addition of gold to Ni/Al_2O_3 catalysts calcined at 900 °C and 1000 °C, although carbon deposition is increased, no change in carbon-forming trends is observed.

Niakolas *et al.* [12] have shown that the calcination temperature selected during preparation of Au-Ni catalysts can influence the carbon tolerance and that higher calcination temperatures result in an increase in the thermally induced nickel particle size, lowering nickel active sites available for CH_4 dissociation and carbon formation. Further analysis of the type of carbon formed during reforming reactions over both Ni/Al_2O_3 and Au-Ni/Al_2O_3, using SEM, TEM and XPS analysis and vibrational spectroscopy and inelastic neutron scattering spectroscopy (see Appendix D) might give greater insight into the influence of both the calcination temperature and gold addition on the nature of the specific carbon formed during steam methane reforming reactions. This would be particularly useful to compare the type of carbon formed on Au-Ni/Al_2O_3 (600) compared to that formed on Au-Ni/Al_2O_3 (900) and (1000).

8.9 Summary

Both the calcination temperature employed and the presence of gold have resulted in a significant difference between the reforming characteristics of Au-Ni/Al_2O_3 catalysts over the temperature range studied, including low temperature reactivity, $NiAl_2O_4$ reduction and the activity of side-reactions, such as the reverse water-gas shift reaction and carbon formation.

Following the addition of gold to Ni/Al_2O_3 catalysts, low temperature reforming activity is substantially inhibited. During temperature-programmed reactions Au-Ni/Al_2O_3 catalysts exhibit an increase of more than 200 °C in the product gas onset temperatures compared to Ni/Al_2O_3 catalysts.

Catalyst activity is influenced to a lesser extent at higher reaction temperatures. The reduction in activity at low temperatures over Au-Ni/Al_2O_3 catalysts may be attributed to the distribution of gold on the catalyst surface, inhibiting nickel active surface sites. As the reaction temperature is increased, gold sintering may occur, increasing available nickel surface sites and therefore reforming activity, as shown in Figure 8.18. Similarly, Chin *et al*. [3] have also demonstrated that the effect of gold was shown to be more pronounced at lower temperatures during characterisation studies, than during high temperatures employed during steam methane reforming. The calcination temperature used during preparation of Au-Ni/Al_2O_3 catalysts has also been shown to significantly influence the catalyst behaviour. For example, during reactions of methane and steam over Au-Ni/Al_2O_3 (900) activity is significantly reduced under both stoichiometric and methane-rich reaction conditions, compared to Au-Ni/Al_2O_3 (600) and Au-Ni/Al_2O_3 (1000).

Despite the identification of $NiAl_2O_4$ during post-reduction XRD studies and reduction during the reverse temperature-programmed reaction over Au-Ni/Al_2O_3 (1000), the reduction of $NiAl_2O_4$ during isothermal reactions is not observed. As well as the increased stability of $NiAl_2O_4$ in Au-Ni/Al_2O_3 (1000) and requirement for high reduction temperatures, it has also been shown by Chin *et al*. [3] that gold promoted catalysts exhibit a reduction in hydrogen uptake during TPR reactions, attributed to the position of Au atop Ni sties. This could explain why reduction of $NiAl_2O_4$ is not observed during isothermal reactions over Au-Ni/Al_2O_3 (1000). The unreduced $NiAl_2O_4$ phase may also be a contributing factor towards the limited activity observed during reactions over Au-Ni/Al_2O_3 (1000) [13].

The addition of gold to Ni/Al_2O_3 catalysts and the calcination temperature used during catalyst preparation both also influence carbon deposition characteristics. Over Au-Ni/Al_2O_3 catalysts the occurrence of methane decomposition due to incomplete steam methane reforming results in a significant increase in carbon deposition, under both methane-rich and stoichiometric conditions. This differs from previous research [3, 5-7, 12] which shows significantly reduced carbon deposition over gold promoted catalysts. However, Chin *et al.* [3] show that gold promoted catalysts inhibit coke formation most effectively at 450 °C and to a decreasing extent at high

reaction temperatures. Additionally, most of the previous studies have been undertaken at lower reaction temperatures than those employed in this work. As well as increasing carbon-formation reactions, gold also appears to inhibit adsorption of H_2O and carbon gasification in the presence of steam, contributing to the increase in carbon deposition observed during reforming. This is most significantly observed over Au-Ni/Al_2O_3 (900).

Studies shown in Chapter 5 detail catalyst characteristics following preparation (calcination) and activation (reduction). Post-calcination XRD results show diffraction peaks characteristic of nickel oxide and gold, present in the profiles of all Au-NiO/Al_2O_3 catalysts. Following reduction in hydrogen, nickel oxide is reduced to metallic nickel and thus identified in all XRD profiles. Additionally, distinct gold peaks are also observed in all post-reduction XRD profiles. Following gold-doping of Ni/Al_2O_3 catalysts, no detectible shift in the diffraction peak position of either nickel oxide or nickel are observed. In addition, the XPS Ni 2p spectra for Au-NiO/Al_2O_3 catalysts indicate no change in the Ni^{2+} binding energy following the addition of gold to catalysts. Following reduction of Au-Ni/Al_2O_3 catalysts, Ni 2p spectra obtained were not representative of metallic nickel due to re-oxidation during sample preparation. However, the Au 4f spectra showed distinct gold peaks indicating that gold particles may be highly dispersed on the surface following reduction in hydrogen.

The results obtained in this study suggest that following calcination, the majority of gold species are present within the bulk of the sample. However, following reduction, gold is observed both on the catalyst surface by XPS and in the bulk by XRD. There is no indication of a shift in nickel XRD peak positions and thus no change in the lattice parameters of nickel, following gold-doping of the Ni/Al_2O_3 catalyst or reduction in hydrogen. The results confirm that the formation of a nickel-gold alloy during either calcination or reduction is highly unlikely.

No significant interaction between gold and nickel oxide is observed following catalyst calcination of any Au-Ni/Al_2O_3 catalysts [3]. However, results obtained for Au-Ni/Al_2O_3 catalysts following reduction notably contrast with much literature, in that it is widely reported [2, 12, 14] following

reduction diffraction peaks corresponding to a gold phase are not observed, suggesting the absence of bulk gold particles. Maniecki *et al.* [2] also demonstrate that following high temperature reduction, a gradual shift in the nickel XRD diffraction peaks are observed, up to a 2θ value of 4°, and metallic gold peaks are no longer observed. Such modifications in the catalyst structure are attributed to the formation of a surface nickel-gold alloy [2, 3, 5, 12, 14]. Molenbroek *et al.* [14] have shown that in supported nickel-gold catalysts up to 73 % of gold is present as bulk gold, with the remainder present as a surface nickel-gold alloy. The formation of a surface nickel-gold alloy has been shown to increase the catalyst tolerance towards carbon formation, whilst having a minimal influence on the reforming activity [2, 3, 5, 12, 14]. This is primarily attributed to modifications in the electronic properties of nickel following alloy formation, affecting nickel adsorption properties and stability of intermediate adsorbed species [3, 12].

Consequently, the absence of a surface nickel-gold alloy in Au-Ni/Al_2O_3 catalysts in this study may be a significant factor in the variation in reforming characteristics and specifically carbon tolerance compared to catalysts reported in literature. Additionally, this substantiates the suggestion that gold sintering may occur at elevated reaction temperatures (as discussed in Section 8.5), due to the reduced stability of surface gold, thus further influencing reforming characteristics.

In summary, gold addition to Ni/Al_2O_3 catalysts has shown to negatively influence reforming activity, resulting in a substantial reduction in reforming activity at low reaction temperatures and slight reduction at high temperature reforming. Gold addition also appears to inhibit beneficial carbon gasification reactions, resulting in an increase in carbon deposition during reforming.

8.10 References

1. K. Yoshida, N. Begum, S.-i. Ito, and K. Tomishige, *Oxidative steam reforming of methane over Ni/α-Al_2O_3 modified with trace noble metals.* Applied Catalysis A: General, 2009. **358**(2): p. 186-192.
2. T. Maniecki, A. Stadnichenko, W. Maniukiewicz, K. Bawolak, P. Mierczyński, A. Boronin, and W. Jozwiak, *An active phase transformation on surface of Ni-Au/Al_2O_3 catalyst during partial oxidation of methane to synthesis gas.* Kinetics and Catalysis, 2010. **51**(4): p. 573-578.
3. Y.-H. Chin, D.L. King, H.-S. Roh, Y. Wang, and S.M. Heald, *Structure and reactivity investigations on supported bimetallic AuNi catalysts used for hydrocarbon steam reforming.* Journal of Catalysis, 2006. **244**(2): p. 153-162.
4. L. Guczi, G. Stefler, O. Geszti, I. Sajó, Z. Pászti, A. Tompos, and Z. Schay, *Methane dry reforming with CO_2: A study on surface carbon species.* Applied Catalysis A: General, 2010. **375**(2): p. 236-246.
5. I. Gavrielatos, V. Drakopoulos, and S.G. Neophytides, *Carbon tolerant Ni-Au SOFC electrodes operating under internal steam reforming conditions.* Journal of Catalysis, 2008. **259**(1): p. 75-84.
6. N.C. Triantafyllopoulos and S.G. Neophytides, *Dissociative adsorption of CH_4 on NiAu/YSZ: The nature of adsorbed carbonaceous species and the inhibition of graphitic C formation.* Journal of Catalysis, 2006. **239**(1): p. 187-199.
7. H.S. Bengaard, J.K. Nørskov, J. Sehested, B.S. Clausen, L.P. Nielsen, A.M. Molenbroek, and J.R. Rostrup-Nielsen, *Steam Reforming and Graphite Formation on Ni Catalysts.* Journal of Catalysis, 2002. **209**(2): p. 365-384.
8. F. Basenbacher, I. Chorkendorff, B.S. Clausen, B. Hammer, A.M. Molenbroek, J.K. Norkov, and I. Stensgaard, *Design of a Surface Alloy Catalyst for Steam Reforming.* Science, 1998. **279**: p. 1913 - 1915.

9. O.-S. Joo and K.-D. Jung, *CH 4 Dry Reforming on Alumina-Supported Nickel Catalyst.* Bulletin of the Korean Chemical Society 2002. **23**(8): p. 1149-1153.

10. H. He and J.M. Hill, *Carbon deposition on Ni/YSZ composites exposed to humidified methane.* Applied Catalysis A: General, 2007. **317**(2): p. 284-292.

11. N. Sahli, C. Petit, A.C. Roger, A. Kiennemann, S. Libs, and M.M. Bettahar, *Ni catalysts from $NiAl_2O_4$ spinel for CO_2 reforming of methane.* Catalysis Today, 2006. **113**(3-4): p. 187-193.

12. D.K. Niakolas, J.P. Ouweltjes, G. Rietveld, V. Dracopoulos, and S.G. Neophytides, *Au-doped Ni/GDC as a new anode for SOFCs operating under rich CH_4 internal steam reforming.* International Journal of Hydrogen Energy, 2010. **35**(15): p. 7898-7904.

13. Y.-g. Chen and J. Ren, *Conversion of methane and carbon dioxide into synthesis gas over alumina-supported nickel catalysts. Effect of Ni-Al_2O_3 interactions.* Catalysis Letters, 1994. **29**(1): p. 39-48.

14. A.M. Molenbroek, J.K. Nørskov, and B.S. Clausen, *Structure and Reactivity of Ni−Au Nanoparticle Catalysts.* The Journal of Physical Chemistry B, 2001. **105**(23): p. 5450-5458.

9 Reactions of methane and steam over 20 wt % Ni/Al_2O_3 and 5 mol % Au doped 20 wt % Ni/Al_2O_3: Influence of sulfur addition

Although sulfur is commonly classed as a poison and has been shown to deactivate nickel based catalysts [1-4], it has also shown to be beneficial towards some reforming processes [5-7]. As small levels of sulfur are introduced into a steam methane reforming reaction mixture, the rate of carbon formation may be inhibited more than the rate of reforming [5, 7, 8]. It has been shown that carbon nucleation and deposition over a nickel surface can potentially be reduced due to preferential binding of sulfur to nickel step sites [9]. Gold-doping of the nickel catalysts and the addition of sulfur to reforming reactions may influence reforming characteristics in a similar manner. Surface step sites could potentially be occupied and blocked by either gold or sulfur, affecting both the rate of reforming and carbon formation. The influence of sulfur adsorption on carbon nucleation may also be reflected in the morphology of carbon formed [7, 10]. Although low levels of sulfur have been shown to significantly reduce carbon deposition, it has also been reported to promote carbon deposition under some conditions [10, 11], preventing hydrocarbon reforming and reducing carbon gasification.

Reforming studies described in Chapters 6 to 8 have shown that both the calcination temperature and addition of gold to Ni/Al_2O_3 catalysts have a significant influence on the reforming characteristics and promotion of individual surface reaction pathways. It has been shown that the addition of gold to reforming catalysts reduces reforming activity, specifically at low reforming temperatures. The presence of gold has also been shown to inhibit beneficial carbon gasification reactions, providing no reduction in carbon deposition. This has been proposed to occur due to the absence of a surface nickel-gold alloy and gold segregation on the nickel surface in $Au\text{-}Ni/Al_2O_3$

catalysts. It has been shown [12, 13] that the presence of a nickel-gold alloy may induce changes in the electronic properties of nickel and thus alter the adsorption and stability intermediate CH_x species, ultimately reducing carbon formation. Given the reported similarities between gold and sulfur binding on the nickel surface [9, 14] and presence of sulfur in many hydrocarbon reforming fuels, the effect of sulfur addition to the reaction mixture, on catalytic activity and reforming characteristics has been studied in this chapter.

Following a series of preliminary studies, to obtain some insight into the sulfur tolerance of the catalysts, sulfur was added at levels of 80 ppm with respect to the methane concentration. Reactions were carried out over 20 wt % Ni/Al_2O_3 calcined at 600 °C, 900 °C and 1000 °C (Ni/Al_2O_3 (600), Ni/Al_2O_3 (900) and Ni/Al_2O_3 (1000)) and over 5 mol % Au doped 20 wt % Ni/Al_2O_3 calcined at 600 °C, 900 °C and 1000 °C (Au-Ni/Al_2O_3 (600), Au-Ni/Al_2O_3 (900) and Au-Ni/Al_2O_3 (1000)) under methane-rich (methane: steam = 2:1) and stoichiometric conditions (methane: steam = 1:1).

9.1 Effect of sulfur on the reactions of methane and steam under stoichiometric conditions over 20 wt % Ni/Al_2O_3: influence of reaction temperature

The H_2 yield profiles for reactions of methane and steam over Ni/Al_2O_3 (600), Ni/Al_2O_3 (900) and Ni/Al_2O_3 (1000) in the presence of 80 ppm H_2S under stoichiometric conditions at reaction temperatures from 500 °C to 900 °C are shown in Figure 9.1- Figure 9.3, respectively.

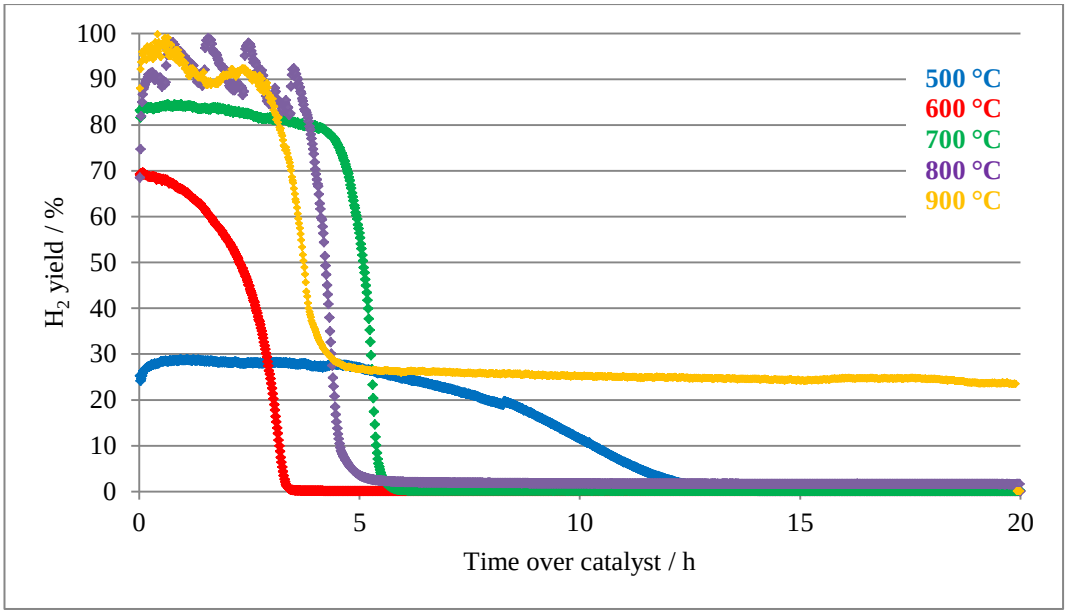

Figure 9.1: **H_2 yield profiles for reactions of methane and steam over Ni/Al_2O_3 (600) for 20 hours under stoichiometric conditions (methane: steam = 1:1) at reaction temperatures 500 °C to 900 °C in the presence of 80 ppm H_2S**

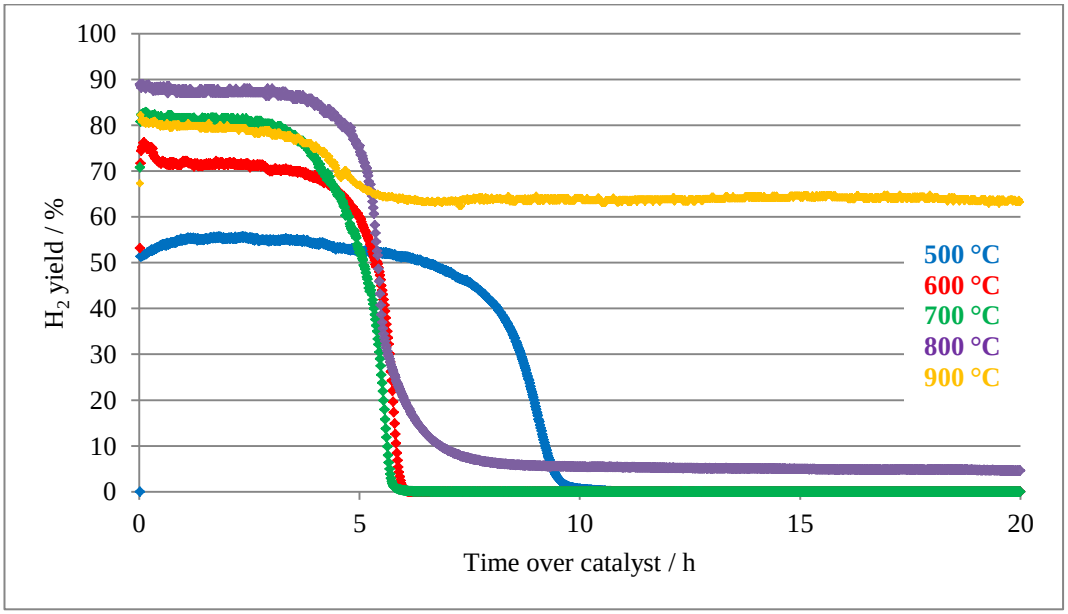

Figure 9.2: **H_2 yield profiles for reactions of methane and steam over Ni/Al_2O_3 (900) for 20 hours under stoichiometric conditions (methane: steam = 1:1) at reaction temperatures 500 °C to 900 °C in the presence of 80 ppm H_2S**

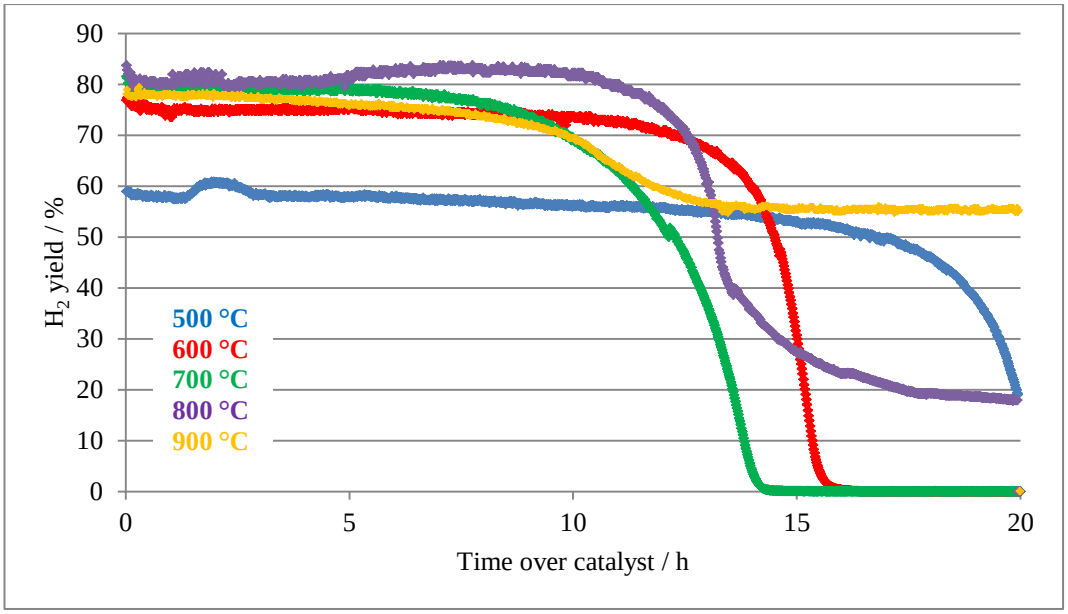

Figure 9.3: **H_2 yield profiles for reactions of methane and steam over Ni/Al_2O_3 (1000) for 20 hours under stoichiometric conditions (methane: steam = 1:1) at reaction temperatures 500 °C to 900 °C in the presence of 80 ppm H_2S**

As well as the initial catalytic activity changing following an increase in the reaction temperature, catalyst deactivation is also significantly affected. Steady initial reforming activity is followed by catalyst poisoning for all reaction temperatures studied, although the extent of poisoning and the reaction profile over time is strongly dependant on both the catalyst and the reaction temperature.

During the reaction over Ni/Al_2O_3 (600) at 500 °C, deactivation initiates after *ca.* 7 hours and occurs gradually over time, finally resulting in complete loss of activity after *ca* 12 hours. Whilst at 600 °C poisoning occurs immediately with rapid loss of activity and complete deactivation after *ca.* 3.5 hours and at *ca.* 5.5 hours at 700 °C. Complete deactivation does not quite occur at 800 °C, and significant activity is retained at 900 °C. A similar trend is observed over all Ni/Al_2O_3 catalysts studied.

During the reaction over Ni/Al_2O_3 (600) at 800 °C, regular sharp peaks are observed in both the product and reactant gas profiles, during both stages of the reaction (prior to and following catalyst

deactivation). The reaction profile for the reaction of methane and steam over Ni/Al_2O_3 (600) at 800 °C in the presence of 80 ppm H_2S are shown in Figure 9.4.

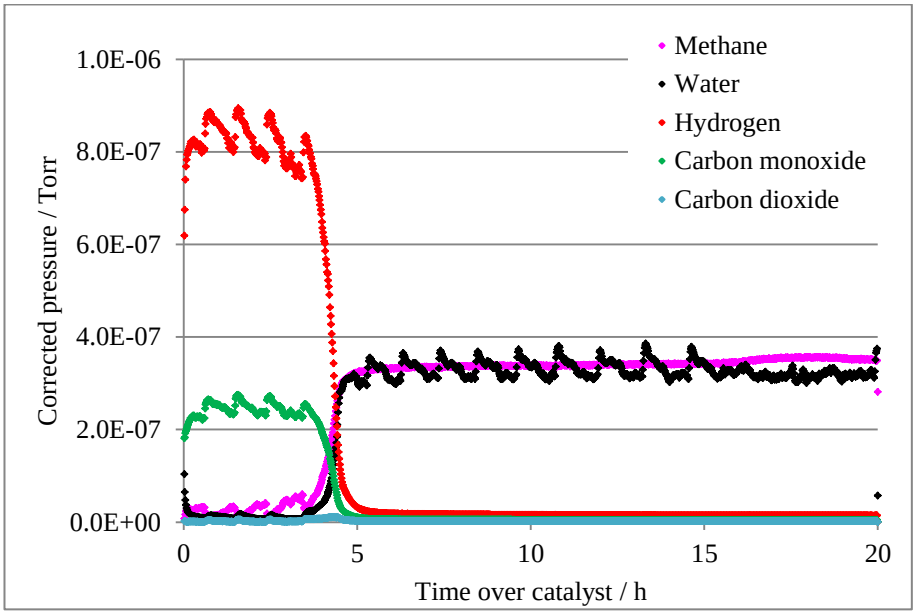

Figure 9.4: Reaction profile for the reaction of methane and steam over Ni/Al_2O_3 (600) for 20 hours under stoichiometric conditions (methane: steam = 1:1) at 800 °C in the presence of 80 ppm H_2S

This cyclic trend observed can be attributed to the successive adsorption and removal of sulfur from the nickel surface at elevated reaction temperatures. This may occur via a number of reactions, including Reactions 9.1 to 9.4.

$$Ni + H_2S \leftrightarrow Ni - S + H_2 \quad (9.1)$$

$$Ni - S + H_2O \rightarrow NiO + H_2S \quad (9.2)$$

$$Ni - S + H_2 \rightarrow Ni + H_2S \quad (9.3)$$

$$NiO + H_2 \rightarrow Ni + H_2O \quad (9.4)$$

The effect of steam on sulfur poisoning of catalysts during steam reforming has been reported by Srinakruang *et al.* [2], who have shown that poisoning is suppressed by the exchange of adsorbed sulfur on the nickel surface with an oxide ion by steam, as shown in Reaction 9.2, and the

subsequent reduction of nickel oxide by hydrogen (Reaction 9.4). There is some evidence of this trend during the reaction over Ni/Al_2O_3 (600) at 900 °C, evident in the H_2 yield profile shown in Figure 9.1. The cyclic adsorption and desorption trend is not observed during other reaction temperatures studied or in the reaction profiles of any other catalyst.

During all reactions undertaken at 900 °C, sulfur poisoning is followed by reduced but stable product gas formation. This suggests partial coverage of the nickel surface by adsorbed sulfur, thus sulfur adsorption does not completely inhibit all nickel active sites available for steam methane reforming at elevated reaction temperatures.

As the calcination temperature is increased, catalyst activity and resistance towards sulfur poisoning is improved. This is particularly the case following calcination at 1000 °C where extended catalyst lifetime is observed. For example, over Ni/Al_2O_3 (1000) catalyst lifetime is increased by over 11 hours compared to Ni/Al_2O_3 (600) during the reaction at 600 °C. Additionally, following calcination at 900 °C, the residual catalyst activity at 800 °C and 900 °C following sulfur poisoning is also significantly high, and H_2 yields of *ca.* 60 % are maintained at 900 °C. This is at variance with results obtained by Srinakruang *et al.* [2] who have shown that over Ni/dolomite catalysts, catalytic activity is reduced as the calcination temperature is increased from 500 °C to 950 °C.

Results obtained over all Ni/Al_2O_3 catalysts under stoichiometric conditions suggest that at lower reaction temperatures kinetic factors dominate over thermodynamic predictions. As the reaction temperature is increased from 500 °C to 700 °C, surface sulfur adsorption and coverage rapidly increases, thus an increased rate of poisoning is observed, overriding thermodynamic factors. At reaction temperatures above 800 °C, thermodynamic factors dominate and although sulfur adsorption rapidly reduces catalytic activity, the rate of sulfur removal also increases rapidly and equilibrium between sulfur adsorption and desorption is reached. This trend has been observed in carbon dioxide reforming studies carried out by Laycock *et al.* [1] who have demonstrated a

reduction in sulfur tolerance and catalyst lifetime as the reaction temperature is increased up to moderate reaction temperatures. Additionally, Ashrafi *et al.* [3] have shown that as the reaction temperature is increased from 700 °C to 900 °C a reduction in catalyst poisoning is observed.

9.2 Effect of sulfur on the reactions of methane and steam under methane-rich conditions over 20 wt % Ni/Al_2O_3: influence of reaction temperature

The H_2 yield profiles for reactions of methane and steam over Ni/Al_2O_3 (600), Ni/Al_2O_3 (900) and Ni/Al_2O_3 (1000) in the presence of 80 ppm H_2S under methane-rich conditions at reaction temperatures 500 °C to 900 °C are shown in Figure 9.5 - Figure 9.7, respectively.

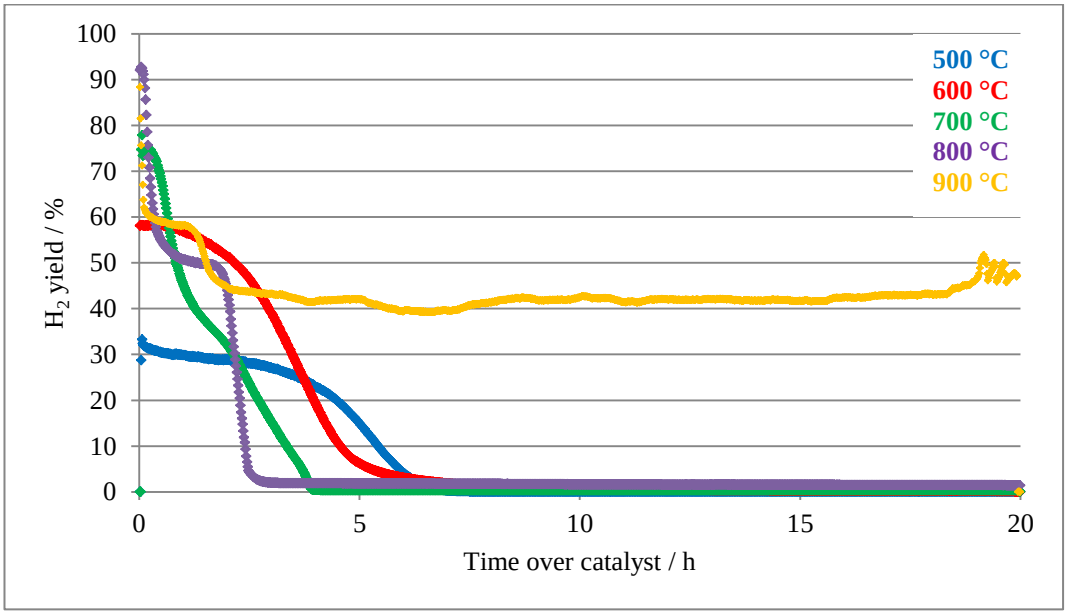

Figure 9.5: **H_2 yield profiles for reactions of methane and steam over Ni/Al_2O_3 (600) for 20 hours under methane-rich conditions (methane: steam = 2:1) at reaction temperatures 500 °C to 900 °C in the presence of 80 ppm H_2S**

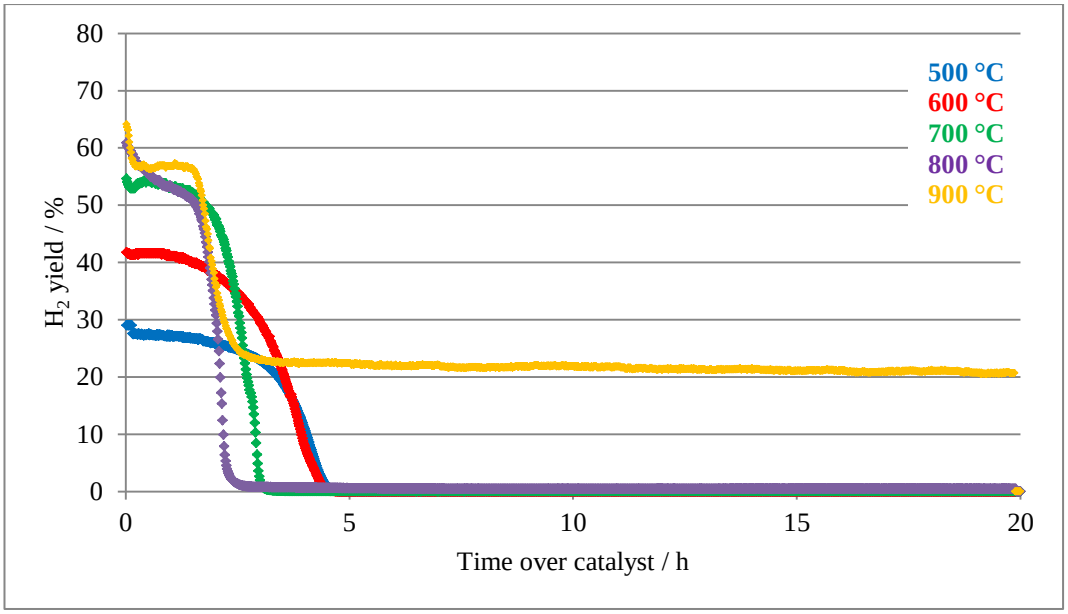

Figure 9.6: **H_2 yield profiles for reactions of methane and steam over Ni/Al_2O_3 (900) for 20 hours under methane-rich conditions (methane: steam = 2:1) at reaction temperatures 500 °C to 900 °C in the presence of 80 ppm H_2S**

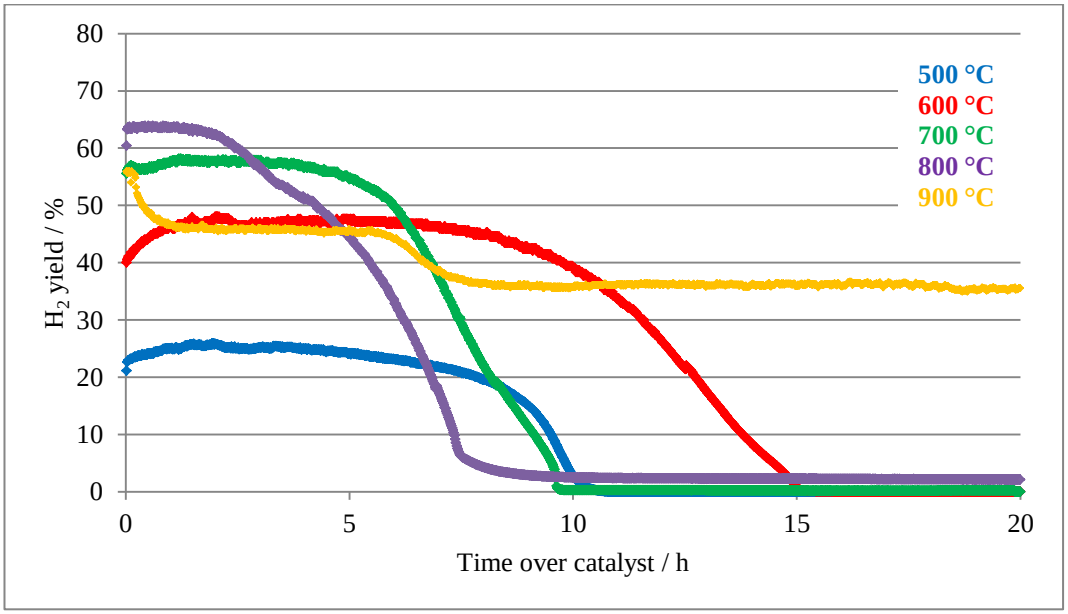

Figure 9.7: **H_2 yield profiles for reactions of methane and steam over Ni/Al_2O_3 (1000) for 20 hours under methane-rich conditions (methane: steam = 2:1) at reaction temperatures 500 °C to 900 °C in the presence of 80 ppm H_2S**

As under stoichiometric conditions, as the reaction temperature is increased from 500 °C to 700 °C an increased rate of sulfur poisoning is observed over all catalysts under methane-rich conditions

During reactions over Ni/Al_2O_3 (600), almost instantaneous sulfur poisoning is observed and a significant reduction in time before complete deactivation of the catalyst compared to reactions under stoichiometric conditions is observed. For example, at 700 °C under stoichiometric conditions, catalyst poisoning is observed after *ca*. 5 hours of reasonably steady activity, whilst under methane-rich conditions steady activity is not observed and poisoning occurs after within minutes of the reaction initiating.

The cyclic trend observed at 800 °C under stoichiometric conditions is not observed under methane-rich conditions, which is consistent with recurring sulfur adsorption and removal from the catalyst surface being facilitated by the presence of excess steam. The sharp initial reduction in activity observed during reactions at 800 °C and 900 °C, may be attributed to instantaneous catalyst poisoning on reaction initiation, or this may be due to reactant gases settling on reaction onset and thus may not be a major factor of catalyst poisoning or deactivation.

As observed over Ni/Al_2O_3 (600), both Ni/Al_2O_3 catalysts calcined at 900 °C and 1000 °C show a reduced lifetime during reactions under methane-rich conditions. For example, under methane-rich conditions the time to complete deactivation is generally reduced by *ca*. 2 hours over Ni/Al_2O_3 (900) and by over 5 hours over Ni/Al_2O_3 (1000), compared to under stoichiometric conditions. Reducing steam concentration influences the behaviour most over Ni/Al_2O_3 (1000), where lifetime is significantly reduced. Despite the reduced catalyst lifetime under methane-rich conditions in the presence of sulfur, Ni/Al_2O_3 (1000) still exhibits the highest resistance towards sulfur poisoning compared to other Ni/Al_2O_3 catalysts.

The sulfur poisoning characteristics and the considerable differences observed over Ni/Al_2O_3 (1000), compared to Ni/Al_2O_3 catalysts calcined at 600 °C and 900 °C, are linked to the morphological and structural differences identified by SEM, XRD, XPS and TPR studies in

Chapter 4. Similarities between the catalyst morphology and reforming characteristics of Ni/Al_2O_3 (1000) and $Au\text{-}Ni/Al_2O_3$ (900) are highlighted in Section 9.3. Additionally, the presence of an unreduced $NiAl_2O_4$ phase, observed during reforming studies in Chapter 6, may also influence sulfur adsorption to active sites and thus catalyst lifetime. Srinakruang *et al.* [2] have reported that catalysts calcined at higher temperatures exhibited a reduction in both activity and sulfur tolerance. This has been attributed to the formation of phases such as $NiMgO_2$, resulting in a reduction in the active metal sites present in the catalyst. The results in this study appear to differ from these findings, although this may be due to differences in reduction characteristics and incomplete reduction of the phases obtained following calcination.

A number of factors may contribute to the increased catalyst poisoning observed under methane-rich conditions. Firstly, the lower levels of steam may reduce catalyst regeneration by Reaction 9.2 and the removal of adsorbed sulfur on the nickel surface with an oxide ion by steam. Secondly, it was observed in Chapter 7 that reduced reforming activity was observed during reactions undertaken in methane-rich conditions, thus lower hydrogen levels would be present, reducing catalyst regeneration, via the reverse of Reaction 9.1.

9.3 Effect of sulfur addition on the reactions of methane and steam under stoichiometric conditions over 5 mol % Au doped 20 wt % Ni/Al_2O_3: effect of gold-doping

The H_2 yield profiles for reactions of methane and steam over $Au\text{-}Ni/Al_2O_3$ (600), $Au\text{-}Ni/Al_2O_3$ (900) and $Au\text{-}Ni/Al_2O_3$ (1000) in the presence of 80 ppm H_2S under stoichiometric conditions at reaction temperatures 500 °C to 900 °C are shown in Figure 9.8 - Figure 9.10, respectively.

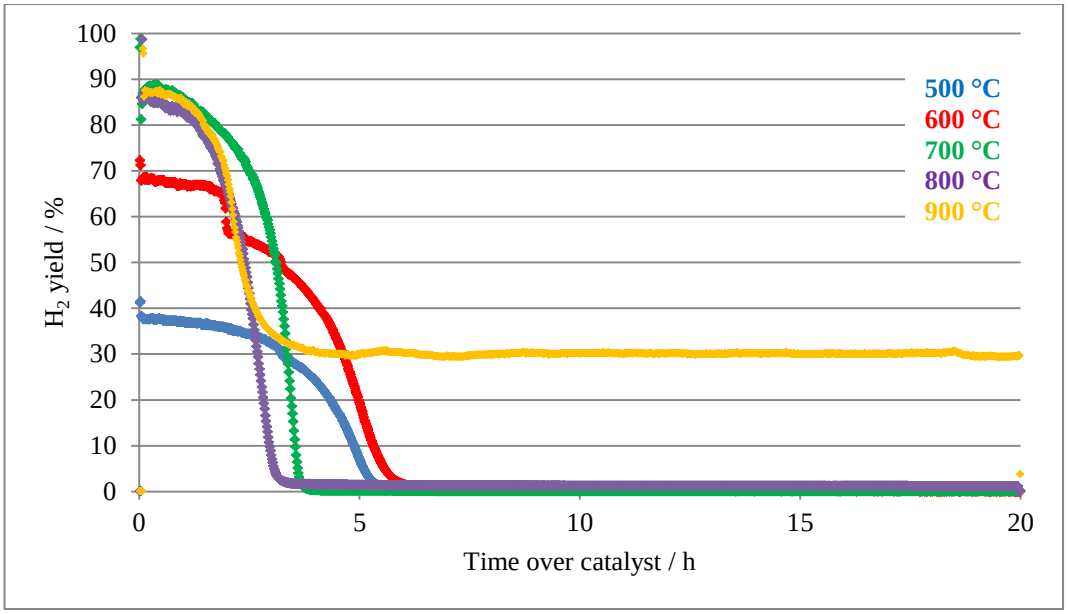

Figure 9.8: **H_2 yield profiles for reactions of methane and steam over Au-Ni/Al_2O_3 (600) for 20 hours under stoichiometric conditions (methane: steam = 1:1) at reaction temperatures 500 °C to 900 °C in the presence of 80 ppm H_2S**

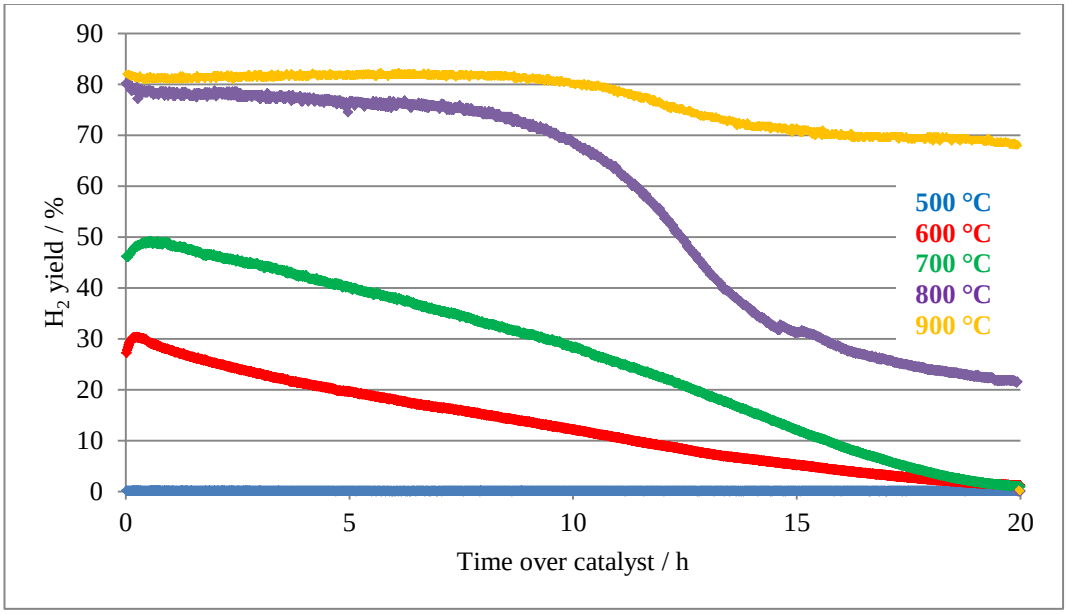

Figure 9.9: **H_2 yield profiles for reactions of methane and steam over Au-Ni/Al_2O_3 (900) for 20 hours under stoichiometric conditions (methane: steam = 1:1) at reaction temperatures 500 °C to 900 °C in the presence of 80 ppm H_2S**

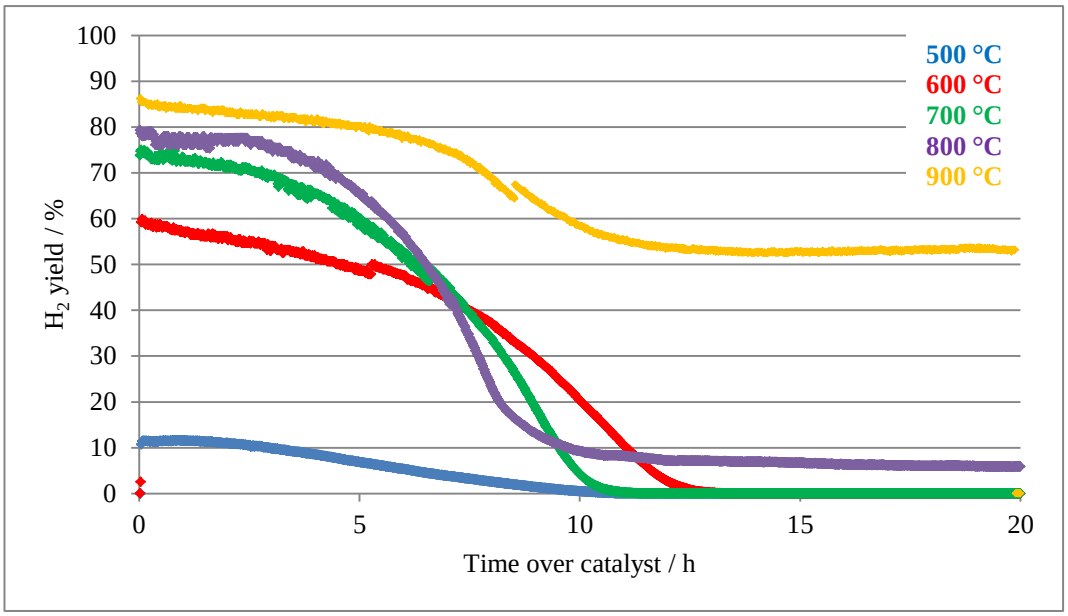

Figure 9.10: **H_2 yield profiles for reactions of methane and steam over Au-Ni/Al_2O_3 (1000) for 20 hours under stoichiometric conditions (methane: steam = 1:1) at reaction temperatures 500 °C to 900 °C in the presence of 80 ppm H_2S**

Following addition of gold to Ni/Al_2O_3 catalysts, considerably different sulfur poisoning behaviour is observed depending on the calcination temperature. For example, the addition of gold to Ni/Al_2O_3 (600) results in a minor reduction in the resistance towards sulfur poisoning, and catalyst lifetime is reduced by over 2 hours over all reaction temperatures, with the exception of the reaction at 600 °C. Similarly, the addition of gold to Ni/Al_2O_3 (1000) results in a reduction in catalyst lifetime by up to 5 hours.

The addition of gold to Ni/Al_2O_3 catalysts calcined at 600 °C and 1000 °C results in reduced tolerance towards sulfur poisoning. Despite the change in poisoning characteristics following gold-doping, the stable activities following poisoning of all catalysts at reaction temperatures of 900 °C are similar to activities observed for Ni/Al_2O_3 catalysts. Results obtained at reaction temperatures above 800 °C, indicate that sulfur adsorption to and removal from the nickel surface are not significantly influenced by the addition of gold.

An increase in catalyst poisoning and reduction in catalyst activity is observed at reaction temperatures below 800 °C. This may be attributed to the location of gold on the nickel surface and adsorption of sulfur to similar active nickel sites [9, 14] at lower reaction temperatures, significantly reducing sites available for steam methane reforming. As the reaction temperature is increased gold agglomeration may be occurring, as discussed in Section 8.7, and sulfur removal becomes more thermodynamically favoured, resulting in increased availability of active nickel sites for high temperature reforming, as shown in the schematic below. Therefore, sulfur adsorption has a greater influence on low temperature reaction characteristics. This phenomenon may also be a significant factor in the similarities observed between the high temperature catalytic activity of Ni/Al_2O_3 and $Au\text{-}Ni/Al_2O_3$ catalysts.

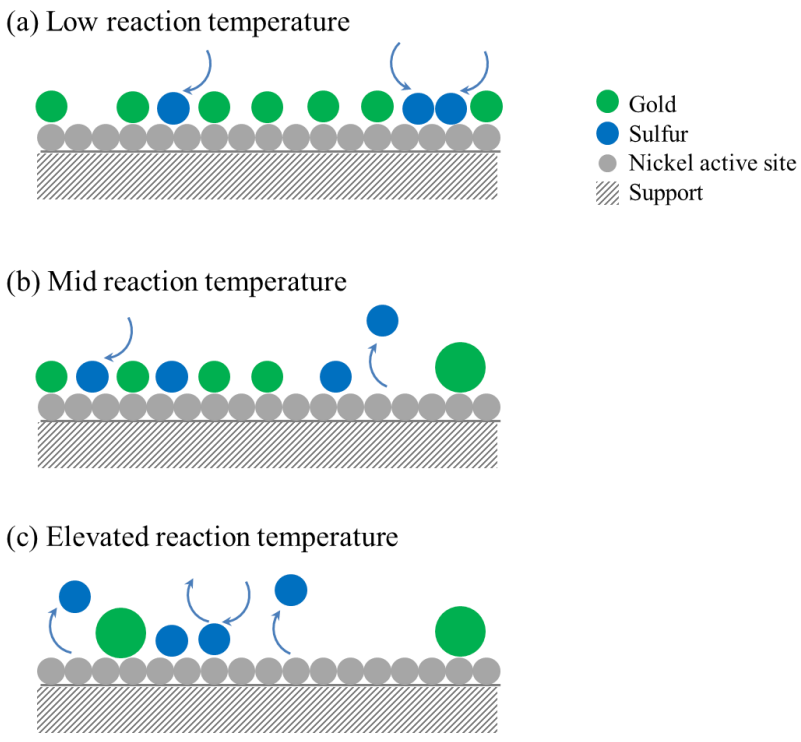

Figure 9.11: Schematic representation of gold sintering and sulfur adsorption/desorption as reaction temperatures are increased, influencing surface active site availability (not to scale)

A substantial variation in the sulfur poisoning behaviour and reaction characteristics are observed following the addition of gold to Ni/Al_2O_3 (900). Over $Au\text{-}Ni/Al_2O_3$ (900), some catalyst

deactivation occurs immediately at lower reaction temperatures but progresses very gradually and almost linearly with time. Complete loss of activity does not occur within 20 hours during reactions at 600 °C and 700 °C, such that the catalyst lifetime is effectively increased by over 15 hours, following addition of gold to Ni/Al_2O_3 (900). During the reaction at 900 °C, sulfur poisoning results a reduction in catalyst activity of only *ca.* 10 %, followed by steady catalytic activity and H_2 yields comparable to those observed over Ni/Al_2O_3 (900). The significant increase in the sulfur tolerance of $Au\text{-}Ni/Al_2O_3$ (900) compared to $Au\text{-}Ni/Al_2O_3$ catalysts calcined at 600 °C and 1000 °C, may be attributed to the morphological and structural differences observed and discussed in Chapter 5. Pre and Post-reduction SEM images shown in Chapter 4 and 5 indicate that $Au\text{-}Ni/Al_2O_3$ (900) has a similar morphological structure to Ni/Al_2O_3 (1000), which has also been shown to have a high sulfur tolerance and extended catalyst lifetime during reforming reactions involving sulfur.

9.4 Effect of sulfur addition on the reactions of methane and steam under methane-rich conditions over 5 mol % Au doped 20 wt % Ni/Al_2O_3: effect of gold-doping

The H_2 yield profiles for reactions of methane and steam over $Au\text{-}Ni/Al_2O_3$ (600), $Au\text{-}Ni/Al_2O_3$ (900) and $Au\text{-}Ni/Al_2O_3$ (1000) in the presence of 80 ppm H_2S under methane-rich conditions at reaction temperatures 500 °C to 900 °C are shown in Figure 9.12 - Figure 9.14, respectively.

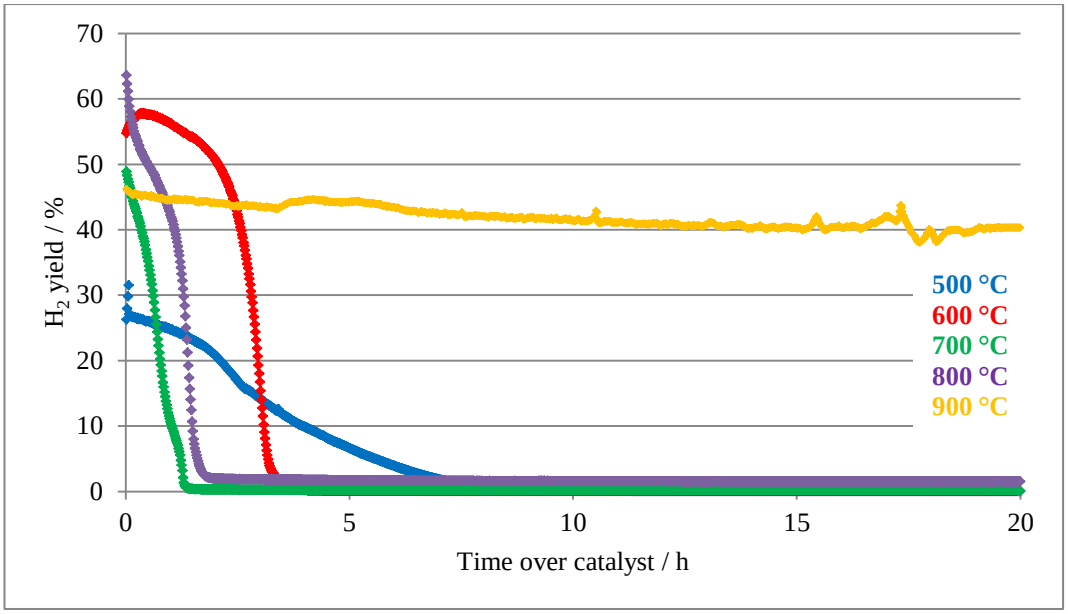

Figure 9.12: **H_2 yield profiles for reactions of methane and steam over Au-Ni/Al_2O_3 (600) for 20 hours under methane-rich conditions (methane: steam = 2:1) at reaction temperatures 500 °C to 900 °C in the presence of 80 ppm H_2S**

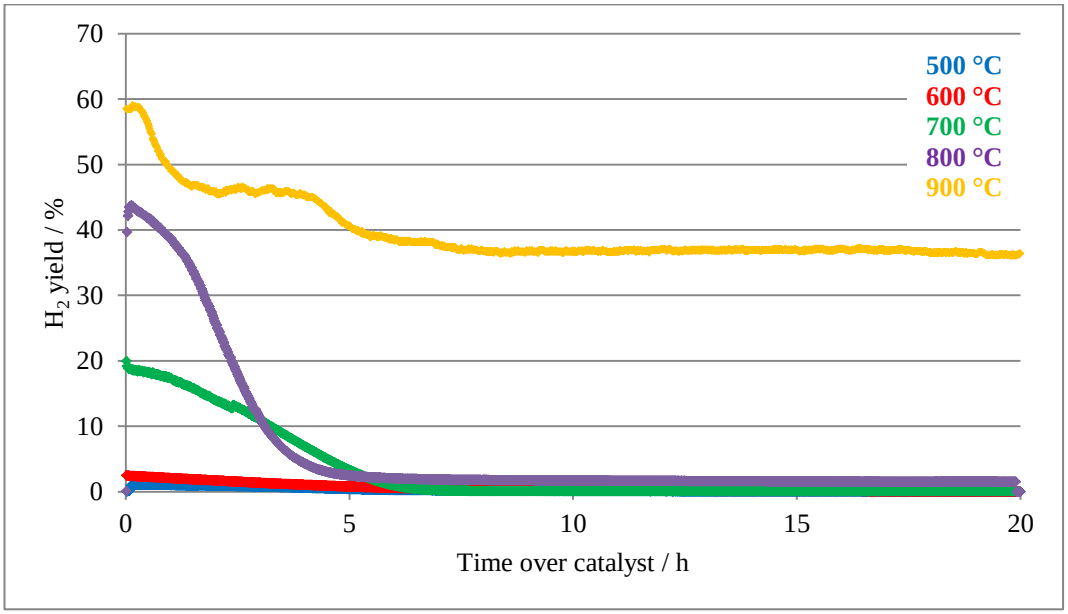

Figure 9.13: **H_2 yield profiles for reactions of methane and steam over Au-Ni/Al_2O_3 (900) for 20 hours under methane-rich conditions (methane: steam = 2:1) at reaction temperatures 500 °C to 900 °C in the presence of 80 ppm H_2S**

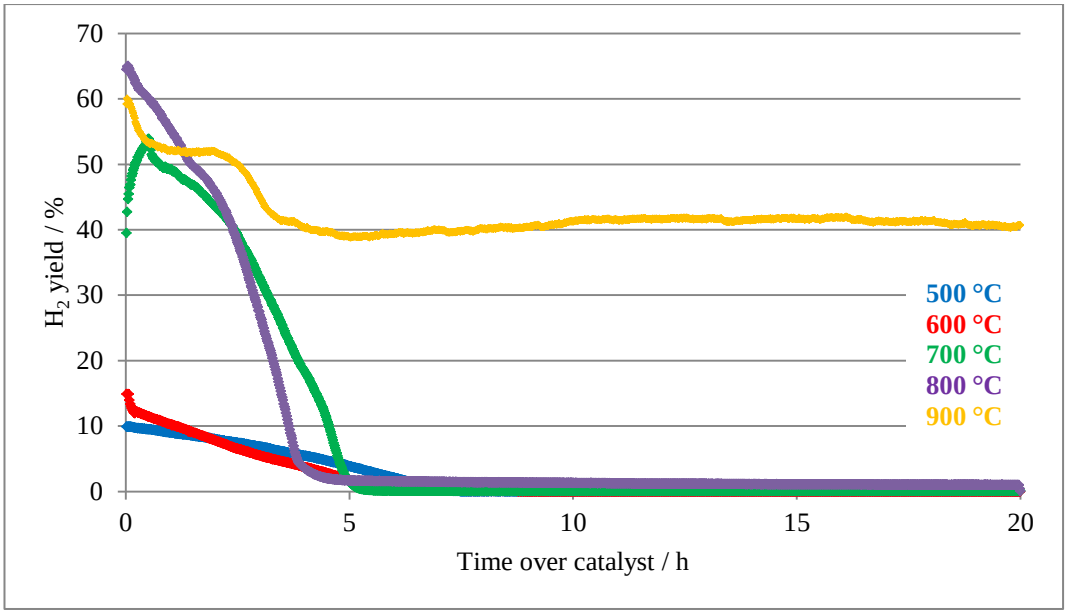

Figure 9.14: **H_2 yield profiles for reactions of methane and steam over Au-Ni/Al_2O_3 (1000) for 20 hours under methane-rich conditions (methane: steam = 2:1) at reaction temperatures 500 °C to 900 °C in the presence of 80 ppm H_2S**

Following addition of gold to Ni/Al_2O_3 (600), catalyst deactivation due to sulfur poisoning occurs almost immediately at lower reaction temperatures and catalyst lifetime is reduced. However, interestingly there is no sign of sulfur poisoning during the reaction over Au-Ni/Al_2O_3 (600) at 900 °C. This may be attributed to the rapid equilibrium between sulfur adsorption and removal being achieved. As observed during reactions under stoichiometric conditions, the addition of gold to Ni/Al_2O_3 (600) has no significant influence on the high temperature sulfur poisoning characteristics during the reactions under methane-rich conditions.

Following the addition of gold to Ni/Al_2O_3 (900) catalyst lifetime is increased by *ca.* 3 hours compared to Ni/Al_2O_3 (900), a similar trend to that observed during reactions under stoichiometric conditions. Although lifetime is not notably altered, under methane-rich conditions sulfur poisoning is steady over time and the rate of deactivation is considerably reduced following the addition of gold to Ni/Al_2O_3 (900). The behaviour at 900 °C is particularly noteworthy, and significantly improved activity is observed compared to Ni/Al_2O_3 (900). Similarly, following the addition of gold to Ni/Al_2O_3 (1000), the rate of catalyst poisoning is considerably reduced.

Over both Au-Ni/Al_2O_3 (900) and Au-Ni/Al_2O_3 (1000), the reaction at 900 °C shows evidence of a two stage poisoning process in the initial phase of the reaction. These stages are labelled 1 and 2 in Figure 9.15.

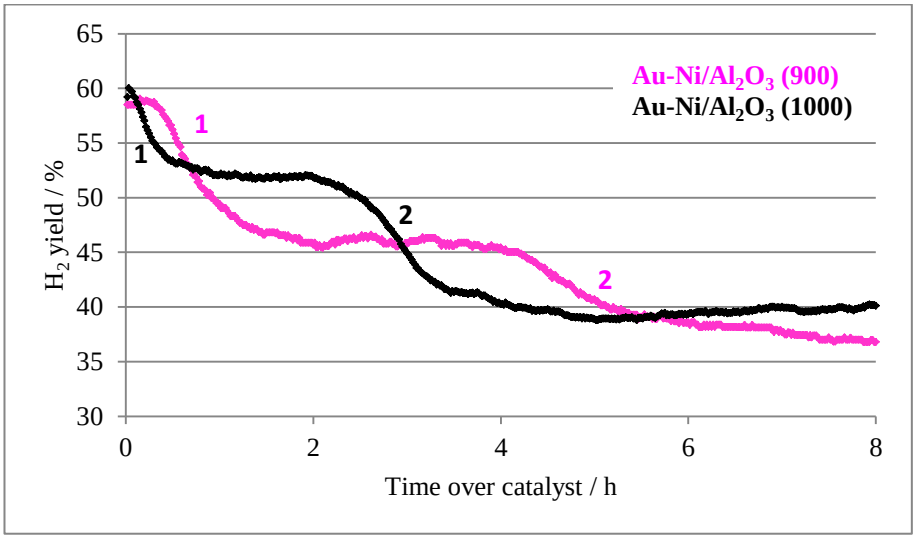

Figure 9.15: **H_2 yield profiles during the initial 8 hours of the reaction for reactions of methane and steam over Au-Ni/Al_2O_3 (900) and Au-Ni/Al_2O_3 (1000) under methane-rich conditions (methane: steam = 2:1) at 900 °C in the presence of 80 ppm H_2S**

Stage 1 occurs following almost immediately, within *ca.* 1 hour of reaction initiation. Initial catalyst deactivation is followed by a period of steady activity. Stage 2 occurs after *ca.* 2 hours for Au-Ni/Al_2O_3 (1000) and *ca.* 4 hours for Au-Ni/Al_2O_3 (900) where a further reduction in activity is observed. Following both poisoning stages, steady syngas production is maintained and no subsequent sulfur poisoning is observed, suggesting a stable equilibrium between sulfur adsorption and removal is reached [15]. This phenomenon may be associated with the adsorption of sulfur on different nickel surface sites or following sulfur adsorption its relocation to different surface sites, followed by further sulfur adsorption.

The addition of gold to Ni/Al_2O_3 (900) results in an increase in sulfur tolerance for both methane-rich and stoichiometric conditions. Sulfur behaviour has been reported by Laycock *et al.* [1] who

have shown that gold-doping Ni/YSZ fuel cell anode materials results in *ca.* 2 hours increase in sulfur tolerance for carbon dioxide reforming. The reduced sulfur tolerance observed over Au-Ni/Al_2O_3 catalysts calcined at 600 °C and 1000 °C may be attributed to the particular change in catalyst morphology and structure following calcination and reduction, as shown in Chapter 5. Srinakruang *et al.* [2] have shown that the calcination temperature used during catalyst preparation can have a significant influence on the sulfur poisoning behaviour, and factors such as the reduction characteristics may also influence the sulfur tolerance characteristics and hence tolerance. In Chapter 5, it was shown that during calcination at high temperatures as well as $NiAl_2O_4$, $AuAl_2O_4$ might also be formed. The presence of such a phase may additionally influence the sulfur tolerance of the catalyst and poisoning behaviour.

A significant difference in the rate of deactivation via sulfur poisoning is also observed over Au-Ni/Al_2O_3 catalysts. This may be attributed to the location of gold on nickel step sites, limiting the adsorption of sulfur to such sites, decreasing the rate of poisoning.

9.5 Long term sulfur tolerance studies over 20 wt % Ni/Al_2O_3 and 5 mol % Au doped Ni/Al_2O_3

The long term tolerance of all the Ni/Al_2O_3 and Au-Ni/Al_2O_3 catalysts under methane-rich conditions in the presence of sulfur was studied in order to determine if the catalytic activity at high reaction temperatures was maintained over a prolonged period of time (100 hours). Figure 9.16 shows a typical reaction profile, in this case over Au-Ni/Al_2O_3 (600) at 900 °C. All reactions were performed for 100 hours.

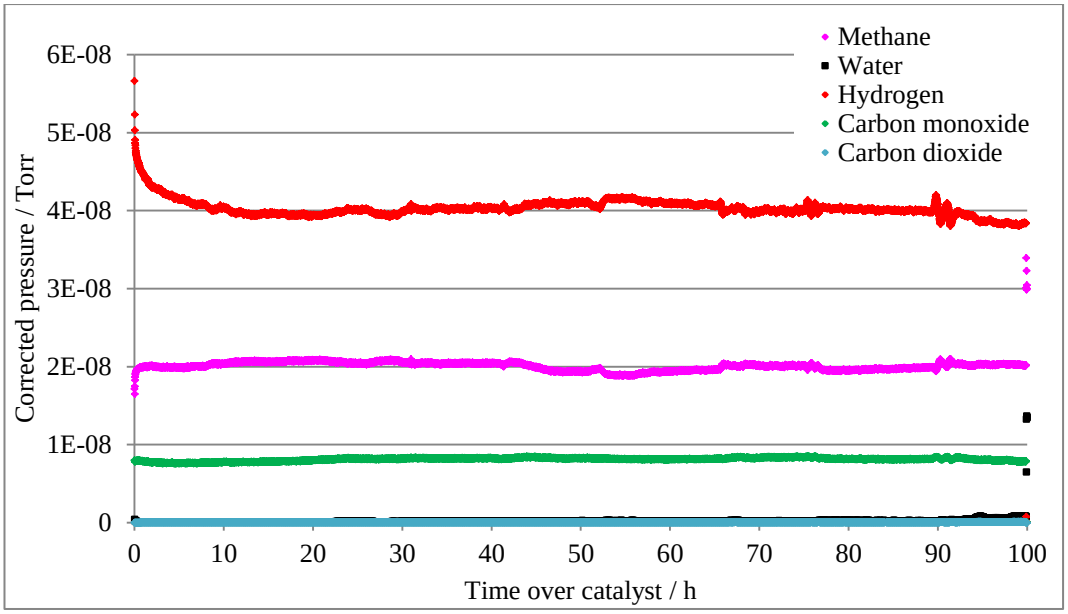

Figure 9.16: Reaction profile for the reaction of methane and steam over Au-Ni/Al_2O_3 (600) for 100 hours under methane-rich conditions (methane: steam = 2:1) at 900 °C in the presence of 80 ppm H_2S

The reaction profile over Au-Ni/Al_2O_3 (600) shown in Figure 9.16 is indicative of all reaction profiles obtained. The catalyst activity remained steady over the 100 hour reaction period and no significant loss in activity was observed over any of the catalysts. Following initial sulfur poisoning of the catalysts, no subsequent catalyst poisoning was observed and equilibrium between sulfur adsorption and removal was maintained.

9.6 Influence of sulfur on carbon deposition during reactions of methane and steam over 20 wt % Ni/Al_2O_3 and 5 mol % Au doped Ni/Al_2O_3

9.6.1 Carbon deposition during reactions of methane and steam under stoichiometric and methane-rich conditions over Ni/Al_2O_3 in the presence of 80 ppm H_2S

The carbon deposition following reactions of methane and steam over Ni/Al_2O_3 catalysts for 20 hours under stoichiometric and methane rich conditions are shown in Figure 9.17 and Figure 9.18,

respectively. Reactions in sulfur-free environments are shown by solid bars and 80 ppm H_2S are shown by dashed bars in both figures.

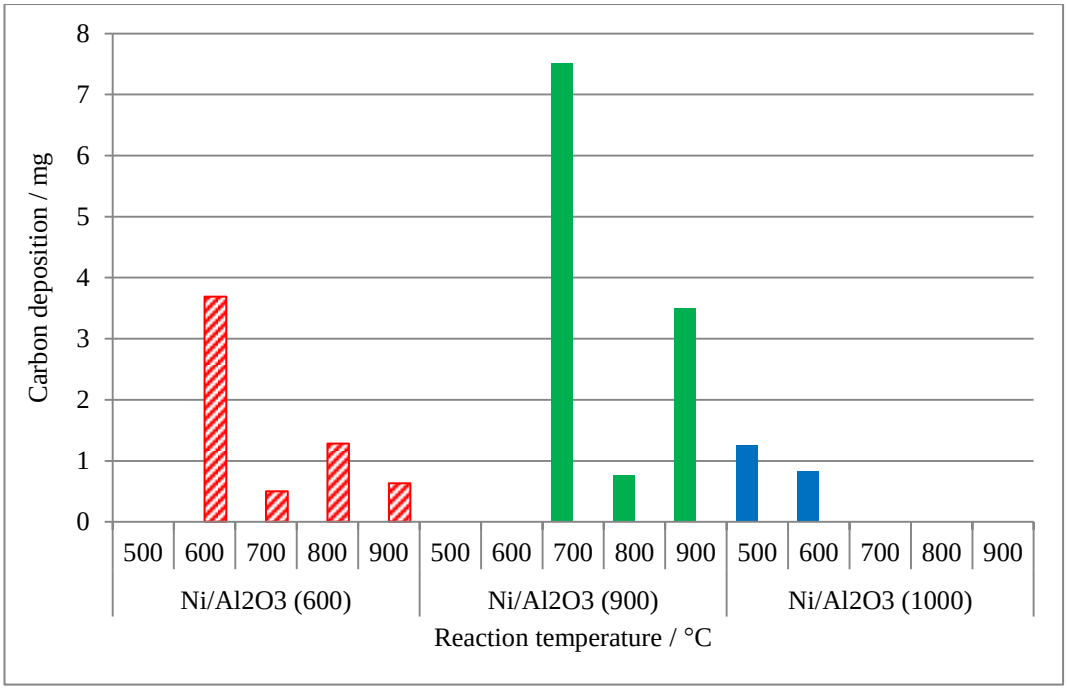

Figure 9.17: Carbon deposition following reactions of methane and steam under stoichiometric conditions at 500 °C and 900 °C in sulfur-free (solid) and 80 ppm H_2S (dashed), over Ni/Al_2O_3 (600), Ni/Al_2O_3 (900) and Ni/Al_2O_3 (1000)

It has been shown in Section 6.3 that carbon gasification in the presence of steam results in complete removal of deposited carbon over Ni/Al_2O_3 (600) under stoichiometric conditions. However, in the presence of H_2S carbon deposition is observed over Ni/Al_2O_3 (600). This is observed to the greatest extent during the reaction at 600 °C, where a cyclic trend is observed during the reforming reaction (Figure 9.4), which has been attributed to the removal of adsorbed sulfur from the surface by steam. The increase in carbon laydown may be attributed to the suppression of carbon gasification [10] through the utilisation of steam in the removal of adsorbed sulfur by Reaction 9.2 or limited adsorption of steam on the catalyst surface.

Over both Ni/Al_2O_3 (900) and Ni/Al_2O_3 (1000), the presence of sulfur eliminates all carbon deposition over all reaction temperatures studied, whereas carbon deposition is observed in the absence of sulfur over these catalysts under the same conditions.

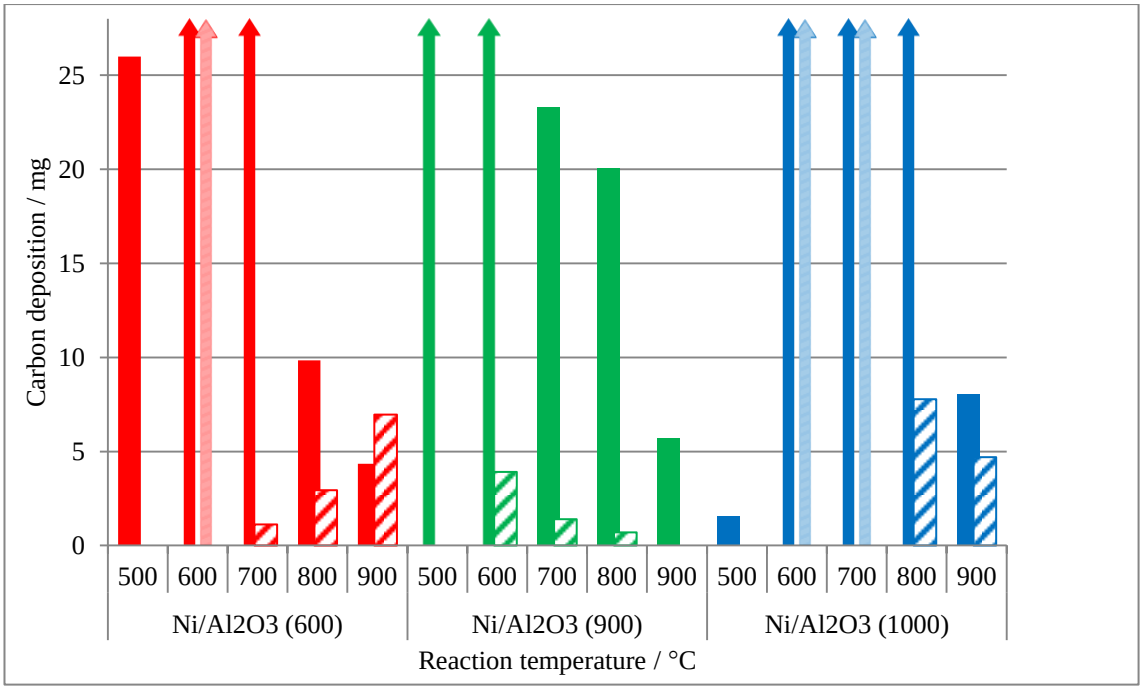

Figure 9.18: Carbon deposition following reactions of methane and steam under methane-rich conditions at 500 °C and 900 °C in sulfur-free (solid) and 80 ppm H_2S (dashed), over Ni/Al_2O_3 (600), Ni/Al_2O_3 (900) and Ni/Al_2O_3 (1000)

During reactions under methane-rich conditions over Ni/Al_2O_3 (600) the addition of sulfur to the reactive gas feed effects the carbon deposition depending on the reaction temperature. It was shown in Section 7.4 that at 500 °C excessive carbon deposition resulted in complete loss of catalytic activity. However, the addition of sulfur to the reactive gas feed completely eliminates carbon formation at this temperature. However, as the reaction temperature is increased carbon deposition is not suppressed to the same extent and considerable carbon deposition is observed at 600 °C. As the reaction temperature is increased from 700 °C to 900 °C an increase in carbon formation is observed in the presence of sulfur, the opposite trend to that observed in the absence of sulfur. The addition of sulfur to the reactive gas feed results in a change in the carbon formation trend observed over Ni/Al_2O_3 (600) at elevated reaction temperatures. This may indicate that the adsorption of sulfur acts to promote methane decomposition or influence the nature of carbon formed over Ni/Al_2O_3 (600) over the reaction temperatures studied. Similarly, Xie *et al*. [10] have shown that

carbon deposition was increased during reactions involving sulfur, although the formation of filamentous carbon was suppressed.

As under stoichiometric conditions, carbon deposition is considerably reduced to minimal levels over Ni/Al_2O_3 (900) in the presence of sulfur, under methane-rich conditions. This is also observed over Ni/Al_2O_3 (1000), although to a lesser extent. Over Ni/Al_2O_3 catalysts calcined at 900 °C and 1000 °C the same trend in carbon deposition with temperature is observed.

Under both stoichiometric and methane-rich conditions carbon deposition has been shown to be most effectively reduced by the presence of sulfur over Ni/Al_2O_3 (900), where carbon deposition is almost completely eliminated.

9.6.2 Carbon deposition during reactions of methane and steam under stoichiometric and methane-rich conditions over Au-Ni/Al_2O_3 a in the presence of 80 ppm H_2S

The carbon deposition following reactions of methane and steam over Au-Ni/Al_2O_3 catalysts for 20 hours under stoichiometric and methane rich conditions are shown in Figure 9.19 and Figure 9.20, respectively. Reactions in sulfur-free environments are shown by solid bars and 80 ppm H_2S are shown by dashed bars in both figures.

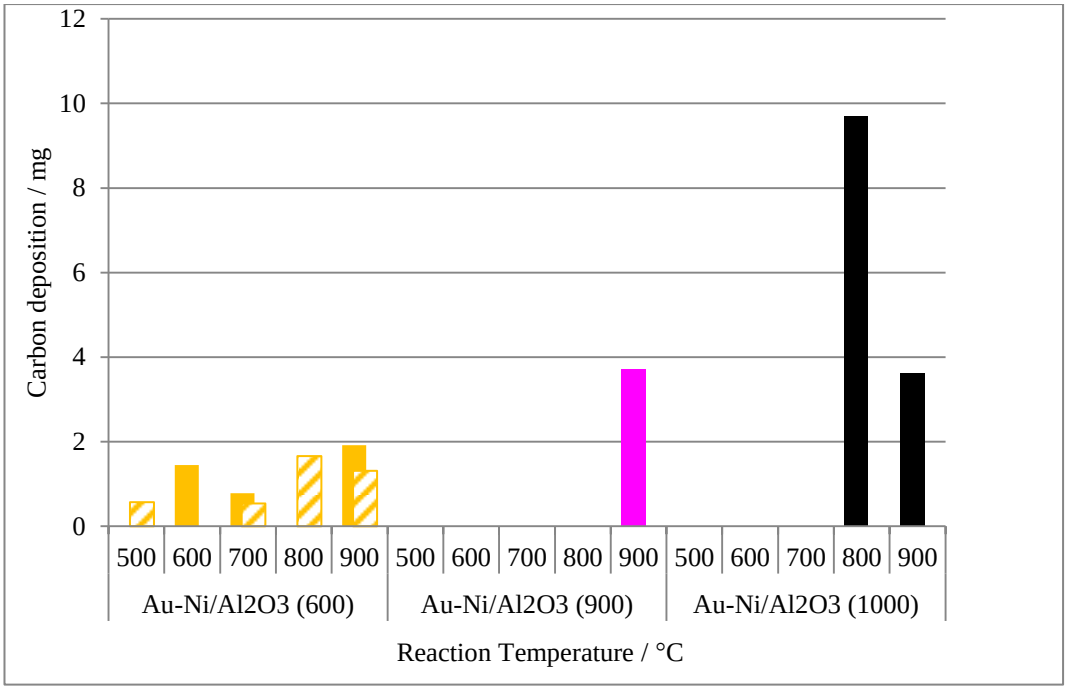

Figure 9.19: Carbon deposition following reactions of methane and steam under stoichiometric conditions at 500 °C and 900 °C in sulfur-free (solid) and 80 ppm H_2S (dashed), over Au-Ni/Al_2O_3 (600), Au-Ni/Al_2O_3 (900) and Au-Ni/Al_2O_3 (1000)

Over Au-Ni/Al_2O_3 (600) the effect of added sulfur on carbon deposition is minimal. Results obtained indicate that sulfur adsorption on Au-Ni/Al_2O_3 (600) acts in a similar manner to the addition of gold to Ni/Al_2O_3 (600). Thus, gold and sulfur may be limiting carbon gasification through the inhibition of nickel active sites or the adsorption of steam.

Over both Au-Ni/Al_2O_3 (900) and Au-Ni/Al_2O_3 (1000) elimination of carbon deposition during reactions of methane and steam in the presence of sulfur is observed. The addition of gold to Ni/Al_2O_3 (900) results in increased sulfur tolerance and an increase in catalyst lifetime by *ca.* 15 hours, although no increase in carbon deposition is observed. Over both Au-Ni/Al_2O_3 (900) and Au-Ni/Al_2O_3 (1000) the presence of sulfur in the reactive gas feed acts to effectively eliminate carbon deposition whilst maintaining high steam reforming activity.

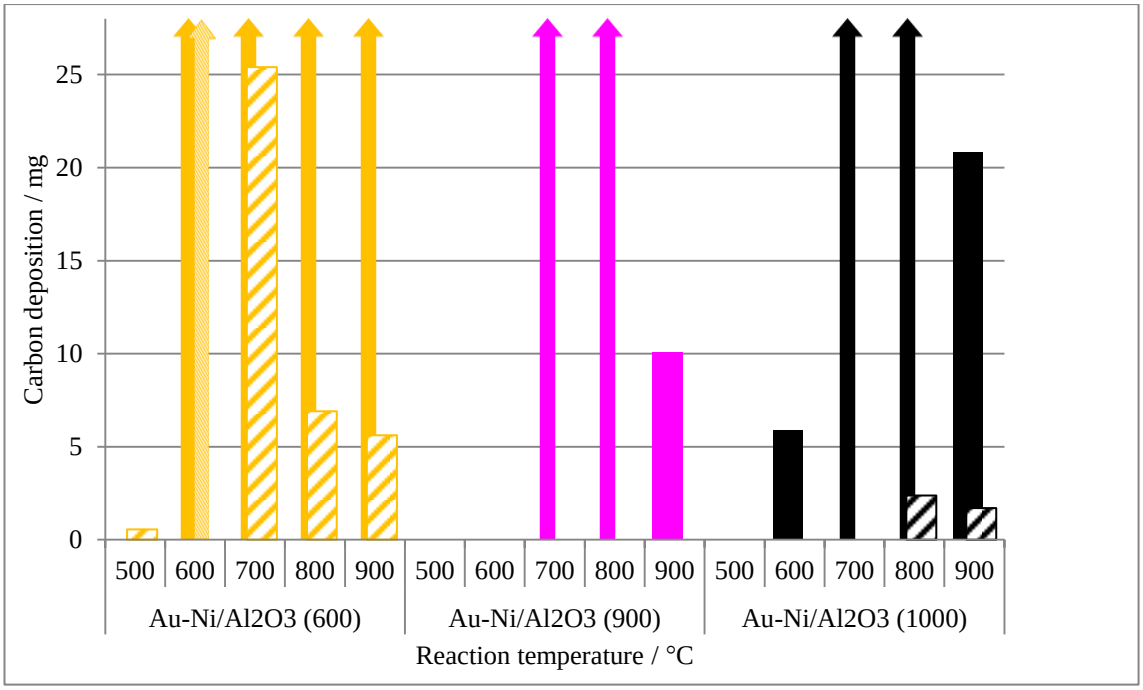

Figure 9.20: Carbon deposition following reactions of methane and steam under methane-rich conditions at 500 °C and 900 °C in sulfur-free (solid) and 80 ppm H_2S (dashed), over Au-Ni/Al_2O_3 (600), Au-Ni/Al_2O_3 (900) and Au-Ni/Al_2O_3 (1000)

Unlike over Ni/Al_2O_3 (600), the carbon deposition trends observed over Au-Ni/Al_2O_3 (600) are not altered following the addition of sulfur to the reactive gas feed. Carbon deposition is significantly reduced following the addition of sulfur, although carbon deposition levels are still relatively high. When sulfur is added to the reactive gas feed over Au-Ni/Al_2O_3 (900) carbon deposition is completely eliminated and over Au-Ni/Al_2O_3 (1000) minimal levels are observed, and only at elevated reaction temperatures. This may be attributed to the combined effects of both gold and sulfur limiting active adsorption sites or altering the stability of intermediate hydrocarbon species on the catalyst surface, thus reducing carbon formation.

There is a considerable difference in the carbon deposition characteristics observed over Au-Ni/Al_2O_3 catalysts calcined at 600 °C, 900 °C and 1000 °C following the addition of sulfur to the methane steam reaction mixture.

9.7 Catalyst regeneration following sulfur poisoning of 20 wt % Ni/Al_2O_3 and 5 mol % Au doped 20 wt % Ni/Al_2O_3 catalysts

It has been shown that catalysts may be at least partially regenerated following sulfur poisoning, recovering some or all of their activity [2, 16, 17]. The addition of oxidising gases to the reaction gas feed, such as CO_2, O_2 and H_2O have been shown to be beneficial towards catalyst regeneration [17, 18], although to varying extents. As well as the addition of oxidising gases to the reaction gas feed, additional methods of catalyst regeneration are also utilised [3], including removal of H_2S, altering the reactant gas composition and increasing the reaction temperature. It has been shown [18] that although catalyst activity may recover following the addition of steam to the reaction gas feed, XPS studies have indicated that adsorbed sulfur is not effectively removed from the surface. This shows that sulfur removal is difficult and although catalyst activity may improve, long term catalyst lifetime and activity may be significantly influenced.

Following reactions of methane and steam in the presence of 80 ppm H_2S under stoichiometric and methane-rich reaction conditions, provisional catalyst regeneration studies were undertaken. The regeneration studies were carried out following sulfur poisoning and complete loss of catalytic activity. Following 2 hours of complete catalyst deactivation and reactive gases passing over the catalyst at the reaction temperature, H_2S was removed from the methane-steam reaction gas feed. This was undertaken for over catalysts at 700 °C and 800 °C.

No improvement in catalytic activity was observed under these conditions, despite carrying out experiments for over 24 hours in the absence of sulfur.

9.8 Summary

The addition of sulfur to reaction mixtures of steam and methane significantly influences the activity of both Ni/Al_2O_3 and $Au\text{-}Ni/Al_2O_3$ catalysts, under stoichiometric and methane-rich conditions. Sulfur poisoning of all catalysts results in some degree of catalyst deactivation.

Generally, as the reaction temperature is increased an increased rate, though not extent, of catalyst poisoning is observed, especially under methane-rich conditions.

A significant variation in the tolerance of catalysts to sulfur poisoning and reaction characteristics are observed over Ni/Al_2O_3 calcined at 600 °C, 900 °C and 1000 °C. Over Ni/Al_2O_3 (600) a cyclic trend is observed during reaction at 800 °C, indicative of successive sulfur adsorption and removal in the presence of steam. This behaviour is not observed over any other catalyst. Over all catalysts, with the notable exception of those calcined at 600 °C, carbon deposition is significantly reduced following the addition of sulfur to the reactive gas feed, in agreement with previous work relating to the SPARG process [7]. This is combined with extended catalyst lifetime and reduced deactivation as calcination temperature is increased, specifically over Ni/Al_2O_3 (1000).

During reactions over catalysts calcined at 600 °C, a difference in the carbon deposition trend is observed. Reactions over both Ni/Al_2O_3 (600) and $Au\text{-}Ni/Al_2O_3$ (600), under stoichiometric conditions, show increased carbon deposition which can be attributed to a reduction in carbon gasification in the presence of sulfur [10]. However, for reactions over Ni/Al_2O_3 (600) under methane-rich conditions, a variation in the carbon deposition trend is observed. The increase in carbon formation at high reaction temperatures observed over Ni/Al_2O_3 (600) may indicate that the adsorption of sulfur acts to promote methane decomposition or supress specific carbon forming reactions. This was also proposed by Xie *et al*. [10], observing that carbon deposition increased during reactions involving sulfur, although the formation of filamentous carbon was suppressed.

The addition of sulfur to reaction mixtures of steam and methane over $Au\text{-}Ni/Al_2O_3$ catalysts results in a variation in the poisoning characteristics and catalyst activity compared to Ni/Al_2O_3 catalysts. In general, the rate of catalyst poisoning and deactivation is considerably reduced over $Au\text{-}Ni/Al_2O_3$ catalysts, most significantly observed during reactions of stoichiometric mixtures where almost linear deactivation over time is observed. This may be attributed to the location of gold at nickel active sites, reducing the sites available for sulfur adsorption, decreasing the rate of

poisoning. Similar reaction characteristics are observed over Au-Ni/Al_2O_3 (900) and Ni/Al_2O_3 (1000), with both catalysts exhibiting significant sulfur tolerance. The similarities in sulfur poisoning characteristics between the two catalysts may be attributed to the morphological and structural similarities of the catalysts observed by SEM shown in Chapter 4 and 5.

The addition of sulfur to the reactive gas feed has impacted steam methane reforming reactions in a comparable manner exhibited following the addition of gold to Ni/Al_2O_3 for catalysts calcined at 600 ºC. For example, sulfur adsorption on Au-Ni/Al_2O_3 (600) acts in a similar manner to the addition of gold to Ni/Al_2O_3 (600), limiting carbon gasification through the inhibition of nickel active sites and the adsorption of steam.

The addition of gold to Ni/Al_2O_3 has shown to increase carbon deposition during specific reactions in the absence of sulfur, as shown in Section 8.11.2. However, the subsequent addition of sulfur to the methane steam reaction mixture over catalysts calcined at 900 °C and 1000 °C results in a significant reduction in carbon formation. For example, over Au-Ni/Al_2O_3 (900) carbon deposition is completely eliminated for sulfur containing reaction mixtures and over Au-Ni/Al_2O_3 (1000) minimal levels are observed following reactions, at elevated reaction temperatures. Despite the reduction in carbon formation during reactions over Ni/Al_2O_3 and Au-Ni/Al_2O_3 catalysts calcined at 900 °C and 1000 °C, reforming activity is reduced and considerable sulfur poisoning is observed. This suggests that for sulfur to be utilised to benefit the reforming process, lower concentrations must be investigated in order to attempt to limit the influence on reforming activity over time, whilst maintaining the reduction in carbon. However, the results do show that under certain conditions some catalysts can be operated in a stable way on sulfur containing gas mixtures, which ultimately has positive implications in the practical catalytic conversion of biogas and sulfur containing hydrocarbon mixtures.

The calcination temperature employed during catalyst preparation significantly influences both the reforming characteristics and tolerance to sulfur poisoning. Calcination at 600 °C, results in an

increase in carbon deposition following sulfur addition. However, high temperature calcination results in significantly increased sulfur tolerance and reduced carbon deposition. The variation in sulfur tolerance and steam reforming properties of the catalysts may be attributed to a number of factors, such as the location of both gold and sulfur on the nickel surface, morphological differences and the presence of additional phases such as $NiAl_2O_4$ or $AuAl_2O_4$. It is evident that both geometric and electronic effects are influencing the surface reaction pathways in the presence of sulfur over the different catalysts, resulting in both increases and decreases in carbon deposition and variations in reforming activity.

9.9 References

1. C.J. Laycock, J.Z. Staniforth, and R.M. Ormerod, *Improving the Sulphur Tolerance of Nickel Catalysts for Running Solid Oxide Fuel Cells on Waste Biogas.* ECS Transactions, 2009. **16**(50): p. 177-188.
2. J. Srinakruang, K. Sato, T. Vitidsant, and K. Fujimoto, *Highly efficient sulfur and coking resistance catalysts for tar gasification with steam.* Fuel, 2006. **85**(17-18): p. 2419-2426.
3. M. Ashrafi, C. Pfeifer, T. Pröll, and H. Hofbauer, *Experimental Study of Model Biogas Catalytic Steam Reforming: 2. Impact of Sulfur on the Deactivation and Regeneration of Ni-Based Catalysts.* Energy & Fuels, 2008. **22**(6): p. 4190-4195.
4. P. Mare´cot, E. Paraiso, J.M. Dumas, and J. Barbier, *Deactivation of nickel catalysts by sulphur compounds: II. Chemisorption of hydrogen sulphide.* Applied Catalysis A: General, 1992. **80**(1): p. 89-97.
5. H.C. Dibbern, P. Olesen, J.R. Rostrup-Nielsen, P.B. Tottrup, and N.R. Udengaard, *Make low H_2/CO syngas using sulfur passivated reforming.* Hydrocarbon Processing, 1986. **65**: p. 71 - 74.
6. J.R. Rostrup-Nielsen, *Chemisorption of hydrogen sulfide on a supported nickel catalyst.* Journal of Catalysis, 1968. **11**(3): p. 220-227.

7. J.R. Rostrup-Nielsen, *Sulfur-passivated nickel catalysts for carbon-free steam reforming of methane.* Journal of Catalysis, 1984. **85**(1): p. 31-43.

8. J.R. Rostrup-Nielsen, I.B. Alstrup, and J.W. Ward, *Ensemble Control By Sulfur Poisoning of Nickel Catalysts for Steam Reforming*, in *Studies in Surface Science and Catalysis*. 1988, Elsevier. p. 725-732.

9. F. Abild-Pedersen, O. Lytken, J. Engbæk, G. Nielsen, I. Chorkendorff, and J.K. Nørskov, *Methane activation on Ni(1 1 1): Effects of poisons and step defects.* Surface Science, 2005. **590**(2-3): p. 127-137.

10. C. Xie, Y. Chen, Y. Li, X. Wang, and C. Song, *Influence of sulfur on the carbon deposition in steam reforming of liquid hydrocarbons over CeO_2-Al_2O_3 supported Ni and Rh catalysts.* Applied Catalysis A: General, 2011. **394**(1-2): p. 32-40.

11. S.L. Lakhapatri and M.A. Abraham, *Deactivation due to sulfur poisoning and carbon deposition on Rh-Ni/Al_2O_3 catalyst during steam reforming of sulfur-doped n-hexadecane.* Applied Catalysis A: General, 2009. **364**(1-2): p. 113-121.

12. I. Gavrielatos, V. Drakopoulos, and S.G. Neophytides, *Carbon tolerant Ni-Au SOFC electrodes operating under internal steam reforming conditions.* Journal of Catalysis, 2008. **259**(1): p. 75-84.

13. Y.-H. Chin, D.L. King, H.-S. Roh, Y. Wang, and S.M. Heald, *Structure and reactivity investigations on supported bimetallic AuNi catalysts used for hydrocarbon steam reforming.* Journal of Catalysis, 2006. **244**(2): p. 153-162.

14. H.S. Bengaard, J.K. Nørskov, J. Sehested, B.S. Clausen, L.P. Nielsen, A.M. Molenbroek, and J.R. Rostrup-Nielsen, *Steam Reforming and Graphite Formation on Ni Catalysts.* Journal of Catalysis, 2002. **209**(2): p. 365-384.

15. M. Ashrafi, C. Pfeifer, T. ProÌˆll, and H. Hofbauer, *Experimental Study of Model Biogas Catalytic Steam Reforming: 2. Impact of Sulfur on the Deactivation and Regeneration of Ni-Based Catalysts.* Energy & Fuels, 2008. **22**(6): p. 4190-4195.

16. C. Laycock, J. Staniforth, and R.M. Ormerod, *Biogas as a fuel for solid oxide fuel cells and synthesis gas production: effects of ceria-doping and hydrogen sulfide on the performance of nickel-based anode materials.* Dalton Transactions, 2011. **40**: p. 5494.

17. S.M. Hashemnejad and M. Parvari, *Deactivation and Regeneration of Nickel-Based Catalysts for Steam-Methane Reforming.* Chinese Journal of Catalysis, 2011. **32**(1): p. 273-279.

18. N. Laosiripojana, S.K. Rajesh, W. Singhto, T. Palikanon, and S. Pengyong, *Effects of H_2S, CO_2, and O_2 on Catalytic Methane Steam Reforming over Ni Catalyst on CeO_2 and Al_2O_3 Supports.* Preceedings of The Third Regional Conference on Energy Technology towards a Clean Environment "Sustainable Energy and Environment (SEE)", 2004: p. 129-133.

10 Conclusion

10.1 Influence of calcination temperature on 20 wt % Ni/Al_2O_3 and 5 mol % Au doped 20 wt % Ni/Al_2O_3 catalysts

The calcination temperature used during catalyst preparation has been shown to significantly influence the morphology, structure and reducibility of Ni/Al_2O_3 and $Au\text{-}Ni/Al_2O_3$ catalysts. As well as the physical and structural characteristics, the calcination temperature also significantly influences reforming activity, carbon laydown and sulphur tolerance of these catalysts.

As the calcination temperature is increased from 600 °C to 800 °C an increase in the interaction between Ni^{2+} and the support is observed, and following calcination at temperatures above 900 °C incorporation of Ni^{2+} into the bulk support structure is observed. 900 °C is a fundamental temperature in the calcination of Ni/Al_2O_3, as the initial stages of nickel aluminate, $NiAl_2O_4$, formation is observed, with the identification of two Ni^{2+} phases. Following calcination at 1000 °C crystalline $NiAl_2O_4$ is formed. High reduction temperatures are required for complete reduction of $NiAl_2O_4$. Despite this, following high temperature reduction a small quantity of $NiAl_2O_4$ remains unreduced in Ni/Al_2O_3 calcined at 1000 °C.

The addition of 5 mol % gold to Ni/Al_2O_3 catalysts results in increased interactions between Ni^{2+} and the support, resulting in a greater quantity of Ni^{2+} that is less reducible. This is bought about because gold significantly influences the formation of $NiAl_2O_4$, confirmed by the formation of a crystalline $NiAl_2O_4$ phase following calcination at 900 °C. As with Ni/Al_2O_3 catalysts, $NiAl_2O_4$ is not formed following calcination of $Au\text{-}Ni/Al_2O_3$ catalysts at temperatures below 900 °C. It is proposed that the increased interaction between Ni^{2+} and support may be attributed to the preparation procedure employed and the influence of pH on the incorporation of nickel into the

support structure. Following reduction of Au-Ni/Al_2O_3 calcined at 900 °C and 1000 °C, more intense gold peaks are observed during XPS analysis. It is proposed that catalyst reduction results in gold segregation to the catalyst surface, facilitated by the high mobility of gold at elevated temperatures. As observed following reduction of Ni/Al_2O_3 (1000), $NiAl_2O_4$ is incompletely reduced following the high temperature reduction of Au-Ni/Al_2O_3 (1000).

In order to ensure no aluminate phases are formed during the preparation of both Ni/Al_2O_3 and Au-Ni/Al_2O_3 catalysts, calcination at temperatures below 800 °C is required. Additionally, high temperature reduction is required to reduce Ni^{2+} species present in both NiO/Al_2O_3 and Au-NiO/Al_2O_3 catalysts. Nickel sintering is not observed following high temperature reduction.

Following re-calcination of reduced catalysts calcined at 1000 °C, *i.e.* those containing the greatest proportion of $NiAl_2O_4$ and requiring the most extreme reduction conditions, reduced nickel species are re-oxidised into their original forms as NiO and $NiAl_2O_4$. It is proposed that although high temperature reduction may reduce Ni^{2+} species, oxidation at high temperatures results in the re-incorporation of Ni^{2+} into the bulk support structure. This behaviour may be completely reversible on successive oxidation – reduction cycles and is a vital factor that must be considered if Ni/Al_2O_3 and Au-Ni/Al_2O_3 catalysts are to be re-used following reforming reactions and subsequent carbon removal by oxidation.

10.2 Steam methane reforming over 20 wt % Ni/Al_2O_3 and 5 mol % Au doped 20 wt % Ni/Al_2O_3 catalysts

Due to the significant effect of calcination temperature on catalyst structure and morphology observed for Ni/Al_2O_3 and Au-Ni/Al_2O_3 catalysts, steam methane reforming studies were performed over catalysts calcined at 600 °C, 900 °C and 1000 °C. Studies were carried out under stoichiometric and methane-rich conditions over a temperature range 500 ºC to 900 ºC. This has

allowed the impact such catalyst modifications have on catalytic reforming activity to be investigated.

Under stoichiometric reaction conditions, carbon is effectively removed during reforming reactions over all reaction temperatures from Ni/Al_2O_3 calcined at 600 °C. However, under methane-rich conditions significant carbon deposition is observed due to significantly reduced carbon gasification, resulting in complete catalyst deactivation at 500 °C. Although high levels of carbon are deposited at higher reaction temperatures, complete catalyst deactivation is not observed. This could indicate that during methane-rich reforming reactions over Ni/Al_2O_3 calcined at 600 °C the nature of the carbon formed on the catalyst surface alters with reaction temperature.

Under stoichiometric reaction conditions Ni/Al_2O_3 calcined at 900 °C appears to be highly active towards the adsorption and subsequent dissociation of H_2O, resulting in increased hydrogen production at elevated reaction temperatures. Consequently, higher levels of surface oxygen are present, increasing carbon gasification and reducing carbon formation. Under methane-rich conditions, the lower steam and higher methane concentrations means this behaviour is not observed.

A significantly different behaviour is observed over Ni/Al_2O_3 calcined at 1000 °C due to the presence of unreduced $NiAl_2O_4$. Low temperature steam methane reforming and carbon-forming activity is reduced due to the low activity of this phase. However, at reaction temperatures above 600 °C, $NiAl_2O_4$ is reduced under reforming conditions increasing both steam reforming and carbon-forming activity. This trend is observed under both stoichiometric and methane-rich conditions.

Following the addition of gold to Ni/Al_2O_3 catalysts, low temperature reforming activity is significantly reduced. However, as the reaction temperature is increased the reduction in activity becomes much less marked. This is attributed to the presence and distribution of gold on the nickel surface, inhibiting highly active nickel surface sites. As the reaction temperature is increased, agglomeration of the gold particles occurs which increases available nickel surface sites, enhancing

reforming activity. XRD shows that gold sintering occurs during calcination at temperatures below 600 ºC but may occur over higher temperatures during reforming due to the temperate reaction conditions compared to those employed during the calcination process.

Although $NiAl_2O_4$ is formed during calcination and identified following the temperature-programmed reduction of Au-Ni/Al_2O_3 calcined at 1000 °C, reduction of this phase is not identified during reforming. This is attributed to the increased stability of $NiAl_2O_4$ and increased interactions between Ni^{2+} and the support following calcination at 1000 °C. It is also possible that the presence of gold reduces hydrogen uptake, limiting reduction under reforming conditions. Methane decomposition and a reduction in carbon gasification is observed over all Au-Ni/Al_2O_3 catalysts, increasing carbon deposition during reactions under stoichiometric and methane-rich conditions.

The addition of gold to Ni/Al_2O_3 catalysts poses no significant long-term benefit towards the activity of catalysts during steam reforming under methane-rich and stoichiometric reaction conditions. Low temperature reforming activity is considerably reduced though activity is similar at higher temperatures, whilst the suppression of carbon gasification increases carbon deposition following the addition of gold to reforming catalysts. This is at variance with previously published work, which has demonstrated that a modest reduction in reforming activity is observed, whilst there is a significant reduction in carbon deposition. This is attributed to the formation of a nickel-gold alloy, inducing electronic changes in the nickel, thus altering the stability of intermediate adsorbed species. However, it has been shown that a surface alloy does not form in Au-Ni/Al_2O_3 during either calcination or reduction in hydrogen and gold is segregated on the nickel surface, accounting for the variation in reforming trends and minimal reduction in carbon deposition over gold-doped catalysts.

This clearly demonstrates the notable impact that the calcination temperature and the reforming conditions can have on the activity and reforming characteristics observed over Au-Ni/Al_2O_3 catalysts. These results suggest that the behaviour of gold-doped nickel based catalysts is highly

sensitive to the preparation method, which can considerably alter the structural and hence surface reaction characteristics of the catalysts.

10.3 Effect of sulfur addition to the reaction gas mixture

Addition of H_2S to the reaction gas feed at a level of 80 ppm, results in significant poisoning of Ni/Al_2O_3 and $Au\text{-}Ni/Al_2O_3$ catalysts and loss of reforming activity at low reaction temperatures. An increase in the rate of catalyst poisoning is observed as the reaction temperature is increased and catalyst lifetime is also reduced up to a reaction temperature of *ca.* 700 °C. A significant reduction in the rate of deactivation as a result of sulfur poisoning is observed over $Au\text{-}Ni/Al_2O_3$ catalysts. This is proposed to occur due to the location of gold on the nickel surface, resulting in a reduction in surface sites available for sulfur adsorption, decreasing the rate of sulfur adsorption and hence catalyst poisoning.

Over all the catalysts, with the notable exception of those calcined at 600 °C, carbon deposition is significantly reduced following the addition of sulfur to the reactive gas feed. However, over both Ni/Al_2O_3 and $Au\text{-}Ni/Al_2O_3$ calcined at 600 °C variations in carbon deposition trends are observed. For example, over Ni/Al_2O_3 calcined at 600 °C a cyclic reforming trend is observed during the reaction at 800 °C under stoichiometric conditions, indicative of successive sulfur adsorption and removal phases in the presence of steam. This results in a slight increase in carbon deposition, attributed to reduced carbon removal. During reactions under methane-rich conditions over Ni/Al_2O_3 calcined at 600 °C a change in the carbon deposition trend is observed. This results in a promotion in methane decomposition reactions at elevated temperatures, as opposed to low temperature carbon formation in the absence of sulfur.

Similar reaction characteristics are observed over $Au\text{-}Ni/Al_2O_3$ calcined at 900 °C and Ni/Al_2O_3 calcined at 1000 °C, attributed to the morphological and structural similarities of the catalysts identified during SEM analysis. The addition of sulfur to the reactive gas feed has a similar effect

on steam methane reforming as that observed following gold-doping of Ni/Al_2O_3 catalysts calcined at 600 ºC. For example, the addition of gold to Ni/Al_2O_3 calcined at 600 °C acts in a similar manner to the adsorption of sulfur to $Au\text{-}Ni/Al_2O_3$ calcined at 600 °C, such that carbon gasification and steam adsorption is limited, increasing carbon formation.

The tandem addition of sulfur to the gas feed and gold to the catalyst has shown to provide additional catalytic benefits, reducing carbon formation whilst also considerably lowering the rate of sulfur poisoning and deactivation over time.

Despite the reduction in carbon deposition during reactions over Ni/Al_2O_3 and $Au\text{-}Ni/Al_2O_3$ calcined at 900 °C and 1000 °C, reforming activity is also reduced and considerable catalyst poisoning is observed over all the catalysts studied, though to a much lower degree at higher reaction temperatures. In order to utilise sulfur in the reaction gas feed to benefit the reforming process lower H_2S concentrations may prove to be more favourable, ensuring a minimal change in catalytic activity whilst improving carbon resistance. Additionally, these catalysts may be used to effectively operate on sulfur containing gas feeds, such as natural gas or biogas, commonly containing sulfur levels much lower than those used in this study.

10.4 Synopsis

The work presented within this thesis is a detailed study for stoichiometric and methane-rich reaction mixtures relating to the use of both Ni/Al_2O_3 and $Au\text{-}Ni/Al_2O_3$ as steam reforming catalysts, and the influence that the calcination temperature and subsequent interactions between Ni^{2+} and the support can have on reforming activity, promotion of side reactions and sulfur tolerance. The amount of and reduction of additional phases, such as $NiAl_2O_4$, has been shown to be an important factor in the resulting catalytic activity under the conditions studied and thus the reforming characteristics of Ni/Al_2O_3 and $Au\text{-}Ni/Al_2O_3$ catalysts.

The addition of gold to Ni/Al_2O_3 catalysts at levels of 5 mol % relative to nickel content provides no long-term substantial benefit relating to reforming activity or carbon deposition during steam methane reforming reactions in the absence of added sulfur.

Sulfur has been introduced into the reaction gas feed at relatively high concentrations compared to those typically present in natural gas or biogas, in order to investigate the sulfur poisoning characteristics on a realistic time frame. The introduction of sulfur to the reactive gas feed reduces carbon deposition, although lower sulfur concentrations may reduce the impact on reforming activity. The combined use of gold as a dopant and sulfur addition to the reactive gas feed may provide additional advantages during the reforming process, limiting the rate of poisoning and reducing carbon deposition, thus extending catalyst lifetime.

This study has allowed initial investigations into the use of Ni/Al_2O_3 and $Au\text{-}Ni/Al_2O_3$ catalysts for the steam reforming of methane-containing fuels, in particular natural gas and biogas, to be undertaken. Catalyst preparation is a major factor in the development of highly active reforming catalysts and one that has often been overlooked. The importance of both the preparation and pre-treatment conditions and their ultimate influence on catalytic activity, as well as the influence of reaction temperature, methane to steam ratio, gold-doping and sulfur addition on alumina supported nickel catalysts has been highlighted within this research.

11 Future work

The research presented within this thesis has provided significant insight into the changes in morphology and structure of both Ni/Al_2O_3 and $Au\text{-}Ni/Al_2O_3$ catalysts following different calcination treatments. The influence these changes have on the reforming activity, tolerance towards carbon deposition and sulphur poisoning of Ni/Al_2O_3 and $Au\text{-}Ni/Al_2O_3$ catalysts has been studied.

Given the complex nature of Ni/Al_2O_3 and $Au\text{-}Ni/Al_2O_3$ catalysts, and the nature of the interactions between the nickel and support phase identified following calcination, as discussed in this work, more detailed characterisation would be desirable to try and gain a greater insight into these interactions and the phase changes which occur during high temperature calcination. The techniques used in this study have allowed the bulk and surface properties to be examined. The use of *in situ* XPS would allow surface properties to be investigated during both calcination and subsequent reduction treatment. TEM and Raman spectroscopy would also provide additional insight into the $NiAl_2O_4$ phase formed and its position and bonding within the support structure. Although *in situ* XRD has been utilised in this work to study high temperature thermal decomposition and oxidation, this technique could also be extended to study reduction and reactions of methane and steam *in situ*. In particular, this could provide some insight into possible structural and phase changes that may be occurring during reforming, including the reduction of $NiAl_2O_4$ during reforming over Ni/Al_2O_3 (1000), as discussed in Chapter 6.

The influence of gold on the catalyst structure, catalytic properties and its dependence on loading, support, preparation method and the calcination temperature and reduction treatments is clearly a complex area and worthy of more detailed investigation than has been possible in this study. This

could focus in particular on the location of gold on the nickel surface and the possible formation of $AuAl_2O_4$ phase, as discussed in Chapter 5. Gold loading has been shown to have a significant impact on the effectiveness of gold as a beneficial addition to reforming catalysts [1-3]. Due to the reduction in reforming activity and increase in carbon deposition observed over Au-Ni/Al_2O_3 catalysts in this study, the influence of gold loading would be a beneficial area of future research. Lower gold loadings may increase low temperature activity and increase the catalyst efficiency in reducing carbon formation.

The results in Chapter 9 show that the presence of sulphur significantly influences both catalytic activity and carbon formation and over the Ni/Al_2O_3 and Au-Ni/Al_2O_3 catalysts studied. This is another important area requiring more detailed study. The results for sulfur-containing reaction feeds over gold-doped Ni/Al_2O_3 are particularly interesting and very positive in terms of reducing carbon deposition and increasing sulfur tolerances. The interplay between sulfur and gold definitely requires further study.

More exclusive regeneration studies involving the addition of O_2 to the reactive gas feed and influence of temperature on catalyst recovery would also be an obvious extension to this work. XPS and XRD [4, 5] may also provide valuable information regarding the poisoning behaviour and regeneration characteristics.

Methane has been used during the steam reforming studies in this work, to reduce complexity. The most common source of methane is natural gas, which contains quite significant levels of sulfur-containing hydrocarbons as well as higher hydrocarbons. Biogas is also currently a very underutilised source of methane which can potentially be utilised in the steam reforming process to produce synthesis gas. Future work should focus on reforming natural gas and potentially reforming actual waste biogas mixtures over Ni/Al_2O_3 and Au-Ni/Al_2O_3 catalysts developed in this study.

11.1 References

1. D.K. Niakolas, J.P. Ouweltjes, G. Rietveld, V. Dracopoulos, and S.G. Neophytides, *Au-doped Ni/GDC as a new anode for SOFCs operating under rich CH_4 internal steam reforming.* International Journal of Hydrogen Energy, 2010. **35**(15): p. 7898-7904.
2. N.C. Triantafyllopoulos and S.G. Neophytides, *Dissociative adsorption of CH_4 on NiAu/YSZ: The nature of adsorbed carbonaceous species and the inhibition of graphitic C formation.* Journal of Catalysis, 2006. **239**(1): p. 187-199.
3. Y.-H. Chin, D.L. King, H.-S. Roh, Y. Wang, and S.M. Heald, *Structure and reactivity investigations on supported bimetallic AuNi catalysts used for hydrocarbon steam reforming.* Journal of Catalysis, 2006. **244**(2): p. 153-162.
4. N. Laosiripojana, S.K. Rajesh, W. Singhto, T. Palikanon, and S. Pengyong, *Effects of H_2S, CO_2, and O_2 on Catalytic Methane Steam Reforming over Ni Catalyst on CeO_2 and Al_2O_3 Supports.* Preceedings of The Third Regional Conference on Energy Technology towards a Clean Environment "Sustainable Energy and Environment (SEE)", 2004: p. 129-133.
5. S.M. Hashemnejad and M. Parvari, *Deactivation and Regeneration of Nickel-Based Catalysts for Steam-Methane Reforming.* Chinese Journal of Catalysis, 2011. **32**(1): p. 273-279.

Appendix A: Influence of calcination time on 20 wt % Ni/Al_2O_3 and 5 mol % Au doped 20 wt % Ni/Al_2O_3 reducibility

---

The calcination temperature selected during preparation has been shown to influence the catalyst morphology and the extent of nickel aluminate formation, Chapter 4. However, the time of calcination may also influence the sample properties and so reducibility of the catalyst, in particular the Ni^{2+} phases present. Numaguchi *et al*. [1] have suggested that as the calcination time is increased the ratio of $NiAl_2O_4$ formed increases and NiO decreases. Despite this, it is observed that the amount of Ni^{2+} species that are difficult to reduce remain constant and that the reducibility of catalysts containing $NiAl_2O_4$ is dependent upon calcination temperature not time.

Calcination over a greater length of time was performed in order to provide information as to the influence such preparation parameters would have on the morphology and structure of alumina supported catalysts. Due to the calcination procedure undertaken samples calcined at higher temperatures undergo calcination for a greater length of time due to the initial temperature increase, therefore, this additional factor must be investigated.

Catalyst precursors, $Ni(NO_3)_2/Al_2O_3$ and $HAuCl_4$ $Ni(NO_3)_2/Al_2O_3$, were calcined at 600 °C for a desired length of time. It has been shown in Chapter 4 and 5 that minimal nickel support interactions are present in samples following calcination at 600 °C, thus in order to investigate if additional interactions between Ni^{2+} and the support occur following calcination over a greater length of time, calcination at 600 °C was investigated. The original samples used during reforming investigations were held for 2 hours, following the initial temperature increase. However, during this study the samples were held for 72 hours in order to investigate the influence a dramatic increase in calcination time has on the catalyst morphology.

1.1 Experimental

Calcination was undertaken as described in Chapter 3, Section 3.2 on pre-calcined prepared undoped and gold doped catalyst samples. The samples were heated up to 500 °C at a heating rate of 1 °C min^{-1}, then up to 600 °C at 5 °C min^{-1}. The temperature was then held for the desired length of time. Following this, the temperature was ramped back down to room temperature at 5 °C min^{-1}.

Temperature-programmed reduction (TPR) analysis was undertaken on both samples in order to investigate the reducibility of Ni^{2+} species present within the sample. Experimental procedures for TPR analysis are described in Chapter 3, Section 3.6.2. Although both hydrogen consumption and water evolution were both measured during TPR studies, only water evolution against temperature is shown in order to show better peak resolution.

1.2 20 wt % Ni/Al_2O_3

Temperature-programmed reduction profiles for NiO/Al_2O_3 (600) samples calcined at 2 hours and 72 hours are shown in Figure A 1 and Figure A 2, respectively.

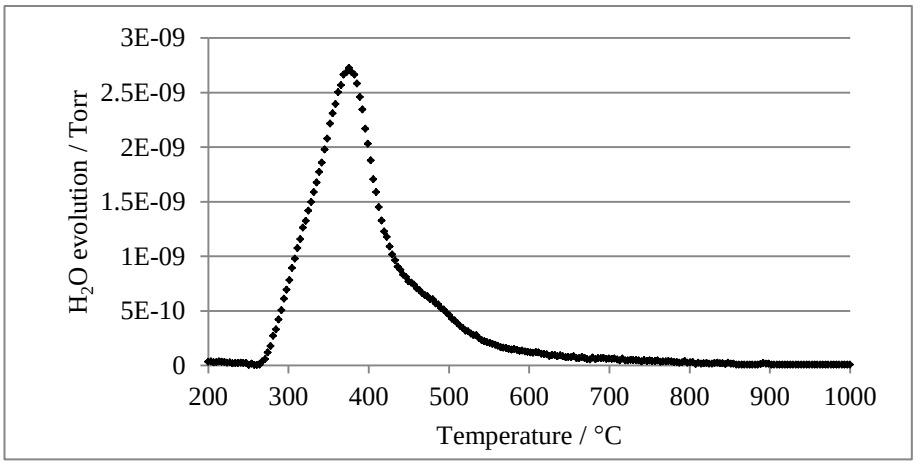

Figure A 1: Temperature-programmed reduction profile for NiO/Al_2O_3 (600) calcined for 2 hours

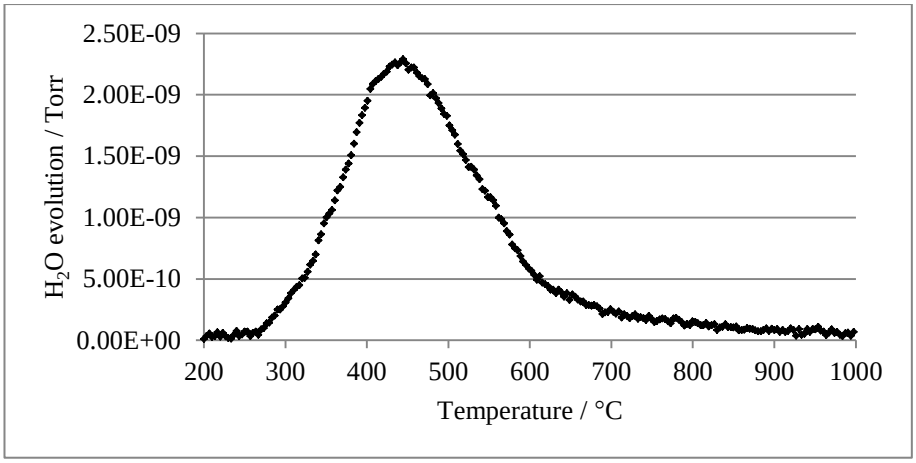

Figure A 2: Temperature-programmed reduction profile for NiO/Al_2O_3 (600) calcined for 72 hours

The temperature at which Ni^{2+} reduction initiates is not affected by length of calcination, under both circumstances reduction initiates at *ca.* 275 °C. However, the peak maxima observed during the reduction of the sample calcined for 72 hours is considerably different from the sample calcined for 2 hours. Following calcination for 2 hours (Figure A 1), reduction is a fast process and the temperature of maximum water evolution is observed at *ca.* 375 °C. Following calcination for 72 hours, Figure A 2, the temperature of maximum water evolution occurs at *ca.* 440 °C and over a wider temperature range. The shoulder observed in the TPR profile for the initial sample is no longer observed following extended calcination. The temperature at which Ni^{2+} is reduced to metallic nickel increases as the calcination length increases, indicating that prolonged calcination increases Ni^{2+} interactions with the support.

1.3 5 mol % Au doped 20 wt % Ni/Al_2O_3

Temperature-programmed reduction profiles for $Au\text{-}NiO/Al_2O_3$ (600) for 2 hours and 72 hours are shown in Figure A 3 and Figure A 4, respectively.

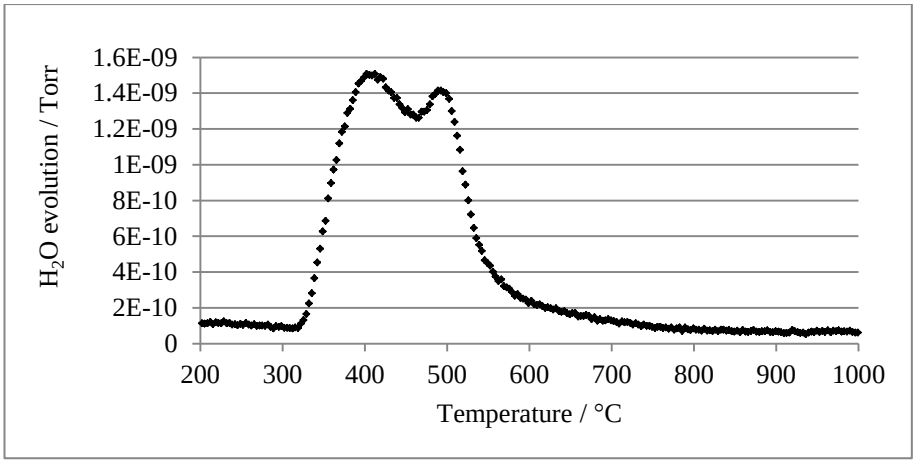

Figure A 3: Temperature-programmed reduction profile for Au- NiO/Al_2O_3 (600) calcined for 2 hours

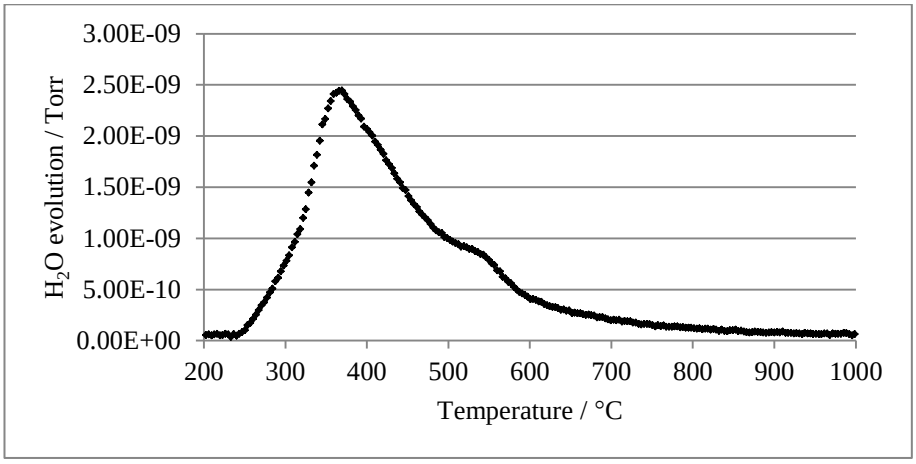

Figure A 4: Temperature-programmed reduction profile for Au- NiO/Al_2O_3 (600) calcined for 72 hours

Following calcination for 72 hours, a significant variation in the reduction of Ni^{2+} species is observed and reduction is influenced by the length of calcination. Ni^{2+} reduction initiates at a reduction temperature *ca.* 100 °C lower than the reduction of the sample calcined for 2 hours. The major peak observed at *ca.* 500 °C for the initial sample (Figure A 3), is present only as a small shoulder following calcination over a prolonged period of time. This could indicate that following long term calcination the structure of the Au-Ni/Al_2O_3 sample is altered, affecting the reducibility of the nickel species. Upon extended calcination gold could become more mobile, forming gold

clusters as opposed to being highly dispersed on the nickel-support surface. This could increase the reducibility of nickel species due to less interaction or inhibition from the gold. The TPR profile shown in Figure A 4, resembles that of Ni/Al_2O_3 (600) calcined for 2 hours shown in Figure A 1. This could indicate that following extended calcination, gold is no longer influencing reduction of nickel species and reduction occurs in a similar manner to Ni/Al_2O_3 samples.

1.4 Summary

Calcination over an extended period of time could prove to be detrimental towards both Ni/Al_2O_3 and Au-Ni/Al_2O_3 catalyst samples. In the case of Ni/Al_2O_3 samples, longer calcination times increase interactions between Ni^{2+} and the support, reducing Ni^{2+} reducibility. However, in Au-Ni/Al_2O_3 doped samples increased time of calcination increases Ni^{2+} reducibility, possibly at the expense of gold dispersion. This could limit the beneficial effects of gold in later reforming investigations.

The study undertaken has highlighted the impact that a dramatic increase in calcination time would have on the reduction of catalysts. However, during the original calcination procedure an increase of *ca.*1 hour per 100 ºC increase in calcination temperature occurs. This is a minimal increase in calcination time, compared to the increase in time investigated in this research. The slight changes observed during this study due to a dramatic increase in calcination time, would most likely not occur for samples calcined in this research. Calcination time is an important factor to be considered in the preparation of catalysts, although due to the short calcination time employed during this study it is not a factor that would significantly influence the catalysts prepared during this research.

1.5 References

1. T. Numaguchi, H. Eida, and K. Shoji, *Reduction of $NiAl_2O_4$ containing catalysts for steam methane reforming reaction.* International Journal of Hydrogen Energy, 1997. **22**(12): p. 1111-1115.

Appendix B: Influence of temperature ramp direction on temperature-programmed reactions involving methane and steam

Forward temperature-programmed reactions involving methane and steam were undertaken over Ni/Al_2O_3 (600) in order to determine if the catalyst was influenced by the presence of an oxidant, such as steam, at low reaction temperatures. Matsumura *et al.* have shown that 20 wt % Ni/Al_2O_3 catalysts can re-oxidise during steam reforming reactions. Following reduction and steam reforming, NiO XRD peaks were observed. This was attributed to re-oxidation of surface nickel during steam reforming reactions at 500 °C, over 5 hours [1].

Prior to the temperature-programmed reaction, the catalyst was fully reduced in hydrogen, as detailed in Chapter 3, Section 3.6.2. Temperature-programmed reactions involving methane and steam were run as previously described in Chapter 3 Section 3.6.3, although during forward temperature-programmed reactions the temperature was linearly increased from 200 °C to 1000 °C at a rate of 5 °C min^{-1}. Reactions were undertaken in near stoichiometric conditions, methane to steam ratio of 1.

1.1 Temperature-programmed reaction of methane and steam over Ni/Al_2O_3 (600) in stoichiometric conditions

To demonstrate the influence of steam on low temperature catalytic reactivity, both forward and reverse temperature-programmed reactions of methane and steam were undertaken. The forward temperature-programmed reaction involving methane and steam over Ni/Al_2O_3 (600) is shown in Figure B 1. For comparison, the reverse temperature-programmed reaction is shown in Figure B 2.

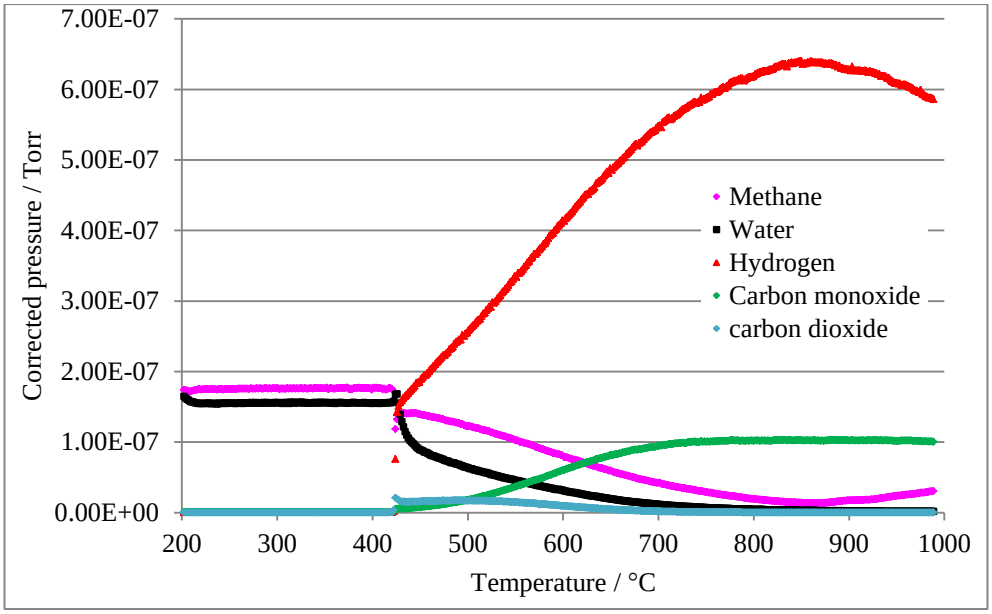

Figure B 1: Forward temperature-programmed reaction involving methane and steam over Ni/Al_2O_3 (600)

During forward temperature-programmed reactions, a sudden reaction onset is observed at *ca.* 450 °C, known as the 'light-off' point. At this point, rapid production of hydrogen, carbon dioxide and carbon monoxide is observed. The 'light-off' point could be attributed to saturation of the surface with adsorbed OH species, at low temperatures. Upon increased reaction temperature, an optimum temperature is reached when surface OH species desorb and surface reactions proceed unhindered. Alternatively, the presence of steam could partially re-oxidise the nickel surface at low temperatures, to NiO, inhibiting the reaction progress as NiO is unreactive towards steam methane reforming [1]. As the temperature is increased the surface re-reduces allowing the reaction to proceed.

When undertaking reactions in the presence of methane and steam in reverse, a 'light-off' point is not observed. The reaction proceeds steadily and catalyst reactivity at low temperatures is able to be accurately monitored. At high temperatures, surface nickel is not in the presence of excess steam as it is utilised during reforming reactions. This ensures that the surface is not saturated by adsorbed OH species or partially re-oxidised during the reaction process.

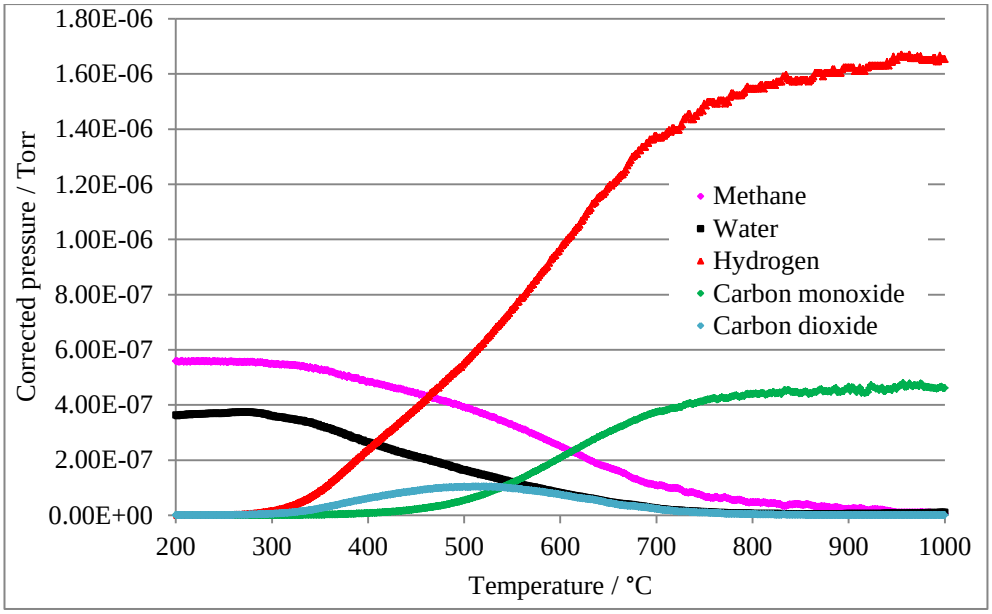

Figure B 2: Reverse temperature-programmed reaction involving methane and steam over Ni/Al_2O_3 (600)

Undertaking reactions in reverse also ensures that additional factors such as carbon deposition do not significantly affect the catalyst activity. catalysts used in this study are highly active towards carbon forming reactions at temperatures between *ca.* 500 °C and 700 °C, as discussed in Chapter 2. During forward temperature-programmed reactions, a reduction in high temperature activity above 850 °C is observed, this could be due to carbon deposition. However, during reverse temperature-programmed reactions this reduction in activity is not observed. Although the influence of carbon deposition on catalyst activity is not able to be eliminated during the reverse temperature-programmed reaction, this reverse reaction process ensures that carbon has less influence on reforming reactions. When undertaking forward temperature-programmed reactions, unwanted side reactions influence both catalytic activity and reactivity hindering accurate reactivity data to be obtained.

1.2 Summary

During forward temperature-programmed reactions, catalytic reactivity is not able to be determined due to the presence of a 'light-off' point and high temperature activity is reduced due to the

deposition of carbon at mid temperatures. In order to gain more accurate temperature-programmed reaction data in the presence of methane and steam, reactions must be undertaken in reverse. This allows the influence of both steam presence and carbon deposition, at all temperatures, to be eliminated or reduced.

1.3 References

1. Y. Matsumura and T. Nakamori, *Steam reforming of methane over nickel catalysts at low reaction temperature.* Applied Catalysis A: General, 2004. **258**(1): p. 107-114.

Appendix C: Carbon gasification in the presence of steam

As discussed in Chapter 2, amongst other carbon-forming reactions, CO reduction (Reaction 3.1) can occur during reforming reactions, producing carbon. Thermodynamic predictions suggest that as the reaction temperature is increased ΔG^{Θ} becomes more positive, limiting the forward reaction. This is shown in Table C 1. The forward reaction is favoured at temperatures below *ca.* 672 °C. At temperatures above this, thermodynamic predictions indicate that it is possible for the carbon gasification in the presence of steam (reverse CO reduction) to occur.

$CO + H_2 \leftrightarrow C + H_2O$ (3.1)

Table C 1: Thermodynamic predictions for CO reduction produced using data from [1]

	$\Delta G^{\Theta}_{298\ K}$ / kJ mol^{-1}	$\Delta G^{\Theta}_{1200\ K}$ / kJ mol^{-1}	$T_{\Delta G=0}$ / K	$T_{\Delta G=0}$ / °C
$CO + H_2 \leftrightarrow C + H_2O$	-89.8	35.4	945.0	672.0

The reaction undertaken in this study will provide an indication as to the extent of carbon gasification by steam. During reforming reactions the influence of steam on carbon gasification may vary due to the catalytic influences and reaction processes occurring. Therefore, this study must be viewed with care as reactions are carried over a known amount of unsupported carbon, not carbon deposited on catalysts during reforming reactions.

Temperature-programmed reactions involved passing steam over 15 mg of carbon, while the temperature was linearly ramped from 100 °C to 1000 °C, at a rate of 10 °C min^{-1}. This allowed the

the effect that steam has on carbon gasification to be determined. The steam pressure used during the reaction was the same as that employed during reactions involving methane and steam under stoichiometric conditions (the highest steam ratio used during reforming studies).

1.1 Temperature-programmed reaction of steam over carbon

The profile for the reaction of steam over carbon is shown in Figure C 1, whilst an expanded profile of Figure C 1 showing minor gas evolution is shown in Figure C 2.

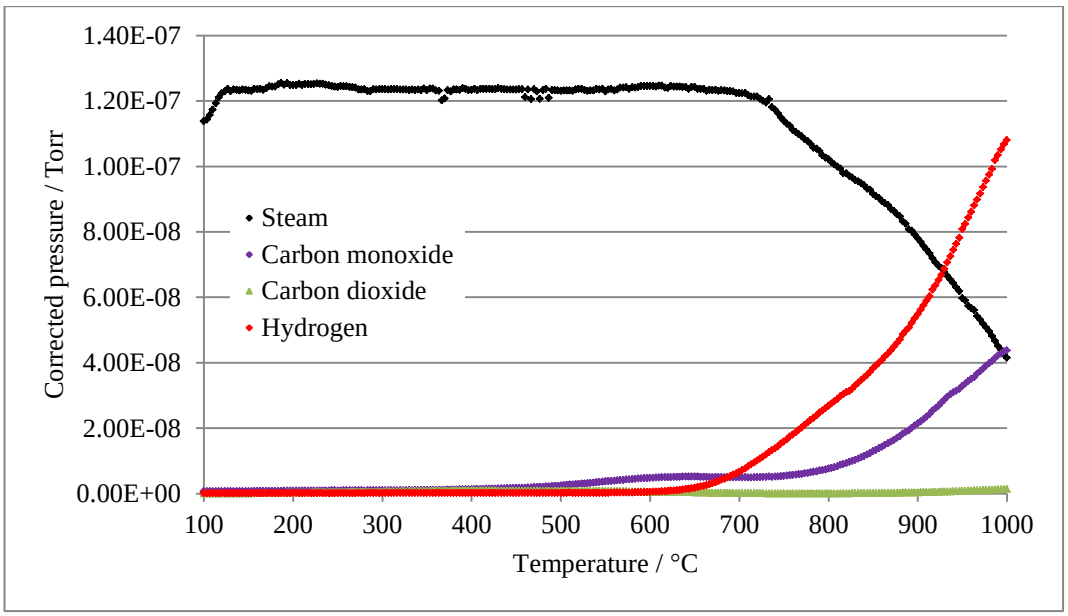

Figure C 1: Reaction of steam over of carbon

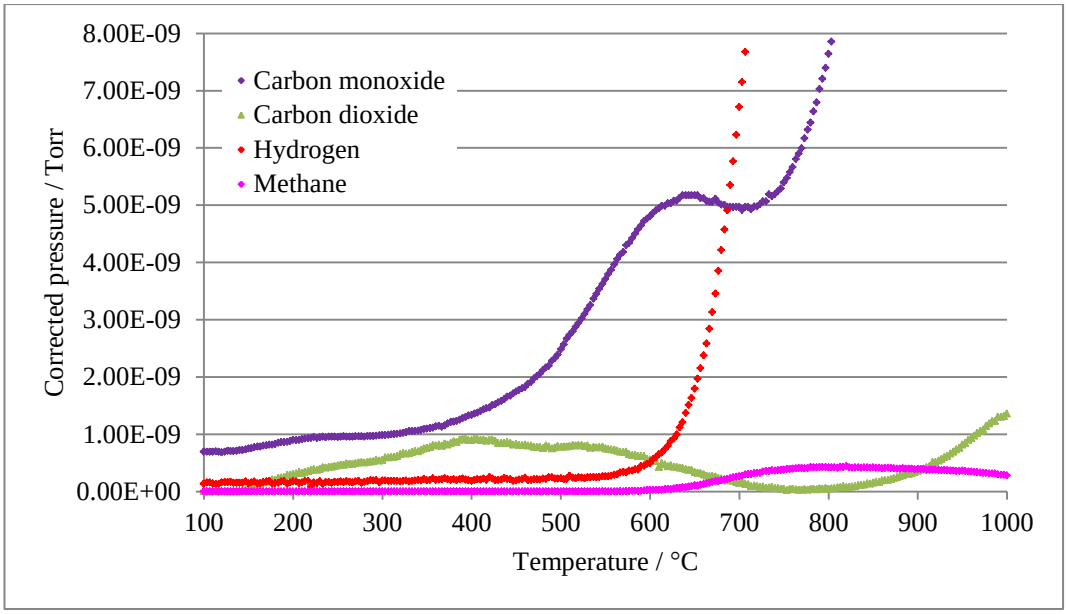

Figure C 2: Expanded profile of Figure C 1, showing minor gas production during reaction of steam over carbon

Carbon monoxide, carbon dioxide, hydrogen and methane are all detected during the reaction of steam and carbon. Two main reaction processes are identified during the reaction of steam and carbon. Initially steam adsorbs on the carbon surface (Reaction 3.2), forming adsorbed oxygen species, which react with carbon to form carbon monoxide and carbon dioxide (Reactions 3.3 and 3.4) at temperatures as low as *ca.* 150 °C. Hydrogen does not desorb until significantly higher temperatures of *ca.* 550 °C via Reaction 3.6.

The second reaction process occurs at *ca.* 610 °C. Following the production of hydrogen, some methane is produced, whilst carbon monoxide and carbon dioxide are consumed. This is proposed to occur via Reactions 3.7 and 3.8. Carbon dioxide and carbon monoxide signals are clearly reduced as they are consumed in the production of methane. As the temperature is increased above 800 °C, carbon dioxide is produced in excess of the requirements of Reaction 3.7 and is detected. Hydrogen, carbon monoxide and carbon dioxide production all increase significantly as the temperature is increased above 800 °C and Reactions 3.2 – 3.6 occur to a greater extent.

$H_2O \rightarrow 2{*}H + {*}O$ (3.2)

$$*O + C \rightarrow CO \quad (3.3)$$

$$2*O + C \rightarrow CO_2 \quad (3.4)$$

$$*CO + *O \rightarrow CO_2 \quad (3.5)$$

$$2*H \rightarrow H_2 \quad (3.6)$$

Where * denotes adsorbed species

$$4H_2 + CO_2 \rightarrow CH_4 + 2H_2O \quad (3.7)$$

$$4H_2 + CO \rightarrow CH_4 + H_2O \quad (3.8)$$

Carbon gasification is proposed to occur predominantly by the reverse of Reaction 3.1 via the main reaction steps proposed above (Reactions 3.2, 3.3 and 3.6), due to the predominant production of hydrogen and carbon monoxide. Carbon gasification by steam can clearly occur at temperatures as low as 150 °C and increases as the temperature is increased, with a particularly marked increase at temperatures above *ca.* 700 °C.

Although the amount formed is relatively low, methane is produced through an additional side reaction in the presence of hydrogen, carbon monoxide and carbon dioxide (Reactions 3.7 and 3.8).

1.2 Summary

Although this study was performed over unsupported carbon and not on catalyst samples it provides a very useful insight into the influence that steam has on carbon gasification. It has been shown that carbon gasification by steam can occur predominantly by the reverse of CO reduction, at extremely low temperatures (below 200 °C). As the reaction temperature is increased the production of hydrogen, carbon monoxide and carbon dioxide increases through the gasification of carbon by steam. Methane is formed by a side reaction, in the presence of hydrogen, carbon

monoxide and carbon dioxide from *ca.* 610 °C. The rate of carbon removal by steam increases very markedly at temperatures above *ca.* 700 °C.

Results gained indicate that during reactions involving methane and steam, any carbon produced can be gasified in the presence of steam. A range of reaction temperatures have been investigated in this study, from 500 °C to 900 °C. The results shown here indicate that carbon gasification may occur over all reforming temperatures investigated but significantly at temperatures above *ca.* 700 °C. During steam methane reforming there will be competition between both carbon-forming reactions and carbon gasification, affecting the amount of carbon formed and influencing the reaction products.

1.3 References

1. *CRC Handbook of Chemistry and Physics*, ed. D.R. Lide. 1995-1996 76h Edition: CRC Press.

Appendix D: Overview of studies undertaken in collaboration with the University of Glasgow

Part of this project has involved an EPSRC funded collaboration with the Surface Chemistry and Heterogeneous Catalysis Group led by Dr Lennon at the University of Glasgow and Dr Stewart Parker at the ISIS neutron source at Rutherford Appleton Laboratory. A variety of techniques including *in situ* inelastic neutron scattering (INS), Raman and infrared spectroscopy, transition electron microscopy (TEM) and X-ray diffraction (XRD) have been used to investigate the catalysts used in this research study. A number of Ni/Al_2O_3 and $Au\text{-}Ni/Al_2O_3$ catalysts with different gold and nickel loadings, calcination and reduction treatments were prepared using the procedure outlined in Chapter 3. Catalytic reaction measurements involving steam and carbon dioxide were performed over *ca.* 20 g of catalyst, presenting some significant challenges relating to catalyst preparation and catalytic testing. Temperature-programmed and isothermal reactions were carried out for the first time at the ISIS facility, as well as at Glasgow, enabling post-reaction INS spectroscopy to be performed.

A recent joint paper has involved the examination of carbon dioxide methane reforming over Ni/Al_2O_3 and $Au\text{-}Ni/Al_2O_3$ catalysts, through the combination of vibration spectroscopy and thermal characterisation methods, to obtain a much greater insight into the nature of carbon deposited during reforming reactions at different reforming temperatures [1]. More specifically, this has involved the application of *in situ* INS spectroscopy as a major characterisation tool, allowing hydrogen retention on the catalyst surface to be examined for the first time and a qualitative description of the carbon dioxide methane reforming reaction kinetics to be proposed. A variety of techniques have been applied in this study enabling a more detailed understanding into

the specific deposition characteristics during carbon dioxide reforming to be built-up. Post-reaction temperature-programmed oxidation has allowed the determination of the total amount of retained carbon. Raman spectroscopy and XRD have suggested the bulk of the carbon over-layer material is a framework of carbon rings and graphic carbon is identified, whilst TPO and INS studies suggest that graphitisation is relatively low, and no filamentous or graphic carbon is observed during TEM studies. This has led to the conclusion that both catalysts are extremely efficient in the cycling of hydrogen during the process and amorphous carbon is formed during carbon dioxide reforming of methane. INS spectroscopy has allowed unambiguous characterisation of low levels of hydrogen associated with deposited carbon. This multi-technique approach has ultimately led to a kinetic insight into the primary reactions occurring during the formation of carbon during reforming reactions. A generalised kinetic scheme that accounts for the partitioning of carbon and hydrogen within the reaction system has been proposed including the following elementary reactions: a) dissociative adsorption of methane, b) re-combinative desorption of adsorbed hydrogen atoms, c) oxidation of adsorbed carbon atoms and d) polymerisation of adsorbed carbon to form amorphous carbon. A high carbon to hydrogen ratio of the active catalysts has indicated that molecular hydrogen species are neither formed nor retained in any substantial quantity on the catalyst surface. Therefore, bulk carbon formed during the reforming process is predominantly bonded to other carbon atoms. It has also been shown during this work that the addition of gold to Ni/Al_2O_3 catalysts provides no benefit during carbon dioxide reforming of methane at elevated reaction temperatures and in fact increases catalyst deactivation during the reforming reactions undertaken.

Additional studies have focused on the use of Ni/Al_2O_3 catalysts during methane reforming of steam [2]. INS spectroscopy studies have allowed the retention of hydrogen in the carbonaceous outer layer to again be examined and during mid-temperature processes carbon deposition has shown to occur primarily in the form of filamentous coke. It has also been shown that steam is a superior oxidant to carbon dioxide, reducing carbon deposition to a greater extent.

These studies have provided fundamental information regarding hydrogen retention during reforming studies and carbon formation, allowing kinetic schemes to be determined for both steam and carbon dioxide reactions. This research has involved the utilisation of *in situ* INS spectroscopy as a novel technique for the identification and quantification of hydrogen retention on hydrocarbon reforming catalyst surfaces and the subsequent use of this information, alongside other vibrational spectroscopy, additional characterisation techniques and catalytic data, to propose kinetic schemes. A third paper will focus on the use of isotope labelling to give additional insight into the reaction pathways.

1.1 References

1. I.P. Silverwood, N.G. Hamilton, A.R. McFarlane, J. Kapitan, L. Hecht, E.L. Norris, R. Mark Ormerod, C.D. Frost, S.F. Parker, and D. Lennon, *Application of inelastic neutron scattering to studies of CO_2 reforming of methane over alumina-supported nickel and gold-doped nickel catalysts.* Physical Chemistry Chemical Physics, 2012.
2. I.P. Silverwood, E.L. Norris, R.M. Ormerod, C.D. Frost, S.F. Parker, and D. Lennon, *The application of inelastic neutron scattering to investigate the steam reforming of methane over alumina-supported nickel catalysts.* Journal of Catalysis, paper in preparation.

PCCP

Cite this: DOI: 10.1039/c2cp42745a

www.rsc.org/pccp

PAPER

Application of inelastic neutron scattering to studies of CO_2 reforming of methane over alumina-supported nickel and gold-doped nickel catalysts

Ian P. Silverwood,[a] Neil G. Hamilton,[a] Andrew R. McFarlane,[a] Josef Kapitán,[a] Lutz Hecht,[a] Elizabeth L. Norris,[b] R. Mark Ormerod,[b] Christopher D. Frost,[c] Stewart F. Parker[c] and David Lennon*[a]

Received 6th August 2012, Accepted 7th August 2012
DOI: 10.1039/c2cp42745a

The methane reforming reaction with carbon dioxide as the oxidant over alumina-supported nickel and gold-doped nickel catalysts is studied using a variety of techniques such as reaction testing, vibrational spectroscopy (inelastic neutron scattering (INS), Raman scattering and infrared absorption), temperature-programmed oxidation (TPO), transmission electron microscopy and X-ray powder diffraction. The quantities of retained carbon and hydrogen are determined by TPO and INS, respectively. Minimal hydrogen retention indicates these catalysts to be very efficient at cycling hydrogen. The relative partitioning of hydrogen within the reaction media is used to formulate a qualitative description of the reaction kinetics. The presence of the gold modifier does not appear to provide any improvement in catalyst performance under the specified reaction conditions.

1. Introduction

The importance of oil to the current eco-political world order cannot be overstated. However, stocks are dwindling and prices are increasingly unstable. The lure of alternative energy sources and chemical feedstocks consequently grows on a virtually daily basis. One possibility for a primary chemical feedstock is the use of methane from natural gas, which is still relatively abundant.[1] The key to exploiting methane in this way is the production of synthesis gas (CO and H_2), which may subsequently be used in the Fischer–Tropsch reaction to form higher hydrocarbons,[2] or in other chemical processes such the synthesis of methanol or ammonia.[3] Commercially, steam reforming of methane as described in eqn (1) is most frequently used, although this reaction demands relatively high energies and produces syngas rich in hydrogen.[4] The use of CO_2 as an alternative oxidant ('dry' reforming), as described in eqn (2), offers environmental benefits, and the synthesis gas produced has a lower H_2 : CO ratio which is more suited to Fischer–Tropsch synthesis.[5] The topic of syngas manufacture has recently been reviewed by Rostrup-Nielsen and Christiansen.[6]

$$\text{Steam reforming:}\quad CH_4 + H_2O \rightarrow CO + 3H_2, \quad (1)$$

$$\text{"Dry" reforming:}\quad CH_4 + CO_2 \rightarrow 2CO + 2H_2. \quad (2)$$

Nickel catalysts are commonly used for both 'dry'- and steam-reforming, although they are known to deactivate rapidly through coke formation.[7,8] Investigations into the use of nickel doped with noble metals have shown less coke deposition and higher activities. However, despite these benefits, their use has not proved to be economically viable.[9] For the steam reforming reaction, it has been shown that disruption of the nickel catalyst surface with sulfur,[10] tin,[11] gold[12] or silver[13] can inhibit coke growth. Various broad classifications of carbon forms are used for the carbon linked to deactivation.[8] Highly reactive monatomic carbon has been suggested to function as a reaction intermediate, commonly denoted C_α. In addition to CO production, this carbon may dissolve in nickel to form a bulk carbide, C_γ, or polymerise to constructs of amorphous carbon, C_β. Further, the growth of filamentous carbon may cause physical damage to the catalyst and generate pressure rises within the reactor. However, this mechanical growth process does not inhibit chemical activity.[14] Chemical inhibition is caused by encapsulating carbon, which covers the nickel surface and prevents reactants from accessing the active catalytic sites. At high temperatures crystalline graphite (C_c) may form, which will also have a deactivating effect.

In any coke-forming reaction, a range of carbon species is likely to be formed and the conversion between materials and their morphology is complex. Due to the nature of carbon deposits, thermal methods are often the only characterisation tool employed, which may misrepresent the materials' true nature and mask minority species. It has been shown that optical spectroscopy is applicable to highly absorbing, coked, catalyst samples[15,16] and vibrational spectroscopy with neutrons can also be used on completely absorbing materials.[17]

[a] *School of Chemistry, Joseph Black Building, University of Glasgow, Glasgow, G12 8QQ, Scotland, UK. E-mail: David.Lennon@glasgow.ac.uk; Tel: +44 (0)141-330-4372*
[b] *School of Physical and Geographical Sciences, Keele University, Staffs, ST5 5BG, UK*
[c] *ISIS Facility, STFC Rutherford Appleton Laboratory, Chilton, Didcot Oxon OX11 0QX, UK*

Characterisation methods combining vibrational spectroscopy with thermal methods consequently promise a more complete investigation into the materials deposited on catalyst surfaces.

This study is a continuation of studies summarised in previous articles describing the use of inelastic neutron scattering (INS) to characterise the CO_2 reforming of methane over alumina-supported nickel catalysts.[18,19] Specifically, this communication seeks to apply the INS technique to compare the performance of a representative nickel catalyst with a gold-doped nickel catalyst. Pioneering work from Clausen, Nørskov and co-workers has demonstrated that gold-doped nickel catalysts may be used in the steam reforming of methane in order to minimise deactivation.[20,21] On the basis that the most active sites on nickel catalysts are those which are located at steps and edges,[22,23] the gold atoms in the promoted catalysts are thought to block these sites that are responsible for coking. However, the improved coking resistance cannot be exclusively attributed to this effect, as an electronic effect may need to be additionally invoked.[23] Model studies have shown that the addition of gold slightly decreases the ability of the catalyst to dissociate methane. More importantly, however, the active monatomic carbon intermediate C_α is destabilised, so that it is more likely to be oxidised (to CO) than to polymerise into coke, C_β.[21] Rostrup-Nielsen has demonstrated that a larger "ensemble" of active metal sites is required to form coke than is needed for the desired reaction.[10] Atoms, which are well distributed, will therefore work to disrupt the larger ensembles and thus improve catalyst longevity. These atoms are not required to be metallic, as demonstrated by the use of sulphur in the SPARG (Sulfur PAssivated ReforminG) process.[10]

In contrast, the use of gold-modified catalysts applied to the 'dry' CO_2 reforming of methane is much less studied. A Japanese patent was granted in 1999 for the production and use of Ni catalysts on ZSM-5 for 'dry' reforming, with promotion by Pt and Au being mentioned.[14] Zhu reports on the use of a Ni/Au catalyst for 'dry' reforming.[24] Triantafyllopoulos and Neophytides have examined the addition of gold to nickel partial oxidation catalysts, with gold being hypothesised to increase the lifetime, stability and concentration of CH_x species.[25] Further, Guczi *et al.* have examined the 'dry' reforming of methane on a Ni/Au spinel, with gold being thought to inhibit the conversion of monatomic carbon to carbon nanotubes and graphite.[26] The conclusions by both Triantafyllopoulos and Guczi are compatible with electronic effects reported by Clausen and co-workers.[21]

The central theme of this communication is the evaluation of the extent of hydrogen retention in an alumina-supported nickel catalyst, acting as a generic methane reforming catalyst, and the comparison of the performances of Ni/Al_2O_3 and gold-modified Ni/Al_2O_3. This comparison is achieved by the application of inelastic neutron scattering (INS). We have recently demonstrated that INS may be used to (i) identify hydrogen retained by heterogeneous catalysts and (ii) quantify the extent of that retention.[18] This information may subsequently be used to comment on mass balance relationships for particular catalytic systems, which is of particular use for the 'dry' reforming of methane, as the reverse water gas shift reaction, as described in eqn (3), may complicate mass balance estimates:

$$CO_2 + H_2 \rightarrow CO + H_2O. \quad (3)$$

Specifically, hydrogen produced from the methane reforming reaction (eqn (2)) may react with the oxidant to produce carbon monoxide and water. The amount of water generated is difficult to quantify, compromising the reliability of assessing the hydrogen content within the catalyst matrix. INS offers the opportunity to determine directly the quantity of hydrogen at the catalyst surface.[18,27] Combining the information deduced from INS with traditional carbon retention measurements such as temperature-programmed oxidation (TPO), permits possible kinetic schemes to be discussed.

As this work has been driven by the evaluation of routes that contribute to catalyst deactivation, the 'dry' reforming reaction is performed using a methane rich feedstream: $CH_4 : CO_2 = 2 : 1$.[28] Also, acknowledging the numerous factors that may influence the morphology of carbon formed at the catalyst surface, such as the nature of support material, catalyst calcination temperature, reaction temperature, *etc.*,[29–31] the catalysts considered in this study are operated in a regime that leads to the formation of amorphous carbon. Firstly, conventional micro-reactor testing is used to define a suitable set of reaction conditions, which are subsequently used to prepare samples for INS measurements utilising a larger scale reactor.[32] Secondly, temperature-programmed oxidation studies supplemented with Raman scattering, infrared absorption measurements, transmission electron microscopy and X-ray diffraction studies combine to determine the relative partitioning of hydrogen and carbon within the reaction media. This information leads to a qualitative description of the reaction kinetics. The effectiveness of the use of gold as a modifier in the 'dry' reforming reaction is also briefly discussed.

2. Experimental

2.1 Catalyst preparation and reaction testing

A 45 wt% Ni/Al_2O_3 catalyst and a 5 mol% gold-doped 45 wt% Ni/Al_2O_3 catalyst were prepared by wet impregnation of α-alumina (Sumitomo, lot no. YE6 Y01, BET surface area 1.93 $m^2\ g^{-1}$) with nickel nitrate and hydrogen tetrachloroaurate, followed by calcination at 1173 K. For the non-doped material, nickel nitrate hexahydrate was dissolved in a minimal amount of water, to which alumina was added subsequently. Water was driven off the suspension using a hot plate, before drying in an oven at 393 K for 6 days. Finally, the material was calcined in static air by heating to 773 K at 1 K min^{-1}, then to 1173 K at 5 K min^{-1}. The temperature was maintained for one hour before cooling to room temperature. This procedure resulted in a 45.1 wt% Ni/Al_2O_3 catalyst. The doped material followed the same synthesis, but used nickel nitrate hexahydrate with hydrogen tetrachloroaurate(III) trihydrate and alumina to generate a catalyst 43.1% Ni and 4.77% Au by mass. Hydrogen tetrachloroaurate(III) trihydrate (99.9% purity) was supplied by Acros Organics and nickel(II) nitrate hexahydrate (99.8%) by BDH. Samples were stored under ambient conditions in sealed glass containers in between preparation and reaction/analysis.

2.2 Micro-reactor measurements

Reaction testing was performed in a quartz-tube micro-reactor. Reactant and calibration gases were controlled by mass flow controllers (Hastings HFC302 controlled by Teledyne THPS-400)

to meter gas into a flow system constructed of 1/8″ diameter stainless steel tubing. Gas flows were mixed before the reactor in a volume containing glass beads to ensure a turbulent flow, and a reactor bypass permitted the gases to be sampled without catalyst contact. The reactor was a 6 mm outside diameter quartz tube connected to the gas lines using 1/4″ compression fittings (Cajon). The reactor passed through a tube furnace (Carbolite MTF 10/15/30) with integrated PID control. Approximately 5–20 mg of the catalyst was loaded into the reactor between quartz wool plugs. Temperature was measured using a K-type thermocouple located at the catalyst bed and recorded by the mass spectrometer software. Prior to reaction, the catalyst was reduced for 2 h at 1123 K under a flow of 3 sccm H_2 (BOC, 99.999%) in 40 sccm He (BOC, 99.999%). Reactions used 2 sccm CH_4 (CK gas, 99.95%) with 1 sccm CO_2 (CK gas, 99.995%) diluted in 40 sccm He as before. The reaction conditions provide a total gas hourly space velocity (GHSV, defined as the ratio of the total volumetric flow at the inlet and the reactor bed volume) of 1.2×10^4 h^{-1} and a space time (the volume of the catalyst bed divided by the flow) of 0.3 s.[33] All reactions were performed at least twice, so that the results presented here are representative of the trends observed. Temperature-programmed oxidation measurements were performed *in situ* after reaction using 20 sccm of a 5% O_2–He mix (BOC) using a temperature ramp of 10 K min^{-1} to 1223 K. The instrumental response was calibrated by oxidation of known masses of graphite (Sigma-Aldrich, >99.5%), as well as the thermal decomposition of calcium carbonate (BDH, >98%). Reaction monitoring for all of these experiments used a quadrupole mass spectrometer (Hiden HPR 20), which was attached to the reactor exhaust line using a T-fitting. The mass spectrometer data were normalised against the recorded pressure of the He carrier gas to remove any potential effects of pressure variation.

2.3 Inelastic neutron scattering

INS measurements were performed at the ISIS Facility of the STFC Rutherford Appleton Laboratory using the TOSCA[34] and MAPS[27] spectrometers. TOSCA is an indirect geometry time-of-flight spectrometer with a spectral range of 16−4000 cm^{-1} and exhibits a resolution of 1.25% of the energy transfer.[27] MAPS is a direct geometry chopper instrument, which uses a Fermi chopper to monochromate the incident neutron beam to produce incident energies in the range 120–6000 cm^{-1}. The energy resolution is 1.5% of the incident energy at the largest energy transfer and degrades with decreasing energy transfer.[27] In order to achieve reasonable resolution over a wide spectral range (40–4000 cm^{-1}), spectra on the MAPS spectrometer are measured at different incident energies.[27] For this study, the S chopper package[27] was used at the following incident energies: 4840, 2017 and 484 cm^{-1}.

Due to sensitivity constraints, large catalyst masses (*ca.* 10 g) are typically required for INS studies of heterogeneous catalysts,[17] which amounts to *ca.* 200 times more sample than is normally used in conventional micro-reactor measurements (Section 2.2). A recent communication outlines a number of procedures which may be used to ensure integrity of the catalyst samples analysed by INS.[32] A brief description of the sample handling procedures used for this work is described below.

A quartz U-tube reactor was used.[32] Three 0–100 ml_{N2} min^{-1} flowmeters (Platon NGX series) were used to control flows of H_2, CO_2 and CH_4. One 2 l_{N2} min^{-1} flowmeter (Platon) controlled the He diluent. A length of 1″ diameter stainless steel tube fitted in front of the reactor and filled with Ballotini glass spheres ensured a homogeneous gas phase entered the reactor. Research grade CH_4, CO_2 and H_2 were supplied by CK gases, with purities of 99.95%, 99.995%, and 99.999% respectively. The He diluent was UHP grade from Air Products (99.9992%).

Sintered quartz discs are fitted at the base of each arm of the reactor to support Raschig rings on the inlet and the catalyst on the outlet. The inlet arm was designed to pre-heat the gas before encountering the catalyst. The Raschig rings were used to ensure a convoluted flow path in order to achieve efficient heat transfer. Shut-off valves were placed immediately above the reactor allowing the sample to be isolated under helium after reaction. The reactor was held inside an Instron bucket furnace (model no: TF105/3/12/F) attached to a Eurotherm temperature controller (model 3508). A quartz wool plug at the top of the furnace minimised heat loss due to convection. A quadrupole mass spectrometer (Spectra Microvision plus) sampling the effluent gases was used to monitor the progress of the reaction.

A charge of approximately 20 g of catalyst was loaded into the reactor. The samples were reduced by heating to 1023 K at 5 K min^{-1} in flowing hydrogen (140 ml min^{-1} H_2 diluted with 1250 ml min^{-1} He) and held at this temperature until hydrogen consumption ceased. Maintaining the helium flow, the sample temperature was increased to 1073 K and reaction commenced by flowing CH_4, CO_2 and He over the catalyst at respective flow rates of 70, 35 and 1250 sccm. Reaction was maintained (GHSV = 4.9×10^3 h^{-1}, space time 0.72 s) for 6 hours with methane conversions comparable to those observed with the micro-reactor arrangement (Section 2.2). It is the increased mass of catalyst required for the INS experiments[27] that restricts the space velocities/times accessible with the large scale quartz U-tube reactor compared to the micro-reactor measurements.

After six hours on-stream, the heating was stopped and the sample isolated and allowed to cool to ambient temperature. The quartz reactor was transferred to an indium-sealed gas tight aluminium sample cell inside an argon-filled glove box (MBraun UniLab MB-20-G, $[H_2O] < 1$ ppm, $[O_2] < 2$ ppm). The cell was then transferred to the INS spectrometer, for the recording of INS spectra at 20 K. Background measurements were also performed on the alumina used in the catalyst synthesis. A sample of the α-alumina was initially treated in flowing hydrogen at 823 K for 2 h (140 ml min^{-1} H_2 diluted with 1250 ml min^{-1} He); subsequently CH_4, CO_2 and He were passed over the sample at the same temperature (respective flow rates of 70, 35 and 1250 sccm). Methane conversion was not detected to any extent under these conditions.

After these INS measurements, the induced activity from the INS cell was allowed to decay to a safe level before the catalysts were recovered and further analysed using a combination of elemental analysis, TPO measurements, Raman scattering,

infrared absorption, transmission electron microscopy and powder X-ray diffraction.

2.3.1 Post-reaction analysis of INS samples. Elemental analysis was carried out using an Exeter Analytical C440 Elemental Analyser. Measurements for both the reacted Ni/Al_2O_3 and the $Ni–Au/Al_2O_3$ samples yielded 'zero' values for hydrogen content, indicating the retained hydrogen values to be less than the detection limit of the instrument (*ca.* 0.3%). *Ex situ* TPO measurements were performed using the apparatus described in Section 2.2. Post-reaction samples exhibited a strong black colouration. Visual inspection of these samples after a TPO run showed the samples to resemble strongly the green colouration of the original catalyst, indicating that the TPO runs had successfully oxidised all of the residual carbon.

Raman scattering measurements were undertaken using a custom instrument utilising backscattering geometry,[35] 532 nm excitation wavelength, spectral resolution of 6.5 cm^{-1} and laser power at the sample of 20 mW. Higher laser powers were observed to damage the sample. A holographic transmission grating and a back-thinned CCD detector were employed for spectral analysis and data collection. Samples were ground with KBr in an approximately 15 : 1 ratio and pressed in a 13 mm die to provide a robust, self supporting tablet suitable for mounting in the horizontal beam arrangement at the laser focus. Data were collected for approximately two minutes.

Transmission infrared absorption measurements were performed using a Bruker Vertex 70 FTIR spectrometer. Thin discs were pressed without diluent in a 13 mm diameter die under 10 tonnes of applied pressure. The resulting fragile discs required careful handling but provided acceptable levels of transmission. IR spectra recorded from samples pressed with KBr displayed interference patterns caused by reflections at the surfaces of the disc. Spectra were recorded using a high D* MCT detector at 4 cm^{-1} resolution and 512 scans were summed.

The microstructure of the post-reaction catalyst samples was studied by transmission electron microscopy (TEM) using a Technai T20 microscope with an accelerating voltage of 200 keV. Samples were dispersed in methanol before being deposited on holey carbon film (300 μm mesh grid, Agar scientific) prior to inspection. Powder X-ray diffraction measurements were carried out on a Siemens D5000 diffractometer with a Cu_α source and Be detector. Approximately 200 mg of sample were placed in a rotating sample holder. Measurements were taken from 5–85° at 1.3° min^{-1}.

3. Results

3.1 Micro-reactor measurements

The catalysts were tested for reforming performance under both temperature-programmed and isothermal regimes. Fig. 1 shows the temperature-programmed reaction profiles for the Ni/Al_2O_3 and $Ni–Au/Al_2O_3$ catalysts, with the two samples displaying similar trends. The reaction initiates at 708 K and then exhibits three distinct regimes. Hydrogen production increases with temperature until 873 K followed by a slight decrease before hydrogen production increases again. Hydrogen production appears to reach a second maximum at 1183 K before decreasing again. The local maximum in the hydrogen production at 873 K corresponds to increased methane consumption and a maximum in the water production, whilst the CO and CO_2 traces do not show any inflection. This observation suggests that carbon is being retained by the catalyst at this point. Methane decomposition is producing additional H_2, some of which is reacting with CO_2 in the reverse water gas shift reaction, eqn (3). As the temperature rises, this reaction pathway becomes less important, and H_2O production decreases, whilst the desired synthesis gas product begins to dominate. Above 1100 K total conversion of CO_2 is observed, and although the CH_4 concentration increases, the CO signal also continues to climb. Hydrogen production also decreases in this region and appears to be matched to the CH_4 conversion, indicating rapid and efficient release of hydrogen from the catalyst. CO production, however, appears more complicated, possibly illustrating deposition of carbon at low temperature, which is later oxidised upon further heating. At 1073 K there is high conversion, with little contribution from the reverse water gas shift reaction, making it a suitable temperature for isothermal measurements.

The reaction profiles for the catalysts under extended reaction at 1073 K are shown in Fig. 2. With increasing time-on-stream, deactivation of the Ni/Al_2O_3 catalyst produces less hydrogen, and more methane is apparent in the exit gases. Production of

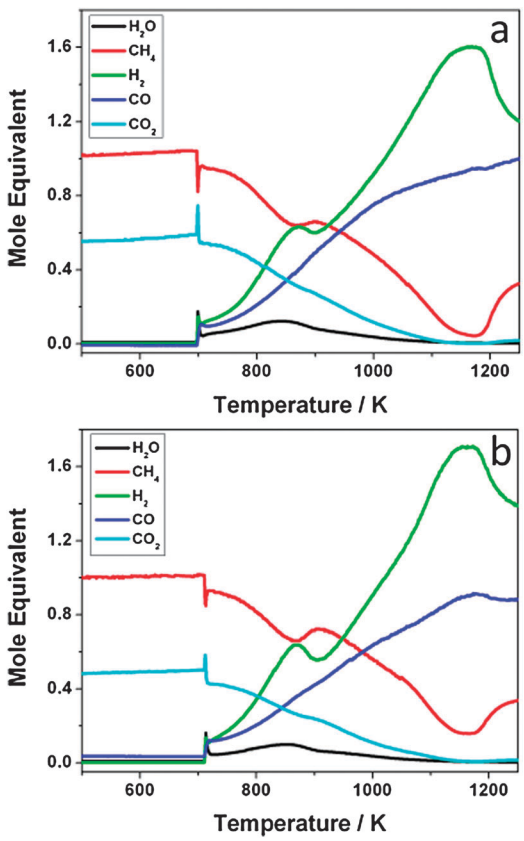

Fig. 1 Temperature-programmed reaction (500–1300 K) within the micro-reactor for a 2 : 1 mixture of CH_4 and CO_2 over (a) the Ni/Al_2O_3 catalyst and (b) $Ni–Au/Al_2O_3$ catalyst. Gas composition = CH_4 4.7%, CO_2 2.3%, He 93%.

CO and CO_2 also increase with time. This process appears to continue, even after 300 min. The Ni–Au/Al_2O_3 profile is very similar but the changes in exit gas composition caused by deactivation occur more quickly, indicating a comparatively more rapid deactivation of this sample. For example, the CO concentration for Ni–Au/Al_2O_3 exceeds H_2 production after 15 minutes, yet for Ni/Al_2O_3 this characteristic production profile begins at 180 minutes. Both catalysts appear to approach steady-state operation after 300 minutes.

Post-reaction (at 1073 K) TPO measurements of the micro-reactor samples are presented in Fig. 3, which are dominated by a single broad and intense feature with a desorption maximum at about 900 K for both the Ni/Al_2O_3 and Ni–Au/Al_2O_3 catalysts. The desorption range of 710–1010 K is indicative of a polymeric amorphous coke, C_β.[36] Peak maxima for the two samples vary between 850 and 918 K, indicating some variation in morphology of the carbonaceous deposits. The oxidation of graphite used for calibration of the system (Section 2.2) yields a sharp peak at 1060 K, suggesting that the detected carbon is not of a graphitic nature. However, it is acknowledged that the metal could catalyse graphitic oxidation, resulting in a reduction in the maximum desorption temperature.[37] Further experimental evidence is consequently required before a classification of the deposited carbonaceous material can be safely attempted.

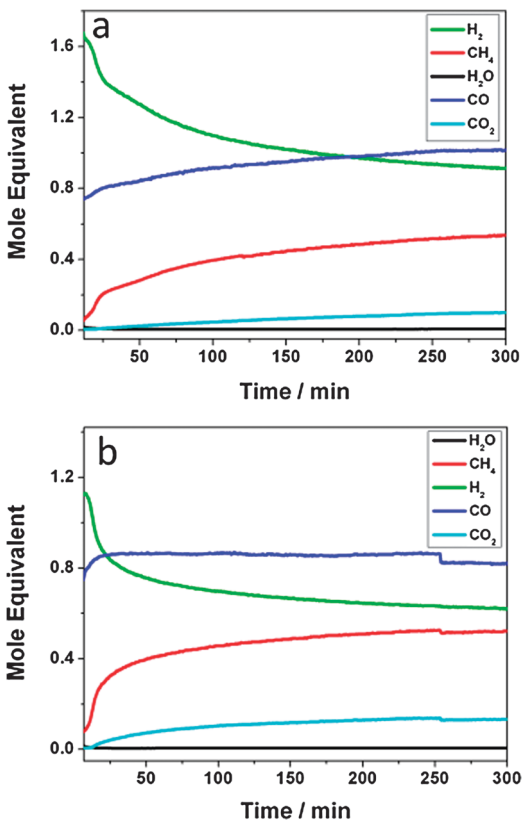

Fig. 2 Extended reaction in micro-reactor at 1073 K of a 2 : 1 mixture of CH_4 and CO_2 over (a) the Ni/Al_2O_3 catalyst and (b) Ni–Au/Al_2O_3 catalyst. Gas composition = CH_4 4.7%, CO_2 2.3%, He 93%.

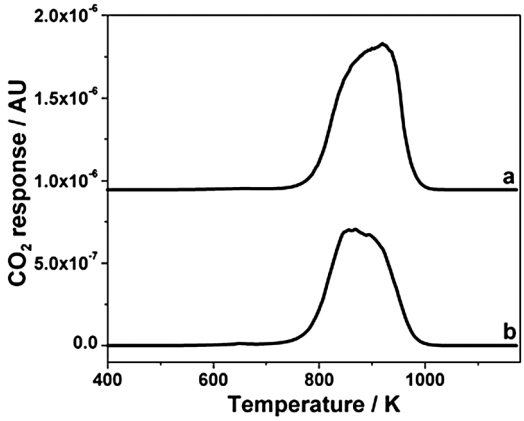

Fig. 3 Temperature-programmed oxidation profile for (a) the Ni/Al_2O_3 and (b) the Ni–Au/Al_2O_3 catalysts after isothermal micro-reactor runs at 1073 K.

3.2 Inelastic neutron scattering

3.2.1 TOSCA spectrometer. The INS spectrum for the reacted Ni/Al_2O_3 sample recorded using the TOSCA spectrometer is presented in Fig. 4. The spectrum has a similar profile to that previously reported for a 26 wt% Ni/Al_2O_3 catalyst that had operated in methane 'dry' reforming conditions at 823 K.[19] The most notable feature of Fig. 4 is the poor signal : noise ratio. This indicates a relatively low quantity of hydrogen to be associated with the sample, which is consistent with the results from elemental analysis (Section 2.3.1). Spectral features are evident at 789, 660, 532, 307 and 222 cm^{-1}. The bands at 789, 660 and 532 cm^{-1} are assigned to in-plane hydroxyl deformation modes of the support material, whilst the bands at 307 and 222 cm^{-1} are attributed to out-of-plane hydroxyl deformation features.[19] The operating principle of the TOSCA spectrometer[27] means that the associated support hydroxyl stretching features are not observed in the spectrum. Whereas background subtraction routines for the 26 wt% Ni/Al_2O_3 TOSCA spectrum revealed a weak spectrum characteristic of an industrial grade carbon black,[19] no new features are observed on background subtraction for the higher loading Ni/Al_2O_3 sample under investigation here. This indicates, in agreement with other studies,[38] that the nature

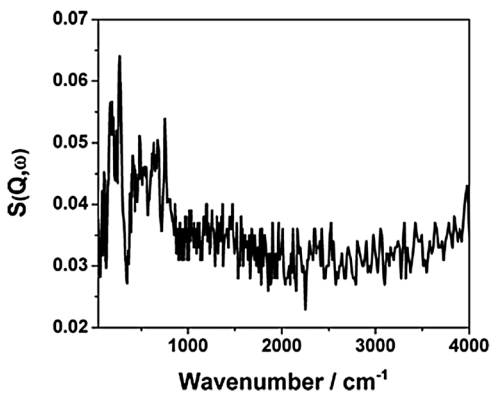

Fig. 4 INS spectrum of the Ni/Al_2O_3 catalyst after 6 hours reaction of a 2 : 1 mixture of CH_4 and CO_2 at 1073 K. The spectrum is recorded using the TOSCA spectrometer.

and extent of the carbon formed is sensitive to the catalyst specification. It is also noted that there is no evidence for graphitic domains, which are discernible with this spectrometer,[17] or for any C–H vibrations.

3.2.1 MAPS spectrometer. Recent studies have established that the MAPS spectrometer is more sensitive than TOSCA,[27] so the reacted samples were also examined using the direct geometry instrument. Fig. 5 presents the spectra in the 2000–4500 cm^{-1} region. The spectrum of the α-alumina support material (no metal) that has experienced a reduction treatment is shown in Fig. 5(e) and is characterised by a flat background with the exception of a very small feature observed at 2900 cm^{-1} which is thought to originate in a C–H stretch of residual aliphatic hydrocarbon. α-Alumina has a low hydroxyl density[40] and no ν(O–H) is evident in the spectrum. Fig. 5(a) shows the spectrum of a reduced Ni/Al_2O_3 catalyst and Fig. 5(b) presents the spectrum the same catalyst post-reaction. The spectrum displayed in Fig. 5(a) is dominated by a relatively intense band measured at 3300 cm^{-1}, that is assigned to ν(O–H) of hydroxyl groups that are thought to be present on the alumina support material. Given the absence of such a feature in Fig. 5(e), it is assumed that the hydroxyl population has been introduced to the catalyst during the preparative stage. This is thought not to be a generic outcome as further studies examining comparable nickel catalysts that have been prepared using a different α-alumina support material exhibit no extra hydroxyl signal in the INS spectrum.[39] Thus, the tendency of α-alumina to retain hydroxyl groups during impregnation of a metal component is thought to be specific to the type and sample history of that particular alumina. Post reaction, the spectrum of Ni/Al_2O_3 exhibits an attenuated ν(O–H) band that is accompanied by a feature centred at 2940 cm^{-1} (Fig. 5(b)), which is attributed to a C–H stretch of aliphatic hydrocarbon species. Consistent with the TOSCA spectrum (Fig. 4), the intensity of this band is low, indicating a relatively low hydrocarbon concentration.

The same sets of spectra are presented in Fig. 6 and 7 for the respective energy ranges of 400–1700 and 60–400 cm^{-1}. For 400–1700 cm^{-1}, the spectrum in Fig. 6 shows the alumina to have a flat background. The reacted Ni/Al_2O_3 and $Ni–Au/Al_2O_3$ catalysts exhibit a small feature observed at 1460 cm^{-1} that is attributed to a C–H deformation mode. Features recorded at 760 and 560 cm^{-1} are assigned to hydroxyl deformation modes.[41] For 60–400 cm^{-1}, Fig. 7 shows the two reacted catalyst samples to exhibit broad features measured at 290 and 170 cm^{-1}. The former is thought to be an out-of-plane deformation of hydroxyl groups,[41] γ(O–H), whereas the latter is ascribed to a nickel phonon mode.[42] The grouping of the spectra recorded at the three primary energies (Fig. 5–7) produces the vibrational spectrum for reduced and activated samples over a wide spectral range (60–4000 cm^{-1}). Few techniques could achieve this outcome. Importantly, the spectra for both catalyst samples are remarkably similar and indicate a low hydrocarbon population that co-exists with a slightly greater hydroxyl population, which is thought to reside on the support material. Unfortunately, there is insufficient spectral information contained within Fig. 5–7 to specify unequivocally the nature of the hydrocarbonaceous deposit.

Utilising procedures described previously,[18] the spectral intensities evident in Fig. 5 can be used to determine the number of hydrogen atoms associated with oxygen and carbon atoms at the surface of the two catalysts. This information is presented in Table 1. Post reaction, the ν(O–H) and ν(C–H)

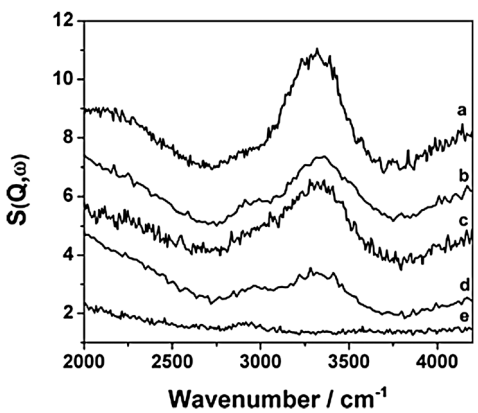

Fig. 5 High energy-transfer INS spectra of (a) reduced Ni/Al_2O_3, (b) reacted Ni/Al_2O_3, (c) reduced $Ni–Au/Al_2O_3$, (d) reacted $Ni–Au/Al_2O_3$ and (e) reduced alumina. Spectra were collected on the MAPS spectrometer operating at an incident energy of 4840 cm^{-1}.

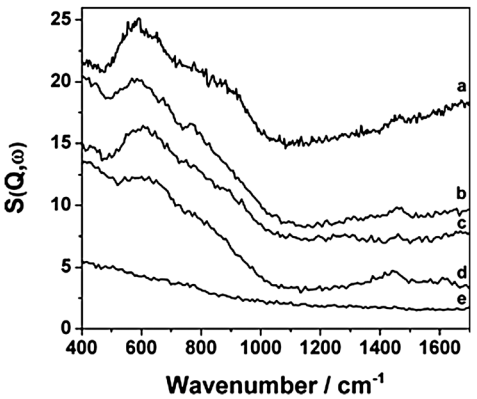

Fig. 6 Medium energy-transfer INS spectra of (a) reduced Ni/Al_2O_3, (b) reacted Ni/Al_2O_3, (c) reduced $Ni–Au/Al_2O_3$, (d) reacted $Ni–Au/Al_2O_3$, and (e) reduced alumina. Spectra were collected on the MAPS spectrometer operating at an incident energy of 2017 cm^{-1}.

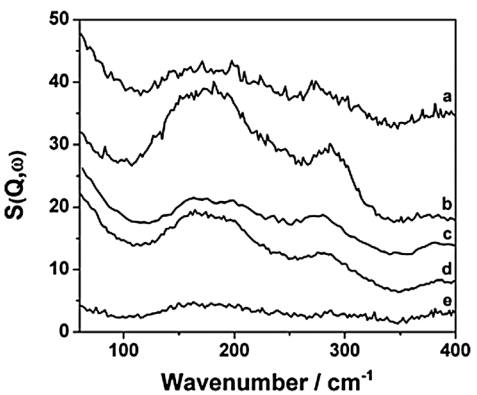

Fig. 7 Low energy-transfer INS spectra of (a) reduced Ni/Al_2O_3, (b) reacted Ni/Al_2O_3, (c) reduced $Ni–Au/Al_2O_3$, (d) reacted $Ni–Au/Al_2O_3$ and (e) reduced alumina. Spectra were collected on the MAPS spectrometer operating at an incident energy of 484 cm^{-1}.

modes for the Ni/Al_2O_3 sample equate to respectively 718 ± 43 and 68 ± 4 μmol H $g^{-1}_{(cat)}$; the equivalent values for the $Ni–Au/Al_2O_3$ sample are 195 ± 12 and 87 ± 5 μmol H $g^{-1}_{(cat)}$.

3.3 Post-reaction analysis of INS samples

3.3.1 Temperature-programmed oxidation. The TPO profiles for the post reaction INS samples are shown in Fig. 8, where both samples exhibit peak maxima at approximately 880 K, closely matching the profiles observed in the micro-reactor experiments (Fig. 3). This coincidence suggests formation of a comparable form of carbon for both catalysts operated in the micro-reactor and the larger volume INS reactor. The quantity of retained carbon for each sample is presented in Table 1, with the Ni and Ni–Au samples equating to 10.9 ± 0.9 and 15.2 ± 1.2 mmol C $g^{-1}_{(cat)}$, respectively. Interestingly, it is the gold modified catalyst that retains the larger proportion of carbon. This fact, combined with the observation that the Ni–Au catalyst does not appear to offer any advantage in terms of sustained syngas yield in the isothermal measurements (Fig. 2) indicates that in contrast to the steam reforming case,[43] the Au additive is providing little beneficial effect for reforming using CO_2.

It is acknowledged that the micro-reactor measurements utilised a higher space velocity (shorter space time) than that achievable with the INS runs, which required a substantially greater quantity of catalyst. Nevertheless, the similarity of the reaction profiles (qualitatively described in Sections 2.2 and 2.3) and the TPO results are an indication that the catalysts are performing in a comparable fashion in the two reactor configurations.

As discussed in the Introduction, the extent of carbon retention in methane reforming catalysts is a well documented phenomenon,[44,45] whereas assessments for hydrogen retention are much less prevalent.[46] It is consequently informative to consider how hydrogen might be incorporated within a carbonaceous matrix, especially since it is not possible to discern the form of a hydrocarbonaceous molecular species from the spectral information contained within Fig. 5–7. The ν(C–H) signal originates in hydrogen associated with carbon and we can use the TPO data to determine the total carbon retention. Thus, this information can be used to provide a C : H ratio, as listed in Table 1.

If hydrogen was associated with a hydrocarbonaceous molecular species the C : H ratio might provide some information on the possible nature of that particular species. However, Table 1 reports C : H values for the reacted Ni/Al_2O_3 and $Ni–Au/Al_2O_3$ samples of 160 ± 13 : 1 and 175 ± 14 : 1 respectively. These values, effectively the same for both catalysts, significantly exceed those of candidate hydrocarbon

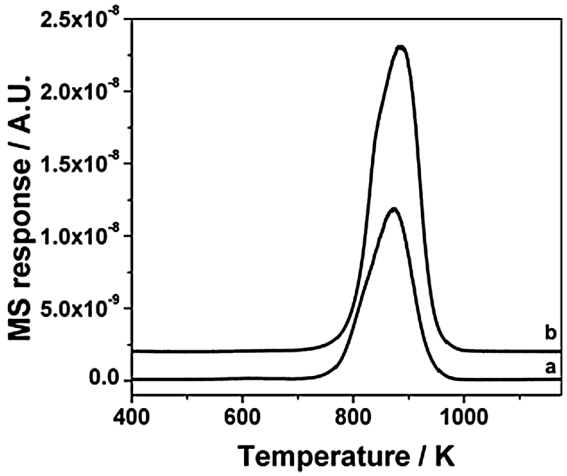

Fig. 8 Temperature-programmed oxidation profile for (a) Ni/Al_2O_3 and (b) the $Ni–Au/Al_2O_3$ catalysts after 6 hours reaction of a 2 : 1 mixture of CH_4 and CO_2 in the quartz U-tube reactor at 1073 K (INS measurements).

moieties such as alkanes or polycyclic aromatic hydrocarbons and consequently indicate that the hydrogenous signal most probably represents hydrogen decorating the edges of a carbonaceous matrix.

We have previously reported the INS spectrum in the range 2500–4000 cm^{-1} for a different batch of the 45% w/w Ni/Al_2O_3 catalyst reacted under comparable conditions that returned a C : H ratio of 171 : 1,[18] which is similar to the 160 : 1 observed in this study. Given that these measurements involved different batches of the Ni/Al_2O_3 catalyst with separate reaction testing and spectroscopic measurements, this outcome shows the methodology adopted in preparing, reacting and handling these sensitive materials to be reproducible within experimental errors.

3.3.2 Raman scattering and infrared spectroscopy. Raman spectra for the reacted Ni/Al_2O_3 and $Ni–Au/Al_2O_3$ samples are shown in Fig. 9. The sharp band observed at 1556 cm^{-1} originates in an atmospheric oxygen plasma and is an artefact of the measurement technique. Two bands consistent with the formation of a carbonaceous overlayer are measured. The G band, which occurs in spectra of all graphitic materials, is recorded at 1582 cm^{-1}.[47] The band detected at 1351 cm^{-1} is the D band, which arises from structural disorder breaking the translation symmetry of the material.[48] Although the ratio of intensities of these two bands is often used as a measure of disorder and may be related to the in-plane crystallite size of existing graphite domains,[49] the laser excitation wavelength should also be taken into account. Cançado *et al.*[50] have

Table 1 Values of carbon and hydrogen moieties in Ni/Al_2O_3 and $Ni–Au/Al_2O_3$ samples after reaction and INS measurement. The errors quoted for the TPO and INS values correspond to 1 standard deviation in the triplicate measurement of reference standards for both techniques

	Ni/Al_2O_3	$Ni–Au/Al_2O_3$
TPO/$carbon_{(ad)}$	10.9 ± 0.9 mmol C $g^{-1}_{(cat)}$	15.2 ± 1.2 mmol C $g^{-1}_{(cat)}$
INS/ν(O–H)	718 ± 43 μmol H $g^{-1}_{(cat)}$	195 ± 12 μmol H $g^{-1}_{(cat)}$
INS/ν(C–H)	68 ± 4 μmol H $g^{-1}_{(cat)}$	87 ± 5 μmol H $g^{-1}_{(cat)}$
C : H	160 ± 13 : 1	175 ± 14 : 1

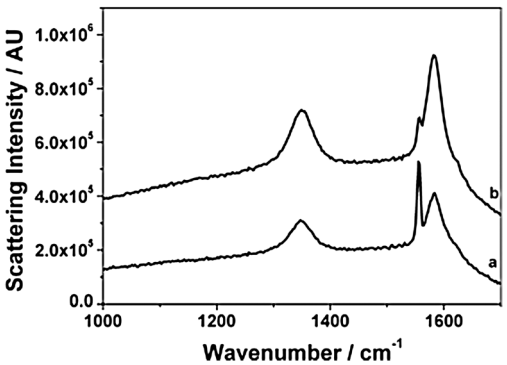

Fig. 9 Raman spectra of (a) Ni/Al_2O_3 and (b) $Ni–Au/Al_2O_3$ catalysts after reaction and INS measurement.

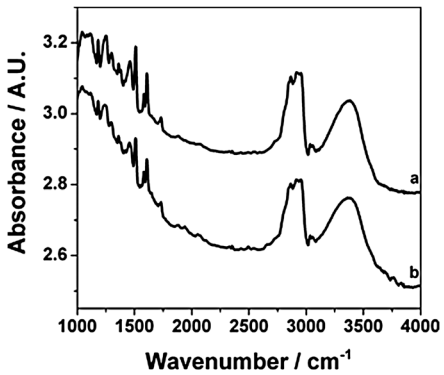

Fig. 10 Transmission infrared absorption spectra of (a) Ni/Al_2O_3 and (b) $Ni–Au/Al_2O_3$ catalysts recorded after reaction and INS measurement.

developed a method for the determination of in-plane crystallite sizes of nano-structured graphites which is based on the following relationship:

$$L_a(\text{nm}) = (2.4 \times 10^{-10})\ \lambda_l{}^4 \left(\frac{I_G}{I_D}\right), \qquad (4)$$

with L_a denoting the in-plane crystallite size, λ_l representing the laser wavelength (measured in nm), and I_D and I_G characterising the integrated peak intensities of the D and G bands, respectively. Calculations using the experimental data presented in Fig. 9 provide crystallite domains of 27 and 39 nm for Ni/Al_2O_3 and $Ni–Au/Al_2O_3$, respectively.

It is acknowledged that these values would lead to a C : H ratio substantially greater than the $\approx$160 : 1 reported in Section 3.3.1. The recorded Raman spectra show contributions from sample fluorescence and were collected close to the limit of the detector, where non-linearity may complicate the instrument response. Further, the existence of the G band does not necessitate the presence of graphite, as merely six conjugated rings are needed to reproduce this spectrum.[51] Also, Raman active vibrations in the region of the G band are observed for benzene.[52,53] Whilst the intensity ratio approach has been shown to work successfully for well-ordered homogeneous materials, justification for its application is weaker with materials of uncertain character.[54] Caution must consequently be exercised for interpretation of the data relating to the calculated graphite crystallite size. Nevertheless, the fact that the two bands in Fig. 9 are separated and well defined suggests that heterogeneity within the coke is relatively low.[55] Signals that may be assigned to hydrogenous species[56] are not observed.

The infrared absorption spectra of the two catalysts post-reaction are displayed in Fig. 10, which shows the two spectra to be very similar. Major peaks and their assignments are shown in Table 2. The broad hydroxyl stretch observed at 3373 cm^{-1} is ascribed to the presence of surface hydroxyls on the alumina support and also some retained water. A small bifurcated C–H stretching peak with maxima measured at 3036 and 3057 cm^{-1} may be attributed to either aromatic or alkene groups. The dominant peak centred at approximately 2900 cm^{-1} is evidence for the presence of saturated hydrocarbons. A weak feature observed at 1732 cm^{-1} is tentatively assigned to a carbonyl stretch, being consistent with the incorporation of oxygen into the deposited material. A low energy shoulder is apparent on this carbonyl band, probably demonstrating that more than one type of carbonyl group is present. A small peak recorded at 1610 cm^{-1} is attributed to the deformation mode of adsorbed water. Peaks below this energy may be due to either hydrocarbon deformations (1457, 1415, 1381, 1361 and 1298 cm^{-1}), skeletal aromatic ring vibrations (1583, 1510 cm^{-1}) or carbonate species, which may be connected with the alumina support or, alternatively, associated with the deposited carbon (1583, 1510, 1457, 1415 cm^{-1}). The peak measured at 1583 cm^{-1} has previously been characterised as a "coke band" and is attributed to the carbon–carbon stretch of microcrystalline graphite.[57] Almost all of the features in the infrared absorption spectrum may be exclusively connected to the persistent carbonaceous deposits formed during reaction, with great similarity apparent between the two catalysts.

Table 2 Infrared assignments for spectra obtained from samples of Ni/Al_2O_3 and $Ni–Au/Al_2O_3$ after reaction and INS measurement

Energy/cm^{-1}	Assignment
3373	ν(OH)
3057	$\nu_{asym}(CH_2)$ alkene; ν(CH) aromatic
3036	ν(CH) alkene; ν(CH) aromatic
2955	$\nu_{asym}(CH_3)$; $\nu_{sym}(CH_2)$ alkene
2917	$\nu_{asym}(CH_2)$ alkane
2866	$\nu_{sym}(CH_3)$
2847	$\nu_{sym}(CH_2)$ alkane
1732	ν(CO)
1609	δ(OH) $water_{ads}$; skeletal aromatic ring mode
1583	$\nu_{sym}(CO_2^-)$ organic; skeletal aromatic ring mode
1510	$\nu(CO_2^-)$; skeletal aromatic ring mode
1457	$\nu(CO_2^-)$; alkane CH_2 scissor; methyl asym deform
1415	$\nu_{sym}(CO_2^-)$ inorganic; alkene CH_2 scissor
1361	Methyl sym bend
1298	Alkene CH rock

Accepting the different emphasis of the IR technique compared to INS,[27] the spectra in Fig. 10 are consistent with the equivalent INS spectra. Namely, the significant aliphatic (C–H) and (O–H) stretches seen in the INS spectra of both catalysts (Fig. 5) are reproduced in the optical spectra. Although the IR spectrum does provide access to non-hydrogeneous modes otherwise inaccessible by INS, it is restricted to a limited spectral range and quantification of the specific modes for these materials is rarely achievable.

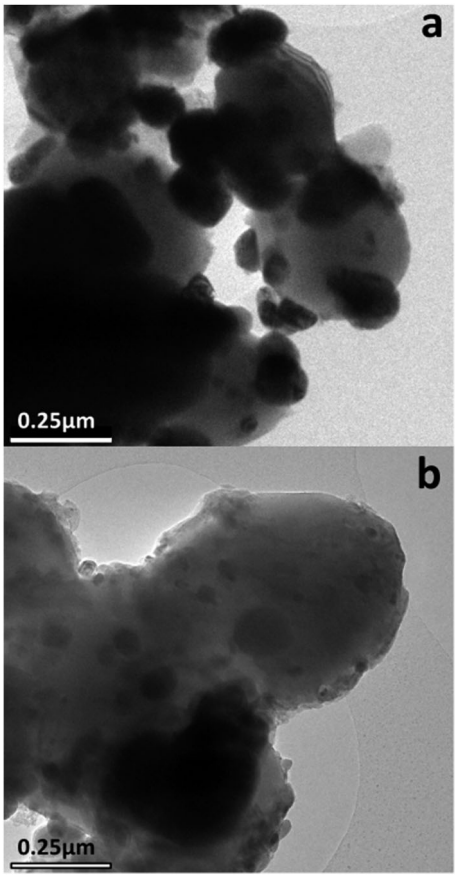

Fig. 11 Transmission electron micrographs of (a) Ni/Al_2O_3 and (b) $Ni–Au/Al_2O_3$ catalysts after reaction and INS measurement.

3.3.3 TEM and XRD. TEM images of Ni/Al_2O_3 and $Ni–Au/Al_2O_3$ recorded after reaction are shown in Fig. 11. The micrographs show large, dispersed, dense structures which represent nickel particles covered by amorphous carbon. The distribution of the particle sizes (20–100 nm) is a reflection of the high calcination, reduction and reaction temperatures used. Evidence for filamentous carbon formation was not detected, neither was it possible to discern graphitic regions.

Diffraction patterns for post-reaction Ni/Al_2O_3 and $Ni–Au/Al_2O_3$ are shown in Fig. 12. The major peaks of all identified phases are labelled; minor peaks are consistent with these assignments, but have not been labelled for clarity. The patterns of both catalysts are dominated by the α-alumina support and nickel. Peaks that are close in position, for example Ni at 51.6 and Al_2O_3 at 52.3°, are resolved, although this may not be apparent from the figure. Small, broad peaks due to crystalline gold are visible in the $Ni–Au/Al_2O_3$ catalyst at 38.2, 64.8 and 77.9°. The peak at 38.2° shows asymmetry that may indicate that the gold is present as anisotropic platelets. The pattern displayed in Fig. 12 shows no evidence for alloy formation. A peak at 26.2° is visible with patterns for both catalysts, which is assigned to graphite, indicating that coking has occurred. Although the graphite peak overlaps another feature and the resolution of the acquired data is limited, the moderately broad nature of this feature indicates limited long range order in the carbon material. *Via* application of the Scherrer equation[58] and accepting the usual

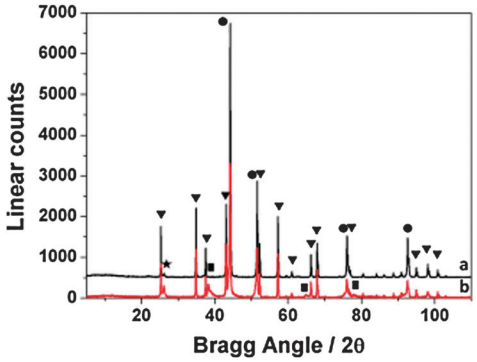

Fig. 12 Powder XRD patterns of spent catalysts (a) Ni/Al_2O_3 and (b) $Ni–Au/Al_2O_3$ showing reflections for α-alumina (triangle), nickel (circle), graphite (star) and gold (square) phases.

caveats,[59] the graphite size domains of the Ni/Al_2O_3 and $Ni–Au/Al_2O_3$ catalysts are determined to be 20 and 16 nm respectively. These dimensions broadly correspond to that determined *via* Raman spectroscopy (Section 3.3.2).

It is apparent that graphite formation has occurred during reaction but that the extent of its formation is low, being insufficient to reveal graphitic structures in the TEM images. This perspective is further endorsed by the absence of graphitic features in the TOSCA INS spectrum (Fig. 4).

4. Discussion

The temperature-programmed reaction measurements (Fig. 1) show that there is no major difference between the catalysts' activity under the reaction conditions studied. Extended isothermal measurements (Fig. 2) however suggest that the addition of gold results in a slightly increased deactivation profile, which contrasts with the deactivation profiles measured for steam reforming conditions.[60] It is possible that the high calcination and reduction temperatures used here to stabilise the nickel particles has resulted in diminishing Au dispersion, thereby reducing the metal's effectiveness to impede deactivation.[10]

In the deactivation process, a quantity of coke is formed, which appears similar in form and quantity regardless of the presence or absence of gold. Although the bulk of the coke is carbon, evidence for hydrogen and oxygen containing functional groups is observed. INS measurements have quantified the amount of hydrogen bound to the catalysts and, importantly, demonstrate that the retained hydrocarbonaceous entities are minority species. *This observation indicates that both catalysts are extremely efficient at cycling hydrogen.* The TEM micrographs indicate the presence of an amorphous carbon overlayer, the edges of which are thought to be terminated with hydrogen, leading to observable INS spectra. The infrared absorption spectra (Fig. 10) provide information on the variety of terminations of the carbonaceous deposits, including functional units such as carbonyl groups, which are not detectable in the INS spectra (Fig. 4–7).

Temperature-programmed oxidation of the coke shows carbon deposits that are oxidised across a wide temperature range (Fig. 3 and 8), which is consistent with the type of the carbon being amorphous and composed of domains varying in size.[39,61] Polycyclic aromatic hydrocarbons (PAHs) show similar

bonding to that found in graphene planes, and have been detailed in highly carbonaceous materials such as carbon blacks and coals.[46,62] A difference between PAHs and small graphene sheets is that the PAH is strictly terminated in hydrogen. Graphene terminations can be left as "dangling bonds" or may be hydrogenated. For bulk crystals, this is not important, but for nanocrystalline graphite, the edge may constitute a significant fraction of the material. It is also likely that some of the graphite nano-crystals will terminate with sp^3 bonded carbon. The location of the carbon on the catalyst is not clear. However, it can not apparently significantly obstruct the active metal, at least under reaction conditions, as only minor deactivation is observed. It may cover the metal, but be sufficiently porous to allow the reactants access and products escape.

The INS and infrared absorption spectra have shown the presence of hydrogen bonded to carbonaceous deposits, with the infrared spectra displaying the C–C ring stretch of the "coke band". Bartholomew describes the mechanisms of coke formation in steam reforming as either reactions between atomic C_α to form pure carbons, or CH_x fragments to generate hydrocarbon cokes, which may be dehydrogenated to form pure carbons.[8] Both of these pathways will probably be present in the 'dry' reforming reaction.

The different techniques applied in this study have all contributed to an understanding of the matrix deposited in the dry reforming reaction. Each technique emphasises a different aspect of the matrix and demonstrates the benefits of a multi-technique approach to describe these materials, which are notoriously difficult to characterise. TPO is thought to sample total retained carbon. The Raman and XRD measurements suggest that the bulk of the overlayer material is a framework of carbon rings, although the oxidation temperature (Fig. 3 and 8) and TOSCA spectrum (Fig. 4) suggest the extent of graphitisation to be relatively low. TEM does not observe the production of filamentous carbon nor graphite, yet X-ray diffraction and Raman spectroscopy are consistent with the presence of graphitic regions exhibiting dimensions of approximately 30 nm. This apparent anomaly is consistent with the bulk of the retained carbon being present as amorphous carbon. There is however a minority concentration of carbon present in a graphitic form but this species is variously distributed throughout the sample matrix, so that it is not readily observable by TEM. Thus, the best descriptor of the retained carbon must therefore be "amorphous". The MAPS spectra have enabled detection, specification and quantification of hydrogen between OH and CH forms, whilst the higher resolution infrared absorption spectra show that the retained hydrogen and oxygen in the coke occurs in a variety of chemical forms.

The MAPS spectra show the presence of hydroxyl groups for both catalysts after reduction (Fig. 5a and c), when the INS spectrum of the alumina itself has a negligible hydroxyl population (Fig. 5e). It is thought unlikely that the reduction process could induce the formation of hydroxyl groups, therefore it is expected that this additional functionality arises during the metal salt impregnation process. However, as noted previously (Section 3.2.1), the generality of this observation is thought to be specific to the nature of the support material used here, as further work on comparable catalysts prepared using a different commercial grade α-alumina exhibited no additional presence of hydroxyls in the INS spectra after comparable treatments.[39] These outcomes imply a degree of variability is possible in the properties of similarly specified commercial grade α-aluminas.

Table 1 shows the residual hydrocarbon population post-reaction for both catalysts to be broadly comparable [ν(C–H) Ni–Au/Al_2O_3 $\approx$ 1.3 $\times$ (ν(C–H) Ni/Al_2O_3], which is in line with comparable reaction profiles (Fig. 2). It is therefore probable that the CH density may correlate with catalytic activity. This situation contrasts with the hydroxyl populations post-reaction, where the Au-modified catalyst exhibits a significantly lower concentration compared to the reference catalyst. [Table 1, [ν(O–H) Ni/Al_2O_3 $\approx$ 3.7 $\times$ (ν(O–H) Ni–Au/Al_2O_3]. The fact that this difference in hydroxyl densities of the two catalysts contrasts with their similar reaction profiles suggests that the hydroxyl groups are not directly involved in the process of catalytic turnover. Moreover, it is possible that the lesser hydroxyl contribution of the Ni–Au/Al_2O_3 catalyst could arise due to the gold impeding the initial hydroxyl formation process.

Rigorous quantification of the hydrogen associated with carbon is difficult, but INS has permitted an unambiguous characterisation that shows very low hydrogen content. This observation leads to kinetic insight into aspects of the reaction under consideration. The following reaction steps are thought to be relevant and are shown below with their associated rate coefficients.

$$\begin{aligned}
CH_{4(g)} &\rightarrow CH_{4(ad)} \quad k_1 \\
CH_{4(ad)} &\rightarrow CH_{3(ad)} + H_{(ad)} \quad k_2 \\
CH_{3(ad)} &\rightarrow CH_{2(ad)} + H_{(ad)} \quad k_3 \\
CH_{2(ad)} &\rightarrow CH_{(ad)} + H_{(ad)} \quad k_4 \\
CH_{(ad)} &\rightarrow C_{(ad)} + H_{(ad)} \quad k_5 \\
2H_{(ad)} &\rightarrow H_{2(ad)} \quad k_6 \\
H_{2(ad)} &\rightarrow H_{2(g)} \quad k_7 \\
CO_{2(g)} + C_{(ad)} &\rightarrow 2CO_{(ad)} \quad k_8 \\
CO_{(ad)} &\rightarrow CO_{(g)} \quad k_9 \\
nC_{(ad)} &\rightarrow C_{n(ad)} \quad k_{10}
\end{aligned} \tag{5}$$

$C_{n(ad)}$ is equivalent to C_β. The rate determining step is the dissociation of methane (k_2), which demands a high temperature (> 700 K, Fig. 1) for the reaction to progress. The almost complete lack of hydrogen retained in the reaction (Fig. 4–7) shows that k_6 and k_7 must be greater than k_8. This leads to a reservoir of adsorbed atomic carbon that polymerises with rate k_{10}, in this case to form amorphous carbon (Fig. 3, 4, 9, and 11). Key to the minimisation of coke is maximising k_8 and k_9 with respect to k_{10} in order to produce gas phase CO.

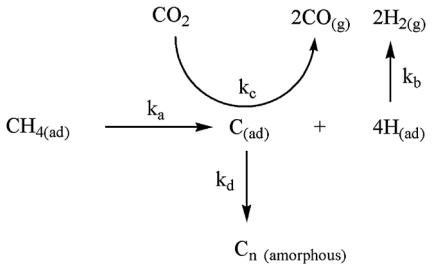

Scheme 1 Schematic representation of principal reactions affecting the partitioning of mass within the reaction system: (a) dissociative adsorption of methane, (b) recombinative desorption of adsorbed hydrogen atoms, (c) oxidation of adsorbed carbon atoms and (d) polymerisation of adsorbed carbon to form amorphous carbon. The rate coefficients for these processes are respectively denoted k_a, k_b, k_c and k_d.

This hypothesis leads to a generalised kinetic scheme that may account for the partitioning of carbon and hydrogen throughout the reaction system. For simplicity, the elementary reactions are approximated to the following four generic processes: (a) dissociative adsorption of methane, (b) re-combinative desorption of adsorbed hydrogen atoms, (c) oxidation of adsorbed carbon atoms and (d) polymerisation of adsorbed carbon to form amorphous carbon. The rate coefficients for these processes are respectively denoted k_a, k_b, k_c and k_d. The connection between these key stages of the reforming process is illustrated in Scheme 1. Accepting that step (a) is rate limiting, the observed trends that correspond to the predominant movement of mass within the chemical system may consequently be described by the magnitudes of the associated rate coefficients exhibiting the following order:

$$k_b \gg k_d > k_c$$

We acknowledge that Scheme 1 is similar to other schemes that have been used to describe this and related chemical systems,[29,63–69] with the proposals of Wei and Iglesia[64] and Xiancai and co-workers[66] in particular describing comparable pathways. However, Scheme 1 is presented here from the perspective of a better quantitative understanding of the partitioning of hydrogen within the reaction system, which additionally endorses some of the concepts explored by the other workers.

The high carbon to hydrogen ratio of the overlayer of the active catalysts (Table 1) indicates that molecular hydrocarbon species are neither formed nor retained in any appreciable quantity. Indeed, the bulk of the carbon is predominantly bonded to other carbon atoms. Terminations of these carbonaceous regions, or possibly surfaces, dominate the infrared absorption spectra and are accessible in the INS spectra. Interestingly, this work also shows that the addition of the gold modifier does not provide any benefit for applications to supported nickel catalysts and the CO_2 reforming of methane at 1073 K. Indeed the extent of deactivation, as evidenced in Fig. 2, was slightly greater for the Au-modified sample than the conventional Ni/Al_2O_3 sample. Additional work is in progress towards a better understanding of the contributors to the carbon deposition process.

Acknowledgements

The authors would like to thank STFC Rutherford Appleton Laboratory for access to the neutron spectrometers and EPSRC for funding (Grant EP/E028861/1). Jim Gallagher and Colin How (University of Glasgow) are thanked for help with the TEM measurements.

References

1 C. Perego, R. Bortolo and R. Zennaro, *Catal. Today*, 2009, **142**, 9.
2 F. Fischer and H. Tropsch, *Brennst.-Chem.*, 1923, **4**, 276.
3 L. Wang, L. Yang, Y. Zhang, W. Ding, S. Chen, W. Fang and Y. Yang, *Fuel Process. Technol.*, 2010, **91**, 723.
4 S. Czernik, R. J. French, K. A. Magrini-Bair and E. Chornet, *Energy Fuels*, 2004, **18**, 1738.
5 A. M. Gadalla and B. Bower, *Chem. Eng. Sci.*, 1988, **43**, 3049.
6 J. Rostrup-Nielsen and L. J. Christiansen, *Concepts in Syngas Manufacture, Catalytic Science Series*, Imperial College Press, 2011, vol. 10.
7 L. Xiancai, L. Shuigen, Y. Yifeng, W. Min and H. Fei, *Catal. Lett.*, 2007, **118**, 59.
8 C. H. Bartholomew, *Catal. Rev. Sci. Eng.*, 1982, **24**, 67.
9 J. R. Rostrup-Nielsen and B. J. H. Hansen, *J. Catal.*, 1993, **144**, 38.
10 J. R. Rostrup-Nielsen, *J. Catal.*, 1984, **85**, 31.
11 A. Nikolla, A. Holewinski, J. Schwank and S. J. Linic, *J. Am. Chem. Soc.*, 2006, **128**, 11354.
12 F. Besenbacher, I. Chorkendorff, B. S. Clausen, B. Hammer, A. M. Molenbroek, J. K. Nørskov and I. Stensgaard, *Science*, 1998, **279**, 1913.
13 N. V. Parizotto, K. O. Rocha, S. Damyanova, F. B. Passos, D. Zanchet, C. M. P. Marques and J. M. C. Bueno, *Appl. Catal., A*, 2007, **330**, 12.
14 D. L. Trimm, *Catal. Today*, 1997, **37**, 233.
15 J. Datka, Z. Sarbak and R. P. Eischens, *J. Catal.*, 1994, **14**, 544.
16 D. G. Blackmond, J. G. Goodwin and J. E. Lister, *J. Catal.*, 1982, **78**, 247.
17 P. C. H. Mitchell, S. F. Parker, A. J. Ramirez-Cuesta and J. Tomkinson, in *Vibrational Spectroscopy With Neutrons*, World Scientific: Singapore, 2005.
18 I. P. Silverwood, N. G. Hamilton, C. J. Laycock, J. Z. Staniforth, R. M. Ormerod, C. D. Frost, S. F. Parker and D. Lennon, *Phys. Chem. Chem. Phys.*, 2010, **12**, 3102.
19 I. P. Silverwood, N. G. Hamilton, J. Z. Staniforth, C. J. Laycock, S. F. Parker, R. M. Ormerod and D. Lennon, *Catal. Today*, 2010, **155**, 319.
20 H. S. Bengaard, J. K. Nørskov, J. Sehested, B. S. Clausen, L. P. Nielsen, A. M. Molenbroek and R. J. R. Nielsen, *J. Catal.*, 2002, **209**, 365.
21 F. Besenbacher, I. Chorkendorff, B. S. Clausen, B. Hammer, A. M. Molenbroek, J. K. Nørskov and I. Stensgaard, *Science*, 1998, **279**, 1913.
22 A. M. Molenbroek, J. K. Nørskov and B. S. Clausen, *J. Phys. Chem. B*, 2001, **105**, 5450.
23 Y.-H. Chin, D. L. King, H.-S. Roh, Y. Wang and S. M. Heald, *J. Catal.*, 2006, **244**, 153.
24 G. Zhu, *Huagong Shikan*, 2009, **23**, 17.
25 N. C. Triantafyllopoulos and S. G. Neophytides, *J. Catal.*, 2006, **239**, 187.
26 L. Guzci, G. Stefler, O. Geszti, I. Sajó, Z. Pászti, A. Tompos and Z. Schay, *Appl. Catal., A*, 2010, **375**, 236.
27 S. F. Parker, D. Lennon and P. W. Albers, *Appl. Spectrosc.*, 2011, **65**, 1325.
28 F. Noronha, A. Shamsi, C. Taylor, E. Fendley, S. Stagg-Williams and D. Resasco, *Catal. Lett.*, 2003, **90**, 13.
29 M. C. J. Bradford and A. M. Vannice, *Appl. Catal., A*, 1996, **142**, 73.
30 P. Chen, Z. Hou, X. Zheng and T. Yashima, *React. Kinet. Catal. Lett*, 2005, **86**, 51.
31 J. Rostrup-Nielsen, *Catalysis Science & Technology*, Springer-Verlag, 1984, vol. 5, p. 1.
32 I. P. Silverwood, N. G. Hamilton, A. R. McFarlane, R. M. Ormerod, T. Guidi, J. Bones, M. P. Dudman, C. M. Goodway, M. Kibble, S. F. Parker and D. Lennon, *Rev. Sci. Instrum.*, 2011, **82**, 034101.

33 R. J. Farrauto and C. H. Bartholomew, in *Fundamentals of Industrial Catalytic Processes*, Blackie, 1997.
34 D. Colognesi, M. Celli, F. Cilloco, R. J. Newport, S. F. Parker, R. V. Albertini, F. Sacchetti, J. Tomkinson and M. Zoppi, *Appl. Phys. A: Mater. Sci. Process.*, 2002, **74**, 64.
35 L. D. Barron, E. W. Blanch, I. H. McColl, C. D. Syme, L. Hecht and K. Nielsen, *Spectroscopy (Amsterdam)*, 2003, **17**, 101.
36 J. R. Anderson and M. Boudart, *Catalysis Science and Technology*, Springer-Verlag, 1984, vol. 5, ch. 1.
37 D. McKee, *Carbon*, 1970, **8**, 623.
38 J. Juan-Juan, M. C. Roman-Martinez and M. J. Illan-Gomez, *Appl. Catal., A*, 2009, **355**, 27.
39 I. P. Silverwood, A. R. McFarlane, E. L. Norris, R. M. Ormerod, C. D. Frost, S. F. Parker and D. Lennon, to be submitted.
40 F. Qi, Z. Chen, B. Xu, J. Shen, J. Ma, C. Joll and A. Heitz, *Appl. Catal., B*, 2008, **84**, 684.
41 A. R. McInroy, D. T. Lundie, J. M. Winfield, C. C. Dudman, P. Jones, S. F. Parker and D. Lennon, *Catal. Today*, 2006, **114**, 403.
42 M. Kresch, O. Delaire, R. Stevens, J. Y. Y. Li and B. Fultz, *Phys. Rev. B: Condens. Matter Mater. Phys.*, 2007, **75**, 104301.
43 Y.-H. Chin, D. L. King, H.-S. Roh, Y. Wang and S. M. Heald, *J. Catal.*, 2006, **244**, 153.
44 M. C. J. Bradford and A. Vannice, *Appl. Catal., A*, 1996, **142**, 73.
45 Z. L. Zhang and X. E. Verykios, *Catal. Today*, 1994, **21**, 589.
46 H. Aso, K. Matsuoka and A. Tomita, *Energy Fuels*, 2003, **17**, 1244.
47 M. A. Pimenta, G. Dresselhaus, M. S. Dresselhaus, L. G. Cançado, A. Jorio and R. Saito, *Phys. Chem. Chem. Phys.*, 2007, **9**, 1276.
48 F. Tuinstra and J. L. Koenig, *J. Chem. Phys.*, 1970, **53**, 1126.
49 L. Nikiel and P. Jagodzinski, *Carbon*, 1993, **31**, 1313.
50 L. G. Cançado, K. Takai, T. Enoki, M. Endo, Y. A. Kim, H. Mizusaki, A. Jorio, L. N. Coelho, R. Magalhães-Paniago and M. A. Pimenta, *Appl. Phys. Lett.*, 2006, **88**, 163106.
51 G. R. Loppnow, L. Shoute, K. J. Schmidt, A. Savage, R. H. Hall and J. T. Bulmer, *Philos. Trans. R. Soc. London, Ser. A*, 2004, **362**, 2461.
52 J. Schwan, S. Ulrich, V. Batori, H. Ehrhardt and S. R. P. Silva, *J. Appl. Phys.*, 1996, **80**, 440.
53 J. McGregor, Z. Huang, E. P. J. Parrott, J. A. Zeitler, K. L. Nguyen, J. M. Rawson, A. Carley, T. W. Hansen, J.-P. Tessonnier, D. S. Su, D. Teschner, E. M. Vass, A. Knop-Gericke, R. Schlögl and L. F. Gladden, *J. Catal.*, 2010, **269**, 329.
54 A. Cuesta, P. Dhamelincourt, J. Laureyns, A. Martínez-Alonso and J. M. D Tascón, *Carbon*, 1994, **32**, 1523.
55 M. Knauer, M. E. Schuster, D. Su, R. Schlögl, R. Niessner and N. P. Ivleva, *J. Phys. Chem. A*, 2009, **113**, 13871.
56 Y. T. Chua and P. C. Stair, *J. Catal.*, 2003, **213**, 39.
57 D. Eisenbach and E. Gallei, *J. Catal.*, 1979, **56**, 377.
58 J. W. Niemantsverdriet, *Spectroscopy in Catalysis*, Wiley-VCH, 2007, ch. 6, p. 151.
59 J. S. J. Hargreaves, *Crystallogr. Rev.*, 2005, **11**, 21.
60 A. M. Molenbroek, J. K. Nørskov and B. S. Clausen, *J. Phys. Chem. B*, 2001, **105**, 5450.
61 P. Wang, E. Tanabe, K. Ito, J. Jiab, H. Morioka, T. Shishido and K. Takehira, *Appl. Catal., A*, 2002, **231**, 35.
62 A. Sadezky, H. Muckenhuber, H. Grothe, R. Niessner and U. Pöschl, *Carbon*, 2005, **43**, 1731.
63 P. Ferreira-Aparicio, I. Rodríguez-Ramos, J. A. Anderson and A. Guerrero-Ruiz, *Appl. Catal., A*, 2000, **202**, 183.
64 J. Wei and E. Iglesia, *J. Catal.*, 2004, **224**, 370.
65 K. Tomishige, O. Yamazaki, Y. Chen, K. Yokoyama, X. Li and K. Fujimoto, *Catal. Today*, 1998, **45**, 35.
66 L. Xiancai, L. Shuigen, Y. Yifeng, W. Min and H. Feib, *Catal. Lett.*, 2007, **118**, 59.
67 L. Basinin and D. Sanfilippo, *J. Catal.*, 1995, **157**, 162.
68 T.-J. Huang, H.-J. Lin and T-C. Yu, *Catal. Lett.*, 2005, **105**, 239.
69 J. Wei and E. Iglesia, *J. Phys. Chem. B*, 2004, **108**, 4094.